

Flow Dynamics and Aeroacoustics of Flow-induced Vibration of Bluff Bodies

by

Zhi Cheng

A thesis
presented to the University of Waterloo
in fulfillment of the
thesis requirement for the degree of
Doctor of Philosophy
in
Mechanical and Mechatronics Engineering

Waterloo, Ontario, Canada, 2023

© Zhi Cheng 2023

Examining Committee Membership

The following served on the Examining Committee for this thesis. The decision of the Examining Committee is by majority vote.

External Examiner: Wei Qiu
Professor, Dept. of Ocean and Naval Architectural Engineering,
Memorial University

Supervisor(s): Fue-Sang Lien
Professor, Dept. of Mechanical and Mechatronics Engineering,
University of Waterloo

Internal Member: William Melek
Professor, Dept. of Mechanical and Mechatronics Engineering,
University of Waterloo

XiaoYu Wu
Professor, Dept. of Mechanical and Mechatronics Engineering,
University of Waterloo

Internal-External Member: Hans De Sterck
Professor, Dept. of Applied Mathematics,
University of Waterloo

Author's Declaration

I hereby declare that I am the sole author of this thesis. This is a true copy of the thesis, including any required final revisions, as accepted by my examiners.

I understand that my thesis may be made electronically available to the public.

Abstract

Flow-induced vibration (FIV), a common phenomenon of fluid-structure interaction (FSI), is found everywhere and at all scales in the applications of marine, civil, aeronautical, and power engineering. The study of FIV phenomenology, ranging from fatigue and concomitant damage of structures to its exploitation for energy extraction, has been an active area of fundamental research. The research on the mechanism supporting the amplifying, stabilizing, and suppressing of FIV has practical implications for the structural design for optimal engineering fatigue control, energy utilization, etc. Moreover, the noise propagation generated from FIV is also accompanying environmental pollution that should not be ignored.

However, past research on the FIV supported by nonlinear spring and the corresponding detailed FSI characteristics are limited. The present study will conduct a numerical FIV study of bluff bodies mounted by linear and nonlinear springs, and analyze the impact of stiffness nonlinearity on the FIV responses, including the amplitude variation, phase change, frequency variation, and wake pattern. The technical method used in this part is direct Computational Fluid Dynamics/Computational Structural Dynamics (CFD/CSD) simulation with the full-order model (FOM), via the coupled Navier-Stokes and body-structure equations.

Additionally, the present study investigates the geometrical influences on FIV response and the mechanism underpinning the transfer from lock-in range to desynchronization or galloping range. Different body shapes, varied Reynolds numbers, and reduced velocity will involve many cases, as a result, expensive time will be consumed if the corresponding grids are generated and FOM calculations are carried out for each case. This part of the research will be mainly based on the data-driven stability analysis using the reduced-order model (ROM), and FOM based on CFD/CSD method will be used as supplementary for comparison. ROM could also provide the modal analysis and physical perspective that are not available for FOM.

Combining ROM and FOM methods, this thesis explores the mode transformation and interaction in the lock-in behavior of laminar flow past a circular cylinder. For the galloping analysis, it is observed very small changes in the windward interior angle of an isosceles-trapezoidal body can provoke or suppress galloping—indeed, a small decrease or increase (low to 1°) of the windward interior angle from a right angle (90°) can result in a significant enhancement and complete suppression, respectively, of the galloping oscillations. This supports our hypothesis that the contraction and/or expansion of the cross-section in the streamline direction is significantly responsible for the galloping response. Furthermore, one novel methodology of data-driven stability analysis via the superposition of 2-D reduced-order modes (SRM) for the purpose of performing modal analysis and stability predictions of 3-D flow-induced vibration with spanwise shear inflow is presented.

Lastly, noise propagation from energy harvesters based on the FIV mechanism also deserves attention. Owing that there is limited past research on noise propagation from oscillating cylinders, an investigation on aeroacoustics study of different oscillation patterns of single cylinder and tandem cylinders is carried out.

Acknowledgements

I would like to owe my first and deepest gratitude to Professor Fue-Sang Lien, my supervisor, for his constant and unconditional support and guidance. He taught me not only how to do research but also what science and engineering are, which reshapes my academic and world-view. It is a good memory of mine to work, study, and research with Professor Fue-Sang Lien and Professor Eugene Yee, which is also the treasurer and a new chapter in my life. I am also deeply grateful to Professor William Melek, Professor XiaoYu Wu, and Professor Hans De Sterck. Their thoughtful suggestions help me improve the research work. I would also like to show my gratitude to Professor Wei Qiu for his detailed review of my thesis and valuable comments. I would like to thank my supervisor during my research visiting time at Duke University, Professor Earl H. Dowell, who provides me with lots of knowledge and support. I am also grateful to my research group members, friends, and visiting scholars in our lab. They are beautiful notes that my life is composed of. It is my pleasure to express my gratitude to my parents, for their financial and spiritual support. This is the most wonderful journey that I have ever experienced. After finishing the thesis, I still realize there is plenty of research work to do in this domain. Knowledge has no limit. But I still wish my thesis could inspire some researchers or engineers in the way that I was inspired. Just as the Chinese modern philosopher JiaYing Chen said, “We have the impulsion to express ourselves and the mission to enlighten others”.

Table of Contents

List of Figures	x
List of Tables	xxvi
List of Symbols	xxvii
List of Abbreviations	xxviii
1 Introduction	1
1.1 Background	1
1.2 Basic principles and preliminary parameters	3
1.2.1 Basic principles	3
1.2.2 Main parameters	7
2 Literature review	10
2.1 Experimental investigations of FIV	10
2.1.1 Response analysis	10
2.1.2 Energy harnessing	13
2.2 Numerical investigations of FIV	14
2.2.1 Computational fluid dynamics	14
2.2.2 Linear stability analysis	17
2.3 Triggering and enhancement of FIV	18
2.3.1 Effect of nonlinear restoring forces on lock-in behavior	18
2.3.2 Modal evolution of lock-in behavior	20
2.3.3 The triggering of galloping behavior	22
2.3.4 FIV with spanwise shear inflow	25
2.4 Aeroacoustics	28
2.4.1 Measurements of flow-induced sound from a stationary body	28

2.4.2	Numerical model	29
2.4.3	Sound generation of the flow past moving bodies	30
2.5	Motivations and novelties	31
2.6	Outline of thesis	33
3	FIV response with nonlinear restoring forces	34
3.1	Methodology	34
3.1.1	Laminar flow model	34
3.1.2	Structure model and fluid-structure interaction with linear or nonlinear restoring forces	35
3.2	Description of the problem	37
3.2.1	Boundary condition and mesh dependency study	37
3.2.2	Validation test of VIV with linear restoring forces	38
3.3	Results and discussion	40
3.3.1	Linear, linear/quadratic and quadratic springs	40
3.3.2	Equivalent natural frequency and identification of branches of the response	48
3.3.3	Wake pattern and DMD analysis	53
3.4	Chapter summary	60
4	2-D linear stability analysis of lock-in behavior with uniform inflow	62
4.1	Methodology of reduced-order model based on eigensystem realization algorithm	62
4.2	Validation of reduced-order model	66
4.2.1	Validation of ROM/ERA fluid model	66
4.2.2	Validation and preliminary analysis of ROM/ERA for VIV system	69
4.3	Summary of key results obtained from the previous LSA on lock-in behavior	73
4.4	New perspectives on the analysis of lock-in range for VIV system based on LSA	75
4.4.1	Uncoupled condition for wake-structure modes	75
4.4.2	Coupled condition for wake-structure modes	78
4.4.3	Interaction between the structural mode and the second wake mode	80
4.4.4	Aerodynamic coefficients and wake patterns	85
4.4.5	Frequency analysis of the modal mechanism	88
4.5	Chapter summary	94

5	2-D linear stability analysis of galloping behavior with uniform inflow	96
5.1	Methodology of Den Hartog stability criterion	97
5.2	Numerical set-up and validation	98
5.2.1	Computational domain and mesh sensitivity	98
5.2.2	Validation of full-order model	100
5.3	Validation of reduced-order model	101
5.4	Effect of windward orientation for various body geometries	103
5.4.1	<i>D</i> -section body (half-cylinder)	103
5.4.2	Isosceles-triangular body	109
5.4.3	Square cylinder	115
5.4.4	Summary	118
5.5	Effect of windward interior angle of trapezoidal body on response	120
5.6	Effect of side ratio of rectangular cylinder on response	124
5.7	Effect of after-body on hard- and soft-galloping	127
5.8	Effect of Reynolds number and mass ratio on galloping	128
5.8.1	Square cylinder	128
5.8.2	Isosceles-triangular body	132
5.9	Chapter summary	134
6	3-D linear stability analysis of FIV system with spanwise shear inflow	138
6.1	Problem definition	139
6.2	Overview of response	141
6.3	Wake pattern	147
6.4	Three-dimensional data-driven stability analysis	149
6.5	Data-driven stability analysis via SROM	150
6.6	Chapter summary	160
7	Aeroacoustics noise propagation	162
7.1	Numerical methods	162
7.1.1	Energy equation	162
7.1.2	Turbulence model	163
7.1.3	Solid body motion	163
7.1.4	Acoustic modelling	164
7.2	Validation of numerical methodology	165
7.2.1	Flow past a stationary cylinder at high Reynolds number	165

7.2.2	Flow past stationary tandem cylinders at high Reynolds number	168
7.2.3	Flow past oscillating tandem cylinders at a Reynolds number of 150	171
7.3	Effect of Reynolds number and number of cylinders on the noise structure	174
7.3.1	Effect of Reynolds number on noise	174
7.3.2	Effect of number of cylinders on noise	177
7.4	Single circular cylinder in forced transverse oscillation at varied frequencies	179
7.5	Single circular cylinder with forced oscillations in the transverse or streamwise directions	183
7.5.1	Analysis of unsteady vortex structures	183
7.5.2	Analysis of the acoustic field	185
7.6	Tandem cylinders with forced oscillations in the transverse or streamwise directions	187
7.6.1	Analysis of average pressure on the cylinder surfaces	187
7.6.2	Analysis of unsteady vortex structures	191
7.6.3	Analysis of acoustic field	191
7.7	Chapter summary	195
8	Conclusions and future work	198
	References	201
A	Appendix: The simplify of one common engineering VIV system mounted by non-linear restoring force	222
B	Appendix: Ffowcs Williams-Hawkings (FW-H) equation with Farassat's formulation 1A	225
C	Appendix: Parameters of turbulence models used in present work	227
D	Appendix: Derivation of equivalent natural frequency	229
E	Published, accepted, and submitted papers	232

List of Figures

1.1	Problems encountered by traditional rotating wind turbines. (a) Birds attacked by blades, and (b) Noise level surrounding rotating wind turbines (source: EWEA, 1991).	2
1.2	Vortices behind the Aleutian Islands [1].	3
1.3	Schematic for boundary-layer separation [2].	4
1.4	Mechanism for the vortex shedding from circular cylinder.	5
1.5	The occurrence of reciprocating motion of a circular cylinder submerged in the uniform incident flow.	6
1.6	Relationship between Reynolds number and Strouhal number [3].	8
2.1	Response of a spring-mounted circular cylinder of self-excited vibration in air [4], V_r , f_{ex} and f_{air} here represents U_r , f_{osc} and f_n in present work.	10
2.2	Amplitude and frequency ratio versus reduced velocity in experiments [5], U^* here is U_r in present work.	11
2.3	Wake modes from vortex-induced vibration summarized by Jauvitis and Williamson [6][7] and Govardhan and Williamson [8][9].	12
2.4	VIVACE energy harnessing units based on VIV [10].	13
2.5	The motivations of this thesis and the corresponding innovations.	32
2.6	Framework of this thesis.	32
3.1	Computational domain and the boundary conditions imposed for simulation of VIV for a cylinder supported by a spring. The subscripts i and j on a vector quantity refer to the component of that quantity in the x (streamwise) and y (transverse) directions, respectively.	37
3.2	The fine mesh (mesh 3) consisting of 45,656 cells used to discretize the computational domain in the present study.	38
3.3	VIV response of a cylinder elastically mounted on a linear spring for $Re = 100$ and $m^* = 10$ compared with those obtained by Singh and Mittal [11] and by Zhang et al. [12].	39

3.4	The response of the (a) maximum amplitude A_{\max} and (b) phase difference Φ between the transverse displacement and the lift force as a function of Re for an elastically-mounted cylinder on a spring subject to linear and/or quadratic restoring forces. It is difficult to identify the lock-in range due to many combinations of (k_1, k_2) here, so the following contents will select a set of (k_1, k_2) with encrypted Re increment and identify the correlated lock-in interval.	40
3.5	Oscillation frequency f_{osc} as a function of Re for a cylinder supported by various types of (non)linear springs characterized by (k_1, k_2)	42
3.6	Time series of the normalized displacement y/D and the lift coefficient C_L for a circular cylinder elastically mounted on (a) a linear spring with $(k_1, k_2, Re) = (0.0063, 0, 100)$ and (b) a linear/quadratic spring with $(k_1, k_2, Re) = (0.003, 0.11, 120)$	44
3.7	The dependence of the maximum amplitude A_{\max} on Re for an elastically-mounted cylinder with various linear/quadratic spring combinations (giving rise to different linear and nonlinear restoring forces) characterized by (k_1, k_2) . It is difficult to identify the lock-in range due to many combinations of (k_1, k_2) here, so the following contents will select a set of (k_1, k_2) with encrypted Re increment and identify the correlated lock-in interval.	44
3.8	Time series of the transverse displacement of an elastically-mounted cylinder on a linear/quadratic spring with $(k_1, k_2) = (0.002, 0.11)$ for various values of Re	45
3.8	Time series of the transverse displacement of an elastically-mounted cylinder on a linear/quadratic spring with $(k_1, k_2) = (0.002, 0.11)$ for various values of Re	46
3.9	(a) The phase difference Φ between the lift force and the transverse displacement and (b) the oscillation frequency f_{osc} of the transverse displacement as a function of Re for an elastically-mounted cylinder on a linear/quadratic spring configuration characterized by (k_1, k_2)	47
3.10	Power spectral density (PSD) of the normalized transverse displacement y/D and the associated phase-plane diagram for an elastically-mounted cylinder on a linear/quadratic spring configuration with (a) $(k_1, k_2) = (0.003, 0.06)$ for $Re = 110, 120$ and 130 and (b) $(k_1, k_2) = (0.003, 0.16)$ for $Re = 120, 130$ and 140	48
3.11	Equivalent natural frequency f_{eq} of the system for a linear and a linear/quadratic spring.	50
3.12	Time series of the (a) instantaneous natural frequency f_n^{ins} and (b) instantaneous stiffness k^{ins} of an elastically-mounted cylinder on a linear/quadratic spring configuration with $(k_1, k_2) = (0.003, 0.11)$ for a flow with $Re = 120$	50
3.13	(a) Normalized structural amplitude A_{\max}/D and phase difference Φ , (b) structural oscillation frequency f_{osc} , original vortex-shedding frequency f_{vs} and equivalent natural frequency f_{eq} , (c) maximum lift coefficient C_L^{max} , and (d) normalized amplitudes of the fluid force (viz., the maximum lift coefficient and the force coefficients associated with the linear (C_{f1}^{max}) and the quadratic (C_{f2}^{max}) contributions of the elastic force as a function of Re for $(k_1, k_2) = (0.002, 0.11)$. The region associated with the start of the initial branch to the beginning of the upper branch is shaded in blue. The upper and lower branches are delineated as the red-shaded region.	51

3.14	Time series of the normalized transverse displacement y/D and the lift coefficient C_L along with the associated power spectral density for these quantities: (a) initial branch with $(k_1, k_2, Re) = (0.002, 0.11, 95)$ and (b) lower branch with $(k_1, k_2, Re) = (0.002, 0.11, 115)$	53
3.15	Isopleths of the vorticity in the wake of an elastically-mounted cylinder on a linear/quadratic spring configuration with (a) $(k_1, k_2) = (0.002, 0.11)$ for seven equally-spaced values of Re from 60 to 120 inclusive and with (b) $(k_1, k_2) = (0.003, 0.11)$ for seven equally-spaced values of Re from 70 to 130 inclusive. Incident flow direction is from left to right in the figure.	54
3.16	The velocity deficit $\delta U \equiv (1 - \ \vec{U}\ /U_0)$ obtained in the wake of an elastically-mounted cylinder on a linear/quadratic spring configuration with $(k_1, k_2) = (0.002, 0.11)$ at (a) $Re = 100$ for seven equally-spaced points in time over one-half cycle of the transverse displacement oscillation (bottom panel) and at (b) $Re = 110$ for five-equally spaced points in time over one-half cycle of the transverse displacement oscillation (bottom panel). Incident flow direction is from left to right in the figure.	55
3.17	Dynamic mode decomposition of velocity time series obtained in the wake of an elastically-mounted cylinder on a linear/quadratic spring configuration with $(k_1, k_2) = (0.002, 0.11)$ at $Re = 60$ summarized in terms of (a) spectrum showing the distribution of the real and imaginary parts of the eigenvalues; (b) amplitudes of the DMD modes normalized by the maximum amplitude and plotted as a function of the frequency; and, (c) real part of the DMD modes depicted using contours of the velocity components and velocity magnitude (white: zero; red: above a given positive threshold; blue: below a given negative threshold).	56
3.18	Dynamic mode decomposition of velocity time series obtained in the wake of an elastically-mounted cylinder on a linear/quadratic spring configuration with $(k_1, k_2) = (0.002, 0.11)$ at $Re = 100$ summarized in terms of (a) spectrum showing the distribution of the real and imaginary parts of the eigenvalues; (b) amplitudes of the DMD modes normalized by the maximum amplitude and plotted as a function of the frequency; and, (c) real part of the DMD modes depicted using contours of the velocity components and velocity magnitude (white: zero; red: above a given positive threshold; blue: below a given negative threshold).	58
3.19	Dynamic mode decomposition of velocity time series obtained in the wake of an elastically-mounted cylinder on a linear/quadratic spring configuration with $(k_1, k_2) = (0.002, 0.11)$ at $Re = 110$ summarized in terms of (a) spectrum showing the distribution of the real and imaginary parts of the eigenvalues; (b) amplitudes of the DMD modes normalized by the maximum amplitude and plotted as a function of the frequency; and, (c) real part of the DMD modes depicted using contours of the velocity components and velocity magnitude (white: zero; red: above a given positive threshold; blue: below a given negative threshold).	59
4.1	Schematic diagram summarizing the procedure used to obtain state-space model for the total system involving the coupling of a fluid dynamics ROM (with input h and output C_L) to a structural dynamics model (with input C_L and output h). The fluid dynamics ROM is constructed using ERA.	63

4.2	The streamwise velocity contours exhibited using the line integral convolution (LIC) visualization methodology for a base flow past a stationary circular cylinder at (a) $Re = 60$ and (b) $Re = 100$. The direction of the flow is from left to right.	67
4.3	Distribution of the first 30 singular values (HSV) of the Hankel matrix $H(1 : r, 1 : s)$ with $(r, s) = (500, 200)$ for $Re = 60$	68
4.4	(a) The growth rate as characterized by $\text{Re}(\lambda)$ of the first wake mode as a function of Reynolds number Re , and (b) the predictions of the C_L impulse response obtained using FOM/CFD and the corresponding ROM/ERA at $Re = 20, 40$, and 60 . The cases at $Re = 20$ and 40 correspond to stable wake flows, whereas that at $Re = 60$ corresponds to an unstable wake flow.	69
4.5	The root loci for a FSI system consisting of the flow past a circular cylinder elastically mounted on a linear spring for $(Re, m^*) = (60, 50)$. The present results are compared with those of Zhang et al. [12] and with the case of a stationary circular cylinder. The eigenvalue corresponding to the wake mode for this case is strictly positive.	70
4.6	Delineation of the lower and upper boundaries of the unstable region for flow past a circular cylinder mounted on a linear spring for $Re = 33$. The results obtained using the present ROM/ERA are compared with those obtained by Zhang et al. [12] using ROM/ARX and by Mittal and Singh [13].	71
4.7	(a) The real and imaginary parts of the two leading eigenvalues obtained from ROM/ERA and (b) the oscillation frequency F as a function of the reduced natural frequency F_s for FOM/CFD conducted by Zhang et al. [12] for the case of flow past a circular cylinder mounted on a linear spring with $(Re, m^*) = (60, 50)$	72
4.8	The real and imaginary parts of eigenvalues corresponding to the two leading eigenmodes plotted as a function of the reduced natural frequency F_s for flow past a circular cylinder mounted on a linear spring with $(Re, m^*) = (60, 20)$. The analysis is conducted using ROM/ERA and compared with the global LSA of Navrose and Mittal [14].	73
4.9	Root loci obtained from ROM/ERA for a flow past a circular cylinder mounted on a linear spring for (a) $(Re, m^*) = (60, 20)$ and (b) $(Re, m^*) = (60, 5)$. The solid red square corresponds to the case of a stationary circular cylinder.	74
4.10	Real and imaginary parts of the two leading eigenvalues obtained from ROM/ERA for a flow past a circular cylinder mounted on a linear spring for (a) $(Re, m^*) = (60, 20)$ and (b) $(Re, m^*) = (60, 5)$	75
4.11	The VIV response as a function of F_s for a flow past a circular cylinder mounted on a linear spring at $(Re, m^*) = (40, 10)$ obtained using (a) ROM/ERA and (b) FOM/CFD [14]. The lock-in range is delineated as the region shaded in red.	76
4.12	The VIV response as a function of F_s for a flow past a circular cylinder mounted on a linear spring at (a) $(Re, m^*) = (60, 50)$ for ROM/ERA; (b) $(Re, m^*) = (100, 10)$ for ROM/ERA; (c) $(Re, m^*) = (60, 50)$ for FOM/CFD conducted by Zhang et al. [12]; and, (d) $(Re, m^*) = (100, 10)$ for FOM/CFD. The lock-in range is delineated as the region shaded in red.	77

4.13	The VIV response as a function of F_s for a flow past a circular cylinder mounted on a linear spring at $(Re, m^*) = (60, 5)$ obtained using (a) ROM/ERA; and, (b) FOM/CFD conducted by Navrose and Mittal [14]. The lock-in range is delineated as the region shaded in red.	79
4.14	Root loci parameterized by the reduced natural frequency F_s for different mass ratios m^* obtained from ROM/ERA for a flow past a circular cylinder mounted on a linear spring. The structural mode interacts primarily with the first wake mode for the cases (a)-(c), whereas for cases (d)-(f), with the second wake mode.	80
4.15	The VIV response as a function of F_s for flows past a circular cylinder mounted on a linear spring for (a) $(Re, m^*) = (120, 10)$ obtained using ROM/ERA; (b) $(Re, m^*) = (140, 10)$ obtained using ROM/ERA; (c) $(Re, m^*) = (120, 10)$ obtained using FOM/CFD; and, (d) $(Re, m^*) = (140, 10)$ obtained using FOM/CFD. These two cases correspond to a coupled condition in which the structural mode is coupled to the second wake mode. The lock-in range is delineated as the region shaded in red. The points marked with ‘o’ are data obtained using FOM/CFD and these points are connected with solid lines for visualization purposes only.	81
4.16	Time series of the displacement in the transverse direction for a VIV system consisting of a flow past a circular cylinder mounted on a linear spring for (a) $(Re, m^*, F_s) = (120, 10, 0.1163)$; (b) $(Re, m^*, F_s) = (120, 10, 0.05)$; and, (c) $(Re, m^*, F_s) = (120, 10, 0.0125)$ obtained using FOM/CFD.	83
4.17	The VIV response as a function of F_s for a flow past a circular cylinder mounted on a linear spring at $(Re, m^*) = (180, 10)$ obtained from (a) ROM/ERA and (b) FOM/CFD. This case corresponds to the structural mode coupling with the second wake mode. The lock-in range is delineated as the region shaded in red. The points marked by ‘o’ are data obtained using FOM/CFD and these points are connected with solid lines for visualization purposes only.	84
4.18	Root-mean-square value of the lift coefficient (C_L) as a function of F_s for (a) $Re = 60$ [15]; (b) 70 [15]; (c) 100; (d) 120; (e) 140; and, (f) 180 obtained using FOM/CFD with $m^* = 10$. The lock-in range is delineated as the region shaded in red. The red dotted vertical line, marking the location of the maximum value of $rms(C_L)$, corresponds to the initial branch.	86
4.19	Time series of the lift coefficients for flow past a circular cylinder mounted on a linear spring for $(Re, U_r, F_s) = (100, 4.6, 0.217)$ (top left panel, initial branch), $(Re, U_r, F_s) = (100, 4.8, 0.208)$ (top right panel, upper branch), $(Re, U_r, F_s) = (120, 4.4, 0.227)$ (bottom left panel, initial branch) and $(Re, U_r, F_s) = (120, 4.6, 0.217)$ (bottom right panel, upper branch). The time series were obtained using FOM/CFD. The location in the envelope of the amplitude response for two of the cases of U_r at $Re = 100$ and 120 can be obtained from Figs 4.12d and 4.15c, respectively.	87
4.20	Isopleths of the instantaneous vorticity for flow past a circular cylinder mounted on a linear spring at $(Re, m^*) = (120, 10)$ obtained using FOM/CFD for (a) $F_s (U_r) = 0.238 (4.2)$; (b) 0.227 (4.4); (c) 0.217 (4.6); (d) 0.143 (7.0); (e) 0.125 (8.0); and, (f) 0.122 (8.2). The flow is from left to right.	88

4.21	Time series of the transverse displacement and the corresponding power spectrum of this displacement for a VIV system consisting of flows past a circular cylinder mounted on a linear spring at $(Re, m^*) = (120, 10)$ obtained using FOM/CFD for values of (a) $F_s = 0.227$; (b) 0.217; (c) 0.125; and, (d) 0.122 which span the entire lock-in range.	89
4.22	Time-frequency spectrum of the time series of the transverse displacement for $(Re, m^*, U_r) = (120, 10, 8)$	90
4.23	Time series of C_L and the associated power spectrum for a flow past a circular cylinder mounted on a linear spring with $(Re, m^*, U_r) = (180, 10, 4.2)$ obtained using FOM/CFD.	92
4.24	DMD of VIV system consisting of a flow past a circular cylinder mounted on a linear spring with $(Re, m^*, U_r) = (180, 10, 4.2)$. (a) Distribution of eigenvalues in the complex plane. (b) Mode amplitudes $ \alpha $ (normalized by the maximum amplitude) and their associated frequencies. (c) The real parts of two DMD modes of the streamwise velocity (white: zero; red: above a positive threshold; blue: below a negative threshold).	92
4.25	Time series of C_L and the corresponding power spectrum for a flow past a circular cylinder mounted on a linear spring with $(Re, m^*, U_r) = (180, 10, 6.2)$ obtained using FOM/CFD.	93
4.26	DMD of VIV system consisting of a flow past a circular cylinder mounted on a linear spring with $(Re, m^*, U_r) = (180, 10, 6.2)$. (a) Distribution of eigenvalues in the complex plane. (b) Mode amplitudes $ \alpha $ (normalized by the maximum amplitude) and their associated frequencies. (c) The real part of the dominant DMD mode of the streamwise velocity (white: zero; red: above a positive threshold; blue: below a negative threshold).	93
4.27	Characteristics of the vortex-induced vibration (VIV) and the relationship of these characteristics with the modal distribution of root loci obtained from ROM/ERA.	94
5.1	The total fluid force acting on a downward-moving body can be resolved into two components: a lift force F_L and a drag force F_D	97
5.2	The computational domain used for the simulations of the flow past a bluff body elastically-mounted on a linear spring. The prescribed boundary conditions on the flow velocity used in the simulations are shown.	99
5.3	The fine mesh (mesh 3) used for the simulation of the flow past a square cylinder: (a) tessellation of the computational domain showing the overset and a partial background mesh surrounding the square cylinder; (b) close-up view of the overset mesh around the square cylinder; and, (c) expanded view of mesh in the immediate vicinity of the walls of the square cylinder.	100
5.4	The normalized maximum transverse displacement y_{\max}/D as a function of the reduced velocity U_r of a FIV system consisting of the flow past an elastically-mounted square cylinder at $(Re, m^*) = (150, 10)$. The results were obtained using FOM/CFD and compared with results obtained by Li et al. [16].	101

5.5	Contours of the vorticity field obtained for an equilibrium base flow past a stationary square cylinder at $Re = 150$. The direction of the flow is from left to right.	102
5.6	The root loci (parameterized by the reduced natural frequency $F_s = U_r^{-1}$) for the flow past a forward equilateral triangular cylinder elastically-mounted on a linear spring at $(Re, m^*) = (60, 10)$. This result is compared with that obtained by Yao and Jaiman [15]. The red solid square corresponds to the stationary body.	103
5.7	Elastically-mounted D -section body (half-cylinder) in the (a) forward and (b) backward orientations with respect to the incident flow.	104
5.8	(a) Normalized maximum amplitude y_{\max}/D and (b) normalized oscillation frequency $f_{\text{osc}}D/U_0$ in the transverse direction as a function of U_r for a flow past an elastically-mounted D -section body with forward and backward orientations at $(Re, m^*) = (60, 10)$. The inset plot in (a) shows an expanded view of the variation of y_{\max}/D around $U_r \approx 6$ for the backward D -section body.	104
5.9	Root loci obtained from a ROM/ERA model of the FIV system (parameterized by the reduced natural frequency $F_s = U_r^{-1}$) for the flow past an elastically-mounted forward and backward D -section body at $(Re, m^*) = (60, 10)$. The red solid squares correspond to the case of the flow past a stationary half-cylinder in the forward and backward orientations.	105
5.10	Growth/decay rate $\text{Re}(\lambda)$ and eigenfrequency $\text{Im}(\lambda)/2\pi$ as a function of $F_s = U_r^{-1}$ for the FIV system consisting of the flow past an elastically-mounted D -section body (half-cylinder) in the (a) backward and (b) forward orientations at $(Re, m^*) = (60, 10)$. The structure mode SM_c , which is hidden in the coupled WSMI and WSMII modes, is marked with open red circles. The dashed line corresponds to the function $f = F_s$	106
5.11	Contours of the vorticity field for a flow past a D -section body in the forward orientation at $(Re, m^*) = (60, 10)$ for 12 different values of the reduced velocity U_r	108
5.12	The lift coefficient C_L and drag coefficient C_D for the base flow of a forward and backward D -section body (half-cylinder) at $Re = 60$ with rotation angle α of -1° , 0° and 1° . The value of Den Hartog function $H(\alpha)$ is given for a rotation angle $\alpha = 0^\circ$	109
5.13	Elastically-mounted isosceles-triangular body in the forward and backward orientations relative to the incident flow. The triangular body has $SL/TL = 1/2$	110
5.14	Root loci (obtained from ROM/ERA) for a FIV system consisting of the flow past an elastically-mounted isosceles-triangular body at $(Re, m^*) = (120, 10)$ in the forward and backward orientations. The inset plot displays the part of the root loci for the backward isosceles-triangular body corresponding to the wake mode 1 (WM1) loop (which collapses to a near-point structure) in the right half of the complex frequency plane. The red solid squares show the results for the flow past the stationary isosceles-triangular body in the forward and backward orientations.	111

5.15	Growth/decay rate $\text{Re}(\lambda)$ and eigenfrequency $\text{Im}(\lambda)/2\pi$ as a function of F_s of the modes associated with the flow past an elastically-mounted isosceles-triangular body at $(Re, m^*) = (120, 10)$ in the (a) backward and (b) forward orientations. The single uncoupled wake mode is identified using black open circle markers and the structure mode hidden in the coupled WSMI/WSMII modes is identified using red open circle markers.	112
5.16	Time series of the normalized transverse amplitude y/D and lift coefficient C_L obtained from FOM/CFD simulation for the flow past a backward elastically-mounted isosceles-triangular body at $(Re, m^*) = (120, 10)$ with U_r changing (abruptly) in time from 19 to 6 to 10 and, finally, to 14.	113
5.17	Time series of the normalized transverse amplitude y/D and lift coefficient C_L obtained from FOM/CFD simulation for the flow past a forward elastically-mounted isosceles-triangular body at $(Re, m^*) = (120, 10)$ with U_r changing (abruptly) in time from 25 to 7 to 14 to 25 and, finally, to 62.	114
5.18	Power spectral density (PSD) of the normalized transverse amplitude y/D and the lift coefficient C_L for the flow past a forward elastically-mounted isosceles-triangular body at $(Re, m^*) = (120, 10)$ (cf. figure 5.17) for (a) $100 < tU_0/D < 250$ (early stage of regime 1), (b) $600 < tU_0/D < 800$ (late stage of regime 1), and (c) $1250 < tU_0/D < 1350$ (regime 2). The power spectra were obtained at $U_r = 25$	115
5.19	The lift C_L and drag C_D coefficients for the base flow past a forward and backward elastically-mounted isosceles-triangular body at $Re = 120$. The body is oriented relative to the incident wind direction with a rotation angle $\alpha = -1^\circ, 0^\circ$ and 1° . The Den Hartog function $H(\alpha)$ is provided for a rotation angle of $\alpha = 0^\circ$	116
5.20	(a) Time series of the normalized transverse displacement y/D and (b) 2S vortex shedding mode arising from the response (desynchronization branch) of a FIV system consisting of the flow past a square cylinder with $(\theta, Re, m^*, U_r) = (45^\circ, 150, 10, 20)$	117
5.21	Root loci for a FIV system consisting of the flow past an elastically-mounted square cylinder oriented at $\theta = 0^\circ$ (blue open square markers) and 45° (black open circle markers) at $(Re, m^*) = (140, 10)$. The arrows point in the direction of increasing U_r along the root loci. The solid red squares correspond to the root loci for the stationary square cylinder oriented at $\theta = 0^\circ$ and 45° . The root loci were obtained using a ROM/ERA of the FIV system.	118
5.22	The lift C_L and drag C_D coefficients for the base flow past an elastically-mounted square cylinder at $Re = 120$ for two angles of attack $\theta = 0^\circ$ and 45° . At each value of θ , the square cylinder is oriented relative to the incident wind direction with a rotation angle $\alpha = -1^\circ, 0^\circ$ and 1° . The Den Hartog function $H(\alpha)$ is provided for a rotation angle of $\alpha = 0^\circ$	119

5.23	Summary of the response characteristics of a FIV system consisting of the flow past an elastically-mounted body with three different geometries at two different orientations: namely, a D -section body (or, half-cylinder) in the forward and backward orientations, an isosceles-triangular body in the forward and backward orientations, and a square cylinder at two angles of attack $\theta = 0^\circ$ and 45° . The symbols \times and \blacksquare are used to indicate the absence or presence, respectively, of the response mode (resonance or flutter-induced lock-in, pre-galloping, soft-galloping, hard-galloping).	119
5.24	Isosceles-trapezoidal bodies with windward interior angles of 85° , 90° (square cylinder), 91° and 95° . All the isosceles-trapezoidal bodies have the same values of TL and SL	120
5.25	Time series of the normalized transverse displacement y/D obtained for a FIV system consisting of the flow past an elastically-mounted isosceles-trapezoidal body at $(Re, m^*) = (160, 10)$ with a windward interior angle of (a) 85° , (b) 90° , (c) 91° , and (d) 95° . For each configuration, the reduced velocity U_r is changed (abruptly) in time in accordance to the sequence of values shown along the top each panel.	121
5.26	(a) The root loci and (b) the variation of the growth/decay rate $\text{Re}(\lambda)$ and eigenfrequency $\text{Im}(\lambda)/2\pi$ as a function of F_s for a FIV system consisting of the flow past an elastically-mounted isosceles-trapezoidal body at $(Re, m^*) = (160, 10)$ with windward interior angles of 85° , 90° , 91° , and 95° . The structure mode SM_c that is hidden in the coupled WSMI/WSMII modes is demarcated with crossed open symbols. The dotted line corresponds to the relationship $f = F_s$	122
5.27	The lift C_L and drag C_D coefficients for the base flow past an elastically-mounted isosceles-trapezoidal body at $Re = 160$ for various values of the windward interior angle. The body is oriented relative to the incident wind direction with a rotation angle $\alpha = -1^\circ$, 0° and 1° . The Den Hartog function $H(\alpha)$ is provided for a rotation angle of $\alpha = 0^\circ$	124
5.28	The root loci for the flow past an elastically-mounted rectangular cylinder for various values of the side ratio SR at $(Re, m^*) = (150, 10)$. Regimes 1 and 2 represent the range of values of U_r where galloping and flutter lock-in occur, respectively. The direction of the black arrow points towards increasing values of U_r	125
5.29	The lift C_L and drag C_D coefficients for the base flow past an elastically-mounted rectangular cylinder at $Re = 150$. The cylinder is oriented relative to the incident wind direction with a rotation angle $\alpha = -1^\circ$, 0° and 1° . The Den Hartog function $H(\alpha)$ is provided for a rotation angle of $\alpha = 0^\circ$	126
5.30	Time series of the normalized transverse displacement y/D and the lift coefficient C_L obtained for a FIV system consisting of the flow past a (a) backward and (b) forward elastically-mounted D -section body at $(Re, m^*) = (120, 10)$. For each of these two orientations of the body, the reduced velocity U_r is changed (abruptly) in time in accordance to the sequence of values shown along the top of each panel.	127
5.31	Power spectrum of the transverse displacements y and lift coefficients C_L at different values of the reduced velocity U_r for a flow past a (a) backward and (b) forward elastically-mounted D -section body at $(Re, m^*) = (120, 10)$	129

5.32	Root loci for a FIV system consisting of the flow past an elastically-mounted square cylinder for (a) $20 \leq Re \leq 120$ and (b) $140 \leq Re \leq 180$ with $m^* = 10$. The arrows point in the direction of increasing U_r along the root loci. The root loci were obtained using a ROM/ERA of the FIV system.	130
5.33	A summary of the the modal characteristics of a FIV system (obtained using ROM/ERA) consisting of the flow past an elastically-mounted square cylinder at various values of the Reynolds number Re ranging from 20 to 180, inclusive, with $m^* = 10$	130
5.34	(a) The root loci and (b) the variation of the growth/decay rate $\text{Re}(\lambda)$ and eigenfrequency $\text{Im}(\lambda)$ as a function of F_s for a FIV system consisting of the flow past an elastically-mounted square cylinder for $m^* = 5, 10$ and 50 at $Re = 140$. The root loci were obtained using a ROM/ERA of the FIV system. Only the structure mode is shown in (b).	131
5.35	Root loci for a FIV system consisting of the flow past an elastically-mounted isosceles-triangular body in the forward orientation for $m^* = 10$ and 60 at $Re = 60$. The root loci were obtained using a ROM/ERA of the FIV system.	132
5.36	The variation of the growth/decay rate $\text{Re}(\lambda)$ and the eigenfrequency $\text{Im}(\lambda)/2\pi$ as a function of the reduced natural frequency F_s for a FIV system consisting of the flow past an elastically-mounted isosceles-triangular body in the forward orientation for (a) $m^* = 10$ and (b) $m^* = 60$ at $Re = 60$. The corresponding root loci for this case are displayed in figure 5.35.	132
5.37	Time series of the normalized transverse displacement y/D obtained for a FIV system consisting of the flow past an elastically-mounted isosceles-triangular body in the forward orientation at (a) $(Re, m^*) = (60, 10)$ and (b) $(Re, m^*) = (60, 60)$. For each case, the reduced velocity U_r is changed (abruptly) in time in accordance to the sequence of values shown along the top of each panel: namely, U_r varies from 7 to 14 to 25 and, finally, to 50.	133
5.38	Time series of the normalized transverse displacement y/D obtained for a FIV system consisting of the flow past an elastically-mounted isosceles-trapezoidal body in the forward orientation at (a) $(Re, m^*, U_r) = (60, 10, 4)$ and (b) $(Re, m^*, U_r) = (60, 60, 4)$	134
6.1	Diagram of the physical configuration for the flow-induced vibration of a circular cylinder with inflow sheared in spanwise (z) direction. Reynolds number Re increases linearly in positive z (spanwise) direction. $Re_{-5D} = U(-5D)D/\nu = 25$, $Re_0 = U(0)D/\nu = 35$, and $Re_{5D} = U(5D)D/\nu = 45$	139
6.2	Size and boundary conditions of the 3-D computational domain for the configuration of a circular cylinder elastically mounted by linear spring in a spanwise shear flow.	140
6.3	The fine mesh (mesh 3) used for the 3-D simulation of a flow past a circular cylinder: (a) the translucent view showing the background and an overset mesh surrounding the circular cylinder; (b) the background mesh; and, (c) overset mesh and expanded view of the mesh in the immediate vicinity of the walls of the circular cylinder.	142

6.4	(a) Normalized maximum structural amplitude y_{\max}/D , (b) root mean square (rms) value of lift coefficient C_L^{rms} , (c) normalized structural oscillation frequency $f_{\text{osc}}D/U_0$, and (d) phase difference θ as a function of U_r . The lock-in region with amplified structural amplitude (or, with $y_{\max}/D > 0.1$) are delineated with red shading.	143
6.5	Time series of the instantaneous normalized structural amplitudes y_{\max}/D and instantaneous lift coefficients C_L of FIV systems that have achieved the equilibrium state at $U_r =$ (a) 5.6, (b) 6.0, (c) 7.0, (d) 8.0, (e) 9.0, (f) 9.5, (g) 10.0, and (h) 10.5.	144
6.6	Time series of instantaneous normalized structural amplitudes y_{\max}/D through the overall FIV development (first panel), the corresponded time-frequency spectrum (second panel), and power spectral density (PSD) of y_{\max}/D at final equilibrium state (third panel) at $U_r =$ (a) 6.0 and (b) 9.0. The data of the time series used for PSD analysis in the third panel is sourced from the area delineated by the red-line box in the first panel.	145
6.7	The variation in vortex-shedding behavior manifested in spanwise direction at $U_r = 5.8$: (a) view of the circular cylinder in $x - z$ plane, (b) time series of the z -components of vorticity along the span at $(x, y) = (2D, 0)$, (c) frequency spectrum along the span corresponding to the data series in (b), and (d) vortex-shedding frequency for uniform inflow past a stationary circular cylinder at Reynolds number ranging from 25 to 45.	146
6.8	Reynolds number $Re(\text{mean})_x$ corresponding to the x -component of mean velocity on the $x - z$ plane at $y = 0$ when the FIV system reaches equilibrium state at $U_r = 6.0$	147
6.9	Instantaneous iso-surfaces of magnitudes of vorticity downstream of the cylinder at $U_r =$ (a) 5.6, (b) 6.0, (c) 9.0, and (d) 9.5.	148
6.10	Instantaneous streamline around the circular cylinder at $U_r =$ (a) 6.0, (b) 7.0, (c) 8.0, and (d) 9.0.	149
6.11	The three-dimensional translucent contour of vorticity magnitudes of the base flow for shear inflow past a stationary circular cylinder with Re ranging from 25 to 45.	149
6.12	(a) The root loci and (b) the variation of the growth/decay rate $\text{Re}(\lambda)$ and eigenfrequency $\text{Im}(\lambda)/2\pi$ as a function of U_r for the studied FIV system. The structure mode SM is demarcated with red symbols. The dotted line corresponds to the relationship $f = F_s$	150
6.13	Illustration of a simple superposition case: the procedure for dividing a circular cylinder with linear shear inflow (with incident velocity ranging from 0 to $2U_0$) into three identically sized elements each subject to a uniform inflow along the spanwise direction.	151
6.14	(a) The overall root loci and (b, c, d) the variation of the growth/decay rate $\text{Re}(\lambda)$ and eigenfrequency $\text{Im}(\lambda)/2\pi$ as a function of U_r for the 2-D FIV system with uniform inflow at $Re =$ (b) 25, (c) 35, and (d) 45. In (b, c, d), the structure mode and wake mode are demarcated using red and blue symbols, respectively.	152

6.15	Diagram showing the division of the cylinder column equally along the spanwise direction into (a) 3 and (b) 5 elements for the superposition of 2-D ROMs (SRROM1).	153
6.16	The root loci, obtained by the SRROM1 with (a) 3 and (b) 5 elements, for the studied FIV system with spanwise shear inflow.	153
6.17	The variation of the growth/decay rate $\text{Re}(\lambda)$ and eigenfrequency $\text{Im}(\lambda)/2\pi$ as a function of U_r , obtained using SRROM1-5E, for the studied FIV system with spanwise shear inflow. The structure mode and wake modes are demarcated with red and black symbols, respectively, and the dotted line corresponds to the relationship $f = 1/U_r$	154
6.18	Diagram showing division of the cylinder column with the spanwise length of the two end elements set to half of the intermediate elements for the superposition of 2-D ROMs (SRROM2). The increment of Reynolds number in (a), (b), and (c) are 2.5 (fine division), 5 (medium division), and 10 (coarse division), respectively.	155
6.19	The root loci, obtained using the SRROM2 with (a) 3 and (b) 5 elements, for the FIV system being studied with spanwise shear inflow.	156
6.20	Growth/decay rate $\text{Re}(\lambda)$ and eigenfrequency $\text{Im}(\lambda)/2\pi$ as a function of U_r , obtained by SRROM2-5E, for the FIV system with spanwise shear inflow being studied.	156
6.21	(a) The root loci and (b) the variation of the growth/decay rate $\text{Re}(\lambda)$ and eigenfrequency $\text{Im}(\lambda)/2\pi$ as a function of U_r , obtained by SRROM2-9E, for the FIV system being studied.	157
6.22	Time series of the normalized transverse displacement y/D for the studied FIV system with spanwise shear inflow at $U_r =$ (a) 5.6, (b) 5.7, (c) 9.4, and (d) 9.5 obtained using FOM/CFD. The logarithmic scale is used for the zoomed-in subgraphs in (b, c).	158
6.23	The comparison of the trend of growth rate $\text{Re}(\lambda)$ obtained using SRROM2-9E and lagging time obtained using FOM/CFD at different U_r values in the lock-in regime.	159
6.24	The predictions of the C_L impulse response obtained using direct 3D-ROM, SRROM2-3E, SRROM2-5E, and SRROM2-9E. The encapsulated subplot utilizes a larger y -axis scale for the first 10 time steps to allow for a complete presentation of the C_L impulse response.	160
6.25	Instability boundaries, predicted by SRROM2-9E, of the flutter lock-in range as a function of mass ratio m^* for the studied FIV system.	160
7.1	Schematic of experiment conducted by Oguma et al. [17] involving the flow past a stationary circular cylinder with a diameter $D = 0.03$ m and a length of $L_c = 0.5$ m. The incident velocity on the cylinder is $U_0 = 22.5$ m s ⁻¹ to give a Reynolds number for the flow of $Re = 40,000$	165
7.2	Boundary conditions and computational mesh used for the validation case consisting of the flow past a stationary circular cylinder at a high Reynolds number ($Re = 40,000$). The permeable FW-H surface used for the prediction of the noise field is shown in (a) as PS0.	166

7.3	Comparison of (a) the mean surface pressure around the cylinder and (b) the downstream variation of the mean streamwise velocity along the computational domain centerline in the spanwise direction ($y/D = 0$) between the present simulation and results reported by Fujisawa and Takeda [18], Oguma et al. [17] and Dong et al. [19].	167
7.4	Comparison of the velocity and pressure fields between the present simulations and the experimental data reported by Oguma et al. [17].	167
7.5	Comparison of the power spectrum of the sound pressure level obtained at the microphone location ($x = 0, y = 1.5 \text{ m}, z = 0$) between the present study and the experimental measurements reported by Oguma et al. [17]. The present simulations of the sound pressure level use both an impermeable (cylinder walls) and a permeable (PS0) FW-H surface for the sound source.	168
7.6	Layout of tandem circular cylinders separated in the streamwise direction by $3.7D$. Each cylinder has a diameter of $D = 0.05715 \text{ m}$. The incident wind speed on the cylinder is $U_0 = 44.0 \text{ m s}^{-1}$ to give a Reynolds number for the flow of $Re = 166,000$. This configuration of two cylinders is used in the present simulations and in the experiments reported by Jenkins et al. [20].	169
7.7	Boundary conditions and mesh used for the numerical simulations of the case of two tandem circular cylinders separated in the streamwise direction. The permeable FW-H surfaces used for the prediction of the noise field are shown in (a) as PS1 and PS2.	169
7.8	Comparison of mean pressure coefficient C_p along the surface of the cylinders obtained from the present numerical simulations and from the QFF experiments [21] for the (a) upstream and (b) downstream cylinders.	170
7.9	Mean streamwise velocity at $y = 0$ for downstream fetches in the range $0.5 \leq x/D \leq 3.3$ between the cylinders and in the range $4.0 \leq x/D \leq 6.0$ corresponding to the wake of the rear cylinder. The mean streamwise velocity is compared between the present numerical simulations and the experimental measurements reported by Jenkins et al. [20].	171
7.10	The PSD of the fluctuating surface pressure for the front (upwind) and rear (downwind) cylinders obtained from the present numerical simulations and from the BART experiments [22].	172
7.11	Power spectral density of the sound pressure level at the observer (microphone) location $(x/D, y/D, z/D) = (-8.33, 27.815, 0)$: (a) comparison of the present predictions of the SPL PSD with those obtained by Guillaume et al.[23] and David et al.[24] and with experimental measurements of the SPL PSD obtained from the QFF experiment [21]; and, (b) comparison of the present predictions of the SPL PSD obtained using three different FW-H surfaces (one impermeable surface coinciding with the walls of the cylinders and two permeable surfaces shown as PS1 and PS2 in Fig. 7.7(a)).	173
7.12	Configuration of tandem cylinders used in the DNS conducted by Hattori and Komatsu [25]—the front (upstream) cylinder is fixed and the rear (downstream) cylinder is oscillating in transverse (or, y -) direction. The center-to-center separation between the two cylinders in the streamwise (or, x -) direction is $L = 4D$	173

7.13	The SPL directivity for the configuration of tandem cylinders shown in Fig. 7.12 obtained in the x - y plane (at $z/D = 0$) at a radial distance of $80D$ from the midpoint between the two in-line cylinders for angular positions in the range $0^\circ \leq \theta \leq 180^\circ$. The prediction obtained from the present numerical simulation are compared to that obtained from the DNS conducted by Hattori and Komatsu [25].	174
7.14	(a) The computational domain and boundary conditions and (b) the computational mesh used in the simulation of the tandem cylinders case. The permeable FW-H surfaces used in the prediction of the noise field are shown as PS1 and PS2 in (a).	175
7.15	The location of the microphones used for monitoring the sound pressure from the noise field generated by a flow over tandem cylinders (viz., a pair of cylinders whose center-to-center separation in the streamwise direction is $L = 3D$).	175
7.16	The sound pressure level PSD at different angular positions θ in the x - y plane (at $z/D = 0$) at a radial distance of $10D$ from the midpoint between the stationary tandem cylinders in the streamwise direction. The surfaces of the two cylinders are taken as the impermeable FW-H surface for determination of the noise field generated by a flow past the tandem cylinders.	176
7.17	(a) The sound pressure level PSD at an angular position of $\theta = 135^\circ$ and (b) the SPL directivity pattern for angular positions in the range $0^\circ \leq \theta \leq 180^\circ$ for three different values of the Reynolds number Re . The sound pressure level is determined in the x - y plane (at $z/D = 0$) at a radial distance of $10D$ from the midpoint between the tandem cylinders in the streamwise direction. The surfaces of the two cylinders are taken as the impermeable FW-H surface for determination of the noise field generated by a flow past the tandem cylinders.	177
7.18	The sound pressure level PSD obtained in the x - y plane at $z/D = 0$ at a radial distance of $10D$ for three angular positions $\theta = 90^\circ, 135^\circ$, and 180° for the flow past a single and tandem cylinder(s) at $Re = 120,000$. An impermeable FW-H surface coinciding with the surfaces of the cylinder(s) is used for the prediction of the noise field generated by the flow past a single or tandem cylinder(s).	178
7.19	The SPL directivity pattern in the x - y plane at $z/D = 0$ at a radial distance of $10D$ obtained for the flow past a single and tandem cylinder(s) at $Re = 120,000$. An impermeable FW-H surface coinciding with the surfaces of the cylinder(s) is used for the prediction of the noise field generated by the flow past a single or tandem cylinder(s).	179
7.20	Root-mean-square (r.m.s.) values of the fluctuating pressure p' . The results correspond to the noise generated by the flow past a transversely oscillating cylinder at $Re = 120,000$ with an oscillation amplitude $A = 0.2D$ and an oscillation frequency f ranging from 5 to 50 Hz. The five microphones (observers) are positioned in the x - y plane at $z/D = 0$ at a radial distance of $10D$ at angular positions of $\theta = 0^\circ, 45^\circ, 90^\circ, 135^\circ$, and 180° . The horizontal dashed lines correspond to the r.m.s. values of p' obtained for the stationary cylinder.	180

7.21	Power spectrum of the fluctuating pressure p' obtained from a microphone (observer) positioned in the x - y plane at $z/D = 0$ at a radial distance of $10D$ at an angular position of $\theta = 135^\circ$. The p' power spectrum for the stationary cylinder is compared with a cylinder with oscillation frequencies f of 20, 25, 30, 35, and 50 Hz.	181
7.22	The r.m.s. value of the fluctuating pressure p' (Pa) obtained for an oscillating cylinder with oscillation frequency f (equivalently Sc) of 0 Hz (stationary cylinder), 20 Hz, 25 Hz and 50 Hz in the x - y plane at $z/D = 0$ at a radial distance of $10D$ at angular positions of 0° (upstream direction), 45° , 90° , 135° and 180° (downstream direction). An impermeable FW-H surface (cylinder walls) is used to determine the noise field generated by the flow past the cylinder. Under each column associated with a particular angular position, the total sound pressure, loading noise, and thickness noise are highlighted in the white, blue and yellow boxes, respectively.	182
7.23	FW-H predictions of (a) the power spectrum of the fluctuating pressure p' obtained from a microphone (observer) positioned in the x - y plane at $z/D = 0$ at a radial distance of $10D$ and an angular position of $\theta = 135^\circ$ for a cylinder oscillating with frequencies f of 20, 25, and 50 Hz and (b) the power spectral density of the SPL obtained using an impermeable (cylinder walls) and a permeable (PS0) FW-H control surface for a cylinder oscillating with a frequency f of 50 Hz.	183
7.24	Three cases: (a) single stationary cylinder; (b) single cylinder oscillating in the transverse (or, y -) direction; and, (c) single cylinder oscillating in the streamwise (or, x -) direction. For cases (b) and (c), the cylinder is oscillating with an amplitude $A = D$ and a frequency $f = 20$ Hz.	184
7.25	Isopleths of the (a) second invariant Q and (b) third invariant R obtained when the cylinder passes through the initial position (viz., the stationary position for the oscillating cylinder) after several oscillation cycles for three cases: namely, a stationary cylinder, a cylinder oscillating in the transverse (y -) direction, and a cylinder oscillating in the streamwise (x -)direction.	185
7.26	The SPL PSD obtained for (a) a stationary cylinder and (b) a cylinder oscillating in the streamwise (x -) direction at a microphone positioned in the x - y plane at $z/D = 0$ at a radial distance of $10D$ and at an angular position of $\theta = 135^\circ$. The FW-H methodology is applied in both cases for an impermeable (cylinder walls) and a permeable (PS0) FW-H surface. (c) The SPL directivity pattern obtained for a stationary cylinder, a cylinder oscillating in the transverse direction, and a cylinder oscillating in the streamwise direction at the same microphone location as in (a) and (b) using an impermeable FW-H surface coinciding with the cylinder walls.	186
7.27	Five cases (scenarios) of tandem cylinders: (1) Scenario (a)—front and rear cylinders stationary; (2) Scenario (b)—front cylinder oscillating in transverse direction and rear cylinder stationary; (3) Scenario (c)—front cylinder oscillating in streamwise direction and rear cylinder stationary; (4) Scenario (d)—front cylinder stationary and rear cylinder oscillating in transverse direction; and, (5) Scenario (e)—front cylinder stationary and rear cylinder oscillating in streamwise direction.	187

7.28	The average surface pressure PSD for the front and rear cylinders for five cases (scenarios): (a) front and rear cylinders stationary; (b) front cylinder oscillating in the transverse direction and rear cylinder stationary; (c) front cylinder oscillating in the streamwise (in-line) direction and rear cylinder stationary; (d) front cylinder stationary and rear cylinder oscillating in the transverse direction; and, (e) front cylinder stationary and rear cylinder oscillating in the streamwise (in-line) direction.	188
7.29	The sound pressure level PSD at various angular positions θ on the surface of the front (upstream) and rear (downstream) cylinders for the case where the front cylinder is oscillating in the streamwise (in-line) direction and the rear cylinder is stationary (Scenario (c)).	189
7.30	The mean pressure coefficient C_P as a function of the arclength $s \equiv \pi D\theta/360$ along circular arcs at (a) two spanwise positions on the surface of the front and rear cylinders. The dependence of C_P on s for the front and rear cylinders is summarized for five different scenarios: (b) Scenario (a)—front and rear cylinders stationary; (c) Scenario (b)—front cylinder oscillating in the transverse direction and rear cylinder stationary; (d) Scenario (c)—front cylinder oscillating in the streamwise (in-line) direction and rear cylinder stationary; (e) Scenario (d)—front cylinder stationary and rear cylinder oscillating in the transverse direction; and, (f) Scenario (e)—front cylinder stationary and rear cylinder oscillating in the streamwise (in-line) direction.	190
7.31	Isopleths of the two invariants Q and R taken when the cylinder passes through the initial position (viz., the stationary position for an oscillating cylinder) after several cycles of oscillations for five different scenarios of tandem cylinders. . . .	192
7.32	SPL PSDs obtained at various angular positions at a radial distance of $10D$ from the midpoint between the two cylinders with the front cylinder stationary and the rear cylinder oscillating in the transverse direction.	193
7.33	SPL PSD obtained at an angular position of $\theta = 135^\circ$ at radial distance of $10D$ from the midpoint between the two cylinders for five different scenarios.	194
7.34	Directivity of the SPL obtained at a radial distance of $10D$ from the midpoint between the pair of cylinders for five different scenarios involving tandem cylinders: directivity predicted using (a) an impermeable FW-H control surface (taken as the cylinder walls) and (b) the permeable FW-H control surface PS1.	195
A.1	VIV system oscillating in Y direction supported by two linear springs in X and Y direction.	222
A.2	Integral spring forces in Y direction with different k_a and L_a	223
A.3	VIV system with nonlinear restoring force of quadratic and cubic orders, structural damping is zero.	224

List of Tables

3.1	Root-mean-square lift and drag coefficients for flow past a stationary cylinder at $Re = 100$ for four different meshes.	38
3.2	Comparison of the maximum amplitude of the lift coefficient C_L^{\max} and Strouhal number S_f for flow past a stationary circular cylinder at $Re = 100$	39
4.1	The length of the recirculation region (measured from the center of the cylinder) normalized by the cylinder diameter D for a base flow past a stationary circular cylinder at $Re = 60$ and 100 . The results of the present simulations are compared with those of previous investigators.	67
5.1	Aerodynamic coefficients (root-mean-square lift and drag coefficients) of flow past a <i>stationary</i> square cylinder at $Re = 100$ for four different meshes.	100
5.2	The length of the recirculation region (steady wake) normalized by the cylinder diameter (side length) D for a base flow past a stationary square cylinder. The results of the present simulations are compared with those reported by Mao and Blackburn [26].	102
6.1	Aerodynamic coefficients (root-mean-square lift and drag coefficients) of shear flow past <i>stationary</i> circular cylinder with Re ranging from 25 to 45 for different mesh conditions.	141

List of Symbols

\mathbf{A}_{rs}	transfer matrix of reduced fluid-structure coupling system
C_L	lift coefficient
C_D	drag coefficient
D	characteristic length
f	normalized structural oscillation frequency ($\equiv f_{osc}D/U_0$)
f_{osc}	structural oscillation frequency
f_{eq}	equivalent natural frequency
F_n	structural natural frequency
F_s	reduced natural frequency ($\equiv F_nD/U_0$)
$\text{Im}(\lambda)/2\pi$	eigenfrequency obtained from \mathbf{A}_{rs}
m^*	mass ratio, the ratio of the solid body density to the fluid density
Re	Reynolds number
$\text{Re}(\lambda)$	growth rate obtained from \mathbf{A}_{rs}
S_t	Strouhal number
U_0	free-stream velocity
U_r	reduced velocity ($\equiv F_s^{-1}$)
y	transverse displacement
y_{\max}, A_{\max}	maximum transverse displacement
ζ	structural damping ratio
θ	angle of attack
Φ	phase difference

List of Abbreviations

ARX	AutoRegressive with eXogenous model
CFL	Courant-Friedrichs-Lewy
DMD	dynamic mode decomposition
DES	detached eddy simulation
ERA	eigensystem realization algorithm
FOM	full-order model
FIV	flow-induced vibration
FSI	fluid-structure interaction
FW-H	Ffowcs Williams-Hawkings
LSA	linear stability analysis
LES	large eddy simulation
POD	proper orthogonal decomposition
PSD	power spectral density
Q	second invariant of the velocity gradient tensor under a Galilean transformation
R	third invariant of the velocity gradient tensor under a Galilean transformation
ROM	reduced-order model
SPL	sound pressure level
SROM	superposition of two dimensional ROM (SROM)
SM	structure mode
SM_c	structure-dominated mode for coupled condition
VIV	vortex-induced vibration
WM	wake mode
WMI	first wake mode
WMII	second wake mode
WSMI	first wake-structure mode in coupled condition
WSMII	second wake-structure mode in coupled condition

Chapter 1

Introduction

1.1 Background

Energy is essential to humanity since it serves as the foundation for social and economic progress. Countries that were overly dependent on oil and gas were badly impacted after the two oil crises of the 1970s, and as a result, they started looking for other energy sources as an oil substitute. At the same time, people began to progressively grasp that beyond the 1980s, the conventional fossil fuels supporting human civilization would unavoidably begin to decline. Moreover, as dangerous compounds are released during the burning of the fuel, it not only pollutes the environment in which people really live but also has a severe effect on their ability to survive and develop. During the 1990s, all nations studied energy countermeasures and national energy policies for the sake of sustainable development, searched for innovative, clean, safe, and dependable sustainable energy systems, and accelerated the production and use of renewable clean energy. The UK government has set a goal of cutting carbon dioxide emissions by 50% compared to 1990 levels by 2050 [27]. International Energy Agency (IEA) (2012) reports that 4,206 TWh of electricity from renewable sources, including wind energy and hydropower, were generated in 2010, making up 20% of the total amount of electricity produced worldwide. The IEA (2012) New Policies Scenario predicts a 270 percent growth in renewable power between 2010 and 2035.

Solar energy, hydro energy, ocean energy, wind energy, and geothermal energy are currently classified as renewable energy sources. In particular, wind and hydro energy are widely used as clean energy sources. At present, the rotating turbine is mainly used to harness those kinds of energy, which uses the fluid to drive the blades to generate electricity. However, the performance of those turbines is limited by the fluid velocity, making it infeasible to utilize wind or hydro energy in the places/environments with the low-speed incident flow. In addition, the traditional rotary turbines, especially the small-scale machine designed for distributed energy, is encountered the problems of safety and noise. For example, underwater rotary turbines will cause damage to migratory turtles or fish, traditional wind turbines pose a threat to birds, and small-scale wind power generators close to residential areas can cause damage to human limbs and ears (cf. with Fig. 1.1). Based on the above consideration, looking for new devices that can utilize the fluid energy of nature becomes a key point for consideration.

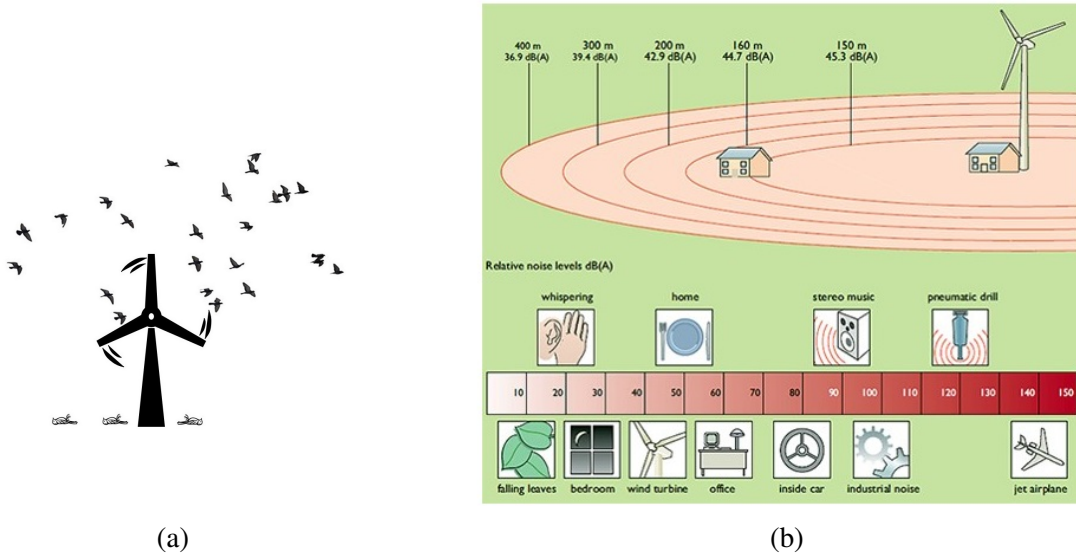


Figure 1.1: Problems encountered by traditional rotating wind turbines. (a) Birds attacked by blades, and (b) Noise level surrounding rotating wind turbines (source: EWEA. 1991).

Flow-induced vibration (FIV) is a common phenomenon of fluid-structure interaction (FSI) that is relevant to the applications of marine, civil, aeronautical, and power engineering. With respect to the characteristics of the structural response, FIV mainly includes the patterns of motion associated with lock-in (resonance and flutter), galloping, buffeting, and surge [28, 29, 30]. Among these various patterns of motion, the instability of lock-in and galloping are most likely to induce a large-amplitude oscillation in structures and, consequently, understanding the physical mechanisms underpinning those two phenomenon is an important and active area of fundamental research. Taking the most representative phenomenon—vortex-induced vibration (VIV), as an example herein, vortex shedding occurs periodically on both sides of a non-streamlined structure under the action of water or air currents, which will form periodic external force on the structure and cause structural vibration. When the amplitude reaches a certain level, it will cause damage to the structure. Therefore, scholars and engineers have been considering VIV as a harmful phenomenon for decades. However, it is found that in the case of low velocity flow, the VIV behavior can produce a large amplitude, and most of the kinetic energy of the fluid is absorbed by the structure, forming a stable periodic oscillation. This dynamics feature makes it possible to use the VIV phenomenon as the mechanism support underpinning a certain kind of energy harvester. Lee [31] reported that Vortex Induced Vibration Aquatic Clean Energy (VIVACE) generator with a single cylinder (Diameter = 3.5", Axial length = 36") can generate electricity from 0.4 m/s water flow, and its maximum power is 15.85 W at 1.11 m/s flow velocity.

As one kind of unstable vibration, the resonance pattern of VIV occurs in a certain range in which the vortex-shedding frequency approaches the natural frequency of the structural system, and can produce effective vibration in a wide range of velocity and Reynolds number. But in reality, VIV is only one widely known case within the varied patterns of flow-induced vibration (FIV). Therefore, effective transverse kinetic energy can be obtained from the low-speed flow by using FIV, which can be converted into electric energy with an appropriate energy driving transmission device. This idea has important practical implications for the utilization of low-speed water or wind energy. If the power generation device driven by FIV can be widely used, not only can the utilization range of water and wind energy resources be greatly expanded, but also

the fluid with low velocity will assist to alleviate the energy shortage. In addition, the dynamic problem of energy generators using FIV is also related to structural design and parameter optimization, which can be used as the research basis for complex multiple vibration systems. From this preceptive, the research on FIV has practical significance for optimizing energy structure, promoting clean energy development, coping with climate change, and developing a low-carbon economy.

Moreover, the disturbance of the bluff body and the vibration of the rod will be accompanied by aeroacoustics noise. Low-frequency noise affects human physiological and mental health, the academic research on low-frequency noise radiated from structural motion has also become a hot topic. For example, the aerodynamic noise produced by high-speed trains and aircraft has brought serious environmental pollution. Among them, the cylindrical rod including bogie structures and pantograph is an indispensable and important part of these trains, and the generated aerodynamic noise is extremely prominent. Hence, the noise caused by FIV deserves particular attention from researchers while the application of FIV phenomena is combined with commercial power generation. Compared to the aeroacoustics study on the flow passing fixed bluff body, the study of noise on flow pass oscillating bluff body is still limited.

As mentioned above, the trend of how to transfer the FIV energy to accessible and stable power is a very promising research direction. The structural energy within FIV is mainly located at the regimes with amplified amplitudes, so what factors are associated with the magnitude of these regimes and the accompanied amplitudes deserve to be studied in depth. Moreover, the noise problem brought by body oscillation in FIV is also a research direction that demands attention.

1.2 Basic principles and preliminary parameters

1.2.1 Basic principles

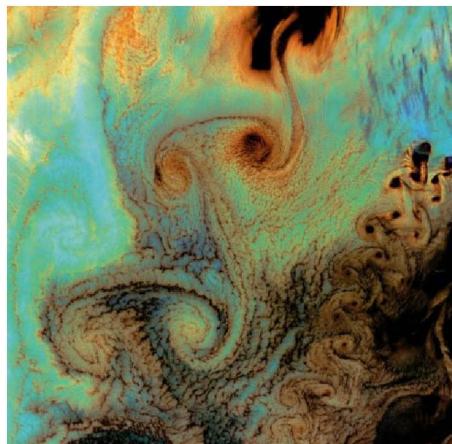


Figure 1.2: Vortices behind the Aleutian Islands [1].

As one of the most widely known cases of fluid-solid coupling instability, the appearance of resonance lock-in should be accompanied with the unstable wake dynamics (or, vortex-shedding behavior), so called ‘vortex-induced vibration (VIV)’. The resonance (lock-in) pattern herein is

correlated to the mechanism underpinning ‘VIV’. The phenomenon of flow around bluff body exists widely in nature, and Fig. 1.2 shows a series of vortices formed by the airflow around the Aleutian Islands captured by NASA Landsat 7. One of the most significant phenomena found by Von Karman in the experiment of flow around a cylinder is that when the Reynolds number increases to a certain value (viz., critical Reynolds number Re_{cr}), the fluid vortices will alternately fall off from the tail of the cylinder and form regular, reverse and alternating vortex series in the wake, which is called Karman vortex street. The flow past a circular cylinder is the most classical one among all situations of the flow around a blunt body. Scholars have tried to explain this physical mechanism, among which Gerrard [32]’s shear layer interaction model has been widely recognized.

For viscous flow, when the uniform incoming fluid flows through the cylinder surface, a boundary layer is formed on the cylinder surface. However, the velocity of each point outside the boundary layer is different from that of the plate boundary layer. As shown in Fig. 1.3, the velocities of points A, B, C and D in the figure are different. Boundary layer separation is an important phenomenon on a cylinder. When the incoming velocity U_0 is close to the surface of the upstream side of the object, on the front stagnation point A where the maximum pressure point appears, the velocity is zero. This is because the pressure increases due to the obstruction at point A. With respect to point B outside the boundary layer, the velocity is the maximum, but the pressure is the minimum. After point B, the pressure increases but the velocity decreases. Consequently, the fluid in the boundary layer is not only affected by the friction resistance, but also by the pressure difference opposite to the flow direction. Before point C, only the velocity on the wall is equal to zero, while after point C, the kinetic energy of fluid near the wall of the boundary layer is exhausted, so the fluid near the wall stagnates and reverses under the action of high pressure in the back section. The pressure distribution in the boundary layer along the surface of the cylinder is identical to the pressure distribution of the fluid outside the boundary layer since the boundary layer is extremely thin.

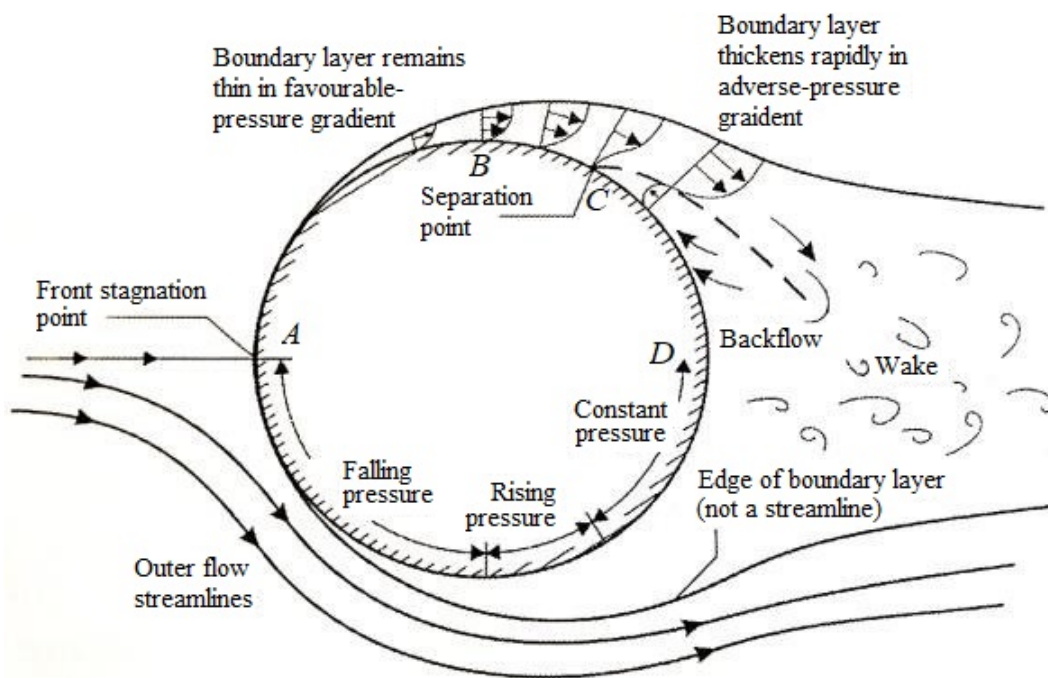


Figure 1.3: Schematic for boundary-layer separation [2].

Point C is usually referred as the separation point S. At the separation point, the boundary layer separates from the cylinder surface and forms a free shear layer, which extends downstream, as shown in Fig. 1.4a. The wake region is between the shear layers on both sides, and the velocity in the outer part of the shear layer is greater than that in the inner part, so the fluid generates wake vortices and falls off downstream, forming several wake vortices. A series of wake vortices behind the cylinder are called ‘vortex street’, as shown in Fig. 1.4b. The wake vortex occurs alternately on the left and right sides of the cylinder. When the wake vortex occurs at the separation point on one side, the circumferential velocity v_1 opposite to the rotation direction of the wake is caused on the cylinder surface, as shown in Fig. 1.4c. The velocity $v + v_1$ of the wake side is larger than the original velocity v , and the $v - v_1$ of the other side is less than the original velocity v . Therefore, a pressure difference is formed on the cylinder surface perpendicular to the incoming flow, which is called lift force F_L . Next, the next wake falls off from the other side and generates lift in the opposite direction. Therefore, each ‘pair’ wake has the opposite lift force and forms an alternating force period perpendicular to the flow direction. The coupling effect between the fluid and the structure gets intense when the structure natural frequency approaches the lift force frequency. Meanwhile, the drag force F_D will be produced in the flow direction of the cylinder. F_D is one order of magnitude smaller than F_L in quantity, so its influence on the whole structure is not as important as F_L .

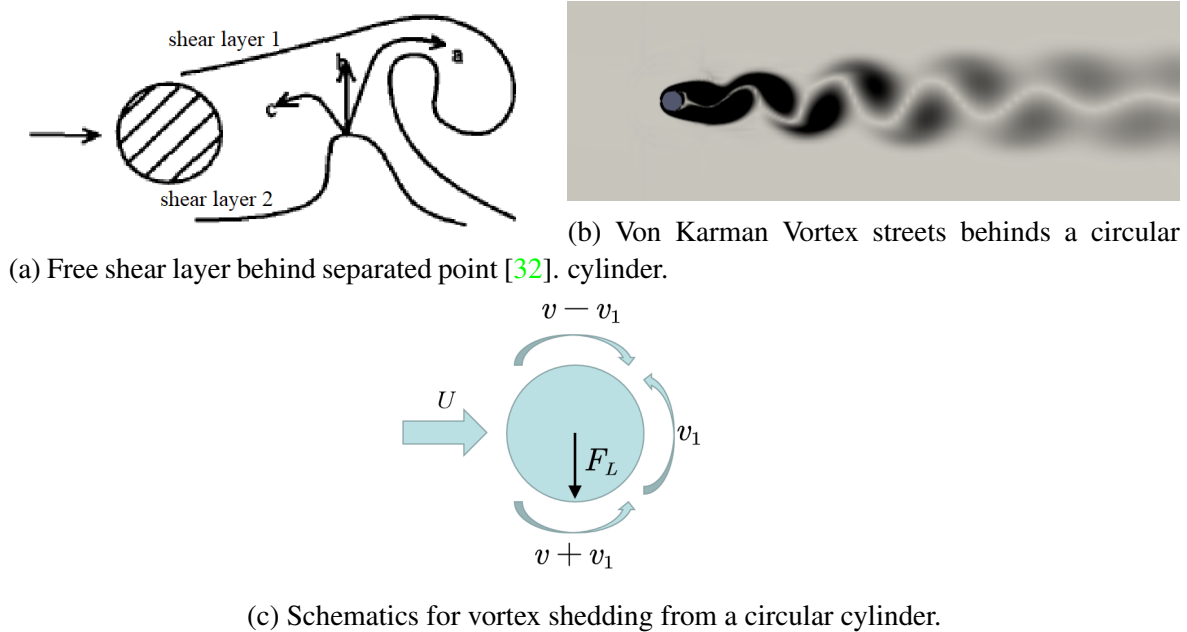


Figure 1.4: Mechanism for the vortex shedding from circular cylinder.

Based on above introduction, we know that when a fluid flows through a bluff body, the vortex shedding phenomenon will appear in the wake under certain flow conditions. As the vortex shedding frequency approaches the natural frequency of the object, a periodic fluid force will be induced on the body surface perpendicular to the direction of the incoming flow, thus causing the body to vibrate and generating periodic shedding vortices on both sides of the back of the body alternately. The vibration of body in turn changes the shape of wake flow and vortex shedding. This fluid-structure interaction is termed VIV. As shown in Fig. 1.5, due to the influence of the added mass, the falling frequency of the vortex is locked at the vibration frequency of the cylinder in a wide range near the natural frequency, rather than limited to it. Therefore, the VIV

is a kind of self-excited response phenomenon. The result of ‘lock-in’ phenomenon leads to the unstable dynamic interaction between structure and fluid.

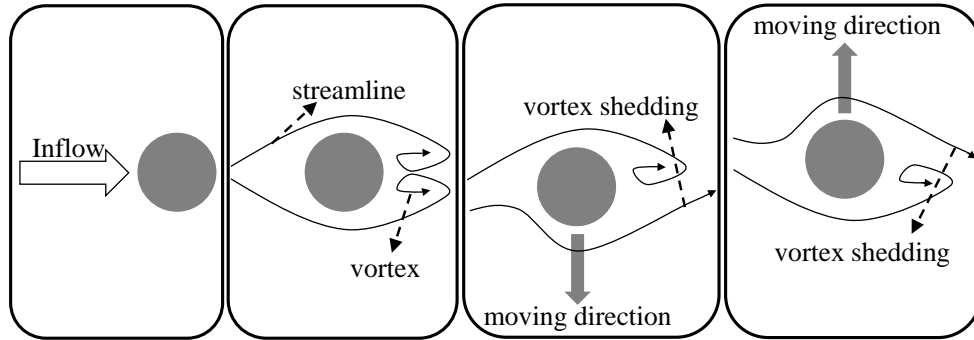


Figure 1.5: The occurrence of reciprocating motion of a circular cylinder submerged in the uniform incident flow.

As explained above, the critical Reynolds number Re_{cr} means the largest Reynolds number for flow past a stationary cylinder to generate a shedding vortex, and consequently, no external fluid forces would act on the stationary body surface at the subcritical Reynolds number. However, with respect to one FIV system with a Reynolds number below the critical Reynolds number, certain behaviors of structural instability will also appear, and flutter lock-in is one representative case herein. Based on the modal analysis of Zhang et al. [12], flutter lock-in is the root cause owing to the unstable structural mode, supporting the assertion of Langre [33] that frequency lock-in is caused by coupled-mode flutter.

Among these various patterns of motion, the galloping instability—a special kind of unbounded vibration—is most likely to induce a large-amplitude oscillation in structures and, consequently, understanding the physical mechanisms underpinning this phenomenon is an important and active area of fundamental research. Galloping behavior is commonly encountered for elastically-mounted objects with non-circular cross-sections submerged in high-speed liquid or air [34]. For instance, unlike the flow-induced vibration (FIV) response of a circular cylinder which will transfer into desynchronization after the lock-in range with increasing inflow velocity, the FIV response of a square cylinder will involve galloping instability [35, 36]. The lock-in phenomenon will occur only when the structural natural frequency is comparable to the vortex-shedding frequency, leading to induced oscillations with limited vibration amplitude. In marked contrast, the galloping instability will appear over a broad range of the incident velocity of the incoming flow (implying that the structural natural frequency does not have to be comparable to the vortex-shedding frequency) and, moreover, the amplitude of vibration for this phenomenon is known to increase with increasing incident flow velocity [35, 37, 36]. Furthermore, galloping is generally a low-frequency oscillation (viz., occurring at frequencies that are much lower than the vortex shedding frequency).

Galloping instability has important consequences for engineering applications and, in particular, for construction engineering. For example, slender structures with a square section are widely used in engineering construction (e.g., high-rise and towering structures, transportation trestle bridges, and corridors). However, owing to the aerodynamic characteristics of a square section, these structures may gallop under the action of the wind and this buffeting response may lead to fatigue damage to various structural components and connections, which can lead to an

increased probability of physical harm, property loss, or environmental impact. The galloping of an ice-coated transmission line is a common example of such concerns. The ice coating can change the shape of the cross-section of the transmission line by forming crescent-shaped, fan-shaped, or D -shaped cross-sections [38]. This change in the cross-sectional shape of the power line in conjunction with the slenderness of the structure and the presence of a crosswind can potentially induce large-amplitude wind-induced vibrations in the structure, leading to fatigue of and damage to conductors and even to dragging down the transmission tower. From the perspective of modal analysis, galloping and flutter are considered by Li et al. [16] to have similar intrinsic motivating factors. However, there is still insufficient research on the triggering factors of galloping, which will be further explored in this thesis.

1.2.2 Main parameters

1. Reynolds number Re .

As an important and basic parameter in fluid mechanics, Reynolds number directly affects the form of vortex shedding pattern, which is expressed by the ratio of inertial force to viscous force:

$$Re = \frac{U_0 D}{\nu}, \quad (1.1)$$

where U_0 is the velocity of incoming flow, D is the diameter of cylinder section, ν is the kinematic viscosity coefficient of fluid. When the Reynolds number is very small, the viscous force is dominant and the flow is relatively stable. With the increase of Reynolds number, the inertial force becomes stronger and flow develops into turbulence. Reynolds number has the greatest influence on the wake shape.

2. Strouhal number S_t .

f_{vs} represents the vortex shedding frequency of flow past stationary cylinder. In the flow past fixed bluff body, the intrinsic physical properties of boundary layer separation and flow instability can be associated with vortex shedding frequency f_{vs} and Strouhal number S_t ,

$$f_{vs} = \frac{S_t U_0}{D}, \quad (1.2)$$

S_t is the most mysterious and robust parameter in the flow past cylinder. As shown in Fig. 1.6, the S_t number is related to the Re [3]. It can be seen that in the subcritical region ($300 < Re < 1.5 \times 10^5$), the S_t number is relatively stable and about 0.20, which indicates that the vortex shedding in the wake is orderly. In the critical region, the S_t is dispersed and the spectrum band of vortex shedding frequency is wider. In moving cylinder cases, f_{mvs} represents the vortex shedding frequency of a forced or self-excited body in motion.

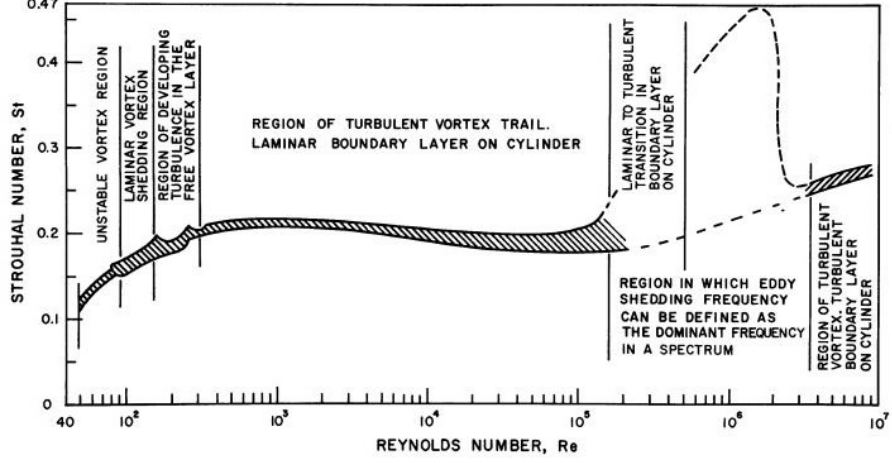


Figure 1.6: Relationship between Reynolds number and Strouhal number [3].

3. Frequency ratio f^* .

f_{osc} represents the oscillation frequency of a vibrating body (either forced or self-excited) regardless of whether lock-in or galloping is present. Frequency ratio is shown as ratio:

$$f^* = \frac{f_{osc}}{F_n}, \quad (1.3)$$

here F_n represents the natural frequency of structural part of FIV system:

$$F_n = \frac{1}{2\pi} \sqrt{\frac{k}{m_s + m_a}}, \quad (1.4)$$

in which, k is the stiffness of linear spring, m_s is the body mass of the structural part, m_a is the added mass on the natural frequency of the structure. In fluid mechanics, added mass is the inertia added to a system because an accelerating or decelerating body must move (or deflect) some volume of surrounding fluid as it moves through it. Added mass is a common issue because the object and surrounding fluid cannot occupy the same physical space simultaneously. For simplicity, added mass can be modeled as some volume of fluid moving with the object, though in reality "all" the fluid will be accelerated, to various degrees, and $m_a (= C_a m_D)$. $m_D (= \pi \rho_f D^2 / 4)$ is the mass of fluid corresponding to body volume of unit length. C_a is the added mass factor, which could be neglected while the fluid medium around the structure is air, because its added mass has limited influence on F_n of the structure. The effect of the added mass is non-negligible when the fluid medium is water, and C_a is set as 1 normally [39].

4. Reduced velocity U_r .

The reduced velocity U_r represents the ratio of the movement distance of one vibration period to the characteristic length, diameter for circular cylinder, of the structure, and the reduced velocity is also a dimensionless parameter:

$$U_r = \frac{U_0}{F_n D}, \quad (1.5)$$

5. Mass ratio m^* and structural damping ratio ζ .

Mass ratio m^* is defined as the ratio of the oscillation body mass m_s to the fluid mass m_D corresponding to body volume, also the ratio of the body's density ρ_s to the surrounding fluid density ρ_f :

$$m^* = \frac{m_s}{m_D} = \frac{\rho_s}{\rho_f}. \quad (1.6)$$

The structural damping ratio ζ represents the energy consumption due to structure's own properties when the structure vibrates:

$$\zeta = \frac{c}{2\sqrt{k(m_s + m_a)}}, \quad (1.7)$$

where c is the structural damping. A mass-damping ratio parameter $m^*\zeta$ is obtained by combining the mass ratio with the damping ratio [40]. By changing the mass ratio m^* and damping ratio ζ separately, the FIV experiment of elastically supported rigid cylinder was carried out by Khalak and Williamson [5] in a towing tank to study the influence of these two parameters on the FIV response. They indicate that the amplitude of the elastically supported rigid cylinder depends on $m^*\zeta$, the smaller $m^*\zeta$ is, the larger the FIV amplitude peak value is.

6. Lift coefficient C_L and drag coefficient C_D .

The transverse force of fluid on the unit length structure is called the lift force F_L , and the dimensionless coefficient is called the lift coefficient C_L :

$$C_L = \frac{F_L}{\frac{1}{2}\rho_f U_0^2 D}. \quad (1.8)$$

Periodic vortex shedding can induce periodic fluid force on the structure, and long-term FIV will damage the structure. In the practical application of ocean engineering and bridge engineering, there are many phenomena of fluid induced structural vibration. For example, the galloping of transmission lines, the ringing of cables, the winding vibration of heat exchange pipes, and the vibration of skyscrapers, bridge piers and offshore drilling structures can cause destructive vibration accidents. The structural damage caused by FIV has been studied extensively by scholars in recent decades. Due to the obvious unstable relationship between fluid and solid in FSI system, many issues concerning FIV dynamics have not been fully understood.

Chapter 2

Literature review

2.1 Experimental investigations of FIV

2.1.1 Response analysis

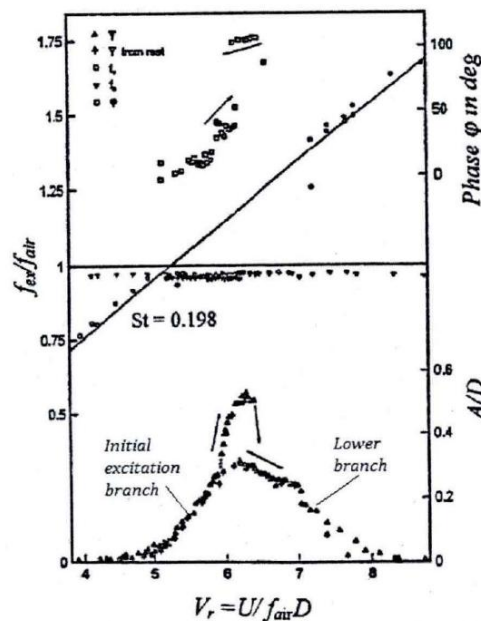


Figure 2.1: Response of a spring-mounted circular cylinder of self-excited vibration in air [4], V_r , f_{ex} and f_{air} here represents U_r , f_{osc} and f_n in present work.

Vortex-induced vibration (VIV) of the single circular cylinder is the most fundamental part in the FIV research. In 1968, Feng [4] first carried out a pioneering experimental study on a single rigid circular cylinder, which has been regarded as a classic example of VIV experiment for decades. The experiment was carried out in a wind tunnel and the cylinder's motion direction is limited in transverse direction, with a high mass ratio $m^* = 248$, a damping ratio = 0.00103, and a Reynolds number range of $(1 - 5) \times 10^4$. Feng measured the amplitude ratio A/D , actual vibration frequency, wake variation frequency and phase angle of VIV system and studied the

relationship between amplitude ratio and reduced velocity, as shown in Fig. 2.1. Since 1996, Williamson and his team have carried out many VIV experiments of a rigid circular cylinder with low mass ratio and elastic support [5, 41]. They have changed the mass ratio by modifying the stiffness coefficient, adjusting the system mass and changing the diameter of the cylinder. Different from Feng’s experiment [4], Khalak and Williamson [5, 41] used low mass ratio and low mass-damping ratio in the experiment to measure the lift forces, drag forces, displacement and frequency response of the structure.

While comparing Feng’s high- m^* experiment [4] with air as the fluid medium and Khalak and Williamson’s low- m^* experiment [5] with water as the fluid medium, several obviously differences could be observed with respect to the responses. In Feng’s experiment, there are only two branches of the displacement response, which are the initial branch and the lower branch. When the reduced velocity changes from small to large or from large to small, the displacement response has some shift around reduced velocity of 6, as shown in Fig. 2.1. In the low- m^* experiment of Khalak and Williamson [5], whose mass-damping parameter is 0.013, the maximum displacement response is larger than that of Feng [4] in which the mass-damping parameter is roughly 30. Therefore, in addition to the initial branch and the lower branch, another branch is defined: the upper branch, as shown in Fig. 2.2a. Similarly, Khalak and Williamson [41][42][8] also obtained varied branches of amplitude response while m^* is different with the lower Reynolds number range ($Re = 2 \times 10^3 - 1 \times 10^4$). The amplitude jump behavior was accompanied by the phase angle (between displacement and lift forces) showing a 180° jump.

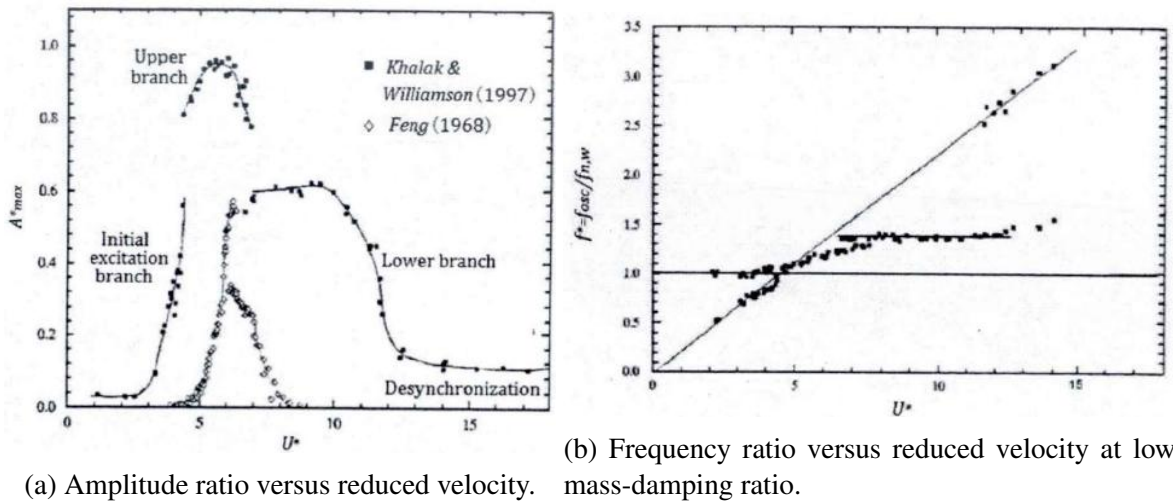


Figure 2.2: Amplitude and frequency ratio versus reduced velocity in experiments [5], U^* here is U_r in present work.

In Feng’s experiment [4] which is conducted in the air, the mass ratio is very large ($m^* = 248$). The vibration frequency of the cylinder approaches the structural natural frequency, and consequently the frequency ratio f^* is about 1. However, with respect to the VIV response in water, the oscillation frequency of the cylinder with low mass ratio is obviously higher than the natural frequency in the resonance regime (U_r is about 5-12). Therefore, the frequency ratio f^* is no longer near 1.0 but about 1.4, as shown in Fig. 2.2b. Govardhan [43] studies the relationship between frequency ratio f^* and reduced velocity at low mass ratio. The smaller the mass ratio is, the larger the frequency ratio is, and the range of lower branch increases with the decrease of mass ratio m^* . What’s interesting is that Govardhan and Williamson [44] also observed the

extreme mass ratio m^* in the experiment: when m^* drops to about 0.5, the upper limit of the lock-in area is very large. No matter how the flow rate increases, the system will always be locked in the state with large VIV amplitude, the vibration frequency is also obviously greater than the structural natural frequency of the system.

In terms of the wake dynamics of FIV, the periodic vibration of the cylinder results in different vortex modes in wake, which are different from the classical Karman vortex street. Jauvitis and Williamson [6][7] and Govardhan and Williamson [8][9] summarized various forms of vortex shedding behaviours, including ‘2S’, ‘2P’, ‘P + S’, ‘2C’ and ‘2T’. It is proposed that there is a certain corresponding relationship between the vortex shedding pattern and the amplitude and frequency of FIV response, such as initial branch corresponds to the ‘2S’ pattern and the lower branch corresponds to the ‘2P’ pattern. Braka and Laneville [45] also observed the ‘2P’ mode through the free vibration experiment of a cylinder, and the premise of this kind of vortex shedding is to use as small structural damping as possible. It should be pointed out that ‘2T’ wake mode occurs only when $m^* < 6$ and its appearance depends heavily on mass ratio m^* , while ‘2C’ wake shape appears only in the vibration of rotationally elastically-supported cylinder [9]. The diagrams of various wake shedding modes are shown in Fig. 2.3. ‘2S’ in the figure indicates that there are two single shedding vortex in each vibration cycle, ‘2P’ indicates that there are two pairs of counter-rotating shedding vortex in each vibration cycle, ‘2C’ represents two pairs of co-rotating vortex shedding in each half of the vibration cycle, and ‘2T’ represents that there are three shedding vortex in each half cycle.

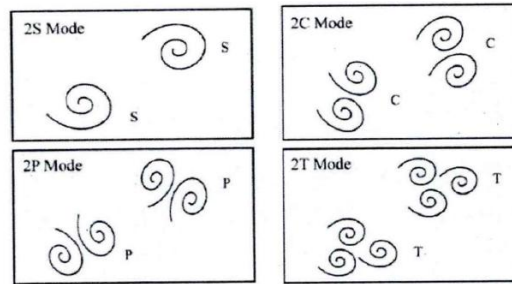


Figure 2.3: Wake modes from vortex-induced vibration summarized by Jauvitis and Williamson [6][7] and Govardhan and Williamson [8][9] .

With respect to the studies on galloping behaviors, Zhao et al. [46] experimentally investigated the dynamic response (including lock-in and galloping) of the flow past an elastically-mounted forward- or backward-facing D -section. While the forward-facing D -section exhibited lock-in and galloping regimes in turn as the reduced velocity was increased, the backward-facing D -section only exhibited the lock-in regime. This study [46] also applied Den Hartog’s stability criterion (discussed later) in order to explain the differences in response caused by the different facing orientations of the obstacle in the flow.

The flow-induced vibration of a large side-ratio elastically-mounted rectangular cylinder in a turbulent flow was investigated experimentally by Zhao et al. [35]. These investigators found that as the ratio of the cross-flow side width to the streamwise side width varies from 2 to 5, the response of the FIV system exhibits a significant and sudden change. More specifically, it was found that side ratios from 2 to 4 display a galloping instability with the amplitude increasing with the reduced velocity. In contrast, for a side ratio of 5, the system was found to transition abruptly to a desynchronization branch after the lock-in range. This is the so-called “galloping-

collapse” behavior. However, the investigation conducted by Zhao et al. [35] did not provide a theoretical explanation for this sudden disappearance of the galloping instability with increasing ratio of the cross-flow to streamwise side width.

Brankovic and Bearantz [47] has carried out experiments on the free vibration of a single circular cylinder in the range of Reynolds number from 3000 to 21000. The mass ratio m^* is higher than 0.8, but the damping ratio is very small and about 0.002. Through the experiments, the relationship between the transverse fluid force/the phase angle and the reduced velocity is obtained, and the jumping phenomenon of the phase angle is observed. In addition, Parkinson and Ferguson [48][49], Griffin and Ramberg [50][51], Sumer and Fredsoe [52], Gerrard [53], Zdravkovich [54] and others have discussed the natural characteristics of FIV in their papers or monographs. Pantazopoulos [55], Bearman [56], Gabbai and Benaroya [57] and Sarpkaya [40] have also made a good review of various types of FIV experiments.

2.1.2 Energy harnessing

FIV can cause fatigue damage of slender structures, which has a negative impact on the smooth development of ocean, road and bridge engineering, but it may also benefit us. When FIV occurs, the structure will produce periodic vibration, which can be converted into useful electrical energy by means of transmission device or piezoelectric generator [58][59][60]. This kind of power can be used for industrial applications, such as power supply for roads, bridges, street lights, underwater monitoring devices, offshore platform facilities, etc.

In the past decade or so, many researchers have used experimental and numerical methods to study how to capture energy by FIV of rigid cylinder, and have derived the prediction model of FIV of rigid cylinder coupled with energy capture device. Bernitsas’s research group at University of Michigan [10][61] proposed the design scheme of laying the bundle of rigid cylindrical tubes underwater to obtain energy, which is relatively comprehensive research for energy acquisition based on VIV, as shown in Fig. 2.4. The VIV-based energy utilization unit is referred to as VIVACE Converter.

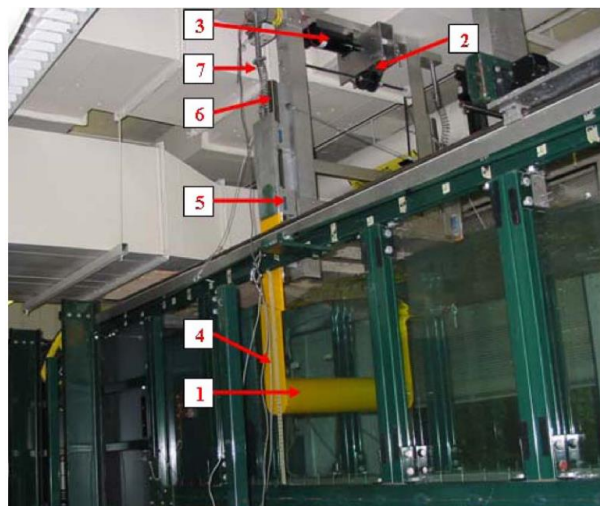


Figure 2.4: VIVACE energy harnessing units based on VIV [10].

Kim [62] try to maximize the synergy of multiple parallel cylinders in fluid induced motion (FIM) to realize the utilization of water kinetic energy. Kim studied the effect of tandem spacing,

staggering, passive turbulence control (PTC), mass ratio, spring stiffness, damping, and cylinders number on FIM response. Two kinds of channel are used in their research, including the old Low Turbulence Free Surface Water (LTFSW) Channel and the new LTFSW Channel, new channel could help the FIM system to get the high oscillation amplitude. VIVACE is tested in the old LTFSW Channel with high Reynolds numbers in the range of $28,000 < Re < 120,000$, and four cylinders with identical diameter $D = 3.5$ cm and length $L = 36$ cm are solidly connected. The maximum amplitude reached $2.2D-2.8D$ which was the limit of the old LTFSW Channel in the galloping region of FIM. In the investigation of VIVACE operating in the new LTFSW Channel, tandem spacing of cylinders in the range of $28,000 < Re < 120,000$ was conducted. For this smallest spacing of $1.43D$, both smooth and roughened cylinders exhibited distinct response with higher amplitude and lower oscillation frequency compared with those of other spacings.

Sun et al. [63][64][65] continued the research on VIVACE in University of Michigan, and studied the effect of damping, mass-ratio and stiffness with respect to the energy conversion of a single cylinder in VIV. The oscillator have the ability to harness energy from water flow with velocity low to 0.3946 m/s. The synchronous branch will be shifted to a higher Reynolds number by the increase in spring stiffness, resulting in the gap between VIV and galloping, in which the power output will drop. A company named VORTEX Bladeless [66] in Spain is also trying to develop a VIV-based wind generator, which is funded by the European Union's Horizon 2020 research and innovation.

Besides the application of energy harvester using lock-in behavior as the fundamental underpinning theory, the academics also try to apply galloping phenomena to harness power. The topological equivalent aerodynamic method is introduced by Zhao et al. [67] to design a funnel-shape galloping energy harvester with wide working wind-speed range and high normalized harvesting power. Harvey et al. [68] tried to develop one galloping energy harvester, a curved blade oriented perpendicular to the incident flow, which is capable of producing self-sustained oscillations at uncharacteristically low wind speeds. A square cylinder with a V-shaped groove on the windward side in the piezoelectric cantilever flow-induced vibration energy harvester (FIVEH) is presented by Zhao et al. [69] to improve the output power of the energy harvester and reduce the onset velocity for the power output, for the purpose of the self-powered supply of low energy consumption devices in the natural environment with low wind speed.

2.2 Numerical investigations of FIV

2.2.1 Computational fluid dynamics

Because FIV is a complex fluid structure coupling phenomenon, and involves many parameters, the influences of parameters on FIV is difficult to be fully investigated by the experimental system. In addition, it is almost impossible to obtain all the dynamics information of fluid domain only by experiments if various parameters and vibration conditions are considered, and reveal the relationship between flow responses and system parameters. The numerical simulation method, which is not limited by the experimental conditions, can flexibly adjust the parameters, thus revealing the influences from parameters and predicting the results. With the development and progress of computer technology, it has become an important technical tools to simulate VIV by computational fluid dynamics (CFD). With respect to CFD methods, there are three kinds of numerical calculation methods used to undertake the FIV calculations in the literature: Direct

Numerical Simulation (DNS), Large Eddy Simulation (LES), Reynolds Averaged Navier-Stokes (RANS), and the synthesis of the above methods.

Direct numerical simulation (DNS) is to directly solve the N-S equation of turbulent motion. Because there is no skillful or model approximation for the turbulent flow, it is a kind of turbulence numerical simulation method with the highest degree of refinement. The instantaneous flow field of turbulence can be obtained, and all the information of turbulence can be obtained, and the relatively accurate results can be obtained theoretically. Evangelinos et al. [70] used the DNS method to simulate the VIV of a rigid and flexible circular cylinder with $Re = 1000$, and made two assumptions: the structural damping is zero and the structural natural frequency is locked in the St number under the condition of flow passing fixed circular cylinder. Blackburn et al. [71] have carried out two-dimensional(2-D) and three-dimensional(3-D) DNS and experimental research on vortex-induced vibration of a single rigid cylinder at low Reynolds number ($Re < 500$). The numerical simulation and experiment adopt the same parameters. The simulation results are similar to the experimental results with respect to the 3D flow field, and the results of 2-D and 3-D flow field simulation are different under the same Reynolds number. At the same time, the change of phase angle ϕ is also studied by the DNS method with $Re = 500$ [72]. The researchers who use DNS to simulate VIV with higher Reynolds numbers of 3900 and 10000 are Ma et al. [73] and Dong et al. [74] respectively. In recent years, George and Ducoin [75] simulated the three-dimensional incompressible fluids dynamics using DNS and coupled it with the motion equation to investigate the laminar-to-turbulent transition-induced vibration system consisting of a rigid NACA66 hydrofoil supported by the elastic axis by a torsional spring and damper. The hydrofoil is fixed at angle of attack of 4° and limited to move in transverse direction. Re of incident flow is 450,000. The results show that the airfoil vibration strongly affects the pressure gradient of the hydrofoil, thus changing its transition position and boundary layer properties, and in addition these properties are proportional to the amplitude and frequency ratio of the airfoil vibration. Chen et al. [76] used 3-D DNS method to investigate the FIV response of one elastically-mounted circular cylinder near a stationary wall at a subcritical Reynolds number of 500. However, due to the various scale quantities in turbulence, any disturbance on the boundary may lead to the generation of new small-scale quantities or increase the original small-scale quantities. Therefore, DNS will become very expensive in terms of computing resources and can not meet the complex engineering flow problems.

The basic idea of Large Eddy Simulation (LES) is to give up the simulation of eddy motion in the full scale of flow field, and decompose the turbulent motion into two parts: small-scale eddy motion and large-scale eddy motion. The large-scale turbulent motion or vortex passage is directly calculated by the instantaneous Navier-Stokes equation, while the sub grid scale (SGS) model is established to approximate the effect of small-scale motion on large-scale motion, which is shown as an additional sub-grid Reynolds stress term in the equation. In 1941, Kolmogorov proposed the k41 theory of dissipation mechanism [77][78], and considered that the small-scale turbulent motion is approximately isotropic. The Large Eddy Simulation (LES) with engineering significance was first carried out by Deardorff [79] in 1970. Subsequently, LES has been successfully applied to the numerical simulation of various turbulent flows. Dalheim [80] and Herjford et al. [81] also used LES method to simulate the free vibration of a single circular cylinder subjected to uniform incoming flow. Zhang and Dalton [82] used LES method to simulate the 2-D transverse vibration of a circular cylinder with $Re = 13000$. Janocha et al. [83] performed the LES calculation to investigate the flow past a vibrating cylinder in the subcritical Reynolds number regime at $Re = 3900$.

Although DNS and LES methods can provide insight into the interaction mechanism of wake boundary layer in FIV response, the Reynolds Averaged Navier-Stokes (RANS), which has the advantages of robustness and less running time, has become the main numerical calculation method to solve the turbulence problem. In this method, instantaneous quantity is decomposed into its time-averaged and fluctuating quantities, and then the governing equations are time averaged. When the turbulence model is used to simulate the turbulence effect, the calculation results are greatly affected by the kinds of turbulence model. Pan et al. [84] used RANS code to simulate the two-dimensional VIV of an elastically-supported rigid cylinder with low mass damping ratio. In the upper and lower branches, the 2P vortex shedding mode is consistent with the experimental results. The vortex mode changes accompanied by the change of frequency ratio through the lock-in region. Guilmineau and Queutey [85] also used the two-dimensional incompressible Reynolds averaged N-S equation to simulate the VIV of a rigid cylinder with $k-\omega$ turbulence model, the Re range is 900-15000, and the vibration of the cylinder in the flow direction is limited. The maximum amplitude is consistent with the results from the experiment of Khalak and Williamson [41], but the upper branch does not show good conformance. Wanderly et al. [86] numerically solved the two-dimensional RANS equation to study the static status and VIV of rigid cylinder. The $k-\epsilon$ turbulence model was used to close the governing equations. The lift, drag coefficient and St number are basically consistent with the numerical and experimental results of other researchers. The VIV response of two rigidly connected circular cylinders in side-by-side and tandem arrangements is numerically investigated by Zhao et al. [87] with RANS SST $k-\omega$ model. The vortex-shedding phenomenon from the upstream cylinder disappears for the gap ratio of 0.5 in the tandem unit at large reduced velocity, and the accompanied structural response is determined as galloping behavior. The Arbitrary Lagrangian Eulerian (ALE) scheme is also used here for solving the governing equations. Furthermore, Catalano et al. [88] simulated the VIV with $Re = 0.5 \times 10^6$ and 1×10^6 in Fluent CFD software using RANS method (standard $k-\epsilon$ model) and LES method (with wall model implementation), and compared the results of the two methods. The results show that the accuracy of RANS results is within the allowable error range, and the lift, drag coefficient and S_r number are more consistent with the experimental results than LES model. In addition, Xu & Zhu [89] used RANS solver combined with SST $k-\omega$ turbulence model to simulate the transverse and in-line motion of elastic support cylinder with a low mass ratio, and the ‘2T’ vortex shedding mode were captured. Khan et al. [90] undertook the CFD investigation of the VIV system using RANS models (SST $k-\omega$ model) in ANSYS FLUENT, and the Reynolds number is fixed at 10,000. The results exhibit high conformance to that using DES, LES, and DNS models. The vortex-shedding phenomenon from the upstream cylinder disappears for the gap ratio of 0.5 in the tandem unit at large reduced velocity, and the accompanied structural response is determined as galloping behavior.

In terms of the energy harnessing researches based on VIV with numerical method, Barrero-Gil et al. [91], Luo et al. [92] and Wang et al. [93] studied the sensitivity of energy harnessing efficiency of rigid cylindrical structure to system parameters under 1-DOF by numerical method. The results show that the mass-damping ratio, Reynolds number, natural frequency and reduced velocity have significant effects on the harnessing efficiency. Naseer et al. [94] studied the effect of additional magnetic poles on the energy trapping performance of a conventional rigid cylindrical VIV piezoelectric energy harvesting structure, and additional magnetic pole is used to increase the bandwidth of the ‘lock-in’ region of the VIV of a rigid cylinder. Pan et al. [95] studied the energy capture characteristics of a rigid cylinder based on piezoelectric units by means of experiments and multi-body dynamics simulation. The results show that the trapping charge

level is related to the flow velocity and cylinder diameter. The maximum electromechanical conversion efficiency can reach 17.8 %. Based on the wake oscillator model, Franzini and Bunzel [96] studied the energy capture characteristics of VIV of rigid cylinder with 1-DOF and 2-DOF by numerical method. The results show that the maximum energy harvesting efficiency can reach 50 % with proper parameters. In addition, they also studied the parameter sensitivity of the wake oscillator model in the model, and pointed out that the parameter selection of the wake oscillator model must be based on, otherwise the calculation results will be greatly affected. Chen et al. [97] used the immersed boundary method to study the structural and wake responses of the FIV system consisting of laminar flow past elastically-mounted D -section body at varied angles of attack with $Re = 100$. However, the lack of small vortex resolution in RANS model will limit its use in aeroacoustics calculations. Therefore, this thesis will use DES, the combined model of LES and RANS, to resolve the flow field in the calculations of aerodynamic noise propagation.

2.2.2 Linear stability analysis

Accurate hydrodynamic model is an important basis for analysis, control and optimization. For example, the analysis of maneuverability and stability in flight mechanics, the flutter analysis in aeroelasticity and the FIV problem studied in this thesis need to rely on high-precision unsteady flow simulation to obtain accurate aerodynamic parameters. A simple and accurate flow analysis model is also of great significance to understand the complex flow mechanism of high-dimensional and nonlinear, and to carry out flow control [98].

In order to establish accurate unsteady hydrodynamic and aerodynamic models, researchers have developed various methods based on linearization theory since 1990s, such as quasi steady Grossman and Theodorsen models for two-dimensional problems, vortex lattice method and dipole grid method for three-dimensional wing. For hypersonic flow, piston theory and its improved method have been developed. The computational fluid dynamics (CFD) has gradually become the most widely used aerodynamic method in the fluid mechanics field with the rapid evolution of computer technology. Based on the high-dimensional and nonlinear governing equations of unsteady flow field (such as Euler equation and Navier-Stokes equation) and high-precision numerical solution technology, CFD method can accurately describe the detailed information of unsteady flow field evolution with time with full-order model (FOM), and reproduce the physical characteristics of flow, so as to accurately obtain the unsteady aerodynamic characteristics. However, the aerodynamic simulation method based on unsteady CFD technology not only has a large amount of calculation and time-consuming, but also involves the solution of high-dimensional flow equation, which is not convenient for the qualitative analysis of the system, and brings many difficulties for the development of model engineering and the mechanism interpretation of complex flow phenomena. In view of this, a simple and accurate flow analysis model is also of great significance to understand and gain deeper physical insights into the characteristics of the complex and highly nonlinear fluid flow underpinning FIV [98].

Models used in the context of theoretical investigations should be accurate, efficient, elegant, and intuitive. To this purpose, researchers have developed a variety of reduced-order models [99, 100] in order to reduce the computational cost of full-order fluid flow simulations and to extract the main characteristics of the fluid system in order to provide the basis for the interpretation and analysis of the complex system. By using numerical data obtained from a small number of high-fidelity computational fluid dynamics (CFD) simulations, ROMs can be developed which can achieve levels of accuracy comparable to those obtained from a full CFD simulation, thereby

reducing the computational cost of unsteady aerodynamic/aeroelastic prediction by one-to-two orders of magnitude while maintaining good accuracy. This advantage makes it easy to couple various component-level ROMs into a system-of-systems simulation and to apply it to applications involving multidisciplinary analysis, control, and optimization design allowing one to analyze the dynamical behaviour of these complex systems quickly.

Dowell et al. [101] believes that the unsteady aerodynamic models can be divided into three categories: Firstly, pure linear models. That is to say, the static and dynamic aerodynamic forces of the research object conform to the linear characteristics. Secondly, the static nonlinearity is accompanied by the dynamic linear model. This situation means that the flow is non-linear in space (for example, there is discontinuity in space) and obeys linear relationship in time, which is also called time linearization model. The linear system identification method and the state space method are all of this kind of model. The model is usually applicable to the unsteady flow of structures under small disturbance when shock wave and flow separation exist at transonic speed and high angle of attack. Thirdly, dynamic nonlinear model. With the increase of the amplitude of motion, the aerodynamic characteristics of dynamic nonlinearity gradually become obvious, and the hypothesis of small disturbance is invalid. Since the complete linear model is usually suitable for steady and quasi steady small disturbances, the unsteady aerodynamic ROM based on system identification mainly focuses on the latter two dynamic characteristics.

It is important to note that FIV systems are nonlinear in general. As a result, linear stability analysis (LSA) can be used to analyze such systems (and, in particular, to study their dynamical characteristics) only when the effects arising from the nonlinear interactions are not dominant [101]. In this case, the information embodied in the eigenvalues of the coupled system that models the interaction between the vibrating structure and the surrounding fluid flow can be used to assess the stability characteristics of this system. More specifically, in order to apply LSA to a system, a time-linearized aerodynamic model needs to be obtained using some form of a system identification methodology such as the eigensystem realization algorithm (ERA) [102] or an autoregressive with exogenous input (ARX) model [103]. Both of these methodologies can be (and have been) used to construct mathematical models of the dynamical characteristics of a VIV system from the measured input and output data. The detailed introduction to the specific LSA analysis and modal evaluations on lock-in and galloping behaviors will be presented in the following sections 2.3.2 and 2.3.3.

2.3 Triggering and enhancement of FIV

2.3.1 Effect of nonlinear restoring forces on lock-in behavior

The studies referenced above concern the nature of FIV for a body (structure) supported by a linear spring-damper system whereby the stiffness of the spring is constant implying that the spring force is linearly proportional to the displacement of the supported body. However, most spring support systems used in engineering problems, which include various applications in vehicle, civil, traffic and ocean engineering are nonlinear in nature implying that the stiffness of the spring does not remain constant as a function of the displacement of the body. Moreover, the characteristics of a nonlinear spring-damper system is different from that of a linear spring-damper system, and will require further research when such a system is coupled with a fluid dynamical system.

In recent years, some experimental studies of the VIV effects on a structure supported on a nonlinear spring-damper system have demonstrated that the nonlinear restoring forces in the system have a significant impact on the lock-in range of reduced velocity and on the amplitude of the induced vibration. Stappenbelt [104] experimentally investigated the influence of compliance nonlinearity on the VIV response of an elastically-mounted rigid cylinder in a steady, uniform flow. The point at which the initial lock-in occurs seems to remain unchanged in comparison to the case of linear compliance, but the whole lock-in range becomes greater with the nonlinear restoring forces. Wang et al. [105], Ramesh et al. [106] and Barton et al. [107] conducted careful studies on the effect of nonlinear restoring forces on the operation of energy harvesting devices. These researchers found that the increased lock-in range and the enhanced amplitude of the concomitant vibrations arising from the nonlinear restoring forces are conducive to the optimization of the energy harvesting quality of the devices through an enhancement of the flow-induced motions in the system.

Huynh et al. [108] numerically and experimentally investigated the VIV response for two types of nonlinear stiffness, namely bi-stable stiffness and hardening stiffness. The bi-stable stiffness has the potential to allow the system to operate in water flows at lower velocity. On the other hand, the hardening stiffness has the potential to extend the operating range into water flows at high velocity, which could improve potentially the overall performance of a VIV-based energy converter. However, the numerical model used in the study conducted by Huynh et al. [108] was based on a simple wake oscillator model, with a simple periodic excitation force included in the structural equation, rather than on a more rigorous fully-coupled FSI model. Sun et al. [109] experimentally investigated hydrokinetic power conversion using flow-induced vibrations with nonlinear (adaptive piecewise-linear) springs. Results for the amplitude response, frequency response, and energy harvesting efficiency are presented and discussed in this study. Moreover, Sun et al. [109] divided the experimental amplitude response into four performance zones according to the VIV response. Finally, in this study, it was shown that an optimal power harnessing can be achieved by changing the nonlinear piecewise-constant spring function.

In spite of these studies, it is noted that research on the VIV phenomenology associated with structures supported by nonlinear spring-damper systems is rather limited. Wang et al. [110] studied the effects of a cubic stiffness nonlinearity on the VIV of a circular cylinder for a low-Reynolds number flow, with a nonlinear spring incorporating the hardening spring nonlinearity and the softening spring nonlinearity. It was shown that the softening spring nonlinearity alters the amplitude of the lock-in range, but does not change the distribution of the various branches associated with this lock-in range. On the other hand, with increasing hardening spring nonlinearity, it was shown in the study that the branch distribution of the lock-in range is significantly altered accompanied by a relatively large amplitude of oscillation over a wider range of reduced velocity U_r . In short, the VIV phenomenology for structures that are supported by a nonlinear spring-damper system are significantly different than those supported by a linear spring-damper system.

Badhurshah et al. [111] studied the effect of a bi-stable spring (rather than a linear spring) on the VIV response of a circular cylinder submerged in uniform laminar flow at $Re = 150$. This numerical study was conducted using an immersed boundary method to address a moving boundary value problem on a two-dimensional domain. The results of these simulations showed that a bi-stable spring could increase the lock-in range compared to that of a linear spring for high mass ratios, with the implication that a VIV system mounted on a bi-stable spring may be useful for the design of energy harvesters. Mishra et al. [112] numerically investigated the VIV

of a rigid circular cylinder coupled to a Standard Linear Solid (SLS) device at $Re = 150$ in order to study the viscoelastic effect. The SLS could be regarded as a normal linear spring-damping unit superposed in parallel with an nonlinear spring-undamping unit. The mass ratio was fixed at 2.546, and the effect of the nonlinearity on the VIV response was investigated by adjusting the parameters associated with the strength of the nonlinearity in the structural control equation. The results obtained in this study, which include the increased lock-in range arising from the use of an nonlinear spring and the effects of the nonlinearity in hardening and softening springs on the VIV response, are consistent with the findings reported by Wang et al. [110].

In view of above discussion, the chapter 3 of present thesis will focus on a two-dimensional (2D) numerical VIV study of a circular cylinder mounted on linear and nonlinear springs for a low Re -number flow. To this purpose, we analyze the impact of the spring nonlinearity on the VIV response, focusing specifically on the differences in the amplitude variation, the phase change, the frequency variation and characteristic wake pattern between the linear and nonlinear spring-mounted cylinder.

2.3.2 Modal evolution of lock-in behavior

Section 2.2.2 presents the background information and past development of linear stability analysis (LSA), this section will introduce some practical applications of LSA as well as the data-driven analysis in the FIV investigations in recent years.

Zhang et al. [12] used a ROM to study the physical mechanisms of VIV for flow past a circular cylinder at a Reynolds number of 60. Zhang et al. showed that a ROM can provide some deeper insights into the underlying modal mechanism of VIV, whereby the modes so obtained from the model can be divided into structural and wake modes according to the characteristics of the root loci (in contrast with the results obtained from a FOM). Furthermore, these investigators found that the lock-in range can be divided into a resonance and a flutter regime. The resonance lock-in mechanism is interpreted to be caused by the frequency proximity of the structural and wake modes, while the flutter lock-in mechanism is instead correlated with an unstable structural mode arising from the modal coupling interaction. The modal behavior of a FIV system is either coupled or uncoupled, depending on whether there is a clear distinction between the root loci associated with the structure and wake modes. For a FIV system with two coupled modes (which we label herein as WSMI and WSMII), it is necessary to determine which of these two modes represent the hidden structure mode at each value of the natural frequency F_s —indeed, the hidden structure model (labelled as SM_c herein) can be WSMI at one value of F_s and switch to WSMII at another value of F_s (or vice-versa), a process which is described as “mode veering” by Gao et al. [113]. The proper identification of the hidden structure mode SM_c for a FIV system in a coupled modal condition will be investigated later in this thesis.

Zhang et al. [12] obtained their reduced-order model for the fluid dynamics using an ARX identification methodology. The ARX model is a linear dynamic model based on a discrete difference equation. The basis of this model is to represent the current system output as the linear superposition of current input and the previous (in time) inputs and outputs. An alternative to the ARX model is the autoregressive moving average (ARMA) model [114].

Navrose and Mittal [14] subsequently investigated the lock-in phenomenon for flow past an elastically-supported cylinder using global LSA based on the linearized Navier-Stokes equations, with the main conclusions similar to those obtained by Zhang et al. [12]. For the case of low

and high mass ratios, the interaction between the fluid and the solid modes are coupled and uncoupled, respectively. Furthermore, Navrose and Mittal [14] analyzed the transfer of energy (kinetic energy of the cylinder, potential energy of the spring, and disturbance energy of the wake flow) within the lock-in range for cases involving different mass ratios.

Yao and Jaiman [15] investigated vortex-induced vibration of bluff bodies with different cross-sectional shapes using a reduced-order model. The shapes include an ellipse, a forward triangle, a diamond, and squares with varied rounding radii. In this study, Yao and Jaiman [15] constructed a stability phase diagram summarizing succinctly the dominant lock-in types (resonance or flutter) for different cross-sectional shapes in the Reynolds number range of $30 < Re < 100$ based on the characteristics of the root loci. To this purpose, Yao and Jaiman used ERA, which is a linear system identification method based on the impulse response of the system. ERA was originally formulated by Juan and Pappa [115] who used it to investigate the modal parameter identification of structures associated with the space shuttle. Because ERA is based on the minimum realization principle of control theory and has a sound theoretical basis, it has been widely applied in aerodynamic modelling problems involving linear dynamics. For example, Silva and Bartels [116] developed a reduced-order model for aeroelastic analysis and flutter prediction using ERA and applied it to the aeroelastic stability analysis of an AGARD445.6 wing [117]. Brunton et al. [118] established aerodynamic models of two-dimensional flat plates and three-dimensional wings in the test environment using ERA. The results show that this method can accurately establish aerodynamic models under different equilibrium positions. In some further work, Yao and Jaiman [119] applied an active feedback consisting of a uniform blowing and suction on the surface of a circular cylinder in order to achieve the suppression of the vortex street and the VIV in the elastically-mounted structure. The analysis here was based on a model reduction for the VIV of the circular cylinder using ERA. The feedback control system, based on an actuator configuration with a blowing and suction over the porous surface of a circular cylinder, was shown to be capable of suppressing the nonlinear saturated state of vortex shedding in the wake of the circular cylinder.

Chizfahm and Jaiman [120] obtained a reduced-order model for the fluid dynamics of a sphere using ERA and constructed a coupled FSI model. Moreover, the effects of the near-wake jet (attached on the downstream side of the sphere) on the VIV response was investigated in this study. These results showed that this arrangement resulted in the suppression of large-amplitude oscillations and can be regarded as a suppression control device. Li et al. [121] applied ARX to investigate the wake-induced vibration for a configuration consisting of two identical circular cylinders in an in-line tandem arrangement and used this arrangement to investigate the stability of the downstream cylinder for a spacing between the two cylinders of twice the cylinder diameter. This study showed that the Reynolds number and mass ratio have significant effects on the structural response of the downstream cylinder. An important advancement of the application of stability analysis to high-Reynolds number flows was made by Chizfahm and Jaiman [122], who used a recurrent neural network (based on a long short-term memory cell) in conjunction with the ERA, in order to obtain a nonlinear state-space model for the VIV of a freely vibrating sphere at Reynolds numbers up to 2000.

According to Yao and Jaiman [15], the application of the ARX method to VIV does not have a rigorous mathematical basis and, moreover, is sensitive to the input signal. In contrast, ERA has a more rigorous theoretical basis in fluid dynamics and, hence, is more appropriate for the analysis of the unstable linear system generated by VIV. In view of this, following the work of Yao and Jaiman [15], Flinois et al. [123] and Ma et al. [124], ERA will be used as the system

identification method to build a low-order fluid model in the present study.

In spite of the research cited above, there still remains much that is unknown regarding the physical mechanisms underlying the fluid-structure coupling of a single circular cylinder and, as a result, this canonical case needs to be investigated further on a fundamental level. Yao and Jaiman [15] investigated the modal mechanisms responsible for a VIV system consisting of a flow past a cylinder. In this investigation, the authors suggested that the frequency lock-in for VIV is solely the result of a flutter-induced lock-in for $Re > 70$. Indeed, this suggestion is still open to discussion as conclusions from previous studies such as Zhang et al. [12] and Navrose and Mittal [14] are all conducted for flows with Reynolds number less than 100. To this point, we shall carry out systematically a large number of simulations of flow past a circular cylinder for various combinations of the Reynolds number Re , the mass ratio m^* , and the reduced natural frequency F_s ; and, more specifically, for Re ranging from 20 to 180, for m^* ranging from 5 to 50, and for F_s ranging from 0.05 to 0.30. This comprehensive set of simulations will allow us to address the important issue of the effect of Reynolds number on the relevant mechanisms underlying VIV and, moreover, will allow us to re-examine the Yao and Jaiman assertion alluded to above.

Critically, the present work will focus on introducing some novel modal behaviors which include various mode transformations and interactions, which are then used to explain some subtle features such as the beating phenomenon which occurs in the initial branch and the significant lag time that ensues between the initial branch and the occurrence of the fully-developed response in the lower branch that have been overlooked previously. In so doing, this bridges some important gaps in our current understanding of this phenomenon and, indeed, the results from the careful analysis conducted herein will be used to redress some of these key limitations and to reduce some critical knowledge gaps on the VIV response of a circular cylinder arising from some prior efforts. Towards this objective, FOM/CFD will be used in conjunction with ROM/ERA and supplemented with power spectral analysis and dynamic mode decomposition to provide deeper insights and a better understanding of the physical processes underlying the lock-in phenomenon and to study in greater depth the influence of the Reynolds number on the fluid-structure interaction. Using this approach, we reveal and explain the characteristics of the vibration response for each branch (initial, lower, and upper) of the lock-in range.

It is acknowledged that the Neimark-Sacker bifurcation may have a possible effect on the VIV response of an elastically-mounted cylinder at Reynolds number of about 180. One needs to be careful in the interpretation of the dynamical characteristics of a VIV system obtained using LSA based on ROM/ERA as the nonlinear effects in the system may not be accounted for properly (especially for flows at higher Reynolds numbers). With this caveat, we follow the lead of prior efforts in the application of LSA to the analysis of FIV systems (e.g., flow past a sphere at $Re = 300$ [120] or a square cylinder at $Re = 150$ [16]) and use ROM/ERA to elucidate the modal dynamics associated with a flow past an elastically-mounted circular cylinder for $20 \leq Re \leq 180$.

2.3.3 The triggering of galloping behavior

Among the various patterns of FIV motion, the galloping instability—a special kind of unbounded vibration—is most likely to induce a large-amplitude oscillation in structures and, consequently, understanding the physical mechanisms underpinning this phenomenon is an important and active area of fundamental research. Galloping behavior is commonly encountered for

elastically-mounted objects with non-circular cross-sections submerged in high-speed liquid or air [34]. For instance, unlike the FIV response of a circular cylinder which will transfer into desynchronization after the lock-in range with increasing inflow velocity, the FIV response of a square cylinder will involve galloping instability [35, 36]. The lock-in phenomenon will occur only when the structural natural frequency is comparable to the vortex-shedding frequency, leading to induced oscillations with limited vibration amplitude. In marked contrast, the galloping instability will appear over a broad range of the incident velocity of the incoming flow (implying that the structural natural frequency does not have to be comparable to the vortex-shedding frequency) and, moreover, the amplitude of vibration for this phenomenon is known to increase with increasing incident flow velocity [35, 37, 36]. Furthermore, galloping is generally a low-frequency oscillation (viz., occurring at frequencies that are much lower than the vortex shedding frequency).

Galloping instability has important consequences for engineering applications and, in particular, for construction engineering. For example, slender structures with a square section are widely used in engineering construction (e.g., high-rise and towering structures, transportation trestle bridges, and corridors). However, owing to the aerodynamic characteristics of a square section, these structures may gallop under the action of the wind and this buffeting response may lead to fatigue damage to various structural components and connections, which can lead to an increased probability of physical harm, property loss, or environmental impact. The galloping of an ice-coated transmission line is a common example of such concerns. The ice coating can change the shape of the cross-section of the transmission line by forming crescent-shaped, fan-shaped, or *D*-shaped cross-sections [38]. This change in the cross-sectional shape of the power line in conjunction with the slenderness of the structure and the presence of a crosswind can potentially induce large-amplitude wind-induced vibrations in the structure, leading to fatigue of and damage to conductors and even to dragging down the transmission tower.

As introduced in section 2.1.1, through theoretical analysis, numerical simulations, and experiments, it is known that the shape of the outline of a structure and the angle of attack (or, direction of the incoming flow) are important factors that determine whether galloping instability occurs. Additionally, a key difference from the lock-in behavior is that the initial state of the FIV system can sometimes determine whether the galloping instability occurs. More specifically, galloping can be classified as patterns of soft-galloping or hard-galloping [125, 126]. Soft-galloping is thought to be a self-initiated oscillation that requires no initial displacement, velocity, or external forces. In contrast, the triggering of hard-galloping requires an initial structural displacement (or, velocity) to exceed a certain threshold [126]. Lien et al. [127] conducted experiments on the responses associated with soft-galloping and hard-galloping of elastically-mounted isosceles-triangular prisms (where the base of the isosceles triangle is perpendicular to the incident flow) in a water channel with a Reynolds number $Re \approx 10^5$. This study investigated the influences of the structural mass, stiffness, damping, and aspect ratio (viz., ratio of the height to the base of the isosceles triangle) on the response. The resulting measurements demonstrated that a low-aspect ratio (less than about 0.866) will initiate a hard-galloping of the isosceles-triangular prisms. In the study of *D*-sections conducted by Zhao et al. [46] mentioned previously, it was found that the forward-facing *D*-section can gallop “softly” from rest, in marked contrast to the characteristics of the hard-galloping response of *D*-sections reported by some previous investigations [128, 129]. Taken as a whole, these experimental studies seem to suggest the following hypothesis: the shape of the after-body of an object determines whether the galloping instability belongs to either the hard or soft patterns of flow-induced vibration response.

In addition to numerical simulations and experimental tests, theoretical analysis has been applied to the investigation of galloping instability. However, the application of theoretical methods for investigating galloping is challenging owing to the complexity of the underlying dynamics. The seminal theoretical investigations of galloping instability can be traced back to the work of Den Hartog [130, 131]. In accordance to Den Hartog, when an object is immersed in a fluid flow with a uniform and constant velocity, the lateral oscillation of the object will cause the relative speed of the incoming flow to vary in magnitude and direction with time. As a result, the angle of attack will change with time which, in turn, will affect (modify) the aerodynamic forces acting on the object. Under certain circumstances, the influence of the varying aerodynamic forces on the object will result in a negative damping in the FIV system, causing the structure to continuously absorb energy from the surrounding fluid and, consequently, to generate violent oscillations. Owing to the validity and clear physical insights provided by Den Hartog’s stability criterion, this criterion has been widely used in the analysis and assessment of the structural stability in various fluid-structure coupling applications of engineering interest [49, 34, 46].

However, owing to the fact that Den Hartog’s stability criterion considers only the change in the aerodynamic force as a function of the incident fluid flow direction, the application of this criterion is rather limited for the general and comprehensive analysis of fluid-solid coupling problems. As a consequence, Den Hartog’s stability criterion has been utilized essentially as a kind of quasi-steady analysis in these types of problems. From this perspective, other quasi-steady models [132, 133] that have been proposed and developed subsequently are all subject to the same limitations—namely, the inability to accurately predict certain special galloping behaviors and the value of the onset reduced velocity U_r that triggers the galloping instability. In spite of this, Den Hartog’s stability criterion is still useful in that it can provide researchers with an analytical framework to better understand certain aspects of the galloping phenomenology. As a consequence, we will use this analytical framework for certain analysis conducted in this thesis with a clear recognition of its limitations. To this purpose, the derivation of Den Hartog’s stability criterion and the limitations of its application will be discussed in detail herein.

Research breakthroughs on understanding the physical mechanisms underpinning the galloping phenomenon, which build on insights obtained from experimental investigations, computational simulations and theoretical analysis, have still not provided a complete understanding of this complex phenomenon.

As presented above, the application of linear stability analysis (LSA) [12, 15, 14] has provided deeper insights into the underlying physical mechanisms underpinning FIV phenomenon. While investigating the influence of sharp-corner rounding on the flow dynamics of an elastically-mounted square cylinder, the range of Re used in the study conducted by Yao and Jaiman [15] was too low to observe the triggering of the galloping instability and, in this sense, the study was limited primarily to the lock-in behavioural characteristics of the square cylinder. However, it can be argued that galloping is perhaps the most significant phenomenon that needs to be considered in the stability analysis for the vibration of bodies with non-circular cross-sections, leaving an important gap in our current knowledge of the effects of shape in the transition of the vibration response characteristics from lock-in to galloping.

Following the work of Zhang et al. [12], Li et al. [16] sought to explain the galloping instability of the square cylinder by utilizing the idea of modal competition (viz., the interaction between SM and WM that can result in a “winning” mode which ultimately dominates the vibration). In this study, this idea was explored using ROM/ARX, FOM/CFD, and dynamic mode decomposition (DMD). The result of the analysis was that modal competition was found to be

present throughout the entire range of the reduced velocity U_r (which include the lock-in, galloping, and desynchronized regimes). This work demonstrated that the instability of the structure mode (SM) leads to large-amplitude and low-frequency vibrations of the structure, whereas the instability of the wake mode leads to high-frequency vortex-shedding from the blunt-body. However, Li et al. [16] did not provide an explanation for how the structure mode becomes unstable and why a particular mode (either SM or WM) eventually dominates the dynamics (resulting in the different dynamical regimes observed as part of this complex phenomenology). Furthermore, it is noted that Li et al. [16] seems to have mistakenly identified one of the coupled modes as a pure structure mode in the modal coupled condition and, as a result, did not correctly distinguish the structure modes from the coupled-modes, potentially leading to an interpretation error.

Following on from the investigation of Yao and Jaiman [15], Bukka et al. [134] applied LSA on a FIV system using the ROM/ERA methodology and attempted to suppress the FIV response of the system through the inclusion of passive suppression devices in the tail of structure. The shapes of the suppression devices considered in this study encompass a number of interesting configurations: namely, a fairing (two strips affixed tangent to the upper and lower ends of the cylinder), a splitter-plate (a strip attached perpendicular to the tail section of the cylinder), and a connected- C (a C -shaped foil of different radii fastened to the cylinder). The FIV behavior of the connected- C device was observed to be similar to that of a fairing in the sense that both devices were shown to suppress successfully the occurrence of flow-induced vibration. Indeed, it was shown that the root loci obtained using ROM/ERA for the two types of passive suppression devices were nearly identical to each other. As a comparison, the results from both the FOM/CFD and ROM/ERA simulations indicated that the cylinder-splitter configuration resulted in a galloping instability at higher values of the reduced velocity. The study conducted by Bukka et al. [134] clearly demonstrated that a linear stability analysis based on ROM/ERA can be used to provide physically-insightful explanations for the FIV response of an elastically-supported structure in terms of the underlying modal mechanisms.

2.3.4 FIV with spanwise shear inflow

With respect to the research on FIV, a uniform incident flow is usually regarded as the ambient situation of the flow field for simplicity/convenience, and this treatment widely appears in the past experimental and numerical studies [11, 135, 136, 12, 14, 15, 137, 16, 134]. However, non-uniform inflow, a more widespread natural behavior to be encountered than uniform inflow, will induce more complicated characteristics in the corresponding wake fields and structural responses of the system. As one specific situation in non-uniform inflow, an incoming shear flow is a widely encountered fluid environment in engineering applications, which include rotating blades with airfoil cross-sections, bladeless turbines with circular cross-sections, and tall slender buildings with square cross-sections. Regarding the structural response and wake dynamics for shear flow past a cylindrical obstacle, academics have also undertaken large amounts of analysis on stationary [138, 139, 140, 141, 142, 143] and moving structures [144, 145, 146, 147].

In terms of the FIV of elastically-mounted structures with shear inflow, Gsell et al. [148] and Ding et al. [149] investigated the vortex-induced vibration (VIV) of an elastically-supported cylinder with a planar shear flow in the 2-D computational domain using the traditional computational fluid dynamics (CFD), where planar shear flow means that the incoming flow velocity varies in value along the cross-flow direction. De and Sarkar [150] further considered the shear profile of inflow velocity in both planar (cross-flow) and spanwise directions in a VIV study of

a circular cylinder in the 3-D domain via direct numerical simulations. Although the incoming flow in which an object/structure is immersed for practical problems may have velocity varying along several directions, for the flow-induced vibration of a slender object, the change of inflow velocity along its spanwise direction should always be of paramount importance to consider due to its predominant presence and dynamical complexity.

Depending on the spanwise length and stiffness of the 3-D rod/cylinder, it could be treated as a rigid or flexible body in dynamic analysis. For significantly long or slender rods, the corresponding flow-induced vibration will have to account for the deformation of the rod itself in motion. In marked contrast to the rigid rods, flexible rods contain a large number of structural modes that result in more complex dynamical responses when they interact with fluids. Bourguet et al. [151, 152] numerically investigated the vortex-induced vibrations of a long flexible cylinder in shear flow via traditional CFD methodology, with a length-to-diameter ratio up to 200 and Reynolds numbers ranging from 110 to 1100. Observations indicated that the wake dynamics could be locked at different frequencies at various spanwise locations, but the lock-in of fluid-solid coupling is a locally mono-frequency event owing to the fact that the vortex formation is generally synchronized with a single vibration frequency at a given location. Wang and Xiao [153] considered a vertical flexible riser subject to both the uniform and linearly sheared currents, and the numerically predicted FIV response was in good agreement with the experimental tests. The results indicated that the number of dominant modes and the corresponding frequencies, structural amplitudes, and resulting fatigue damage increase with the inflow velocity. The wake flow near the position where the maximum structural amplitudes appeared displayed the 2P mode, while the 2S mode is observed to be the dominant pattern for the overall vortex-shedding behavior.

A rod-shaped cylinder with relatively high structural strength can be regarded as a rigid structure and a non-deformable object for the purpose of analyzing the characteristics of its motion. To our knowledge, there are still limited studies on the FIV of such rigid cylinders with finite length under spanwise shear inflow. Zhao [154] applied the traditional CFD method to numerically investigate the vortex-induced vibration of a rigid cylinder mounted by a linear spring with a length-to-diameter ratio of 19.2 immersed in a spanwise shear flow. The effect of different mass ratios and shear inflow angles are considered with the Reynolds number fixed at 500. The fluid-solid response, phase variation, and wake pattern are analyzed at different reduced velocities. The results revealed that the maximum structural amplitude and regime width of lock-in are comparable with their counterparts for a cylinder in a uniform flow. Furthermore, the researcher concluded that the sectional lift forces along certain spanwise lengths of the cylinder stimulate the vibration, while those along other parts in the spanwise direction suppress the vibration. These distributions associated with stimulation and suppression of vibration depend on the reduced velocity.

Additionally, the FIV of the bluff body at subcritical Reynolds numbers has always been an area of intense focus by researchers. The critical Reynolds number Re_{cr} represents the largest Reynolds number that allows for the appearance of vortex-shedding behavior for flow past a stationary body, which is equal to 46.8 for the case of the circular cylinder. Previous works [155, 156, 157] have demonstrated that the FIV of a circular cylinder would also occur for subcritical Reynolds numbers as low as 18 in a 2-D computational domain with uniform inflow.

The vortex-induced vibration (VIV) of a flexible cylinder with uniform inflow at a subcritical Reynolds number (Re) was explored numerically by Bourguet [158]. The onset Re for the VIV of the flexible cylinder to appear was found to be 20, which is almost consistent with the previ-

ously reported onset Re for VIV of the rigid cylinder. Further detailed assessment of the variation of system parameters (including the mass ratio and damping coefficients) at $Re = 25$ was conducted to investigate the corresponding effects on the structural responses and wake dynamics. The lock-in regimes are found to correspond to different ranges of reduced velocity because the flexible cylinder contains many orders of structural modes, leading to varying structural natural frequencies. Additionally, the flow dynamics would be temporally and spatially locked with structural motion once the cylinder vibrates. Accompanied by the formation of cellular wake patterns, the cross-flow standing-wave responses are synchronized regardless of which structural modes are involved during the FIV.

Investigations on the response of FIV, especially the lock-in behavior, rely on many research methods/models such as CFD, the wake oscillator model, and linear stability analysis, to gain physical insight from different perspectives. As mentioned by the Hollenbach et al. [159] and Sanders [160], the traditional CFD method (used by the literature works introduced above), as one full-order model (FOM), has no ability to provide physical insight into the generation of flow-induced vibrations including the lock-in behavior. Moreover, with respect to the VIV study using a non-uniform velocity as the incident flow, the necessary 3-D computation using FOM/CFD is significantly time-consuming and yet unable to expose the underlying modal situation. Ge et al. [161] applied the wake oscillator (one kind of empirical formula) model to the FIV study of long flexible rods. The three-dimensional structure of the flexible cylinder is divided into several elements, and the interaction between each structure element and the fluid is represented by the two-dimensional control equations. Inside the control equations, the wake oscillator model represents the flow dynamical equation, and the structural control equation uses the common structural vibration model, in which the spring stiffness is replaced by the terms corresponding to the material properties, such as the bending stiffness of the rod material. In addition, while the rod faces non-uniform inflow, the parameters of the wake oscillator in the governing equation of each element can be adjusted according to the dynamic properties corresponding to different Reynolds numbers (or, inflow velocity). Using the methodology introduced above which employs the wake oscillator model, the FIV of three-dimensional flexible rods can be studied in the case of non-uniform inflow [162]. This chapter will focus on the study of spanwise shear flow-induced vibration at subcritical Reynolds numbers based on LSA, and consequently, resonance lock-in is excluded from the present analysis.

The investigation of an FIV system with spanwise shear inflow must be carried out in the 3-D computational domain. Compared with the previous 2-D LSA works mentioned above, to our knowledge there are few precedents for the using 3-D LSA for the study of FIV in the past. Chizfahm and Jaiman [120] obtained a ROM for the fluid dynamics of a sphere at $Re = 300$ using the eigensystem realization algorithm (ERA) and constructed the associated coupled FSI model to study the effects of the near-wake jet (attached to the downstream side of the sphere) on the VIV response. The construction process of the fluid ROM, including the obtainment of the base flow for a sphere and the dynamic response (or, lift coefficients) when subjected to an impulse, is performed in the 3-D computational domain. The results show that the direct 3-D LSA is capable of capturing the effect of the near-wake jet on the FIV response in terms of trend, but cannot predict the lock-in range very accurately.

The following work herein also encounters such errors in the direct 3-D LSA of the shear flow-induced vibration of a rigid cylinder. Therefore, in addition to carrying out direct 3-D LSA, a novel/original LSA methodology is proposed here—the rigid cylindrical structure is segmented into several elements in the spanwise direction, and the aerodynamic characteristics of each

element are simplified into 2-D situations with uniform inflow. ERA identification is conducted for each element to provide the separate 2-D fluid ROM, and the integral fluid ROM for the 3-D cylinder with shear inflow is obtained via the superposition of all 2-D fluid reduced-order models (ROMs). Then, the LSA could be achieved via the coupling of the integral fluid ROM and the structural equation. This differential idea of partitioning a slender structure (with a relatively large length-to-chord ratio) into small elements and then superimposing the dynamical features of each small element is similar to the Blade-Element-Momentum (BEM) theory [163, 164, 165], which is a mature concept frequently applied in the research of wind turbines. The detailed information of the proposed methodology will be introduced later in sub-section 6.5. In addition, before performing direct 3-D and superimposed 2-D LSA, this study performs detailed 3-D calculations based on FOM/CFD and systematically analyzes the lock-in range, spectrum features, wake response, etc. Although the determination of the lock-in boundary via FOM/CFD (which involves a large number of calculations corresponding to different reduced velocity U_r cases) is very time-consuming, it could provide a detailed understanding of the lock-in behavior of the FIV system being studied and also establish a credible validation for the subsequent LSA analysis.

2.4 Aeroacoustics

Vortex shedding results in periodic fluctuations of the lift and drag forces which, in turn, generates sound waves referred to as Karman vortex sound [166]. Since the work of Strouhal [167] on aeolian tones, the mechanism of noise generation for the flow past a cylinder has been of great interest to researchers. The generation of aeolian tones was attributed to the vortex shedding behind a circular cylinder [168, 169].

2.4.1 Measurements of flow-induced sound from a stationary body

Several experimental investigations of sound generation have been conducted for the flow past a stationary cylinder. Oguma et al. [17] carried out experimental measurements of the acoustic field emitted from a flow past a stationary circular cylinder at $Re = 4 \times 10^4$. The pressure fluctuations of the flow were evaluated by measuring the instantaneous velocity field using particle image velocimetry (PIV) implemented in conjunction with the pressure Poisson equation. The sound pressure fluctuations were measured simultaneously by a microphone in the far field. The results of these experiments showed that the shear layers around the cylinder and in the near-wake were significant sound sources. The peak frequency of the sound power spectral density (PSD) occurred at about 146 Hz.

Xing et al. [170] conducted a parametric study concerning the control of the far-field noise using helical cables wrapped along the cylinder span. The results of these experiments revealed that the noise control depends primarily on the dimensionless thread pitch and the cable density. Subsequently, the study conducted by Li et al. [171] provided an explanation of the noise reduction mechanism of the helical-cable technique and these researchers extended their investigation to tandem cylinders. In particular, this study found that the helical cables suppress noise by interrupting the two-dimensional vortex-shedding process and by disrupting the in-phase relationship of the flow pulsations along the cylindrical span by creating a three-dimensional trailing edge. Moreover, it was found that noise suppression control on the upstream cylinder is more important

than that on the downstream cylinder in terms of the noise generated by the flow past two tandem cylinders.

The tandem cylinder data collected by the Basic Aerodynamics Research Tunnel (BART) [20, 22] and the Quiet Flow Facility (QFF) [21] at the National Aeronautics and Space Administration (NASA) Langley Research Center are the most widely used measurements for the validation of numerical aeroacoustic models. These measurements include stable surface pressures, detailed off-surface measurements of the flow fields using PIV and hot-wire measurements in the rear cylinder wake, unsteady surface pressure data, and far-field noise. The data from these experiments were conducted at $Re = 1.66 \times 10^5$. These data are used to validate one of our test cases in the present work.

2.4.2 Numerical model

Numerical methods for computational aeroacoustics are mainly classified as either hybrid methods or direct methods. In terms of direct simulation, on the basis of compressible Navier Stokes equation, Yokoyama et al. [172] carried out direct numerical simulation of the flow field and sound field, in order to clarify the fluid-acoustic interaction of the opening and closing sound holes in the actual recorder. Hildebrand et al. [173] carried out direct numerical simulation (DNS) to study the acoustic free flow disturbance radiated by turbulent boundary layer, along the contour nozzle wall in a rectangular test section of a supersonic wind tunnel.

Osamu and Hatakeyama [174] used direct numerical simulation (DNS) to study the sound produced by a two-dimensional circular cylinder in a uniform flow. This DNS study showed that when a vortex is shed from one side of the cylinder, a negative pressure pulse is generated from that side and a positive pressure pulse is generated from the other side. The alternating vortex shedding from the upper and lower sides of the cylinder produces negative and positive pulses and, in consequence, results in the generation of sound pressure waves. The dipolar nature of this generated sound was confirmed. Moreover, it was found that the lift dipole dominates the sound field.

Compared with DNS, hybrid methods significantly reduce computational demands by allowing coarser grids and larger time steps to be used in the numerical simulation while providing reasonable accuracy in the solution. For this reason, hybrid methods are widely used in computational aeroacoustics. The commonly used sound models in many commercial software packages are based on the Ffowcs Williams-Hawkins (FW-H) equation [175, 176], and the simplified integral method [177].

The British scientist Lighthill [178][179] established the acoustic analogy theory in 1950s and derived the famous Lighthill equation. Thus, the research on hydrodynamic acoustics has officially become a new discipline. The fruitful work of Lighthill is considered to be a milestone in the birth of modern hydrodynamic acoustics theory. The solution of Lighthill equation is assumed to be obtained in free space, which is applicable to free turbulent radiation noise in unbounded space, such as jet noise, but it has some limitations for sound generation problems with solid boundary or moving boundary. In fact, in engineering practice, there are a lot of acoustic problems of fluid solid interaction (FSI). In order to solve this problem, Curle [180] in 1955 extended Lighthill acoustic analogy theory to consider the influence of static solid boundary. On the basis of Lighthill equation and generalized function theory, the FW-H acoustic wave equation of sound field caused by moving object is derived by Ffowcs Williams and Hawings

[181] with using the generalized function theory, and the influence of moving solid boundary on noise is displayed. In terms of the studies on the aeroacoustics from uniform flow past a cylinder, researchers have also used the hybrid simulation approach to calculate the noise generation [182][183][184]. The FW-H wave equation will be discussed in following section.

There are some other studies about the differential methods for acoustics simulation, including Acoustics Perturbation Equation (APE) [185][186], Linearized perturbed compressible equations (LPCE) [187][188] and etc. However, the differential acoustics simulation has high requirements on the mesh quantity and time step size, which will bring expensive calculation costs, especially in far-field noise study. The present study in this thesis will mainly focus on the FW-H method in acoustics simulation and analysis.

2.4.3 Sound generation of the flow past moving bodies

Noise propagation has also been a key research area for renewable energy, as extracting energy from the wind often results in a highly turbulent and noisy wake. For example, the noise generated by both traditional wind [189, 190] and tidal [191, 192] turbines has been heavily investigated. As introduced above, new types of energy harvesting devices have been recently proposed involving the extraction of energy from flow-induced vibration (FIV). In particular, certain energy harvesting devices can be tuned to resonate under vortex-induced vibration (VIV) which, in turn, can transfer energy into the vibrating structure. The kinetic energy of this vibration can be initiated from a low-speed flow and this vibrational kinetic energy can then be converted into electric energy with an appropriate generator [95, 61]. This idea has important implications for the use of low-speed water or wind energy and can be widely used as a source of distributed energy [96, 10].

However, the noise generated by a VIV energy harvester can be of concern. While a large body of literature exists concerning the flow dynamics around oscillating cylinders, including experimental [193, 194, 195, 196] and numerical [197, 198, 199] studies, the noise generated by this flow has not been studied in detail. Ganta et al. [200, 201] simulated the sound generation by a two-dimensional laminar flow past a circular cylinder performing rotary oscillations using a DNS approach. The DNS studies were performed over a wide range of forcing frequencies and rotary oscillation amplitudes, specifically in the synchronization region. The rotary oscillation of a cylinder modifies the vortex-shedding patterns in the wake region which, in turn, results in the generation of different noise patterns.

The distinct wake patterns in VIV result in a distinct acoustic behaviour. For example, some studies of the flow past a cylinder in forced oscillation exhibited reduced sound generation compared to that of the flow past a stationary cylinder. The directivity of the sound field is also affected by the amplitude of the rotary oscillations. Hattori and Komatsu [25] investigated the sound propagation from a single or tandem circular cylinder(s) at $Re = 150$ using DNS. This study demonstrated that the acoustic field predicted by DNS is in excellent conformance with that obtained using the FW-H methodology. Interestingly, the oscillation of the cylinder suppresses the noise generation—the aeroacoustic energy of the flow past an oscillating cylinder at $0.14 < Sc < 0.17$ is significantly less than that of the flow past a stationary cylinder at the same Reynolds number (Sc is the Scruton number defined as $Sc \equiv f_{osc}D/U_0$ where f_{osc} is the oscillation frequency, D is the cylinder diameter, and U_0 is the inflow velocity). Moreover, this study showed that the acoustic power generated by the flow past tandem cylinders depends strongly

on the in-line spacing between the two cylinders because the vortex-shedding pattern behind the front (upstream) cylinder depends critically on this spacing.

2.5 Motivations and novelties

The above discussion implies that the investigations on the mechanism underpinning FIV behaviors and the associated detailed responses are valuable. More specifically, researches on lock-in and galloping regimes are the most important focus, and the correlated applications to energy utilization will also be the future research hotspot. With respects to the industrial fields, most engineering springs are nonlinear with varied configurations and different orders. However, the FIV studies about the effects of nonlinear restoring forces are still limited, and how it affects the characteristics of lock-in behaviors is unclear. As a consequence, the FIV responses with the nonlinear restoring forces deserve to be further studied.

In addition, there are abundant researches on the FIV system consisting of flow passing elastically-mounted bluff bodies including circular, square and triangle cylinders, and the concerned FIV behaviors (accompanied by structural instability) involves flutter, resonance, and galloping patterns. Nevertheless, the key factors, such as the variations of cross-sectional shapes, triggering structural instability are still unclear and remain to be investigated. On the one hand, changing cross-sections of bluff body will bring a lot of case studies, which is expensive for the traditional FOM/CFD calculations. On the other hand, the traditional CFD method, as one full-order model (FOM), has no ability to provide physical insight into the generation of flow-induced vibrations. As a consequence, the linear stability analysis (LSA) using the ROM/ERA methodology will be applied herein for both the studies of lock-in and galloping behaviors. Furthermore, except for the conventional LSA used in the exploration of the 2-D FIV system consisting of different cross-section bodies submerged in uniform flow, one new/original LSA based on the superposition of 2-D fluid ROMs will be proposed and applied for the 3-D FIV system with spanwise shear inflow (similar to the practical working scenario of bladeless wind turbines).

Energy utilization will inevitably bring various forms of pollution, and the aerodynamics of noise propagation has been one of the research focuses for traditional wind turbines and tidal turbines. As a result, the aeroacoustics problems brought by the FIV energy harvester will also be the object of concern. Present work will conduct research on aeroacoustics propagation from forced vibration of single and tandem cylinders, especially in the turbulent situation which could emulate the actual life situation.

To sum up, the right panel of figure 2.5 structures the motivations of this thesis, in which the innovations corresponding to separate contents are also indicated. The research objectives in the present work cover three parts:

1. The influences of restoring force with nonlinearity on FIV response.
2. The influences of parameters and configurations setting such as different cross-sections of bluff bodies on FIV response.
3. Aeroacoustics propagation originating from oscillations of the cylinder (array).

The novelties of current research are also summarizes in the left panel of Fig. 2.5. Combined with the discussion in Section 2.3, the previous work on the above-introduced contents/researches are relatively scarce, and correlated further explorations will be very valuable. In addition, if the

lock-in or galloping phenomenon enhanced by the above methods is applied in practical energy utilization, the inevitable noise pollution is valuable to pay attention to. However, the researches on the aerodynamic noise of vibrating cylinders in the turbulent situation are also very limited so far.

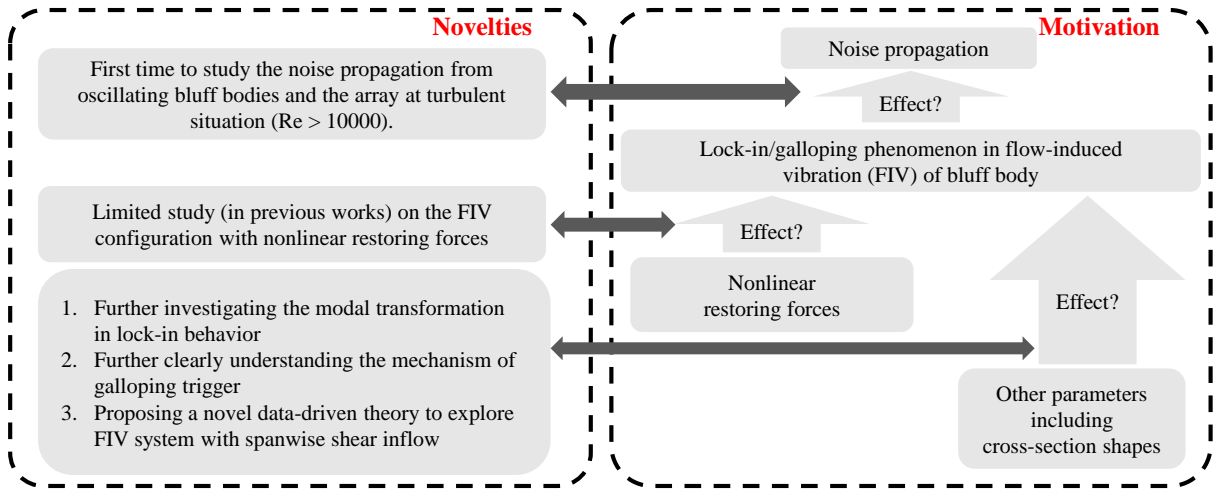


Figure 2.5: The motivations of this thesis and the corresponding innovations.

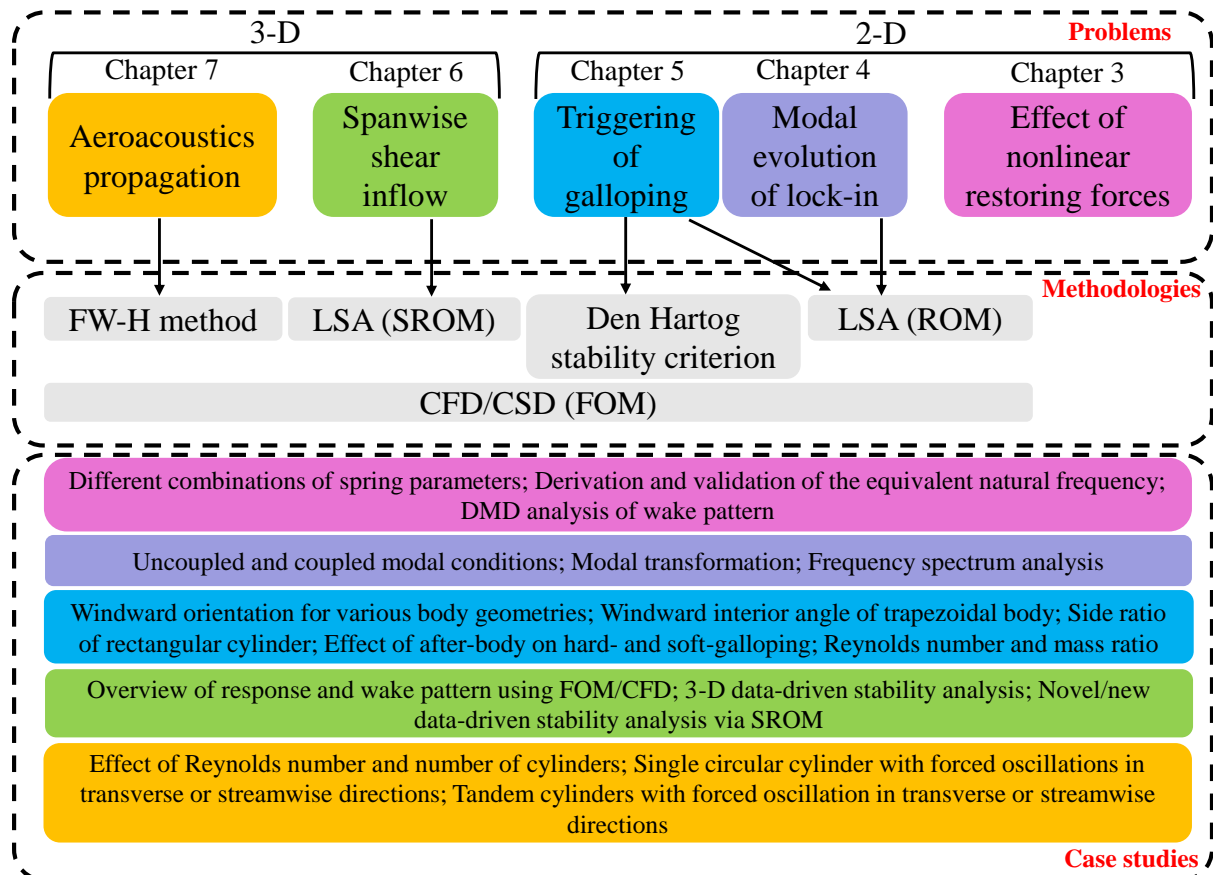


Figure 2.6: Framework of this thesis.

2.6 Outline of thesis

The framework consisting of the main contents in this thesis is exhibited in figure 2.6. The correspondence between the problem/chapters in the first (top) panel and the detailed case studies in the third (bottom) panel is distinguished by the box color in which it is located. Term one of above-mentioned research will be undertaken in chapter 3, corresponding to the research focus with respects to the effect of nonlinear restoring forces herein. This problem is analyzed with the help of FOM/CFD and the corresponded to-be-explored contents are displayed in the third panel of figure 2.6. It is noted that the methodology of FOM/CFD is used in all problems (chapters) to be studied in the present thesis, but different problems may involve other additional methodologies for assistant analyzes.

The second term of above-mentioned research would contain three sub-parts, all involving the application of linear stability analysis (LSA). More specifically, chapter 4 focuses on the dynamics characteristics especially the modal evolution of the lock-in behavior. In chapter 5, the mechanism underpinning the galloping behavior is investigated from various perspectives. In this stage, this thesis will investigate the relationship between different cross-sectional shapes and structural instability using Den Hartog stability criterion. Furthermore in chapter 6, one novel data-driven theory using the superposition of 2-D ROMs is proposed for the stability prediction of a 3-D FIV system with spanwise shear inflow. The detailed contents of the case studies are shown in the third panel.

In terms of the noise problem (studied in chapter 7), the preliminary FW-H model is used herein to calculate aeroacoustics propagation from cylinders' oscillation. Firstly, the proposed thesis will compare present simulation results with measurement results based on the units of fixed single cylinder and fixed tandem cylinders. Secondly, the noise propagation from single-cylinder with different oscillation patterns will be analyzed. Thirdly, the noise propagation from tandem cylinder array with different oscillation patterns will be compared.

It is reminded that the concerned problems in chapters 3, 4, and 5 are all two-dimensional (2-D) situations, whereas three-dimensional FIV systems are investigated in chapters 6 and 7.

Chapter 3

FIV response with nonlinear restoring forces

This chapter will focus on a two-dimensional (2D) numerical FIV study of a circular cylinder mounted on linear and nonlinear springs for a low Re -number flow. All forms of nonlinearity can be approximately replaced by polynomials through Taylor expansions. The quadratic nonlinear term is the basis of all polynomials, and consequently, the research on it will be representative. For this purpose, we analyze the impact of the spring nonlinearity on the FIV response, focusing specifically on the differences in the amplitude variation, the phase change, the frequency variation, and characteristic wake pattern between the linear and nonlinear spring-mounted cylinder. More specifically, we study the FIV response of a circular cylinder mounted on a linear/quadratic spring. The Reynolds number studied in this chapter is larger than the critical Reynolds number, and consequently, vortex-shedding behaviors will occur for flow passing stationary cylinder at the same Reynolds number. In this case, the term ‘vortex-induced vibration (VIV)’ is applied in this thesis when the studied Reynolds number is larger than the critical Reynolds number. To the best of our knowledge, this is the first study that is focused on the influence of a quadratic spring nonlinearity on the VIV dynamics of an elastically-spring-mounted cylinder (with previous studies focusing primarily on a cubic spring nonlinearity). Indeed, the quadratic nonlinearity is the first higher-order nonlinear term in the Taylor series expansion of the restoring force for a general nonlinear spring and, hence, is important to investigate. For this purpose, the equivalent natural frequency for the VIV system is derived for the first time and the relationship between this equivalent natural frequency and the characteristics of the induced VIV oscillation is investigated. Furthermore, a seminal investigation involving the application of a dynamic mode decomposition (DMD) is used herein, allowing one to compare different wake models for the FIV response of a system that includes the influences of a nonlinear restoring force.

3.1 Methodology

3.1.1 Laminar flow model

In this chapter, we will focus on the analysis of VIV for a cylinder supported by a nonlinear spring and immersed in a laminar flow. The incident velocity U_0 of the flow into the computational domain is constant at the inlet plane. The mass and momentum conservation laws for the

laminar flow are given by

$$\frac{\partial u_i}{\partial x_i} = 0, \quad (3.1)$$

and

$$\frac{\partial u_i}{\partial t} + (u_j - \tilde{u}_j) \frac{\partial u_i}{\partial x_j} = -\frac{1}{\rho} \frac{\partial p}{\partial x_i} + \nu \frac{\partial^2 u_i}{\partial x_j \partial x_j}, \quad (3.2)$$

where $\tilde{u}_j = dx_j/dt$ is the j -th component of the grid velocity arising from the motion of the cylinder (structure) immersed in the flow; x_i is i -th component of a Cartesian coordinate vector \vec{x} with $i, j \equiv 1, 2, 3$ corresponding to the x -, y - and z -directions, respectively; t is the time; p is the pressure; ρ is the density of the fluid; ν is the kinematic viscosity of the fluid; and, u_i represents the i -th component of fluid velocity.

The open source computational fluid dynamics (CFD) toolbox OpenFOAM [202] is used to simulate the flow field. The Navier-Stokes equations are discretised with a finite-volume method (FVM). To this purpose, a second-order accurate implicit Euler scheme is employed to discretize the transient term, while a second-order-accurate Gaussian integration scheme is used for discretization of the advection, pressure gradient and diffusion terms in the momentum transport equation. The same discretization schemes have been used by Wang et al. [110] in their numerical simulation of VIV of a circular cylinder supported on a spring with a cubic stiffness nonlinearity. The large time-step transient PIMPLE algorithm which combines the semi-implicit method for pressure-linked equations (SIMPLE) with the pressure-implicit with the splitting of operators (PISO) algorithm is used to solve the continuity and momentum transport equations together in a segregated manner. All these algorithms are iterative solvers, but PISO and PIMPLE are used for transient problems, whereas SIMPLE is used for steady-state problems. The pressure-velocity coupling provided by the PIMPLE algorithm results in better stability and higher accuracy [203]. The time step size is adjusted to control the maximum Courant-Friedrichs-Lewy (CFL) number CFL_{\max} which is specified to be 0.4 at each time step in the PIMPLE algorithm. The maximum CFL number CFL_{\max} is defined as $CFL_{\max} \equiv \|\vec{u}\| \Delta t / \Delta x_{\min}$ where Δx_{\min} is the size of the smallest grid cell in the computational domain and $\|\vec{u}\|$ is the magnitude of the fluid velocity \vec{u} .

3.1.2 Structure model and fluid-structure interaction with linear or non-linear restoring forces

As derived in Appendix. A, the nonlinearity relationship between restoring force and structural displacement (in engineering spring) can be transformed into polynomial form. Springs with complex nonlinear restoring forces are required for modeling some practical applications such as an automobile's energy absorbing system or the spring vibration characteristics of elastic rods [204]. These springs with highly nonlinear relations can be modeled using a Taylor expansion of a nonlinear form into a sum of terms involving polynomials of various degrees (viz., the partial sum consisting of the first $(n + 1)$ terms of the Taylor expansion of the nonlinear form yields the n -th Taylor polynomial approximation of the form). As an example, the nonlinear restoring force F_{nr} for a simple spring can be modeled using the third-order Taylor polynomial with the form:

$$F_{nr} = -k_1 \cdot \Delta L - k_2 \cdot \Delta L \cdot |\Delta L| - k_3 \cdot \Delta L^3, \quad (3.3)$$

where ΔL is the total compression or elongation of the spring from its equilibrium length (where $\Delta L = 0$) and k_1, k_2 and k_3 are spring constants. Indeed, this functional form for the restoring force

of a nonlinear spring (acting to restore the spring to its equilibrium length) is commonly used in vibration theory. The spring is linear if k_2 and k_3 are identically equal to 0 and, in this case, $k_1 > 0$ is the usual spring constant that appears in Hooke's law (which states that the force required to compress or stretch a spring by some distance ΔL is proportional to that distance). Retaining the second-order term in Eq.(3.3) yields the simplest form of a nonlinear spring (namely, a quadratic spring). This chapter focuses on the characteristics of the VIV of a structure supported by a spring with quadratic (nonlinear) restoring force characteristics with $k_1 > 0$, $k_2 > 0$, and $k_3 = 0$.

The transverse motion of a circular cylinder mounted on a nonlinear spring and damper system is governed by the following second-order ordinary differential equation (where y corresponds to the displacement of the cylinder in the transverse direction from the equilibrium position):

$$m\ddot{y} + c\dot{y} + k_1y + k_n l_n(y, \dot{y}) = F_y, \quad (3.4)$$

where $l_n(y, \dot{y}) = l_n(y)$ in present study, with special cases corresponding to a quadratic spring if $n = 2$ so $l_2(y, \dot{y}) = y|y|$, a cubic spring with $n = 3$ so $l_3(y, \dot{y}) = y|y|^2$, a quartic spring with $n = 4$ so $l_4(y, \dot{y}) = y|y|^3$, and so on for higher values of n associated with higher-order springs. If $c = 0$ and $n = 2$, the model of Eq. (3.4) reduces to the case of a circular cylinder mounted on a quadratic spring with no structural damping (the case of interest in the present study). Hence, Eq. 3.4 with these simplifications yields

$$m\ddot{y} + (k_1 + k_2|y|)y = F_y, \quad (3.5)$$

where k_1 is the linear spring (stiffness) constant (N m^{-1}), k_2 is the quadratic spring (stiffness) constant (N m^{-2}), m is the mass of the circular cylinder, and F_y is the hydrodynamic force (acting on the cylinder) in the transverse direction (or, y -direction). The numerical scheme used to integrate the equation of motion (viz., Eq. 3.5) is the explicit second-order symplectic method [205]). The fluid-structure interaction in the current study is based on a weakly coupled approach. The numerical procedure [110] executed for each time step in the simulation of the FSI consists of the following key steps:

- The hydrodynamic load on the cylinder is obtained by solving the flow (or Navier-Stokes) equation on the current grid;
- The calculated dynamic load obtained from the flow solution is utilized in the structural dynamic solver to calculate the motion of the cylinder;
- A new grid field (including new grid positions and grid velocities) resulting from the motion of the cylinder is obtained using the spherical linear interpolation of the dynamic grid quantities (positions and velocities) as a function of the distance to the current (updated) location of the surface of the cylinder;
- The velocity boundary conditions corresponding to the moving cylinder are updated;
- The next time step involves the solution of the Navier-Stokes equation on the updated grid to obtain the new hydrodynamic load on the cylinder.

3.2 Description of the problem

3.2.1 Boundary condition and mesh dependency study

The computational domain and the boundary conditions for present study are shown in Fig. 3.1. The computational domain is $42D$ in the streamwise (x -) direction and $30D$ in the cross-stream (y -) direction where D is the diameter of the circular cylinder. The center of the circular cylinder is located along the centerline of the computational domain ($y = 0$) in the cross-stream (transverse) direction and at a streamwise distance of $12D$ from the inflow (inlet) boundary (left edge of the domain shown in Fig. 3.1). A zero-gradient streamwise velocity boundary condition is applied at the lateral boundaries of the domain and a Neumann boundary condition is imposed on the velocity at the outflow (outlet) boundary of the domain. At the inflow boundary, a Dirichlet boundary condition is prescribed for the incident flow velocity $\vec{u} = (U_0, 0)$ where U_0 is the incident streamwise wind speed. The initial conditions used to prescribe the motion of the cylinder are $y = 0$ and $\dot{y} = 0$ (cylinder at rest at $t = 0$). The choice for the computational domain size and boundary conditions used here is consistent with those used in other numerical simulations of VIV involving rigid and flexible cylinders [110, 206].

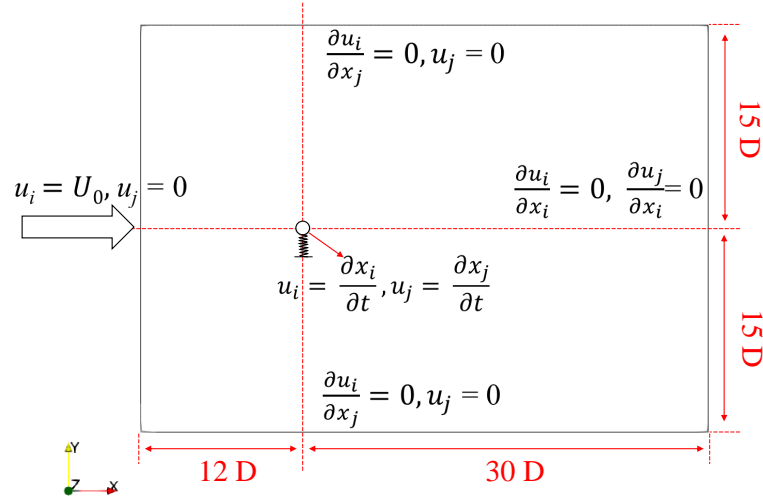


Figure 3.1: Computational domain and the boundary conditions imposed for simulation of VIV for a cylinder supported by a spring. The subscripts i and j on a vector quantity refer to the component of that quantity in the x (streamwise) and y (transverse) directions, respectively.

The simulation of flow past a stationary (fixed) cylinder is conducted and used to assess the sensitivity of the results to the mesh used. Towards this objective, four different meshes with a total number of cells ranging from 17,725 (coarse) to 65,322 (very fine) are used for the simulation of a laminar flow past a stationary cylinder at $Re = 100$ and the root-mean-square (rms) lift C_L^{rms} and drag C_D^{rms} coefficients were computed. The results of this analysis for the four different meshes are summarized in Table 6.1. It can be seen that the differences between the values of C_L^{rms} and C_D^{rms} obtained on meshes 1 (coarse) and 2 (intermediate) are quite large (viz., the discrepancy is 2.3% and 0.6% for the root-mean-square lift and drag coefficients, respectively). However, the differences in the values of C_L^{rms} and C_D^{rms} obtained on meshes 3 (fine) and 4 (very fine) are small (more precisely, the discrepancy in the results for the two meshes is 0.04% for C_L^{rms} and 0.07% for C_D^{rms}).

Based on these considerations, mesh 3 is used for the simulations conducted in this study as it provides the best compromise (balance) between numerical accuracy and computational effort. Mesh 3, exhibited in Fig. 3.2 is a fine mesh consisting of 45,656 cells (see Table 6.1). Using this mesh, the maximum amplitude of the lift coefficient C_L^{\max} and the Strouhal number $S_r \equiv f_{vs}D/U_0$ (where f_{vs} is the vortex shedding frequency and U_0 is the incident wind speed) have been obtained for the flow past a stationary cylinder at $Re = 100$ and summarized in Table 3.2. These results are seen to be in very good conformance those obtained by Lu et al. [207] and by Zhang et al. [12] for the same case.

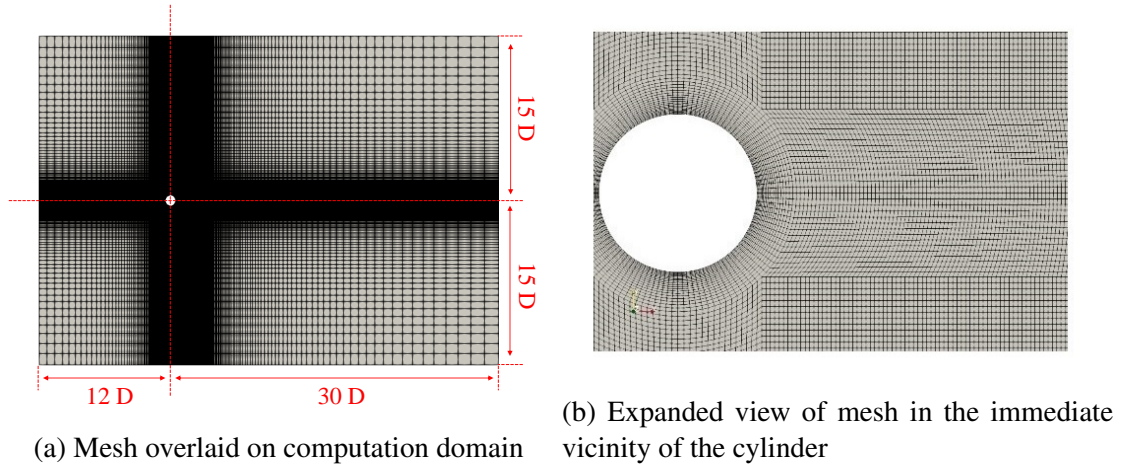


Figure 3.2: The fine mesh (mesh 3) consisting of 45,656 cells used to discretize the computational domain in the present study.

Table 3.1: Root-mean-square lift and drag coefficients for flow past a stationary cylinder at $Re = 100$ for four different meshes.

Mesh	Number of cells	C_L^{rms}	C_D^{rms}
1	17725	0.2234	1.311
2	31933	0.2287	1.319
3	45656	0.2335	1.349
4	65322	0.2336	1.348

3.2.2 Validation test of VIV with linear restoring forces

To validate the accuracy of our fluid-structure interaction numerical model and its implementation, we consider the case of VIV for an elastically-mounted circular cylinder with a linear spring whereby the cylinder is allowed to vibrate in both the streamwise (x -) and transverse (y -) directions. For the case considered, the damping coefficient $c = 0$ (no structural damping in the

Table 3.2: Comparison of the maximum amplitude of the lift coefficient C_L^{\max} and Strouhal number S_t for flow past a stationary circular cylinder at $Re = 100$.

	C_L^{\max}	S_t
Present	0.34	0.169
Lu et al. [207]	0.34	0.167
Zhang et al. [12]	0.34	0.166

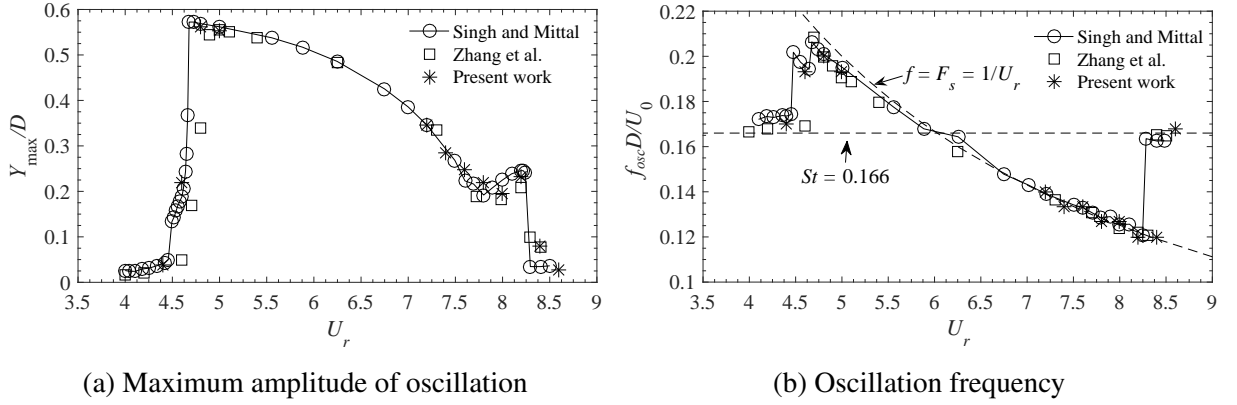


Figure 3.3: VIV response of a cylinder elastically mounted on a linear spring for $Re = 100$ and $m^* = 10$ compared with those obtained by Singh and Mittal [11] and by Zhang et al. [12].

system) and the mass ratio $m^* = 10$. The simulation is conducted for a flow past an elastically-mounted cylinder for a Reynolds number $Re = 100$. The reduced velocity U_r in the problem is varied by changing the natural frequency of the structure (cylinder).

Figure 3.3a shows the maximum amplitude A_{\max} (normalized by the cylinder diameter D) of the oscillation in the transverse direction as a function of the reduced velocity U_r . The maximum amplitude A_{\max} exhibits a sudden jump to its largest value of $A_{\max}/D \approx 0.6$ at $U_r \approx 4.6$ and then slowly decreases with increasing U_r . However, when U_r approaches a value of about 7.6, the maximum amplitude A_{\max} begins to increase again with increasing values of U_r until it reaches a secondary relative maximum value of $A_{\max}/D \approx 0.25$ at $U_r \approx 8.2$. After this value of U_r , the maximum amplitude is seen to exhibit a sudden (discontinuous) jump to a lower value of $A_{\max}/D \approx 0.025$ at a reduced velocity of about 8.3. This behavior in the maximum amplitude as a function of the reduced velocity is in good agreement with the results reported by other investigators [11, 12].

Figure 3.3b displays the oscillation frequency f_{osc} of the vibrations in the transverse direction as a function of reduced velocity U_r . When the reduced velocity U_r is in the range from about 4.7 to 8.2 (which corresponds to a reduced natural frequency $F_s \equiv U_r^{-1} = f_n D/U_0$ in the range from about 0.12 to 0.21), the oscillation frequency f_{osc} is seen to match the natural structural frequency f_n —a condition that is associated with the lock-in phenomenon. Outside this range of reduced velocities, the forced vibration in the system lies outside the lock-in range (viz., the vortex shedding frequency is not close to a natural fundamental frequency of vibration of the cylinder). The Strouhal number (which characterizes the vortex shedding frequency) $S_t \equiv f_{vs} D/U_0 \approx 0.166$ for a cylinder over a wide range of flow velocities (see Table 3.2). Finally, in

Fig. 3.3b, the results for f_{osc} as a function of U_r obtained in our simulations are seen to compare well with similar results reported by other investigators [12, 11].

3.3 Results and discussion

At each value of the Reynolds number Re used in this study, the corresponding flow past a stationary cylinder is calculated and this flow is used subsequently as the initial flow for the VIV calculation involving the elastically-mounted cylinder on a (non)linear spring. For the latter calculation, the initial state of the cylinder mounted on the spring is prescribed (namely, $y = 0$ and $\dot{y} = 0$ at the initial time $t = 0$) and then allowed to vibrate in response to the lift force imposed on it by the flow (viz., when the elastically-mounted cylinder is coupled to the flow). It is stressed that vibrations of the cylinder in the transverse direction are significantly larger than those in the streamwise direction and, as a result, the analysis presented in the remainder of this study will focus on the vibrations in the transverse direction only.

For the simulations reported in this section, we investigate various flows in the Re -number range from 50 to 150 inclusive for each spring stiffness condition with a fixed mass ratio $m^* = 10$ and a structural damping coefficient $c = 0$ (viz., no damping). The variation in the value of Re is achieved by adjusting the value of the inlet velocity U_0 . The spring-mounted cylinder has a diameter $D = 0.1$ m and the flow is assumed to have a kinematic viscosity $\nu = 0.0001 \text{ m}^2 \text{ s}^{-1}$.

3.3.1 Linear, linear/quadratic and quadratic springs

For the first set of simulations, we consider the dynamics of a circular cylinder elastically mounted on (1) a pure linear spring with spring constant $k_1 = 0.0063 \text{ N m}^{-1}$; (2) a linear/quadratic spring combination with $k_1 = 0.003 \text{ N m}^{-1}$ and $k_2 = 0.11 \text{ N m}^{-2}$; and, (3) three different pure quadratic springs with spring constants of $k_2 = 0.14, 0.21,$ and 0.28 N m^{-2} .

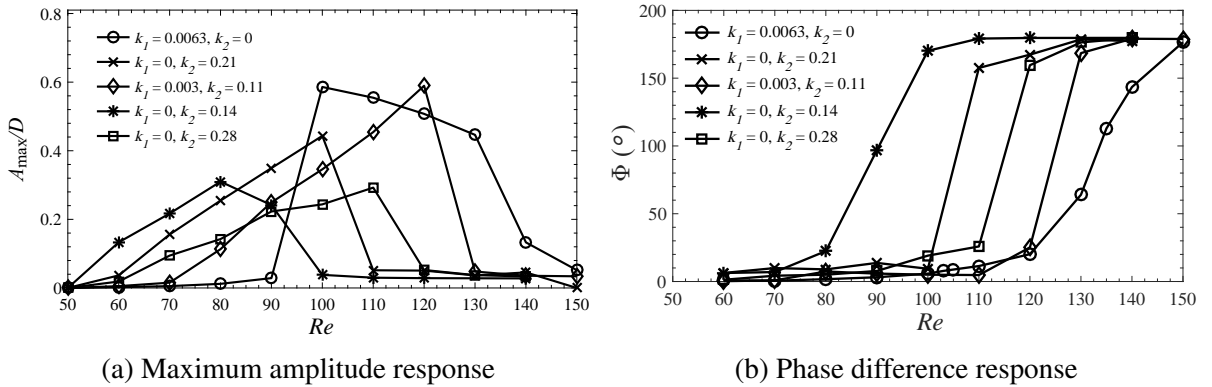


Figure 3.4: The response of the (a) maximum amplitude A_{max} and (b) phase difference Φ between the transverse displacement and the lift force as a function of Re for an elastically-mounted cylinder on a spring subject to linear and/or quadratic restoring forces. It is difficult to identify the lock-in range due to many combinations of (k_1, k_2) here, so the following contents will select a set of (k_1, k_2) with encrypted Re increment and identify the correlated lock-in interval.

As discussed previously, the natural frequency for the VIV of a cylinder elastically mounted on a nonlinear spring will change with the amplitude of oscillation, but this amplitude cannot

be determined *a priori*. In consequence, it is interesting to investigate the variation of this amplitude as a function of Re . To this purpose, the variation of the amplitude and phase of an elastically-mounted circular cylinder on a linear and/or nonlinear spring with Re (the latter of which is related to the inflow velocity U_0) is shown in Fig. 3.4a. The dependence of the maximum amplitude A_{\max}/D on Re is displayed in Fig. 3.4a. The maximum amplitude A_{\max} of the elastically-mounted cylinder is sensitive to the “type” of linear/quadratic spring (as characterized by (k_1, k_2)) used to mount the cylinder. For the case of a linear spring where $k_2 = 0$, the maximum amplitude exhibits a sudden jump to the largest “observed” value of A_{\max} as Re (which depends on U_0) approaches the lower bound of the lock-in range. After this point, the maximum amplitude is seen to decrease slowly with increasing values of Re (or, equivalently, U_0), until the system transitions outside the lock-in range.

In terms of the VIV response for a nonlinear spring (whether for a linear/quadratic or a purely quadratic spring), it is seen that the lock-in range in these cases differ from that for the linear spring. In contrast to the linear spring which exhibits a sudden transition (jump) when the lock-in condition has been achieved, the nonlinear springs transition in a more gradual (approximately linear) manner into the lock-in regime. For example, for the linear/quadratic spring with $(k_1, k_2) = (0.003, 0.11)$, the transition into the nonlinear lock-in regime occurs gradually as Re increases from about 80 to 120 (and, the maximum amplitude of the oscillations is seen to increase linearly (approximately or better) for increasing Reynolds number in this range).

For the pure quadratic spring with $k_1 = 0$ and with an effective stiffness $k_{\text{eff}} \equiv k_2|y|$, the maximum amplitude A_{\max} is seen also to undergo a more gradual (linear) increase with increasing Re , followed by a sudden drop in value after the largest value of amplitude has been achieved in the lock-in regime. Generally, the range of lock-in increases with increasing values of k_2 owing to the fact that larger values of k_2 will facilitate oscillatory motions in the system at the higher value of Re . This phenomenon is consistent with the results obtained by Huynh et al. [108] in their numerical and experimental investigations of nonlinear VIV energy converters.

An appropriate combination of k_1 and k_2 for a linear/quadratic spring can be potentially utilized to enhance the useful lock-in regime for energy conversion, provided both the magnitude of the amplitude response and extent of the range of flow velocities at which lock-in occurs can be simultaneously exploited. Towards this objective, it is noted that the nonlinear lock-in for the cylinder occurs at a lower value of the velocity for the pure quadratic spring than that for the linear spring—but, on the other hand, the maximum amplitude of oscillation obtained for the linear spring in the lock-in regime is larger than that for the pure quadratic spring. More importantly, it is noted that a linear/quadratic spring configuration can potentially inherit the strengths of the linear and pure quadratic springs vis-a-vis the characteristics of the lock-in regime; namely, a lock-in that occurs at a lower velocity (as for a pure quadratic spring) and a maximum amplitude of oscillation that is large within the operational lock-in regime. For example, the linear/quadratic spring configuration with $(k_1, k_2) = (0.003, 0.11)$ exhibits a local synchronization of the vortex shedding frequency and the structural vibration frequency at $Re \approx 80$, but within the range of the lock-in regime the maximum amplitude of oscillation A_{\max}/D attains a value of about 0.6 (equal to the maximum amplitude of oscillation achieved by the linear spring) at $Re \approx 120$ (see Fig. 3.4a).

In terms of the VIV response of a cylinder mounted on a linear spring, four distinct branches in the response have been identified. These different branches of the response emerge as the reduced velocity U_r is increased and are characterized as follows [40]: (1) an initial branch which emerges as the vortex shedding frequency approaches the natural structural vibration frequency

and is characterized by a distinct increase in the amplitude of oscillation; (2) an upper branch as the amplitude of the oscillations transitions to a higher level corresponding to a complete local synchronization of the vortex shedding frequency and the natural structural frequency, a state that is associated with the largest vibrations; (3) a lower branch as the amplitude of the oscillations transitions to a lower level as the vortex shedding frequency diverges more and more from the natural structural frequency; and, (4) desynchronization in which the amplitude of oscillations vanish as desynchronization occurs between the vortex shedding frequency and natural structural frequency leading to lock-out. However, for the VIV response of a circular cylinder mounted on an nonlinear (hardening) spring, the range of Re associated with the start of the initial branch to the start of the upper branch is increased (extended), implying that the envelope of the maximum amplitude of the transverse displacement exhibits a smooth increase with increasing Re . Furthermore, the range of Re corresponding to the upper and lower branches of the response shrinks. In consequence, the value of A_{\max} decreases precipitously (rapidly) (accompanied by a jump in the phase difference between the transverse displacement and the lift coefficient from 0° to 180°) with a small increase in Re after the point when A_{\max} attains its largest (maximum) value in the upper branch of the response. One set of (k_1, k_2) will be chosen and simulations will be conducted for a large number of values of Re in order to investigate the branches of the response in detail, the results of which will be described in sub-section 3.3.2.

Figure 3.4b displays the dependence of the phase difference Φ between the transverse displacement of the cylinder and the lift force as a function of Re . The phase difference Φ as defined here is the same as that used by Govardhan and Williamson [208]. A perusal of the figure shows that Φ exhibits a sharp jump from 0° to 180° within the later stages of the lock-in range. This behaviour is consistent with that reported by Wang et al. [105]. For the pure quadratic spring, the phase difference Φ is approximately 0° for a large range of values of Re (associated with the non-linear lock-in regime) and Φ transitions abruptly (jumps) to about 180° at the end of the lock-in range (corresponding to the local desynchronization between the vortex shedding frequency and the natural structural frequency). A comparison of Figs 3.4a and 3.4b shows that the value of the Reynolds number Re at which A_{\max} decreases abruptly in magnitude coincides (approximately or better) with the value of Re at which Φ increases sharply from 0° to 180° , a characteristic that has also been observed by Wang et al. [105].

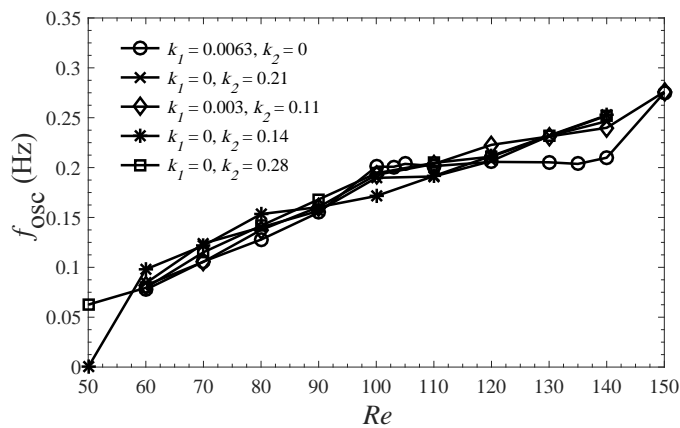


Figure 3.5: Oscillation frequency f_{osc} as a function of Re for a cylinder supported by various types of (non)linear springs characterized by (k_1, k_2) .

The variation of the oscillation (vibration) frequency with Re for different types of springs (characterized by (k_1, k_2)) is displayed in the Fig. 3.5. The frequency corresponding to the peak

with the largest amplitude is selected if there are multiple peaks in the spectrum. An examination of Fig. 3.5 reveals that for a linear spring, the oscillation frequency is constant (approximately or better) over the range of Reynolds numbers from about 100 to 140 implying that over this range the system is in the lock-in condition. This characteristic of the lock-in condition for a linear spring is consistent with results reported previously by Khalak and Williamson [42] and Leontini et al. [209]. This property of a linear spring is in stark contrast with that of a nonlinear spring where the oscillation frequency is seen to vary with Re rather than remain constant. Indeed, an important characteristic feature of a nonlinear spring is that the natural frequency of a system coupled to the spring (e.g., cylinder mounted on a nonlinear spring) is not constant. In consequence, for such systems the oscillation frequency cannot easily achieve lock-in at one constant value. If the nonlinear stiffness (k_2) of the spring is large, the frequency of oscillation is proportional (approximately or better) to the vortex shedding frequency. These characteristics of a linear and nonlinear spring are consistent with those described by Wang et al. [105] who also found that the characteristics of the vibration frequency of a nonlinear spring departs from that of a linear spring.

It is interesting to compare and contrast the transient signals of the transverse displacement and the lift coefficient in the VIV response of a circular cylinder mounted on a linear and linear/quadratic spring. Towards this objective, we consider two specific cases which exhibit comparable maximum amplitudes for the transverse displacement: namely, $(k_1, k_2, Re) = (0.0063, 0, 100)$ and $(0.003, 0.11, 120)$. The time series of the normalized displacement y/D and the lift coefficients C_L for these two cases are shown in Fig. 3.6. Note that for both cases, the maximum normalized transverse displacement y_{\max}/D assumes a value of about 0.6. Furthermore, it can be seen that starting from an initial condition where the cylinder was at rest at $y = 0$, the vibration response of the system with the linear spring achieves equilibrium at $tU_0/D = 100$, in contrast with that of the nonlinear spring which reaches equilibrium at a significantly longer time of $tU_0/D = 280$. Moreover, it is noted that the beating phenomenon appears in the early stage of the vibration response for the nonlinear spring. Finally, it is interesting to note that after the system with the linear and linear/quadratic springs reach equilibrium, the temporal fluctuations in the lift coefficient C_L are very similar and, indeed, the maximum lift coefficient has a value of about unity in both cases. Nevertheless, a careful persual of Fig. 3.6 shows that the maximum lift coefficient attained by the system with the linear/quadratic spring (with a value of about 1.37) is slightly larger than that attained by the system with the linear spring.

Next we consider two sets of cases for a linear/quadratic spring combination summarized as follows: (1) linear spring constant fixed at a value of $k_1 = 0.003 \text{ N m}^{-1}$ and the quadratic spring constant assuming values of $k_2 = 0.06, 0.11$ and 0.16 N m^{-2} ; and, (2) quadratic spring constant fixed at a value of $k_2 = 0.11 \text{ N m}^{-2}$ and the linear spring constant taking values of $k_1 = 0.002, 0.003$ and 0.004 N m^{-1} . Note in the two sets, one case overlaps; namely $(k_1, k_2) = (0.003, 0.11)$ so there are actually only five linear/quadratic spring combinations here.

Figure 3.7 displays the dependence of the maximum amplitude A_{\max} on Re for the linear/quadratic spring combinations summarized above. The results in this figure can be interpreted as two series: namely, one where k_1 is fixed at a value of 0.003 N m^{-1} with k_2 taking values of $0.06, 0.11$ and 0.16 N m^{-2} and another where k_2 is fixed at a value of 0.11 N m^{-2} with k_1 taking values of $0.002, 0.003$ and 0.004 N m^{-1} . For the first series, the maximum amplitude response associated with $k_2 = 0.06 \text{ N m}^{-2}$ (for a fixed value of k_1) has a broader (wider) peak as a function of Re than that associated with the larger values of $k_2 = 0.11$ and 0.16 N m^{-2} , implying that the case with the smallest value of the quadratic spring constant provides a response

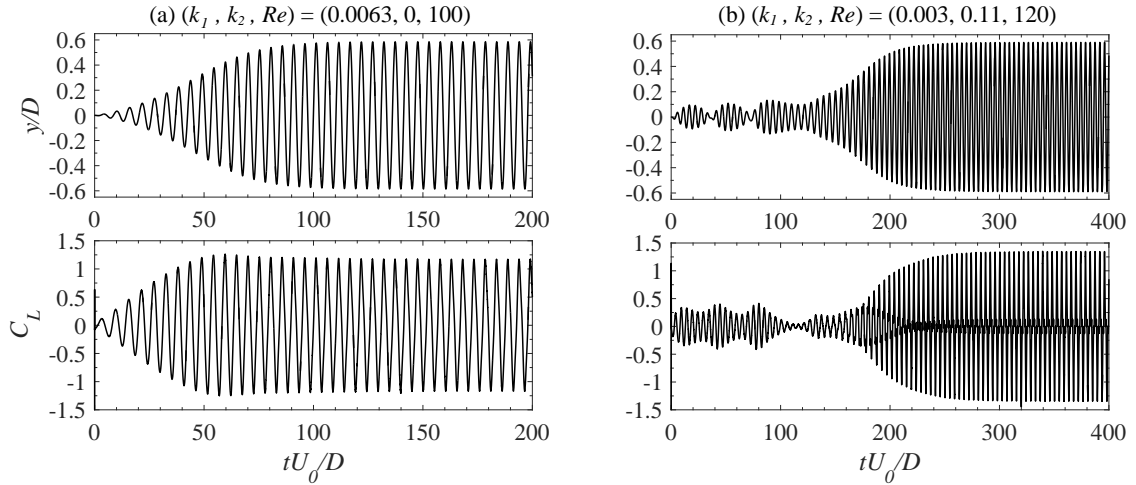


Figure 3.6: Time series of the normalized displacement y/D and the lift coefficient C_L for a circular cylinder elastically mounted on (a) a linear spring with $(k_1, k_2, Re) = (0.0063, 0, 100)$ and (b) a linear/quadratic spring with $(k_1, k_2, Re) = (0.003, 0.11, 120)$.

with the largest values of the maximum amplitude over the largest range of Reynolds number. In contrast, for the second series, the maximum amplitude response corresponding to $k_1 = 0.004 \text{ N m}^{-1}$ (for a fixed value of k_2) exhibits a broader peak as a function of Re than that corresponding to the smaller values of $k_1 = 0.002$ and 0.003 N m^{-1} , suggesting that the case with the largest value of the linear spring constant gives a response with the largest values of A_{\max} over the largest range of values of Re . Taken together, these results imply that selecting a linear/quadratic spring combination with a larger value of k_1 and a smaller value of k_2 will result a VIV system with a wider range of lock-in.

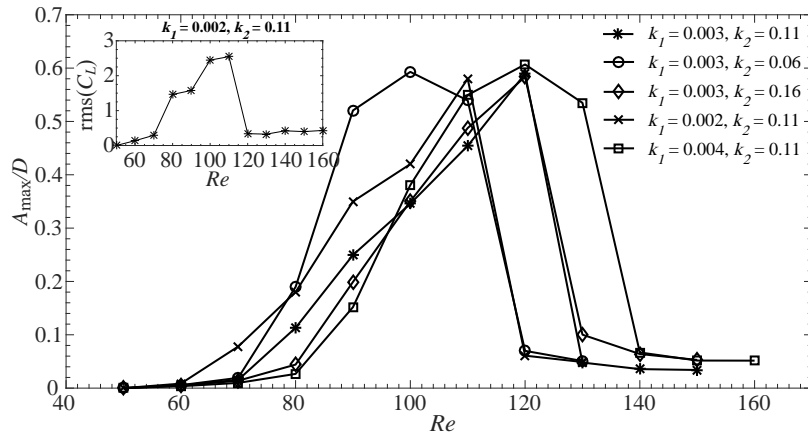


Figure 3.7: The dependence of the maximum amplitude A_{\max} on Re for an elastically-mounted cylinder with various linear/quadratic spring combinations (giving rise to different linear and nonlinear restoring forces) characterized by (k_1, k_2) . It is difficult to identify the lock-in range due to many combinations of (k_1, k_2) here, so the following contents will select a set of (k_1, k_2) with encrypted Re increment and identify the correlated lock-in interval.

The inset plot in Fig. 3.7 shows the dependence of the root-mean-square of the lift coefficient C_L as a function of the Reynolds number for the linear/quadratic spring combination $(k_1, k_2) = (0.002, 0.11)$. Note that the variation of $\text{rms}(C_L)$ with Re mirrors that of the variation of the

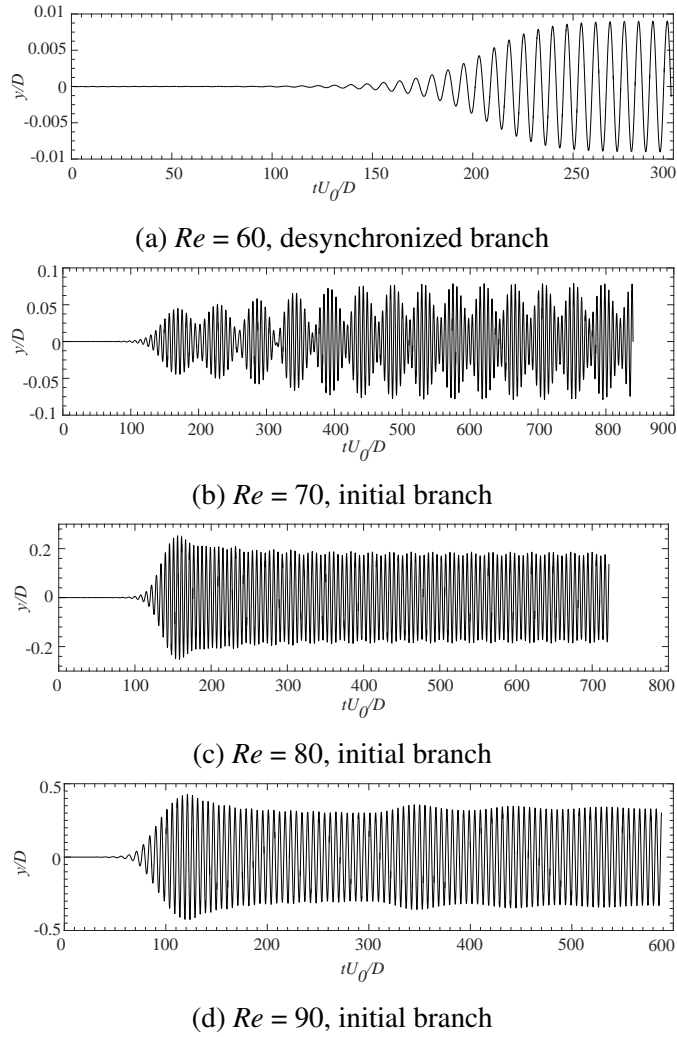


Figure 3.8: Time series of the transverse displacement of an elastically-mounted cylinder on a linear/quadratic spring with $(k_1, k_2) = (0.002, 0.11)$ for various values of Re .

corresponding A_{\max} with Re which is not surprising as a large lift force acting on the elastically-mounted cylinder will result in a large maximum amplitude for the transverse displacement y of the cylinder. Nevertheless, it should be emphasized that there is a phase difference between the lift force and the resulting transverse displacement. This will be discussed more fully below.

Figure 3.8 exhibits the time history of the transverse displacement oscillations for an elastically-mounted cylinder on a linear/quadratic spring configuration with $(k_1, k_2) = (0.002, 0.11)$ for six different Reynolds numbers spanning the range of flows from $Re = 60$ to 120 inclusive. A perusal of this figure indicates that the oscillations of the transverse displacement are periodically stable over the lock-in range. The range of Re spans the various branches of the amplitude response. More specifically, we note that the desynchronized branch occurs at $Re = 60$ and 120. The range of Re from about 70 to 110 corresponds to the transition through the lock-in range as the pattern of oscillations progresses from the initial branch to the upper branches of the amplitude response. For increasing values of Re in this range, the maximum amplitude of the response increases monotonically (approximately or better) attaining the largest A_{\max} at $Re = 110$. For Re in the range 80 to 100, the transverse displacement amplitude first increases to a maximum value and then decreases to a slightly smaller (but more stable) value of the amplitude. At $Re = 110$,

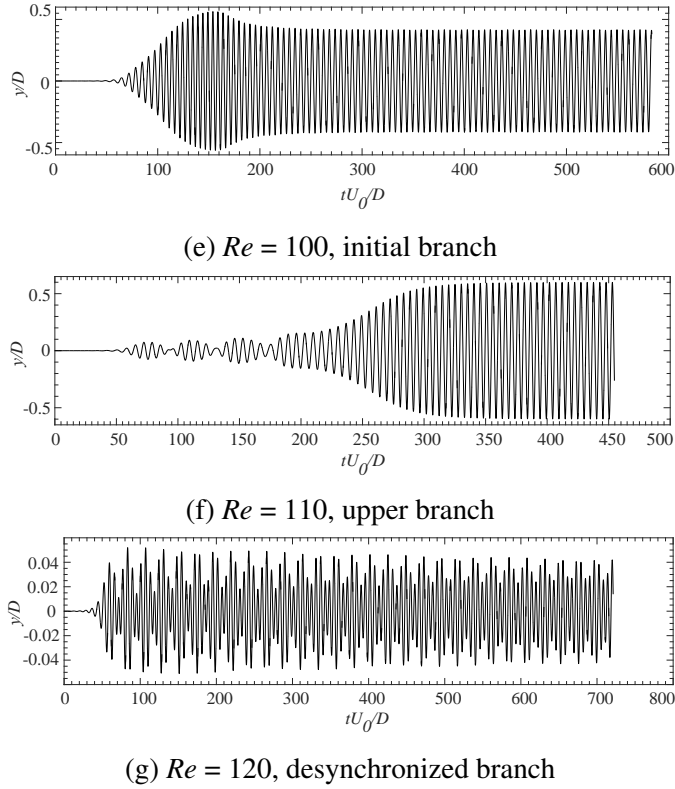


Figure 3.8: Time series of the transverse displacement of an elastically-mounted cylinder on a linear/quadratic spring with $(k_1, k_2) = (0.002, 0.11)$ for various values of Re .

the transverse displacement oscillations exhibit the largest maximum amplitude. These oscillations undergo a long transient period of fluctuations before transitioning into a stable (and large amplitude) oscillation. During this transient period, the oscillations are seen to exhibit a beating phenomenon that is associated with a mode change or a mode competition [210, 211]. This beating phenomenon is seen to still occur in the time series of the transverse displacement associated with the desynchronised branch of the response at $Re = 120$, albeit the amplitude of the response is much smaller than that in the upper and lower branches.

Figure 3.9 encapsulates the phase difference Φ between the lift force and the transverse displacement and the oscillation frequency f_{osc} of the transverse displacement as a function of Re . A perusal of the figure shows that the transition of the phase difference from 0° to 180° occurs at larger values of Re for the linear/quadratic spring configuration with the larger values of both k_1 and k_2 . The value of Re at which Φ transitions from 0° to 180° is consistent with the value of Re where the maximum amplitude A_{max} exhibits the sudden drop in value after the largest value of amplitude has been achieved in the lock-in range. As discussed previously, with respect to the hardening spring VIV system, the square of the equivalent natural frequency $\omega_{\text{eq}}^{(2)}$ of a linear/quadratic spring configuration is proportional to the amplitude a of the transverse displacement. In consequence, the quadratic spring contribution implies that the equivalent natural frequency will depend on Re (owing to the fact that the amplitude depends on Re) which, in turn, suggests that the oscillation frequency cannot be locked at one constant structural natural frequency in the initial branch even though the VIV system exhibits a large-amplitude response. Indeed, the vortex shedding frequency is proportional to Re which, in turn, affects the oscillation frequency of the VIV system for the nonlinear lock-in range. A more detailed comparison and

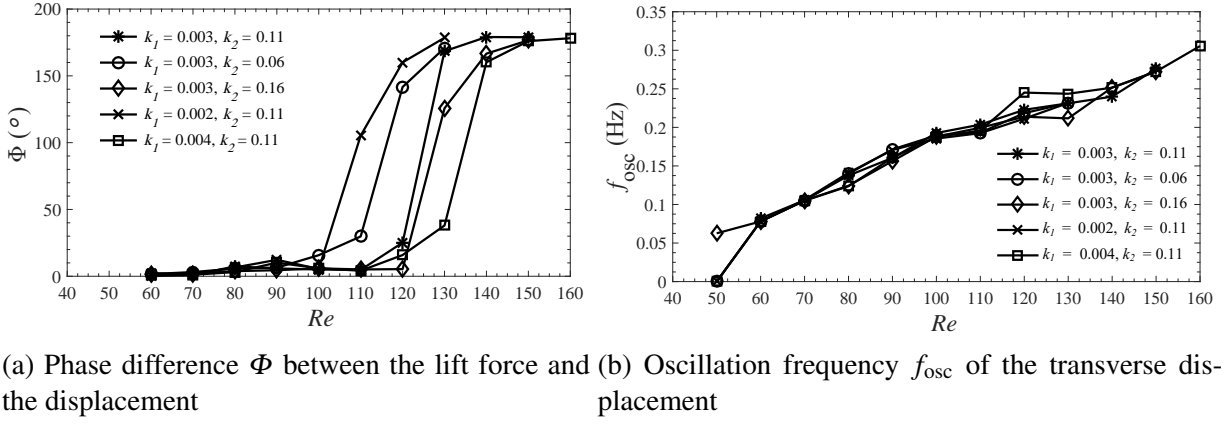


Figure 3.9: (a) The phase difference Φ between the lift force and the transverse displacement and (b) the oscillation frequency f_{osc} of the transverse displacement as a function of Re for an elastically-mounted cylinder on a linear/quadratic spring configuration characterized by (k_1, k_2) .

analysis of the frequencies of the structural oscillations, the fluid force (or, lift coefficient), and the nature of the vortex shedding will be provided later in the study for one particular case.

Figure 3.10 displays the power spectral density (PSD) of the normalized transverse displacement oscillations $y(t)/D$ and the associated phase-plane diagrams (viz., plots of the normalized transverse displacement y/D versus the transverse velocity $d(y/D)/dt$ of the normalized displacement). The results shown are stratified in terms of Re for two cases of an elastically-mounted cylinder on a linear/quadratic spring configuration characterized by $(k_1, k_2) = (0.003, 0.06)$ and $(0.003, 0.16)$. It is noted that the results for the linear/quadratic spring system with $(k_1, k_2) = (0.003, 0.06)$ for $Re = 110, 120$ and 130 (two leftmost columns of panels in Fig. 3.10) and with $(k_1, k_2) = (0.003, 0.016)$ for $Re = 120, 130$ and 140 (two rightmost columns of panels in Fig. 3.10) show the behavior of the transverse displacement oscillations in the upper to desynchronised branches of the amplitude response. In the former case for $Re = 110$ and in the latter case for $Re = 120$, the PSD of the transverse displacement exhibits one peak (corresponding to one dominant frequency of oscillation) and the associated phase-plot diagram is consistent with the dynamics associated with a periodic system. The behavior is consistent with the appearance of the time series plots of the transverse displacement oscillations shown in Fig. 3.8 and, more specifically, with the time series corresponding to $Re = 110$ in that figure which is associated with the upper or lower branches of the lock-in range.

For $(k_1, k_2) = (0.003, 0.06)$ at $Re = 120$ and $(k_1, k_2) = (0.003, 0.16)$ at $Re = 130$ in Figs 3.10(a) and (b), respectively, the power spectra of the normalized transverse displacements exhibit two peaks and the associated phase-plane diagrams consist of two lobes (which we will refer to simply as a “binocular” effect). The “binocular” phenomenon observed herein implies that the equilibrium point of the transverse displacement oscillations does not correspond simply to $y = 0$. Rather, there are two equilibrium points in the oscillations and the dynamics switches (transitions) from one point to the other in the course of the temporal evolution of $y(t)$. This behavior is consistent with the beating phenomenon in the transverse displacements discussed previously with reference to Fig. 3.8 (and, more particularly with reference to part (g) of that figure corresponding to $Re = 120$) which is associated with the transition of the dynamical system out of the lock-in range [110]. The “binocular” effect observed in the phase-plane diagrams here is clearly associated with the beating effect whereby two oscillations in the transverse displacement of very

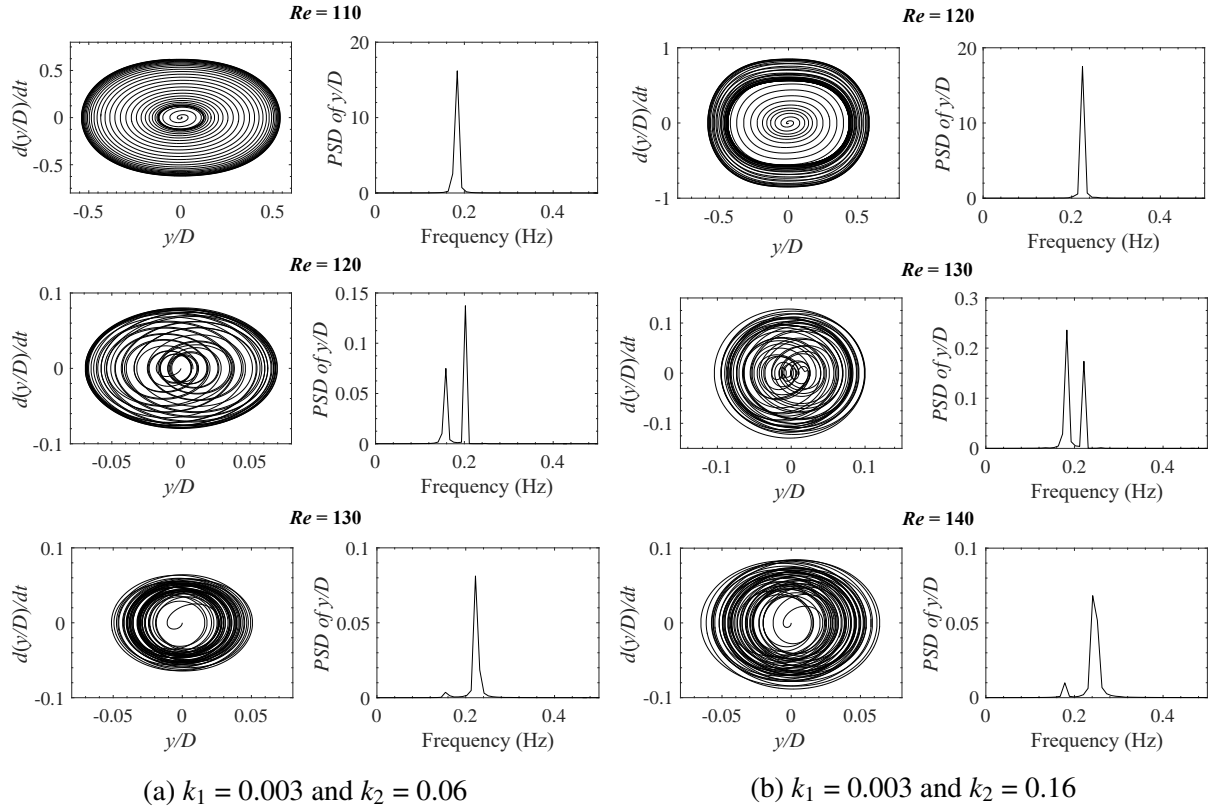


Figure 3.10: Power spectral density (PSD) of the normalized transverse displacement y/D and the associated phase-plane diagram for an elastically-mounted cylinder on a linear/quadratic spring configuration with (a) $(k_1, k_2) = (0.003, 0.06)$ for $Re = 110, 120$ and 130 and (b) $(k_1, k_2) = (0.003, 0.16)$ for $Re = 120, 130$ and 140 .

similar frequencies interfere with one another, producing periodic and repeating modulations in the vibrations (viz., beats).

It is noted that as Re increases, the “binocular” effect vanishes as the amplitude response of the VIV system transitions into the desynchronised branch. When this occurs, the oscillations of the transverse displacement of the cylinder correspond to a single dominant frequency and the constant amplitude of the oscillations decreases to a level consistent with the transition out of the lock-in range (associated with the desynchronised branch of the amplitude response). The signature of this effect is clearly seen in Fig. 3.10 at $Re = 130$ for $(k_1, k_2) = (0.003, 0.06)$ and at $Re = 140$ for $(k_1, k_2) = (0.003, 0.16)$ in both the power spectra of the transverse displacement and in the corresponding phase-plot diagrams.

3.3.2 Equivalent natural frequency and identification of branches of the response

As discussed above, in a cylinder mounted on a nonlinear spring and subject to VIV, the natural structural frequency of the system changes with the oscillation amplitude. In consequence, it is beneficial to derive an equivalent natural frequency f_{eq} for such a VIV system which can be used for interpretation of the phenomenon. To this purpose, a useful procedure is the describing function (equivalent linearization) technique which was first applied in control theory to pro-

vide approximate solutions to (weakly) nonlinear systems subject to random excitations [212]. In this technique, each nonlinear term (element) in the system is replaced with a (quasi) linear term (element) with an appropriate functional form (describing function) that approximates the input-output response of the nonlinear element [213]. The gain of the linear element (obtained as part of the equivalent linearization of the nonlinear system) is a function of the amplitude of the input, with the form of the function (or, describing function) depending on the type (nature) of the input. Two examples of describing functions that are used in the equivalent linearization technique are the sinusoidal input describing function (SIDF) [214, 215] and the random input describing function (RIDF) [216].

To obtain an equivalent natural frequency for an oscillating cylinder mounted elastically on a linear/nonlinear spring with no structural damping ($c = 0$), we re-cast Eq. 3.4 as follows:

$$\ddot{y} + \omega_1^2 y + \frac{k_n}{m} l_n(y, \dot{y}) = f_y, \quad (3.6)$$

where $\omega_1 \equiv \sqrt{k_1/m}$ (natural frequency of linear spring) and $f_y \equiv F_y/m$. Equation 3.6 could be recast as

$$\ddot{y} + \omega_{\text{eq}}^{(n)2} y = f_y, \quad (3.7)$$

where $\omega_{\text{eq}}^{(n)}$ is the equivalent frequency for the linear/nonlinear spring system. It is assumed that the displacement y can be approximated by a sinusoid with a slow modulation of the amplitude and phase as follows (sinusoidal input describing function):

$$y(t) = a(t) \sin\left(\omega_{\text{eq}}^{(n)} t + \phi(t)\right). \quad (3.8)$$

Using the equivalent linearization methodology described by Caughey [213], the equivalent frequency $\omega_{\text{eq}}^{(n)}$ can be obtained for a linear/nonlinear spring system. The derivation of $\omega_{\text{eq}}^{(n)}$ is described in Appendix A for a general linear/nonlinear spring. The key result required for the current analysis can be succinctly summarized as follows. For a linear/quadratic spring system (when $n = 2$), the equivalent frequency $\omega_{\text{eq}}^{(2)}$ is given by

$$\omega_{\text{eq}}^{(2)2} = \omega_1^2 \left(1 + \varepsilon_2 \frac{2}{\sqrt{\pi}} \langle a^2 \rangle^{1/2}\right), \quad (3.9)$$

where $\langle a^2 \rangle$ is the mean-square amplitude of the transverse oscillations and $\varepsilon_2 \equiv k_2/k_1$. During the lock-in range, when the amplitude and phase is constant (approximately or better) so $a(t)$ and $\phi(t)$ are *not* slowly-varying functions of time t , the equivalent frequency assumes the following form:

$$\omega_{\text{eq}}^{(2)2} = \omega_1^2 \left(1 + \varepsilon_2 \frac{8}{3\pi} a\right), \quad (3.10)$$

where a is the maximum amplitude of the transverse oscillations. Note that for a linear/quadratic spring system, the equivalent natural frequency varies as the square root of the root-mean-square amplitude (for transverse oscillations with a slow modulation in the amplitude and phase) or with the square root of the (maximum) amplitude (for transverse oscillations whose amplitude and phase are constant in time).

Figure 3.11 shows the equivalent natural frequency $f_{\text{eq}} \equiv \omega_{\text{eq}}/(2\pi)$ for a linear spring with $k_1 = 0.0063 \text{ N m}^{-1}$ and a linear/quadratic spring with $k_1 = 0.003 \text{ N m}^{-1}$ and $k_2 = 0.11 \text{ N m}^{-2}$.

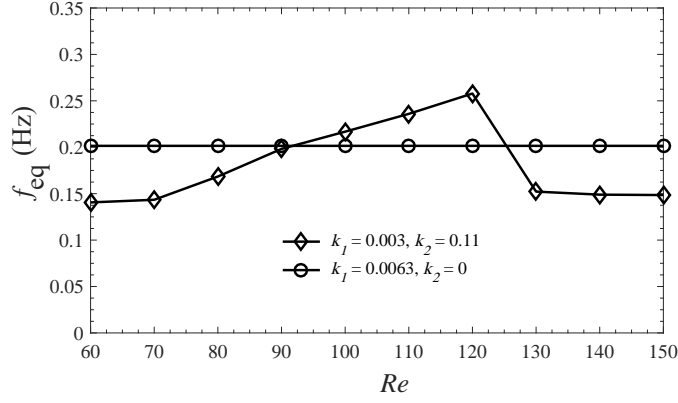


Figure 3.11: Equivalent natural frequency f_{eq} of the system for a linear and a linear/quadratic spring.

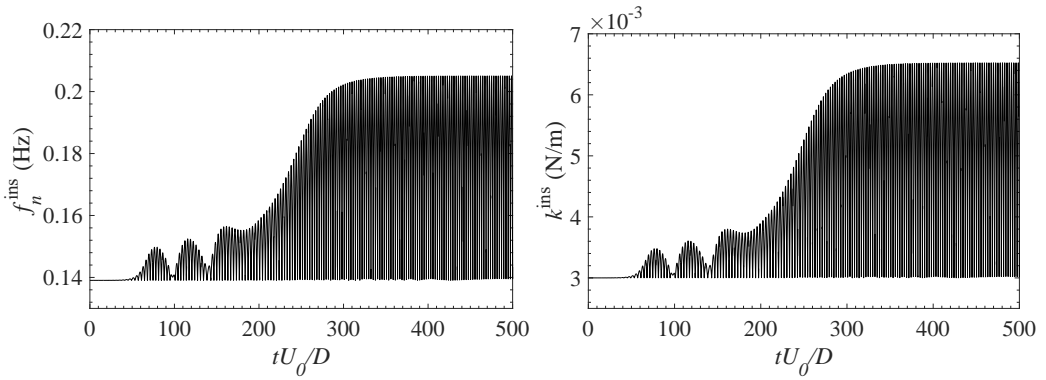


Figure 3.12: Time series of the (a) instantaneous natural frequency f_n^{ins} and (b) instantaneous stiffness k^{ins} of an elastically-mounted cylinder on a linear/quadratic spring configuration with $(k_1, k_2) = (0.003, 0.11)$ for a flow with $Re = 120$.

The sudden decrease in the maximum amplitude at $Re \approx 120$ exhibited in Fig. 3.4a for the linear/quadratic spring with $(k_1, k_2) = (0.003, 0.11)$ corresponds to the sharp decrease in f_{eq} at $Re \approx 120$ for the linear/quadratic spring as seen in Fig. 3.11. Here, the equivalent natural frequency is seen to be the natural frequency of the linear spring with $k_1 = 0.003 \text{ N m}^{-1}$ after the sharp decrease in value for Re greater than about 120. This suggests that the natural frequency arising from the linear part of the linear/quadratic spring system is stable and determines the minimum value of the natural frequencies inherent in the linear/quadratic spring, a contention which is supported by Fig. 3.12. More specifically, Fig. 3.12 displays the instantaneous stiffness $k^{\text{ins}} \equiv k_1 + k_2|y|$ and the instantaneous natural frequency $(2\pi)f_n^{\text{ins}} \equiv \sqrt{k^{\text{ins}}/m}$. If the nonlinear restoring forces arise from the combination of a linear part (k_1) and a quadratic part (k_2) of linear/quadratic spring combination, the instantaneous natural frequency will vary over a range of frequencies with the minimum value in the range determined by the natural frequency of the linear spring (characterized by k_1).

To obtain a deeper understanding of the behavior of each branch of the VIV response of a circular cylinder mounted on a linear/quadratic spring, and further explore the relationship between the derived equivalent natural frequency and oscillation frequency, we conducted a series of simulations for the case $(k_1, k_2) = (0.002, 0.11)$ at twenty-five different values of Re in the range from 50 to 140. The variation of the maximum normalized amplitude A_{max}/D of the trans-

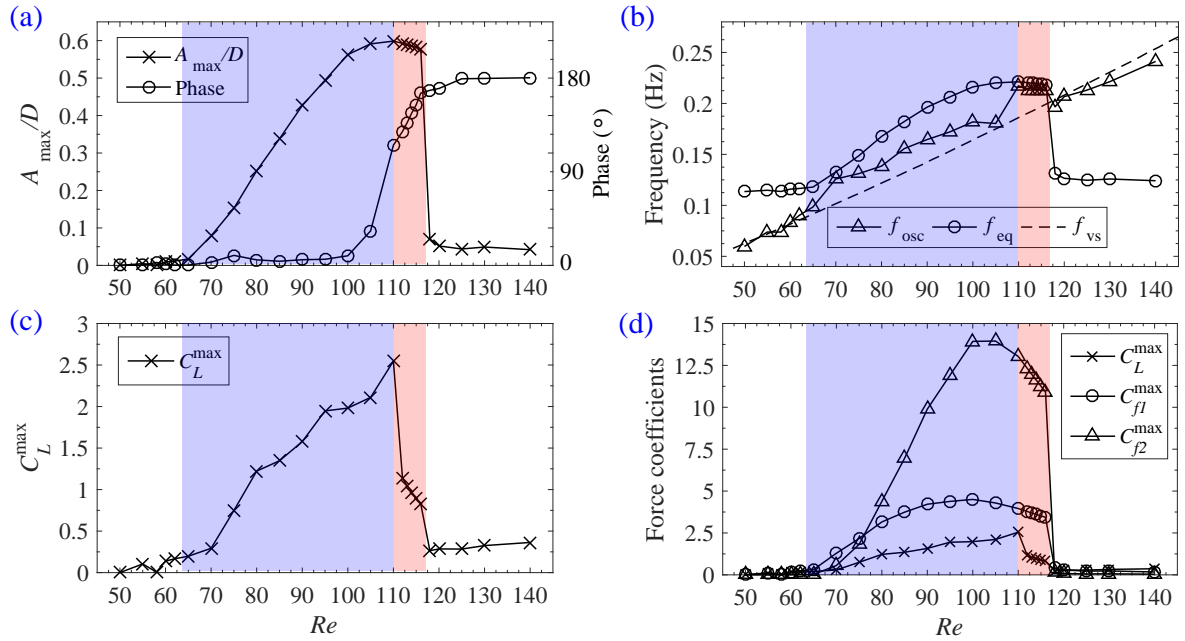


Figure 3.13: (a) Normalized structural amplitude A_{\max}/D and phase difference Φ , (b) structural oscillation frequency f_{osc} , original vortex-shedding frequency f_{vs} and equivalent natural frequency f_{eq} , (c) maximum lift coefficient C_L^{\max} , and (d) normalized amplitudes of the fluid force (viz., the maximum lift coefficient and the force coefficients associated with the linear (C_{f1}^{\max}) and the quadratic (C_{f2}^{\max}) contributions of the elastic force as a function of Re for $(k_1, k_2) = (0.002, 0.11)$. The region associated with the start of the initial branch to the beginning of the upper branch is shaded in blue. The upper and lower branches are delineated as the red-shaded region.

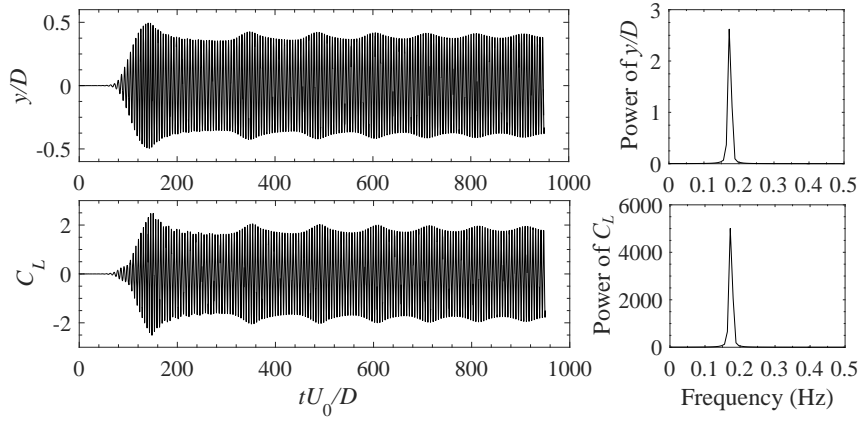
verse displacement and the maximum lift coefficient C_L^{\max} as a function of Re is summarized in Figs 3.13(a) and (c). The maximum amplitude A_{\max}/D exhibits a monotonic increase with increasing Re for Re in the range from 65 to 110 (delineated as the blue-shaded region) and this monotonic increase in the maximum amplitude is associated with a corresponding monotonic increase in C_L^{\max} over the same range of Re . For the range $110 < Re < 117$ (delineated as the red-shaded region), it is observed that A_{\max}/D exhibits a small decrease in value from about 0.599 to 0.578. This small decrease in A_{\max}/D just before the transition out of the lock-in range is consistent with those observed for $(k_1, k_2) = (0.003, 0.06)$ and $(0.004, 0.11)$ in Fig. 3.7 and for $(0, 0.14)$ in Fig. 3.4a. In marked contrast, over this range of Re , the corresponding C_L^{\max} displays a sudden (rapid) decrease in value. In accordance with the characteristics of the branches of a VIV system supported by a linear spring [11], C_L^{\max} is known to rapidly increase in the initial branch to a maximum value (associated with the start of the upper branch) and then gradually decrease in value as the VIV system transitions from the upper to the lower branch. The range of Re associated with the initial branch for a VIV system with a linear spring is very narrow. In contrast, compared to a linear restoring force, the nonlinear restoring force associated with the response of a VIV system with a nonlinear spring will exhibit an increased (extended) range of Re corresponding to the transition from the initial branch to the upper branch (or, equivalently, from the smallest to largest values of A_{\max}/D or C_L^{\max}), while the range of Re associated with upper and lower branches is reduced. An examination of Fig. 3.13(a) shows that the phase difference Φ between the lift force and the transverse displacement is small ($\Phi \lesssim 10^\circ$) in the early stages of the initial branch. When the Reynolds number Re approaches values associated with

the beginning of the upper branch ($100 < Re < 110$), the phase difference Φ begins to increase, slowly at first and then rapidly in the upper/lower branch as Φ tends to 180° . When the system transitions out of the lock-in range, Φ maintains a value of about 180° as Re increases further.

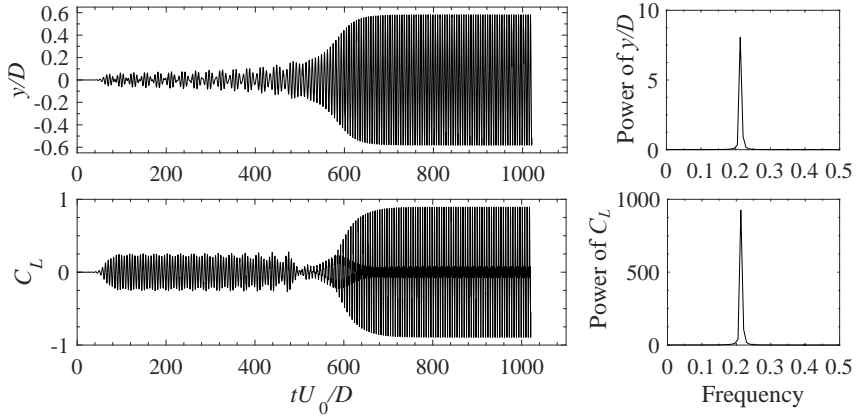
Next, we investigated in detail the frequency response of the VIV system with a linear/quadratic spring in order to validate the equivalent natural frequency derived earlier (with details given in Appendix A). To this purpose, the structural oscillation frequency f_{osc} , the original vortex-shedding frequency f_{vs} and the equivalent natural frequency f_{eq} as a function of Re are compared Fig. 3.13(b). Firstly, in the region outside the blue- and red-shaded areas, the VIV system is in the desynchronized branch. The variation of f_{osc} with increasing Re approaches the dashed line corresponding to the vortex-shedding frequency f_{vs} , indicating that the behavior of the VIV system corresponds to that of a forced vibration. Secondly, in the blue-shaded region (which is associated with the start of the initial branch to the beginning of the upper branch), the value of the oscillation frequency f_{osc} is larger than that of the vortex-shedding frequency f_{vs} and smaller than the equivalent natural frequency f_{eq} . This suggests that the structural natural frequency and the vortex-shedding frequency together affect the vibration, and the structural oscillation frequency f_{osc} cannot be locked at one constant value. However, when the system enters the red-shaded region (associated with the upper and lower branches), f_{osc} is essentially identical to f_{eq} (approximately or better) and is effectively constant as Re increases, indicating that the system has entered the lock-in regime which is similar to that of a VIV system with a linear spring. Furthermore, this implies that the equivalent natural frequency f_{eq} derived herein is correct and can be used to study the characteristics of the natural frequency of the VIV system with a linear/quadratic spring which extends (generalizes) the results reported by Wang et al. [110].

Figure 3.13(d) exhibits the variation of the force coefficients C_L^{\max} , C_{f1}^{\max} , and C_{f2}^{\max} as a function of Re . Here, $C_L^{\max} \equiv F_y^{\max}/(\rho U_0^2 D/2)$ is the maximum lift coefficient; and, $C_{f1}^{\max} \equiv (k_1 A_{\max})/(\rho U_0^2 D/2)$ and $C_{f2}^{\max} \equiv (k_2 A_{\max}^2)/(\rho U_0^2 D/2)$ are the maximum force coefficients corresponding to the linear and quadratic contributions of the elastic force, respectively. The maximum values of C_{f1}^{\max} and C_{f2}^{\max} occur at a value of $Re \approx 100$, whereas the maximum value of C_L^{\max} occurs at a value of $Re \approx 110$. In the red-shaded region (associated with the upper and lower branches of the response), all three force coefficients are seen to decrease with increasing Re in this region. Furthermore, the force coefficient associated the quadratic contribution to the elastic force displays the largest amplitude owing to its nonlinear character. This implies that the quadratic spring plays a dominant role in this VIV system.

To compare the variation of the transient signal in the initial and lower branches of the VIV response, we investigate two cases: namely, $(k_1, k_2, Re) = (0.002, 0.11, 95)$ (for the initial branch) and $(0.002, 0.11, 115)$ (for the lower branch). Time series of the normalized transverse displacement y/D and the lift coefficient C_L and the corresponding power spectral densities for these quantities are shown in Fig. 3.14. It is noted that the power spectrum was calculated for that portion of the time series when the quantity (displacement or lift coefficient) has reached equilibrium. Similar to our discussion of Fig. 3.8, it is seen that the time required for the transverse displacement and the lift coefficient to reach equilibrium at $Re = 95$ and 115 is shorter for the displacement than for the lift coefficient. Furthermore, the time variation of y/D and C_L at $Re = 95$ exhibits a small modulation in their amplitudes. In both the initial and lower branches of the response, the fluctuation frequency of C_L is locked to the structural oscillation frequency. The development of y/D in the lower branch for $(k_1, k_2, Re) = (0.002, 0.11, 115)$ can be partitioned into two regimes with the boundary separating these two regimes occurring at the normalized time $tU_0/D = 500$. In the first regime with the normalized time ranging from 0 to 500, the time



(a) Initial branch: $(k_1, k_2, Re) = (0.002, 0.11, 95)$.



(b) Lower branch: $(k_1, k_2, Re) = (0.002, 0.11, 115)$.

Figure 3.14: Time series of the normalized transverse displacement y/D and the lift coefficient C_L along with the associated power spectral density for these quantities: (a) initial branch with $(k_1, k_2, Re) = (0.002, 0.11, 95)$ and (b) lower branch with $(k_1, k_2, Re) = (0.002, 0.11, 115)$.

series of the transverse displacement and the lift coefficient displays a modulation. In second regime with $500 < tU_0/D < 1000$, modulations in the time series of y/D and C_L are absent. Finally, at the end of the first regime, the amplitude of C_L decreases to near zero and is subsequently amplified in concert with the increase in the amplitude of the transverse displacement.

3.3.3 Wake pattern and DMD analysis

Williamson and Roshko [217] classified wake patterns observed in VIV systems into three classes: namely, ‘P’ corresponding to vortex pairs, ‘S’ corresponding to a single vortex and ‘SP’ associated with a configuration consisting of a ‘S’ and ‘P’ mode. It was normally considered that the patterns in the wake vortex dynamics model for VIV were related (correlated) to the transverse displacement of the cylinder.

Figure 3.15 exhibits the vorticity isopleths illustrating the wake vortex dynamics of an elastically-mounted cylinder with a linear/quadratic spring configuration of $(k_1, k_2) = (0.002, 0.11)$ and $(k_1, k_2) = (0.003, 0.11)$ at various values of Re corresponding, as such, to various values of the maximum amplitude A_{\max}/D . The patterns of vorticity shown in the leftmost column of panels in

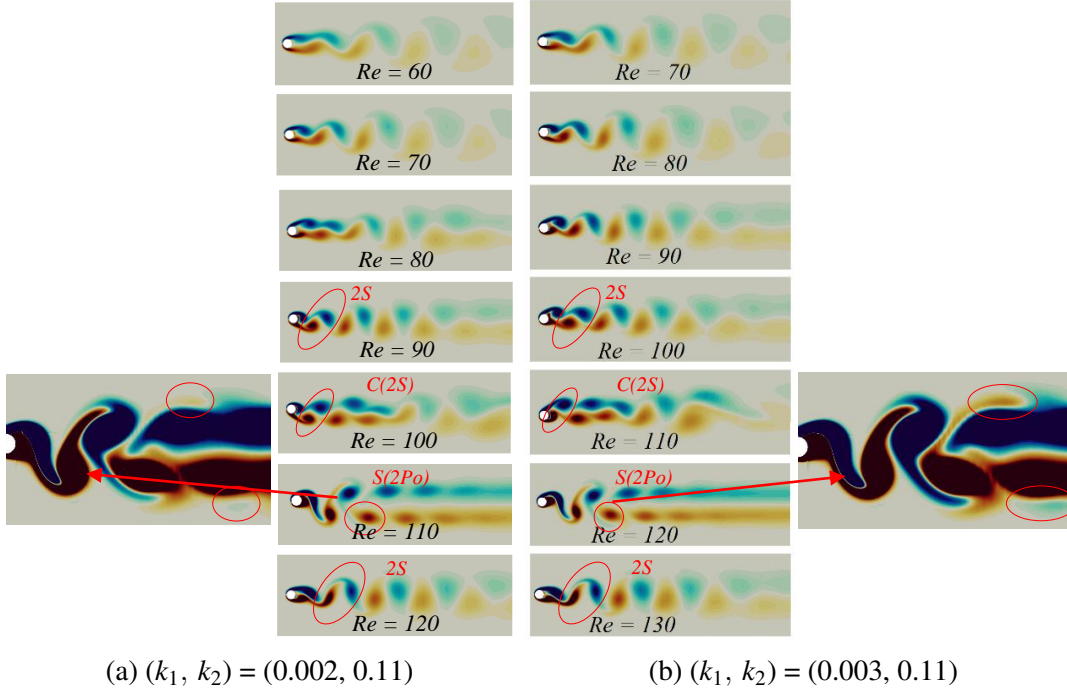


Figure 3.15: Isoleths of the vorticity in the wake of an elastically-mounted cylinder on a linear/quadratic spring configuration with (a) $(k_1, k_2) = (0.002, 0.11)$ for seven equally-spaced values of Re from 60 to 120 inclusive and with (b) $(k_1, k_2) = (0.003, 0.11)$ for seven equally-spaced values of Re from 70 to 130 inclusive. Incident flow direction is from left to right in the figure.

this figure are associated with the temporal evolution of the transverse displacement y/D shown in Fig. 3.8. Owing to the small amplitude displacement for $(k_1, k_2) = (0.002, 0.11)$ at $Re = 60$ or $(k_1, k_2) = (0.003, 0.11)$ at $Re = 70$, the wake vortex dynamics are seen to be statistically stationary (approximately or better) and the vortex shedding regime here displays a 2S wake pattern. When the maximum amplitude A_{\max}/D of the transverse displacement increases to $A_{\max}/D = 0.41$ for $(k_1, k_2, Re) = (0.002, 0.11, 100)$ or to 0.46 for $(k_1, k_2, Re) = (0.003, 0.11, 110)$, the topology of the vortical wake pattern changes to C(2S). The topology (as more clearly seen in the enlarged sub-figures of Fig. 3.15 with the darkened colors) of the vortical wake pattern is consistent with that identified in the investigation of Huang et al. [218], namely the so-called S(2Po) pattern. The smaller vortices (identified by the red ellipses in enlarged plots) in the up/down pairs are located at the top/bottom of the strong vortex, and is quickly damped out in wake region due to the low Reynolds number. It is noted that for Re ranging from 60 to 100 for $(k_1, k_2) = (0.002, 0.11)$ and from 70 to 110 for $(k_1, k_2) = (0.003, 0.11)$, the response here belongs to the initial branch; and, for $Re = 110$ at $(k_1, k_2) = (0.002, 0.11)$ and for $Re = 120$ at $(k_1, k_2) = (0.003, 0.11)$, the response here belongs to the upper branch. Overall, this observed transition in the wake oscillatory pattern with increasing oscillation amplitude is consistent with the results reported by Lambert and Olivier [219] and by Prasanth and Mittal [135].

Figure 3.16 exhibits the velocity deficit $\delta U \equiv (1 - \|\vec{U}\|/U_0)$ ($\|\vec{U}\|$ is the Euclidean norm of the flow velocity \vec{U} and U_0 is the incident wind speed) in the wake of a cylinder mounted elastically on a linear/quadratic spring configuration with $(k_1, k_2) = (0.002, 0.11)$. Note that both the maximum amplitude of the transverse displacement y/D and the velocity deficit δU increase as Re increases from 100 to 110. These characteristics are correlated with the transition in the vortex shedding regime from C(2S) for $Re = 100$ to 2P for $Re = 110$ as shown in Fig. 3.15(a).

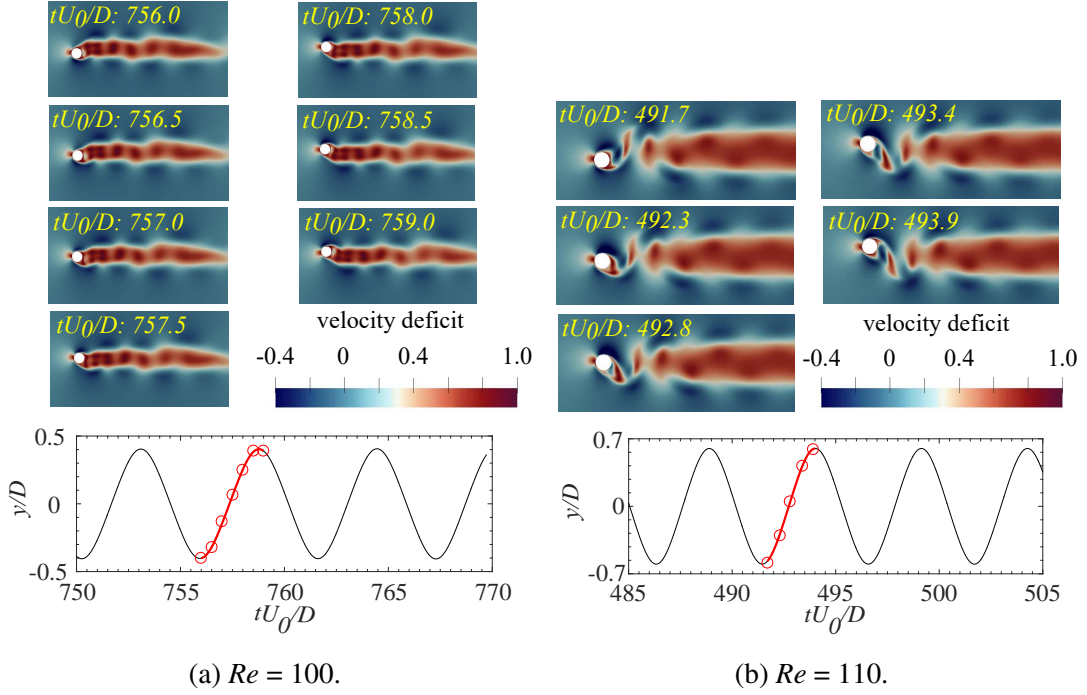


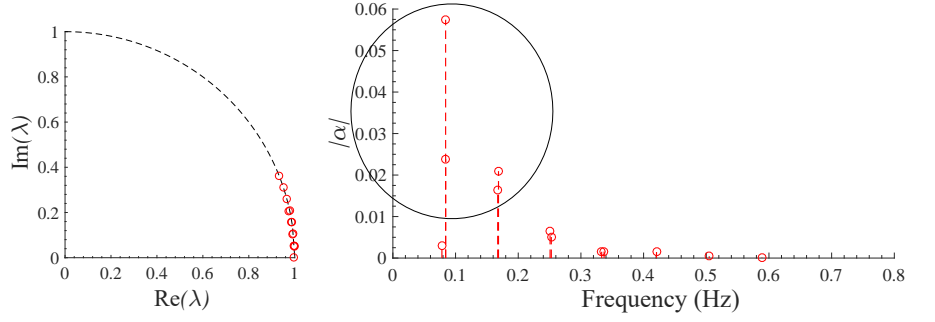
Figure 3.16: The velocity deficit $\delta U \equiv (1 - \|\vec{U}\|/U_0)$ obtained in the wake of an elastically-mounted cylinder on a linear/quadratic spring configuration with $(k_1, k_2) = (0.002, 0.11)$ at (a) $Re = 100$ for seven equally-spaced points in time over one-half cycle of the transverse displacement oscillation (bottom panel) and at (b) $Re = 110$ for five-equally spaced points in time over one-half cycle of the transverse displacement oscillation (bottom panel). Incident flow direction is from left to right in the figure.

Furthermore, velocity deficit region in the cylinder wake is wider in the transverse direction and the wake vortices initially attached to the surface of the cylinder are swept away more quickly from the surface for $Re = 110$ than for $Re = 100$.

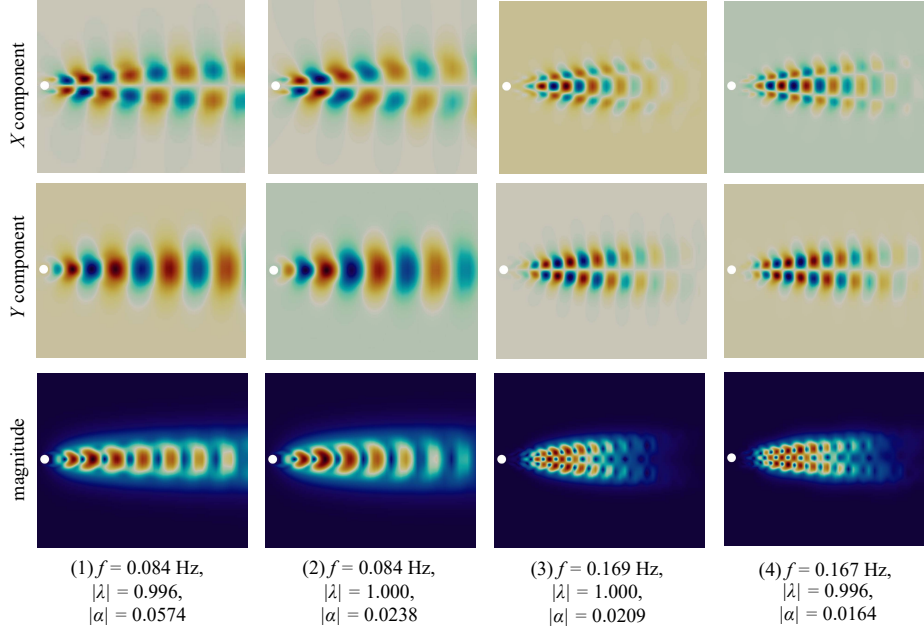
Next, the wake oscillatory dynamics is analyzed using dynamic mode decomposition (DMD) which is used here identify characteristic features in the vortical motions that can be associated with physically meaningful damped (or driven) sinusoidal (periodic) behavior. To this purpose, the velocity field is sampled at a point in the wake of an elastically-mounted cylinder at a rate of 50 samples per oscillation cycle for a total sampling time of 40 oscillation cycles. These sequential snapshots of the velocity field at a given location are stacked into columns of a data matrix \mathbf{X} from which the DMD modes and eigenvalues can be computed using a DMD algorithm.

An examination of Figs 3.17, 3.18 and 3.19 shows that the DMD velocity modes are symmetrically or anti-symmetrically distributed with respect to the centerline. According to the proper orthogonal decomposition (POD) analysis of Qu et al. [220] and Konstantinidis et al. [221], the antisymmetric distributions represent the antisymmetric vortex-shedding modes, while the symmetric distributions correspond to the symmetric shedding process.

The modes extracted from the DMD analysis are correlated with characteristic harmonics (frequencies) associated with both the vortex shedding of the stationary cylinder (viz., cylinder that has not been coupled to a spring) and the VIV oscillations of the elastically-mounted cylinder on the linear/quadratic spring. Figure 3.17 exhibits the results of the DMD analysis for an elastically-mounted cylinder on a linear/quadratic spring configuration with $(k_1, k_2) =$



(a) Spectrum of eigenvalues (b) Amplitude of DMD modes (data within circle visualized in (c))



(c) The four largest DMD modes sorted by decreasing amplitude

Figure 3.17: Dynamic mode decomposition of velocity time series obtained in the wake of an elastically-mounted cylinder on a linear/quadratic spring configuration with $(k_1, k_2) = (0.002, 0.11)$ at $Re = 60$ summarized in terms of (a) spectrum showing the distribution of the real and imaginary parts of the eigenvalues; (b) amplitudes of the DMD modes normalized by the maximum amplitude and plotted as a function of the frequency; and, (c) real part of the DMD modes depicted using contours of the velocity components and velocity magnitude (white: zero; red: above a given positive threshold; blue: below a given negative threshold).

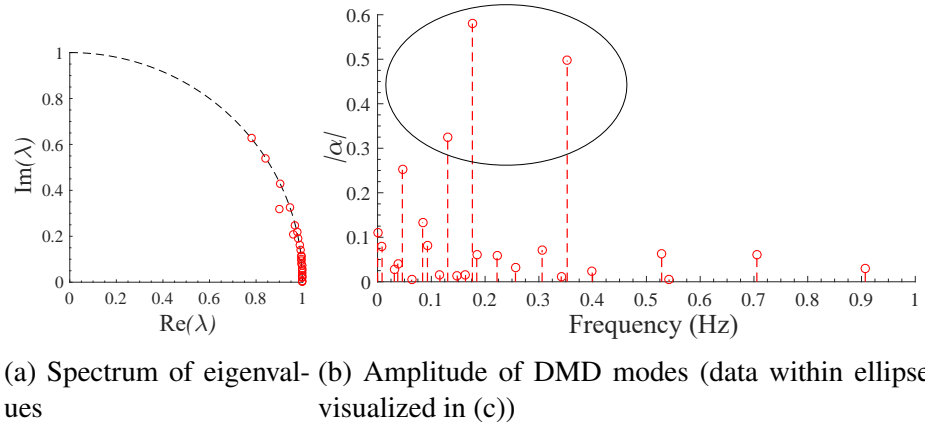
$(0.002, 0.11)$ for $Re = 60$ where the maximum displacement amplitude is only $A_{\max}/D = 0.008$ (suggesting that the oscillations of the transverse displacements can be interpreted as being approximately statistically stationary). An examination of Fig. 3.17a shows that the modulus of the (complex) eigenvalues is unity (viz., $|\lambda| = 1$), so all the eigenvalues lie on the unit circle in the complex plane. This implies that the wake oscillatory dynamics of the flow is approximately linear (or, quasi-linear) which is consistent with similar results reported by Hemati et al. [222] and Sarkar et al. [223].

The amplitudes of the various DMD modes normalized by the maximum amplitude are displayed Fig. 3.17b as a function of their associated frequency. It is noted that the first two modes

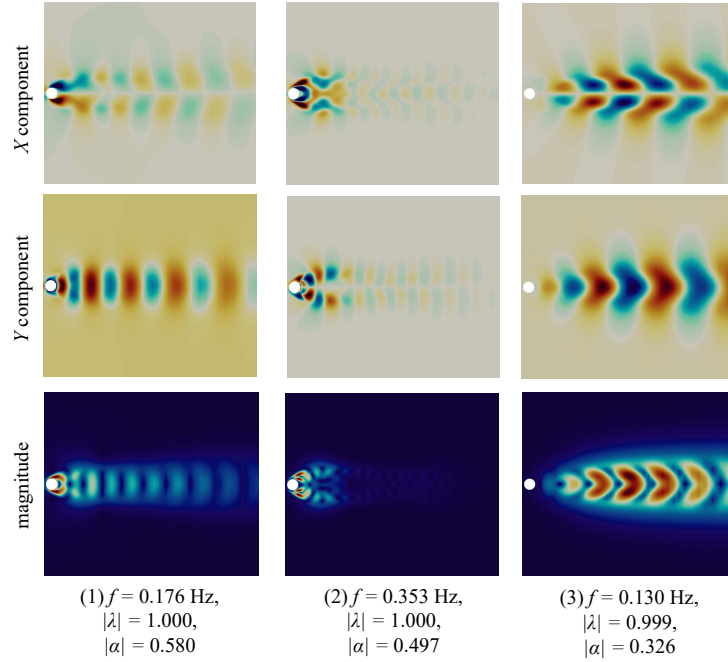
corresponding to a frequency f of 0.084 Hz (or, equivalently, to a Strouhal number of $St = 0.14$) are associated with the largest magnitude in energy. According to Kozlov et al. [224] and Qu et al. [225], the Strouhal number St for flow past a stationary cylinder for $Re = 60$ is 0.14 which is consistent with the characteristic frequency associated with the first two DMD modes. In consequence, these first two DMD modes are associated with wake oscillatory motions (and concomitant vortex shedding structures, so-called ‘Kármán street modes’) of the stationary cylinder at $Re = 60$. The real parts of the first four DMD modes with the largest amplitude (data highlighted within the circle in Fig. 3.17b corresponding to the first four dominant modes) are visualized as color isopleths of the velocity components and the magnitude of the velocity in Fig. 3.17c. The spatial pattern of the first two DMD modes are similar, albeit with a phase difference. Similarly, the third and fourth dominant modes are seen to have a similar spatial pattern. All these dominant modes exhibit a symmetry/anti-symmetry pattern. The features of modal similarity, symmetry/anti-symmetry, and phase shift have been observed in the principal orthogonal decomposition (POD) analysis conducted Siegel et al. [226] in the context of the low-dimensional modeling of a transient cylinder wake.

Figure 3.18 summarizes the DMD analysis of the velocity in the wake of an elastically-mounted cylinder on a linear/quadratic spring configuration with $(k_1, k_2) = (0.002, 0.11)$ for $Re = 100$ with a maximum displacement amplitude of $A_{\max}/D = 0.41$. Again, it is seen that the moduli of almost all the eigenvalues are unity and so lie on the unit circle of the complex plane. The first three dominant DMD modes are enclosed by the ellipse in Fig. 3.18b. Of these three modes, the first two dominant modes are associated with dominant frequencies of 0.176 Hz (or, $St = 0.176$) and 0.353 Hz (or, $St = 0.353$). These two dominant frequencies are correlated with the first and second harmonics for the elastically-mounted cylinder on the linear/quadratic spring configuration with $(k_1, k_2) = (0.002, 0.11)$ at $Re = 100$. These results can be compared to Fig. 3.9b where it can be seen that $f_{\text{osc}} \approx 0.17$ Hz at $Re = 100$ for $(k_1, k_2) = (0.002, 0.11)$, which is coincident with the first harmonic frequency of the elastically-mounted cylinder and with the frequency associated with the first dominant DMD mode, the so-called ‘body vibration mode’. It is interesting to note that the spatial pattern for the third dominant mode at $Re = 100$ is very similar to that for the dominant mode at $Re = 60$ (cf. with Fig. 3.17c). Furthermore, this spatial pattern is similar to the spatial pattern of vortex shedding for flow past a stationary cylinder as reported in Noack et al. [227]. Assimilating all this information, it is suggested that the third dominant DMD mode at $Re = 100$ is connected (linked) to the ‘Kármán street mode’ from a stationary cylinder at the same Reynolds number. Even so, the link seems tenuous owing to the fact that $St = 0.168$ for flow past a stationary cylinder at $Re = 100$, whereas the frequency associated with the third dominant mode is 0.130 Hz (or, equivalently, $St = 0.130$).

Figure 3.19 shows the results of a DMD analysis for the flow in the wake of an elastically-mounted cylinder on a linear/quadratic spring configuration with $(k_1, k_2) = (0.002, 0.11)$ at $Re = 110$ where the maximum amplitude of the transverse displacement is $A_{\max}/D = 0.6$. In contrast with the DMD results for $Re = 60$ and 100 (cf. Figs 3.17 and 3.18) the DMD mode that is linked to wake oscillations (or, ‘Kármán street mode’) behind the stationary cylinder is absent. Physical insights can be obtained by combining the information about the DMD modes with that concerning the maximum amplitude of the transverse displacement. For flow past a stationary cylinder, the vortex shedding arises from the periodic boundary-layer separation from the surface of the cylinder. At $Re = 110$, the significant vibrations associated with the wake oscillations obliterate this periodic boundary-layer separation from the cylinder surface and, as a consequence, the vortical wake structures are the result of the VIV of the cylinder. In this case, the ‘Kármán street



(a) Spectrum of eigenvalues (b) Amplitude of DMD modes (data within ellipse visualized in (c))

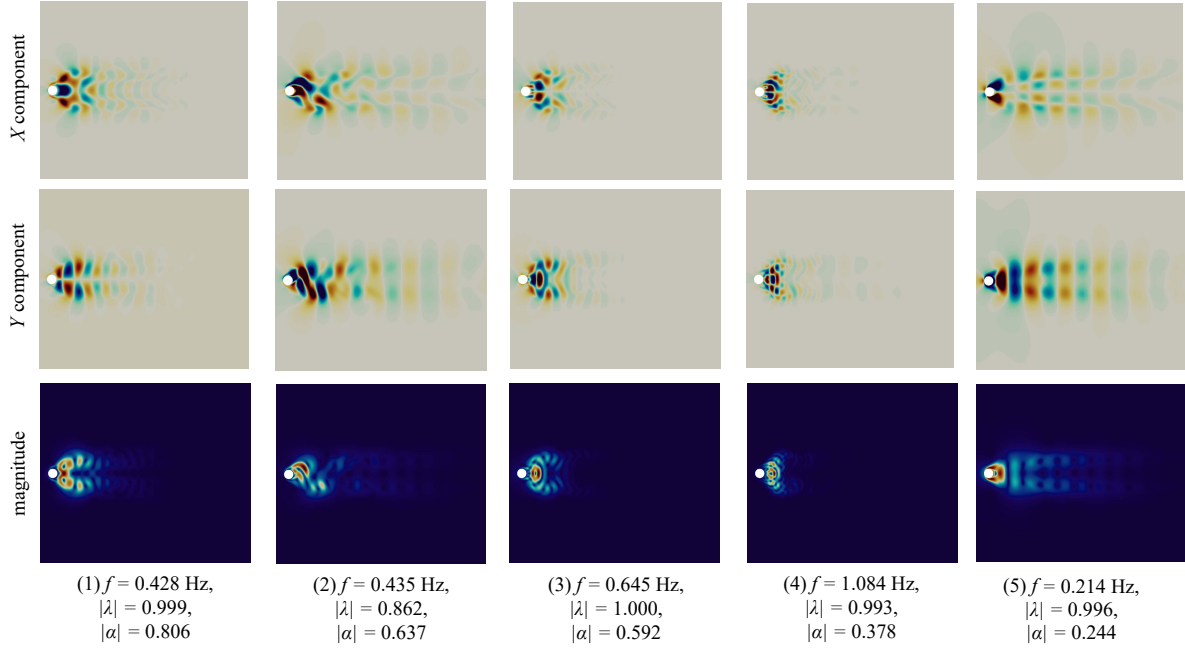
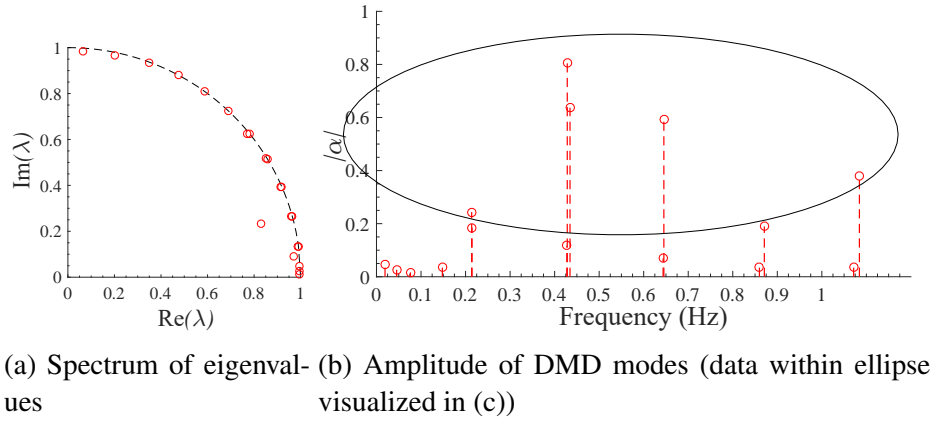


(c) The three largest DMD modes sorted by decreasing amplitude

Figure 3.18: Dynamic mode decomposition of velocity time series obtained in the wake of an elastically-mounted cylinder on a linear/quadratic spring configuration with $(k_1, k_2) = (0.002, 0.11)$ at $Re = 100$ summarized in terms of (a) spectrum showing the distribution of the real and imaginary parts of the eigenvalues; (b) amplitudes of the DMD modes normalized by the maximum amplitude and plotted as a function of the frequency; and, (c) real part of the DMD modes depicted using contours of the velocity components and velocity magnitude (white: zero; red: above a given positive threshold; blue: below a given negative threshold).

mode' disappears and the 'body vibration mode' dominates the wake modal pattern.

From Fig. 3.19b, the fifth dominant DMD mode corresponding to a frequency of 0.214 Hz (or, equivalently, to $St = 0.195$) is correlated with the first harmonic in the 'body vibration mode' of the elastically-mounted cylinder at $Re = 110$. Additionally, this frequency is consistent with the oscillation frequency f_{osc} summarized in Fig. 3.9b for $(k_1, k_2) = (0.002, 0.11)$ at $Re = 110$. The first dominant DMD mode with a dominant frequency of 0.428 Hz corresponds to the second harmonic in the VIV-motion (or, 'body vibration mode') of the elastically-mounted cylinder



(c) The five largest DMD modes sorted by decreasing amplitude

Figure 3.19: Dynamic mode decomposition of velocity time series obtained in the wake of an elastically-mounted cylinder on a linear/quadratic spring configuration with $(k_1, k_2) = (0.002, 0.11)$ at $Re = 110$ summarized in terms of (a) spectrum showing the distribution of the real and imaginary parts of the eigenvalues; (b) amplitudes of the DMD modes normalized by the maximum amplitude and plotted as a function of the frequency; and, (c) real part of the DMD modes depicted using contours of the velocity components and velocity magnitude (white: zero; red: above a given positive threshold; blue: below a given negative threshold).

with $(k_1, k_2) = (0.002, 0.11)$ at $Re = 110$. Interestingly, the second dominant DMD mode has an eigenvalue magnitude less than unity (and, hence lies inside the unit circle in the complex plane) implying a damped mode (viz., a mode whose amplitude decreases with time). As a result, the second dominant DMD mode does not seem to be associated with either the ‘Kármán street mode’ of the stationary cylinder or with the ‘body vibration mode’ of the elastically-mounted cylinder.

3.4 Chapter summary

In this chapter, one degree-of-freedom VIV in the transverse direction of an elastically-mounted circular cylinder (resulting in nonlinear restoring forces) is investigated using two-dimensional computational fluid dynamics simulations for a range of Re from 50 to 150 inclusive. The damping in the system is assumed to be absent (so damping coefficient $c = 0$). The characteristics of VIV for the fluid-structure interaction of an elastically-mounted cylinder on a linear, linear/quadratic and quadratic spring are analyzed and compared.

The equivalent natural frequency f_{eq} for an elastically-mounted cylinder on a linear/nonlinear spring is derived and it is found that unlike a linear spring, the equivalent natural frequency is dependent on the amplitude of the transverse displacement and so cannot be determined *a priori*. More specifically, the square of the equivalent natural frequency for a linear/quadratic spring configuration is proportional to the (constant) amplitude of the transverse displacement (or, more generally to the root-mean-square of the amplitude of the transverse displacement for the case where the amplitude and phase of the sinusoidal oscillations can exhibit a slow modulation in time).

The maximum amplitude of the transverse displacement of an elastically-mounted cylinder on a linear/quadratic spring will increase with increasing Re (at low values of Re starting at around 60 as determined in the present study). However, the presence of the linear spring component in the configuration will limit the maximum amplitude of the VIV at the higher values of Re (e.g., this self-limiting mechanism is observed to occur at $Re = 120$ in the present study). The increase in the maximum amplitude A_{max} of the transverse displacement with increasing Re in the VIV system with a quadratic (nonlinear) component in the spring configuration will be smooth and, at sufficiently large values of Re will exhibit a sudden drop in A_{max} as the response transitions from the upper branch to the lower branch to the desynchronised branch. In this study, it was found that the lock-in range for a VIV system with a nonlinear restoring force is more extensive than that for a linear restoring force only, but the maximum amplitude of the response does not change significantly between these two cases.

The phase difference Φ between the lift force and the transverse displacement for a VIV system with a quadratic (nonlinear) restoring force exhibits a sudden jump from $\Phi \approx 0^\circ$ (or, more precisely, from a small phase difference of less than about 10°) to about 180° for the same Re (approximately or better) at which the system exhibits a sudden drop in the maximum amplitude A_{max} . Both of these conditions are the signature of the transition out of the lock-in range for the VIV system. It is noted that larger values of k_2 (implying a larger nonlinear restoring force for the VIV system) are associated with a sharper transition in Φ as a function of Re as it jumps from 0° to 180° in the desynchronised branch.

For a VIV system with a quadratic (nonlinear) restoring force, the range of Re corresponding to the transition from the start of the initial branch to the start of the upper branch is increased (extended), and the upper/lower branches of the response are suppressed compared to that with a linear spring. The derived equivalent natural frequency f_{eq} is equal to the structural oscillating frequency f_{osc} in the suppressed upper and lower regions of the response.

For Re corresponding to the end of the lock-in range where the maximum amplitude of the transverse displacement exhibits a sudden drop to a smaller level (transition from the lower branch to the desynchronised branch of the amplitude response), a beating phenomenon is observed in the oscillations of the transverse displacement. The signature of the latter physical

effect is apparent from the fact that the power spectrum of the transverse displacement exhibits two dominant peaks at two slightly different frequencies and the associated phase-plane diagram displays a characteristic “binocular” structure. This beat phenomenon in the transverse displacement oscillations disappears at still larger values of Re .

The vortical wake structure for a VIV system with a quadratic (nonlinear) restoring force is similar to the classical von Kármán vortex street where regions of concentrated vorticity are shed downstream from opposite (alternate) sides of a cylinder. The wake oscillatory pattern is related to the amplitude response of the elastically-mounted cylinder (VIV system). For smaller values of the amplitude response, the vortex shedding regime exhibits a characteristic 2S pattern with a single-row configuration which occurs during the initial branch of the amplitude response (viz., associated with the lower amplitude response in the initial branch). As the amplitude response of the VIV system increases, the vortex shedding regime transitions into a 2P pattern with a double-row vortex street in the upper branch.

The DMD analysis of the velocity in the wake of an elastically-mounted cylinder on a linear/quadratic spring showed that the transverse extent of the DMD modes is larger for larger values of the maximum amplitude of the transverse displacement. The characteristic frequencies associated with the dominant DMD modes are correlated with either the wake vortex structure (‘Kármán street mode’) of the stationary cylinder or the vortical wake structure arising from the VIV (‘body vibration mode’) of the elastically-mounted cylinder. Furthermore, strong VIV oscillations of the elastically-mounted cylinder can significantly alter the wake oscillatory pattern of the stationary cylinder.

Chapter 4

2-D linear stability analysis of lock-in behavior with uniform inflow

This chapter will focus on introducing some novel modal behaviors which include various mode transformations and interactions, which are then used to explain some subtle features such as the beating phenomenon which occurs in the initial branch and the significant lag time that ensues between the initial branch and the occurrence of the fully-developed response in the lower branch that have been overlooked previously. In so doing, this bridges some important gaps in our current understanding of this phenomenon and, indeed, the results from the careful analysis conducted herein will be used to redress some of these key limitations and to reduce some critical knowledge gaps on the FIV response of a circular cylinder arising from some prior efforts. Towards this objective, FOM/CFD will be used in conjunction with ROM/ERA and supplemented with power spectral analysis and dynamic mode decomposition to provide deeper insights and a better understanding of the physical processes underlying the lock-in phenomenon and to study in greater depth the influence of the Reynolds number on the fluid-structure interaction. Using this approach, we reveal and explain the characteristics of the vibration response for each branch (initial, lower, and upper) of the lock-in range.

This chapter is organized as follows. The numerical methods for reduced-order models used in the present study are described in section 4.1. The accuracy of reduced-order models is validated in section 4.2. Section 4.3 provides a review of the limitations and conclusions obtained from past investigations of the modal mechanisms of FIV systems based on reduced-order modelling. Section 4.4 provides a detailed analysis of the mode transformation and interaction in the vortex-induced vibration for laminar flow past a circular cylinder using FOM/CFD, ROM/ERA, power spectral analysis and DMD.

4.1 Methodology of reduced-order model based on eigensystem realization algorithm

The reduced-order model for the simplified representation of the FIV of the system is obtained using the eigensystem realization algorithm. Figure 4.1 displays the key steps in the construction of an ERA-based ROM for the VIV of the system. As a system consisting of a coupled fluid-structure interaction, the ROM for the system consists of two parts—the first part

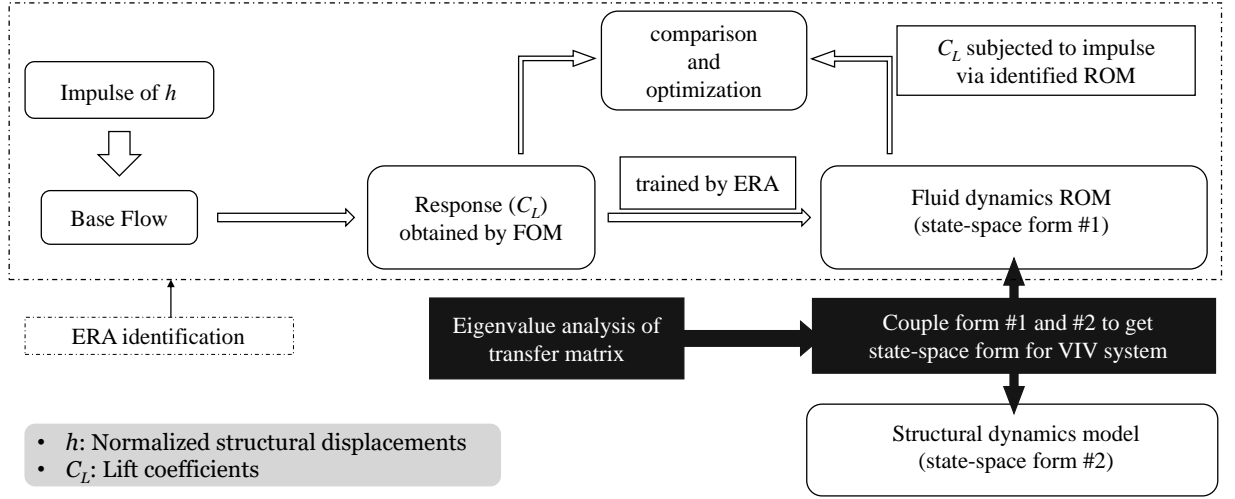


Figure 4.1: Schematic diagram summarizing the procedure used to obtain state-space model for the total system involving the coupling of a fluid dynamics ROM (with input h and output C_L) to a structural dynamics model (with input C_L and output h). The fluid dynamics ROM is constructed using ERA.

is the reduced, linear fluid model whose input is the normalized transverse displacement $h \equiv y/D$ (where y is the transverse displacement and D is the diameter of the cylinder) and whose output is the lift coefficient C_L and the second part is the linear structural model whose input is the lift coefficient C_L and whose output of normalized transverse displacement h . Once these two models have been obtained, they are recast into a state-space form and coupled together to obtain the final state-space model for the total system.

A reduced-order model for the fluid dynamics is obtained using the ERA. However, it is impossible to identify a linear aerodynamics model based on an unsteady vortex flow. The linearization of the mean flow [228] or the use of an equilibrium base flow [12, 15] are two of the most commonly used methodologies for the application of LSA to FIV systems. Here, we will follow the examples of Zhang et al. [12] and Yao and Jaiman [15] and apply ROM/ERA with respect to an equilibrium base flow to provide a linear aerodynamics model for the flow past an elastically-mounted cylinder. To this purpose, the required base flow is obtained by solving the Navier-Stokes equations (cf. Eqs (3.1) and (3.2)) using a large dimensionless time step value of 10 and a maximum of 30 iterations for one single time step. The equilibrium base flow is obtained once the value of the lift force has stabilized in the iterative solution of the Navier-Stokes equations.

Once the equilibrium base flow has been completed, the ERA can be used to provide a low-dimensional linear input-output model for the fluid dynamics system. To this end, we model the fluid dynamics system using a discrete-time multiple-input multiple-output (MIMO) state-space model as follows:

$$x_r(k+1) = \tilde{A}_r x_r(k) + \tilde{B}_r u_r(k) , \quad (4.1)$$

$$y_r(k) = \tilde{C}_r x_r(k) + \tilde{D}_r u_r(k) , \quad (4.2)$$

where $x_r(k)$ is the N_x -dimensional state vector, $u_r(k)$ is the N_u -dimensional input vector, and $y_r(k)$ is the N_y -dimensional output vector obtained at discrete-time step k . Here, it is noted

that $t_k \equiv k\Delta t$ is the time associated with the k -th discrete-time step, where Δt is the time-step size. Furthermore, \tilde{A}_r , \tilde{B}_r , \tilde{C}_r , and \tilde{D}_r are the $(N_x \times N_x)$ -system, $(N_x \times N_u)$ -input, $(N_y \times N_x)$ -output, and $(N_y \times N_u)$ -feedthrough matrices, respectively. Note that for the special case of a single-input single-output (SISO) state-space model, $N_u = N_y = 1$. The ERA is constructed using impulse response measurements of the system and, in this context, a discrete-time Kronecker delta function input u_r^δ (or, unit impulse function) assumes the following form:

$$u_r^\delta(k) \equiv u_r^\delta(k\Delta t) = \begin{cases} I_{N_u}, & k = 0; \\ 0, & k = 1, 2, 3, \dots, \end{cases} \quad (4.3)$$

where I_{N_u} is an $(N_u \times N_u)$ identity matrix. The output responses for the unit impulse inputs are given by

$$y_r^\delta(k) \equiv y_r^\delta(k\Delta t) = \begin{cases} \tilde{D}_r, & k = 0; \\ \tilde{C}_r \tilde{A}_r^{k-1} \tilde{B}_r, & k = 1, 2, 3, \dots \end{cases} \quad (4.4)$$

Note that $y_r^\delta(k)$ are $(N_y \times N_u)$ matrices (viz., N_u impulse responses are obtained corresponding to each of the N_u unit impulse input signals, each of which gives an output impulse response of dimension N_y as a function of time).

The output responses are collected for each unit impulse input and used by ERA to determine (estimate) the system matrices $(\tilde{A}_r, \tilde{B}_r, \tilde{C}_r, \tilde{D}_r)$. ERA is a data-driven algorithm consisting of the following steps. Firstly, the Hankel matrix $H(1:r, 1:s)$ is constructed by stacking the shifted time sequences of impulse response measurements y_r^δ into an $(N_y r \times N_u s)$ matrix as follows:

$$H(1:r, 1:s) = \begin{bmatrix} y_r^\delta(1) & y_r^\delta(2) & \cdots & y_r^\delta(s) \\ y_r^\delta(2) & y_r^\delta(3) & \cdots & y_r^\delta(s+1) \\ \vdots & \vdots & \ddots & \vdots \\ y_r^\delta(r) & y_r^\delta(r+1) & \cdots & y_r^\delta(s+r-1) \end{bmatrix}. \quad (4.5)$$

Next, a singular value decomposition of the Hankel matrix $H(1:r, 1:s)$ is applied to give (superscript T denotes matrix transposition)

$$H(1:r, 1:s) = U \Sigma V^T = [U_1 \ U_2] \begin{bmatrix} \Sigma_1 & 0 \\ 0 & \Sigma_2 \end{bmatrix} \begin{bmatrix} V_1^T \\ V_2^T \end{bmatrix}, \quad (4.6)$$

where the small singular values in the diagonal matrix Σ_2 are truncated (viz., Σ_2 is ignored) and only the first l singular values in Σ_1 are retained. In consequence, the truncated Hankel matrix estimated as $\hat{H} \approx U_1 \Sigma_1 V_1^T$ represents the significant temporal patterns in the time sequence data. Finally, the reduced-order model is constructed as follows using a second shifted Hankel matrix $\tilde{H} \equiv H(2:r+1, 2:s+1)$:

$$\bar{A}_r = \Sigma_1^{-1/2} U_1^T \tilde{H} V_1 \Sigma_1^{-1/2}; \quad (4.7)$$

$$\bar{B}_r = \Sigma_1^{1/2} V_1^T E_m; \quad (4.8)$$

$$\bar{C}_r = E_r U_1 \Sigma_1^{1/2}; \quad (4.9)$$

$$\bar{D}_r = y_r^\delta(0). \quad (4.10)$$

Here,

$$E_m = [I_q \ 0]^T \quad \text{and} \quad E_t = [I_p \ 0] \quad (4.11)$$

are $(N_u s \times q)$ and $(p \times N_y r)$ matrices consisting of the $(q \times q)$ and $(p \times p)$ identity matrices I_q and I_p , respectively, which used to extract the first q columns and the first p rows in the construction of \bar{B}_r and \bar{C}_r . In the present study, the input u_r and the output y_r are the dimensionless displacement $h \equiv y/D$ and lift coefficient C_L , respectively, so $p = q = 1$. In summary, the input-output dynamics of the ROM assumes the following form which constitute the discrete-time state-space equations for the fluid flow model (reduced system obtained from using the FOM/CFD data):

$$x_r(k+1) = \bar{A}_r x_r(k) + \bar{B}_r u_r(k) , \quad (4.12)$$

$$y_r(k) = \bar{C}_r x_r(k) + \bar{D}_r u_r(k) , \quad (4.13)$$

where (in a slight abuse of notation) x_r is an l -dimensional state vector for the reduced system. Moreover, the input-output dynamics for the ROM/ERA in Eqs (4.12) and (4.13) are determined by the $(l \times l)$ -system matrix \bar{A}_r , the $(l \times q)$ -input matrix \bar{B}_r , the $(p \times l)$ -output matrix \bar{C}_r and the $(N_y \times N_u)$ -feedthrough matrix \bar{D}_r .

In order to couple the reduced fluid model with the structural model, the discrete-time state-space form (cf. Eq. (4.12)) must be converted into the continuous-time state-space form. This can be accomplished as follows:

$$\begin{aligned} \dot{x}_r(t) &= A_r x_r(t) + B_r u_r(t) , \\ y_r(t) &= C_r x_r(t) + D_r u_r(t) , \end{aligned} \quad (4.14)$$

where $A_r = \Delta t^{-1} \ln(\bar{A}_r)$, $B_r = A_r [\bar{A}_r - I]^{-1} \bar{B}_r$, $C_r = \bar{C}_r$, and $D_r = \bar{D}_r$. Here, I is an identity matrix with the same size as \bar{A}_r [229].

The dimensionless structural equation for a transversely vibrating body has the following form:

$$\ddot{h} + 4\pi F_s \zeta \dot{h} + (2\pi F_s)^2 h = a_s C_L / m^* , \quad (4.15)$$

where $F_s = f_n D / U_0 \equiv U_r^{-1}$ is the reduced natural frequency (f_n is the structural natural frequency, D is the cylinder diameter, U_0 is the free-stream velocity, and U_r is the reduced velocity); $m^* = \rho_s / \rho$ is the mass ratio (ρ_s is the density of the cylinder and ρ is the density of the fluid); h is the non-dimensional transverse displacement (viz., the transverse displacement y normalized by D); and, ζ is the damping coefficient. The characteristic length scale factor a_s is determined by the body geometry as follows:

$$a_s = \frac{1}{A_b} \cdot \frac{L_b^2}{2} , \quad (4.16)$$

where A_b and L_b are the area and the characteristic length of the cross-section of the bluff body. It is noted that $a_s = 1/2$ and $2/\pi$ for a square and circular cylinder, respectively. Following from this, the structural equation can be recast into a continuous-time state-space form as follows:

$$\begin{aligned} \dot{x}_s(t) &= A_s x_s(t) + q B_s y_r(t) , \\ h(t) &= C_s x_s(t) + q D_s y_r(t) , \end{aligned} \quad (4.17)$$

with the state vector $x_s \equiv (h, \dot{h})^T$, $q \equiv a_s/m^*$, and

$$\begin{aligned} A_s &= \begin{bmatrix} 0 & 1 \\ -(2\pi F_s)^2 & -4\pi F_s \zeta \end{bmatrix}; & B_s &= \begin{bmatrix} 0 \\ 1 \end{bmatrix}; \\ C_s &= [1 \ 0]; & D_s &= [0]. \end{aligned} \quad (4.18)$$

As alluded to in Fig. 4.1, the state-space model for the fluid dynamics [cf. Eq. (6.1)] can be coupled with the state-space model for the structural dynamics [cf. Eqs (4.17) and (4.18)] to yield the linear and reduced-order coupled model for the VIV system. This yields the ROM for the total system consisting of the structural part given by Eq. (4.17) and the fluid part given by Eq. (6.1), so the linear and reduced coupled-model for the VIV system is obtained as follows:

$$\dot{x}_{rs}(t) = \mathbf{A}_{rs} x_{rs}(t) \equiv \begin{bmatrix} A_s + qB_s D_r C_s & qB_s C_r \\ B_r C_s & A_r \end{bmatrix} x_{rs}(t), \quad (4.19)$$

$$h(t) = [C_s \ 0] x_{rs}(t), \quad (4.20)$$

where $x_{rs} \equiv (x_s, x_r)^T$.

The VIV stability problem can be investigated by analyzing the behaviour of the eigenvalues of the system matrix \mathbf{A}_{rs} exhibited in Eq. (4.18). The two or three leading eigenvalues (which depends on the Reynolds number) are associated with the most unstable modes of the system which, necessarily, include both the structural and wake modes. The methodology that we use for identifying the structural and wake modes will be described later. Our interpretation of the physical processes associated with the behaviour of these modes will be described in Sections 4 and 5. We note that the eigenvalues determine the growth/decay rate and oscillatory characteristics of the associated (eigen)mode. In particular, the positivity or negativity of the real parts of the eigenvalues determine the growth or decay rate of the mode, respectively. The imaginary part of each eigenvalue is associated with the oscillatory frequency of the associated mode, with the eigenfrequency (in continuous time) given by $\text{Im}(\lambda)/(2\pi)$ where λ is the (complex) eigenvalue and $\text{Im}(\cdot)$ denotes the imaginary part of a complex number.

4.2 Validation of reduced-order model

Sub-section 3.2.1 already demonstrates that the present method of FOM/CFD provides good accuracy for obtaining the base flow required for the ERA identification as well as for the provision of high-quality FOM/CFD datasets for the subsequent analysis, And consequently, the parameter definition such as mesh situation, computational domain, boundary condition, etc. are consistent with those of Sub-section 3.2.1. This section focuses on validating the fluid reduced model and the coupled FSI reduced model using ERA.

4.2.1 Validation of ROM/ERA fluid model

The ROM/ERA is constructed using the equilibrium base flow owing to the fact that the variation of the dynamic force associated with a small displacement of the body (cylinder) around

the base flow is linear. This assertion will be validated later by a comparison of the results obtained from the FOM and ROM. Figure 4.2 exhibits the contours of the streamwise velocity for flow past a stationary cylinder at $Re = 60$ and 100 . In this figure, the line integral convolution (LIC) vector field visualization methodology [230, 231] is used to display the characteristics of the base flow around the circular cylinder. The LIC vector field visualization cannot provide information on the orientation (clockwise or counter-clockwise) of the flow such as that provided by flow streamlines. Nevertheless, the LIC vector visualization methodology is an effective means for identifying the recirculating regions in the flow. The LIC vector field in Fig. 4.2 clearly shows the extent of the recirculating region in the wake of the cylinder. Table 5.2 compares the length of the recirculating region for base flows past a stationary cylinder at $Re = 60$ and 100 . The length of the recirculating region is defined as the distance in the streamwise direction along the centerline of the cylinder between the base point (which is taken as the center of cylinder) and the stagnation point in the wake. We note that the length of the recirculating regions in the wake of a stationary cylinder at $Re = 60$ and 100 obtained in our current simulations are in very good conformance with the results of other investigators [232, 15, 26].

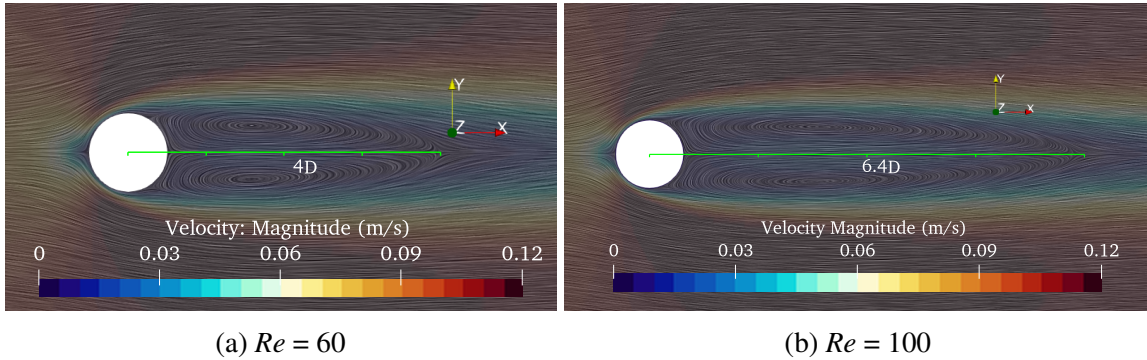


Figure 4.2: The streamwise velocity contours exhibited using the line integral convolution (LIC) visualization methodology for a base flow past a stationary circular cylinder at (a) $Re = 60$ and (b) $Re = 100$. The direction of the flow is from left to right.

Table 4.1: The length of the recirculation region (measured from the center of the cylinder) normalized by the cylinder diameter D for a base flow past a stationary circular cylinder at $Re = 60$ and 100 . The results of the present simulations are compared with those of previous investigators.

Re	Present	Flavio and Paolo [232]	Yao and Jaiman [15]	Mao and Blackburn [26]
60	4.0	4.1	4.1	4.2
100	6.4	6.6	—	6.5

The magnitude of the input impulse signal is important for ROM identification. On the one hand, the signal needs to excite the relevant modes in the underlying flow. On the other hand, the amplitude of the input impulse cannot be too large; otherwise, the nonlinear characteristics of the underlying flow will dominate the dynamics. Insufficient data in the regime of the flow where linear dynamics dominate would make it impossible to construct an unsteady fluid flow model using ROM/ERA to obtain the low-dimensional linear input-output model from the impulse response data. Furthermore, at larger values of Re , the flow past a circular cylinder exhibits significant Hopf bifurcation resulting in the formation of a periodic vortex street. Based on these considerations, the dynamic responses for impulse values of $\delta = 10^{-2}$, 10^{-3} , and 5×10^{-4} are compared.

It is noted that the nonlinearity arising for $\delta = 10^{-2}$ develops too quickly with the result that it is not possible to extract sufficient data for ERA identification. In contrast, values of $\delta = 10^{-3}$ and 5×10^{-4} are appropriate for LSA in the sense that these values for the impulse allow sufficient time for the dynamical response to evolve linearly to enable enough data to be obtained for ERA identification. As a consequence, the input impulse signal for the non-dimensional transverse displacement h used in our numerical experiments is prescribed as $\delta = 10^{-3}$ (normalized by the cylinder diameter D) in a Reynolds number range from 20 to 180.

In accordance to Yao and Jaiman [15] and Juang and Pappa [102], the dimensions of the Hankel matrix H from Eq. (4.5) for a SISO system (where $N_u = N_y = 1$) can be tall ($r > s$), wide ($r < s$) or square ($r = s$), depending on the choice of r and s . For the current study, $(r, s) = (500, 200)$ was found to be sufficient to obtain a good match between the predictions provided by FOM/CFD and ROM/ERA for the dynamic response (C_L) of the system when subjected to an impulse input signal (viz., an impulse in the non-dimensional transverse displacement h). The dimensionless time step Δt is chosen as 0.05, which is sufficient for the resolution of the discrete-time impulse response $y^\delta \equiv C_L$, the latter of which is used to construct the matrix $H(1 : r, 1 : s)$ in accordance to Eq. (4.5). If the data corresponding to the first 700 ($r + s$) time steps are used to construct the ROM, then for a specific combination of (Re, m^*) , the computational efficiency in the prediction of structural instability using ROM/ERA will be more than 300 times that of using FOM/CFD. For the system matrix \bar{A}_r , the retention of the first $l = 30$ singular values of $H(1 : r, 1 : s)$ is sufficient to capture the dominant temporal patterns in the fluid flow. Figure 4.3 displays the first 30 singular values (HSV) of the Hankel matrix where it can be seen that the singular values monotonically and rapidly decrease to zero implying that the dominant dynamics of the system occur on a low-dimensional space. In consequence, a ROM can be used to approximate well the dynamics of the VIV system.

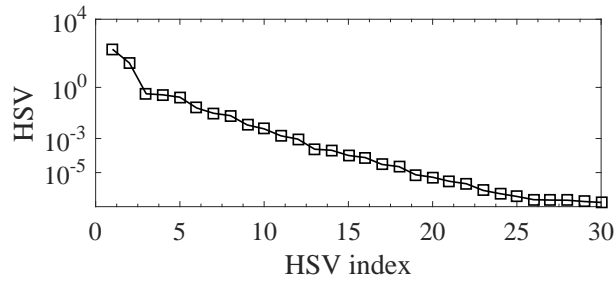
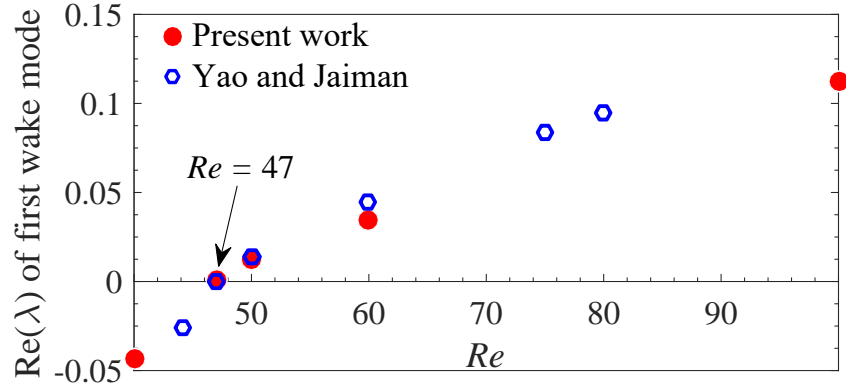


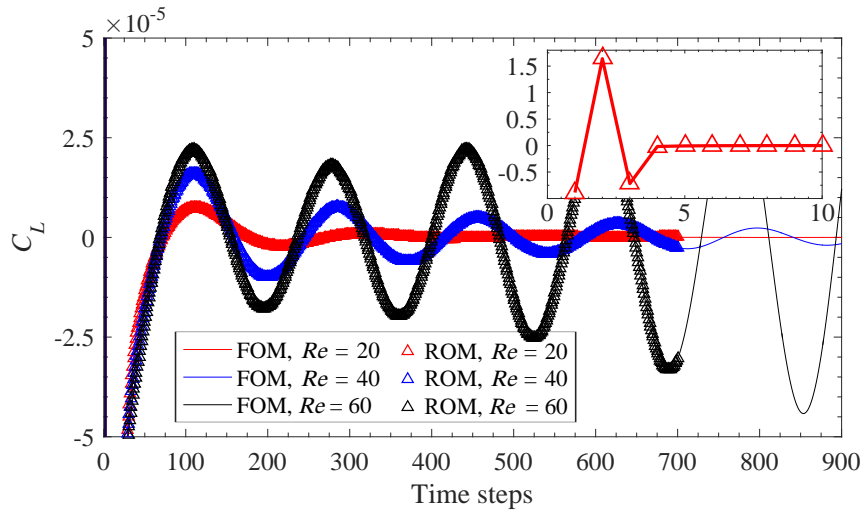
Figure 4.3: Distribution of the first 30 singular values (HSV) of the Hankel matrix $H(1 : r, 1 : s)$ with $(r, s) = (500, 200)$ for $Re = 60$.

Figure 4.4a exhibits the rate of growth characterized by $\text{Re}(\lambda)$ of the first wake mode as a function of Reynolds number Re . The dynamic response of the wake mode for different values of Re is consistent with the results reported by Yao and Jaiman [15] and, more generally, with the prevailing knowledge—in particular, that the minimum Re required for the generation of a periodic vortex street in the wake of a circular cylinder is 46.8 [232, 233, 234]. For Re greater than 47, the increasing fluctuating amplitude of C_L for increasing Re results in the generation of a periodic vortex street in the wake of a circular cylinder as the flow begins to lose its stability through the Hopf bifurcation. For Re less than 47, the vibration amplitude of C_L decreases gradually, and the wake of a circular cylinder tends to be stable with no vortex street formation. The impulse response of C_L (arising from the impulse input signal $u^\delta \equiv h$) obtained from FOM/CFD over 1000 time steps and from the corresponding ROM/ERA over 900 time steps are displayed

in Fig. 4.4b. It can be seen that there is a very good conformance in the impulse response obtained from the full-order model and the reduced-order model. Indeed, the system identification method based on ROM/ERA has a high predictive accuracy for the time development of the dynamic coefficient C_L for both the stable ($Re < 47$) and unstable ($Re > 47$) behaviours in the wake of a circular cylinder. In particular, the first 10 time steps obtained from both FOM/CFD and ROM/ERA at $Re = 20$ are shown in the inset plot of Fig. 4.4b, demonstrating that there is excellent agreement between these two predictions.



(a) $Re(\lambda)$ of first wake mode



(b) The C_L impulse response

Figure 4.4: (a) The growth rate as characterized by $Re(\lambda)$ of the first wake mode as a function of Reynolds number Re , and (b) the predictions of the C_L impulse response obtained using FOM/CFD and the corresponding ROM/ERA at $Re = 20, 40$, and 60 . The cases at $Re = 20$ and 40 correspond to stable wake flows, whereas that at $Re = 60$ corresponds to an unstable wake flow.

4.2.2 Validation and preliminary analysis of ROM/ERA for VIV system

Figure 4.5 shows the root loci of the eigenvalues of the coupled FSI system (flow past a circular cylinder elastically supported on a linear spring) as a function of the reduced natural frequency F_s for $(Re, m^*) = (60, 50)$. The current results obtained with ROM/ERA are seen to be

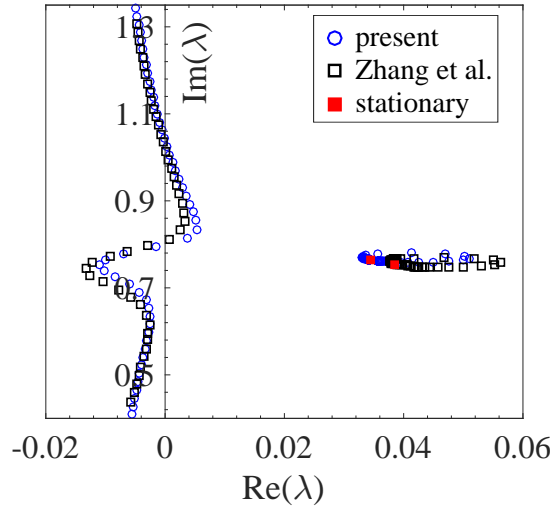


Figure 4.5: The root loci for a FSI system consisting of the flow past a circular cylinder elastically mounted on a linear spring for $(Re, m^*) = (60, 50)$. The present results are compared with those of Zhang et al. [12] and with the case of a stationary circular cylinder. The eigenvalue corresponding to the wake mode for this case is strictly positive.

in very good agreement with those obtained by Zhang et al. [12] based on ROM/ARX. Following the convention established by Yao and Jaiman [15], Cossu and Morino [235], and Zhang et al. [12], the two most unstable modes (or, the two leading eigenvalues) are significant in this case and are referred to as SM (corresponding to a “nearly structural mode”) and WM (corresponding to a “von Karman mode/wake mode”). The identification of these modes is useful for analyzing and comparing the behaviour of the root loci for different cases and, as a result, the identification of these characteristic modes will be an underlying focus of this chapter. A perusal of Fig. 4.5 shows that when the natural frequency of the SM is close to the frequency of the WM, the SM crosses the imaginary axis and enters the right-half plane, and the VIV system becomes unstable. It is suggested that the fundamental reason for the instability of an elastically supported bluff body under subcritical flow is the interaction between the SM and WM. It should be noted that the linear growth rate does not necessarily correlate with the dominance of one specific mode. More specifically, the growth rate as measured by $Re(\lambda)$ of the structural mode predicted by LSA represents the increasing growth rate of the amplitude in the initial linear regime of the VIV response predicted by FOM for flutter lock-in [121]. In the above discussion, the WM for a flow past a circular cylinder with Re greater than 46.8 is unstable and, as a consequence, the signature of this instability is revealed through the fact that the real part of the WM is always positive. Additionally, it is seen that the trajectories of the SM and WM are disconnected corresponding, as such, to an uncoupled modal condition.

Figure 4.6 shows the behaviour of the unstable region (or, lock-in range) for the FSI system as a function of the mass ratio m^* for flow past a circular cylinder mounted on a linear spring at $Re = 33$. Because there is no resonance lock-in for $Re = 33$, the boundaries of the unstable region (viz., lock-in regime) in this case are defined by the flutter lock-in. It can be seen that the mass ratio has little effect on the upper boundary of the unstable region. As the mass ratio decreases to less than about 30, the lower boundary of the unstable region is seen to decrease more rapidly. Our current results based on ROM/ERA are in good agreement with the results obtained using an FOM by Mittal and Singh [13] and those obtained using ROM/ARX by Zhang et al. [12]. In

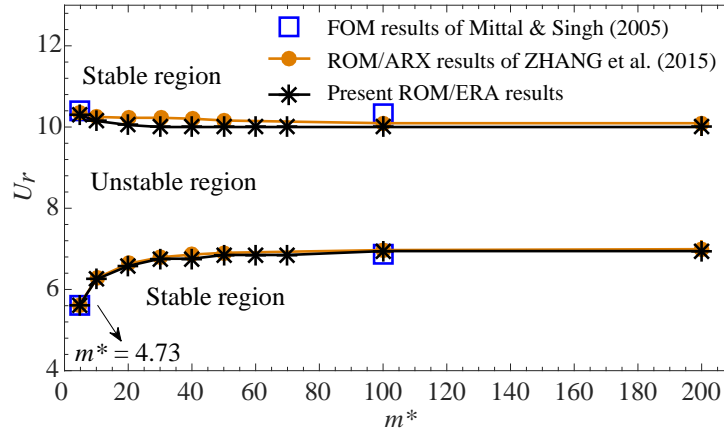
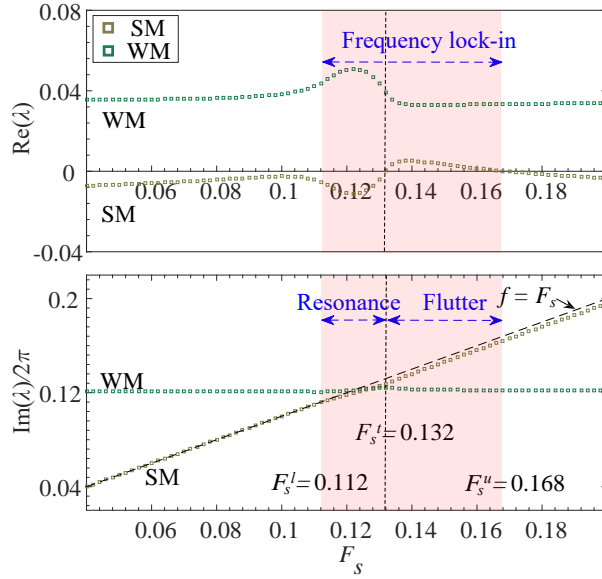


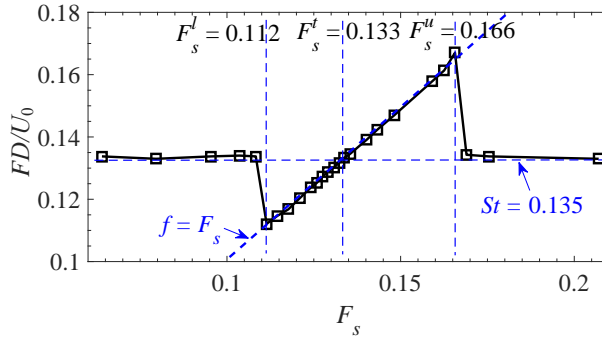
Figure 4.6: Delineation of the lower and upper boundaries of the unstable region for flow past a circular cylinder mounted on a linear spring for $Re = 33$. The results obtained using the present ROM/ERA are compared with those obtained by Zhang et al. [12] using ROM/ARX and by Mittal and Singh [13].

particular, the lower and upper boundaries of the unstable region are predicted accurately—more specifically, the lower boundary of $U_r^l = 5.6$ and the upper boundary of $U_r^u = 10.4$ for $m^* = 4.73$ and the lower boundary of $U_r^l = 6.8$ and the upper boundary of $U_r^u = 10.3$ for $m^* = 100$ agree well with those obtained by Mittal and Singh [13] using a full-order model. It should be noted that Mittal and Singh analyzed the phenomenon of VIV using two (both) degrees of freedom; namely, those in the transverse and the streamwise directions. Our current results show that the degree of freedom in the transverse direction is the dominant effect in the determination of the stability of the VIV system.

Figure 4.7a shows the real part $\text{Re}(\lambda)$ and imaginary part $\text{Im}(\lambda)$ of the complex eigenvalue λ (which determines the growth/decay and characteristic frequency of the mode, respectively) as a function of the reduced natural frequency F_s for the coupled FSI system based on the ROM/ERA. The Reynolds number Re , mass ratio m^* , and structural damping ζ for the flow past a circular cylinder mounted on a linear spring are 60, 50 and 0, respectively. In the discussion of Zhang et al. [12], the lock-in region of the flow is delineated into two regimes: namely, that due to resonance-induced lock-in and that due to flutter-induced lock-in. Resonance-induced lock-in appears when $\text{Im}(\lambda)$ associated with the SM and WM are close in value—a region defined by the lower F_s^l and upper F_s^t boundary in the reduced natural frequency. In contrast, the flutter-induced lock-in is correlated with the unstable structural mode (viz., when the real part of the eigenvalue associated with the SM is positive, so $\text{Re}(\lambda) > 0$) and arises from the coupled interaction between the SM and WM—in a region defined by the lower F_s^t and upper F_s^u boundary in the reduced natural frequency. These two kinds of lock-in phenomena constitute the frequency lock-in range. The identification of these two regimes of lock-in are exhibited in Fig. 4.7a. Moreover, as is evident in Fig. 4.7b, outside the frequency lock-in interval either when $f < F_s^l$ or when $f > F_s^u$, the coupled system displays the characteristics of a forced-vibration under the effect of an unsteady aerodynamic load. The current results obtained using ROM/ERA agree with both the ROM/ERA and FOM/CFD results presented by Zhang et al. [12] for $(Re, m^*) = (60, 50)$. In the following analysis, the identification of the left-hand (or lower) and right-hand (or upper) bounds of the lock-in range are determined based on a characteristic signature of the frequency lock-in—namely, the lower and upper bounds of the lock-in are associated with abrupt changes



(a) Real and imaginary parts of complex eigenvalues (ROM/ERA)



(b) Oscillation frequency (FOM/CFD)

Figure 4.7: (a) The real and imaginary parts of the two leading eigenvalues obtained from ROM/ERA and (b) the oscillation frequency F as a function of the reduced natural frequency F_s for FOM/CFD conducted by Zhang et al. [12] for the case of flow past a circular cylinder mounted on a linear spring with $(Re, m^*) = (60, 50)$.

in the variation of Y_{\max}/D or F/f_n as a function of the reduced natural frequency F_s .

In the global linear stability analysis (LSA) of Navrose and Mittal [14] for a VIV system, the two leading uncoupled eigenmodes are defined as the fluid mode (FM) and the elastic mode (EM). The definitions for FM and EM are same as those for WM and SM as proposed by Zhang et al. [12] and used in the analysis conducted herein. To demonstrate that the results produced by the global LSA method and the reduced VIV model are essentially identical, we consider the case of a flow past a circular cylinder mounted on a linear spring for $(Re, m^*) = (60, 20)$. Figure 4.8 shows the variation of the real and imaginary parts of the eigenvalues as a function of reduced natural frequency F_s obtained using ROM/ERA. A careful examination of the figure shows that the latter results are in excellent conformance with those obtained using the global LSA [14]. With reference to the real parts of the eigenvalues, it is seen that both the FM from the global LSA and the WM from the ROM/ERA are unstable for all values of F_s . Furthermore, the maximum growth rate for the FM and WM is achieved when $F_s = 0.125$. Finally, both the SM and EM are

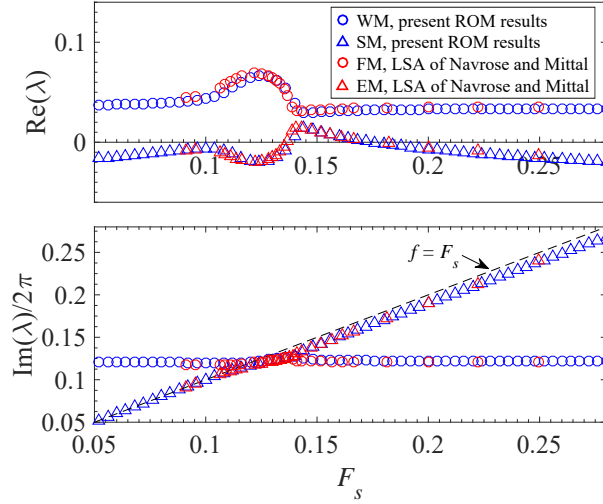


Figure 4.8: The real and imaginary parts of eigenvalues corresponding to the two leading eigenmodes plotted as a function of the reduced natural frequency F_s for flow past a circular cylinder mounted on a linear spring with $(Re, m^*) = (60, 20)$. The analysis is conducted using ROM/ERA and compared with the global LSA of Navrose and Mittal [14].

seen to be unstable over the range of reduced natural frequency where $0.137 < F_s < 0.172$ and, in this range, the growth rate of the modes are essentially identical (approximately or better).

4.3 Summary of key results obtained from the previous LSA on lock-in behavior

This section synthesizes and summarizes the key results obtained by previous studies concerning the relationship between the response (e.g., lock-in range) of a VIV system and the behaviour of the eigenvalues for the system obtained using LSA conducted by Zhang et al. [12], Navrose and Mittal [14], and Yao and Jaiman [15]. The differences between coupled and uncoupled modes will also be considered within the context of the identification of specific patterns of lock-in.

- With reference to Fig. 4.7, Zhang et al. [12] remarked that the lock-in range can include two physical mechanisms for lock-in; namely, a resonance lock-in (occurring in the range of reduced natural frequency (F_s^l, F_s^t) in Fig. 4.7a) and a flutter lock-in (occurring in the range of reduced natural frequency (F_s^t, F_s^u) in Fig. 4.7a).
- With reference to Figs 4.9a and 4.10a, for the uncoupled condition at $(Re, m^*) = (60, 20)$ computed herein, there is a clear distinction between the wake and structure modes, referred to as WM (or, FM) and SM (or, EM) respectively, as mentioned previously. The resonance lock-in appears when the eigenfrequencies $\text{Im}(\lambda)/(2\pi)$ corresponding to the SM and WM are close to each other in value. The flutter lock-in, on the other hand, is due to the coupling flutter between the SM and WM and, simultaneously, when the real part $\text{Re}(\lambda)$ of the eigenvalue associated with the SM is positive.

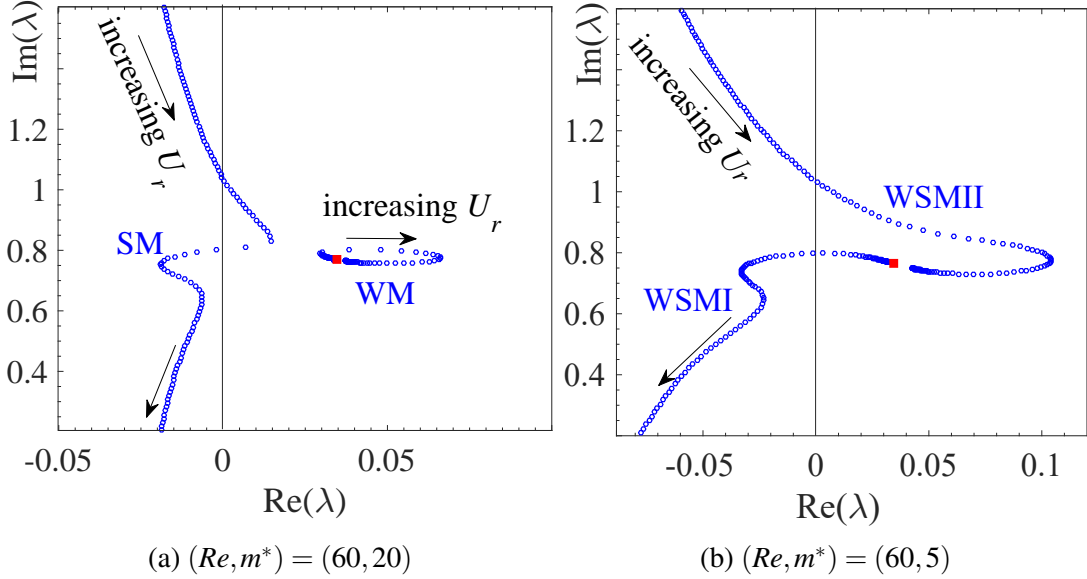


Figure 4.9: Root loci obtained from ROM/ERA for a flow past a circular cylinder mounted on a linear spring for (a) $(Re, m^*) = (60, 20)$ and (b) $(Re, m^*) = (60, 5)$. The solid red square corresponds to the case of a stationary circular cylinder.

- With reference to Figs 4.9b and 4.10b, for the coupled condition at $(Re, m^*) = (60, 5)$ computed herein, there is no distinction between the wake and structure modes. This is in stark contrast to the uncoupled condition, where an independent SM can be identified. Moreover, two coupled modes referred to as WSMI and WSMII can be defined based on the behaviour of the root loci for the two leading eigenvalues [15]. In this case, one needs to ascertain which of the two coupled modes WSMI or WSMII is associated with the hidden structural mode from the behavior of these modes as a function for the reduced natural frequency F_s —this will be one of the focal points in this study. The hidden structural mode in the coupled condition will be referred to as “SM_c” herein. Following from this, Zhang et al. [12] argues that this structural mode is associated with the eigenvalue possessing the smaller real part. In the case of Fig. 4.10b, the role of SM_c is assumed by WSMI and WSMII alternately (tracked using the red arrow in the figure), with the mode-switching point occurring at the value of F_s where the mode associated with the eigenvalue possessing the smallest real part switches over. Zhang et al. [12] argue that the flutter lock-in range will be bounded by the two intersections of the real part ($Re(\lambda)$) of the complex eigenvalue λ associated with SM_c with the horizontal axis (viz., where $Im(\lambda) = 0$).
- Yao and Jaiman [15] indicated that the lower (left) boundary of the resonance lock-in range cannot be precisely determined based on the behaviour of ROM root loci owing to the overlap of the SM and WM trajectories in the complex plane.
- Yao and Jaiman [15] argue that when the real part of the eigenvalue associated with the SM is always negative (cf. the behaviour of the root loci for a square cylinder with sharp corners conducted at $(Re, m^*) = (60, 10)$), the lock-in regime is entirely dominated by the resonance lock-in.
- Yao and Jaiman [15] suggested that the frequency lock-in of VIV for a flow past a circular cylinder is due only to a flutter-induced instability for $Re > 70$.

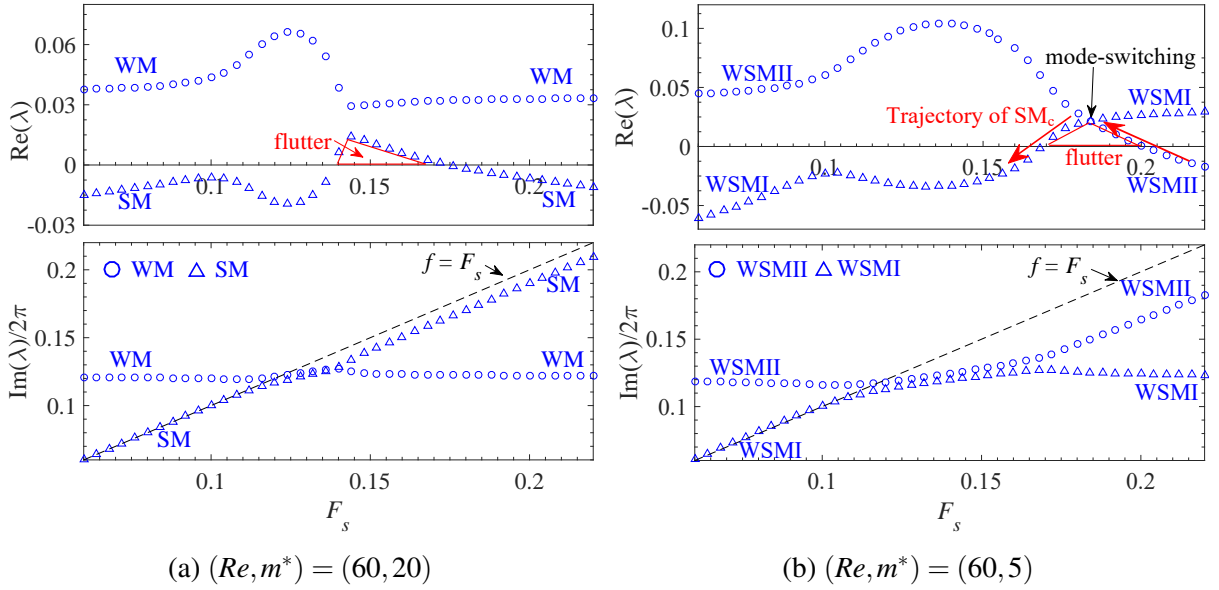


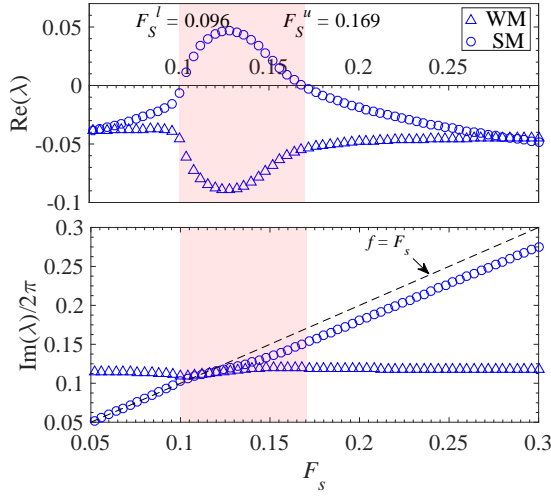
Figure 4.10: Real and imaginary parts of the two leading eigenvalues obtained from ROM/ERA for a flow past a circular cylinder mounted on a linear spring for (a) $(Re, m^*) = (60, 20)$ and (b) $(Re, m^*) = (60, 5)$.

4.4 New perspectives on the analysis of lock-in range for VIV system based on LSA

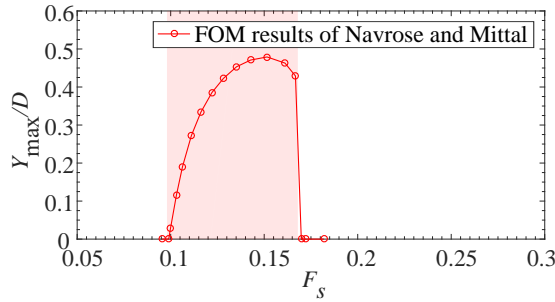
This section summarizes our investigations of the stability of the fluid-structure interaction associated with VIV response (e.g., frequency lock-in, desynchronization) using simulation data obtained from ROM/ERA and FOM/CFD. The analysis presented herein will involve higher Reynolds numbers than considered in previous investigations reported by Zhang et al. [12], Navrose and Mittal [14] and Yao and Jaiman [15] for a flow past a circular cylinder. This is important since higher Reynolds numbers will result in more complex mode interactions in the FSI (and, these type of interactions have not been studied previously).

4.4.1 Uncoupled condition for wake-structure modes

Figure 4.11a displays the real and imaginary parts of the two leading eigenvalues as a function of F_s for a flow past a circular cylinder mounted on a linear spring at $(Re, m^*) = (40, 10)$. This case corresponds to the uncoupled condition. The wake mode is stable over the entire F_s range (since the real part of the eigenvalue associated with the WM is strictly negative) owing to the fact that Re is less than the critical Reynolds number of $Re_{cr} \approx 47$ for a flow past a stationary circular cylinder. The lock-in phenomenon in this case arises entirely from the mechanism of flutter lock-in, an observation that is consistent with the results reported by Yao and Jaiman [15] for the same case. Therefore, a large-amplitude VIV is present, even though there is no excitation of the motion arising from the resonance between the wake and structure modes. The VIV amplitude response (normalized transverse displacement as a function of F_s) obtained by Navrose and Mittal [14] using FOM/CFD is shown in Fig. 4.11b. This result demonstrates that significant vibrations of the cylinder will occur even though there is no initial periodic vortex



(a) Leading eigenvalues (ROM/ERA)



(b) Maximum amplitude obtained by Navrose and Mittal [14] (FOM/CFD)

Figure 4.11: The VIV response as a function of F_s for a flow past a circular cylinder mounted on a linear spring at $(Re, m^*) = (40, 10)$ obtained using (a) ROM/ERA and (b) FOM/CFD [14]. The lock-in range is delineated as the region shaded in red.

street generated in the wake, which corroborates the flutter lock-in mechanism alluded to above.

Figure 4.12a displays the real and imaginary parts of the two leading eigenvalues for a flow past a circular cylinder mounted on a linear spring at $(Re, m^*) = (60, 50)$. Following the convention proposed by Zhang et al. [12], the lock-in range is divided into the resonance lock-in and the flutter lock-in. For the case of $(Re, m^*) = (60, 50)$, the range of values of F_s associated with the resonance lock-in and the flutter lock-in do not overlap one another. As the reduced velocity U_r increases (or, equivalently, as the reduced natural frequency F_s decreases), the regime of flutter lock-in transitions into the regime associated with resonance lock-in. In the range of F_s associated with the resonance lock-in, the real part of the eigenvalue corresponding to the WM increases, which is consistent with an increase in the instability of the wake flow. The closeness in the values of the frequencies associated with the SM and WM is the underlying reason for the resonance lock-in. In the flutter lock-in regime, the real part of the eigenvalue associated with the SM is positive. Following from these considerations, we infer that the instability in the SM leads to the onset of the flutter lock-in. It is known that the lock-in regime consists of three characteristic branches (cf. Fig. 4.12c). These branches consist of (1) the initial branch, which is characterized by a distinct increase in the amplitude of the oscillations; (2) the upper branch, where the amplitude of the oscillations transitions to a higher level corresponding to a complete local synchronization of the vortex shedding frequency with the natural structural frequency, a

state that is associated with the largest vibrations; and, (3) the lower branch, where the amplitude of the oscillations transitions to a lower level. A comparison of the ROM/ERA results of Fig. 4.12a with the FOM/CFD results of Fig. 4.12c shows that the flutter and resonance lock-in are associated with the upper and lower branches, respectively (provided, of course, that both lock-in regimes are present).

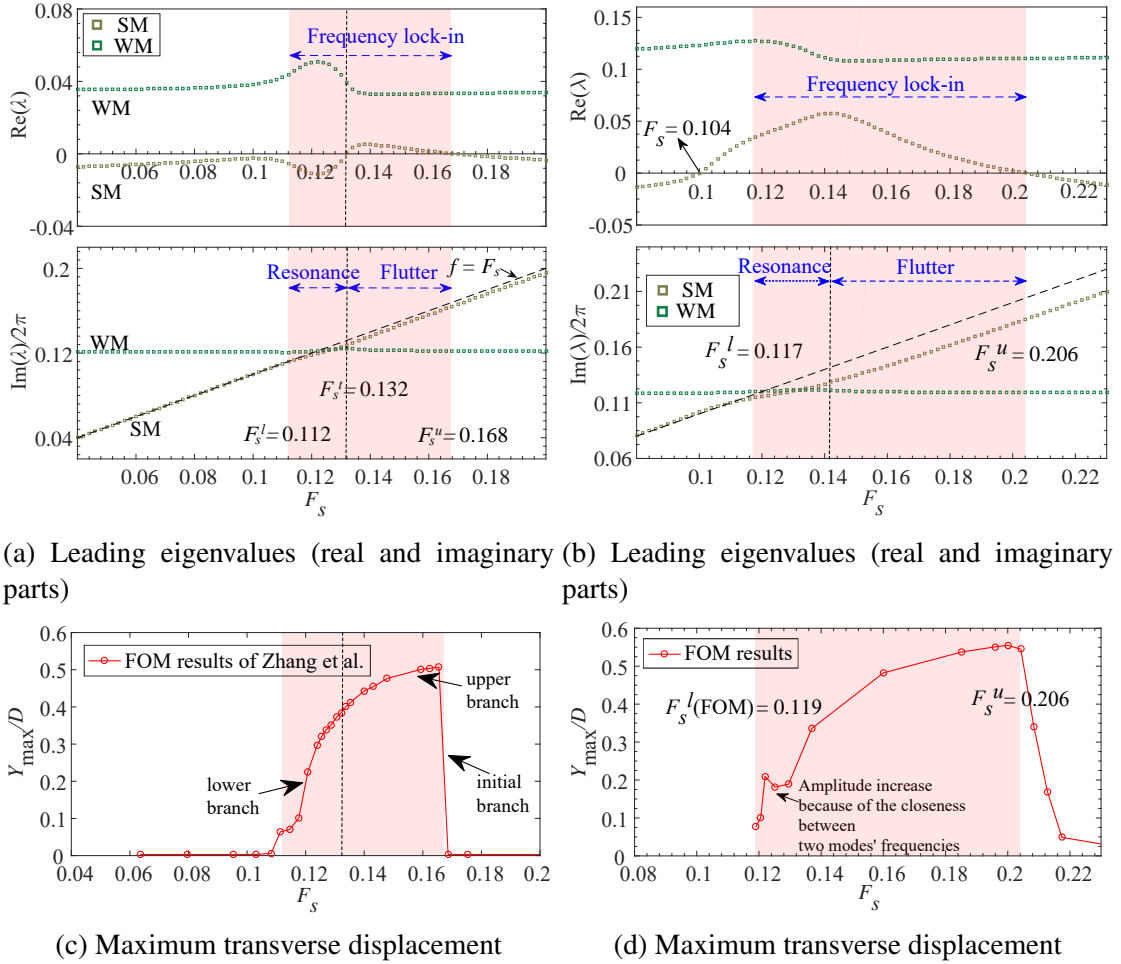


Figure 4.12: The VIV response as a function of F_s for a flow past a circular cylinder mounted on a linear spring at (a) $(Re, m^*) = (60, 50)$ for ROM/ERA; (b) $(Re, m^*) = (100, 10)$ for ROM/ERA; (c) $(Re, m^*) = (60, 50)$ for FOM/CFD conducted by Zhang et al. [12]; and, (d) $(Re, m^*) = (100, 10)$ for FOM/CFD. The lock-in range is delineated as the region shaded in red.

Figure 4.12b displays the real and imaginary parts of the two leading eigenvalues for a flow past a circular cylinder mounted on a linear spring at $(Re, m^*) = (100, 10)$. The results shown in this figure agree well with those reported by Yao and Jaiman [15] for the same values of (Re, m^*) . Interestingly, the range of F_s where the $Re(\lambda) > 0$ for the SM completely overlaps that associated with the resonance lock-in. As a consequence, Yao and Jaiman [15] argued that the frequency lock-in for this VIV system is the result of a pure flutter instability only. However, we assert that the flutter instability is not the only physical mechanism producing the frequency lock-in at $Re = 100$. To this assertion, it can be seen from Fig. 4.12d that the lower boundary of the frequency lock-in range obtained using a high-fidelity FOM/CFD occurs at $F_s = 0.119$. On the other hand, the ROM/ERA predictions exhibited in Fig. 4.12b suggest that this lower boundary occurs instead at $F_s = 0.104$ (which corresponds to the value of F_s at which the real part of the

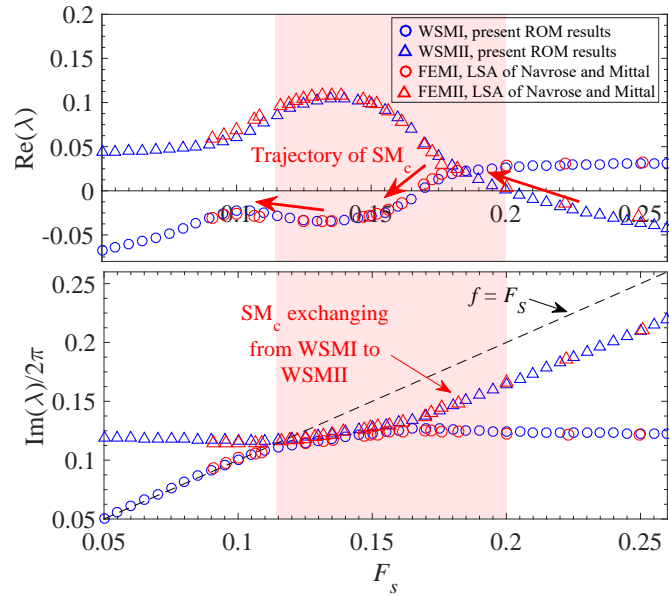
eigenvalue associated with the SM first becomes positive). This incompatibility implies that it is necessary to find another condition of the eigenvalue distribution that can be used to identify the lower boundary in F_s that defines the termination of the lock-in. To this purpose, it is noted that if the lower boundary of the lock-in range is identified by the value of F_s where the slope of $\text{Im}(\lambda)/(2\pi)$ first deviates from the reference line $f = F_s$ (dashed line in Fig. 4.12b), this yields a lower boundary at $F_s = 0.117$. Interestingly, this value of the lower boundary is comparable with that obtained from FOM/CFD—namely, $F_s = 0.119$. In view of this, we can infer that as F_s decreases (or, equivalently, as U_r increases) and the resonance lock-in first appears (viz., the SM frequency approaches the WM frequency), the positive growth rate of the SM will no longer affect the lock-in (i.e., the flutter lock-in disappears) and resonance lock-in will dominate the FSI until it too disappears (when F_s decreases to values less than the lower boundary identified above). The analysis to further support this argument will be provided in the following sub-sections.

After the termination of the resonance lock-in, if the SM is still unstable (viz., if $\text{Re}_{\text{SM}}(\lambda) > 0$), the VIV system will transition into either the galloping or desynchronization regime depending on the specific shape of the body. Li et al. [16] presented a similar argument and suggested that the instability of the SM is intimately linked to the galloping phenomenon for a square cylinder. In consequence, the instability condition of the SM at small values of F_s (or, equivalently, at large values of U_r) is not directly correlated with the lock-in range, but may lead to the galloping phenomenon for specific body cross-sections such as a square cylinder. A body with a circular cross-section is not susceptible to galloping, so the flow-induced oscillations cannot be maintained as the reduced velocity U_r increases past the termination of the lock-in, suggesting that these oscillations will rapidly disappear in this case.

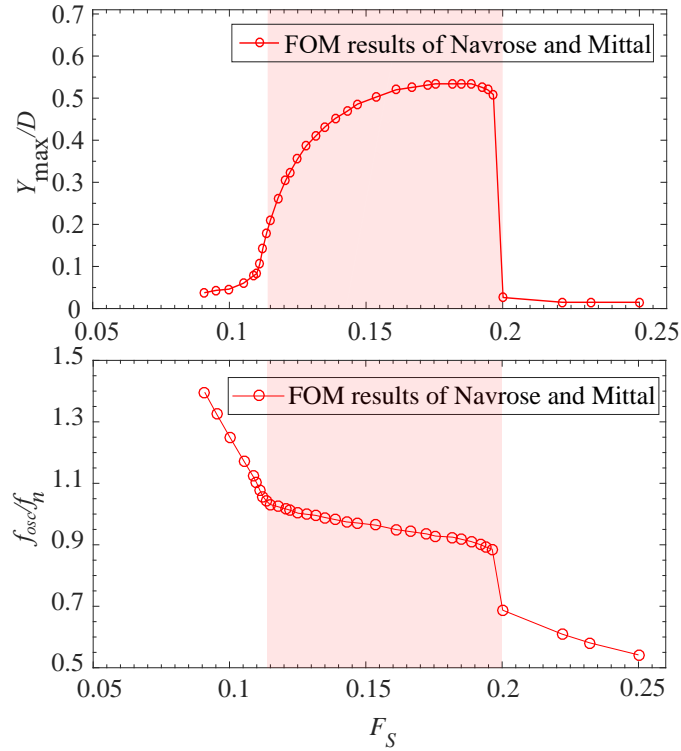
4.4.2 Coupled condition for wake-structure modes

The discussion in the previous sub-section are for cases where the structural and wake modes are uncoupled. In this sub-section, cases where the structural and wakes modes are coupled will be investigated. For the uncoupled condition, the SM can be unambiguously identified. For the coupled condition, the structural mode is now identified with either WSMI or WSMII (depending on the situation). In this thesis, we will refer to the latter mode as SM_c (to emphasize its distinctive properties).

Figure 4.13a displays the real and imaginary parts of the two leading eigenvalues for a flow past a circular cylinder mounted on a linear spring at $(Re, m^*) = (60, 5)$. There is a good conformance between the global LSA conducted by Navrose and Mittal [14] and the current predictions provided by ROM/ERA. In this case, the structural and wake modes are coupled owing to the small mass ratio m^* , and the stability roles of WSMI and WSMII switch at a specific value of the reduced natural frequency F_s [12, 15]. Moreover, no distinction can be made between the SM and the WM, but the coupled modes WSMI and WSMII can be defined. With reference to Fig. 4.10, previous researchers [12, 15] suggested that the resonance lock-in and flutter lock-in dominate the lock-in range in succession with no overlap between the two. The real parts of the eigenvalues associated with WSMI and WSMII intersect—and, the point of intersection, functions as the switching point. More specifically, WSMI and WSMII alternately represents the SM_c over different intervals of F_s , a phenomenon referred to as ‘mode veering’ by Gao et al. [113].



(a) Two leading eigenvalues (real and imaginary parts)



(b) Maximum transverse displacement and oscillation frequency

Figure 4.13: The VIV response as a function of F_s for a flow past a circular cylinder mounted on a linear spring at $(Re, m^*) = (60, 5)$ obtained using (a) ROM/ERA; and, (b) FOM/CFD conducted by Navrose and Mittal [14]. The lock-in range is delineated as the region shaded in red.

4.4.3 Interaction between the structural mode and the second wake mode

The wake mode that interacts with the structural mode, such as in the coupled and uncoupled conditions corresponding to $(Re, m^*) = (60, 5)$ and $(100, 10)$, respectively, is referred to as the first WM (WMI). This characteristic behaviour is evident also in Figs 4.14a, 4.14b and 4.14c which show the root loci obtained from ROM/ERA for various flows past a circular cylinder conducted at Re values of 40, 60, and 100, respectively, for various mass ratios m^* . Moreover, it is noted that for the root loci at $Re = 100$ exhibited in Fig. 4.14c, the second wake model WSII is seen to approach the structural mode SM from the left side of the coordinate axis, exerting its influence on the SM together with the WMI. As Re increases to 120, it is the second wake mode that primarily dominates the structural-wake mode interaction and the loop in the complex plane representing the first wake mode WMI shrinks as shown by the root loci of Fig. 4.14d. Increasing the value of Re to 180, the loop in the complex plane associated with WMI shrinks to a single point, as is evident on perusal of Fig. 4.14f. This indicates that the wake mode interacting with the structural mode will transition from the first wake mode to the second wake mode as the Reynolds number increases. The coupling of the structural mode with a second wake mode was also found by Li et al. [16] using a ROM for the galloping phenomenon of a square cylinder.

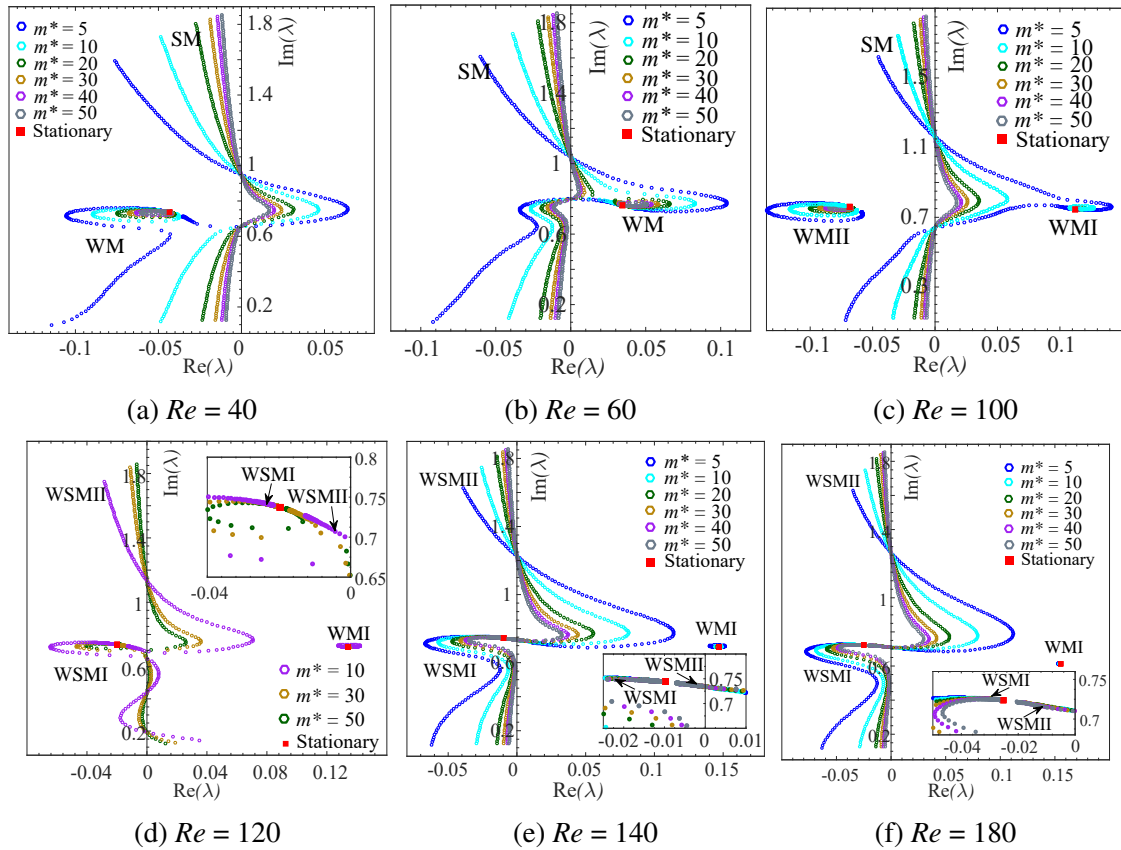
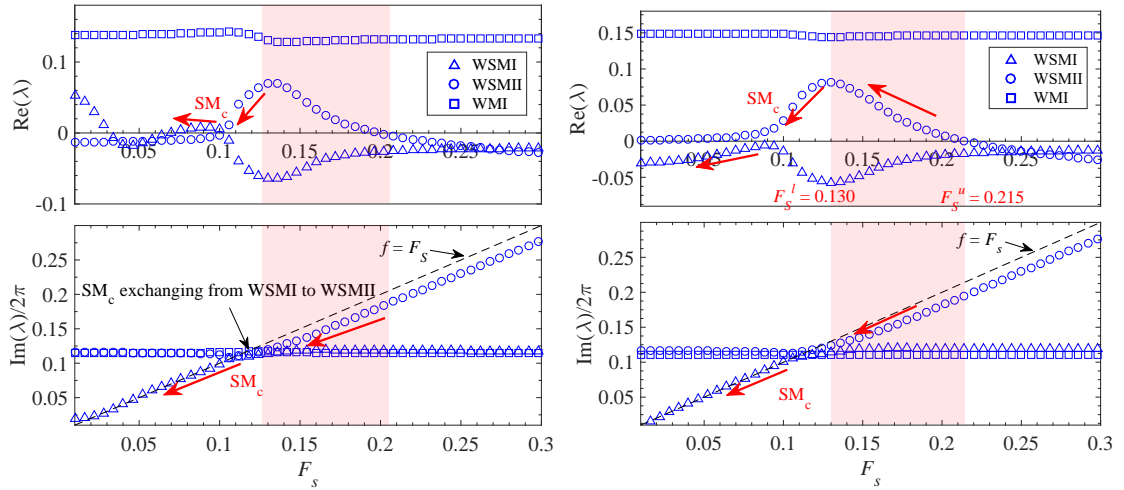


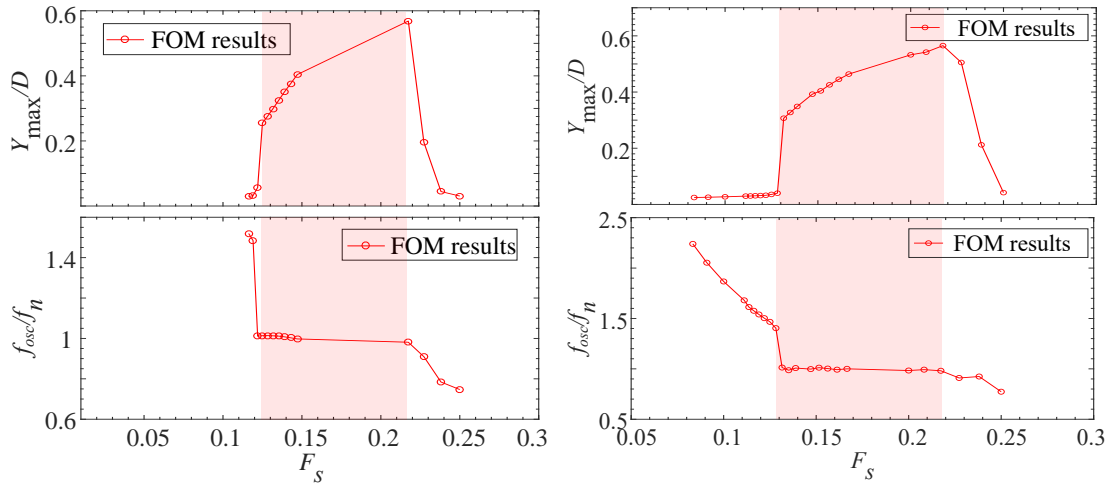
Figure 4.14: Root loci parameterized by the reduced natural frequency F_s for different mass ratios m^* obtained from ROM/ERA for a flow past a circular cylinder mounted on a linear spring. The structural mode interacts primarily with the first wake mode for the cases (a)-(c), whereas for cases (d)-(f), with the second wake mode.

As the mass ratio m^* decreases for a fixed value of Re , the real part of the eigenvalue associated with the structural mode becomes more positive (viz., moves further into the right half

of the complex plane). As a consequence, the structural instability increases and the vortex-induced vibration exhibits a larger amplitude of oscillation. Furthermore, the range of reduced velocity U_r for which vortex-induced vibration occurs increases. The fact that a reduction of the mass ratio leads jointly to an increase in the oscillation amplitude and a widening of the velocity range associated with lock-in has been observed in some previous experimental investigations [5, 41, 44].



(a) Leading eigenvalues (real and imaginary parts) (b) Leading eigenvalues (real and imaginary parts)



(c) Maximum traverse displacement and oscillation frequency (d) Maximum traverse displacement and oscillation frequency

Figure 4.15: The VIV response as a function of F_s for flows past a circular cylinder mounted on a linear spring for (a) $(Re, m^*) = (120, 10)$ obtained using ROM/ERA; (b) $(Re, m^*) = (140, 10)$ obtained using ROM/ERA; (c) $(Re, m^*) = (120, 10)$ obtained using FOM/CFD; and, (d) $(Re, m^*) = (140, 10)$ obtained using FOM/CFD. These two cases correspond to a coupled condition in which the structural mode is coupled to the second wake mode. The lock-in range is delineated as the region shaded in red. The points marked with 'o' are data obtained using FOM/CFD and these points are connected with solid lines for visualization purposes only.

Figure 4.15a displays the real and imaginary parts of the leading eigenvalues for a flow past a circular cylinder mounted on a linear spring at $(Re, m^*) = (120, 10)$. Here, the terms

WMI_c/WMI_c are introduced to more aptly describe the first/second wake modes (depending on Reynolds number), which is represented by WSMI and WSMII successively in a coupled modal situation. When one of WSMI/WSMII represents SM_c, the other mode represents WMI_c (for $Re \leq 100$) or WMI_c (for $Re \geq 120$). Therefore, we observe that it is mainly the second wake mode (WMI_c) that interacts with the structural mode. However, based on the trajectory of the eigenvalue λ associated with WMI in Fig. 4.15a, it is seen that $\text{Re}(\lambda)$ exhibits a slight variation around $F_s = 0.132$ (located at the lower boundary of the lock-in area delineated as the region shaded in red). This implies that there still exists some interaction between WMI and SM_c (SM_c is represented by WSMI/WSMII in turn). To identify the trajectory of SM_c and which specific mode is undertaking this role at a certain F_s , the variation of $\text{Im}(\lambda)$ is one criterion to use. This is because the eigenfrequency associated with SM_c should adhere closely to the dotted line ($f = F_s$) (representing reduced natural frequency) throughout the entire F_s range. In consequence, there should be one SM_c switching location around $F_s = 0.1$, where the mode acting as SM_c changes from WSMII (marked by \circ) to WSMI (marked by \triangle). In terms of the variation of $\text{Re}(\lambda)$, it can therefore be inferred that the intersection point of WSMI and WSMII around $F_s \approx 0.1$ should be the mode switching point. The intersection point located on the right side of the $\text{Re}(\lambda)$ plot between WSMI and WSMII ($F_s \approx 0.26$) does not affect the modal representation of SM_c in that WSMII continues to act as SM_c in this range.

Figure 4.15c presents the results obtained using FOM/CFD showing the dependence of the normalized maximum amplitude Y_{\max}/D and the normalized oscillation frequency f_{osc}/f_n on the reduced natural frequency F_s for $(Re, m^*) = (120, 10)$. It is stressed that if there are multiple peaks in the frequency spectrum of the oscillations at a given value of F_s , the frequency corresponding to the largest peak in the spectrum is the one that is plotted here. With respect to the lock-in range, the lower and upper boundaries for this range are given by $F_s^l = 0.125$ and $F_s^u = 0.215$, respectively. The upper boundary F_s^u obtained from FOM/CFD is not exactly equal to the largest value of F_s for which $\text{Re}_{\text{SM}_c}(\lambda) > 0$ (cf. Fig. 4.15a). Moreover, the value of F_s^l (which is associated with the lower boundary of the resonance lock-in) obtained from FOM/CFD is consistent with the value of F_s where the frequencies associated with the wake and structural modes converge.

A careful examination of $\text{Re}(\lambda)$ in Fig. 4.15a reveals that for values of F_s less than about 0.03, $\text{Re}_{\text{SM}_c}(\lambda)$ transitions from a negative value to a positive value. The positivity of $\text{Re}_{\text{SM}_c}(\lambda)$ at large values of U_r (or, equivalently, at small values of F_s) may be due to a galloping instability. To explore this hypothesis, we conducted high-fidelity FOM/CFD simulations of flow past a cylinder at $(Re, m^*) = (120, 10)$ for $U_r = 8.6, 20, \text{ and } 80$ (or, equivalently, for $F_s = 0.1163, 0.05, \text{ and } 0.0125$, respectively).

Figures 4.16a, 4.16b and 4.16c exhibit time series of the structural displacement in the transverse direction of flows past a circular cylinder with $(Re, m^*, F_s) = (120, 10, 0.1163), (120, 10, 0.05)$ and $(120, 10, 0.0125)$, respectively. The vibration amplitudes for $U_r = 20$ and 80 are still rather small (with the maximum amplitude smaller than $0.03D$), indicating that the system is not in the lock-in or galloping range. However, the displacement equilibrium positions about which the vibrations occur are shifted to 0, 0.008, and 0.1 for $F_s = 0.1163, 0.05, \text{ and } 0.0125$, respectively. This suggests that the equilibrium position of the vibrating body is displaced in the transverse direction with respect to the original equilibrium position at $Y/D = 0$. Moreover, larger values of U_r are associated with larger displacements of the equilibrium position of the body. In view of this, we suggest that this overall deflection of the structure to a new equilibrium position corresponds to a kind of structural mode instability—associated with $\text{Re}_{\text{SM}_c}(\lambda) > 0$, but distinct from

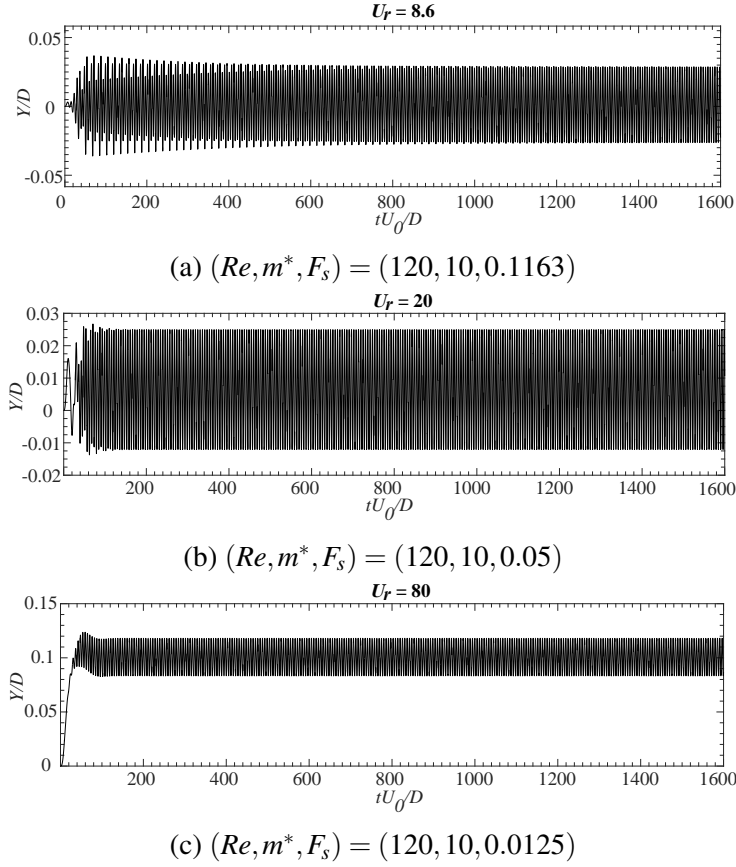


Figure 4.16: Time series of the displacement in the transverse direction for a VIV system consisting of a flow past a circular cylinder mounted on a linear spring for (a) $(Re, m^*, F_s) = (120, 10, 0.1163)$; (b) $(Re, m^*, F_s) = (120, 10, 0.05)$; and, (c) $(Re, m^*, F_s) = (120, 10, 0.0125)$ obtained using FOM/CFD.

the conventional notions of lock-in and galloping. Furthermore, the current simulations define the values for F_s and U_r by changing the structural stiffness while keeping Re constant. More specifically, large values of U_r are associated with a small spring stiffness which, in turn, implies that the restoring force on the elastically-mounted cylinder is smaller, resulting in a larger overall structural deflection.

Figure 4.15b displays the real and imaginary parts of the leading eigenvalues for a flow past a circular cylinder mounted on a linear spring at $(Re, m^*) = (140, 10)$. An interesting feature revealed in this figure is that the real and imaginary parts of the eigenvalue associated with WMI are constant (approximately or better) over the entire range of F_s . Moreover, with reference to Figs 4.12a and 4.12b, the eigenvalues associated with the interacting modes appear to be “pulled” toward each other in the lock-in range. From this perspective, it seems that the first wake mode (WMI) has no influence on the structural mode SM_c in the case of $(Re, m^*) = (140, 10)$. Also, consistent with the case of $(Re, m^*) = (120, 10)$, the right-side intersection point (at $F_s \approx 0.25$) of $Re(\lambda)$ for $(Re, m^*) = (140, 10)$ also does not exhibit SM_c track switching. Note that in the latter case, the real parts of the eigenvalues associated with WSMI and WSMII do not intersect for values of $F_s < 0.15$, unlike that of the former case. Nevertheless, we suggest that there still exists a SM_c transition point at a smaller value of F_s and that this transition occurs where the difference in values of $Re(\lambda)$ for WSMI and WSMII are at a minimum. This transition point

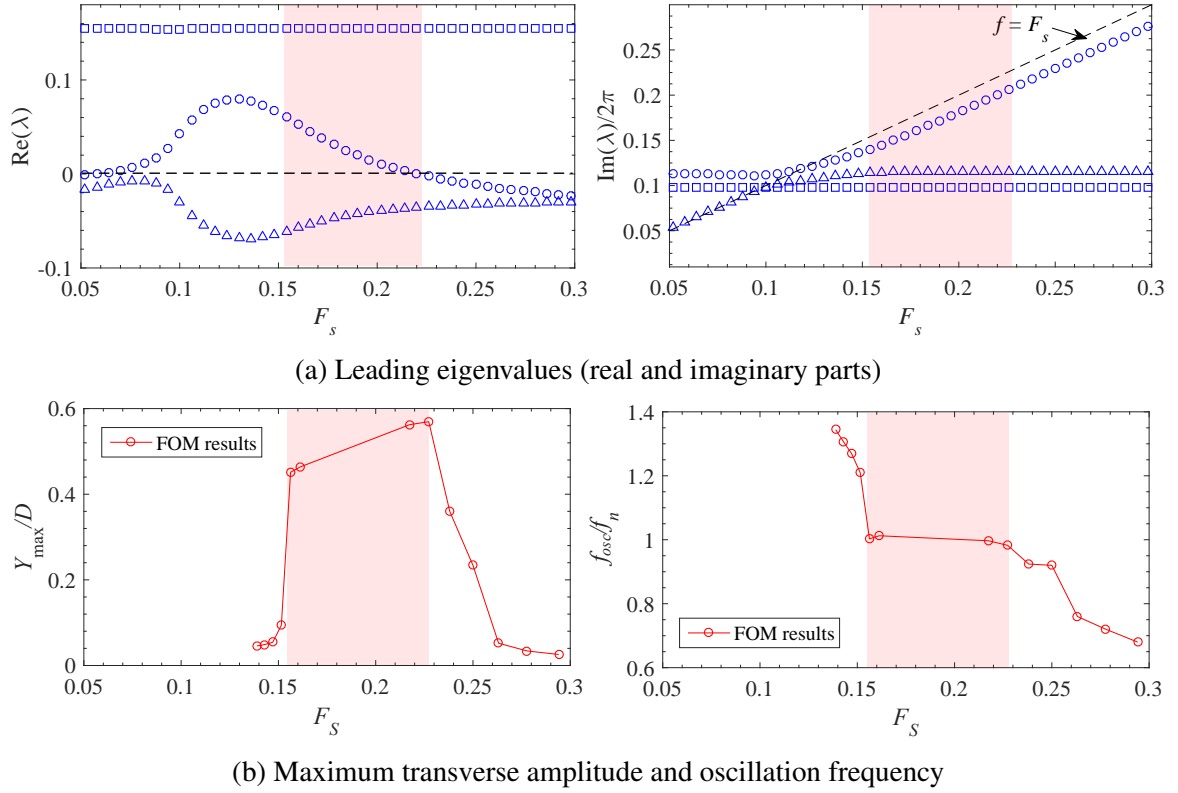


Figure 4.17: The VIV response as a function of F_s for a flow past a circular cylinder mounted on a linear spring at $(Re, m^*) = (180, 10)$ obtained from (a) ROM/ERA and (b) FOM/CFD. This case corresponds to the structural mode coupling with the second wake mode. The lock-in range is delineated as the region shaded in red. The points marked by ‘o’ are data obtained using FOM/CFD and these points are connected with solid lines for visualization purposes only.

also coincides with the point where $\text{Im}(\lambda)$ first converges to the reduced natural frequency [the latter of which is shown as the dotted line ($f = F_s$) in the bottom panel of Fig. 4.15b].

To provide further insights on the lock-in range for $(Re, m^*) = (140, 10)$, Fig. 4.15d presents the normalized maximum amplitude Y_{\max}/D and normalized oscillation frequency f_{osc}/f_n as a function of F_s obtained using FOM/CFD. The lower and upper bounds of the lock-in range are given by $F_s^l = 0.128$ and $F_s^u = 0.217$, respectively. A comparison Fig. 4.15b with Fig. 4.15d shows that the upper boundary of the flutter lock-in obtained from ROM/ERA (i.e., the value of F_s where $\text{Re}_{\text{SM}_c}(\lambda)$ transitions from a positive to a negative value) matches well with the upper boundary of the lock-in range obtained from FOM/CFD.

Figures 4.15a and 4.15b both imply F_s associated with the left-end of the region where $\text{Re}_{\text{SM}/\text{SM}_c}(\lambda) > 0$ is smaller than the lower boundary of the lock-in range obtained from FOM/CFD at $Re = 120$ and 140. This supports the current argument that the condition $\text{Re}_{\text{SM}/\text{SM}_c}(\lambda) > 0$ does not necessarily imply the presence of a flutter lock-in because under this condition if the modal frequencies are also observed to converge (viz., approach one another), then a resonance lock-in is expected to be the dominant mechanism “driving” the lock-in. Consistent with the analysis of Yao and Jaiman [15], the lower (or, left) boundary of the resonance range cannot be determined accurately based on the behaviour of the ROM root loci. Li et al. [16] suggest that this inconsistency is due to the nonlinear competition between the leading wake mode and the structural mode.

At larger values of Re (viz., for $Re \geq 100$), the predictions of FOM/CFD show that the lower boundary of the lock-in range exhibits a sharp decrease in the maximum amplitude response with decreasing F_s , whereas the maximum amplitude response at the smaller values of Re (e.g., for $Re = 40$ and 60) exhibits a smoother transition with decreasing F_s . Furthermore, we found that the lower boundary associated with the region where $\text{Re}_{\text{SM}/\text{SM}_c}(\lambda) > 0$ for $Re = 100, 120,$ and 140 is larger than that of the lower boundary of the resonance lock-in range. Furthermore, we found that the region where $\text{Re}_{\text{SM}/\text{SM}_c}(\lambda) > 0$ for $Re = 100, 120,$ and 140 covers the lower boundary of the resonance lock-in range. Here, the interaction between the wake and the structural modes involves two cases: namely, the uncoupled interaction between SM and WMI for $(Re, m^*) = (100, 10)$ and the coupled interaction between SM_c and WMII_c for $(Re, m^*) = (120, 10)$ or $(140, 10)$.

Figure 4.14f shows the root loci trajectory for a flow past a circular cylinder mounted on a linear spring for $(Re, m^*) = (180, 10)$. The area of the complex plane associated with the WMI loop is very small (almost converging to a single point) and is associated with a constant value (approximately or better) for $\text{Re}_{\text{WMI}}(\lambda)$ and $\text{Im}_{\text{WMI}}(\lambda)$. This characteristic behaviour suggests that WMI has no influence on the structural mode SM_c . Owing to the fact that the frequency associated with WMI is essentially constant over the entire range of values of F_s , we assert that WMI is correlated with the wake mode corresponding to the flow past the stationary cylinder and that WMII_c is correlated with the wake mode induced by the structural oscillations.

The discussion above, in conjunction with the results presented in Fig. 4.14, show that at a low Reynolds number (e.g., $Re = 60$) only the first wake mode interacts with the structural mode, so WMI appears to be related to the modes for both the flow passing the stationary cylinder and for the structural oscillations. For $Re > 100$, the wake mode representing the flow past a stationary cylinder (WMI) acts as a trigger for the phenomenon of resonance lock-in, but WMI and WMII_c jointly interact with the structural model during VIV. Furthermore, as shown by Fig. 4.17a (which exhibits the real and imaginary parts of the leading eigenvalues for a flow past a circular cylinder mounted on a linear spring for $(Re, m^*) = (180, 10)$), the eigenfrequency gap between WSMI and WSMII_c increases as Re increases to 180. While the eigenfrequencies $\text{Im}(\lambda)/(2\pi)$ associated with WSMI and WSMII are close to each other for a limited range of values of F_s ($0.1 < F_s < 0.16$), these eigenfrequencies diverge from each other with a certain spacing, indicating that the coupling between WSMI and WSMII is weaker at these larger F_s values. Owing to this weaker interaction, the resonance lock-in range for this case terminates at $F_s = 0.155$, whereas for the case of $Re = 120$ and 140 the termination of the resonance lock-in occurs at $F_s = 0.125$ and 0.130 , respectively. This behaviour corroborates the relatively narrow lock-in range (delineated as the region shaded in red) obtained from FOM/CFD in Fig. 4.17b.

4.4.4 Aerodynamic coefficients and wake patterns

Yao and Jaiman [15] is at variance with Zhang et al. [12] concerning the conclusion that the root-mean-square (rms) lift coefficient is suppressed in the resonance regime but strengthened in the flutter regime, because they state that the mechanism of flutter lock-in is responsible entirely for the observed lock-in for $Re \geq 70$. However, the present work suggests that the resonance lock-in still exists for the flow past a circular cylinder at $Re \geq 70$. Indeed, the results presented here lends support for Zhang et al.'s [12] view concerning the relationship between the root-mean-square (rms) lift coefficient and the mechanism responsible for the lock-in.

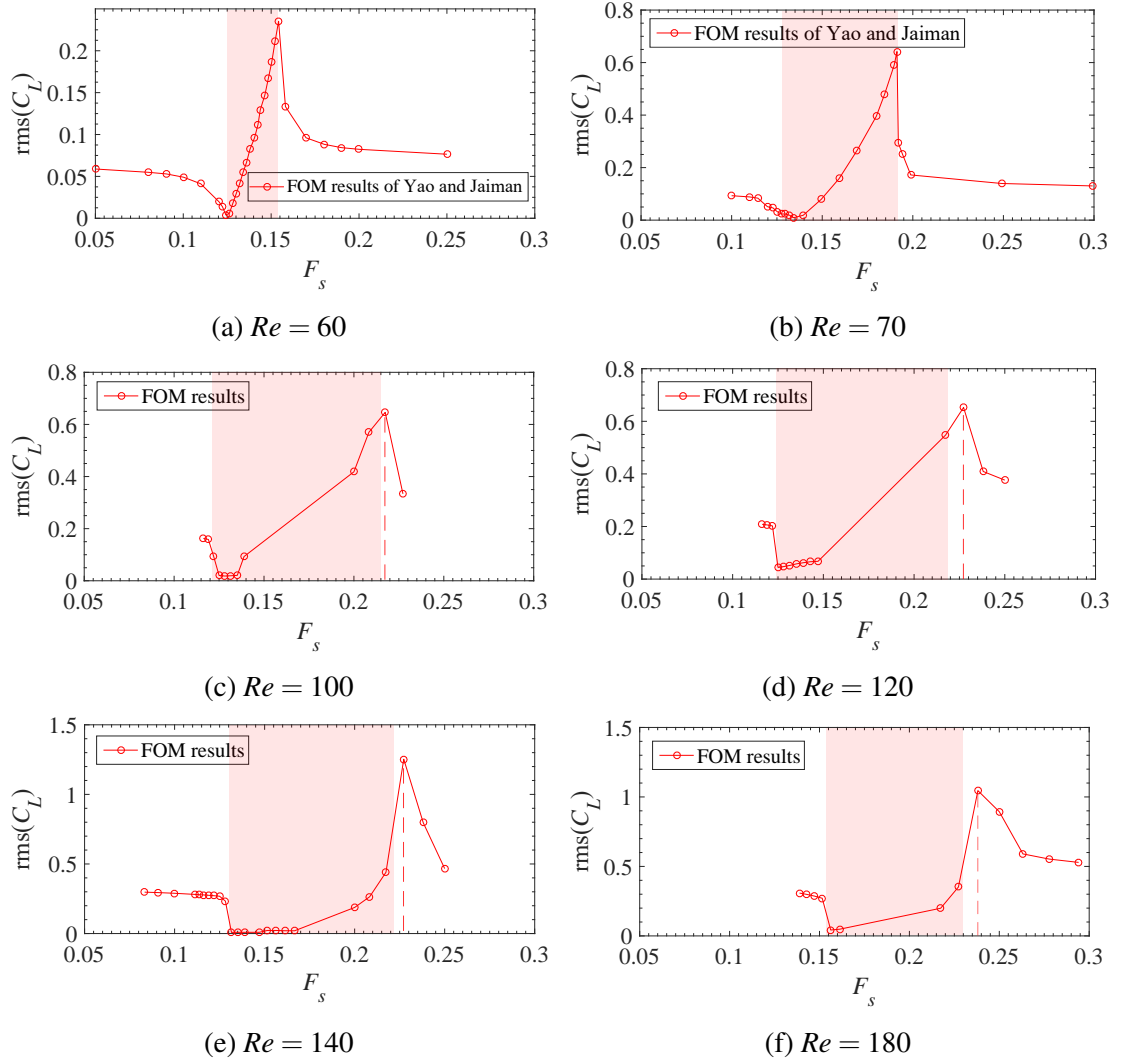


Figure 4.18: Root-mean-square value of the lift coefficient (C_L) as a function of F_s for (a) $Re = 60$ [15]; (b) 70 [15]; (c) 100; (d) 120; (e) 140; and, (f) 180 obtained using FOM/CFD with $m^* = 10$. The lock-in range is delineate as the region shaded in red. The red dotted vertical line, marking the location of the maximum value of $\text{rms}(C_L)$, corresponds to the initial branch.

Figures 4.18a and 4.18b exhibit the root-mean-square values of the lift coefficient ($\text{rms}(C_L)$) as a function of F_s obtained using FOM/CFD. The data shown in these two panels of Fig. 4.18 were extracted from Yao and Jaiman [15]. For $Re = 60$ and 70, the upper bound of the lock-in range (delineated as the region shaded in red) is located precisely at the value of F_s associated with the maximum value of $\text{rms}(C_L)$. Figures 4.18c, 4.18d, 4.18e, and 4.18f summarize how the $\text{rms}(C_L)$ varies with F_s for $(Re, m^*) = (100, 10)$, $(120, 10)$, $(140, 10)$, and $(180, 10)$, respectively. A perusal of Fig. 4.18 shows that for $Re \geq 100$, the upper bound of the lock-in range occurs at a smaller value of F_s than that associated with the maximum of $\text{rms}(C_L)$ (viz., with the reduced natural frequency corresponding to $\max(\text{rms}(C_L))$ shown by the dotted vertical lines in each of the panels for Fig. 4.18). The $\max(\text{rms}(C_L))$ in the present FOM/CFD simulations for $Re = 100, 120, 140,$ and 180 is associated with the initial branch, where the oscillation amplitude is amplified but does not attain the largest value of the amplitude with increasing U_r .

Figure 4.19 shows time series of C_L obtained using FOM/CFD for various combinations of

(Re, U_r, F_s) . These time series display a modulation in the amplitude of oscillations for the initial branch of the lock-in range for $Re = 100$ and 120 , and this modulation disappears as the system enters the upper branch of the lock-in range. The beating phenomenon present in the initial branch leads to increased values of $\text{rms}(C_L)$ compared to those of the upper branch. Moreover, the beating phenomenon evident in the initial branch suggests that there is a balanced competition between the structure and wake modes so the VIV response in this case is unable to achieve a stable (stationary) state. This conclusion reinforces that advocated by Li et al. [16] where these researchers argue that it is the modal competition that determines whether galloping occurs.

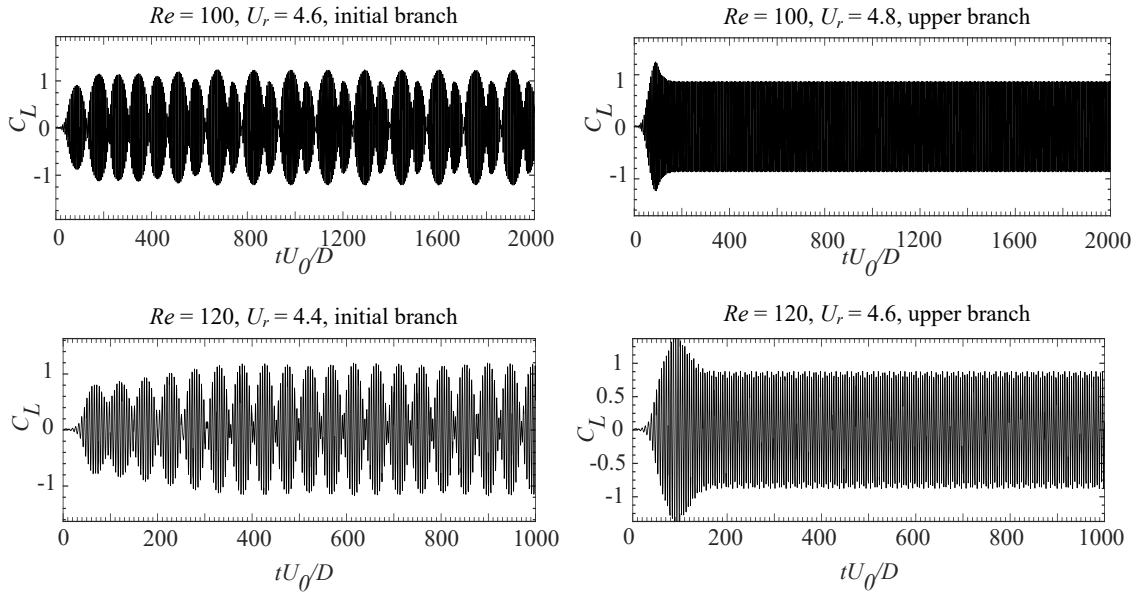


Figure 4.19: Time series of the lift coefficients for flow past a circular cylinder mounted on a linear spring for $(Re, U_r, F_s) = (100, 4.6, 0.217)$ (top left panel, initial branch), $(Re, U_r, F_s) = (100, 4.8, 0.208)$ (top right panel, upper branch), $(Re, U_r, F_s) = (120, 4.4, 0.227)$ (bottom left panel, initial branch) and $(Re, U_r, F_s) = (120, 4.6, 0.217)$ (bottom right panel, upper branch). The time series were obtained using FOM/CFD. The location in the envelope of the amplitude response for two of the cases of U_r at $Re = 100$ and 120 can be obtained from Figs 4.12d and 4.15c, respectively.

Figure 4.20 exhibits the vortical flow pattern in the wake of a circular cylinder mounted on a linear spring at $(Re, m^*) = (120, 10)$ obtained using FOM/CFD. The various panels in the figure document the development of the VIV system at it transitions through various stages: namely, desynchronization, initial branch, upper branch, lower branch, and then back to desynchronization for increasing values of U_r . The results of the current simulations are seen to exhibit various vortex shedding patterns which are consistent with similar outcomes reported by Lambert and Olivier [219] and Prasanth and Mittal [135]. The modes of vortex shedding include the ‘P’ mode which corresponds to the shedding of vortex pairs, the ‘S’ mode which corresponds to the shedding of a single vortex, and the ‘C(2S)’ wake mode which generally appears with a relatively large amplitude at the initial branch of the VIV system consisting a flow past a circular cylinder mounted on a linear spring. We note that Fig. 4.20b displays the 2S mode of vortex shedding in the initial branch owing to the fact that the normalized maximum transverse amplitude Y_{\max}/D does not meet the threshold for the triggering of the ‘C(2S)’ wake mode. For a reduced velocity of $U_r = 4.6$, the flutter lock-in is in the upper branch and the VIV system exhibits the 2P mode of

vortex shedding as is evident from an examination of Fig. 4.20c. On the other hand, for $U_r = 8.0$ corresponding to a resonance lock-in in the lower branch, the VIV system displays a 2S mode of vortex shedding as can be seen in Fig. 4.20e.

Furthermore, our results support Yao and Jaiman [15] who questioned the interpretation provided by Zhang et al. [12] on the relationship between the nature of the wake pattern and the mechanism responsible for the lock-in (i.e., resonance or flutter). Indeed, the modes of vortex shedding depend on the body shape, the amplitude of the oscillations, and the characteristic frequencies of shedding and have no direct link to whether the lock-in is induced by resonance or flutter. In general, the transition of the wake dynamics from the desynchronization, the initial branch, the upper branch, and the lower branch and, finally, back to the desynchronization regions of the VIV (as U_r increases or, equivalently, as F_s decreases), the wake will exhibit the ‘2S’, ‘2S/C(2S)’, ‘2P’, ‘2S’, and ‘2S’ modes of vortex shedding, respectively, for the flow past a circular cylinder.

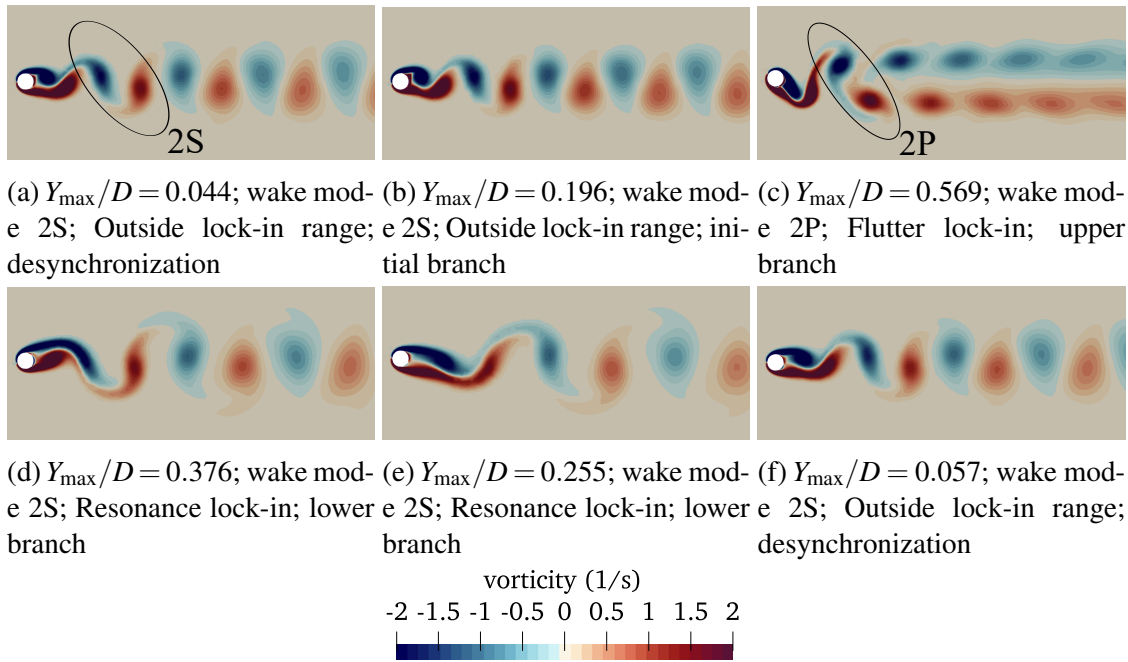


Figure 4.20: Isopleths of the instantaneous vorticity for flow past a circular cylinder mounted on a linear spring at $(Re, m^*) = (120, 10)$ obtained using FOM/CFD for (a) F_s (U_r) = 0.238 (4.2); (b) 0.227 (4.4); (c) 0.217 (4.6); (d) 0.143 (7.0); (e) 0.125 (8.0); and, (f) 0.122 (8.2). The flow is from left to right.

4.4.5 Frequency analysis of the modal mechanism

Figure 4.21 shows time series for the normalized transverse displacement Y/D of motion and the corresponding power spectral density (PSD) for a VIV system consisting of the flow past a circular cylinder mounted on a linear spring at $(Re, m^*) = (120, 10)$ obtained using FOM/CFD. The information contained here can be used to ascertain the possible presence of the interaction between the wake mode (characterized by a frequency of 0.175 Hz for flow past a stationary circular cylinder at $Re = 120$) and the structural mode (whose characteristic frequency will depend

on the reduced natural frequency F_s) for different values of U_r .

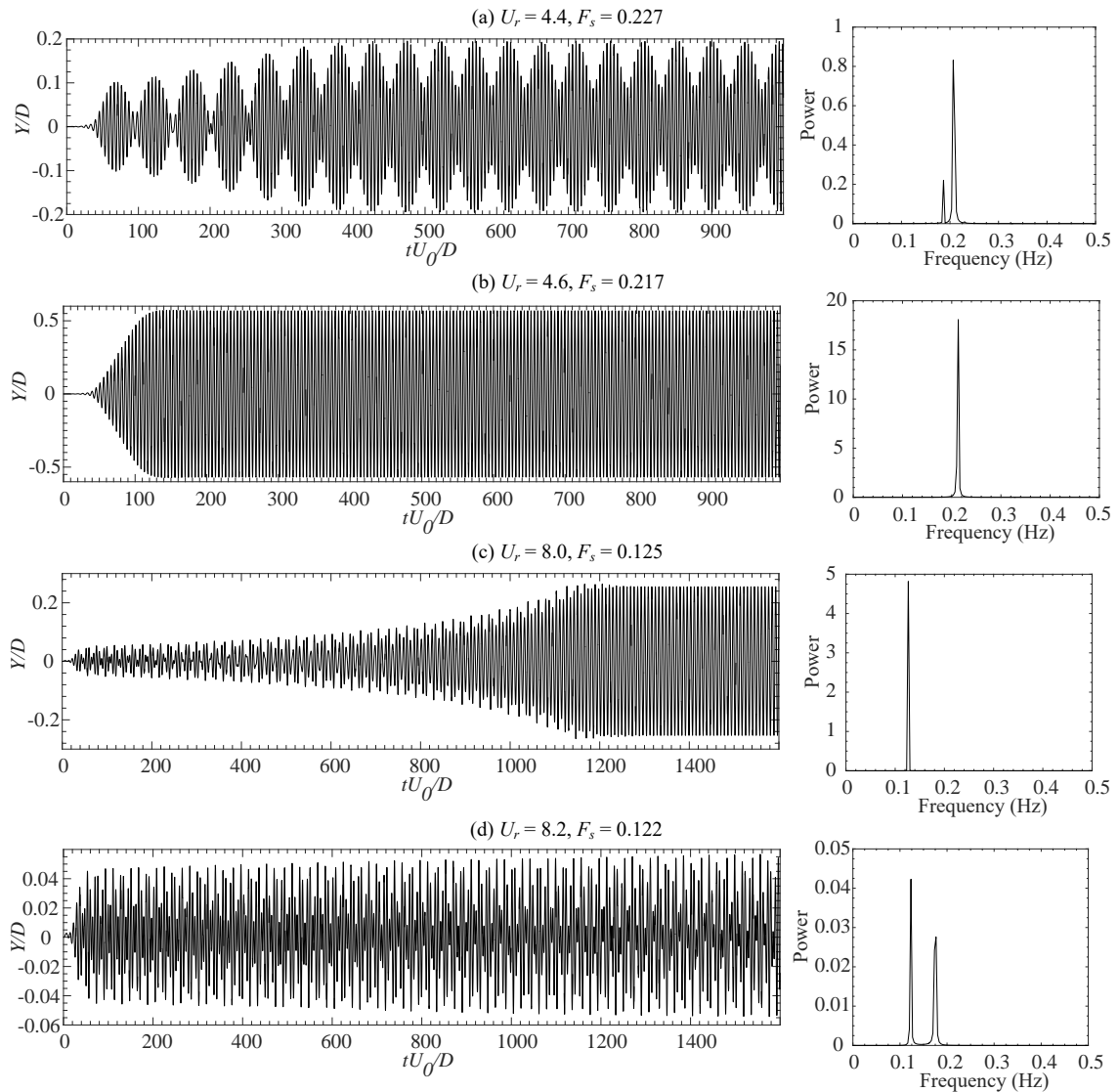


Figure 4.21: Time series of the transverse displacement and the corresponding power spectrum of this displacement for a VIV system consisting of flows past a circular cylinder mounted on a linear spring at $(Re, m^*) = (120, 10)$ obtained using FOM/CFD for values of (a) $F_s = 0.227$; (b) 0.217; (c) 0.125; and, (d) 0.122 which span the entire lock-in range.

The top panel in the Fig. 4.21, obtained at $U_r = 4.4$, exhibits the presence of the beating phenomenon in the transverse displacement which remains even when the flow-induced vibration is fully developed. The amplitude of oscillations here displays the characteristic modulation associated with the beating phenomenon. The characteristic frequencies associated with both the SM and WM are seen to be present in the time series of the transverse displacement as is evident from a perusal of the PSD plot. In the power spectrum, the first spectral peak is associated with the WM (with a corresponding frequency of 0.175 Hz) and the second spectral peak is associated with the SM (with a corresponding frequency of 0.227 Hz). The system is at the edge (initial branch) of the lock-in range.

For the second panel in Fig. 4.21, obtained at $U_r = 4.6$, the amplitude of oscillations, after

equilibrium (stationarity) has been achieved, is characterized by a single frequency. In this case, the reduced natural frequency F_s is close to Strouhal number St for flow past a stationary cylinder, so the lock-in phenomenon occurs quickly and the system enters the upper branch.

The third panel in Fig. 4.21, obtained at $U_r = 8.0$, exhibits a substantial transient in the time development of the transverse displacement amplitude before the system finally achieves an equilibrium or stationary state. According to Zhang et al.'s [12] analysis, the wake and structural modes coexist in the early stages of the time development here. Owing to the role of resonance, the structural frequency gradually dominates the flow-induced vibration and at the later stages of the time evolution, the system achieves a periodic stability characterized by a single oscillation frequency. In this example, the system enters the lower branch.

The bottom panel in Fig. 4.21, obtained at $U_r = 8.2$, exhibits an interesting vibration pattern. In this case, the system transitions out of the lock-in range so the transverse displacement amplitude is very small (viz., the vibration almost disappears). The power spectrum of this low-amplitude vibration shows that the frequencies induced by the structural and wake modes co-exist. The first spectral peak corresponds to the SM (with a characteristic frequency of 0.122 Hz) and the second spectral peak is associated with the WM (with a characteristic frequency of 0.175 Hz). In general, as the VIV system transitions into the lock-in range, the vibration will be dominated by the structural natural frequency after a sufficient time has elapsed for the VIV system to develop.

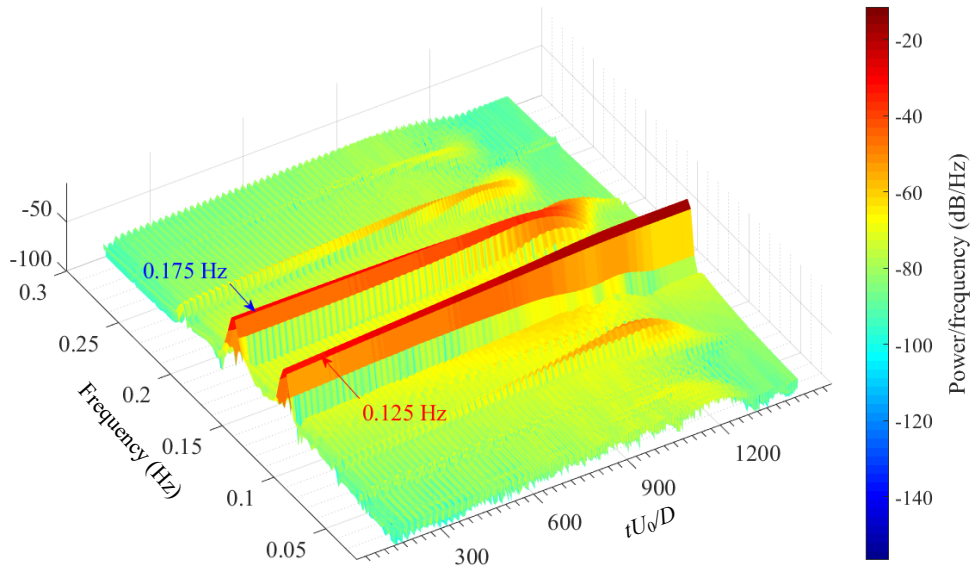


Figure 4.22: Time-frequency spectrum of the time series of the transverse displacement for $(Re, m^*, U_r) = (120, 10, 8)$.

Next, we apply a time-frequency analysis to the time series exhibited in the third panel of Fig. 4.21 for the case $U_r = 8.0$. The result of the time-frequency analysis is shown in Fig. 4.22. A careful examination of this figure shows the presence of two prominent spectral peaks corresponding to frequencies of 0.125 Hz and 0.175 Hz which are associated with the SM and WM, respectively. With increasing time tU_0/D , it is seen that the power of the spectral peak associated with the SM increases monotonically (approximately or better), while that associated with the WM decreases (albeit slowly) until it disappears altogether at $tU_0/D \approx 1200$. The calculation at $U_r = 8.0$ in Fig. 4.21 also indicates that the vibration achieves stability for $tU_0/D > 1200$. Follow-

ing from this, it is apparent that there is a strong modal competition occurring here, but the SM ultimately wins this competition and dominates the dynamics of the VIV system. Furthermore, it is asserted that it is this balanced competition between initially two equally “strong” structural and wake modes that results in the very long transient seen in the third panel of Fig. 4.21. Owing to the closeness of the two frequencies associated with the SM and WM (reflecting the onset of a resonance), the competition between the SM and WM persists for a long time leading to the long transient development seen in the time series. This provides support for our argument that it is the mechanism of resonance rather than that of flutter that dominates the lower branch region of the VIV response.

To follow on, we use dynamic mode decomposition (DMD) to investigate the dynamics of the wake flow. DMD is a data-driven methodology that can be used to extract dynamical information from data acquired from either experimental measurements or numerical simulations of time-varying phenomena [236]. To this purpose, we apply DMD to identify the dominant modes responsible for the dynamics of a flow past a circular cylinder and, more specifically, to identify a low-order dynamics model for the underlying unsteady flow phenomenon. The DMD version applied in our analysis is the streaming total DMD (STDMD) [237, 238], which has been implemented in OpenFOAM v2006 [202].

Despite the existence of many versions of the DMD algorithm [222, 237, 238], the most important feature of the analysis is that every DMD mode is associated with a characteristic complex frequency (or, eigenvalue) and corresponds to a low-dimensional coherent spatiotemporal pattern in the data set. The (complex) eigenvalues describe the growth/decay and oscillatory characteristics of the associated DMD (dynamical) mode. The magnitude $|\lambda|$ of the (complex) eigenvalue represents the growth/decay rate of the associated DMD mode. More specifically, damped (decaying) modes are associated with eigenvalues whose magnitude is less than unity, whereas amplified (growing) modes are associated with eigenvalues whose magnitude is greater than unity. Furthermore, DMD modes associated with eigenvalues where $|\lambda| = 1$ (which lie on the unit circle in the complex plane) are purely oscillatory in nature. The amplitude $|\alpha|$ of the DMD modes can be arranged in decreasing order of magnitude where the modes with the largest amplitude are considered to be dominant (and provide generally a good approximation of the underlying dynamics in a low-rank subspace). To this purpose, the amplitudes of the DMD modes can be computed using data snapshots and normalized with respect to the maximum mode amplitude [239]. For the DMD conducted herein, the velocity snapshots are sampled sixty times per oscillation cycle and fifty oscillation cycles are used for the analysis. We apply the DMD methodology to analyze the wake flow for a VIV system consisting of flow past a circular cylinder mounted on a linear spring for $(Re, m^*, U_r) = (180, 10, 4.2)$ and $(180, 10, 6.2)$ in order to obtain a deeper insight into the nature of the vortical wake dynamics and to garner a better understanding of the mode competition predicted by ROM/ERA.

Figure 4.23 presents a time series of C_L and the corresponding power spectrum for a flow past a circular cylinder mounted on a linear spring for $(Re, m^*, U_r) = (180, 10, 4.2)$ which belongs to the initial branch region of VIV. The power spectrum consists of two predominant peaks at frequencies of 0.219 Hz and 0.194 Hz. The spectral peak at 0.194 Hz is consistent with the Strouhal number St for a flow past a stationary cylinder at $Re = 180$ [240], whereas the spectral peak at 0.219 Hz is associated with the structural mode. Owing to the equal interaction between the structural and wake modes in the initial branch, the dominant spectral peak at 0.219 Hz deviates from the structural natural frequency $F_s \equiv U_r^{-1} = 0.238$ Hz.

Figure 4.24 shows the spectra, mode amplitudes, and isopleths of two representative D-

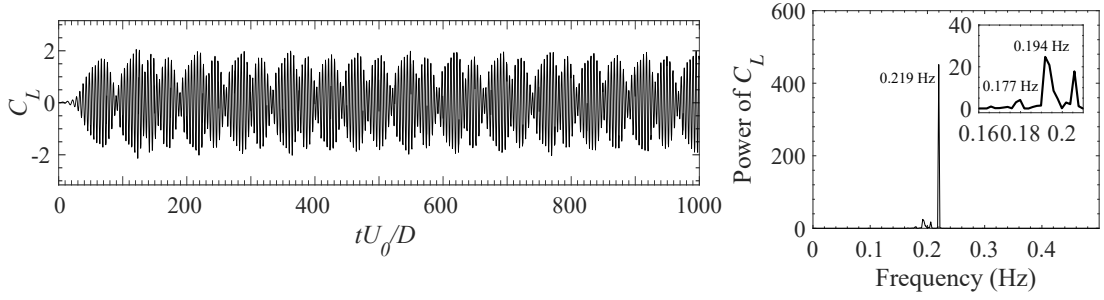


Figure 4.23: Time series of C_L and the associated power spectrum for a flow past a circular cylinder mounted on a linear spring with $(Re, m^*, U_r) = (180, 10, 4.2)$ obtained using FOM/CFD.

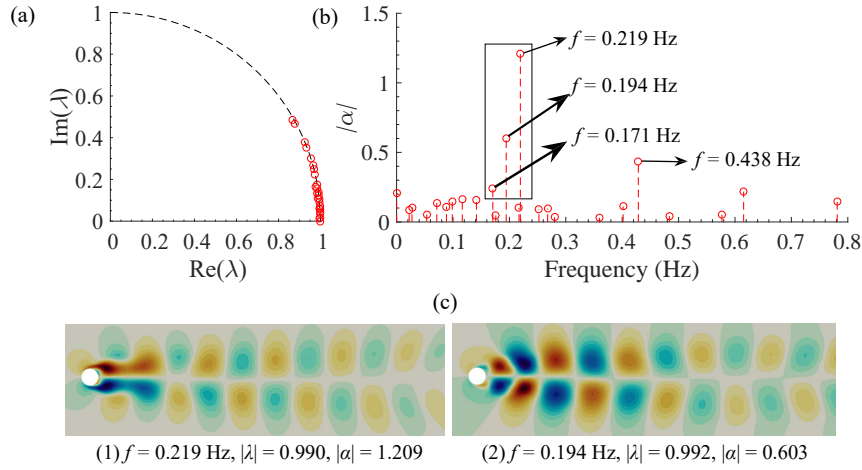


Figure 4.24: DMD of VIV system consisting of a flow past a circular cylinder mounted on a linear spring with $(Re, m^*, U_r) = (180, 10, 4.2)$. (a) Distribution of eigenvalues in the complex plane. (b) Mode amplitudes $|\alpha|$ (normalized by the maximum amplitude) and their associated frequencies. (c) The real parts of two DMD modes of the streamwise velocity (white: zero; red: above a positive threshold; blue: below a negative threshold).

MD models for a flow past a circular cylinder mounted on a linear spring at $(Re, m^*, U_r) = (180, 10, 4.2)$. It is seen that the magnitude of all the eigenvalues are unity (viz., the eigenvalues lie on the unit circle $|\lambda| = 1$ in the complex plane suggesting that the flow is in a near-equilibrium (or, quasi-equilibrium) state where the dynamics are linear (approximately or better)). Similar observations were reported by Hemati et al. [222] and Sarkar et al. [223]. The two dominant mode amplitudes exhibited in Fig. 4.24(b) are at 0.219 Hz and 0.194 Hz which are consistent with the power spectrum shown in Fig. 4.23. The first two DMD modes for the streamwise velocity are exhibited in Fig. 4.24(c). The modes are consistent with the notion that the first DMD mode (at 0.194 Hz) is consistent with the signature of von Kármán vortex shedding, whereas the second DMD mode (at 0.219 Hz) is associated with the signature of the SM. In conformance with the discussion above, the WM and SM involve a competing equilibria, which manifests itself in a modulation in the time variation of C_L . This, in turn, shapes the nature of the vortical wake patterns revealed by the DMD modes.

Figure 4.25 depicts the time series of C_L and the corresponding power spectrum for a flow past a circular cylinder mounted on a linear spring with $(Re, m^*, U_r) = (180, 10, 6.2)$ which belongs to the lower branch region of the lock-in range. The power spectrum exhibits a single dominant

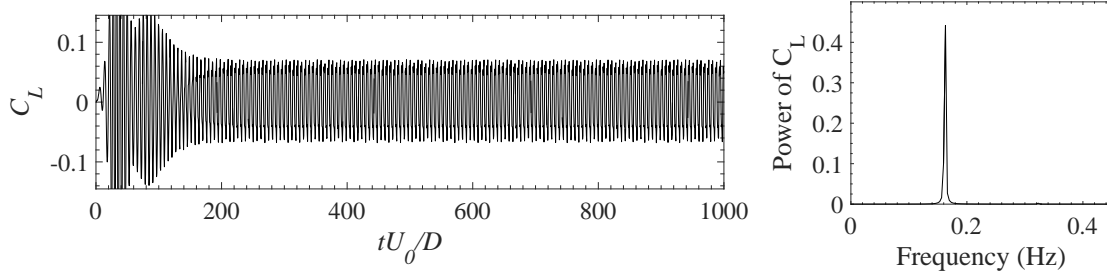


Figure 4.25: Time series of C_L and the corresponding power spectrum for a flow past a circular cylinder mounted on a linear spring with $(Re, m^*, U_r) = (180, 10, 6.2)$ obtained using FOM/CFD.

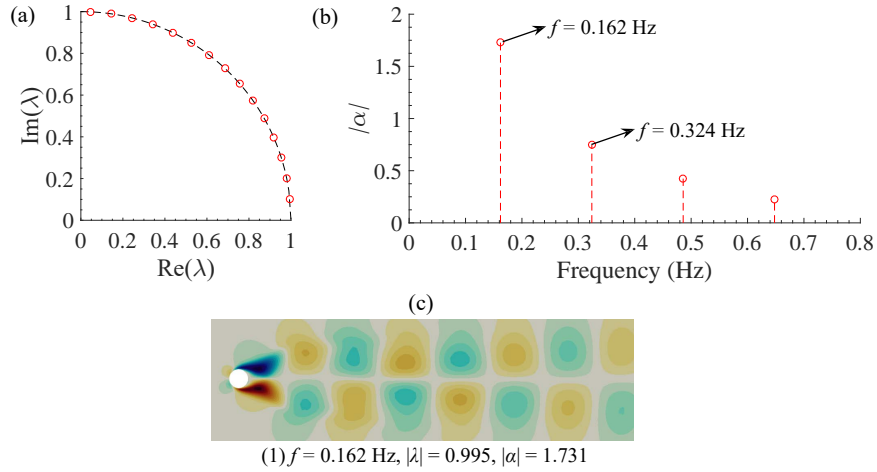
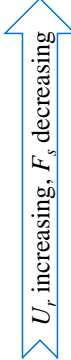


Figure 4.26: DMD of VIV system consisting of a flow past a circular cylinder mounted on a linear spring with $(Re, m^*, U_r) = (180, 10, 6.2)$. (a) Distribution of eigenvalues in the complex plane. (b) Mode amplitudes $|\alpha|$ (normalized by the maximum amplitude) and their associated frequencies. (c) The real part of the dominant DMD mode of the streamwise velocity (white: zero; red: above a positive threshold; blue: below a negative threshold).

peak corresponding to a frequency of 0.162 Hz associated with the structural mode. Indeed, in the case, it is evident that the structural mode dominates the VIV response. Moreover, the structural natural frequency $F_s \equiv U_r^{-1} = 0.162$ Hz is precisely equal to the oscillation frequency, owing to the fact that the structural mode completely dominates the mode interaction in this case with the result that modal competition between the SM and WM disappears as the VIV settles into an equilibrium state.

Figure 4.26 shows the spectra, mode amplitudes and isopleths of the first DMD mode for a flow past a circular cylinder mounted on a linear spring with $(Re, m^*, U_r) = (180, 10, 6.2)$. This figure shows that the eigenvalues are distributed uniformly on the unit circle of the complex plane implying that the eigenvalues are associated with a fundamental frequency and positive integer multiples of this fundamental frequency (viz., the various harmonics). The fundamental frequency corresponds to an oscillation frequency of 0.162 Hz which is consistent with the power spectrum shown in Fig. 4.25. The DMD mode corresponding to the fundamental frequency of the streamwise velocity is shown in Fig. 4.26(c). These results support the notion that the VIV system in this example is locked at the structural natural frequency.

	Modes	Existence		Distribution of root loci
		Yes	No	
	Galloping		Circular cylinder	$\text{Re}(\lambda)$ of 'SM/SM _c ' > 0, at high U_r
	Resonance	$Re > Re_{cr}$	$Re < Re_{cr}$	$\text{Im}(\lambda)$ of 'SM/SM _c ' is close to that of wake modes
	Flutter	Circular cylinder		$\text{Re}(\lambda)$ of 'SM/SM _c ' > 0, at low U_r

Notes: 'SM' refers to SM for uncoupled condition, and SM_c (the mode represents SM role) for coupled condition.

Figure 4.27: Characteristics of the vortex-induced vibration (VIV) and the relationship of these characteristics with the modal distribution of root loci obtained from ROM/ERA.

4.5 Chapter summary

The present work provides a synthesis of the key characteristics for the dynamics of a VIV system consisting of the flow past a circular cylinder elastically mounted on a linear spring. The important results of this investigation are summarized in Fig. 4.27. For Re less than a critical Reynolds number Re_{cr} (which is approximately 47 for a circular cylinder) required to trigger vortex shedding for the flow past a stationary cylinder, the wake modes are stable and flutter is the only mechanism responsible for triggering the lock-in. When the structural modes are stable over the full range of values of F_s (viz., there is no flutter lock-in), the frequency lock-in will be completely determined by the mechanism of resonance lock-in. In present work, we argue that the flutter is not necessarily the only factor responsible for the frequency lock-in at $Re = 100$ for the flow past a circular cylinder. This is contrary to the contention of previous investigators [15] who have stated that the frequency lock-in for a VIV system arises only from a pure flutter mode instability for $Re \geq 70$.

With increasing U_r , a resonance lock-in manifests itself (viz., when the structural natural frequency and vortex shedding frequency are close to one another). The instability of the SM is not the dominant effect in the VIV system (i.e., the flutter lock-in disappears altogether) and the resonance lock-in will be the primary mechanism influencing the lock-in until this resonance disappears.

After the resonance lock-in disappears, the flutter lock-in will not reappear even if $\text{Re}_{SM}(\lambda) > 0$ (as shown for a flow past a circular cylinder at $Re = 100$ investigated herein as well as the results reported by Yao and Jaiman [15]). Nevertheless, the condition $\text{Re}_{SM}(\lambda) > 0$ is related to the galloping instability at large values of U_r , but the occurrence of galloping (which gives rise to large-amplitude vibrations) is determined by the specific body shape. To summarize, the condition $\text{Re}_{SM}(\lambda) > 0$ is correlated with a flutter lock-in or a galloping instability, but a resonance lock-in will be the primary mechanism governing VIV when the frequencies corresponding to the structural and wake modes are close to one another. In the latter case, the resonance lock-in will be responsible for the frequency lock-in (and not the flutter instability).

Occasionally, the condition $\text{Re}_{SM/SM_c}(\lambda) > 0$ at large values of U_r is linked to an overall

deflection of the vibrating structure to a new equilibrium position with respect to the original equilibrium position at $Y/D = 0$. This occurs for a circular cylinder supported by a spring with a small string stiffness. This phenomenon is independent of either the flutter lock-in or the galloping instability (e.g., refer to the case of the flow past a circular cylinder elastically mounted on a linear spring with $(Re, m^*, F_s) = (120, 10, 0.0125)$).

There exist numerous wake modes and the wake dynamics will become increasingly more unstable as the Reynolds number increases. In the complex plane, the trajectories of the root loci corresponding to the full spectrum of wake modes will tend to move from the negative half-plane to the positive half-plane. During this process, the particular wake mode that is nearest to the structural mode in frequency will interact with it, potentially resulting in either a coupled or uncoupled condition. A resonance lock-in occurs when the frequency corresponding to the SM is close to the frequency corresponding of any of the wake modes—and not, necessarily, the first wake mode.

As Re varies over 100, 120, 140, and 180, the area of the first wake mode WMI loop in the complex plane decreases monotonically. In consequence, the interaction between WMI and the SM decreases with an increasing Reynolds number, while the second wake mode WMII exhibits a stronger interaction with the SM owing to the modal transformation of the wake flow. At a certain value of Re (e.g., $Re = 140$), an increasing m^* is correlated with a weaker interaction in the VIV system and with a smaller WMI loop area. The latter condition is also correlated with a constant value (approximately or better) for imaginary part of the eigenvalue associated with WMI. The transition out of the lock-in range is faster at $Re = 180$ than at either $Re = 140$ or 160, owing to the weaker interaction (coupling) between WSMI and WSMII, implying a weaker coupling between the structural and wake modes. This observation lends support for the dominance of the resonance lock-in in the lower branch region of VIV.

The balanced competition between the wake and structural modes is the cause of the beating phenomenon observed in the time series of the transverse displacement for the initial branch of the VIV. The upper branch is correlated with the flutter lock-in, in which the structural mode dominates the interaction, and where the structural oscillations rapidly settle into an equilibrium state. The mode interaction in the lower branch region of VIV, associated with resonance lock-in, exhibits a long transient in the temporal development of the transverse displacement before it finally settles into an equilibrium or stationary state. This observation provides support for the assertion that the resonance lock-in dominates the lower branch region of VIV, even when the real part of the eigenvalue for the SM is positive (implying a growth rate in the SM).

Chapter 5

2-D linear stability analysis of galloping behavior with uniform inflow

This chapter focus on investigating the mechanism underlying the triggering of galloping behavior in elastically-mounted structures. Considering the literature review and summary in Chapter 2, although past experiments and numerical simulations undertaken by the research community have extensively explored the influence of various shapes on the galloping response, there still remains much that is poorly understood regarding the physical mechanisms that determine galloping—for example, what particular characteristics in the cross-sectional shape of a body result in the generation of galloping and what determines whether this galloping is “hard” or “soft” are currently unanswered questions. Our present state of understanding and our current gaps of knowledge with respect to the galloping phenomenon will be discussed later. From this perspective, further detailed studies of the galloping phenomenon (with the objective of providing a more complete characterization and deeper physical insights into the complex dynamics of this phenomenology) are needed, particularly as it concerns the problem of obtaining a better and more unified understanding of the precise conditions and underlying physical reasons for the triggering of galloping. The studies in this chapter will be significant for the amplification and suppression of flow-induced vibration in practical engineering issues.

In this chapter, the detailed characterization of the galloping response in a FIV system is based on the mechanistic insights and predictions of the complex dynamics provided by: (1) a full-order model obtained using high-fidelity computational fluid dynamics; (2) a linear stability analysis undertaken using a reduced-order model constructed from the eigensystem realization algorithm; and, (3) a quasi-steady analysis conducted using the Den Hartog stability criterion. The results obtained herein provide a unified approach for studying the effects of body geometry (shape), Reynolds number, and mass ratio on the nature of the galloping instability and the associated chaos in the galloping structure and, in so doing, provide a deeper and better understanding of the physical processes responsible for galloping. From this perspective, we first use these results to ameliorate certain oversights in the LSA of galloping conducted by Li et al. [16] and, thereby, extend the utility of their work. Next, we propose some novel factors that may be responsible for the triggering of the galloping instability, particularly with reference to the sensitive influence of the cross-sectional shape of the object for self-excited motion to occur. To this purpose, we investigate the geometry effects on galloping and, more specifically, how even small (minute) changes in the cross-sectional shape of a trapezoidal body in the windward direction can trigger the galloping instability.

Following from this analysis, we undertake a seminal investigation of the influence of the after-body shape (geometry) on the causation of either hard-galloping or soft-galloping from a purely modal perspective. In addition, we apply a quasi-steady theory to explain the influence of the side-ratio of rectangular cylinders on galloping oscillations but, even so, we describe and emphasize the specific limitations of this theory when applied to other body geometries. Finally, the influence of the Reynolds number and the mass ratio on the galloping mechanism is investigated systematically, with the result that certain special modal characteristics associated with galloping (viz., uniformity of the eigenfrequency of the structure mode at the value of the reduced velocity U_r associated with the onset of galloping) are reported for the first time. Critically, this study provides the first comprehensive and detailed investigation on the specific mechanisms underlying the triggering (initiation) conditions for the galloping instability and, in so doing, addresses a key limitation of prior efforts in this regard.

5.1 Methodology of Den Hartog stability criterion

Besides the methodologies of FOM/CFD and ROM/ERA already introduced above, this chapter would also use the Den Hartog stability criterion, one quasi-steady model, to explore the galloping phenomenon. Hartog [pp. 370–371] [131] proposed a stability criterion to determine the potential susceptibility of a FIV system to develop a galloping behavior from the equilibrium position. Figure 5.1 shows a bluff body that is moving in the downward direction (transverse to the incident flow U) and, as a result of this motion, the incoming flow U_{rel} relative to the moving body is incident from below at an angle $\alpha = \tan^{-1}(v/U)$, where v is the downward (transverse) velocity of the body.

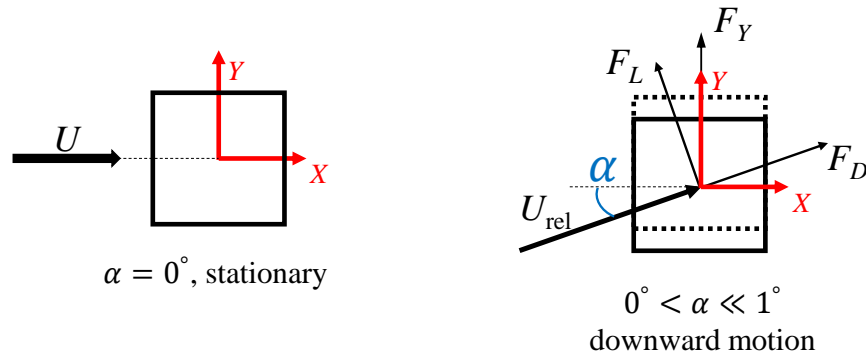


Figure 5.1: The total fluid force acting on a downward-moving body can be resolved into two components: a lift force F_L and a drag force F_D .

The lift F_L and drag F_D forces acting on the downward-moving body have y-components (opposite of the direction of the moving body) given by $F_L \cos \alpha$ and $F_D \sin \alpha$, respectively, which results in a total upward force F_Y acting on the body that retards its downward motion:

$$F_Y = F_L \cos \alpha + F_D \sin \alpha . \quad (5.1)$$

The condition for aerodynamically unstable behavior for the moving (vibrating) body is given

by

$$\frac{dF_Y}{d\alpha} < 0, \quad (5.2)$$

which, in view of (5.1), can be recast in terms of the static force coefficients for a unit spanwise length as follows:

$$\begin{aligned} \frac{dF_Y}{d\alpha} &= \cos \alpha \left(\frac{dF_L}{d\alpha} + F_D \right) + \sin \alpha \left(-F_L + \frac{dF_D}{d\alpha} \right) \\ &\approx \left(\frac{dF_L}{d\alpha} + F_D \right) \\ &= \frac{1}{2} \rho U^2 D \left(\frac{dC_L(\alpha)}{d\alpha} + C_D(\alpha) \right) < 0, \end{aligned} \quad (5.3)$$

where the penultimate line follows from the assumption that $\alpha \ll 1$ so $\cos \alpha \approx 1$ and $\sin \alpha \approx 0$. Here, C_L and C_D are the lift and drag coefficients respectively, and U is the flow speed.

From (5.3), it is seen that a positive value for the derivative of the lift coefficient with respect to α corresponds to an aerodynamically stable behavior for the vibrating body, whereas an negative value for the derivative of the lift coefficient with respect to α can potentially lead to an aerodynamically unstable behavior for the body. The Den Hartog stability condition can only be used to assess the stable behavior of a body with a specific shape at a certain angle of attack α and, from this perspective, the parameters that define the elastically-supporting device (e.g., spring) that may be attached to the body are not taken into consideration. Clearly, the Den Hartog stability condition has limitations, and the analysis conducted herein will clarify some of these restrictions in the application of this stability criterion (based on a quasi-steady theory for addressing aerodynamic problems).

5.2 Numerical set-up and validation

5.2.1 Computational domain and mesh sensitivity

Structural amplitude of galloping response could achieve a value much larger than that of lock-in behavior. As a consequence, the domain size used here is sufficiently large to allow for possible large-amplitude vibrations of the body. Figure 5.2 shows the computational domain and the boundary conditions used for the FOM/CFD simulations conducted in present galloping study. A number of two-dimensional (2-D) numerical simulations of the flow-induced vibration of a bluff body mounted on a linear spring is undertaken at low Reynolds number Re . The computational domain is $48D$ in the streamwise (x -) and $50D$ in the cross-stream or transverse (y -) directions, where D as a characteristic length of the bluff body. To facilitate comparisons of the results of the simulations for the different bluff body geometries, we use the same transverse length TL for every body geometry studied herein. This transverse length is taken to define the characteristic length D for each of the body geometries.

The center of the bluff body is located along the centerline of the computational domain at $y = 0$ and at a distance of $12D$ downstream from the inlet boundary (left edge of the domain). The boundary conditions applied here are consistent to those within section 3.2.1. For all the simulations in this chapter, the characteristic length D of the bluff body, the incident wind speed

U_0 at the inlet boundary, and fluid density ρ are 0.1 m, 0.1 m s⁻¹, and 1.2 kg m⁻³, respectively. The Reynolds number Re is changed by adjusting the kinematic viscosity ν of the fluid.

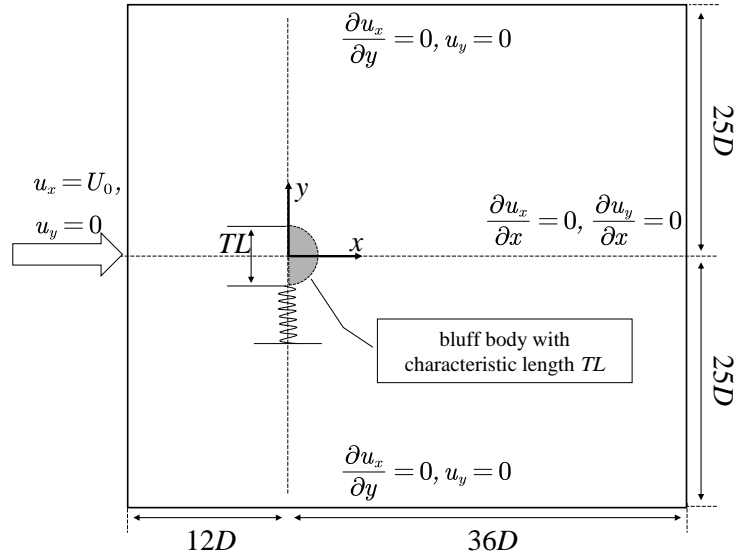


Figure 5.2: The computational domain used for the simulations of the flow past a bluff body elastically-mounted on a linear spring. The prescribed boundary conditions on the flow velocity used in the simulations are shown.

To investigate the galloping instability for which the amplitude of vibration of the body is expected to be significantly larger than that for vortex-induced vibration, an overset mesh (implemented in OpenFOAM/v2006 [202]) is used with a computational domain size that is large enough so that the entire motion of the elastically-mounted body in the transverse (y -) direction is well contained within the domain. To begin, the simulation of the flow past a *stationary* square cylinder is conducted and used to assess the sensitivity of the results to the mesh used. For this assessment, we used four different mesh sizes with the number of cells in the different meshes ranging from 58,032 to 82,810. The flow past a stationary square cylinder at the Reynolds number $Re = 100$ was simulated using these four meshes. For each of these simulations, we extracted the root-mean-square (rms) lift C_L^{rms} and drag C_D^{rms} coefficients. The values for these two dynamical force coefficients are compared in table 6.1 for each of the four meshes. In addition, these results are compared with those reported by Zhao et al. [241] and Li et al. [16] for the same case.

The percentage differences in the values of C_L^{rms} and C_D^{rms} obtained in going from mesh 1 (coarse) to mesh 2 (intermediate) are 1.4% and 3.9%, respectively. This discrepancy is quite large. However, in going from mesh 3 (fine) to mesh 4 (very fine), the percentage differences in the values of C_L^{rms} and C_D^{rms} are reduced considerably, being only 0.16% and 1.8%, respectively. Based on these considerations, mesh 3 is used for all the simulations conducted herein. Mesh 3 provides the best compromise between numerical accuracy and computational cost. Moreover, the values of C_L^{rms} and C_D^{rms} obtained for mesh 3 are in good agreement with those obtained by Zhao et al. [241] and Li et al. [16]. In particular, our current values for the root-mean-square lift and drag coefficients lie between those obtained by these previous investigators. Figure 5.3 displays mesh 3—the hybrid overset mesh used in our simulations of the flow past a square cylinder elastically-supported on a linear spring. More specifically, this figure shows the overall mesh used in the tessellation of the computational domain and two increasingly expanded views of the mesh in the vicinity of the square cylinder.

Mesh	Cell number	C_L^{rms}	C_D^{rms}
1	58032	0.1786	0.0049
2	65995	0.1812	0.0051
3	78752	0.1895	0.0054
4	82810	0.1898	0.0055
Zhao et al. [241]	—	0.1908	0.0057
Li et al. [16]	—	0.1817	0.0052

Table 5.1: Aerodynamic coefficients (root-mean-square lift and drag coefficients) of flow past a *stationary* square cylinder at $Re = 100$ for four different meshes.

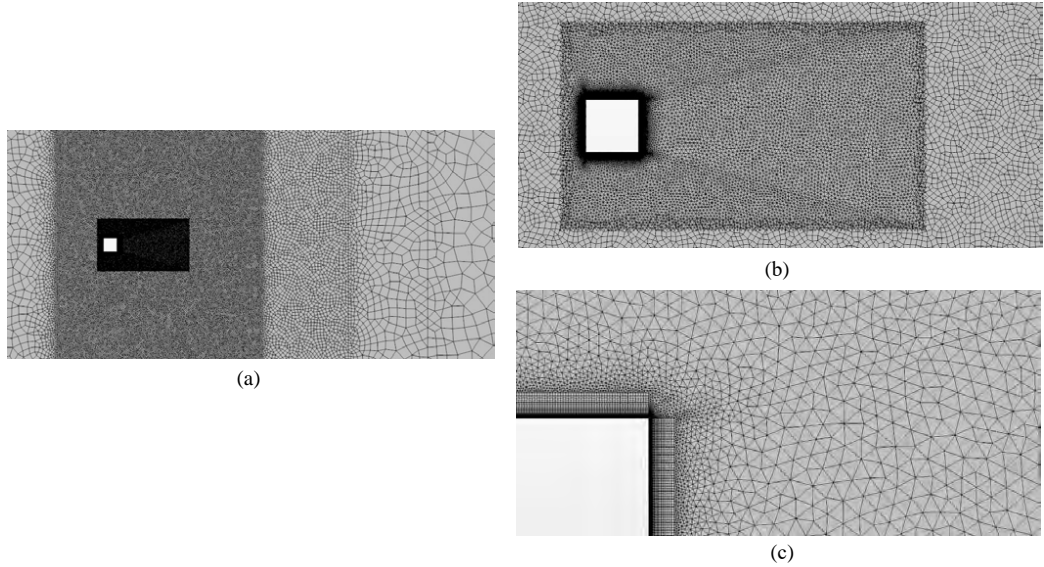


Figure 5.3: The fine mesh (mesh 3) used for the simulation of the flow past a square cylinder: (a) tessellation of the computational domain showing the overset and a partial background mesh surrounding the square cylinder; (b) close-up view of the overset mesh around the square cylinder; and, (c) expanded view of mesh in the immediate vicinity of the walls of the square cylinder.

5.2.2 Validation of full-order model

The previous section 3.2.2 already validates the predictive accuracy of the FOM/CFD and its implementation with respect to the lock-in behavior. In this section, we will focus on the FOM/CFD validation for galloping response using the simulation of the flow past a square cylinder elastically mounted on a linear spring. The square cylinder is free to move in the cross-stream (y -) direction. The physical parameters for this simulation are as follows: the structural damping coefficient $\zeta = 0$, the mass ratio $m^* = 10$, and the Reynolds number $Re = 150$. The reduced velocity U_r is varied by changing the structural natural frequency f_n .

Figure 5.4 shows the variation of normalized maximum transverse displacement y_{max}/D as a function of the reduced velocity U_r for the FIV system consisting of the flow past an elastically-supported square cylinder. The normalized maximum transverse displacement y_{max}/D exhibits

a sudden increase to a value of 0.14 at $U_r \approx 5.75$, and then decreases slowly thereafter with increasing values of U_r . When U_r reaches a value of between 17 and 18, y_{\max}/D exhibits a rapid increase in value with increasing U_r . The amplification of y_{\max}/D associated with this range of values of U_r is unbounded (viz., the motion here is not self-limiting) and corresponds to a galloping instability. The variation of y_{\max}/D as a function of U_r predicted here for the elastically-supported square cylinder is in excellent conformance with the results reported by Li et al. [16]. Based on these considerations, it is concluded our current FOM/CFD simulations provide good accuracy for providing the high-fidelity FOM/CFD data sets needed for the analysis of the triggering of galloping in structures and for securing the equilibrium base flow required for the application of ROM/ERA to fluid-structure interaction problems studied herein.

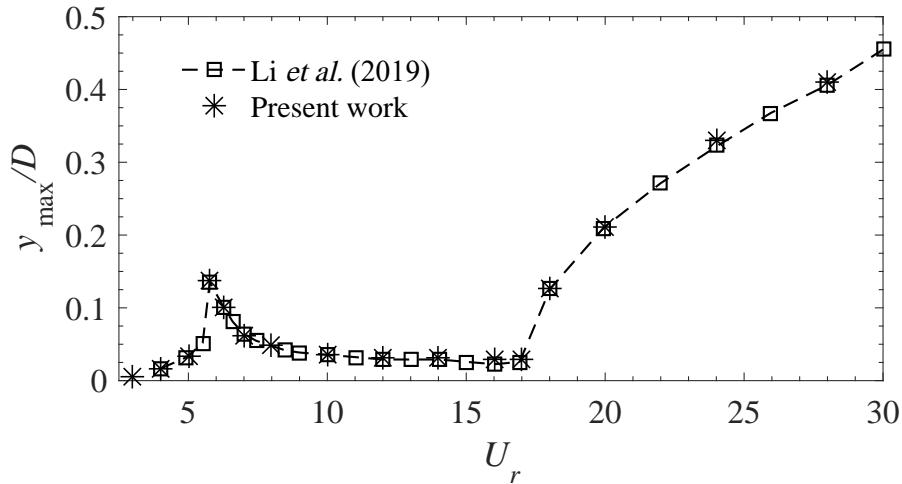


Figure 5.4: The normalized maximum transverse displacement y_{\max}/D as a function of the reduced velocity U_r of a FIV system consisting of the flow past an elastically-mounted square cylinder at $(Re, m^*) = (150, 10)$. The results were obtained using FOM/CFD and compared with results obtained by Li et al. [16].

5.3 Validation of reduced-order model

As an example of an equilibrium base flow for LSA investigation of galloping response, figure 5.5 shows the isopleths of the vorticity field for a flow past a stationary square cylinder at $Re = 150$.

Table 5.2 compares the length of the recirculating region (steady wake) for a base flow past a stationary square cylinder at three different values of the Reynolds number: namely, at $Re = 100$, 125 and 150. The length of the recirculating region is defined as the distance in the streamwise direction along the centerline of the cylinder between the base point (which is taken as the geometric center of square cylinder) and the stagnation point in the wake. The length of the recirculating region in the wake of a stationary square cylinder at $Re = 100$, 125 and 150 obtained in our current simulations is in very good agreement with the corresponding results reported by Mao and Blackburn [26] in their investigations of the nature of the primary instability modes in the steady wake of a square cylinder. More specifically, the discrepancy in our current predictions of the length of the recirculating bubble in the steady wake of the square cylinder is 2.4%, 1.8%

Re	Present	Mao and Blackburn [26]
100	8.4	8.6
125	11.0	11.2
150	14.1	14.4

Table 5.2: The length of the recirculation region (steady wake) normalized by the cylinder diameter (side length) D for a base flow past a stationary square cylinder. The results of the present simulations are compared with those reported by Mao and Blackburn [26].

and 2.1% at $Re = 100, 125$ and 150 , respectively, when compared with those obtained by Mao and Blackburn [26].

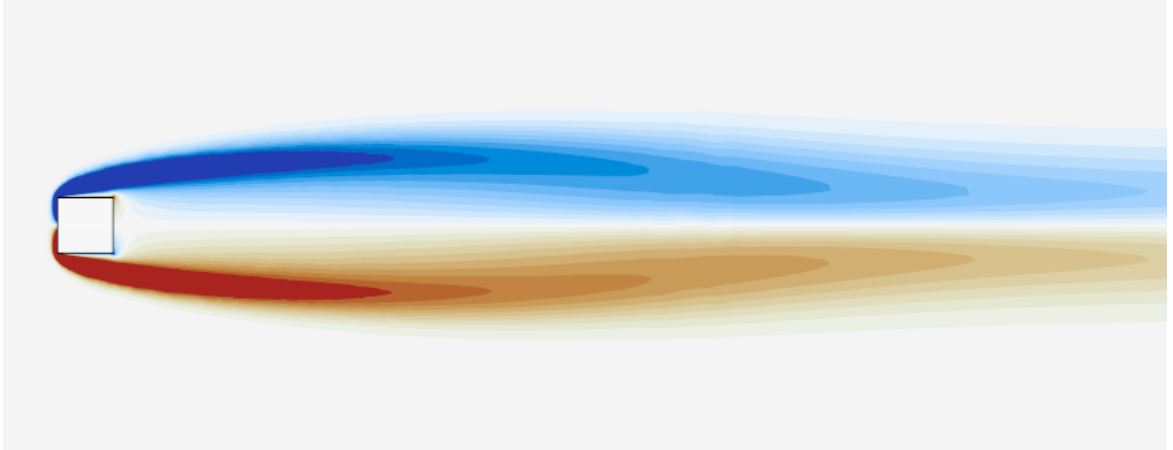


Figure 5.5: Contours of the vorticity field obtained for an equilibrium base flow past a stationary square cylinder at $Re = 150$. The direction of the flow is from left to right.

Since the work reported here focuses on the factors that trigger the galloping instability, we validate ERA/ROM for the flow past a forward equilateral triangular cylinder (with one side perpendicular to the incident flow) mounted on a linear spring at $(Re, m^*) = (60, 10)$. The root loci obtained for this case are shown in figure 5.6. The root loci clearly show the coupling between the structure and wake modes. Here, it is seen that either WSMI or WSMII alternately assumes the role of the structure mode depending on the value of the reduced natural frequency F_s . The value of $\text{Re}(\lambda)$ over the interval where $\text{Im}(\lambda) < 0.9$ is strictly positive which is in agreement with the result reported by Yao and Jaiman [15]. This implies that the structure mode is unstable as F_s decreases (or, equivalently, as the reduced velocity U_r increases). Moreover, these modal characteristics are indicative of the fact that a FIV system involving a forward equilateral triangular cylinder will transition into galloping (distinguished by their large-amplitude and low-frequency oscillations) after lock-out, in contradistinction to the dynamical response of a circular cylinder at large values of U_r . It is noted that FOM/CFD simulations described later for the flow past a forward isosceles-triangular cylinder provide further validation of this result (viz., this case is seen to exhibit galloping also). The maximum amplitude of oscillations of the forward equilateral triangular cylinder continues to increase with increasing U_r after the system transitions out of lock-in (which is a characteristic signature of a galloping instability).

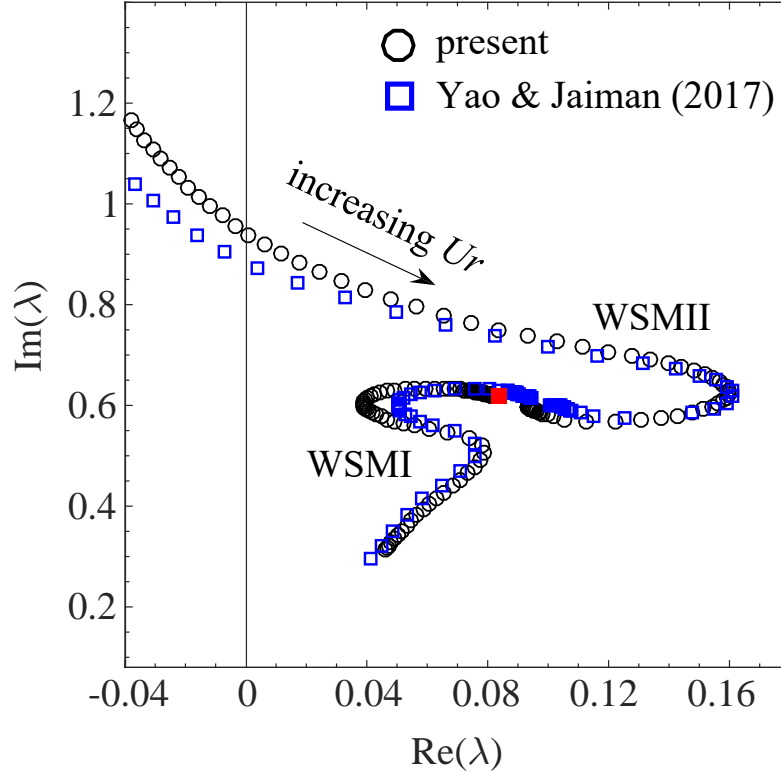


Figure 5.6: The root loci (parameterized by the reduced natural frequency $F_s = U_r^{-1}$) for the flow past a forward equilateral triangular cylinder elastically-mounted on a linear spring at $(Re, m^*) = (60, 10)$. This result is compared with that obtained by Yao and Jaiman [15]. The red solid square corresponds to the stationary body.

5.4 Effect of windward orientation for various body geometries

This section examines the relationship between the galloping instability and the windward orientation of the cross-section of the body (D -section, triangular-section, or square-section) using simulations obtained from FOM/CFD. We use this information to investigate the modal mechanisms that are responsible for the observed features of the dynamics using an LSA based on ROM/ERA. Finally, we study the stability of different body geometries at the system equilibrium point using a quasi-steady stability analysis. This approach will help to unravel the specific conditions and mechanisms that trigger the galloping instability.

5.4.1 D -section body (half-cylinder)

To begin, we study the flow past a D -section (or, semi-circular) body at $(Re, m^*) = (60, 10)$ with reference to the galloping instability. The dynamic response of an elastically-mounted D -section body in a uniform flow has been investigated by various researchers [242, 129, 128]. These efforts provided insights on the importance of an after-body for the generation vortex-induced vibrations [46]. Here, we investigate the flow past an elastically-mounted D -section body in order to study galloping. More specifically, we use the results of our simulations of

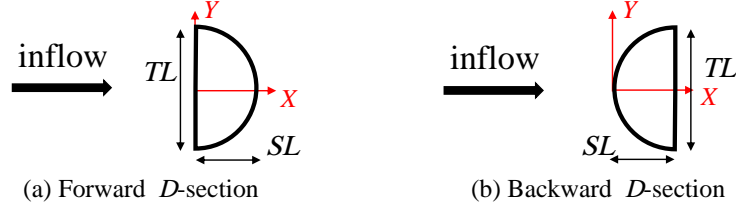


Figure 5.7: Elastically-mounted D -section body (half-cylinder) in the (a) forward and (b) backward orientations with respect to the incident flow.

the flow past a D -section body mounted on a linear spring to explain the underlying modal mechanisms of the galloping instability for this case using linear stability analysis and examine the identification of the hidden structure mode for the coupled modal condition. We will use the descriptor forward or backward D -section body (half-cylinder) to describe the configurations when the flat face of the half-cylinder is facing into (windward of) or away from (leeward of) the incident wind direction, respectively, as shown in figure 5.7.

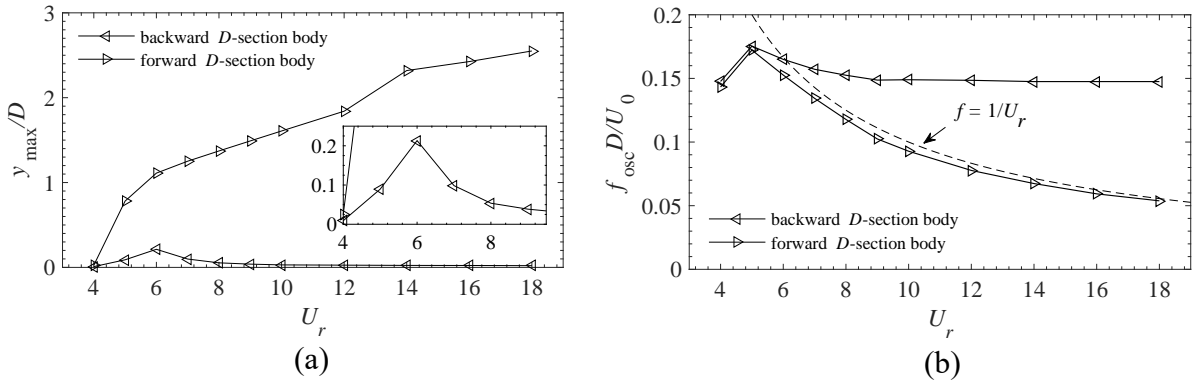


Figure 5.8: (a) Normalized maximum amplitude y_{\max}/D and (b) normalized oscillation frequency $f_{\text{osc}}D/U_0$ in the transverse direction as a function of U_r for a flow past an elastically-mounted D -section body with forward and backward orientations at $(Re, m^*) = (60, 10)$. The inset plot in (a) shows an expanded view of the variation of y_{\max}/D around $U_r \approx 6$ for the backward D -section body.

Figure 5.8(a) shows the variation of the maximum amplitude y_{\max}/D as a function of U_r for the FIV system consisting of a flow past an elastically-mounted D -section body at $(Re, m^*) = (60, 10)$ in the forward and backward orientations. These predictions were obtained using FOM/CFD — the solution (structural dynamic response and flow field) obtained at given value of U_r was used as the initial state of the system at the next larger value of U_r in the calculations. For these simulations, the variation in the reduced velocity U_r is achieved by adjusting the structural spring stiffness while keeping the Reynolds number Re at the prescribed fixed (constant) value. As a consequence, the initial state of the system encodes the potential energy of the spring and the kinetic energy of the body. A perusal of figure 5.8(a) shows that the maximum amplitude of the vibrations in the transverse direction for the forward D -section body is significantly larger than that for the backward D -section body. Moreover, y_{\max}/D for the forward orientation increases monotonically with increasing U_r in stark contrast with the backward orientation where the maximum amplitude is seen to increase to a peak value at a reduced velocity $U_r \approx 6$ and then decrease monotonically from this peak value with increasing U_r .

Figure 5.8(b) displays the normalized oscillation frequency $f_{\text{osc}}D/U_0$ of the transverse vibrations as a function of U_r for an elastically-mounted D -section body at $(Re, m^*) = (60, 10)$ in the forward and backward orientations. For the forward D -section body, the dependence of the oscillation frequency f_{osc} on U_r is consistent (approximately or better) with the relationship $f = U_r^{-1}$ (viz., the oscillation frequency is inversely proportional to the reduced velocity) for $U_r \gtrsim 5$. In stark contrast, the oscillation frequency for the backward D -section body does not conform to the relationship $f = U_r^{-1}$, although at $U_r \approx 6$ the normalized oscillation frequency for the backward orientation is approximately equal to the inverse of the reduced velocity U_r . Note that the backward D -section also exhibits the maximum value of y_{max}/D at $U_r \approx 6$ (see figure 5.8(a)). The FIV system for the backward orientation exhibits the behavior of a forced vibration for $U_r \gtrsim 6$. Moreover, the elastically-mounted forward and backward D -section bodies will transition to galloping and the desynchronization range, respectively, after leaving the lock-in range. Finally, for the lock-in or galloping regimes, the structural oscillation frequency is dominated (determined principally) by the corresponding structural natural frequency.

The results presented in figure 5.8 are consistent with those obtained from an experimental investigation of the flow past an elastically-mounted D -section body (for both the forward and backward orientations) conducted by Zhao et al. [46] (for Reynolds numbers in the range $1080 \leq Re \leq 9000$). In these experiments, the forward D -section body was observed to exhibit a galloping instability. Moreover, for the backward D -section body, the maximum amplitude of the transverse vibrations was observed to occur at a value of the reduced velocity of $U_r \approx 6$. These observations are in good agreement with our simulations for the D -section body (albeit for laminar flow, rather than for the turbulent flow in the experiments of Zhao et al. [46]). Finally, our present calculations also support the conclusion reached by Zhao et al. [46] that an after-body is not strictly required for the appearance of a significant amplitude response in a FIV system.

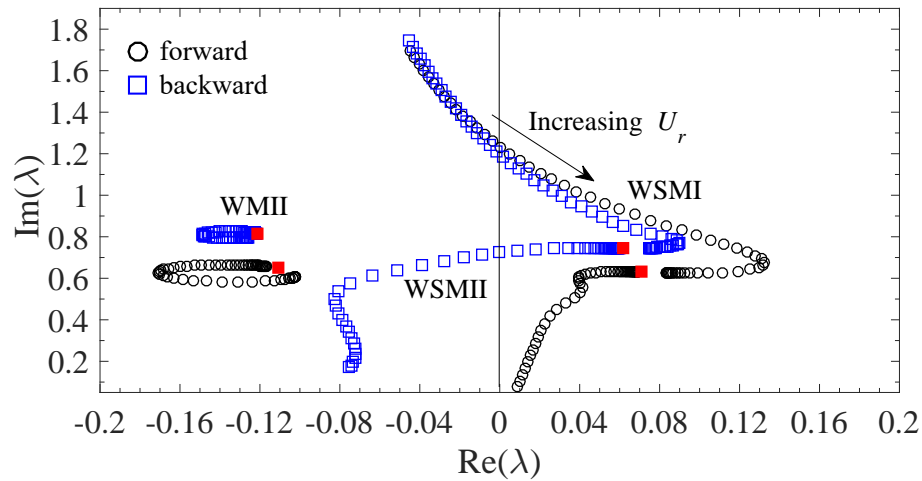


Figure 5.9: Root loci obtained from a ROM/ERA model of the FIV system (parameterized by the reduced natural frequency $F_s = U_r^{-1}$) for the flow past an elastically-mounted forward and backward D -section body at $(Re, m^*) = (60, 10)$. The red solid squares correspond to the case of the flow past a stationary half-cylinder in the forward and backward orientations.

Figure 5.9 shows the root loci obtained from ROM/ERA for a flow past a forward and backward elastically-mounted D -section body at $(Re, m^*) = (60, 10)$. A perusal of this figure suggests that the FIV response of both the forward and backward half-cylinders is in a coupled state involving the structure and first wake modes. However, with increasing U_r , $Re(\lambda)$ associated with

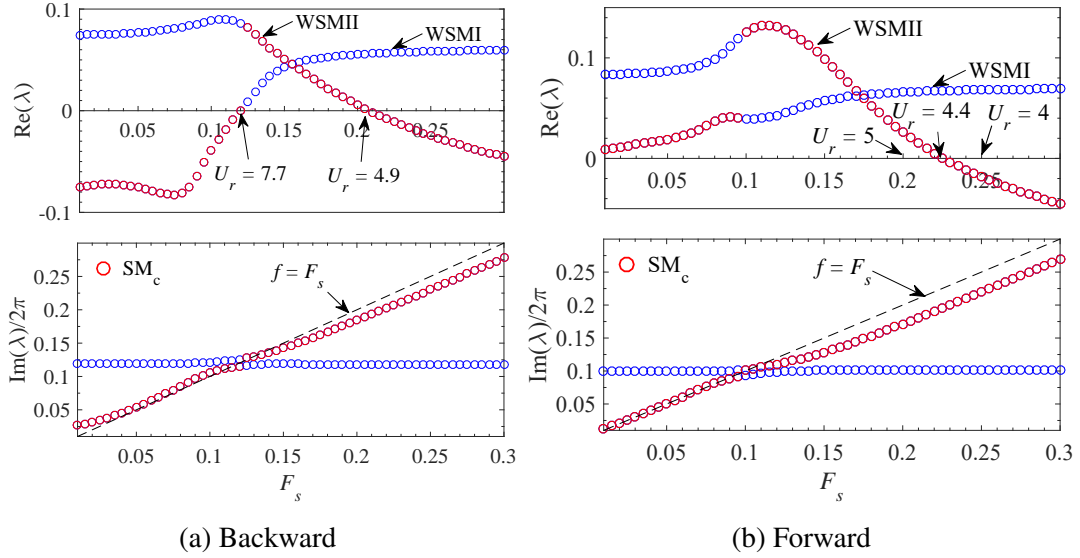


Figure 5.10: Growth/decay rate $\text{Re}(\lambda)$ and eigenfrequency $\text{Im}(\lambda)/2\pi$ as a function of $F_s = U_r^{-1}$ for the FIV system consisting of the flow past an elastically-mounted D -section body (half-cylinder) in the (a) backward and (b) forward orientations at $(Re, m^*) = (60, 10)$. The structure mode SM_c , which is hidden in the coupled WSMI and WSMII modes, is marked with open red circles. The dashed line corresponds to the function $f = F_s$.

the root loci for the forward half-cylinder is positive while that for the backward half-cylinder becomes negative (viz., crosses over to the left half of the complex plane). This stark difference in the modal variation indicates that there are significant differences in the dynamics between the forward and backward orientations of an elastically-mounted D -section body in an uniform flow. In other words, the structure mode associated with the forward D -section body is associated with an instability for increasing values of U_r , which is a characteristic signature for galloping phenomenon. This signature is similar to the modal behavior of the forward equilateral triangular body presented previously in figure 5.6.

The variation of $\text{Re}(\lambda)$ and $\text{Im}(\lambda)$ as a function of the reduced velocity U_r is critical for providing a clearer understanding of the modal dynamics associated with the galloping instability. Towards this objective, the variation of the eigenvalues associated with the two leading unstable modes as a function of the reduced natural frequency F_s (or, equivalently, the inverse of the reduced velocity) is shown in figure 5.10. More specifically, figures 5.10(a) and (b) show the growth/decay rates and eigenfrequencies of WSMI and WSMII for the backward and forward half-cylinders, respectively, as a function of F_s .

When a coupling condition occurs between the wake and structure modes, a mode-switching action must occur because the eigenfrequency (or, imaginary part of the eigenvalue) associated with the structure mode is a function of the reduced natural frequency F_s . The coupled mode that is associated with an eigenfrequency that is closest in value to the reduced natural frequency F_s is identified as SM_c . The subscript ‘c’ in this identification of the structure mode is used to remind the reader that this mode is associated with the coupled condition. In order to determine which of the coupled modes in figure 5.10 represents the SM, the modes whose associated eigenfrequencies are closest to F_s are depicted using the red markers. Nevertheless, we note that the application of this criterion cannot be used to determine the location of the mode-switching with absolute accuracy within the overlapping region where the frequencies associated with the

two modes approach each other in value, as a result of their strong modal interaction.

For the D -section in the backward orientation, it is seen from figure 5.10(a) that SM_c is unstable in the interval $F_s \in (0.130, 0.204)$ (or, equivalently, for $U_r \in (4.9, 7.7)$). This interval, which is associated with an unstable SM_c , is consistent with the results shown in figure 5.8(a) (see inset here)—for the D -section body in the backward orientation, $y_{\max}/D > 0$ in $U_r \in (4.9, 7.7)$ (approximately or better). This implies that for the D -section body in this orientation, the structure mode is unstable in a certain interval (viz., lock-in range) due to the proximity of the structural natural frequency to the vortex-shedding frequency. This is evident on an examination of figure 5.10(a)—the eigenfrequencies $\text{Im}(\lambda)$ associated with the coupled modes are close to one another. This observation supports the assertion made by Zhao et al. [46] that an after-body is not a necessary condition for the occurrence of significant amplitude vibrations in VIV.

For the D -section body in the forward orientation, it is seen from figure 5.10(b) that $\text{Re}(\lambda)$ associated with SM_c (marked with the red open circles) is positive for $F_s < 0.227$ (or, equivalently, for $U_r > 4.4$). This observation, in turn, is consistent the result in figure 5.8(a) that $y_{\max}/D > 0$ for $U_r > 4.4$ for the forward D -section body. According to the modal analysis conducted by Li et al. [16] for a square cylinder, the instability of the structure mode at large values of U_r (viz., values greater than about 10) leads to a low-frequency galloping vibration of the structure, which is consistent with our current results. Furthermore, Li et al. [16] partitioned the induced response into three distinct regions: namely, VIV, pre-galloping, and galloping obtained from an examination of their FOM/CFD simulations for the square cylinder (cf. with figure 17 in Li et al. [16]). Pre-galloping is defined as the range of values of U_r where the structure mode is unstable as predicted using LSA, but galloping has not yet occurred (the latter of which can be determined from an analysis of FOM/CFD simulations).

Li et al. [16] concluded that LSA significantly underestimates the value of U_r associated with the onset of galloping. Indeed, figure 15 in Li et al. [16] concluded that a square cylinder at $(Re, m^*) = (150, 10)$ results in a coupling between the structure and wake modes. This implies that one of the two coupled modes must correspond to the structure mode, in turn, so that there must exist one mode-switching point (also demonstrated previously in work reported by past works [12, 15]). However, in figure 17 of Li et al. [16] for the square cylinder at the same $(Re, m^*) = (150, 10)$, the authors asserted that the full coupled-mode (labelled as WMSI in our work) can be interpreted as a pure structure mode for the purposes of analysis. This interpretation of the underlying modal dynamics appears to be incorrect and seems to have resulted in an underestimation of the value of U_r associated with the onset of galloping (and, ultimately, to the conclusion reached by Li et al. [16] that the value of U_r linked to the onset of galloping as predicted using LSA is much lower than that derived using FOM/CFD).

In contradistinction to these conclusions, we suggest that an unstable structure mode leads to galloping and that LSA does not significantly underestimate the value of U_r associated with the onset of galloping. Furthermore, we assert that pre-galloping does not necessarily have to occur and, indeed, this assertion is consistent with our current results for the forward D -section body. Finally, galloping can be divided into two regimes: namely, hard-galloping and soft-galloping [127]. Soft-galloping occurs without the need to impose any initial excitation (either an initial nonzero displacement and/or an initial nonzero velocity) in the FIV system. In contrast, hard-galloping requires an initial excitation of the FIV system and the magnitude of this excitation must also exceed a certain (minimum) threshold. An analysis of the effects of the initial excitation on the nature of the galloping response and the relationship between soft- and hard-galloping and the cross-sectional shape of the body will be addressed later.

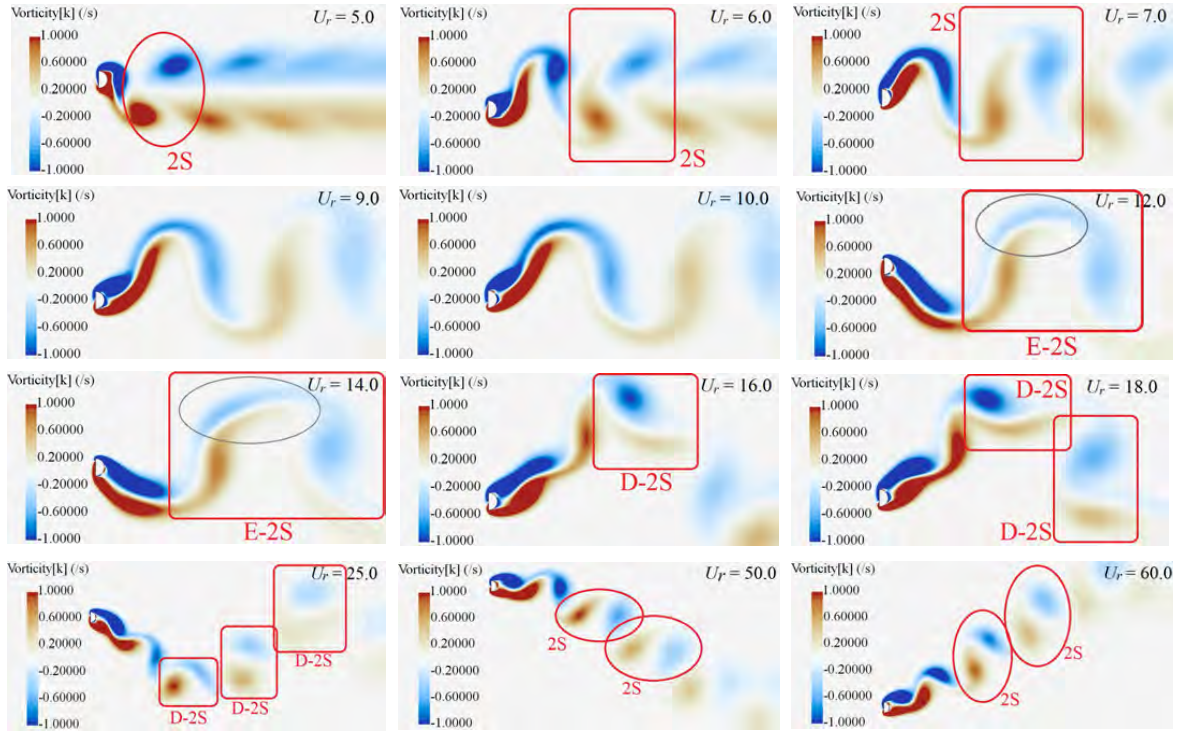


Figure 5.11: Contours of the vorticity field for a flow past a D -section body in the forward orientation at $(Re, m^*) = (60, 10)$ for 12 different values of the reduced velocity U_r .

Figure 5.11 exhibits the contours of the vorticity field for a flow past the forward D -section body at $(Re, m^*) = (60, 10)$ for various values of the reduced velocity U_r that span regimes from lock-in to galloping. The values of $U_r = 5, 6$ and 7 correspond to the lock-in regime for the FIV system and the wake mode is associated with a typical 2S pattern of vortex shedding in which two single vortices are shed during each cycle of oscillation. For values of $U_r = 9$ and 10 , the vortex-shedding mode is similar to a 2S pattern, but the spacing between the vortices is increased. As the values of U_r increase to 12 and 14 , the vortex-shedding modes are stretched or elongated and there is a region in the wake (delineated by the grey ellipse) where the two vortex structures appear to be parallel to one another (approximately or better). We refer to this vortex-shedding mode as an elongated-2S (E-2S) pattern. When U_r reaches a value of 16 , the associated reduced natural structural frequency $F_s = 1/16 = 0.0625$ is smaller than the normalized vortex-shedding frequency $F_{vs} = 0.147$ and, as a result, the behavior of the vortex shedding is no longer locked-in to the natural structural frequency. In this case, the moving body can be regarded simply as a moving source of vortex shedding and, owing to the relatively slow speed of motion of the body, the vortex-shedding pattern is similar to the vortex shedding pattern at the lower values of U_r , except for the fact that the contours of the vorticity field are slightly deformed (with one normal vortex and another that is slightly stretched in the streamwise direction). We refer to this vortex-shedding mode as deformed-2S (D-2S) and this vortex pattern occurs for values of $U_r = 16, 18$ and 25 as seen in figure 5.11. At still larger values of U_r (e.g., $U_r = 50$ and 60), the oscillation amplitude of the body is further increased and accompanied by a further decrease in the oscillation frequency. Owing to the very slow transverse motion of the body, the vortex-shedding pattern is a 2S mode seen at the very small values of U_r , but the pattern is spatially displaced as a whole in the transverse direction as the body moves (as if it were frozen in the flow). For reference, it is noted that $y_{\max}/D = 3.15, 5.64$ and 6.63 for $U_r = 25, 50$ and 60 ,

respectively.

Figure 5.12 summarizes the stability of a forward and backward D -section body at $Re = 60$. The results were obtained using a quasi-steady analysis. We note that the values of lift coefficient C_L and the drag coefficient C_D for rotation angles $\alpha = -1^\circ, 0^\circ$ and 1° are obtained from the base flow in order to remove any fluctuations in these force coefficients arising from the vortex-shedding. Overall, it is seen that C_D exhibits a very small change for small variations in the rotation angle α , whereas C_L exhibits a much larger change for the same variations in α . In addition, C_L essentially vanishes at $\alpha = 0^\circ$ owing to the symmetry of the body relative to the flow direction for this rotation angle. As the body is rotated clockwise from -1° to 1° , the lift coefficient C_L for the forward D -section body changes from a positive value of 0.0285 to a negative value of -0.0277 , whereas that for the backward D -section body changes from a negative value of -0.00457 to a positive value of 0.00466. The Den Hartog function $H(\alpha) \equiv dC_L(\alpha)/d\alpha + C_D(\alpha)$ at $\alpha = 0^\circ$ is negative- and positive-valued for the forward and backward D -section body, respectively. The gradient of $C_L(\alpha)$ with respect to α for the forward D -section body is negative and if the absolute value of this quantity exceeds the associated drag coefficient $C_D(\alpha)$, then the FIV system will be negatively damped and, as a result, the structure will be prone to instability. In consequence, the elastically-mounted forward D -section body is expected to exhibit a galloping instability for a flow at $Re = 60$. Finally, it should be noted that an analysis of experimental data for the forward and backward D -section body (half-cylinder) at $Re = 4880$ based on a quasi-steady approach also suggests that the forward half-cylinder manifests a galloping instability [46].

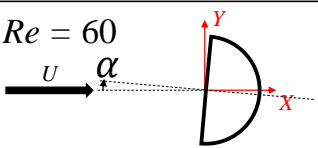
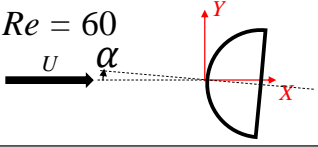
<i>Diagram</i> \ α	-1°	0°	1°
$Re = 60$ 	$C_L = 0.0285$ $C_D = 1.5118$	$C_L = 4.15 \times 10^{-4}$ $C_D = 1.5116$ $H(\alpha) = -0.09821$	$C_L = -0.0277$ $C_D = 1.5118$
$Re = 60$ 	$C_L = -0.00457$ $C_D = 1.34739$	$C_L = -5.53 \times 10^{-5}$ $C_D = 1.34712$ $H(\alpha) = 1.61180$	$C_L = 0.00466$ $C_D = 1.34736$

Figure 5.12: The lift coefficient C_L and drag coefficient C_D for the base flow of a forward and backward D -section body (half-cylinder) at $Re = 60$ with rotation angle α of $-1^\circ, 0^\circ$ and 1° . The value of Den Hartog function $H(\alpha)$ is given for a rotation angle $\alpha = 0^\circ$.

5.4.2 Isosceles-triangular body

As a common shape for engineering cables and ice-coated wires, an elastically-mounted triangular body is an important geometry for fluid-solid interaction investigations. In view of this, we study a FIV system consisting of the flow past an elastically-mounted isosceles-triangular body at $(Re, m^*) = (120, 10)$ in both the forward and backward orientations when the flat face of the body is facing into (windward of) or away from (leeward of) the incident wind direction, respectively, as shown in figure 5.13. It is mentioned previously that the transverse length TL is the same for all the body geometries investigated herein, so TL for the isosceles-triangular

body is identical to the characteristic length D for the half-cylinder (viz., $TL = D$). Furthermore, $SL/TL = 1/2$ for the isosceles-triangular body (or, diagonally-cut semi-square cylinder) studied herein.

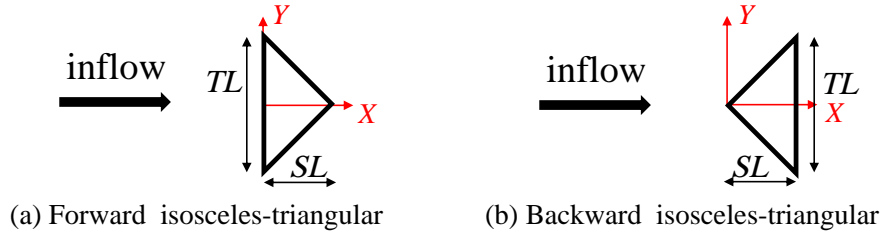


Figure 5.13: Elastically-mounted isosceles-triangular body in the forward and backward orientations relative to the incident flow. The triangular body has $SL/TL = 1/2$.

Figure 5.14 shows the root loci for the FIV system consisting of the flow past an isosceles-triangular body in the forward (black open circle markers) and backward (black open square markers) orientations at $(Re, m^*) = (120, 10)$. The root loci were obtained using ROM/ERA. The root loci for the two orientations exhibit three leading modes: a single wake mode (WM) and two coupled modes (WSMI and WSMII). It should be noted the red solid square markers in the figure correspond to the modes for the flow past the stationary isosceles-triangular body in either the forward or backward orientations. For the body in the forward orientation, the associated red markers lie on the right-hand-side of the complex frequency plane, implying that the flow past the stationary body results in an unstable vortex street at $Re = 120$. For the case of the backward orientation, there is a wake mode I (WMI) and wake-structure coupled modes I and II (WSMI and WSMII). The two modes WSMI and WSMII are confined to the left-half-side of the complex frequency plane for the entire range of values of F_s (or, of U_r), implying that the isosceles-triangular body in the backward orientation does not result in flutter lock-in and galloping at $(Re, m^*) = (120, 10)$ because the growth rate of the vibration represented by $Re(\lambda)$ is strictly negative. Nevertheless, the resonance lock-in will still materialize for that range of values of U_r where the structural mode frequency is close to the frequencies associated with the wake modes. In comparison with the root loci for the backward D -section body (cf. figure 5.9), it is expected that a curved after-body which gives rise to points of flow separation will result in a flutter lock-in. For the case of the forward isosceles-triangular body, the relevant modes governing the dynamics are WSMI, WSMII, and WMII. In this case, the modal characteristics of the body is similar to that of the forward D -section body in that the trajectory of the root loci does not cross over to the left-half-side of the complex frequency plane with increasing values of U_r . This suggests that the forward isosceles-triangular body considered here will exhibit a galloping instability at large values of U_r .

To obtain a clearer view of nature of the modal interaction, we plot the growth/decay rate $Re(\lambda)$ and eigenfrequency $Im(\lambda)/2\pi$ of the modes for the backward and forward isosceles-triangular body as a function of the reduced natural frequency F_s in figures 5.15(a) and (b), respectively. In this figure, the single wake modes WMI and WMII are delineated using the black open circle markers. Among the coupled modes, the mode associated with an eigenfrequency that is closest in value to F_s (shown as the dashed line) is taken to be the structure mode SM_c which is delineated in figure 5.15 with the red markers. It is noted that for the forward isosceles-triangular body (see figure 5.15(b)), the growth rate of the structure mode SM_c is positive for $F_s < 0.05$ implying that body will undergo a galloping instability. However, for the backward isosceles-

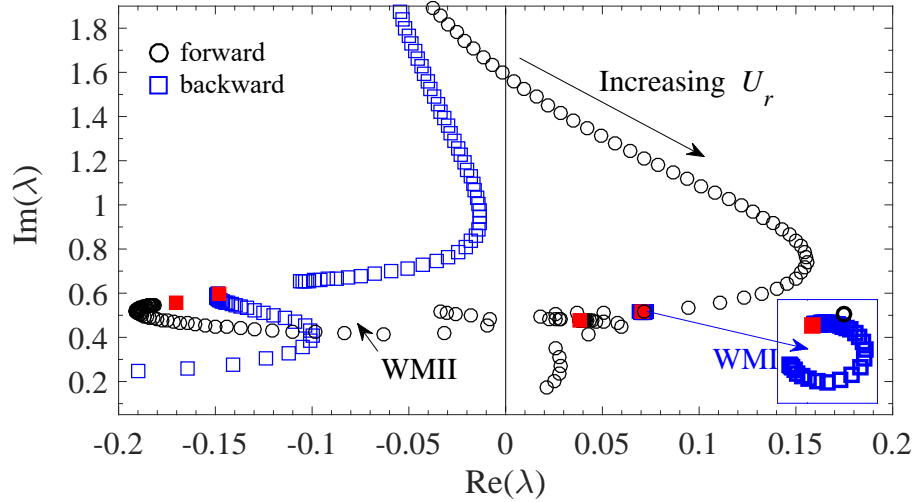


Figure 5.14: Root loci (obtained from ROM/ERA) for a FIV system consisting of the flow past an elastically-mounted isosceles-triangular body at $(Re, m^*) = (120, 10)$ in the forward and backward orientations. The inset plot displays the part of the root loci for the backward isosceles-triangular body corresponding to the wake mode 1 (WM1) loop (which collapses to a near-point structure) in the right half of the complex frequency plane. The red solid squares show the results for the flow past the stationary isosceles-triangular body in the forward and backward orientations.

triangular body, over the range of values of F_s associated with resonance lock-in (identified by red rectangular box in figure 5.15(a)), the frequencies associated with the structure and wake modes move away from one another, implying that the coupling between these modes is weak. This will result in an abrupt termination of the lock-in range as the reduced velocity U_r increases (or, equivalently, as the reduced natural frequency F_s decreases).

To supplement the preceding analysis based on ROM/ERA, we have conducted a number of FOM/CFD simulations of the flow past an elastically-mounted isosceles-triangular body. Figure 5.16 exhibits the time series of the normalized transverse amplitude y/D (recall $TL = D$) and the lift coefficient C_L for flow past an elastically-mounted isosceles-triangular body in the backward orientation at $(Re, m^*) = (120, 10)$. In this FOM/CFD simulation, the value of the reduced velocity U_r was changed (sharply) in time from 19 to 6 to 10 and, finally, to 14 in sequence. The fully-developed state of the FIV system at a given (constant) value of U_r was used as the initial condition for the state of the FIV system at the succeeding value of U_r . A perusal of figure 5.16 shows that a galloping instability does not occur for the backward isosceles-triangular body at $U_r = 19$. However, when U_r is decreased to a value of 6, the triangular body manifests large-amplitude oscillations with $y_{\max}/D \approx 0.30$, implying that the FIV system has transitioned into the lock-in range. As mentioned above, this lock-in range corresponds to the regime of a resonance lock-in. Finally, increasing U_r to either 10 or 14, it is seen that the vibration amplitude is reduced significantly from that observed at $U_r = 6$.

Figure 5.17 exhibits the time series of the normalized transverse amplitude y/D and the lift coefficient C_L obtained from a FOM/CFD simulation for the flow past an elastically-mounted forward isosceles-triangular body at $(Re, m^*) = (120, 10)$. The simulation was conducted with the reduced velocity U_r changing abruptly in time in accordance to the following sequence: 25 to 7 to 14 to 25 and, finally, to 63. For the first value of $U_r = 25$ (regime 1), the FIV system

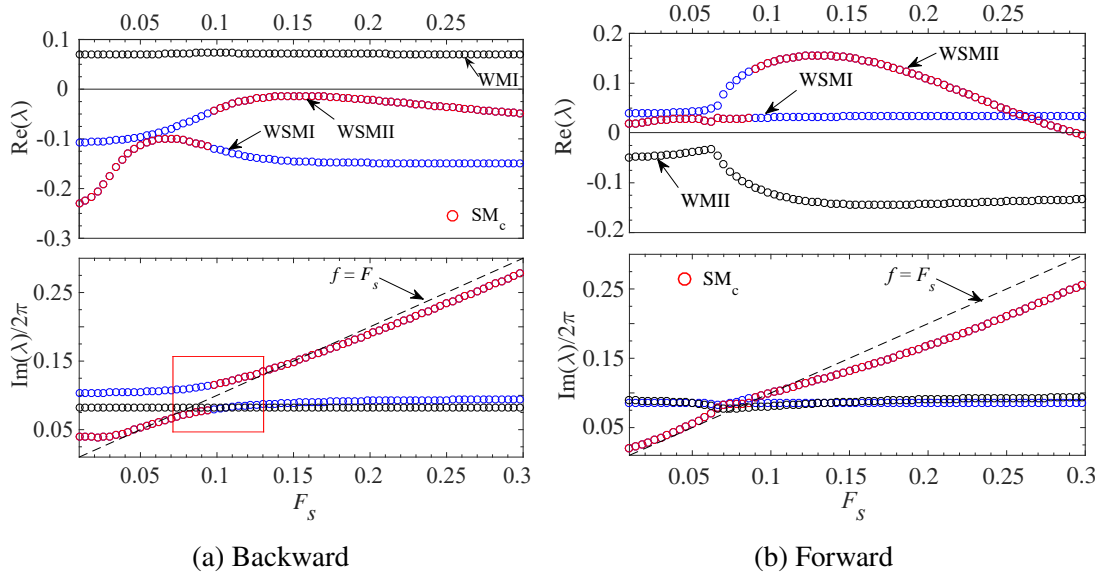


Figure 5.15: Growth/decay rate $\text{Re}(\lambda)$ and eigenfrequency $\text{Im}(\lambda)/2\pi$ as a function of F_s of the modes associated with the flow past an elastically-mounted isosceles-triangular body at $(Re, m^*) = (120, 10)$ in the (a) backward and (b) forward orientations. The single uncoupled wake mode is identified using black open circle markers and the structure mode hidden in the coupled WSMI/WSMII modes is identified using red open circle markers.

was started from an initial condition where the triangular body was at rest (viz., $(y, \dot{y}) = (0, 0)$ at $t = 0$). For the second value of $U_r = 25$ (regime 2), the fully-developed state of the FIV system at the previous value of $U_r = 14$ was used as the initial condition for the state of the FIV system at $U_r = 25$. Note that as the FIV system progresses in time through the sequence of values of U_r —7, 14, 25 and 62—the transverse maximum amplitude of vibrations y_{\max}/D increases monotonically from 1.64 to 3.50 to 6.31 and, finally, to 16.30, respectively. This response implies that the forward isosceles-triangular body will transition to a galloping instability at the larger values of U_r (e.g., at $U_r = 14, 25$ and 62) after it has achieved lock-in at $U_r = 7$. It is interesting to note that when the FIV system is started from rest as for the case of the first value of $U_r = 25$, the system does not exhibit a galloping instability. Moreover, a power spectral analysis of the time series displayed in figure 5.17 indicates that the structural oscillation frequency f_{osc} corresponding to $U_r = 25$ (regime 1), 7, 14, 25 (regime 2) and 63 assumes the values $f_{\text{osc}} = 0.160$ Hz, 0.129 Hz, 0.070 Hz, 0.040 Hz and 0.015 Hz, respectively. Because $U_0 = 0.1 \text{ m s}^{-1}$ and $D = 0.1 \text{ m}$, the non-dimensional oscillation frequency $f_{\text{osc}}D/U_0$ has the same value as the associated dimensional quantity f_{osc} . Keeping this in view, we note that the oscillation frequency f_{osc} corresponding to $U_r = 7, 14, 25$ (regime 2) and 63 is comparable to the reduced natural frequency $F_s \equiv U_r^{-1}$ (approximately or better), suggesting the structure mode dominates the FIV response in the lock-in and galloping regimes. In contrast, the oscillation frequency f_{osc} at $U_r = 25$ (regime 1) is approximately equal to vortex-shedding frequency for flow past the stationary forward isosceles-triangular body, implying the response in regime 1 is that of a forced-vibration. The response of the forward isosceles-triangular body conforms to the characteristics of hard-galloping.

Figure 5.16 shows that for the backward isosceles-triangular body for $U_r = 6$, the large amplitude of the transverse oscillations when the FIV system is in the lock-in range is correlated with small amplitude fluctuations in the lift coefficient C_L . This is in stark contrast with the response of the forward isosceles-triangular body displayed in figure 5.17 where it can be seen that the

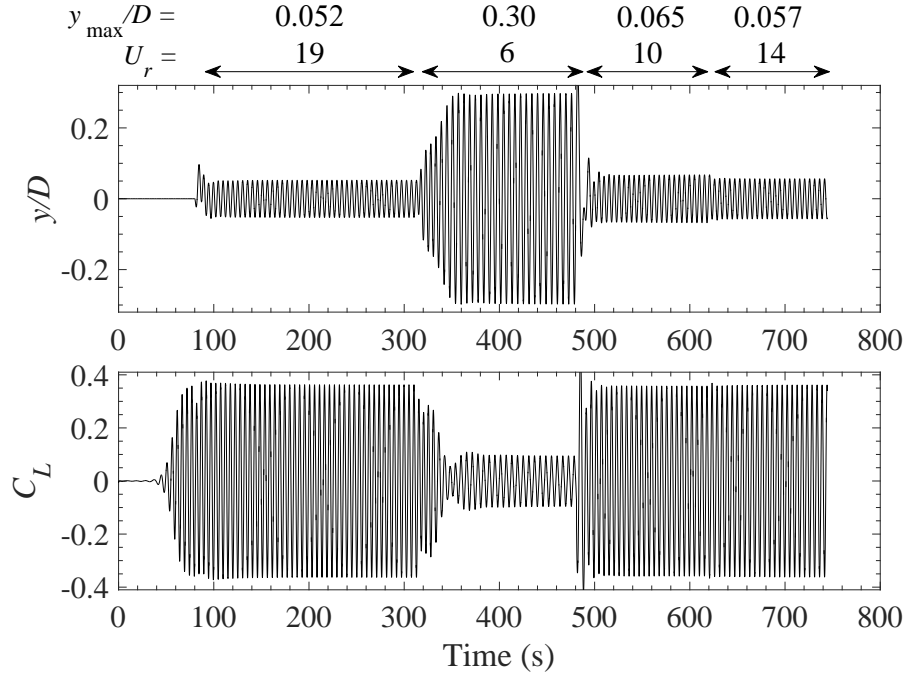


Figure 5.16: Time series of the normalized transverse amplitude y/D and lift coefficient C_L obtained from FOM/CFD simulation for the flow past a backward elastically-mounted isosceles-triangular body at $(Re, m^*) = (120, 10)$ with U_r changing (abruptly) in time from 19 to 6 to 10 and, finally, to 14.

flutter lock-in regime for $U_r = 7$ is correlated with large amplitude fluctuations in the lift coefficient C_L . This result supports the claim made by Zhang et al. [12] that the root-mean-square (rms) lift coefficient is reduced in the resonance lock-in regime, whereas it is increased in the flutter lock-in regime. Furthermore, when the FIV system consisting of the flow past a forward elastically-mounted isosceles-triangular body enters into the galloping regime at $U_r = 14, 25,$ and 62 , the time variation of the lift coefficient appears to be very chaotic (see figure 5.17).

A power spectral analysis was conducted for the time series of the transverse displacement y and the lift coefficient C_L for the forward elastically-mounted isosceles-triangular body shown in figure 5.17. The power spectrum was obtained for the segments of the time series corresponding to $U_r = 25$ —these segments consist of the early portion of regime 1 defined by the time span $tU_0/D \in (100, 250)$, the late portion of regime 1 defined by the time span $tU_0/D \in (600, 800)$ and regime 2 defined by the time span $tU_0/D \in (1250, 1350)$. Recall that $U_0/D = 1 \text{ s}^{-1}$, so the non-dimensional time tU_0/D is equal in value to (viz., has the same magnitude as) the dimensional time t . The power spectrum of these three segments of the time series is exhibited in figure 5.18. The dominant frequency in the power spectrum of the transverse displacement for the early and late portions of regime 1 is 0.04 Hz and 0.16 Hz, respectively, suggesting that the dynamic response here is determined by a competition between the structure and wake modes.

Although the forward elastically-mounted isosceles-triangular body has the potential to manifest a galloping instability at $U_r = 25$, for the early part of regime 1 corresponding to the body starting from a state of rest (viz., $(y, \dot{y}) = (0, 0)$ at $t = 0$), the structure mode with the associated frequency of 0.04 Hz eventually dissipates in the modal competition with the result that the wake mode with the associated frequency of 0.16 Hz eventually dominates the oscillations leading to a

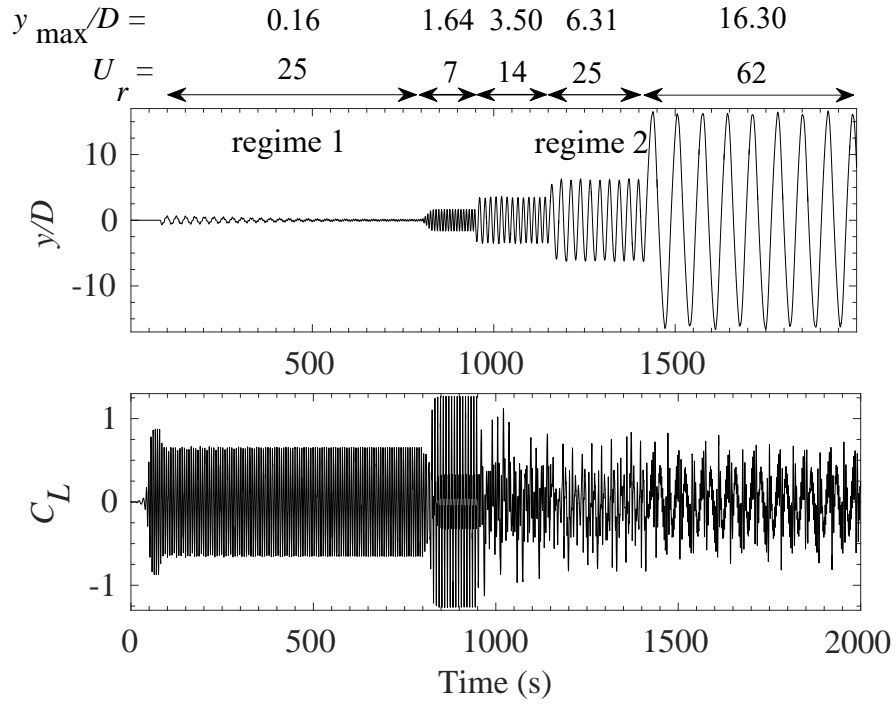


Figure 5.17: Time series of the normalized transverse amplitude y/D and lift coefficient C_L obtained from FOM/CFD simulation for the flow past a forward elastically-mounted isosceles-triangular body at $(Re, m^*) = (120, 10)$ with U_r changing (abruptly) in time from 25 to 7 to 14 to 25 and, finally, to 62.

forced vibration of the FIV system. It is noted that the dominant frequency in the power spectrum of C_L for both the early and late portions of regime 1 occurs at 0.16 Hz owing to the fact that the structural oscillation is weak. This result supports the notion that the galloping instability is associated with a mode competition as proposed by Li et al. [16]. In the early stage of regime 2, the initial motion of the body results in large transverse displacements of the body. During this early period of the vibration, the negative damping in the FIV system reinforces and maintains the large oscillations. These oscillations, in turn, alter the dynamics of the lift coefficient C_L (see the bottom panel of figure 5.18(c) where it is seen that dominant frequencies of C_L occur at both 0.04 Hz and 0.16 Hz, in contradistinction to that for the early and late stages of the dynamics in regime 1). In consequence, if the initial state of the body is not at rest (viz., when the body is subject to an external excitation with $y \neq 0$ and/or $\dot{y} \neq 0$), this leads to a reinforcement of the structure mode in the modal competition.

Figure 5.19 summarizes the stability condition for the FIV system consisting of a flow past a forward and backward elastically-mounted isosceles-triangular body at $Re = 120$. The assessment of the stability was undertaken using a quasi-steady stability analysis. As in the case for the forward and backward elastically-mounted D -section body investigated previously, it is seen that the Den Hartog function $H(\alpha)$ is negative- and positive-valued for the forward and backward isosceles-triangular body, respectively. This implies that the FIV response of the triangular body in the forward and backward orientations is unstable and stable, respectively. This result is consistent with the fact that a forward elastically-mounted isosceles-triangular body was found earlier to exhibit a galloping instability at $Re = 120$. However, as the body oscillates, the value of the rotation angle α can change with the result that the FIV system cannot be negatively damped

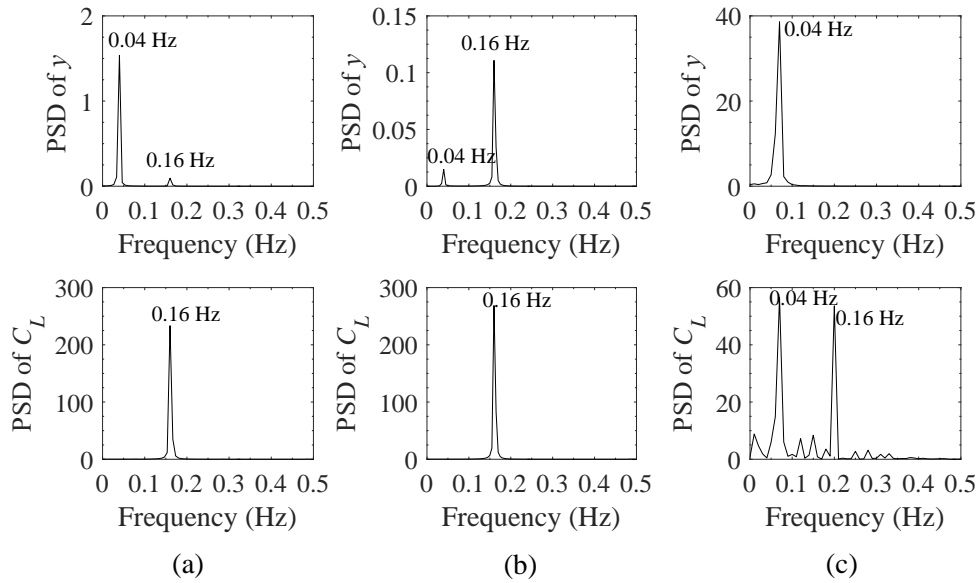


Figure 5.18: Power spectral density (PSD) of the normalized transverse amplitude y/D and the lift coefficient C_L for the flow past a forward elastically-mounted isosceles-triangular body at $(Re, m^*) = (120, 10)$ (cf. figure 5.17) for (a) $100 < tU_0/D < 250$ (early stage of regime 1), (b) $600 < tU_0/D < 800$ (late stage of regime 1), and (c) $1250 < tU_0/D < 1350$ (regime 2). The power spectra were obtained at $U_r = 25$.

throughout the course of these oscillations. In consequence, the amplitude of the transverse displacement cannot increase continuously, with the result that the FIV system will eventually settle into an equilibrium state (indeed, as a so-called limit cycle). Furthermore, we suggest that the structural instability arising from the negative damping in the FIV system is correlated with the galloping instability, but the emergence of lock-in in the system arises from a resonance effect which is totally unrelated to the negative damping.

Bringing together the results of our analysis of the response of the D -section body and the isosceles-triangular body in the forward orientation, we infer that the shape of the after-body is not directly related to whether or not galloping occurs. Rather, the galloping instability appears to be related to the shape of the downstream contraction of the body. This aspect of the FIV response, as well as the influence of the shape of the after-body on the characteristics of hard- or soft-galloping, will be studied in detail later.

5.4.3 Square cylinder

Previous experimental and numerical investigations have shown that the flow past an elastically-mounted square cylinder exhibits galloping instability. Zhao et al. [243] studied experimentally the effects of the angle of attack θ (viz., the angle between the incident flow direction and the normal to the windward face of the square cylinder) on the response of a FIV system consisting of a flow past an elastically-mounted square cylinder in a water channel for a mass ratio $m^* = 2.64$ and a reduced velocity U_r ranging from 3 to 17. The measurements showed that the square cylinder oriented at $\theta = 0^\circ$ and 45° exhibited a transition to a galloping oscillation and to desynchronization, respectively, as the values of U_r increased. A numerical study of the FIV response of a square cylinder was conducted by Li et al. [16] for a square cylinder under the

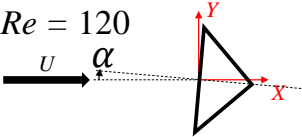
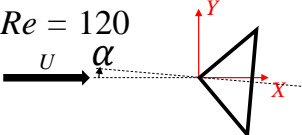
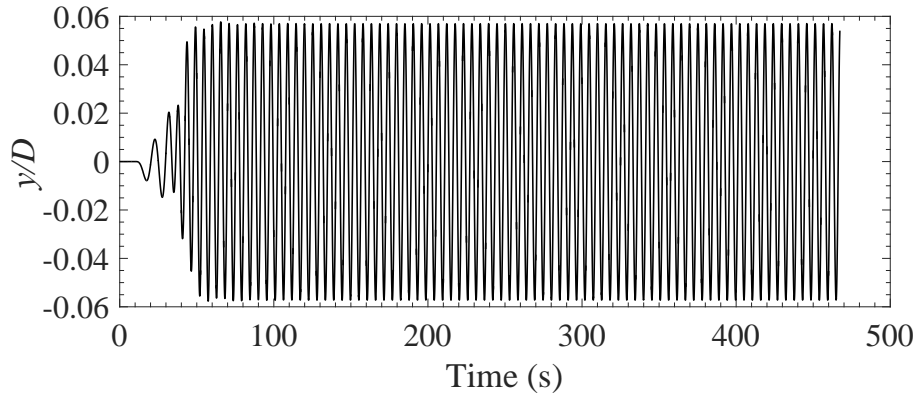
Diagram \ α	-1°	0°	1°
 $Re = 120$	$C_L = 0.0229$ $C_D = 1.3066$	$C_L = 1.28 \times 10^{-5}$ $C_D = 1.3065$ $H(\alpha) = -0.00547$	$C_L = -0.0229$ $C_D = 1.3066$
 $Re = 120$	$C_L = -0.00733$ $C_D = 1.10298$	$C_L = -7.66 \times 10^{-5}$ $C_D = 1.10299$ $H(\alpha) = 1.51976$	$C_L = 0.00722$ $C_D = 1.10288$

Figure 5.19: The lift C_L and drag C_D coefficients for the base flow past a forward and backward elastically-mounted isosceles-triangular body at $Re = 120$. The body is oriented relative to the incident wind direction with a rotation angle $\alpha = -1^\circ, 0^\circ$ and 1° . The Den Hartog function $H(\alpha)$ is provided for a rotation angle of $\alpha = 0^\circ$.

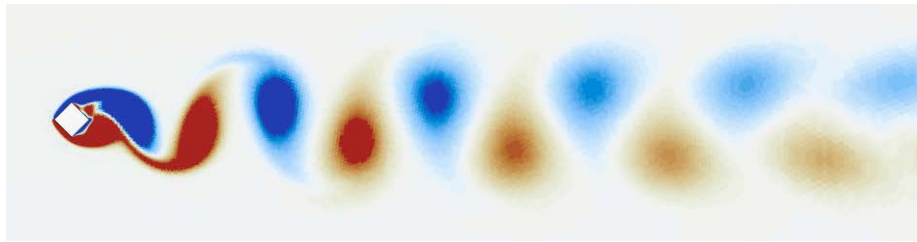
following conditions: $(\theta, Re, m^*, U_r) = (0^\circ, 150, 10, 20)$. This response can be compared to that for $(\theta, Re, m^*, U_r) = (45^\circ, 150, 10, 20)$ which we have conducted using FOM/CFD—the time series of the normalized transverse displacement y/D is displayed in figure 5.20(a). The very small value for the maximum transverse displacement of $y_{\max}/D \approx 0.055$ implies that a galloping instability does not occur in this case in stark contrast to the case with $\theta = 0^\circ$ where a galloping instability was observed with $y_{\max}/D \approx 0.21$ as reported by [16]. Finally, figure 5.20(b) shows that the vortex shedding pattern for the square cylinder oriented at $\theta = 45^\circ$ is consistent with a 2S mode of vortex shedding which corresponds to the desynchronization branch of the FIV response.

Li et al. [16] showed that a square cylinder oriented at $\theta = 0^\circ$ to the incident wind direction does not exhibit galloping until $Re \gtrsim 139$. In view of this, we constructed a ROM/ERA for the flow past an elastically-mounted square cylinder at $(Re, m^*) = (140, 10)$ for $\theta = 0^\circ$ and 45° . The root loci obtained from the ROM/ERA for these two cases of the angle of attack are exhibited in figure 5.21: namely for the square cylinder oriented at $\theta = 0^\circ$ (blue open square markers) and at 45° (black open circle markers) with respect to the incident wind direction. The arrows point in the direction of increasing U_r (or, equivalently, of decreasing F_s). A careful perusal of figure 5.21 shows the first wake mode WMI for $\theta = 0^\circ$ and 45° shrinks down to a point in the complex frequency plane, whereas the second wake mode is coupled to the structure mode (designated herein as WSMI and WSMII).

The root loci corresponding to the square cylinder oriented at $\theta = 45^\circ$ lie primarily in the positive right-half of the complex frequency plane at the smaller values of U_r , implying that the structure mode is associated with a positive growth rate over this range of U_r —which, in turn, is linked to a wider lock-in regime that can include potentially both resonance and flutter as the root cause of the frequency lock-in. Furthermore, at larger values of U_r , the root loci for the square cylinder at $\theta = 45^\circ$ lie in the negative (left) half of the complex frequency plane, implying that the structure mode exhibits a negative (or, decaying) growth rate, so this mode is expected to be stable at the larger values of U_r . In contrast, the growth/decay rate of the structure mode (as characterized by $\text{Re}(\lambda)$) for the square cylinder at $\theta = 0^\circ$ is positive at the larger values of U_r , suggesting the presence of a galloping instability in the FIV response at the larger values of U_r . However, at the smaller values of U_r , the root loci for the square cylinder at



(a) Normalized transverse displacement y/D



(b) 2S vortex shedding mode for square cylinder

Figure 5.20: (a) Time series of the normalized transverse displacement y/D and (b) 2S vortex shedding mode arising from the response (desynchronization branch) of a FIV system consisting of the flow past a square cylinder with $(\theta, Re, m^*, U_r) = (45^\circ, 150, 10, 20)$.

$\theta = 0^\circ$ lie in the negative left-half of the complex frequency plane and, as a result, the structure mode corresponds to a negative or decaying growth rate—so, coupled-mode flutter cannot be the mechanism underlying the lock-in of frequencies here. In view of this, we suggest that the mechanism underlying frequency lock-in for the square cylinder at $\theta = 0^\circ$ is that of resonance. Consequently, the frequency lock-in in this case is associated with a narrow range of values of U_r . This suggestion is supported by FOM/CFD simulations conducted by Li et al. [16]. These simulations showed that the frequency lock-in regime for the square cylinder at $\theta = 0^\circ$ only occurs when $U_r \approx 6$ –7.

Figure 5.22 summarizes the stability characteristics for the FIV system consisting of a flow past an elastically-mounted square cylinder at $Re = 120$ for two angles of attack $\theta = 0^\circ$ and 45° . The assessment of the stability was undertaken using a quasi-steady stability analysis. The stability characteristics of this FIV system is sensitive to the value of θ . An examination of the Den Hartog function $H(\alpha)$ for $\alpha = 0^\circ$ for the flow past an elastically-mounted square cylinder at the angle of attack $\theta = 0^\circ$ is negative-valued—so, in this case, the response of the FIV system will give rise to increasing transverse displacements of the body until a limit cycle (or equilibrium state) is reached. In contrast, for the square cylinder at $\theta = 45^\circ$, $H(\alpha) > 0$ at $\alpha = 0^\circ$ so the FIV system in this case is stable. These results suggest that the nature of the flow-induced vibration of an elastically-mounted square cylinder depends critically on the angle of attack

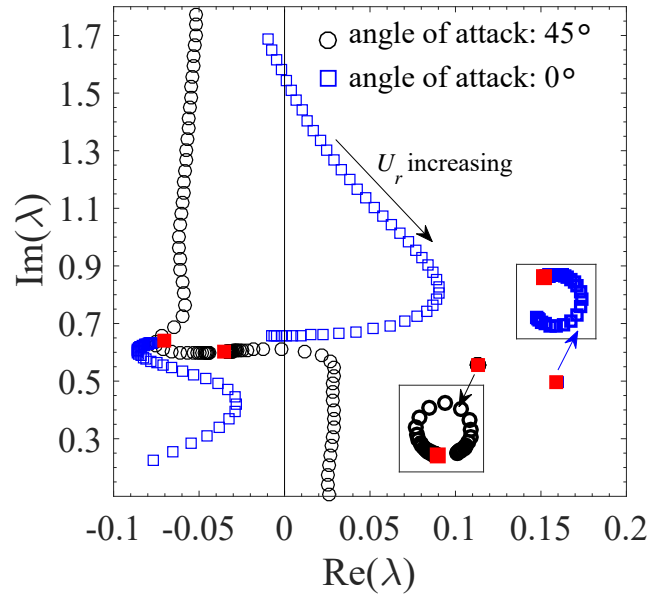


Figure 5.21: Root loci for a FIV system consisting of the flow past an elastically-mounted square cylinder oriented at $\theta = 0^\circ$ (blue open square markers) and 45° (black open circle markers) at $(Re, m^*) = (140, 10)$. The arrows point in the direction of increasing U_r along the root loci. The solid red squares correspond to the root loci for the stationary square cylinder oriented at $\theta = 0^\circ$ and 45° . The root loci were obtained using a ROM/ERA of the FIV system.

θ . If we consolidate the results obtained here for the square cylinder with those for the D -section body described earlier, it appears that the presence of sharp corners in a body is not a sufficient condition for a flow past such a body to provoke structural instabilities. This issue will be investigated in depth in the next section.

5.4.4 Summary

Figure 5.23 summarizes the response characteristics of a number of FIV systems consisting of the flow past an elastically-mounted body with various geometries and orientations: namely, a D -section body (half-cylinder) in the forward and backward orientations, an isosceles-triangular body in the forward and backward orientations, and a square cylinder at angles of attack of $\theta = 0^\circ$ and 45° . The appearance and disappearance of the various modes of response (resonance and/or flutter lock-in, pre-, soft- and hard-galloping) for these FIV systems for increasing values of the reduced velocity U_r are encapsulated in the figure at specific values of (Re, m^*) . Firstly, we note that the appearance of one or more forms of galloping occurs when a flat side of the geometrical body is facing directly into the wind (viz., when the outward unit normal to a flat face of the body is anti-parallel to the direction of the incident wind). Secondly, it is interesting to note that the square cylinder at $\theta = 0^\circ$ does not undergo flutter-induced lock-in but exhibits pre-galloping, in contradistinction to the D -section and isosceles-triangular bodies which do not undergo pre-galloping but exhibit flutter-induced lock-in. Thirdly, resonance lock-in occurs for all the body geometries and orientations shown in figure 5.23 (albeit the range of values of U_r for this type of frequency lock-in will vary with the body shape and orientation). More specifically, resonance lock-in will be present so long as the Reynolds number of the flow exceeds the critical Reynolds number for the formation of a stable vortex street in the wake of the body. Finally, the

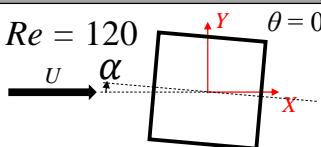
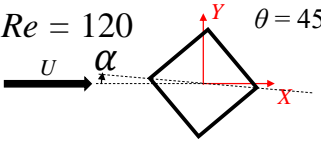
<i>Diagram</i> \ α	-1°	0°	1°
$Re = 120$  $\theta = 0^\circ$	$C_L = 0.0320$ $C_D = 1.1775$	$C_L = 1.23 \times 10^{-4}$ $C_D = 1.1773$ $H(\alpha) = -0.64451$	$C_L = -0.0316$ $C_D = 1.1775$
$Re = 120$  $\theta = 45^\circ$	$C_L = -0.00332$ $C_D = 1.099$	$C_L = 1.76 \times 10^{-4}$ $C_D = 1.099$ $H(\alpha) = 1.27891$	$C_L = 0.00296$ $C_D = 1.099$

Figure 5.22: The lift C_L and drag C_D coefficients for the base flow past an elastically-mounted square cylinder at $Re = 120$ for two angles of attack $\theta = 0^\circ$ and 45° . At each value of θ , the square cylinder is oriented relative to the incident wind direction with a rotation angle $\alpha = -1^\circ$, 0° and 1° . The Den Hartog function $H(\alpha)$ is provided for a rotation angle of $\alpha = 0^\circ$.







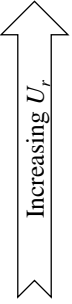
Shape	D-section		Isosceles-triangular		Square cylinder		
Orientations	forward 	backward 	forward 	backward 	angle of attack: 0° 	angle of attack: 45° 	
Hard-galloping	×	×	■	×	×	×	
Soft-galloping	■	×	×	×	■	×	
Pre-galloping	×	×	×	×	■	×	
Resonance lock-in	■	■	■	■	■	■	
Flutter lock-in	■	■	■	■	×	■	
(Re, m^*)	(60, 10)		(120, 10)		(140, 10)		

Figure 5.23: Summary of the response characteristics of a FIV system consisting of the flow past an elastically-mounted body with three different geometries at two different orientations: namely, a D -section body (or, half-cylinder) in the forward and backward orientations, an isosceles-triangular body in the forward and backward orientations, and a square cylinder at two angles of attack $\theta = 0^\circ$ and 45° . The symbols \times and \blacksquare are used to indicate the absence or presence, respectively, of the response mode (resonance or flutter-induced lock-in, pre-galloping, soft-galloping, hard-galloping).

shape of the after-body appears to be related to whether or not the galloping is hard or soft, but the detailed mechanisms underlying this relationship are unknown at present and, as a result, will require further investigation in future studies.

5.5 Effect of windward interior angle of trapezoidal body on response

As shown previously, when a flat face of an elastically-mounted geometrical body (e.g., half-cylinder, isosceles-triangular body, square cylinder) is directed into the incident flow, the body tends to exhibit a galloping instability for sufficiently large values of the reduced velocity U_r . This result leads to the following question—does the value of the interior angle at the vertices of the windward flat face of the geometrical body have any effect on whether galloping occurs or not? To resolve this question we consider a sequence of isosceles-trapezoidal bodies elastically-mounted in a flow at $(Re, m^*) = (160, 10)$. Figure 5.24 depicts the sequence of isosceles-trapezoidal bodies considered herein—the interior angles of the windward flat face of the bodies have values of 85° , 90° (square cylinder), 91° and 95° and the cross-sectional area of each trapezoidal body is equal to that of the square cylinder (trapezoidal body with an interior angle of 90°). The characteristic lengths— TL and SL —of each isosceles-trapezoidal body are the same. The acute and obtuse interior angles of the geometrical bodies correspond to either a contraction or expansion, respectively, of the body in the streamwise direction.

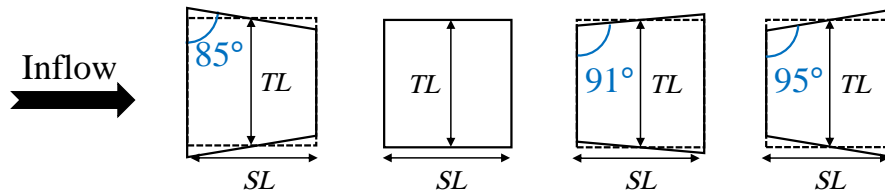


Figure 5.24: Isosceles-trapezoidal bodies with windward interior angles of 85° , 90° (square cylinder), 91° and 95° . All the isosceles-trapezoidal bodies have the same values of TL and SL .

Figure 5.25 shows the time series of the normalized transverse displacement y/D (obtained using FOM/CFD simulations) for a FIV system consisting of the flow past an elastically-mounted isosceles-trapezoidal body at $(Re, m^*) = (160, 10)$ for four different values of the windward interior angle: namely, for 85° , 90° (square cylinder), 91° and 95° . For each of the four configurations considered here, the value of the reduced velocity U_r was changed (abruptly) in time—the sequence of change points of U_r is shown in each panel of the figure. The initial temporal segment for each configuration used an initial condition of $(y, \dot{y}) = (0, 0)$ at $t = 0$ for $U_r = 25$ in order to investigate the presence or absence of soft- or hard-galloping in the response of the FIV system.

The configuration with a windward interior angle of 85° , 90° , 91° , and 95° has a maximum normalized transverse displacement y_{\max}/D at $U_r = 25$ of 1.805, 0.625, 0.013, and 0.014, respectively. A careful perusal of figure 5.25 shows that very small changes in the value of the interior angle at the vertices of the upper and lower sides of the windward face of the body can substantially affect the stability of the system and determine ultimately whether galloping does or does not occur. More specifically, it appears that a windward interior angle of 90° is the tipping point for stability, with the result that galloping disappears suddenly when the windward interior angle of the body increases ever so slightly from a right angle of 90° to an obtuse angle of 91° . On the other hand, when the windward interior angle of the body is acute, the response of the FIV system is unstable and prone to galloping with large transverse displacements of the body (e.g., $y_{\max}/D = 1.805$ and 0.625 for a windward interior angle of 85° and 90° , respectively, at $U_r = 25$).

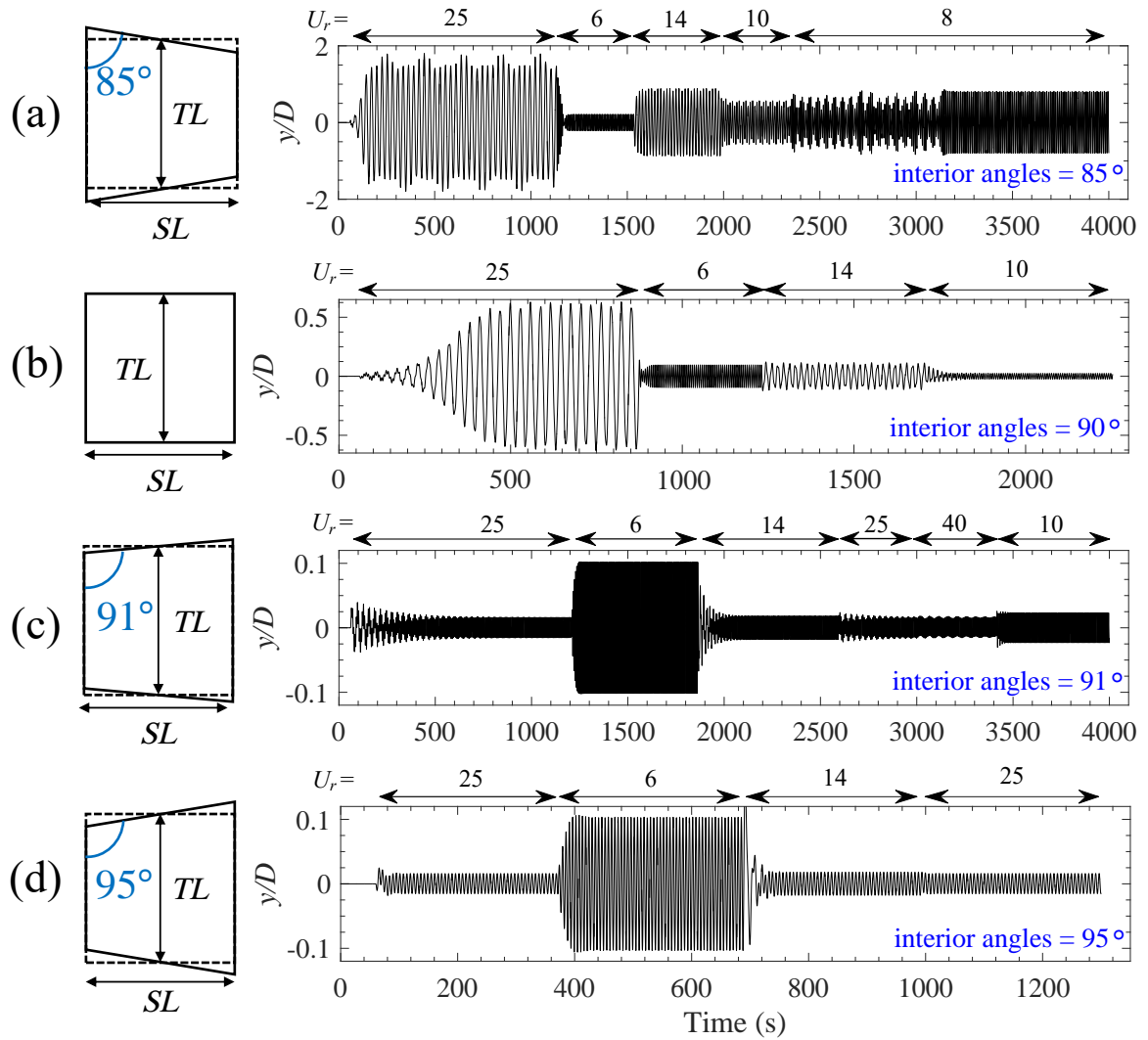


Figure 5.25: Time series of the normalized transverse displacement y/D obtained for a FIV system consisting of the flow past an elastically-mounted isosceles-trapezoidal body at $(Re, m^*) = (160, 10)$ with a windward interior angle of (a) 85° , (b) 90° , (c) 91° , and (d) 95° . For each configuration, the reduced velocity U_r is changed (abruptly) in time in accordance to the sequence of values shown along the top each panel.

It should be noted that all four configurations in figure 5.25 exhibit lock-in at $U_r = 6$, suggesting that the appearance of the lock-in here is not related to the small changes in the windward interior angle of the body. Furthermore, from a careful examination of figures 5.25(c) and (d) involving a windward obtuse interior angle for the body, the FIV system at $U_r = 14, 25$ and 40 enters into the desynchronization region of the response, demonstrating that the two configurations with a windward obtuse interior angle exhibit neither soft- nor hard-galloping.

Figure 5.26(a) shows the root loci for a FIV system consisting of the flow past an elastically-mounted isosceles-trapezoidal body at $(Re, m^*) = (160, 10)$ for windward interior angles of $85^\circ, 90^\circ, 91^\circ$ and 95° . The results were obtained from a ROM/ERA of the FIV system. A perusal of the figure shows that even small changes in the windward interior angle of the body has significant effects on the trajectory of the associated root loci. The root loci for the isosceles-trapezoidal body with windward interior angles of 85° and 90° imply that after leaving the resonance lock-in

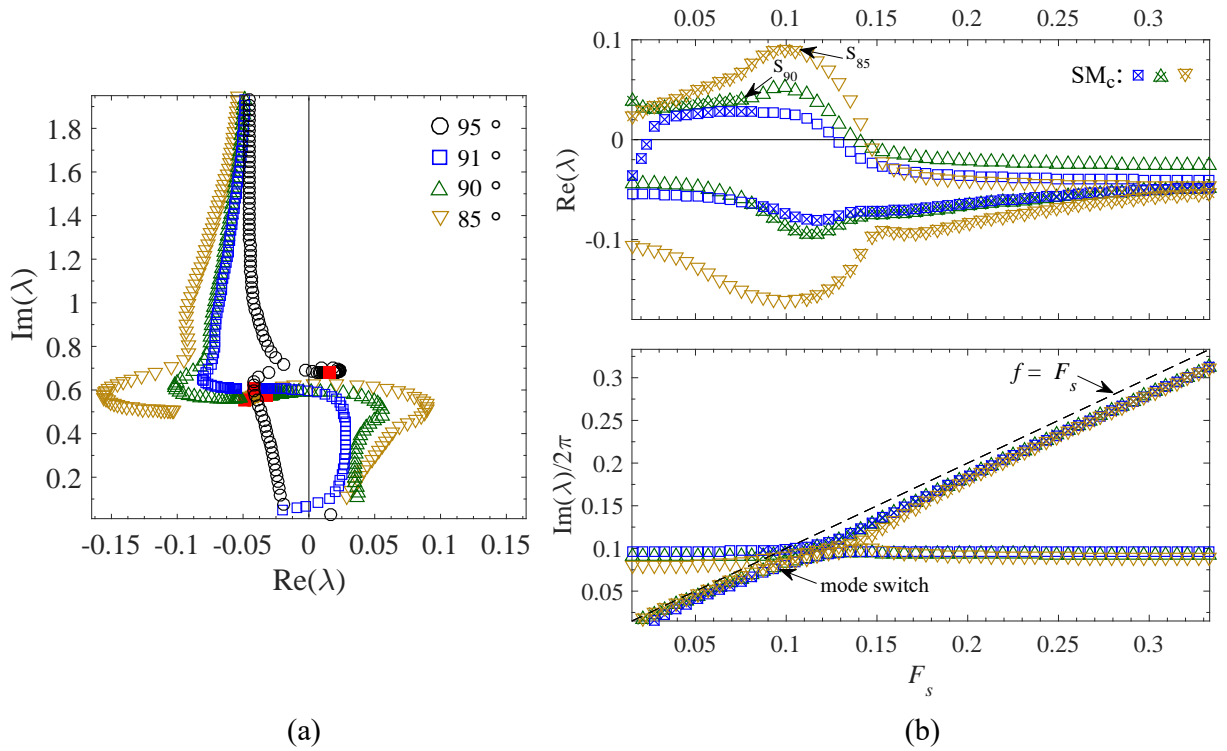


Figure 5.26: (a) The root loci and (b) the variation of the growth/decay rate $\text{Re}(\lambda)$ and eigenfrequency $\text{Im}(\lambda)/2\pi$ as a function of F_s for a FIV system consisting of the flow past an elastically-mounted isosceles-trapezoidal body at $(Re, m^*) = (160, 10)$ with windward interior angles of 85° , 90° , 91° , and 95° . The structure mode SM_c that is hidden in the coupled WSMI/WSMII modes is demarcated with crossed open symbols. The dotted line corresponds to the relationship $f = F_s$.

region with increasing values of U_r , the growth rate (characterized by $\text{Re}(\lambda)$) associated with the structure mode is positive, so the trapezoidal body here has an unstable structure mode that leads to a galloping instability. Moreover, we note that $\text{Re}(\lambda)$ for the structure mode associated with the trapezoidal body with a windward interior angle of 85° is larger than that associated with the square cylinder (or, trapezoidal body with a windward interior angle of 90°). Hence, the response of a trapezoidal body with a windward acute interior angle is more unstable than that with a right angle (viz., a square cylinder) and, in consequence, the former body geometry is more prone to exhibit large amplitude oscillations in the response than the latter body geometry. Our FOM/CFD simulations for $U_r = 14$ shown in figures 5.25(a) and (b) provide further support for this assertion—here, it is seen that the normalized maximum transverse displacement y_{\max}/D for the trapezoidal body with a windward interior angle of 85° is eight times larger than that for the square cylinder with a windward interior angle of 90° (viz., $y_{\max}/D = 0.883$ and 0.115 for the former and latter case, respectively). Finally, as mentioned previously, small changes in the windward interior angle of the trapezoid body do not alter substantially the amplitude response in the resonance lock-in region—for example, for $U_r = 6$ in figures 5.25(a) and (b), the normalized maximum transverse displacement for the trapezoidal body with a windward interior angle of 85° and 90° is $y_{\max}/D = 0.215$ and 0.101 , respectively.

As U_r increases beyond the range of values associated with the resonance lock-in regime for the flow past an isosceles-trapezoidal body with a windward interior angle of 85° and 90° ,

there will be a value of U_r at which galloping will be initiated. The precise value of U_r at which this occurs depends critically on the mode-switching behaviour of SM_c . The locations at which mode switching occurs for the trapezoidal body with a windward interior angle of 85° and 90° are marked as S_{85} and S_{90} in the top panel of figure 5.26(b), respectively. The values of U_r corresponding to the onset of galloping for the trapezoidal body with a windward interior angle of 85° and 90° are 9 and 14, respectively. The time series of the transverse displacement (obtained using FOM/CFD simulations) for the trapezoidal body with a windward interior angle of 85° at the reduced velocity $U_r = 14, 10$ and 8 , shown in figure 5.25(a), suggests that the onset of galloping occurs at $U_r = 8$. Similarly, a perusal of figure 5.25(b) indicates that for the square cylinder, the onset of galloping occurs in the interval $U_r \in (10, 14)$. These results for the value of U_r associated with the onset of galloping are generally consistent with those obtained using ROM/ERA. Interestingly, this result seems to contradict the assertion of Li et al. [16] that the use of LSA will lead to a significant underestimation of the value of U_r associated with the onset of galloping. The discrepancy here is due to the fact that Li et al. [16] did not identify the correct structure mode in their LSA of the square cylinder.

For an isosceles-trapezoidal body with a windward obtuse interior angle, the response of the FIV system is stable—even when the difference between the obtuse angle and a right angle is as small as either 1° or 5° . An examination of figure 5.26(a) shows that the root loci associated with the isosceles-trapezoidal body with a windward interior angle of 95° is located in the left-half-side of the complex frequency plane over the entire range of values of the reduced velocity U_r —so, the structure mode corresponds to a negative growth rate ($\text{Re}(\lambda) < 0$). As a result, this trapezoidal body will exhibit a resonance lock-in region, but no flutter-induced lock-in or galloping. Moreover, a perusal of figure 5.26(b) shows that for the isosceles-trapezoidal body with a windward interior angle of 91° , the structure mode first transitions from a stable to an unstable state with increasing values of U_r (or, equivalently, with decreasing values of F_s) and then switches back to a stable state at an even larger value of U_r (viz., the transition back to the stable state occurs at $F_s \approx 0.025$). The ROM/ERA results here are at variance with the FOM/CFD simulations where it can be seen the isosceles-trapezoidal body with a windward interior angle of 91° does not appear to exhibit a galloping instability (viz., no galloping is evident at $U_r = 10, 14, 25$, and 40 in figure 5.25(c)). In spite of this discrepancy, both the FOM/CFD and ROM/ERA results suggest that even a small increase in the windward interior angle of an isosceles-trapezoid body beyond a right angle (square cylinder) can greatly enhance the structural stability of the body and suppress the galloping instability.

Figure 5.27 summarizes the stability characteristics for the FIV system consisting of a flow past an elastically-mounted isosceles-trapezoidal body at $Re = 160$ for various values of the windward interior angle. Interestingly, the Den Hartog function $H(\alpha)$ at $\alpha = 0^\circ$ is negative for the trapezoidal body regardless of the value of the windward interior angle, implying the body exhibits a galloping instability that does not depend on the windward interior angle. The quasi-steady stability analysis here is incorrect as it has been shown above that a galloping instability does not occur for the isosceles-trapezoidal body with a windward interior angle of 91° and 95° (in contradistinction to predictions provided by the Den Hartog stability criterion). Although the Den Hartog stability criterion has been successfully applied previously for the D -section and isosceles-triangular bodies, it cannot be used to assess the system stability for the isosceles-trapezoidal body and especially with respect to how very small variations in the geometry of the body (e.g., windward interior angle) affects the stability (and, more specifically, whether galloping occurs).

The work presented herein shows that a contraction of the trapezoidal body in the stream-wise direction (viz., in the direction of the incident wind) is correlated with the presence of a galloping instability, and this trend has also been seen for the D -section and isosceles-triangular bodies. Moreover, recent research conducted by Bukka et al. [134] concerning the design of a passive device for the suppression of FIV has provided some interesting and practical results. When compared with a simple circular cylinder, the addition of a fairing device inhibits the VIV response, but the addition of a splitter-plate device causes galloping. Moreover, these investigators found that decreasing the radius of a C -shaped foil in a connected- C will provoke a structural instability and lead to galloping.

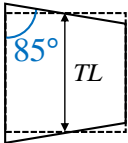
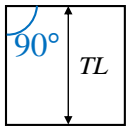
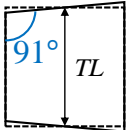
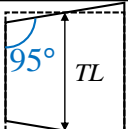
<i>Diagram</i>	α	-1°	0°	1°
$Re = 160$ 		$C_L = 0.04212$ $C_D = 1.2535$	$C_L = 0.000840$ $C_D = 1.2533$ $H(\alpha) = -1.1109$	$C_L = -0.04041$ $C_D = 1.2533$
$Re = 160$ 		$C_L = 0.04386$ $C_D = 1.1099$	$C_L = 0.000598$ $C_D = 1.1100$ $H(\alpha) = -1.3758$	$C_L = -0.04291$ $C_D = 1.1097$
$Re = 160$ 		$C_L = 0.03961$ $C_D = 1.0793$	$C_L = 0.000145$ $C_D = 1.0785$ $H(\alpha) = -1.1796$	$C_L = -0.03924$ $C_D = 1.0793$
$Re = 160$ 		$C_L = 0.02606$ $C_D = 1.0014$	$C_L = -3.8e-5$ $C_D = 0.9996$ $H(\alpha) = -0.5133$	$C_L = -0.02675$ $C_D = 1.0013$

Figure 5.27: The lift C_L and drag C_D coefficients for the base flow past an elastically-mounted isosceles-trapezoidal body at $Re = 160$ for various values of the windward interior angle. The body is oriented relative to the incident wind direction with a rotation angle $\alpha = -1^\circ, 0^\circ$ and 1° . The Den Hartog function $H(\alpha)$ is provided for a rotation angle of $\alpha = 0^\circ$.

5.6 Effect of side ratio of rectangular cylinder on response

Zhao et al. [35] experimentally investigated the galloping instability of the flow past an elastically-mounted rectangular cylinder with various values of the side ratio SR for Reynolds numbers ranging from 1000 to 8000. The side ratio SR is defined as the ratio of the streamwise length SL to the transverse length TL of the rectangular cylinder, so $SR = SL/TL$. These researchers reported on the following interesting phenomenon: namely, with increasing values of the reduced velocity outside the frequency lock-in range, galloping appears when $SR > 0.25$ and the oscillation amplitude continues to increase with increasing U_r . However, when $SR = 0.2$ the rectangular cylinder exhibits bounded galloping—the oscillation amplitude continues to increase with increasing reduced velocity until $U_r = 10.8$, after which it abruptly decreases. The latter corresponds to the system exiting the galloping regime and entering into the desynchronization

branch of the response. Zhao et al. [35] proposed that the collapse of galloping for a rectangular cylinder at $SR = 0.2$ is related to the incident wind direction relative to the cylinder, but does not propose any physical mechanism to explain this phenomenon.

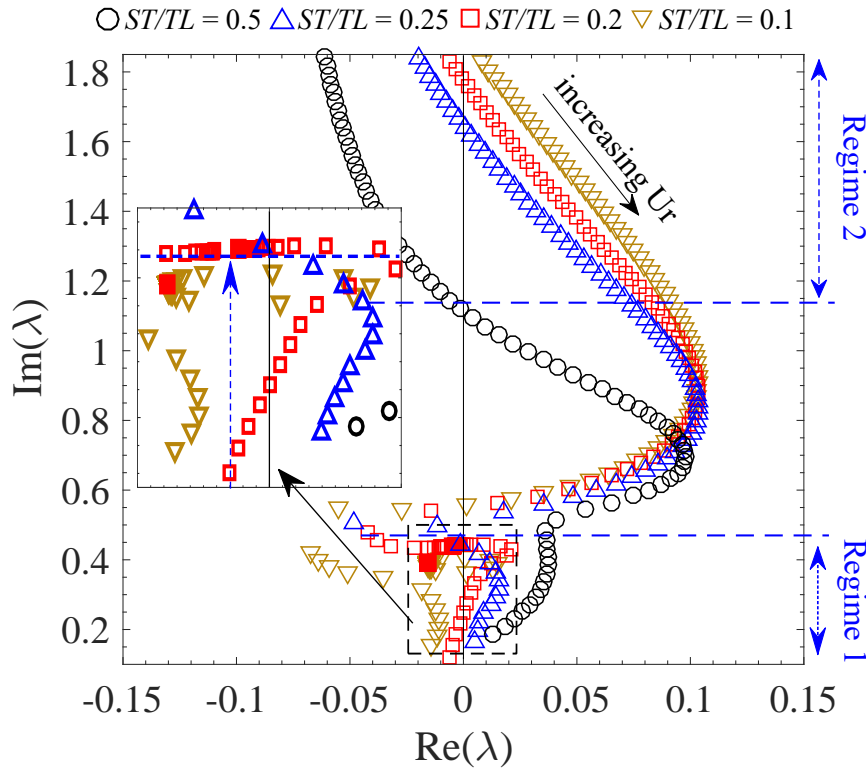


Figure 5.28: The root loci for the flow past an elastically-mounted rectangular cylinder for various values of the side ratio SR at $(Re, m^*) = (150, 10)$. Regimes 1 and 2 represent the range of values of U_r where galloping and flutter lock-in occur, respectively. The direction of the black arrow points towards increasing values of U_r .

In this sub-section, we investigate the phenomenology associated with the collapse of galloping for a cylinder with a rectangular cross-section at specific values of the side ratios SR using LSA (ROM/ERA) and quasi-steady stability analysis. Figure 5.28 exhibits the root loci (obtained using ROM/ERA) for a FIV system consisting of the flow past a rectangular cylinder at $(Re, m^*) = (150, 10)$ for four different values of the side ratio: namely, $SR = 0.5, 0.25, 0.2,$ and 0.1 . The inset plot in figure 5.28 provides a magnified view of the trajectory of the root loci at the large values of U_r . Only the variation of the root loci for the structure mode SM is shown in the figure owing to the fact that the various modes are uncoupled.

For the rectangular cylinder with a side ratio of 0.5 or 0.25, the associated root loci in Regime 1 (demarcated in figure 5.28) lie in the right half of the complex frequency plane—the growth rate $Re(\lambda)$ of the SM is positive and the response of the FIV system in this region corresponds to a galloping instability. However, for the rectangular cylinder with a side ratio of 0.2, it is observed from a perusal of the inset plot of figure 5.28 that the associated root loci crosses over from the right half to the left half of the complex frequency plane at a specific value of U_r . This implies that the unstable SM associated with galloping will suddenly collapse at this specific value of U_r (viz., where $Re(\lambda)$ crosses over from being positive-valued to being negative-valued)—a phenomenon consistent with that reported by Zhao et al. [35]. Moreover, for the rectangular cylinder with a

side ratio of 0.1, the associated root loci in Regime 1 lies in the left half of the complex frequency plane, implying that the galloping instability is inhibited in this case. However, for this case, the value of U_r in Regime 2 (demarcated in figure 5.28) where the root loci first crosses over from the left half to the right half of the complex frequency plane is associated with the onset of the flutter lock-in region. Taken together, these results suggest that a rectangular cylinder having a smaller side ratio results in a more stable FIV system at the larger values of U_r beyond the lock-in region and, at the same time, extends the range of values of U_r associated with the flutter lock-in by decreasing the value of U_r associated with the onset of lock-in. The galloping phenomenon will disappear when the side ratio of the rectangular cylinder is less than some critical threshold.

The Den Hartog stability criterion can be used to provide another perspective on the collapse of galloping for a rectangular cylinder with a specific side ratio. To this purpose, figure 5.29 indicates that the Den Hartog function $H(\alpha) < 0$ at $\alpha = 0^\circ$ for the rectangular cylinder with $SR = 1$ (square cylinder), 0.25, 0.2, and 0.1—which, in turn, implies that the derivative of the lift coefficient C_L with respect to α (viz., $dC_L(\alpha)/d\alpha$) is negative for all these cases. As the side ratio decreases from 1.0 to 0.1, the drag coefficient C_D for the rectangular cylinder with a rotation angle $\alpha = 1^\circ$ increases slowly from a value of 1.122 to 1.226. However, the absolute value of $dC_L(\alpha)/d\alpha$ decreases more rapidly owing to the reduction of the side length SL . As a result, $H(\alpha) \equiv dC_L(\alpha)/d\alpha + C_D(\alpha)$ increases through the sequence of values of -1.261 , -0.068 , -0.015 and 0.075 as the side ratio varies through the sequence of values of 1, 0.25, 0.2 and 0.1, respectively. It is noted that the negative damping (implied by a negative value for $H(\alpha)$) disappears when the side ratio of the rectangular cylinder decreases below some critical value. This critical value depends on the competition between the gradient of the lift coefficient with respect to the rotation angle and the drag coefficient, the latter two quantities of which determine the sign of the Den Hartog stability function.

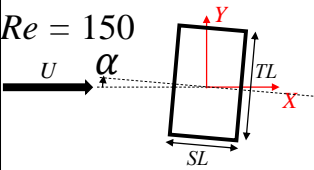
Diagram	α	-1°	0°	1°
Side ratio = SL/TL 	1	$C_L = 0.0420$ $C_D = 1.1219$	$H(\alpha) = -1.2616044$	$C_L = -0.0412$ $C_D = 1.1219$
	0.25	$C_L = 0.0320$ $C_D = 1.1775$	$H(\alpha) = -0.068231345$	$C_L = -0.0316$ $C_D = 1.1775$
	0.2	$C_L = 0.0214473$ $C_D = 1.20713$	$H(\alpha) = -0.014796822$	$C_L = -0.0212032$ $C_D = 1.20697$
	0.1	$C_L = 0.0202$ $C_D = 1.2260$	$H(\alpha) = 0.074354832$	$C_L = -0.0200$ $C_D = 1.2263$

Figure 5.29: The lift C_L and drag C_D coefficients for the base flow past an elastically-mounted rectangular cylinder at $Re = 150$. The cylinder is oriented relative to the incident wind direction with a rotation angle $\alpha = -1^\circ$, 0° and 1° . The Den Hartog function $H(\alpha)$ is provided for a rotation angle of $\alpha = 0^\circ$.

5.7 Effect of after-body on hard- and soft-galloping

The FOM/CFD simulations of the flow past an elastically-mounted forward isosceles-triangular body at $(Re, m^*) = (120, 10)$ (cf. figure 5.17) confirmed the presence of hard-galloping (viz., the galloping here cannot be initiated from a state of rest where there is no initial displacement and/or initial velocity). In order to further investigate the effect of the after-body on the galloping response, we conducted FOM/CFD simulations of the flow past a forward and backward elastically-mounted D -section body at $(Re, m^*) = (120, 10)$, the results of which will be used to compare with those obtained from the flow past an elastically-mounted forward isosceles-triangular body.

An examination of figure 5.30(a) shows that for $U_r = 5$ and 7, the backward elastically-supported D -section body is in the lock-in region—and, as well, the body does not exhibit either hard- or soft-galloping at $U_r = 14$. In marked contrast, the forward elastically-supported D -section body at $U_r = 14$ and 25 shown in figure 5.30(b) clearly exhibits a galloping instability—and, more specifically, soft-galloping in contradistinction to the forward elastically-supported isosceles-triangular body which, as we have mentioned earlier, exhibits hard-galloping. It is noteworthy that the type of galloping that occurs appears to be related to the geometrical shape of the after-body, with a rounded after-body being more likely to initiate soft-galloping.

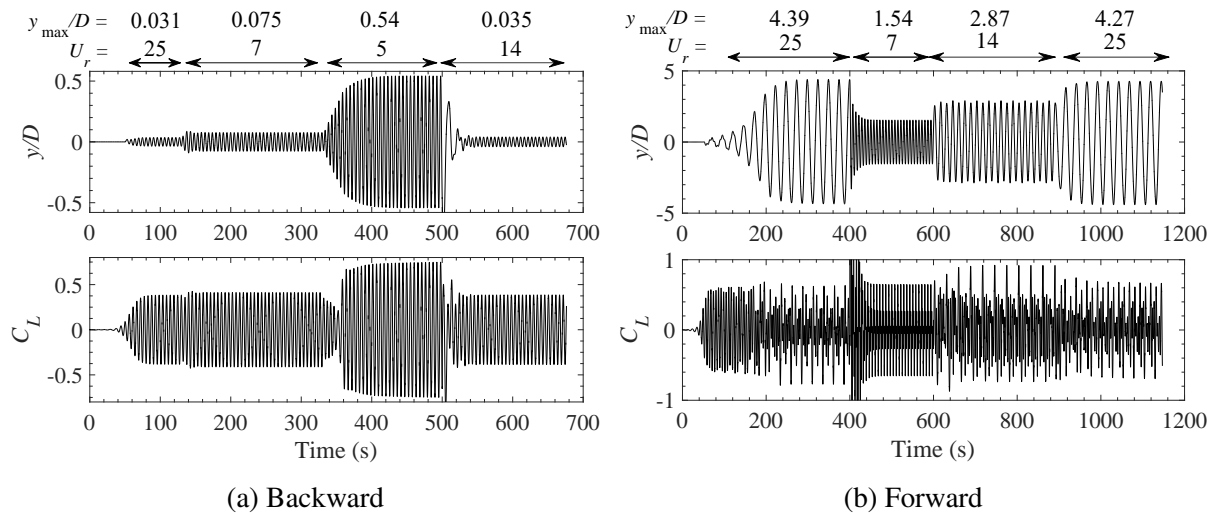


Figure 5.30: Time series of the normalized transverse displacement y/D and the lift coefficient C_L obtained for a FIV system consisting of the flow past a (a) backward and (b) forward elastically-mounted D -section body at $(Re, m^*) = (120, 10)$. For each of these two orientations of the body, the reduced velocity U_r is changed (abruptly) in time in accordance to the sequence of values shown along the top of each panel.

The backward and forward elastically-supported D -section body at $U_r = 7$ shown in figures 5.30(a) and (b), respectively, correspond to the frequency lock-in region (frequency synchronization of the vortex-shedding frequency and the structural natural frequency). In this lock-in region, the temporal fluctuation characteristics of the lift coefficient C_L for the backward D -section body are significantly different than those of the forward D -section body. These differences in the fluctuation characteristics of C_L have also been observed for the isosceles-triangular body in the forward and backward orientations, which is evident from a careful examination of

figures 5.16 and 5.17. Finally, note that as U_r increases from 7 to 14 and, finally, to 25 in figure 5.30(b), the normalized maximum transverse displacement y_{\max}/D increases monotonically; in contradistinction, the maximum amplitude of the lift coefficient C_L does not exhibit such a monotonic increase.

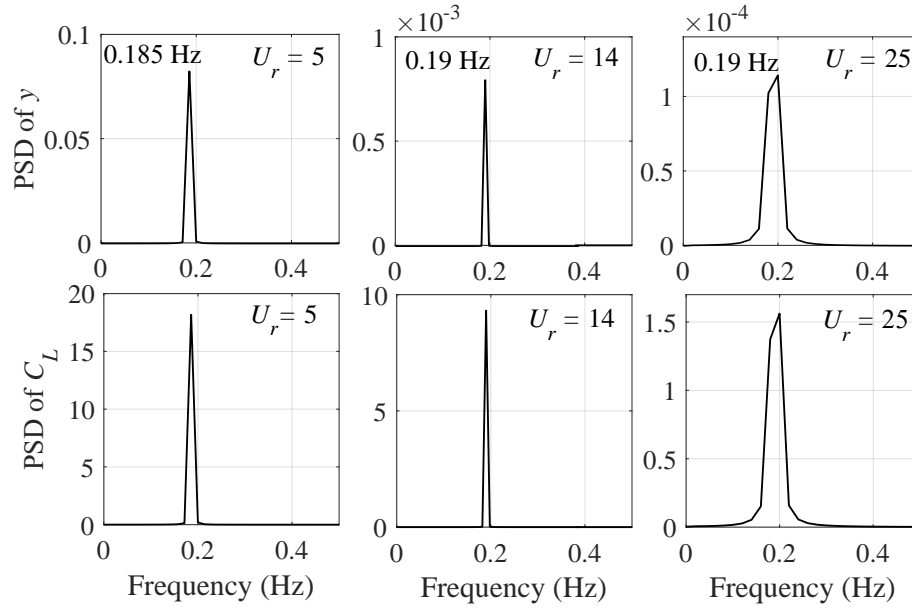
The power spectra of the time series data of the transverse displacement y and the lift coefficient C_L , shown in figure 5.30 for various values of the reduced velocity U_r , have been computed and summarized in figure 5.31. For the backward D -section body in the lock-in region at $U_r = 5$ and in the desynchronization branch of the response at $U_r = 14$ and 25, it is seen from figure 5.31(a) that the power spectra of y and C_L have a dominant peak at a frequency of 0.185 Hz (lock-in range) and at 0.19 Hz (desynchronization regime) which correspond, respectively, to the structural natural frequency and the vortex-shedding frequency of the stationary backward D -section body at $Re = 120$. For the forward D -section body at the values of U_r shown in figure 5.31(b), the power spectra for the transverse displacement y exhibit a single peak at a non-dimensional frequency equal to U_r^{-1} (again, we remind the reader that owing to the fact that $D/U_0 = 1$ s, the non-dimensional frequency is equal in magnitude to the dimensional frequency). To place this in perspective, we note that the vortex-shedding frequency for the stationary forward D -section body is 0.17 Hz at $Re = 120$. As a result, the structural natural frequency at $U_r = 7$ is very close in value to the vortex-shedding frequency of the stationary body, so there is a frequency synchronization of the vortex-shedding frequency and the structural natural frequency in this case (as is evident on examination of the power spectrum of C_L in figure 5.31(b) for $U_r = 7$ which exhibits a dominant peak at the frequency corresponding to the vortex-shedding frequency (approximately or better) as well as a secondary peak at a frequency of 0.42 Hz). Moreover, at $U_r = 14$ (or, equivalently, at $F_s = 0.071$), the power spectrum of the lift coefficient C_L for the forward D -section body is rather complex, exhibiting multiple peaks at a number of different frequencies, including a weak peak at a frequency of 0.071 Hz. Finally, we note that the power spectrum of C_L for the forward D -section body at $U_r = 25$ contains multiple peaks, including a peak at a frequency of 0.17 Hz (vortex-shedding frequency for the stationary forward D -section body owing to the fact that the low-frequency galloping can no longer synchronize in frequency with the vortex-shedding dynamics).

5.8 Effect of Reynolds number and mass ratio on galloping

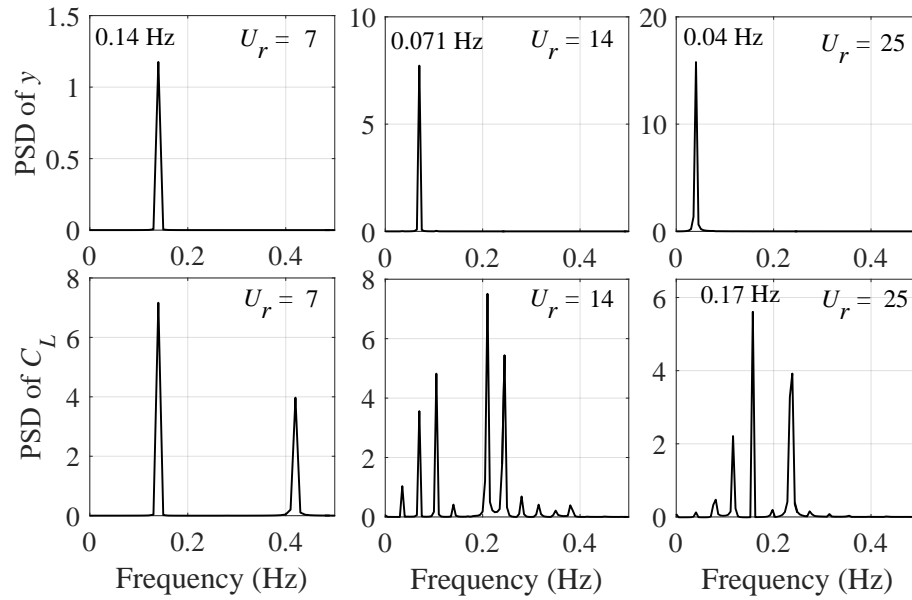
As the Reynolds number Re is increased, the growth rate of the structure and wake modes is amplified and there is a stronger coupling between these modes. Furthermore, the mass ratio m^* has an important effect on the response of a FIV system. In this section, we will use FOM/CFD simulations and ROM/ERA to investigate the effect of Re and m^* on the characteristics of galloping in the flow past an elastically-mounted square cylinder and an isosceles-triangular body.

5.8.1 Square cylinder

Figure 5.32 displays the root loci obtained using ROM/ERA for a FIV system consisting of the flow past an elastically-mounted square cylinder for a number of different values of the Reynolds number Re ranging from 20 to 180, inclusive, with $m^* = 10$. The characteristics of the modes for this case are summarized in figure 5.33. For $Re < 100$, the growth/decay rate $\text{Re}(\lambda)$ of the structure mode is negative for the entire range of values of the reduced velocity (viz.,



(a) Backward



(b) Forward

Figure 5.31: Power spectrum of the transverse displacements y and lift coefficients C_L at different values of the reduced velocity U_r for a flow past a (a) backward and (b) forward elastically-mounted D -section body at $(Re, m^*) = (120, 10)$.

the root loci lie entirely in the left half of the complex frequency plane). In this case, the square cylinder will not exhibit galloping. More specifically, the modes are uncoupled (decoupled modal condition) for $Re = 20$ —the wake mode is stable implying that there is no vortex shedding from the square cylinder. At $Re = 40$, the structure and the first wake mode are coupled and, as well, the wake mode is stable. At $Re = 60$ and 80 , the FIV system corresponds to a decoupled modal condition, but the wake mode is unstable. At $Re = 100$, the root loci for a certain range of values of U_r lie along the imaginary axis of the complex frequency plane (viz., along $Re(\lambda) = 0$) as seen clearly in the inset plot of figure 5.32(a). Here, the structure mode is at the tipping point

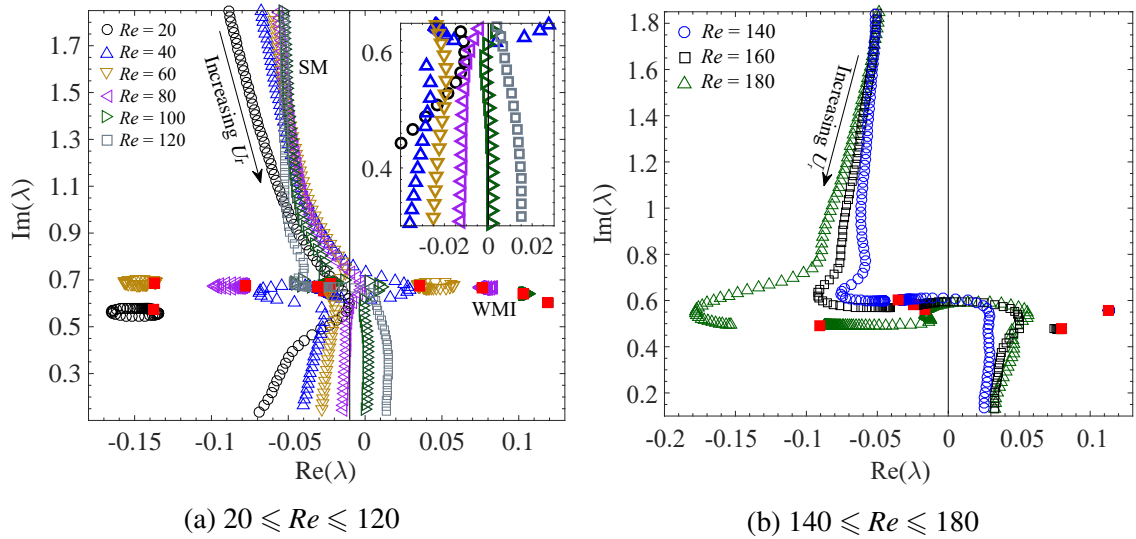


Figure 5.32: Root loci for a FIV system consisting of the flow past an elastically-mounted square cylinder for (a) $20 \leq Re \leq 120$ and (b) $140 \leq Re \leq 180$ with $m^* = 10$. The arrows point in the direction of increasing U_r along the root loci. The root loci were obtained using a ROM/ERA of the FIV system.

Square cylinder, $m^* = 10$							
	$Re < 100$			$Re = 100$	$Re > 100$		
growth rate of structure mode	remains negative			near the vertical axis of 'Re(λ) = 0'	becomes positive after certain U_r		
galloping	no				yes		
	$Re = 20$	$Re = 40$	$Re = 60, 80$	$Re = 100$	$Re = 120, 140$	$Re = 160$	$Re = 180$
modal interaction situation	de-coupled	coupled: structural mode + first wake mode		de-coupled	de-coupled	coupled: structural mode + second wake mode	coupled: structural mode + first and second wake modes
wake mode	stable	stable	unstable	unstable	unstable	unstable	unstable

Figure 5.33: A summary of the modal characteristics of a FIV system (obtained using ROM/ERA) consisting of the flow past an elastically-mounted square cylinder at various values of the Reynolds number Re ranging from 20 to 180, inclusive, with $m^* = 10$.

between stability and instability and galloping is about to take place in the FIV system. For $Re > 100$, the root loci for the structure mode lies in the right half of the complex frequency plane for a certain range of values of U_r , implying the presence of galloping in the response of the FIV system. Furthermore, an increasing Re leads to a stronger interaction between the modes which encompass specific behaviours such as a decoupled modal condition at $Re = 120$ and 140 , a coupled modal condition involving the structure and second wake modes at $Re = 160$ and, finally, a coupled modal condition involving the structure and the first and second wake modes at $Re = 180$ (cf. figure 5.32(b)). Taken together, these collective results show that an increase in the Reynolds number is associated generally with an increase in the degree of instability (viz., larger growth rates) of the modes on the one hand and a greater interaction between the structure and wake modes on the other hand (leading to ever more complex couplings between these various

modes).

Figure 5.34(a) displays the root loci for a FIV system consisting of the flow past an elastically-mounted square cylinder at $Re = 140$ for $m^* = 5, 10,$ and 50 . We note that the structure mode SM is not coupled to any of wake modes and that the first wake mode designated as WMI collapses to a single point in the complex frequency plane (approximately or better). The two modes SM and WMII are closer to one another in the complex frequency plane at $m^* = 5$ than at $m^* = 50$ implying that a smaller mass ratio is associated with a stronger interaction between these two modes. Interestingly, the trajectories of the root loci for $m^* = 5, 10,$ and 50 all intersect the imaginary or vertical axis ($Re(\lambda) = 0$) of the complex frequency plane at exactly the same location: namely, at the location $Im(\lambda) = 0.616$. This may be purely coincidental—indeed, other investigators [12, 15] have also noted this seeming coincidence.

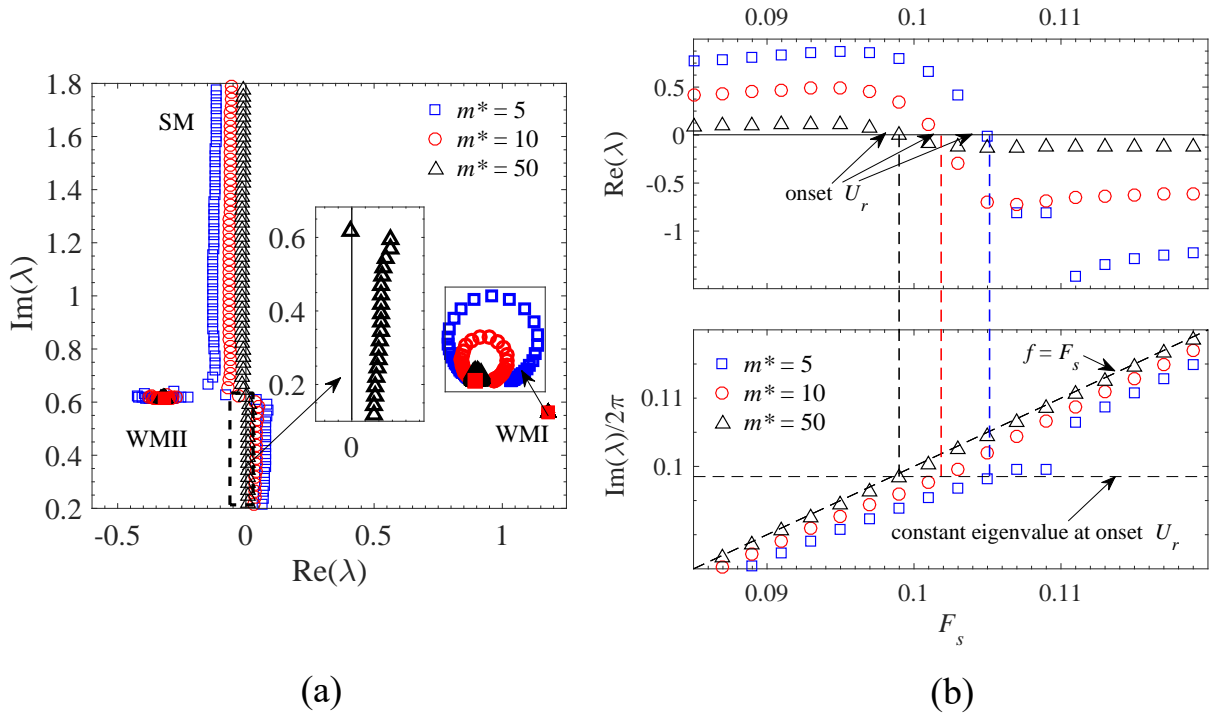


Figure 5.34: (a) The root loci and (b) the variation of the growth/decay rate $Re(\lambda)$ and eigenfrequency $Im(\lambda)$ as a function of F_s for a FIV system consisting of the flow past an elastically-mounted square cylinder for $m^* = 5, 10$ and 50 at $Re = 140$. The root loci were obtained using a ROM/ERA of the FIV system. Only the structure mode is shown in (b).

The real and imaginary parts of the eigenvalue associated with the SM for a FIV system consisting of the flow past an elastically-mounted square cylinder are plotted in figure 5.34(b) as a function of F_s . Firstly, the value of F_s (or, U_r) where $Re(\lambda) = 0$ (see top panel of figure 5.34(b)) corresponds to that value of F_s (or, U_r) associated with the onset of galloping in the FIV system. Note that the onset value of F_s (or, U_r) for galloping decreases (or, increases since $U_r = F_s^{-1}$) as the mass ratio m^* increases. In other words, an elastically-mounted square cylinder with a smaller value of m^* will exhibit galloping at a lower value of the reduced velocity U_r . Interestingly, the value of the eigenfrequency $Im(\lambda)/2\pi$ associated with the structure mode at the onset value of U_r (viz., the value of the reduced velocity at which the FIV system first becomes unstable) is constant with m^* as is evident on a careful examination of figure 5.34(b).

5.8.2 Isosceles-triangular body

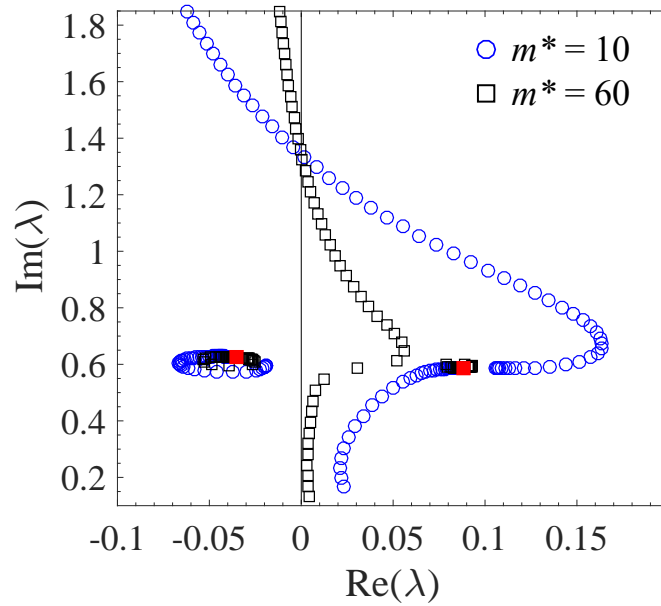


Figure 5.35: Root loci for a FIV system consisting of the flow past an elastically-mounted isosceles-triangular body in the forward orientation for $m^* = 10$ and 60 at $Re = 60$. The root loci were obtained using a ROM/ERA of the FIV system.

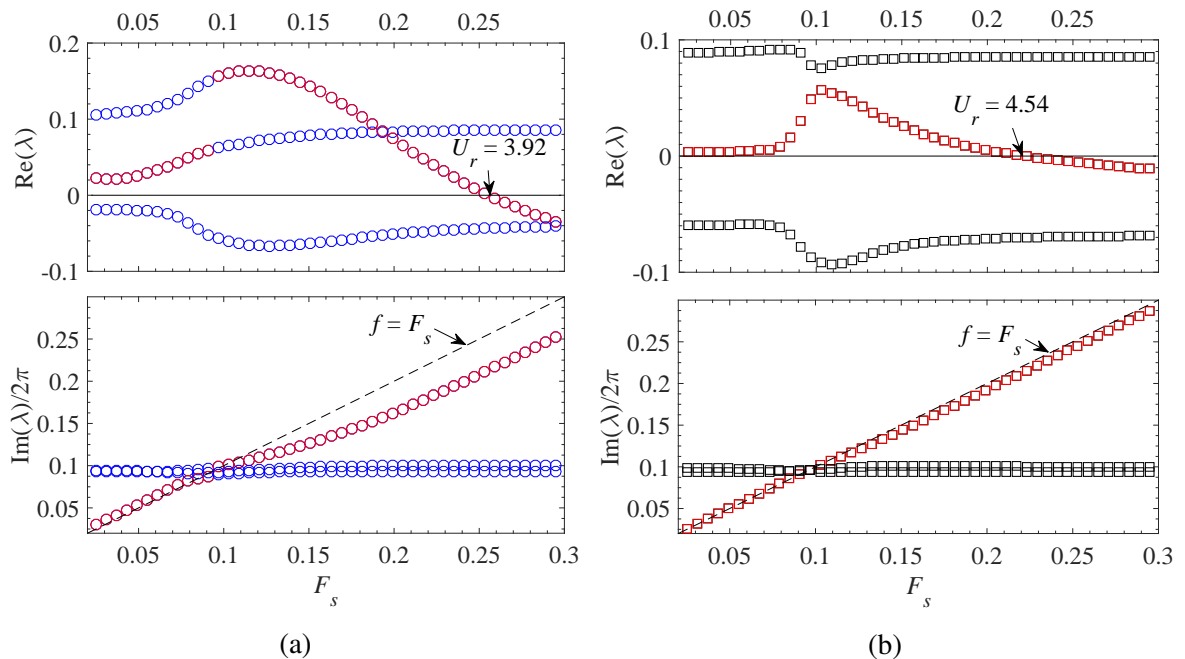


Figure 5.36: The variation of the growth/decay rate $Re(\lambda)$ and the eigenfrequency $Im(\lambda)/2\pi$ as a function of the reduced natural frequency F_s for a FIV system consisting of the flow past an elastically-mounted isosceles-triangular body in the forward orientation for (a) $m^* = 10$ and (b) $m^* = 60$ at $Re = 60$. The corresponding root loci for this case are displayed in figure 5.35.

In this sub-section, we investigate the effects of the mass ratio m^* on the response of a FIV system consisting of the flow past an elastically-mounted isosceles-triangular body in the forward

orientation at $Re = 60$. Figure 5.35 displays the root loci for this FIV system for two values of m^* : namely, $m^* = 10$ and 60. To disentangle this information, figures 5.36(a) and (b) exhibit the growth/decay rate $\text{Re}(\lambda)$ and the eigenfrequency $\text{Im}(\lambda)/2\pi$ as a function of the reduced structural frequency F_s for $m^* = 10$ and 60, respectively (obtained from the complex eigenvalues extracted from the ROM/ERA for the FIV system). The root loci for the FIV system shown in figure 5.35 suggest the modes associated with the response are coupled and uncoupled for $m^* = 10$ and 60, respectively. This suggests that for the forward isosceles-triangular body, the modes in the response of the FIV system are more strongly coupled (and, hence, interact more strongly with one another) at the smaller value of m^* . The result raises the following question—does the stronger interaction between the modes at the smaller value of the mass ratio m^* influence the amplitude of the structural vibrations and alter the range of values of U_r associated with the structural instability?

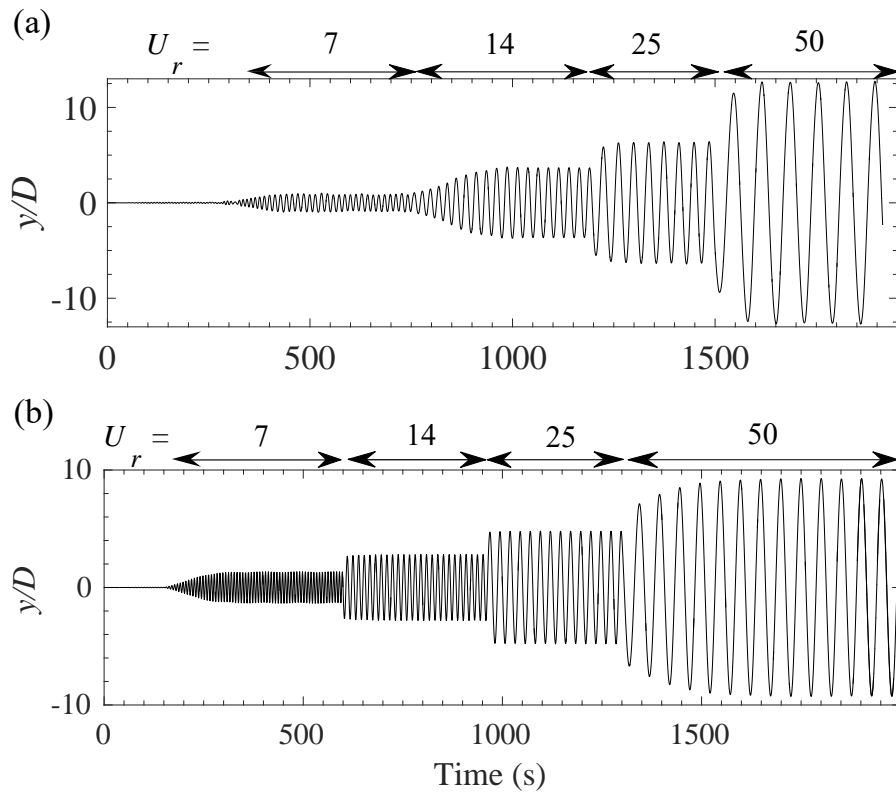


Figure 5.37: Time series of the normalized transverse displacement y/D obtained for a FIV system consisting of the flow past an elastically-mounted isosceles-triangular body in the forward orientation at (a) $(Re, m^*) = (60, 10)$ and (b) $(Re, m^*) = (60, 60)$. For each case, the reduced velocity U_r is changed (abruptly) in time in accordance to the sequence of values shown along the top of each panel: namely, U_r varies from 7 to 14 to 25 and, finally, to 50.

To address this question, FOM/CFD simulations of the flow past an elastically-mounted isosceles-triangular body in the forward orientation were conducted for two values of the mass ratio: namely, for $m^* = 10$ and 60. For these two cases, the reduced velocity U_r is changed (abruptly) at selected change points in time in accordance to the following sequence: $U_r = 7, 14, 25,$ and 50 in that order. The time series of the normalized transverse displacement y/D following from these two simulations are displayed in figure 5.37. It is noted that for $m^* = 10$, the normalized maximum transverse displacement y_{\max}/D was 1.009, 3.692, 6.418, and 12.685 for

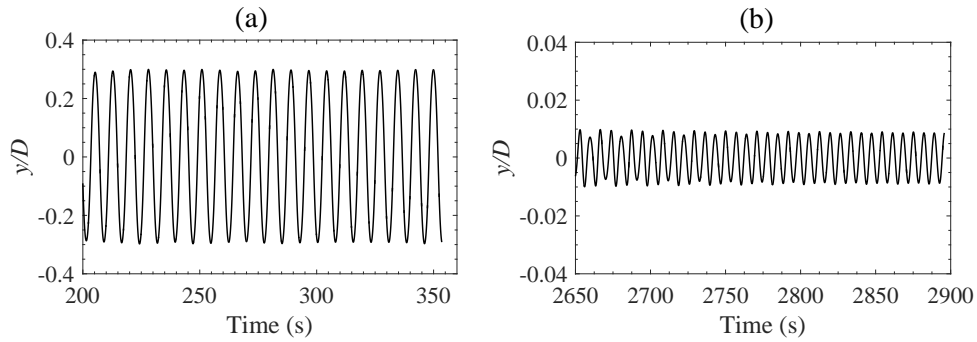


Figure 5.38: Time series of the normalized transverse displacement y/D obtained for a FIV system consisting of the flow past an elastically-mounted isosceles-trapezoidal body in the forward orientation at (a) $(Re, m^*, U_r) = (60, 10, 4)$ and (b) $(Re, m^*, U_r) = (60, 60, 4)$.

$U_r = 7, 14, 25,$ and $50,$ respectively. Similarly, for $m^* = 60,$ the normalized maximum transverse displacement y_{\max}/D was $1.341, 2.818, 4.798,$ and 9.250 for $U_r = 7, 14, 25,$ and $50,$ respectively. A comparison of these two cases shows that in the galloping regime, y_{\max}/D at $m^* = 10$ is $31\%, 33\%$ and 37% larger for $U_r = 14, 25$ and $50,$ respectively, than that at $m^* = 60.$ Moreover, in the frequency lock-in regime at $U_r = 7,$ y_{\max}/D at $m^* = 60$ is 33% larger than that at $m^* = 10.$ Consequently, a smaller mass ratio results in oscillations with reduced amplitude in the lock-in region and with increased amplitude in the galloping region, all other factors (e.g., Reynolds number, reduced velocity) being equal.

A careful examination of figures 5.36(a) and (b) shows that the value of F_s (or, $U_r = F_s^{-1}$) associated with the onset of the flutter-induced lock-in for $m^* = 10$ and 60 is 0.255 ($U_r = 3.92$) and 0.220 ($U_r = 4.54$), respectively. In view of this, we conducted FOM/CFD simulations for the flow past an elastically-mounted isosceles-triangular body in the forward orientation at $Re = 60$ for $U_r = 4$ (or, equivalently, for $F_s = 0.25$) and for $m^* = 10$ and $60.$ The results of these simulations are given in figure 5.38 which shows the time series of the normalized transverse displacement y/D for $m^* = 10$ and $60.$ It is noted that the normalized maximum transverse displacement y_{\max}/D is 0.30 and 0.01 for $m^* = 10$ and $60,$ respectively. The responses of the FIV system shown here belong to the frequency lock-in and desynchronization regimes, respectively. Hence, a smaller value of m^* implies that structural instability is present for a wider range of values of the reduced velocity $U_r.$

5.9 Chapter summary

In this chapter, detailed investigations were conducted to determine the mechanisms responsible for triggering galloping in a flow past an elastically-mounted body, with a particular emphasis on the critical influence of the body geometry on the initiation of a galloping instability. Three methodologies have been used to address this problem: namely, full-order model/computational fluid dynamics simulations, application of linear stability analysis based on the use of a reduced-order model obtained using the eigenvalue realization algorithm, and use of the Den Hartog stability (galloping) criterion (based on a quasi-steady theory) that determines the condition for aerodynamic instability in a single degree-of-freedom oscillator.

In the application of a linear stability analysis based on ROM/ERA to a FIV system, we

show that for a system with coupled modes, singling out one of these coupled modes (e.g., either WSMI or WSMII) and simply designating it to be the pure structure mode as done by Li et al. [16] is not correct. In fact, doing so leads to a significant underestimation of the value of U_r associated with the onset of galloping as has been reported by Li et al. [16]. Rather, it is necessary to carefully identify which of the two coupled modes at any particular value of U_r actually corresponds to the structure mode taking into account possible mode switching. The structure mode so obtained is designated as SM_c herein. The modal stability analysis needs to be based on the trajectory of the root loci associated with SM_c . Furthermore, the range of values of U_r where the real part of SM_c is positive is related to the flutter-induced lock-in region for the smaller values of U_r (normally for $U_r \leq 7$) and to the galloping regime for the larger values of U_r (normally for $U_r \geq 10$) in this range.

The vorticity field for the flow past an elastically-supported forward D -section body at $(Re, m^*) = (60, 10)$ for a range of values of the reduced velocity U_r (obtained from FOM/CFD simulations) was used to study how the wake patterns change as a function of U_r . For $U_r \leq 7$, the FIV system is in frequency lock-in and the vortex wake pattern is 2S (with each period alternatively shedding a single vortex). For values of the reduced velocity in the range $12 \leq U_r \leq 14$, the vortex shedding modes are stretched or elongated in the streamwise direction—a vortex wake pattern which we have named E-2S (or, elongated-2S). For $16 \leq U_r \leq 25$ where the natural structural frequency is less than the vortex-shedding frequency, the vortex wake pattern changes into a so-called D-2S (deformed-2S) mode consisting of a normal vortex (as in 2S) and an elongated vortex (as in E-2S) with each period alternatively shedding a vortex of one type or the other. Finally, for $U_r \geq 50$, owing to the very large amplitude and very low frequency of the oscillations of the galloping regime, the vortex-shedding pattern corresponds to a slow transverse displacement of a 2S mode (as if the 2S vortex pattern were frozen into the flow at any particular time in this spatial displacement).

A detailed study of the two key factors—the cross-section geometry of the body and the angle of attack of the incident flow—was undertaken in this chapter. The key results are summarized below.

A careful analysis of the response and structural stability of a FIV system consisting of the flow past an elastically-supported D -section body (half-cylinder), isosceles-triangular body, and isosceles-trapezoidal body (including a square cylinder) has been undertaken. The upshot of this effort was that both the geometry of the body and the angle of attack has a significant effect on the stability of the FIV system. More specifically, a number of FOM/CFD simulations demonstrated conclusively that galloping appears when the flat face of the body is windward of the incident flow and, alternatively, galloping disappears when the flat face of the body is leeward of the incident flow. Moreover, linear stability analysis based on ROM/ERA showed that the structure mode SM_c is unstable for large values of the reduced velocity U_r when the flat face of the body is windward. Finally, the Den Hartog stability criterion revealed that negative damping in the FIV system, that arises from the occurrence of a negative gradient of the lift coefficient C_L with respect to the angle of attack α at $\alpha = 0^\circ$ (when the oscillations are normal to the incident wind direction), occurs when the flat face of the body is windward (providing the condition for an aerodynamically unstable behavior of a single degree-of-freedom oscillator).

A novel result of the present work concerns the fact very small changes in the windward interior angle of an isosceles-trapezoidal body can have a significant effect on the appearance or disappearance of galloping. Using an isosceles-trapezoidal body with a windward interior right angle (square cylinder) as the reference, it was found that even a small increase in the

value of the windward interior angle (say, from 90° to 91°) can lead to a complete suppression of the galloping instability. Alternatively, a small decrease in the windward interior angle of an isosceles-trapezoidal body to a value below 90° can result in a significant enhancement of the galloping oscillations. These conclusions were supported by our FOM/CFD simulations and linear stability analysis (and, more specifically, ROM/ERA).

We explain, for the first time, some experimental results reported by Zhao et al. [35] concerning the collapse of galloping for a rectangular cylinder when the side ratio decreases below a critical threshold value (between about 0.1 and 0.2). To this purpose, a linear stability analysis showed that when the side ratio of a rectangular cylinder decreases to a value of 0.1, the growth rate associated with the structure mode SM_c at $(Re, m^*) = (150, 10)$ is positive for a certain range of values of U_r and then becomes negative for a further increase in value of U_r outside this range—this observed behavior of the the root loci trajectory associated with SM_c is consistent with the collapse of galloping reported by Zhao et al. [35] (viz., galloping was observed for a certain range of values of U_r and then collapses for a further increase in the value of U_r). This analysis is supported by the Den Hartog stability criterion—as the side ratio of the rectangular cylinder is decreased the negative damping disappears when the side ratio is reduced below some critical value (and, as a result, galloping disappears). The disappearance of the negative damping here occurs when the magnitude of the slope of the lift coefficient $dC_L(\alpha)/d\alpha$ (which is negative) is reduced to the point where it becomes less than the drag coefficient $C_D(\alpha)$.

It was found that a FIV system consisting of the flow past a forward D -section body and an isosceles-triangular body at $(Re, m^*) = (120, 10)$ exhibit soft- and hard-galloping, respectively. The presence of a curved after-body appears to provoke soft-galloping and this seems to be related to the presence of separation points arising in the motion of the shear layer on the body surface. Moreover, the manifestation of hard-galloping for certain body geometries requires a sufficiently large initial displacement of the body—large enough so that it can extract sufficient energy from the surrounding fluid to excite galloping (aided by the negative damping in the initial vibrational cycles).

The effects of the Reynolds number Re and the mass ratio m^* on the characteristics of galloping in the flow past an elastically-supported square cylinder and isosceles-triangular body was studied in this chapter. The results of the linear stability analysis suggest that increasing the Reynolds number and decreasing the mass ratio tends to enhance the coupling between the structure and wake modes and to increase the range of values of the reduced velocity U_r where the structure mode SM_c exhibits a positive growth rate. Furthermore, a smaller value of m^* results in oscillations with decreased amplitude in the frequency lock-in region and with increased amplitude in the galloping region, all other factors (Reynolds number, reduced velocity) being equal.

The synthesis of the results from FOM/CFD simulations, linear stability analysis (ROM/ERA) and application of the Den Hartog stability criterion can provide deeper insights in the mechanisms underlying flow-induced vibrations. For example linear stability analysis (ROM/ERA) can be usefully applied to study the mechanisms responsible for the collapse of the galloping instability in an elastically-mounted rectangular cylinder, but cannot be used to determine whether a bluff body is susceptible to either soft- and hard-galloping. Quasi-steady stability analysis can be applied to particular structures to determine whether they will be subject to an aerodynamically unstable behaviour (albeit under the major limitation that this analysis is valid only for an angle of attack of $\alpha = 0^\circ$). However, quasi-steady theory cannot be used to determine the type of galloping that a structure may exhibit or the influence of small structural changes in the cross-

sectional geometry (e.g., windward interior angle) on the FIV response. The latter can only be ascertained using FOM/CFD simulations.

From a comparison of the FIV response for the flow past an elastically-supported half-cylinder, isosceles-triangular body and isosceles-trapezoidal body with various values for the windward interior angle, it is noted that a contraction towards the after-body will widen structural instability to smaller values of U_r (to approximately 4 or 5), allowing the existence of a flutter lock-in region. Furthermore, the contraction of the isosceles-trapezoidal body in the streamwise direction is associated with the presence of a galloping instability. If we combine these observations with some recent work conducted by Bukka et al. [134] for the design of passive FIV suppression devices, we hypothesize that a body with a cross-sectional geometry that is contractive in the streamwise direction will tend to provoke galloping.

Chapter 6

3-D linear stability analysis of FIV system with spanwise shear inflow

The presented motivations in this thesis are correlated to the application of the FIV phenomenon in energy harvesting devices such as bladeless wind turbines. Additionally, a vertical bladeless wind turbine will often encounter a shear situation in the vertical direction of the incident flow. As a consequence, the FIV system with spanwise shear inflow is valuable to be investigated. As mentioned by the Hollenbach et al. and Sanders [159, 160], the traditional CFD method, as one full-order model (FOM), has no ability to provide physical insight into the generation of flow-induced vibrations including the lock-in behavior. Moreover, with respect to the FIV study using a non-uniform velocity as the incident flow velocity, the necessary 3-D computation using FOM/CFD is significantly time-consuming and yet unable to expose the underlying modal situation.

Compared with the previous 2-D LSA works mentioned above, to our knowledge there are few precedents for the using 3-D LSA for the study of FIV in the past. Chizfahm and Jaiman [120] obtained a ROM for the fluid dynamics of a sphere at $Re = 300$ using the eigensystem realization algorithm (ERA) and constructed the associated coupled FSI model to study the effects of the near-wake jet (attached to the downstream side of the sphere) on the VIV response. The construction process of the fluid ROM, including the obtainment of the base flow for a sphere and the dynamic response (or, lift coefficients) when subjected to an impulse, is performed in the 3-D computational domain. The results show that the direct 3-D LSA is capable of capturing the effect of the near-wake jet on the FIV response in terms of trend, but cannot predict the lock-in range very accurately.

The following work herein also encounters such errors in the direct 3-D LSA of the shear flow-induced vibration of a rigid cylinder. Therefore, in addition to carrying out direct 3-D LSA, a novel/original LSA methodology is proposed in this chapter—the rigid cylindrical structure is segmented into several elements in the spanwise direction, and the aerodynamic characteristics of each element are simplified into 2-D situations with uniform inflow. ERA identification is conducted for each element to provide the separate 2-D fluid ROM, and the integral fluid ROM for the 3-D cylinder with shear inflow is obtained via the superposition of all 2-D fluid reduced-order models (ROMs). Then, the LSA could be achieved via the coupling of the integral fluid ROM and the structural equation. This differential idea of partitioning a slender structure (with a relatively large length-to-chord ratio) into small elements and then superimposing the dynamical features of each small element is similar to the Blade-Element-Momentum (BEM)

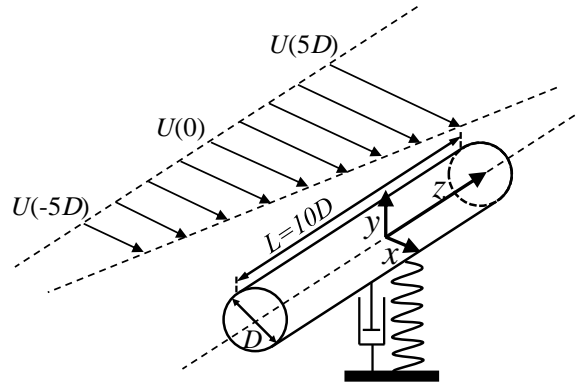


Figure 6.1: Diagram of the physical configuration for the flow-induced vibration of a circular cylinder with inflow sheared in spanwise (z) direction. Reynolds number Re increases linearly in positive z (spanwise) direction. $Re_{-5D} = U(-5D)D/\nu = 25$, $Re_0 = U(0)D/\nu = 35$, and $Re_{5D} = U(5D)D/\nu = 45$.

theory [163, 164, 165], which is a mature concept frequently applied in the research of wind turbines. The detailed information of the proposed methodology will be introduced later in this chapter. In addition, before performing direct 3-D and superimposed 2-D LSA, present work performs detailed 3-D calculations based on FOM/CFD and systematically analyzes the lock-in range, spectrum features, wake response, etc. Although the determination of the lock-in boundary via FOM/CFD (which involves a large number of calculations corresponding to different reduced velocity U_r cases) is very time-consuming, it could provide a detailed understanding of the lock-in behavior of the FIV system being studied and also establish a credible validation for the subsequent LSA analysis.

This chapter is arranged as follows: Section 6.1 presents the problem to be studied. From section 6.2 to 6.3, the detailed FIV responses including structural amplitude, oscillation frequency, lock-in scope, wake pattern, etc. are obtained using FOM calculation and discussed in detail. In section 6.4 and 6.5, the direct 3-D and superimposed 2-D LSA are conducted, with the corresponding results compared and validated with the FOM results. The theory of the data-driven stability analysis via the superposition of 2-D ROMs (SROM) is also explained.

6.1 Problem definition

Fig. 6.1 displays the configuration of one circular cylinder elastically mounted on a linear spring-damping unit and submerged in spanwise shear inflow. The spanwise length is set to be $L = 10D$, where D is the diameter of the circular cylinder. It has been introduced above that the lock-in behavior of the FIV system with Re higher than the critical Reynolds number Re_{cr} will involve the resonance pattern. Due to the fact that the present work focuses on the flutter pattern of flow-induced vibration, the Reynolds number is limited to a value below 45 because the lowest Re for flow past a stationary circular cylinder that can generate a vortex street is $Re_{cr} = 46.8$ [232, 233, 234]. Meanwhile, the minimum Re for the appearance of the structural instability of an elastically-supported circular cylinder is 18 [156]. Considering the points above, the range of the Reynolds number along the spanwise (z) direction of the circular cylinder is set to be $(25, 45)$ for the incident flow used in this study. More specifically, the incident flow velocity

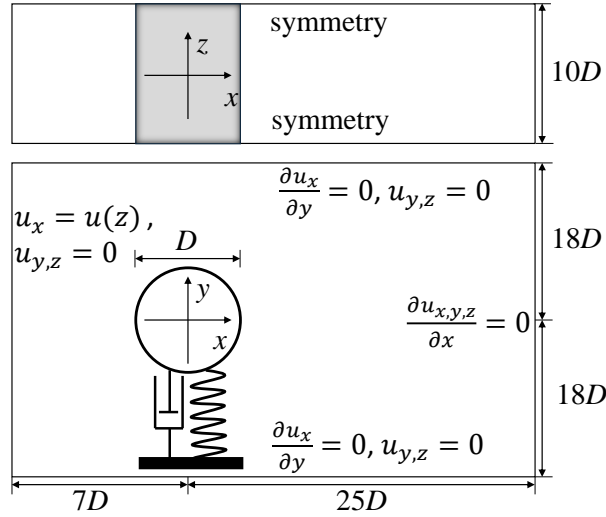


Figure 6.2: Size and boundary conditions of the 3-D computational domain for the configuration of a circular cylinder elastically mounted by linear spring in a spanwise shear flow.

$U(z)$ (viz., $= U_x(z)$) is linearly proportional to the location along the cylinder's length in the z direction, leading to $Re_{-5D} = U(-5D)D/\nu = 25$, $Re_0 = U(0)D/\nu = 35$, and $Re_{5D} = U(5D)D/\nu = 45$. In particular, $U(0)$ (viz., the velocity of incident flow at $z = 0$) is taken to define the reference velocity U_0 in present study. The mass ratio m^* and structural damping coefficient ζ is maintained constant at 10 and 0 throughout the present work. The cylinder is constrained to move in the transverse (y -) direction.

The computational domain and boundary condition for the three-dimensional (3-D) FOM/CFD calculation of FIV response in the present work is shown in Fig. 6.2. The center of the elastically-mounted circular cylinder is at the transversal centerline ($y = 0$), situated at $7D$ in x downstream from the inlet boundary. The streamwise (x -) length, the cross-stream (y -) length, and the spanwise (z -) length of the computational domain are $32D$, $36D$, and $10D$, thus creating a transverse length that is large enough to avoid any blockage effects. A zero-gradient streamwise velocity boundary condition is applied at the lateral boundaries of the domain and a Neumann boundary condition is imposed on the velocity at the outflow (outlet) boundary. A Dirichlet boundary condition was prescribed for the incident flow velocity $\vec{u} = (U_x(z), 0, 0)$ where $U_x(z)$ is the incident streamwise flow speed varying in the spanwise (z -) direction according to the manner described above. Symmetric boundary conditions are used in the two spanwise boundaries, consistent with that used in the past FIV studies [154, 136], which also involved 3-D uniform and spanwise shear inflows. The initial state of the cylinder's motion are assigned to be $y = 0, \dot{y} = 0$ (viz., cylinder at rest at $t = 0$).

The technique of overset mesh (implemented in OpenFOAM [202]) is applied in the present work with the definition of a large background mesh domain to allow sufficient transverse range for the elastically-supported cylinder to move in the transverse direction. The mesh dependency study is conducted via a 3-D simulation of shear flow (with Re ranging from 25 to 45 in the spanwise direction) past a stationary circular cylinder. Four different mesh conditions with cells number ranging from 1956765 to 2843865 are tested, and the corresponding root-mean-square (rms) lift and drag coefficients (C_L^{rms} and C_D^{rms}) are compared in table 6.1. It can be seen that the relative differences of C_L^{rms} and C_D^{rms} between mesh 1 to mesh 2 are considerable, but decrease to 0.25% and 0.11% as the mesh is refined to mesh 3 (fine) and mesh 4 (very fine). Mesh 3

Mesh	Cells number	C_L^{rms}	C_D^{rms}
1	1956765	0.001614	1.541
2	2245860	0.001752	1.654
3	2695420	0.001976	1.778
4	2843865	0.001981	1.780

Table 6.1: Aerodynamic coefficients (root-mean-square lift and drag coefficients) of shear flow past *stationary* circular cylinder with Re ranging from 25 to 45 for different mesh conditions.

is adopted in the present work to achieve the best balance of calculation time and accuracy. Fig. 6.3a and 6.3b display the overview of the hybrid overset mesh and background mesh used in the present study, with the expanded/close-up views of mesh in the immediate vicinity of the circular cylinder shown in Fig. 6.3c.

6.2 Overview of response

This section will provide an overview of the fluid-solid response using a systematic CFD/FOM calculation for one elastically-mounted circular cylinder submerged in a spanwise shear flow with the configuration introduced above. The behavior of the maximum amplitude of transverse displacements y_{\max}/D due to variations in the reduced velocity U_r is shown in Fig. 6.4 (a). First, it can be observed that y_{\max}/D exhibits a sudden increase from 0.0002 at $U_r = 5.6$ to 0.2705 at $U_r = 5.7$. Additionally, y_{\max}/D is 0.1046 and 0.0031 at $U_r = 9.4$ and 9.5, respectively. Based on these data points, the lock-in range which exhibits amplified structural amplitudes (viz., $y_{\max}/D > 0.1$) is determined to be $U_r \in (5.6, 9.5)$, which is denoted with a red background in all four sub-figures of Fig. 6.4. More precisely, y_{\max}/D reaches the largest value at $U_r = 6.2$, and then gradually decreases in the lock-in range.

Figure 6.4 (b) indicates the variation of the root mean square (rms) value of the lift coefficient C_L as a function of reduced velocity U_r . Combined with the other researchers' observations [12, 15], it is asserted that C_L^{rms} would be amplified in the flutter regime and suppressed in the resonance regime compared to that of the desynchronization regime (or, the situation of flow past a stationary cylinder). More specifically, for a system with Re above Re_{cr} , the FIV response will transition through desynchronization, flutter lock-in, resonance lock-in, and finally desynchronization again in sequence as U_r is increased. The accompanied C_L^{rms} suddenly increases to the largest value at the beginning of flutter and then gradually decreases to the lowest value at the end of resonance. In terms of the present configuration with 3-D shear flow, the overall Re are below the critical Re and consequently the flutter pattern dominates the lock-in mechanism. The corresponding behavior is seen where C_L^{rms} suddenly increases to the largest value at the start of the flutter and then gradually drops to a value close to that of a flow past stationary units. This feature is also reported by the 2-D FIV study of a circular cylinder at subcritical Reynolds numbers [155].

Since the wake field is stable at a subcritical Reynolds number outside the lock-in range (i.e., the structural amplitude is negligible), there is no external force excitation from the fluid dynamics, meaning no forced-vibration would appear. Therefore, structural vibrations are completely

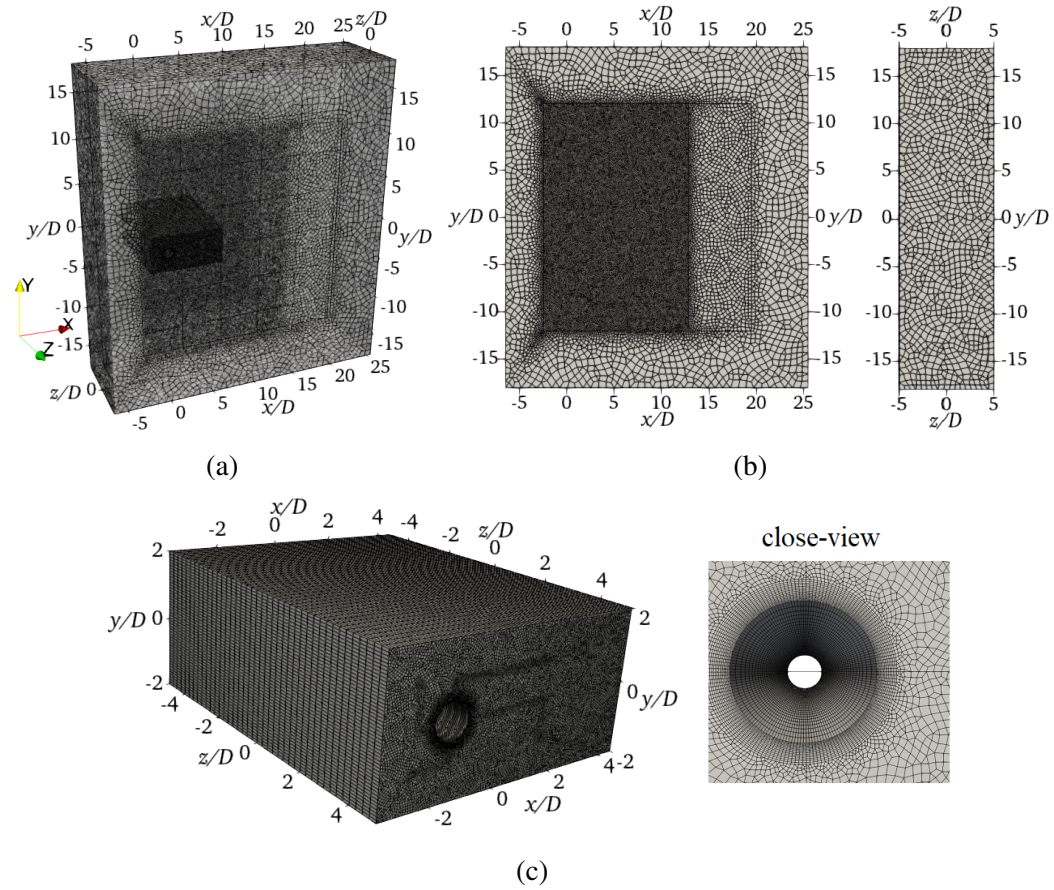


Figure 6.3: The fine mesh (mesh 3) used for the 3-D simulation of a flow past a circular cylinder: (a) the translucent view showing the background and an overset mesh surrounding the circular cylinder; (b) the background mesh; and, (c) overset mesh and expanded view of the mesh in the immediate vicinity of the walls of the circular cylinder.

dominated by the structural natural frequency, as can be seen in Figure 6.4 (c) in which the variation of $f_{osc}D/U_0$ is accompanied by the dashed line representing ' $F_s = 1/U_r$ ' in the lock-in range. This frequency response behavior is also observed in the 2-D FIV study of a circular cylinder at $(Re, m^*) = (40, 10)$ [14].

Fig. 6.4 (d) displays the change of the phase differences $\theta(^{\circ})$ between the real-time fluctuation of displacements and lift coefficients with increasing U_r . Indeed, the equilibrium point of the fluctuation of y/D or C_L is not at zero during the FIV response for certain values of U_r . As a consequence, it is necessary to calculate the phase difference after subtracting its average value (or, the value of the equilibrium point) from the time histories when calculating the phase difference between displacements and lift coefficients. It is evident that the phase difference θ immediately decays to almost 0° as lock-in behavior appears and maintains this constant level until the right boundary of the lock-in range. Based on past FIV investigations of the circular cylinder where Re is greater than Re_{cr} [15, 14, 244], the U_r of the point at which phase difference jumps to a different level and the transition point between the resonance and flutter patterns are found to almost coincide with each other. In other words, the phase difference θ stabilizes at almost exactly 0° and 180° in flutter and resonance lock-in, respectively. The present results demonstrate agreement with this relationship since it is evident that the phase difference θ remains low (close to 0°) throughout the overall lock-in range, in which only the flutter pattern exists. Based on the

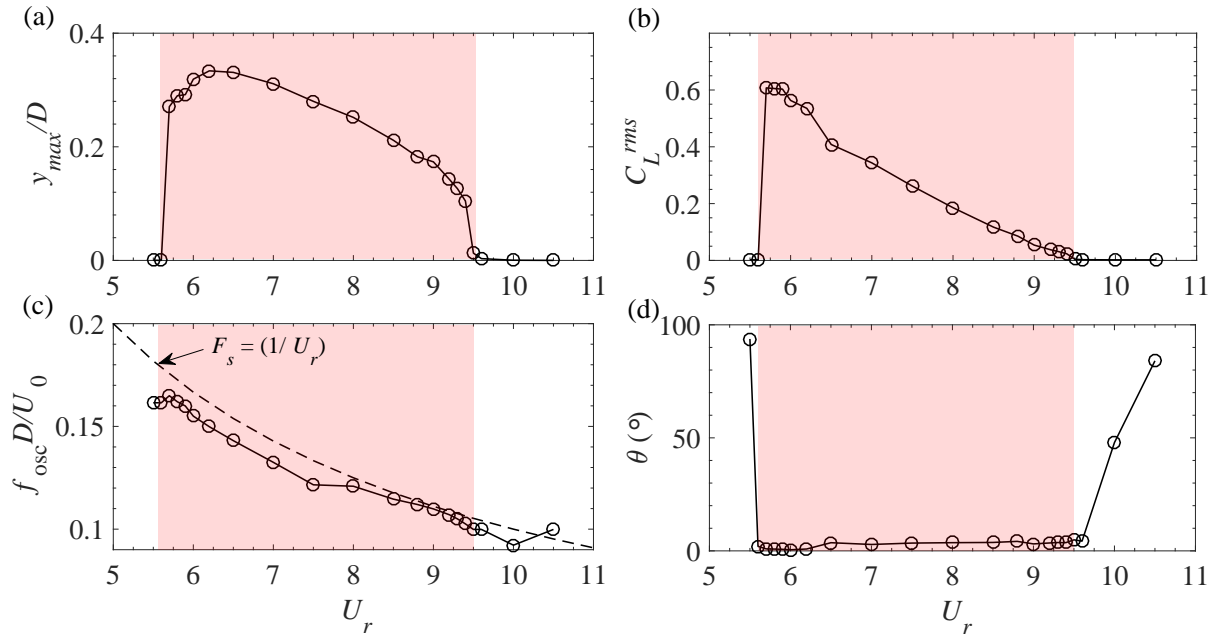


Figure 6.4: (a) Normalized maximum structural amplitude y_{\max}/D , (b) root mean square (rms) value of lift coefficient C_L^{rms} , (c) normalized structural oscillation frequency $f_{osc}D/U_0$, and (d) phase difference θ as a function of U_r . The lock-in region with amplified structural amplitude (or, with $y_{\max}/D > 0.1$) are delineated with red shading.

above analysis, it is also suggested here that the appearance of a jump in phase difference from 0° to 180° is more likely to occur in a FIV response that manifests the resonance pattern.

To further investigate the phase difference $\theta(^\circ)$ between the fluctuation of y and C_L , several representative cases with different U_r values are chosen to be examined in detail with the corresponding real-time histories of y/D and C_L plotted in Fig. 6.5. In terms of the FIV responses at $U_r = 5.6$, the curves reveal that the equilibrium positions of the fluctuation of y/D and C_L are not actually at the zero value (or, $y/D = C_L = 0$). In addition to the fluctuations caused by structural vibrations, the dynamics coefficient is superimposed with small numerical fluctuations, thus exhibiting unsmooth curves. While the structural amplitudes are amplified at $U_r = 6.0$, it is observed that the curve of the fluctuating C_L becomes smooth. In stark contrast, the structural amplitude gradually decays as U_r increases to 7.0, 8.0, and 9.0. This is accompanied by the reappearance of the sawtooth element in the C_L curve and its increasing aggravation (with increasing U_r). Furthermore, the small fluctuation amplitudes of y/D and C_L at $U_r = 9.5$ reveal the reappearance and magnification of the offset of the equilibrium point (away from 0). When the FIV response completely jumps out of lock-in range at $U_r = 10.0$ and 10.5, the structural oscillation completely disappears, as displayed in the last two panels of Fig. 6.5. In these two U_r cases, C_L remains almost constant at 1.9×10^{-3} , and there is also no observable numerical fluctuations. Overall, in all situations where there are visible oscillations in the structural amplitude, the phase difference between it and the lift coefficient excited by structural oscillation remains close to 0° in the present work.

Figure 6.6a and 6.6b show for the cases of $U_r = 6$ and 9, respectively, the real-time history (from initial state to final equilibrium state) of the transverse displacement, the corresponding time-frequency spectrum, and the spectrum for a particular part of the time-series with stabilized responses. It is noted here that the spectrum information of the amplitude response boxed within

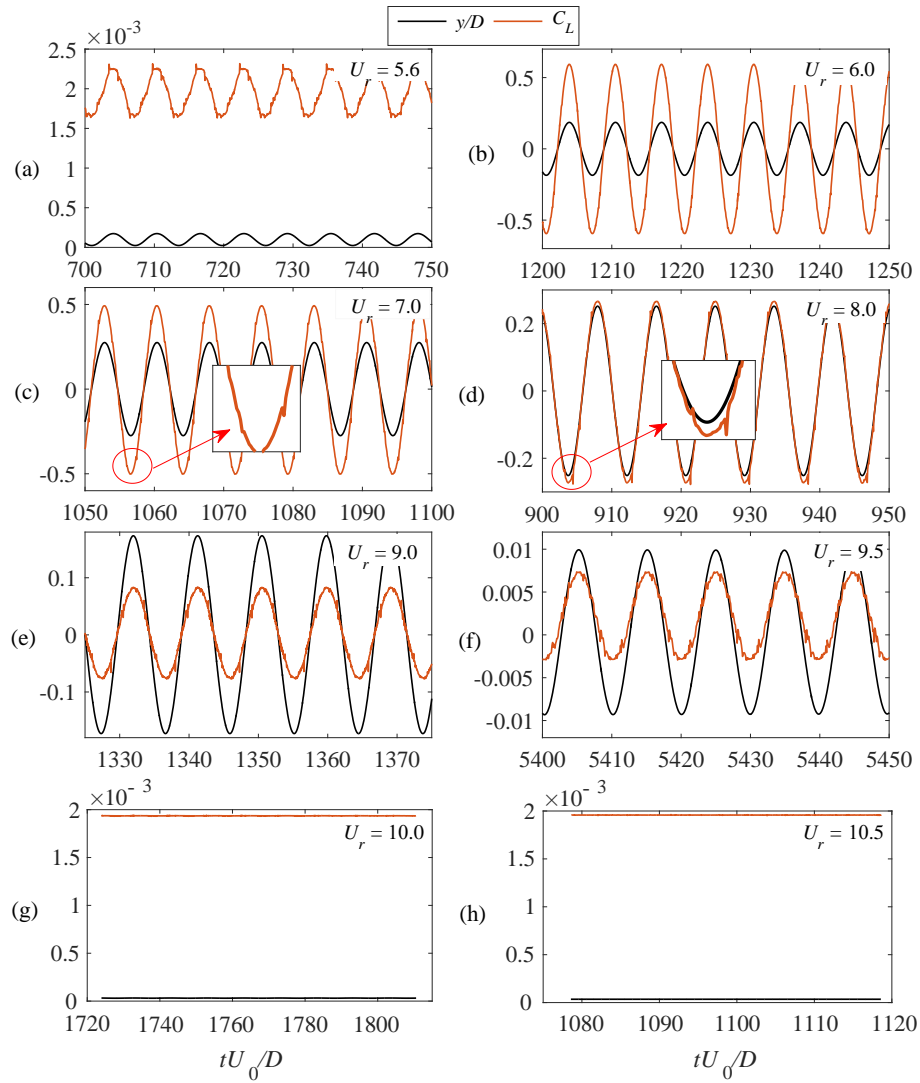
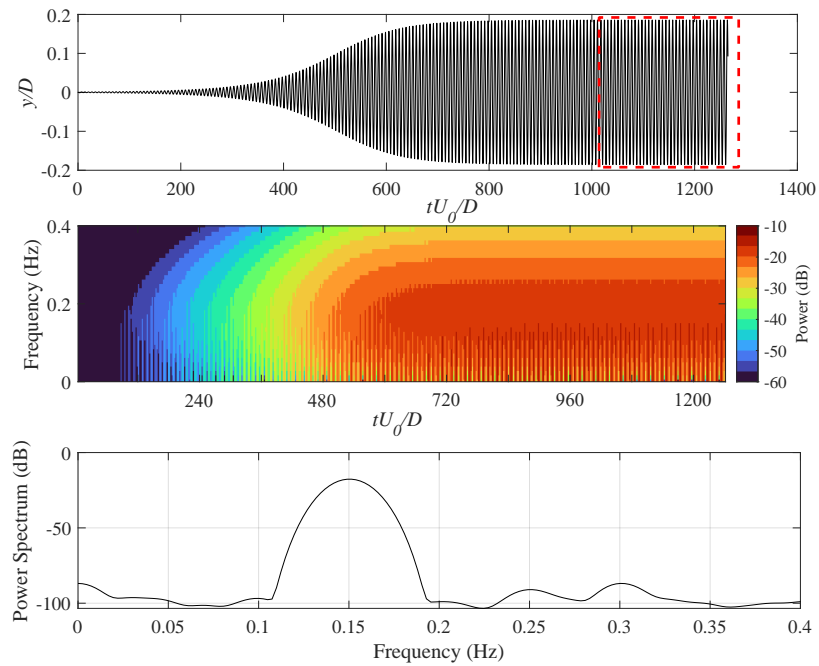
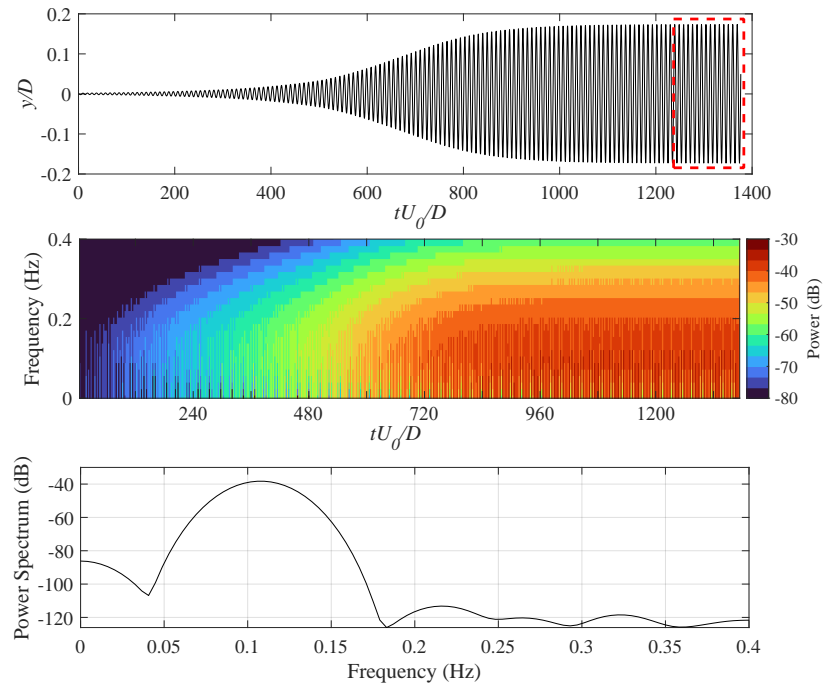


Figure 6.5: Time series of the instantaneous normalized structural amplitudes y_{max}/D and instantaneous lift coefficients C_L of FIV systems that have achieved the equilibrium state at $U_r =$ (a) 5.6, (b) 6.0, (c) 7.0, (d) 8.0, (e) 9.0, (f) 9.5, (g) 10.0, and (h) 10.5.

the red outlines in the first sub-panel is extracted and plotted on the third sub-panel. Firstly, a comparison of the real-time history of transverse displacement (first sub-panel) between $U_r = 6$ and 9 reveals that the FIV responses at $U_r = 9$ requires more lagging time than that at $U_r = 6$. This feature will be explained in the following LSA analysis. Lagging time here refers to the time it takes for an elastically supported cylinder to develop from a stationary state to an equilibrium state of oscillation. It is further observed that in the early-stage of FIV response the time-frequency spectrum (second sub-panel) of $U_r = 6$ and 9 both display the broadband features. With the development of the FIV, an intense peak gradually appears in the spectrum with the dominant frequency equal to the natural frequency. More specifically, as shown in the spectrum (third sub-panel) in Figure 6.6a and 6.6b, the final dominant frequency of transverse displacement for $U_r = 6$ and 9 are 0.155 Hz and 0.110 Hz, respectively. Additionally, although the structural amplitude of the final response reaches a stable value, its spectrum characteristics still do not exhibit the sharp contraction of the single-peak feature often seen in the FIV amplitude response with uniform inflow. The spans/scopes of the corresponding spectral peaks for $U_r = 6$



(a) $U_r = 6.0$



(b) $U_r = 9.0$

Figure 6.6: Time series of instantaneous normalized structural amplitudes y_{max}/D through the overall FIV development (first panel), the corresponded time-frequency spectrum (second panel), and power spectral density (PSD) of y_{max}/D at final equilibrium state (third panel) at $U_r =$ (a) 6.0 and (b) 9.0. The data of the time series used for PSD analysis in the third panel is sourced from the area delineated by the red-line box in the first panel.

and 9 are (0.11, 0.19) Hz and (0.04, 0.18) Hz, respectively. It would be expected that the variation of the incoming velocity of the shear flow could make the vortex-shedding mechanism highly inconsistent in the spanwise direction while generating a pressure difference in the spanwise direction, which consequently has an effect on the structural response during lock-in.

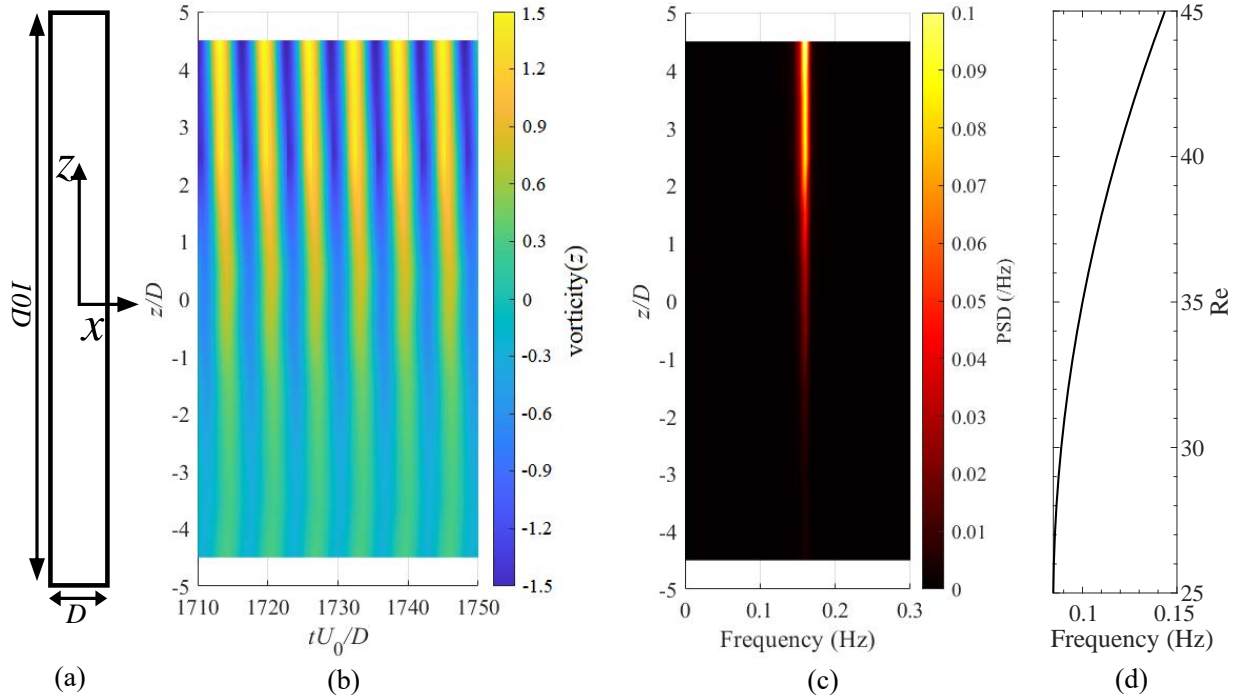


Figure 6.7: The variation in vortex-shedding behavior manifested in spanwise direction at $U_r = 5.8$: (a) view of the circular cylinder in $x - z$ plane, (b) time series of the z -components of vorticity along the span at $(x, y) = (2D, 0)$, (c) frequency spectrum along the span corresponding to the data series in (b), and (d) vortex-shedding frequency for uniform inflow past a stationary circular cylinder at Reynolds number ranging from 25 to 45.

Although the displacement of each part of the rigid body is identical, its fluid characteristics including vortex-shedding behavior vary in the spanwise direction as a result of shear inflow. Figure 6.7 (a) shows the top view (perpendicular to the y -direction) of the circular cylinder. Figure 6.7 (b,c) presents a selected time series of the z -component's fluctuations of vorticity at $(x, y) = (2D, 0)$ and the corresponding power spectral density (PSD) along the spanwise (z -) direction. It is seen in Fig. 6.7 (b) that the overall vortex-shedding behavior is very regular. More specifically, along the positive z -direction which corresponds to an increasing Reynolds number, the vorticity value has an increasing amplitude and the fluctuation of vorticity also shows an incremental lag in phase. Moreover, as observed in Fig. 6.7 (c), the power of the frequency peak becomes stronger due to the enhancement of the vortex strength. However, the peak value of the vortex-shedding spectrum does not change much along the spanwise direction because the vortex-shedding mechanism is locked by the large-amplitude vibrations of the rigid body. More specifically, the spectrum indicates that the vortex-shedding frequency is about 0.171 Hz, which is roughly the same as the structural natural frequency 0.172 Hz ($= U/U_r D = 0.1$ (m/s)/(5.8·0.1 (m))). As a comparison/reference here, in Fig. 6.7 (d) we display the vortex-shedding frequency for uniform inflow past a stationary circular cylinder at a corresponding subcritical Reynolds number ranging from 25 to 45. The data in Figure 6.7 (d) are derived from a dimensionless

fitting formulation/equation based on experimental results (describing the variation of Strouhal number St with Reynolds number) [245]. It is noted that St , which changes based on a varied inflow velocity, is converted into the vortex-shedding frequency shown here.

6.3 Wake pattern

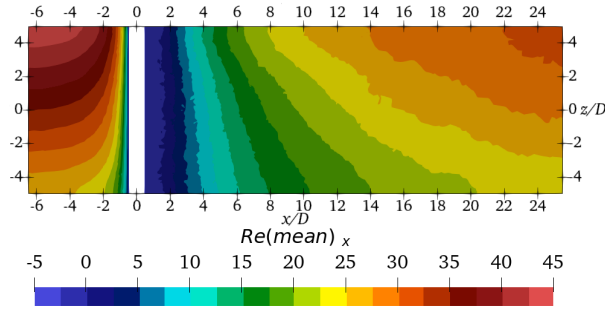


Figure 6.8: Reynolds number $Re(\text{mean})_x$ corresponding to the x -component of mean velocity on the $x-z$ plane at $y = 0$ when the FIV system reaches equilibrium state at $U_r = 6.0$.

Fig. 6.8 displays the x -component of the mean Reynolds number $Re(\text{mean})_x$ on the slice at $y = 0$ for $U_r = 6$, where $Re(\text{mean})_x = U(\text{mean})_x D / \nu$ and $U(\text{mean})_x$ is the x -component of mean velocity. Firstly, figure 6.8 shows that the Reynolds number range of the incoming flow from the left is (25, 45). The incident flow reaches stagnation when it hits the left edge of the slice of the cylinder, and the velocity drops rapidly to zero in the entire spanwise (z -) range. In addition, the cylinder produces a recirculation area in the downstream region of $x/D < 2$. The lengths in the streamline (x -) direction for this recirculation area do not differ substantially in the spanwise (z -) direction. Furthermore, the Reynolds number gradually recovers to the level of the incoming flow as the wake progresses further downstream.

Fig. 6.9 displays the three-dimensional translucent vorticity contour of the FIV response of the circular cylinder at $U_r = 5.6, 6.0, 9.0,$ and 9.5 . Specifically, $U_r = 5.6$ and 9.5 correspond to the left and right bounds of the lock-in range, and the corresponding maximum normalized structural amplitudes y_{\max}/D at the final equilibrium states are both smaller than 0.01. Therefore, at and beyond these bounds the effect of structural oscillation on the wake flow becomes negligible and the FIV response can be regarded as the same as that for a flow past a stationary cylinder. Moreover, as introduced above, the Hopf-bifurcation would not appear at subcritical Reynolds numbers for a circular cylinder. As a consequence, no visible vortex behavior is formed at $U_r = 5.6$ and 9.5 . In addition, since the incoming velocity gradually increases with the positive z -direction due to the shear inflow, the streamwise distance from the right-end of the contour/isosurface at a certain value of the vorticity magnitude to the centerline of the cylinder gradually increases in the positive z -direction. In other words, the vortex contour appears to extend more downstream as z/D increases. In terms of $U_r = 6.0$ and 9.0 in Fig. 6.9b and 6.9c, the vortex is detached from and shed by the wall surface in the wake as a result of the large-amplitude vibration of the structure. A further perusal found that the vortex structure in the wake could be interpreted as a vortex tube, with the tube's centerline also skewed in the streamline (x -) direction as the z -coordinate increases. More specifically, unlike the 2S-2P hybrid wake pattern discovered by Techet et al. [246] in the 3-D wake study of the tapered cylinder oscillating in a uniform flow,

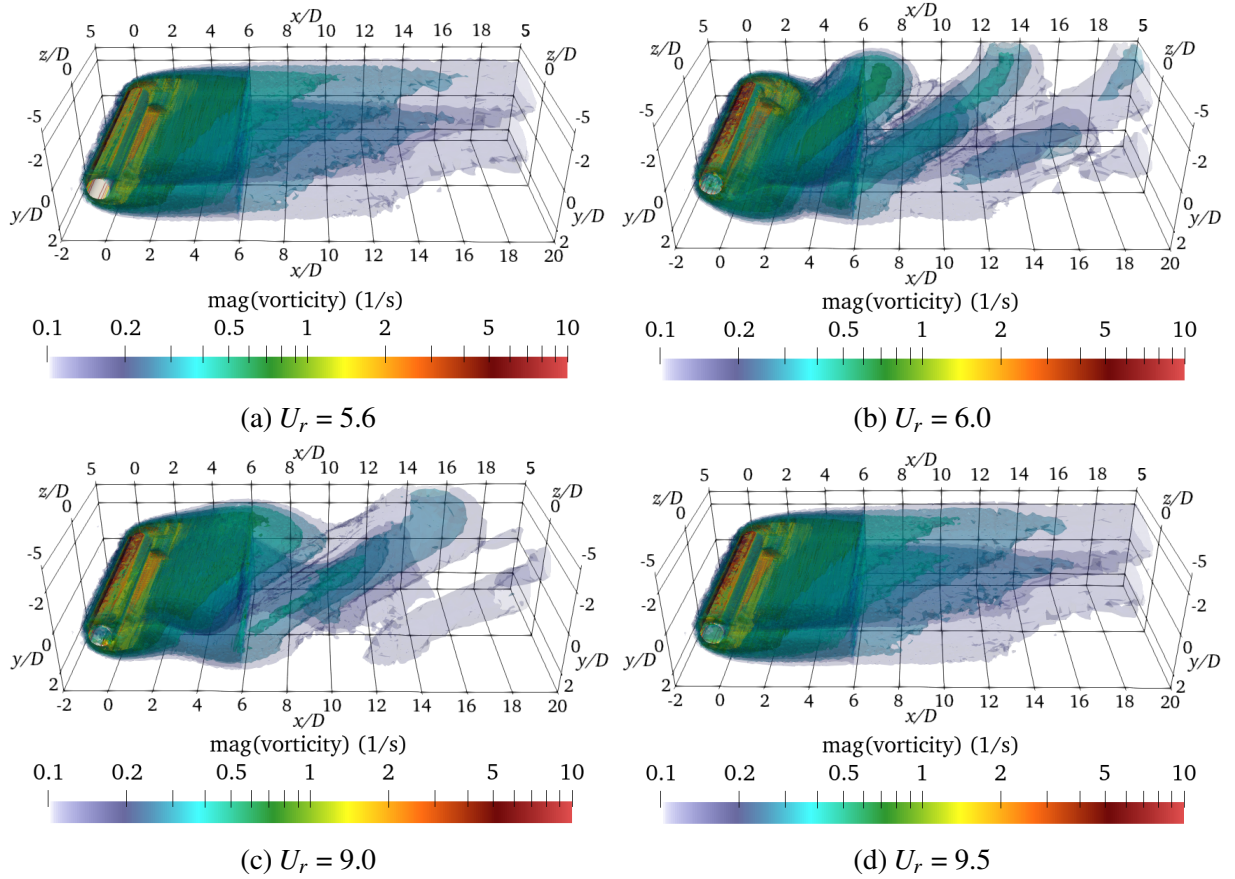


Figure 6.9: Instantaneous iso-surfaces of magnitudes of vorticity downstream of the cylinder at $U_r =$ (a) 5.6, (b) 6.0, (c) 9.0, and (d) 9.5.

the wake flow calculated herein only exhibits a 2S pattern. Moreover, the FIV response at $U_r = 6.0$ with $y_{max}/D = 0.319$ displays a wider transverse (y -) width of the vortex-street than that of $U_r = 9.0$ with $y_{max}/D = 0.173$.

Figure 6.10 displays the three-dimensional streamlines near the cylinder for $U_r = 6.0, 7.0, 8.0,$ and 9.0 . Incidentally, the computational domain of the streamlines exhibited here is chosen to be the fields of the overset meshes designed for this study, which was shown previously in Fig. 6.3c. Firstly, the presence of the cylinder causes a low-pressure region to appear in the wake flow. The velocity gradient of the shear flow in the spanwise direction in the vicinity and downstream of the cylinder creates a pressure gradient in the z -direction, and this pressure gradient then leads to the spanwise stream observable near the core of the main vortex area. Furthermore, at the top boundary which is constrained with symmetric boundary conditions, the spanwise stream is blocked and a vortex perpendicular to the cylinder is formed. These vortices affect and weaken the spanwise vortices. Such observations are also reported by Zhao [154]. With more scrutiny, it is found the flow along the spanwise streams is stronger near the main vortex core of the cylindrical wake for $U_r = 6$ and 7 than for $U_r = 8$ and 9 . This is because the maximum vibration amplitudes corresponding to $U_r = 6$ and 7 are larger than those for $U_r = 8$ and 9 .

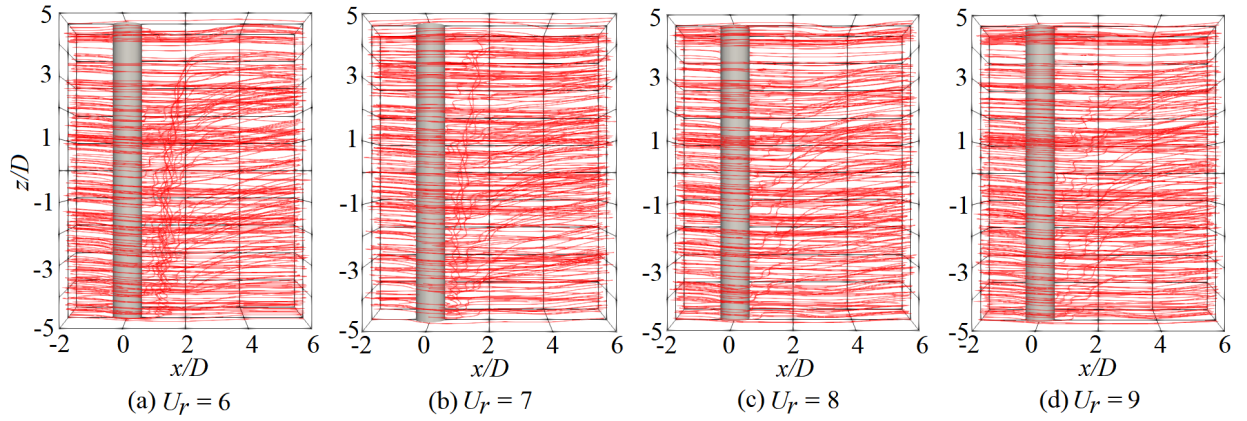


Figure 6.10: Instantaneous streamline around the circular cylinder at $U_r =$ (a) 6.0, (b) 7.0, (c) 8.0, and (d) 9.0.

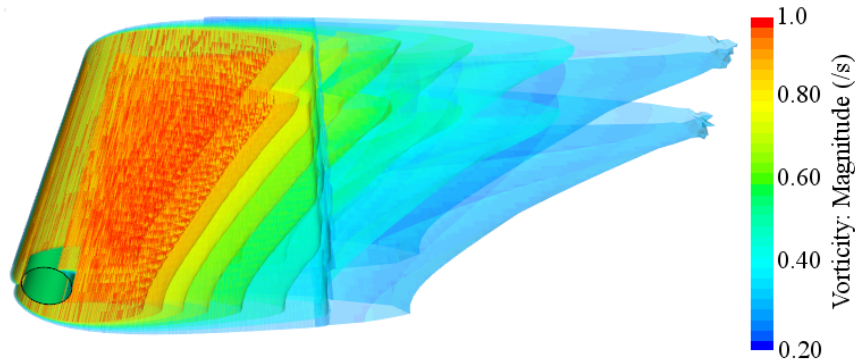


Figure 6.11: The three-dimensional translucent contour of vorticity magnitudes of the base flow for shear inflow past a stationary circular cylinder with Re ranging from 25 to 45.

6.4 Three-dimensional data-driven stability analysis

In this sub-section, the data-driven stability analysis of the FIV response of a circular cylinder with shear inflow is directly undertaken within the 3-D domain. More specifically, the 3-D base flow for spanwise shear flow past the cylinder is first obtained, and then one impulse (input) of transverse (y) displacement is imposed on the cylinder body with the resulting dynamic response of C_L (output) resolved/predicted by FOM/CFD. The ERA identification technology is applied to obtain the ROM of fluid dynamics in the 3-D domain based on the dynamic response of C_L (output). Then, the state-space form of the fluid ROM is coupled with the structural state-space form to construct the coupled 3-D ROM for the FIV system as introduced in previous sub-section introducing ERA method. Within the calculation of lift coefficients C_L in the present work, we note that the reference velocity is maintained as the mean value of inflow velocity and also equal to $U(0)$ at $z = 0$. Fig. 6.11 displays the vorticity contours of the base flow of the stationary circular cylinder subjected to spanwise shear inflow. As a whole, the vorticity distribution of the base flow is analogous to the contour of FIV response at $U_r = 5.6$ and 9.5 with tiny structural amplitudes (cf. with figure 6.9), which is due to the fact that the flow Reynolds number remains in the subcritical Reynolds number range throughout the entire computational domain.

The root loci of the two uncoupled modes SM and WM provided by the direct 3-D ROM of FIV system at $(Re, m^*) = ((25, 45), 10)$ is plotted in Fig. 6.12a. It is noted the trajectory of just one

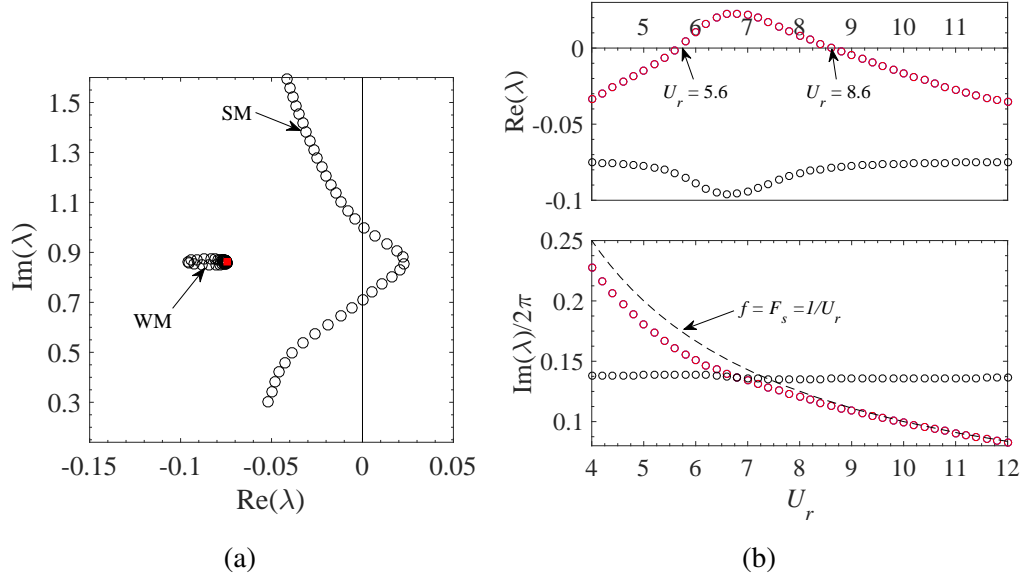


Figure 6.12: (a) The root loci and (b) the variation of the growth/decay rate $\text{Re}(\lambda)$ and eigenfrequency $\text{Im}(\lambda)/2\pi$ as a function of U_r for the studied FIV system. The structure mode SM is demarcated with red symbols. The dotted line corresponds to the relationship $f = F_s$.

WM appears in the determined/chosen range of the complex coordinate system. Additionally, this single WM is located in the stable left-half plane ($\text{Re}(\lambda) < 0$). This is in agreement with the physical fact that no vortex street is generated in this case. The growth rate $\text{Re}(\lambda)$ and eigenfrequency $\text{Im}(\lambda)/2\pi$ as a function of reduced velocity U_r is plotted in Fig. 6.12b. The trajectory of SM is marked in red. A perusal of Fig. 6.12b indicates that the unstable regime of the structural mode SM ranges from a U_r of 5.6 to 8.6. The U_r range for the unstable structural mode (predicted by the data-driven stability analysis) or the lock-in phenomenon (predicted by FOM/CFD) is referred to as \tilde{U}_r , and by this notation \tilde{U}_r (3-D ROM) = (5.6, 8.6). Comparing the \tilde{U}_r (3-D ROM) with \tilde{U}_r (FOM) ($\in (5.6, 9.5)$), it is found that the prediction of the left-boundary is of excellent accuracy, whereas the right-boundaries show a significant difference. It is expected that dynamic interactions in the spanwise (z -) direction would have nonlinear effects on the ERA identification process, thus explaining the prediction flaws of the direct 3-D ROM observed here.

6.5 Data-driven stability analysis via SROM

In advance of conducting a data-driven stability analysis via the novel superposition of 2-D ROM (SROM) for a practical case, a simple example is presented herein to explain how to superimpose 2-D ROMs for the purpose of analyzing an FIV system with a 3-D domain and shear inflow. As presented in Fig. 6.13, the inflow velocity is defined with a smooth linear increase from 0 to $2U_0$ along the z -axis (in the original configuration on the left), with a mean value of velocity of U_0 at $z = 0$. The span length of the circular cylinder is then divided into 3 identically sized elements in the modified configuration shown on the right. Therefore the velocity ranges of element 1, 2, and 3 are $(0, U_0/3)$, $(U_0/3, 2U_0/3)$, and $(2U_0/3, U_0)$, respectively. In this case each element is simplified to be experiencing a uniform inflow velocity so that we can apply a 2-D

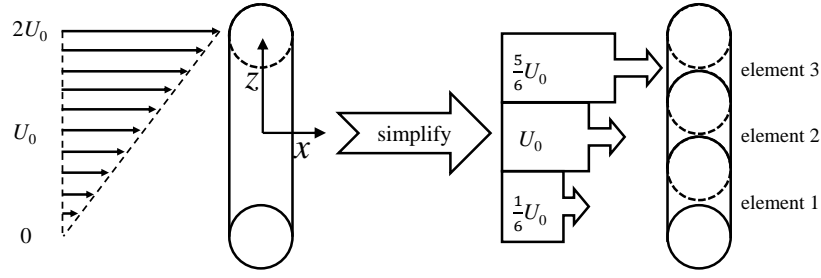


Figure 6.13: Illustration of a simple superposition case: the procedure for dividing a circular cylinder with linear shear inflow (with incident velocity ranging from 0 to $2U_0$) into three identically sized elements each subject to a uniform inflow along the spanwise direction.

calculation to resolve the corresponding domain. After the simplification, the inflow velocity for element 2 is still U_0 , whereas the velocity of inflow for element 1 and 3 are determined based on averaging the velocity at the element bounds to be $U_0/6$ ($= (0 + U_0/3)/2$) and $5U_0/6$ ($= (2U_0/3 + U_0)/2$), respectively.

For each element in a 2-D situation, the ERA identification is undertaken and the corresponding state-space sub-form is thus obtained as follows:

$$\begin{aligned} \dot{x}_r(t) &= A_r^e x_r(t) + B_r^e u_r(t), \\ y_r(t) &= C_r^e x_r(t) + D_r^e u_r(t), \end{aligned} \quad (6.1)$$

with $e = 1, 2$, and 3 denoting element 1, 2, and 3, respectively. For this case (represented by the right diagram in Fig. 6.13) in which the spanwise length along the z -axis is equally divided, the weight of each element is equal, and consequently the overall system matrices are expressed as:

$$(A_r^a, B_r^a, C_r^a, D_r^a) = \sum_{e=1}^3 \frac{1}{3} (A_r^e, B_r^e, C_r^e, D_r^e). \quad (6.2)$$

However, if the ratio of the spanwise length of each element to the total spanwise length is nonuniform across elements, the inner coefficient ($1/3$ in the above equation 6.2) of the sub-system matrices should also be adjusted accordingly when superimposing. Moreover, it is emphasized again that the reference velocity for calculating C_L in the structural formula should be unique/fixed, so it is set as the mean value of the entire shear inflow U_0 herein. As a consequence, the reference velocity used for the calculation of C_L is still U_0 even for element 3 (which has an inflow velocity of $5U_0/6$) and element 1 (which has an inflow velocity of $U_0/6$) during the ERA identification for flow dynamics.

The superposed system matrices $(A_r^a, B_r^a, C_r^a, D_r^a)$ for the fluid dynamics (cf Eq. 6.2) are coupled with the system matrices (A_s, B_s, C_s, D_s) for the structural dynamics (cf. Eqs 4.17) to yield the system matrix \mathbf{A}_{rs}^a of the simplified reduced-order coupled model for the FIV system with 3-D shear inflow:

$$\mathbf{A}_{rs}^a \equiv \begin{bmatrix} A_s + qB_s D_r^a C_s & qB_s C_r^a \\ B_r^a C_s & A_r^a \end{bmatrix}. \quad (6.3)$$

Then, the leading eigenvalues for \mathbf{A}_{rs}^a are extracted for corresponding analysis using a methodology similar to the one introduced in the previous sub-section. The mesh settings and associated parameters for the attainment of individual 2-D ROMs for each element are identical to those

used in our previous work [244].

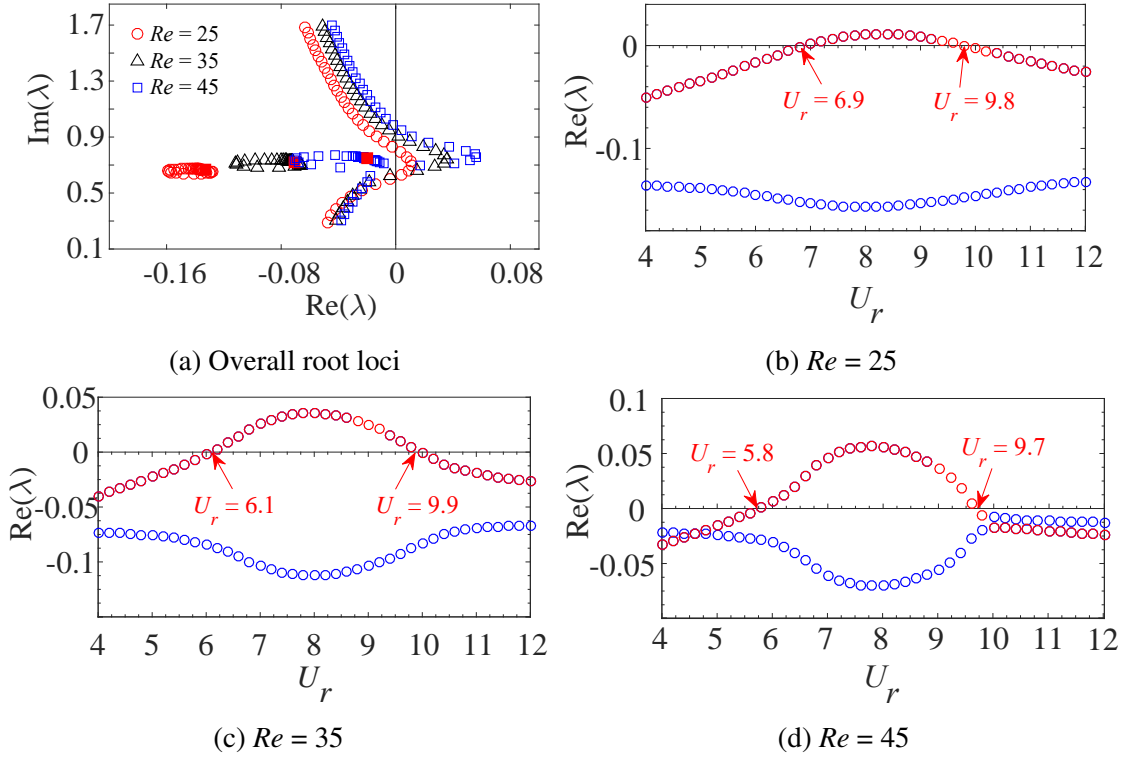


Figure 6.14: (a) The overall root loci and (b, c, d) the variation of the growth/decay rate $Re(\lambda)$ and eigenfrequency $Im(\lambda)/2\pi$ as a function of U_r for the 2-D FIV system with uniform inflow at $Re =$ (b) 25, (c) 35, and (d) 45. In (b, c, d), the structure mode and wake mode are demarcated using red and blue symbols, respectively.

Before performing the novel superposition of 2-D ROMs (SROM) to predict the 3-D VIV response with spanwise shear inflow, the modal root loci for single 2-D ROMs with VIV at separate Re of 25, 35, and 45 are investigated. It is found, as expected, that applying 2-D ROM to predict the lock-in range of VIV response with uniform inflow at subcritical Reynolds numbers is quite accurate/credible. This has been demonstrated by previous chapters and other investigations [156, 14]. The overall root loci for 2-D ROM-based VIV at three Re values are displayed in Fig. 6.14a. It is observed that the eigenvalue distribution at Re of 25 and 35 correspond to the uncoupled modal situation and that at Re of 45 corresponds to the coupled modal situation. Moreover, the wake modes for all three Re values experience the stable state with $Re_{WM}(\lambda) < 0$. The real part $Re(\lambda)$ of eigenvalues as a function of U_r are re-plotted in Fig. 6.14b, 6.14c, and 6.14d, with structural mode SM or SM_c delineated with red circle markers. The U_r ranges of the positive $Re_{SM/SM_c}(\lambda)$ are (6.9, 9.8), (6.1, 9.9), and (5.8, 9.7) for Re at 25, 35, and 45, respectively. The purpose of introducing the VIV response under a 2-D uniform flow here is to prove that in the case of subcritical Reynolds numbers, the U_r lock-in range boundaries for different Reynolds numbers are noticeably different. These considerable discrepancies thus establish a baseline for highlighting the comparative accuracy of the following prediction using SROM.

For the initial attempt of SROM, we divide the structural body into identically sized cylindrical elements with each element subjected to a uniform 2-D incoming flow. This identical-size division strategy is named SROM1 in the present work and is shown in Figure 6.15. For the superpositions (a) and (b) in Fig. 6.15, the spanwise length of the circular cylinder is divided into

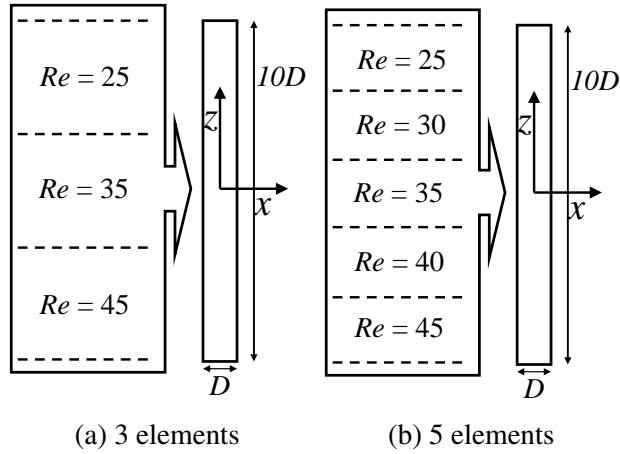


Figure 6.15: Diagram showing the division of the cylinder column equally along the spanwise direction into (a) 3 and (b) 5 elements for the superposition of 2-D ROMs (SRM1).

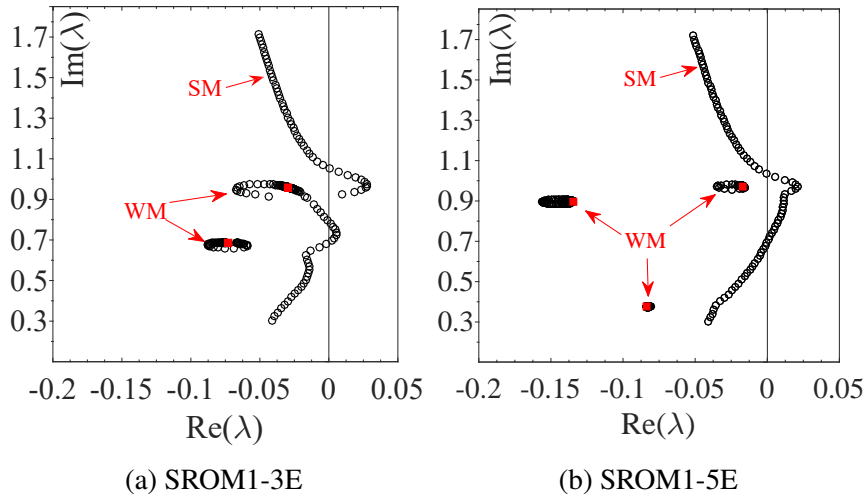


Figure 6.16: The root loci, obtained by the SRM1 with (a) 3 and (b) 5 elements, for the studied FIV system with spanwise shear inflow.

3 and 5 elements with identical lengths, in which Re values at each element are (25, 35, 45) and (25, 30, 35, 40, 45), respectively. This lays out the two SRM1 cases that will be evaluated.

In accordance with the calculation results obtained using FOM/CFD, the response of the FIV configuration studied in this chapter has one single uninterrupted lock-in interval, and the U_r value corresponding to the left- and right-boundaries are 5.6 and 9.5 respectively. In other words, the structural instability occurs in the continuous U_r interval without interruption. In stark contrast, the root loci of SM in Fig. 6.16a moves to the positive plane then returns to the negative plane twice with increasing U_r , which disagrees with the stability situation predicted by the calculation of FOM/CFD. As the element number increases to 5, a continuous instability interval of the structural mode emerges as shown in Fig. 6.16b.

The root loci of the 2-D superposition strategy with 5 identical elements (cf. with Fig. 6.16b) is re-plotted in Fig. 6.17, in which the growth rate $Re(\lambda)$ and eigenfrequency $Im(\lambda)/2\pi$ as a function of reduced velocity U_r are displayed. The trajectory of SM is marked with red. First, the $Im(\lambda)/2\pi$ for the two WM remain almost constant at around 0.15, and the variation of $Im(\lambda)/2\pi$

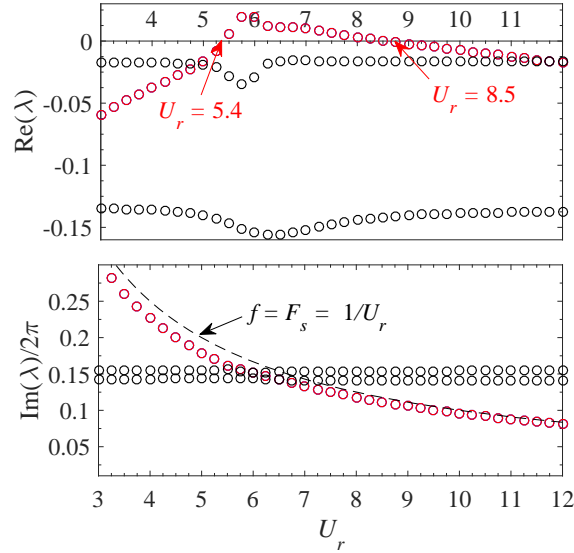


Figure 6.17: The variation of the growth/decay rate $\text{Re}(\lambda)$ and eigenfrequency $\text{Im}(\lambda)/2\pi$ as a function of U_r , obtained using SR0M1-5E, for the studied FIV system with spanwise shear inflow. The structure mode and wake modes are demarcated with red and black symbols, respectively, and the dotted line corresponds to the relationship $f = 1/U_r$.

for SM correlates with the dotted line ($f = F_s$). This demonstrates that the eigenfrequencies of SM and WM are correlated to reduced natural frequency and vortex-shedding frequency respectively. It should be emphasized that vortex-shedding behavior refers to the wake pattern of the FIV response herein, not the fluid dynamics for flow past a cylinder at stationary state due to the fact that the wake mode is stable at $Re < Re_{cr}$ here. Secondly, the U_r value of the left- and right-boundaries for the range of structural instability are 5.4 and 8.5, respectively, still demonstrating non-negligible errors compared to the results predicted by the FOM.

However, it is found after further analysis that the above element-division strategy consists of flaws. The Reynolds numbers of the incoming flow at the two physical boundaries of the circular cylinder in the spanwise direction are 25 and 45, respectively. With this in mind, the length of the elements situated at both ends should be set to half of the length of the intermediate elements when segmenting the cylinder if the Re corresponding to the two boundary elements are predetermined as 25 and 45. When the cylinder is divided into n elements with the spanwise length of the elements at both ends ($e = 1, n$) half that of the elements spanning the middle area between them ($1 < e < n$), the resulting formulation becomes:

$$(A_r^a, B_r^a, C_r^a, D_r^a) = \sum_{e=1, n} \frac{1}{2(n-1)} (A_r^e, B_r^e, C_r^e, D_r^e) + \sum_{e=2}^{n-1} \frac{1}{n-1} (A_r^e, B_r^e, C_r^e, D_r^e). \quad (6.4)$$

Based on this new proposition, the updated strategy, named SR0M2 in the present work, for the superposition of 2-D data-driven stability analysis will be evaluated (cf. with Fig. 6.18). This type of division strategy continuously encodes the partition density of the cylinder with its associated Reynolds number increment between adjacent elements set to 10 (coarse), 5 (medium), to 2.5 (fine), respectively.

The root loci of the VIV system obtained using SR0M2 of the coarse (cf. with Fig. 6.18a) and medium (cf. with Fig. 6.18b) discretization fineness are displayed in Fig. 6.19. As with the case of SR0M1 discretized into 3 identical elements (Fig. 6.16a), the 3-element case in SR0M2

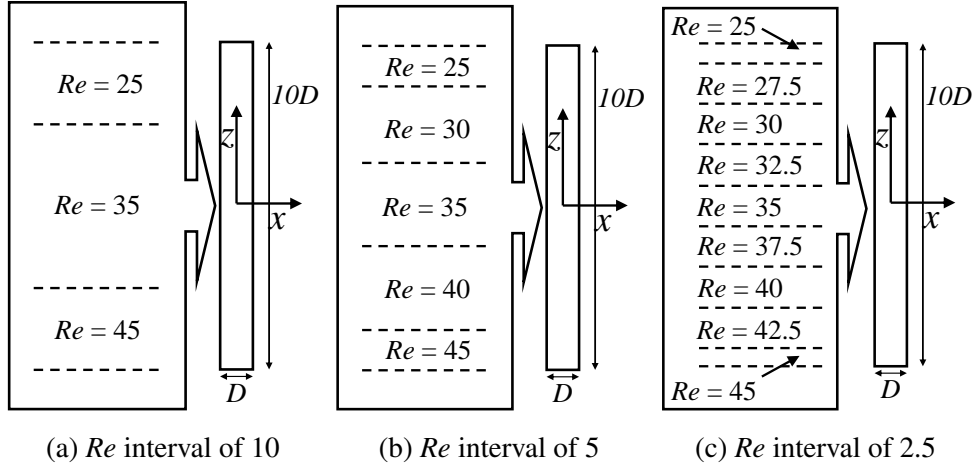


Figure 6.18: Diagram showing division of the cylinder column with the spanwise length of the two end elements set to half of the intermediate elements for the superposition of 2-D ROMs (SRM2). The increment of Reynolds number in (a), (b), and (c) are 2.5 (fine division), 5 (medium division), and 10 (coarse division), respectively.

here (Fig. 6.19a) also predicts discontinuous instability intervals for the structural mode, showing that such few elements prove too coarse to correctly capture the lock-in range. As the interval of Re is reduced to 5 (or, for the case of SRM2-5E), a continuous range of structural instability appears in Fig. 6.19b, and the associated equation for matrix superposition is converted to the form:

$$(A_r^a, B_r^a, C_r^a, D_r^a) = \sum_{e=1,5} \frac{1}{8} (A_r^e, B_r^e, C_r^e, D_r^e) + \sum_{e=2}^4 \frac{1}{4} (A_r^e, B_r^e, C_r^e, D_r^e). \quad (6.5)$$

The root locus is replotted in Fig. 6.20, which describes the variation of $\text{Re}(\lambda)$ and $\text{Im}(\lambda)/2\pi$ with U_r . A perusal of the SM trajectory shows that the range of the positive growth rate $\text{Re}(\lambda)$ of SM starts from $U_r = 5.5$ and ends at $U_r = 9.3$. In comparison to the U_r interval ($\in (5.6, 9.5)$) of flutter lock-in predicted by the FOM/CFD method, considerable errors are still found in the results obtained using SRM2-5E, but the accuracy of the prediction via data-driven stability analysis has already been greatly improved.

To further increase the prediction accuracy of present SRM2 analysis, the superposition configuration in Fig. 6.18c is analyzed and the accompanying equation 6.2 is derived as:

$$(A_r^a, B_r^a, C_r^a, D_r^a) = \sum_{e=1,9} \frac{1}{16} (A_r^e, B_r^e, C_r^e, D_r^e) + \sum_{e=2}^8 \frac{1}{8} (A_r^e, B_r^e, C_r^e, D_r^e). \quad (6.6)$$

The eigenvalue distribution with a fine Re interval of 2.5 (SRM2-9E) is shown in Fig. 6.21. Firstly, it is observed that there is only one dominating wake mode in Fig. 6.21a, which is in line with the physical meaning (the reader is referred to the analysis presented for the direct 3-D LSA). Furthermore, it was asserted in our past work [244] that the second dominant WM will not appear until Re increases to 100 at laminar flow. There should be only one dominant WM at a subcritical Re , which can also be observed in the modal situation (cf. with Fig. 6.12a) for the 3-D data-driven stability analysis presented in sub-section 6.4. Although the prediction of the lock-in boundary via 3-D data-driven stability analysis is inaccurate, its modal physical insights are still valuable and credible. Secondly, the growth rate $\text{Re}(\lambda)$ of SM (marked with red) in Fig. 6.21b indicates that SRM2-9E (with a Re interval of 2.5) provides a prediction of lock-in range with \tilde{U}_r (SRM2-9E) $\in (5.6, 9.5)$, where the growth rate $\text{Re}(\lambda)$ is 0 at these U_r bounds for

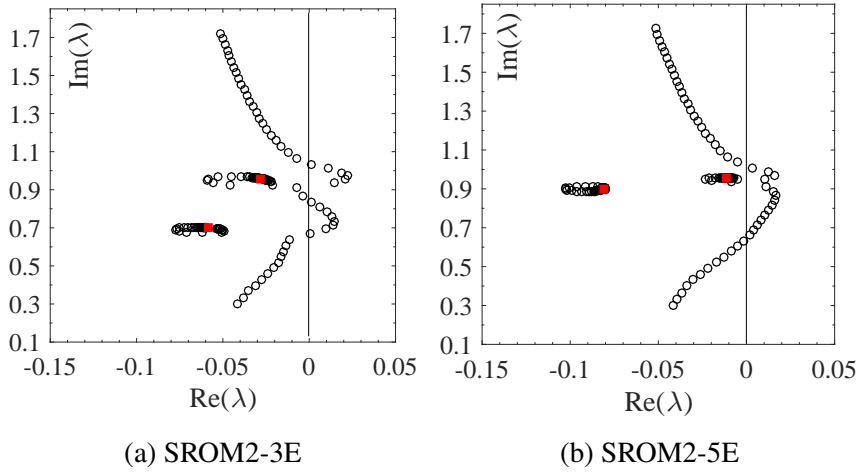


Figure 6.19: The root loci, obtained using the SROM2 with (a) 3 and (b) 5 elements, for the FIV system being studied with spanwise shear inflow.

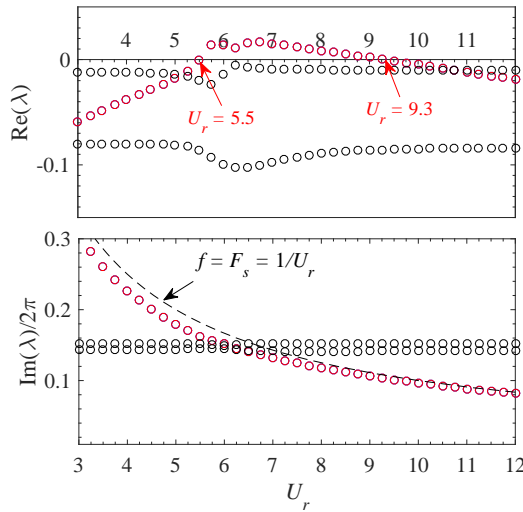


Figure 6.20: Growth/decay rate $\text{Re}(\lambda)$ and eigenfrequency $\text{Im}(\lambda)/2\pi$ as a function of U_r , obtained by SROM2-5E, for the FIV system with spanwise shear inflow being studied.

SM, demonstrating a high-precision agreement with the FOM predictions.

The FSI response at the left and right boundaries of the lock-in reflects the dynamics of the system at the edge of stability. In an effort towards this objective, the structural amplitude time-history for $U_r = 5.6, 5.7, 9.4,$ and 9.5 are displayed in Fig. 6.22. The maximum amplitude y_{max}/D for $U_r = 5.6$ and 9.5 are 0.00017 and 0.009 , respectively, which proves that the structural state is stable in those two cases and conforms to the fact that the growth rate $\text{Re}(\lambda) = 0$ at $U_r = 5.6$ and 9.5 . Based on the above evidence, it can be asserted that SROM2-9E here achieves a near-perfect prediction accuracy in comparison with FOM/CFD results. Moreover, the amplitude responses corresponding to the two lock-in endpoints both show a tendency to expand first and then contract, and the equilibrium position of structural oscillation for $U_r = 5.6$ shifts from the origin position (i.e.: $y = 0$). On the other hand, the y_{max}/D for $U_r = 5.7$ and 9.4 finally reaches 0.271 and 0.105 , respectively, which are considerably large structural amplitudes that demonstrate the FSI system belongs to the lock-in regime. A striking phenomenon is that the FSI system at $U_r=9.4$ consumes considerable time ($tU_0/D > 1500$) before reaching the final equilibrium state.

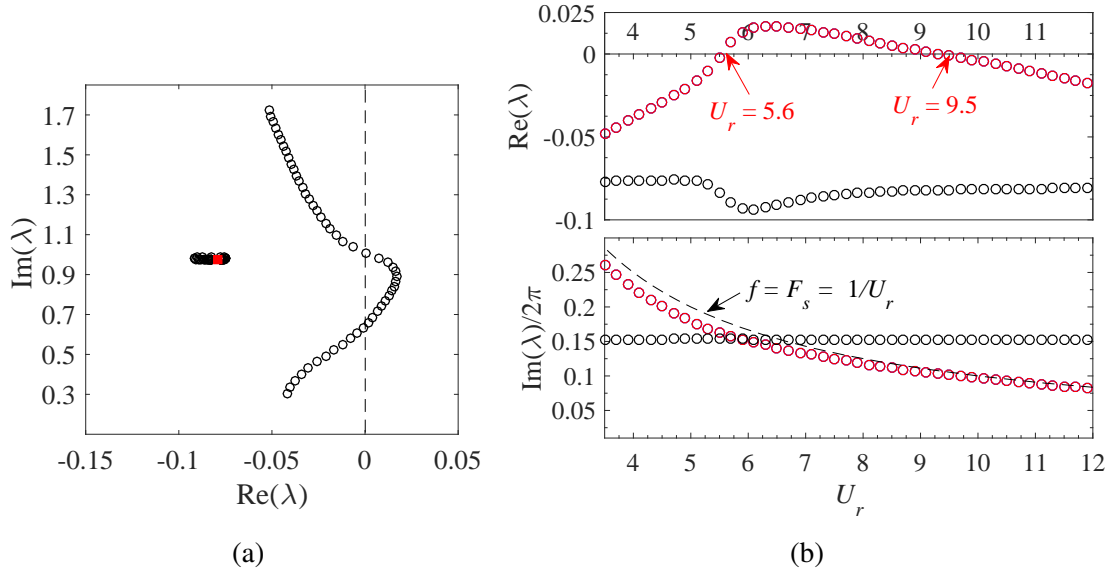


Figure 6.21: (a) The root loci and (b) the variation of the growth/decay rate $\text{Re}(\lambda)$ and eigenfrequency $\text{Im}(\lambda)/2\pi$ as a function of U_r , obtained by SRM2-9E, for the FIV system being studied.

Whether the lagging time of the FIV development implies some hidden physical meaning will be investigated below.

Fig. 6.23 compares the the growth rate $\text{Re}(\lambda)$ and lagging time as a function of reduced velocity U_r . We note that only the FIV response belonging to the lock-in regime (or, with an unstable structural mode) is displayed here. To begin, it could be seen that in the lock-in regime, the value of the growth rate obtained by SRM and the value of lagging time obtained by FOM/CFD show a clear inverse correlation. In the initial stage of FIV development, the dynamic characteristics of FSI could be regarded as a linear relationship, and the expansion rate of the structural amplitude will maintain a nearly constant value throughout this stage. The expansion rate of the amplitude is the physical meaning of growth rate in linear stability analysis [247]. In the smaller sub-plots of Fig. 6.22b and 6.22c, the time-history with a log scale of displacement y is presented, and it is evident that the peak amplitude increases almost linearly with the time variation. It should be emphasized that the linear relationship here is not perfect, because the three-dimensional shearing inflow will pull the wake in the spanwise direction, which would have a certain impact on the linear dynamics features in the initial stage of FIV development. Additionally, the SRM-based LSA method divides the circular cylinder into several elements, which also introduces some simplification/discretization errors. This linear feature is gradually replaced by nonlinear dynamic characteristics with the enhanced body amplitude and the increasing complexity of the flow field, and the structural response finally enters into the limit-cycle. As a consequence, the lagging time is minimum around $U_r = 6.2$ and reaches a maximum value near the right boundary ($U_r > 9$) of the lock-in range.

Since an ERA-based ROM is essentially a linear state-space model, under the same input of displacement input h , the linear (superposition) relationship between the transfer matrices (\tilde{A}_r^e , \tilde{B}_r^e , \tilde{C}_r^e , \tilde{D}_r^e) of the sub-elements can be completely transplanted to the corresponding relationship of its output (of C_L) with no change, that is:

$$y_r^a = \sum_{e=1,n} \frac{1}{2(n-1)} y_r^e + \sum_{e=2}^{n-1} \frac{1}{n-1} y_r^e, \quad (6.7)$$

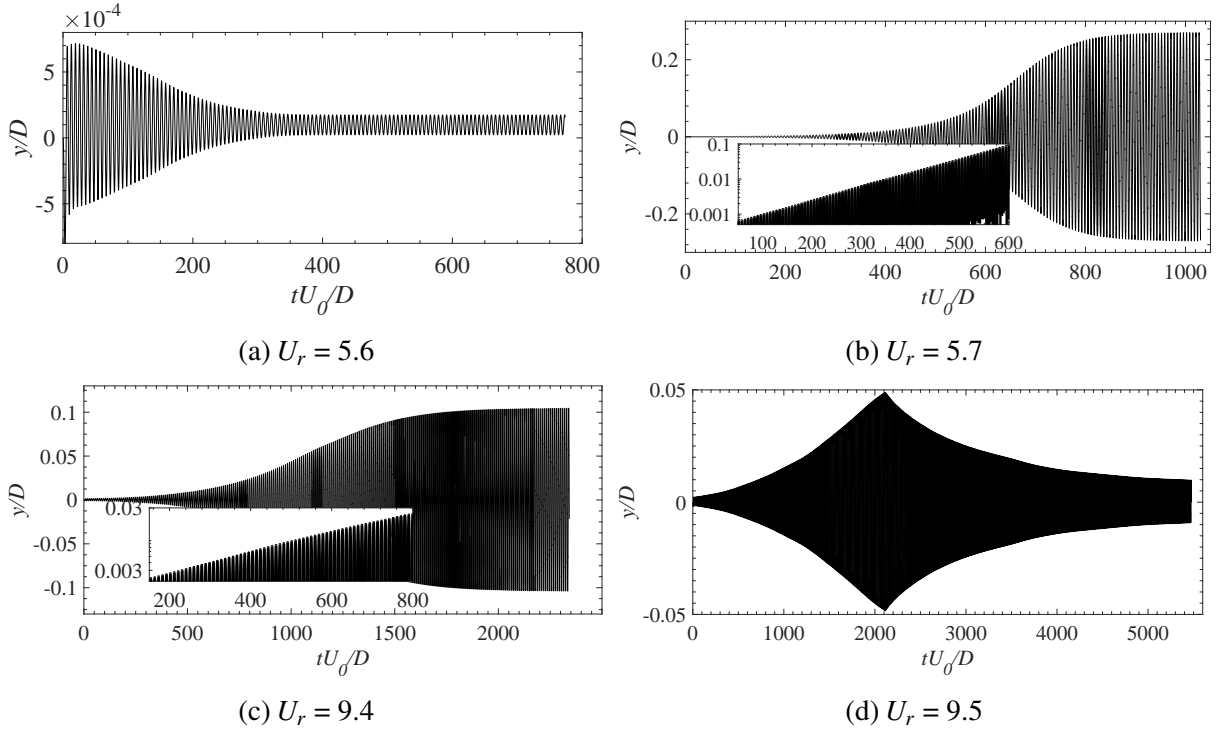


Figure 6.22: Time series of the normalized transverse displacement y/D for the studied FIV system with spanwise shear inflow at $U_r =$ (a) 5.6, (b) 5.7, (c) 9.4, and (d) 9.5 obtained using FOM/CFD. The logarithmic scale is used for the zoomed-in subgraphs in (b, c).

where cylinder is divided into n elements and y_r^a and y_r^e satisfy:

$$x_r^a(k+1) = \tilde{A}_r^a x_r(k) + \tilde{B}_r^a u_r(k), \quad (6.8)$$

$$y_r^a(k) = \tilde{C}_r^a x_r(k) + \tilde{D}_r^a u_r(k), \quad (6.9)$$

$$x_r^e(k+1) = \tilde{A}_r^e x_r(k) + \tilde{B}_r^e u_r(k), \quad (6.10)$$

$$y_r^e(k) = \tilde{C}_r^e x_r(k) + \tilde{D}_r^e u_r(k), \quad (6.11)$$

with $(\tilde{A}_r^{a,e}, \tilde{B}_r^{a,e}, \tilde{C}_r^{a,e}, \tilde{D}_r^{a,e})$ as the discrete-time state-space form converted from $(A_r^{a,e}, B_r^{a,e}, C_r^{a,e}, D_r^{a,e})$.

The above information indicates that the transfer matrix affects the distribution of eigenroots, and the value of the transfer matrix is determined by the C_L response obtained via FOM/CFD. On the basis of the linear relationship described above, we can instead directly compare y_r^a (in equation 6.7) in place of the C_L responses of different ROM strategies, and the associated discrepancy between the SROM2-9E and other strategies are also analyzed herein. Fig. 6.24 shows the overall response of lift coefficients C_L (or, the output y_r^a) obtained using direct 3D-ROM and SROM2. Firstly, in the subplot of Fig. 6.24, the first 10-steps of the response of lift coefficients are presented and no obvious discrepancies of value could be observed among different ROM strategies. Thus, it would be expected that the value of the initial C_L response when subjected to the impulse has no decisive influence on the U_r value of the lock-in boundaries in this case. More specifically, except for the significantly larger C_L responses in the few starting time-steps, subsequent responses in time steps from 50 to 600 evolve quickly back to very small absolute values ($< 2 \times 10^{-5}$), which is illustrated in the main plot of Fig. 6.24. It is noted again here

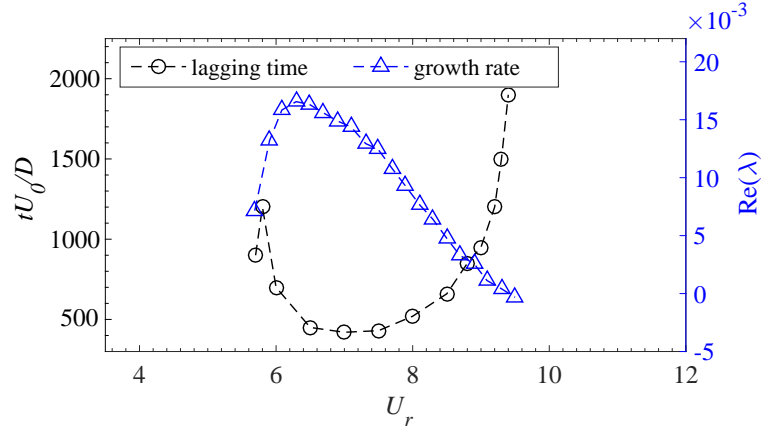


Figure 6.23: The comparison of the trend of growth rate $\text{Re}(\lambda)$ obtained using SRROM2-9E and lagging time obtained using FOM/CFD at different U_r values in the lock-in regime.

that the inflow Reynolds numbers in this study ranged from 25 to 45, which were smaller than the critical Reynolds number. Therefore, the development of C_L will not lead to the appearance of Hopf-bifurcation and will instead gradually stabilize. However, compared to the other three trajectories, the C_L development of SRROM2-3E does not show an obvious contracting trend in the range of 0-600 time steps. The trend development of SRROM2-5E and SRROM2-9E are almost consistent with each other, but there are still small discrepancies, and the extent of this consistency can also be observed by comparing the values of the U_r boundaries of the lock-in regime (refer to Figures 6.21b and 6.20.) Additionally, the trend development of 3D-ROM exhibits a certain degree of lag compared to that of SRROM2-9E. Considering the theoretical basis of obtaining the fluid ROM based on the ERA identification, differences in the C_L response have likely led to prediction errors of the 3D-ROM.

Given that the methodologies of SRROM2-9E and FOM/CFD show excellent agreement on the prediction of lock-in range, the computational efficiency of those two models is compared herein. The time consumed by mesh design/production is not taken into consideration here. In order to precisely determine the lock-in range using FOM/CFD, a total of about 20 cases corresponding to various U_r values are calculated, with an identical cell number of 2695420 for each case. An average of 75,000 time steps are required for each case to reach the final equilibrium state, and each time step involves 15 inner iterations. Applying SRROM2-9E to investigate the modal features necessitates division of the circular cylinder into 9 elements, with each element being treated as a 2D situation with uniform inflow. For each element (at different Re), the base flow should be obtained first and the C_L response subjected to a displacement impulse exerting on the base flow is then calculated. These two processes are conducted via FOM/CFD and the cells number used is 66708. The number of time-steps and iteration numbers (per time-step) for obtaining the base flow is 30 and 25, respectively; the same for calculating the C_L response is 1000 and 15. The time expended on post-processing is also ignored in this comparison. Considering the numbers presented above, a preliminary estimation suggests that the processing efficiency of SRROM2-9E is about 7000 times that of FOM/CFD.

Finally, Fig. 6.25 depicts the evolution of an unstable U_r region, with varying mass ratio m^* , of an FIV response of a system comprised of an elastically-mounted circular cylinder submerged in spanwise shear inflow with Re ranging from 25 to 45. Firstly, the region of unstable structure is delineated with a red shade, and the lower and upper boundaries are marked with the dashed

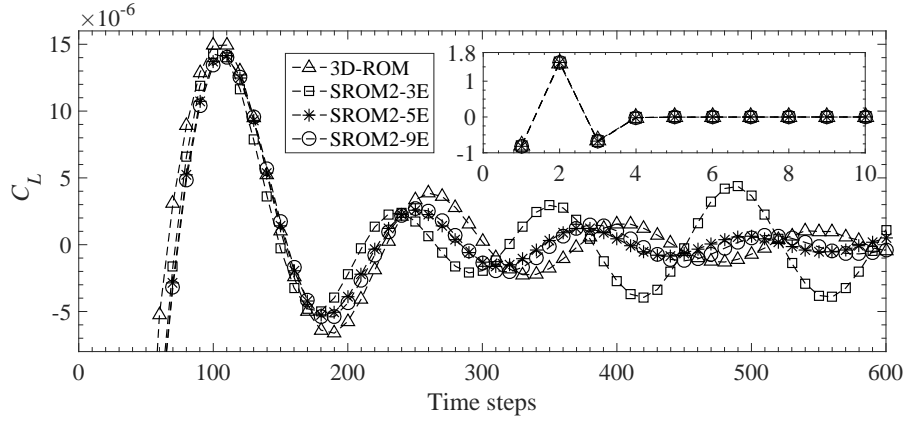


Figure 6.24: The predictions of the C_L impulse response obtained using direct 3D-ROM, SROM2-3E, SROM2-5E, and SROM2-9E. The encapsulated subplot utilizes a larger y-axis scale for the first 10 time steps to allow for a complete presentation of the C_L impulse response.

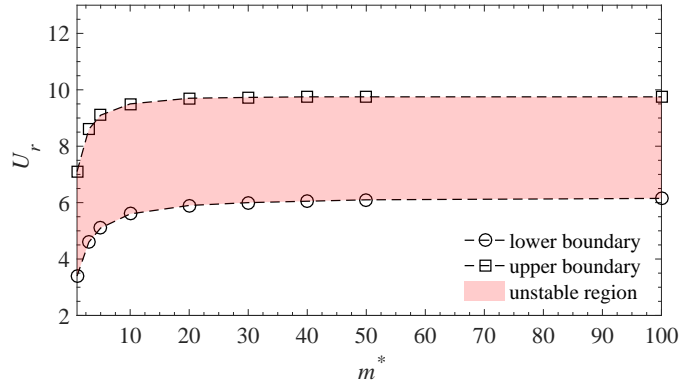


Figure 6.25: Instability boundaries, predicted by SROM2-9E, of the flutter lock-in range as a function of mass ratio m^* for the studied FIV system.

lines. As m^* increases, the U_r values corresponding to the upper and lower boundaries of the unstable region gradually increase and stabilize after $m^* = 30$. As shown by the root loci of the FIV response for which $Re > Re_{cr}$ [12, 244], the U_r span of resonance lock-in widens more significantly as m^* decreases compared to flutter lock-in, which leads to the overall widening of the whole lock-in span. However, it is stressed once more that the lock-in pattern in this study is completely of the flutter mode. Thus, there is no significant change in the U_r span of the whole lock-in scope (which is observable via the difference between the U_r values of the upper and lower boundaries) as m^* varies.

6.6 Chapter summary

In this chapter, we introduced one new methodology of data-driven stability analysis via the superposition of 2-D reduced-order modes (SROM) for the purpose of performing modal analysis and stability predictions of 3-D flow-induced vibration of an elastically-mounted circular cylinder, submerged in spanwise shear inflow at subcritical Reynolds numbers ranging from 25 to 45. The proposed methodology divides the circular cylinder into several elements in a spanwise

direction, and the 2-D fluid ROM is obtained for each element via ERA identification. The 3-D fluid ROM of the studied system is constructed by superimposing the separate 2-D fluid ROMs together and then coupling with the structural control model to achieve the 3-D coupled ROM for the FIV system of interest.

A detailed and time-consuming calculation using the method of FOM/CFD is applied to determine the lock-in range, which is crucial for establishing a reference for verifying subsequent results of the data-driven stability analysis. Due to the fact that the entire lock-in range is subjected to the flutter pattern, the root-mean-square value of the lift coefficient abruptly reaches its maximum value when entering the lock-in interval (as U_r increases), and then gradually decreases and reaches its minimum value (or, the value at the desynchronized branch) at the right bound of the U_r lock-in range. In this flutter lock-in range, the structural oscillation frequency is locked at the structural natural frequency, and the phase differences between transverse displacements and lift coefficients remain close to a value of zero. Additionally, the amplified amplitude of structural response in the lock-in range would induce vortex-shedding behavior, and the accompanied vortex tube is skewed in the streamline direction as the inflow Reynolds number increases in the spanwise direction. Furthermore, the vortex-shedding frequencies along the spanwise direction are identical but there is an enhancement of the spectrum power in the positive spanwise direction. The vortex pattern in the desynchronized branch (or, when the system is out of the lock-in range) is stable, characterized by an absence of Hopf-bifurcation.

The stability prediction of direct 3-D data-driven stability analysis exhibits non-negligible errors in comparison with the results of FOM/CFD calculations. It would be expected the non-linear characteristics caused by the spanwise dynamics interaction have a significant effect on the accurate attainment of the base flow and the process of ERA identification. In terms of the data-driven stability analysis via the superposition of 2-D reduced-order modes, the prediction of the proposed methodology has achieved extremely high consistency with FOM/CFD calculations after several revisions/improvements in the element-division strategy. Considering the time taken by the two methods (SROM and FOM/CFD) for prediction, it is demonstrated that the newly presented theory of data-driven stability analysis (SROM) is both accurate and efficient. Furthermore, this study explains that the growth rate provided by SROM shows a negative correlation to the lagging time for the FIV system during the development from the initial stationary state to the final equilibrium state. Additionally, the evolution of the U_r region for the unstable structural mode indicates that the span of the whole flutter lock-in range reflects only small changes with varying mass ratio m^* .

Chapter 7

Aeroacoustics noise propagation

As introduced above that past studies have focused on the flow dynamics of moving cylinders and aeroacoustics of stationary cylinders, investigations of the noise generated by oscillating cylinders are very limited, especially for turbulent flow at a high Reynolds number Re . Practical engineering problems require an understanding of the aeroacoustics of flow past oscillating cylinders at high Re . The study in this chapter is the first to perform computational aeroacoustics of single/tandem oscillating cylinders in a turbulent flow at high Re (viz., at $Re \geq 50,000$), in a fully three-dimensional computational domain and with structural oscillations in either the streamwise or transverse directions.

Specifically, this chapter investigates the existence of the noise suppression phenomenon for turbulent flows. While this phenomenon has been observed in laminar flow at $Re = 150$, it is of interest to determine whether this phenomenon is applicable for a fully turbulent flow. Additionally, we investigate the effect of various oscillation configurations on the dynamics and aeroacoustics of the flow past both a single or tandem cylinder(s). Furthermore, this thesis also analyzes the vortex structures generated in the wake of these flows.

This chapter is organized as follows. The numerical methodology used in this chapter are discussed in Section 7.1. In Section 7.2, the numerical methodology is validated on a number of test cases: namely, the case of a flow past a stationary cylinder measured by Oguma et al. [17], the case of a flow past stationary tandem cylinders measured by BART/QFF [20, 22, 21], and the case of a flow past oscillating tandem cylinders (at $Re = 150$) simulated by Hattori and Komatsu [25]. Section 7.3 investigates the aeroacoustics of the flow past a single or tandem stationary cylinder(s) at large values of Re ; namely, $Re = 60,000$, $120,000$ and $240,000$. Section 7.4 demonstrates that the noise suppression phenomenon applies to turbulent flow and investigates the underlying mechanism for this suppression. The aerodynamics and aeroacoustics for the flow past a single or tandem oscillating cylinder(s) at $Re = 120,000$ are investigated in Sections 7.5 and 7.6, respectively.

7.1 Numerical methods

7.1.1 Energy equation

The energy equation is the fundamental equation in fluid dynamics and is derived from the first law of thermodynamics [248]. The energy equation is used in combination with RANS or

LES to incorporate the effects of density and temperature in the flow. It could be used for incompressible external flow simulations, and also compressible flow via the combination with the ideal gas law [249].

7.1.2 Turbulence model

The fluid is assumed to be Newtonian and the resulting fluid flow is compressible and unsteady. The accuracy of the aerodynamic noise calculation is closely correlated to the resolution of the vortices in the flow field. According to the literature review, detached eddy simulation (DES) is used to model the turbulence in this chapter. DES is a hybrid method that combines the Reynolds-averaged Navier-Stokes (RANS) and large eddy simulation (LES) methods. In DES, the turbulence model switches from RANS to LES depending on the mesh size in comparison to the turbulence length scale. If the turbulence length scale is larger than the mesh size, then LES can be used as the mesh is sufficient to resolve the larger scales of the turbulence. If the turbulence length scale is smaller than the mesh size, then RANS is used. This switching effectively means that RANS is used near the wall, and LES is used away from the wall. The mesh size and time step required to resolve the boundary-layer flow using RANS are less computationally demanding than would be required if a full LES was used throughout the entire computational domain.

The shear stress transport (SST) DES method [250] is used herein. The k - ω SST turbulence closure model is used in the RANS model to solve the boundary-layer flow. The detailed information of RANS model are shown in Appendix C. The k - ω SST RANS model has been modified for use in the DES model. This modification involves the dissipative term in the turbulent kinetic energy (k) transport equation: namely, the dissipation of k in the SST RANS given by

$$D_{\text{RANS}}^k = \rho \beta^* k \omega = \rho k^{3/2} / l, \quad (7.1)$$

has been modified in the SST DES as

$$D_{\text{DES}}^k = \rho k^{3/2} / \tilde{l}, \quad (7.2)$$

where $\tilde{l} = \min(l, C_{\text{DES}} \Delta)$ is the DES length scale, $l = k^{1/2} / (\beta^* \omega)$ is the RANS length scale, C_{DES} is a calibration constant with a value of 0.82, and Δ is the maximum local grid spacing.

7.1.3 Solid body motion

The fluid is assumed to be Newtonian and the resulting fluid flow is compressible and unsteady. SST-DES is used to model the turbulence in present acoustics simulation, as presented in section 7.1.2. The forced oscillations of the cylinder are characterized by the frequency f and the amplitude $A = x_{i,\text{max}}$, where $x_{i,\text{max}}$ is the maximum imposed amplitude along the i -th Cartesian spatial coordinate. A sinusoidal motion is explicitly imposed on the cylinder at each time step, prior to solving the flow field. More specifically, the sinusoidal motion is prescribed as follows:

$$x_i(t) = x_{i,\text{max}} \sin(2\pi f t), \quad (7.3)$$

where x_i is the i -th Cartesian coordinate direction with $i = 1, 2,$ and, 3 corresponding to the x -, y -, and z -directions, respectively.

The cylinder oscillates independently from the flow, but the wake can be strongly affected by the cylinder motion. The no-slip boundary condition along the surface of the moving cylinder depends on the current cylinder velocity. Continuity of the velocities imposes the following constraint at the solid cylinder wall; namely, $u_i = \dot{x}_i$ where u_i is the i -th component of the fluid velocity vector $\mathbf{u} \equiv (u, v, w)$, and \dot{x}_i is the i -th component of the cylinder velocity. A moving mesh procedure has been developed as a user subroutine. It operates only in a ring surrounding the cylinder and leads to a deformed mesh whose structure is preserved during the oscillations [251]. A second-order accurate implicit Euler scheme is employed to discretize the transient term, while a second-order accurate Gaussian integration scheme is used for the discretization of the advection, pressure gradient and diffusion terms in the momentum transport equation. The calculation of this chapter still use PIMPLE scheme to solve the continuity and momentum transport equations together in a segregated manner. For this iterative solution, we used 12 inner iterations per time step and prescribed under-relaxation factors of 0.3 and 0.7 in the iterative solution for the pressure and velocity fields, respectively.

7.1.4 Acoustic modelling

The Ffowcs Williams-Hawkings (FW-H) equation is an inhomogeneous wave equation derived from the continuity and Navier-Stokes equations. The wave equation includes three noise terms: quadrupole source (turbulence-induced noise term due to unsteadiness in the fluid), dipole source (loading noise term due to dilatation of boundaries) and monopole source (thickness noise term due to fluctuating stresses on the surface). Since the FW-H equation is suitable for predicting the sound generated by arbitrary moving solid surfaces, it has become an important theoretical and numerical basis for engineering noise prediction. A large number of methods has been proposed to solve the FW-H equation.

Since the turbulent term (quadrupole source) is a volume integral, it is difficult to select the integration region and conduct integration in the fluid around the rigid body [252]. The permeable FW-H method starts from establishing a permeable surface, abandoning the assumption of that the normal velocity of the fluid is equal to that of the surface of the rigid body in contact with it, and allowing these two velocities to be distinct (different). In this way, the calculation of the loading and thickness noise on the permeable surface can include the noise caused by turbulence (or, quadrupole source) inside the surface [253, 254]. Farassat et al. [255, 256, 257] introduced the time-domain integration method resulting in the Farassat 1 and Farassat 1A formulae. These formulations have become one of the most widely used methods for computational aeroacoustics, and can be used for permeable and impermeable control surfaces. The Farassat 1A formulation, as applied in this study, is described in detail in Appendix. A. The FW-H model applied in this thesis is based on the work of Epikhin et al. [258] concerning the implementation of the Farassat 1A formulation inside the open-source software OpenFOAM [202]. The present work uses a custom solver to decompose the fluctuating acoustic total noise pressure into loading and thickness components, while applying an impermeable surface as the FW-H control surface.

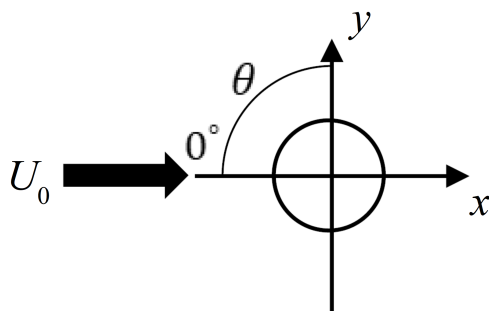


Figure 7.1: Schematic of experiment conducted by Oguma et al. [17] involving the flow past a stationary circular cylinder with a diameter $D = 0.03$ m and a length of $L_c = 0.5$ m. The incident velocity on the cylinder is $U_0 = 22.5$ m s⁻¹ to give a Reynolds number for the flow of $Re = 40,000$.

7.2 Validation of numerical methodology

7.2.1 Flow past a stationary cylinder at high Reynolds number

Oguma et al. [17] conducted measurements of the flow field and noise generated by the flow past a stationary circular cylinder. A simplified schematic of the setup of this experiment is shown in Fig. 7.1. The mean inflow velocity U_0 is 22.2 m s⁻¹ with $Re \equiv U_0 D / \nu = 40,000$, where ν is the kinematic viscosity of air. The circular cylinder has a diameter of 30 mm and a length of 500 mm. The resulting aspect ratio of the cylinder (ratio of the length to the diameter of the cylinder) is 16.7. The aspect ratio of the cylinder is large enough to produce a two-dimensional mean flow at the mid-span of the circular cylinder. A microphone with a diameter of 12.7 mm is located 1.5 m from the top side of the circular cylinder (viz., the microphone is located at the coordinates of $(x, y, z) = (0, 1.515, 0)$ m). The mean velocity in the test section was uniform to within an accuracy of $\pm 1\%$ and the free-stream turbulence level was 1.5%. The free-stream turbulence is an important quantity for aeroacoustics because an increased free-stream turbulence can increase the noise level [259].

Fig. 7.2(a) shows the computational domain and the boundary conditions for the validation case. Dirichlet boundary conditions were imposed for the incoming wind velocity and turbulence intensity. At the top, bottom, and outflow planes of the computational domain, a pressure outlet boundary condition was imposed with the pressure set equal to the standard (ambient) atmospheric pressure. Symmetric boundary conditions are applied at the spanwise boundaries. The velocity at the upstream boundary is fixed at 22.2 m s⁻¹ resulting in a Reynolds number for the flow of $Re = 40,000$. The turbulence intensity was prescribed to be 4.0%. The mesh in the computational domain is shown in Fig. 7.2(b). The maximum dimensionless wall-normal distance $y^+ \equiv y u_\tau / \nu$ (y is the wall-normal distance and u_τ is the friction velocity) of the first cell above the wall is 6 which is sufficient for the application of the $k-\omega$ SST RANS model near the wall. The time step was dynamically adjusted to maintain a maximum CFL number of 0.8 in order to promote numerical stability and accuracy of the solution. The aspect ratio of the first-layer mesh on the column surface here and in the following cases is approximately 5.

Fig. 7.3 compares the simulated velocity and pressure fields to the experimental measurements reported by Oguma et al. [17]. Fig. 7.3(a) shows the variation of the mean surface pressure coefficient $C_p = (P - P_0) / (0.5 \rho_0 U_0^2)$ (ρ_0 is the air density and P_0 is the atmospheric air

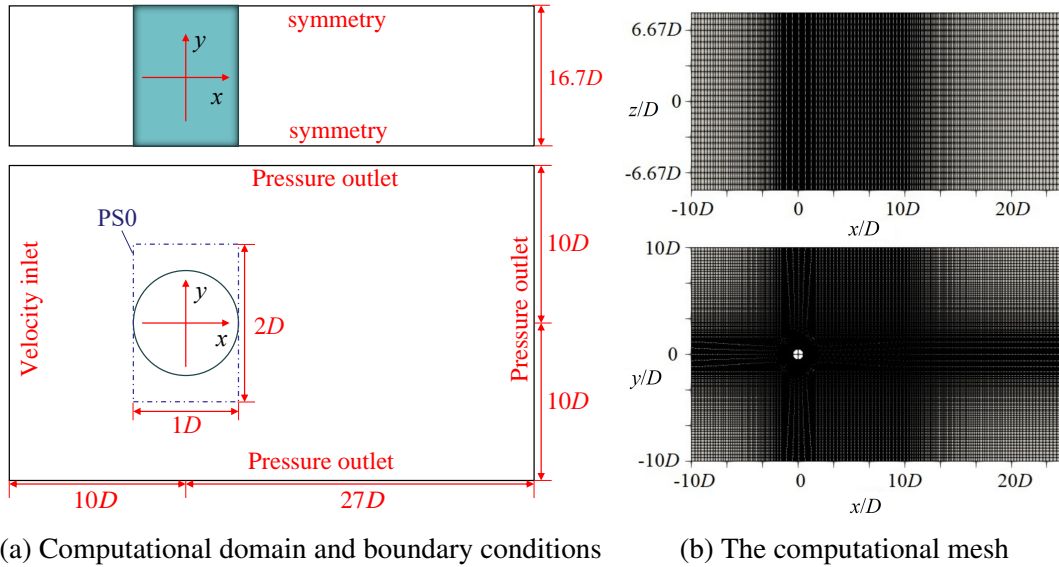


Figure 7.2: Boundary conditions and computational mesh used for the validation case consisting of the flow past a stationary circular cylinder at a high Reynolds number ($Re = 40,000$). The permeable FW-H surface used for the prediction of the noise field is shown in (a) as PS0.

pressure) as a function of the angle θ (measured from the upstream stagnation point) along the cylinder. The mean surface pressure coefficient from the numerical simulation generally agrees well with the experimental data. The base pressure from the present study is in better agreement with the Oguma et al. [17] experiment than with the Fujisawa and Takeda [18] experiment—this observation is consistent with another numerical study conducted by Dong et al. [19]. Fig. 7.3(b) compares the mean velocity measurements along the domain centerline ($y/D = 0$) with the PIV measurements reported by Oguma et al. [17]. Although there are several differences in the setup between the present numerical study and these experiments (e.g., aspect ratio, free-flow turbulence, and cylinder end conditions), nevertheless the time-averaged behaviour of the cylinder wake is consistent with the previous experimental and numerical results.

Fig. 7.4 compares the mean streamwise velocity and pressure coefficient C_p contours around the cylinder. Fig. 7.4(b) shows the mean velocity vectors from the experimental PIV results. The results in Fig. 7.4(c) show that the simulation accurately captures the size of the recirculation zone behind the cylinder. The velocity magnitude increases as the flow moves over the cylinder and a velocity deficit is generated in the near-wake region of the flow. The flow separates near an angle of $\theta = 80^\circ$, measured from the stagnation point. A careful perusal Figs. 7.4(a) and 7.4(c) shows that the mean pressure field from the simulation is also in good agreement with the experimental results. A high-pressure zone is created upwind of the cylinder and a low-pressure zone forms in the near-wake region of the cylinder.

Fig. 7.5 compares the simulated noise generation to the experimental measurements reported by Oguma et al. [17]. Two types of surfaces are used for the representation of the sound source in the FW-H equation: namely, an impermeable FW-H surface (cylinder walls) and a permeable FW-H surface (PS0) as shown in Fig. 7.2(a). The power spectral density (PSD) of the sound pressure level (SPL) at the microphone location (viz., at $(x, y, z) = (0, 1.5, 0)$ m) is given in dB Hz^{-1} (relative to a reference pressure of $P_{\text{ref}} = 20 \times 10^{-6}$ Pa). The experimental spectra are obtained by sampling the data at a frequency of 10 kHz for a temporal duration of 36 s. The

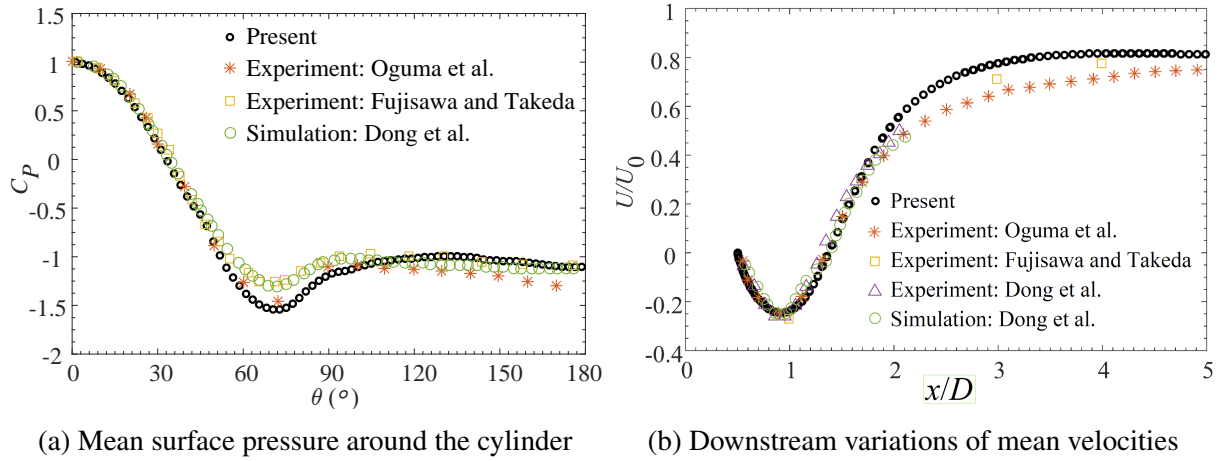


Figure 7.3: Comparison of (a) the mean surface pressure around the cylinder and (b) the downstream variation of the mean streamwise velocity along the computational domain centerline in the spanwise direction ($y/D = 0$) between the present simulation and results reported by Fujisawa and Takeda [18], Oguma et al. [17] and Dong et al. [19].

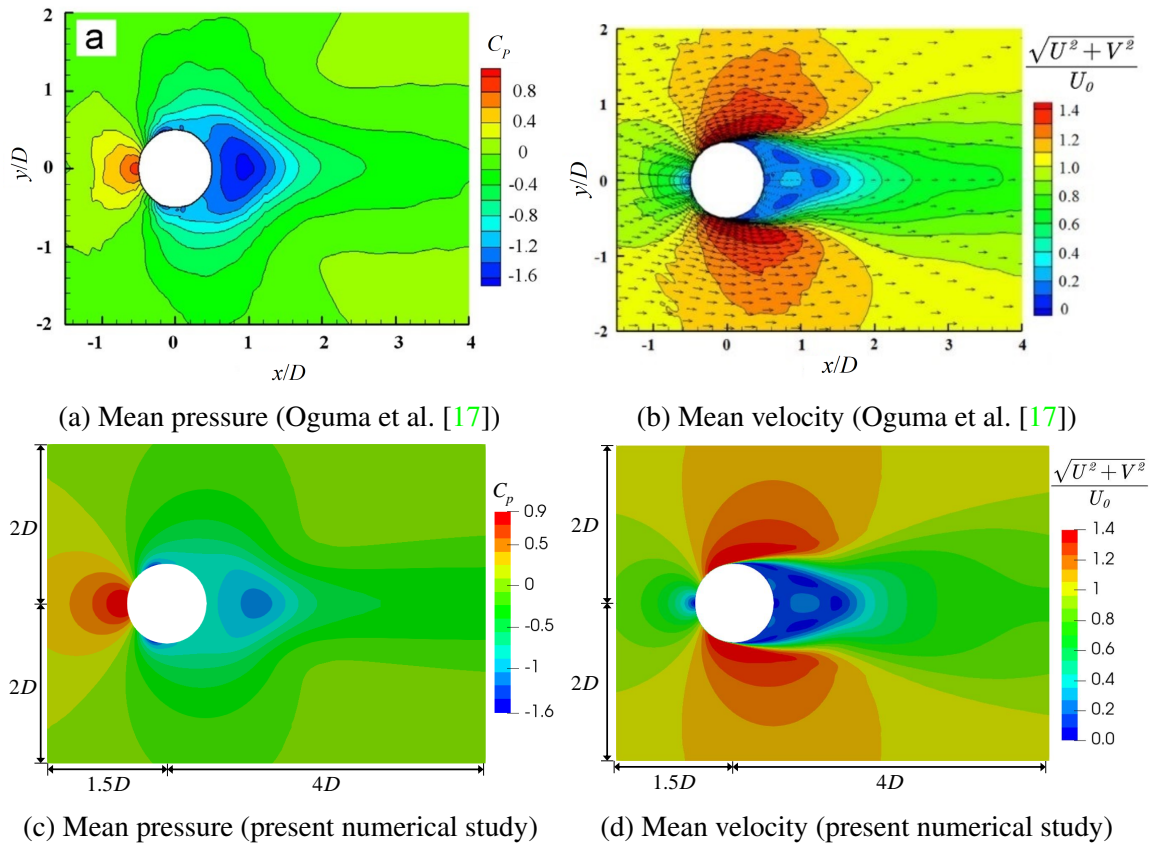


Figure 7.4: Comparison of the velocity and pressure fields between the present simulations and the experimental data reported by Oguma et al. [17].

experimental results show that the sound field is dominated by the vortex-shedding frequency, combined with the broadband noise from the turbulent wake. The first peak frequency is related to the lift force fluctuations and the second peak frequency is due to the weaker energy arising from the drag force fluctuations. The noise predictions obtained from our numerical simulations

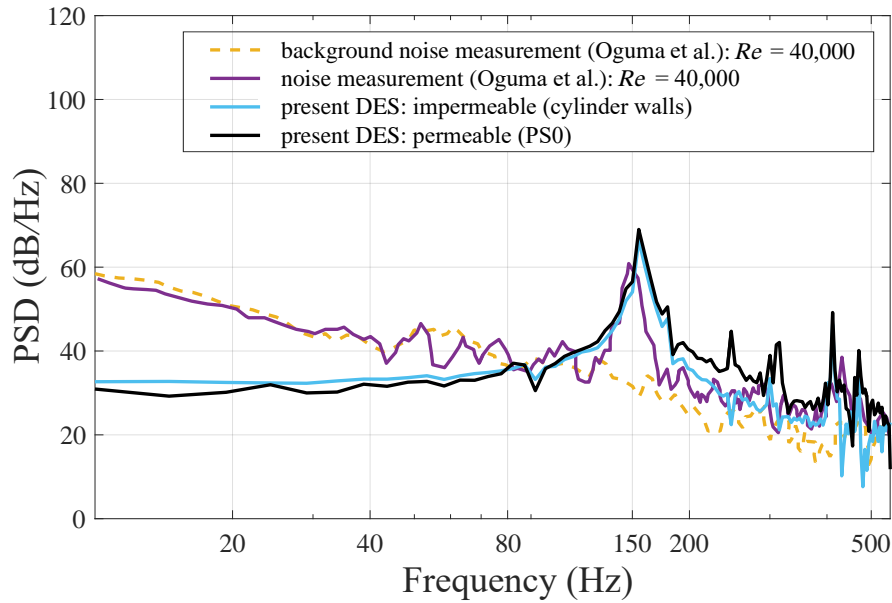


Figure 7.5: Comparison of the power spectrum of the sound pressure level obtained at the microphone location ($x = 0$, $y = 1.5$ m, $z = 0$) between the present study and the experimental measurements reported by Oguma et al. [17]. The present simulations of the sound pressure level use both an impermeable (cylinder walls) and a permeable (PS0) FW-H surface for the sound source.

are in good agreement with the experimental measurements, especially for the peak frequencies. The power spectrum obtained from the permeable FW-H surface is higher than that obtained from the impermeable FW-H surface. The permeable FW-H surface only includes the pressure fluctuations in the boundary layer. However, the predictions of the noise obtained using the two FW-H surfaces are similar. The numerical simulation does not include the background noise, so the sound power at frequencies less than about 80 Hz is smaller than that observed in the experimental measurements.

7.2.2 Flow past stationary tandem cylinders at high Reynolds number

The most widely used noise measurements for numerical validation are the NASA tandem cylinder data obtained at the Basic Aerodynamics Research Tunnel (BART) [20, 22] and the Quiet Flow Facility (QFF) [21] at the NASA Langley Research Center. The data from these experiments include measurements of the surface pressure along the cylinder walls, the flow field around the cylinders obtained using PIV, hot-wire anemometer measurements of the velocity in the wake of the cylinders, and measurements of the noise generated by the flow past the cylinders.

The tandem cylinder case consists of two equal-diameter cylinders aligned in the flow direction. The tandem cylinders of diameter $D = 0.05715$ m are separated by a distance of $3.7D$ in the streamwise direction. The flow Mach number is $M_0 = 0.128$. The experiments were performed at a Reynolds number of $Re = 1.66 \times 10^5$. For the experiments conducted in the closed-loop wind tunnel (BART) and in the open-jet anechoic wind tunnel (QFF), the length of the cylinder is $12.4D$ and $16D$, respectively. Fig. 7.6 shows the arrangement of the cylinders used for the present simulations. The aspect ratio of the cylinders used in these simulations is 12.4—this

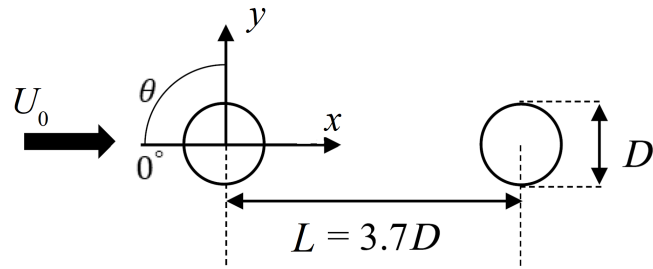


Figure 7.6: Layout of tandem circular cylinders separated in the streamwise direction by $3.7D$. Each cylinder has a diameter of $D = 0.05715$ m. The incident wind speed on the cylinder is $U_0 = 44.0$ m s⁻¹ to give a Reynolds number for the flow of $Re = 166,000$. This configuration of two cylinders is used in the present simulations and in the experiments reported by Jenkins et al. [20].

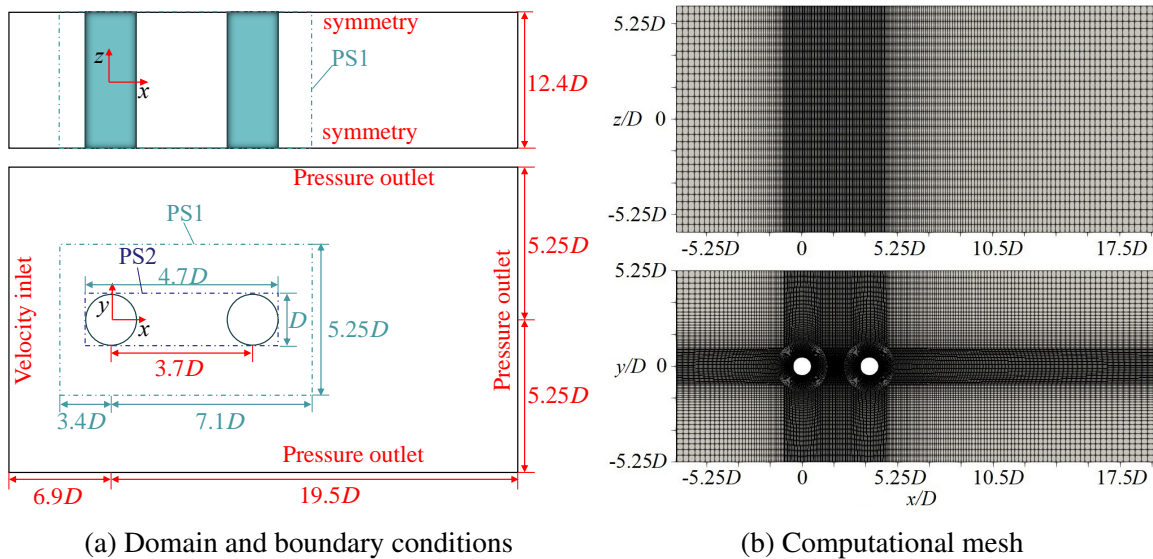


Figure 7.7: Boundary conditions and mesh used for the numerical simulations of the case of two tandem circular cylinders separated in the streamwise direction. The permeable FW-H surfaces used for the prediction of the noise field are shown in (a) as PS1 and PS2.

value is the same as that used in the tandem cylinder experiments conducted at the BART.

Fig. 7.7(a) shows the computational domain, the boundary conditions and the inflow turbulence intensity for the tandem cylinder validation case. The boundary conditions are consistent with the previously discussed single cylinder case. The numerical simulations were conducted for a flow with a Reynolds number of $Re = 166,000$ —this value of Re matches that used in the experimental measurements. The mesh is displayed in Fig. 7.7(b). This mesh maintains a maximum value for the dimensionless wall-normal distance y^+ for the first cell above the wall of 5.

The variation of the mean pressure coefficient C_P along the surface of the front (upstream) and rear (downstream) cylinders is shown in Figs. 7.8(a) and 7.8(b), respectively. For the front cylinder, the pressure coefficient is captured well by the simulation. The simulation correctly predicts the separation point location of $\theta \approx 110^\circ$ for the upstream cylinder. For the rear cylinder, the simulation underestimates the pressure coefficient, in alignment with previous studies [260,

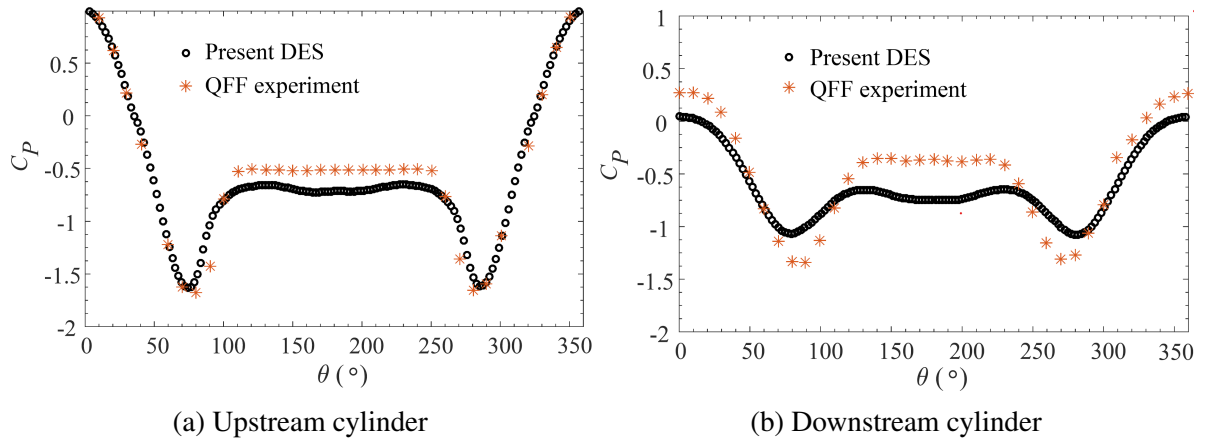


Figure 7.8: Comparison of mean pressure coefficient C_p along the surface of the cylinders obtained from the present numerical simulations and from the QFF experiments [21] for the (a) upstream and (b) downstream cylinders.

261]. However, the separation point at an angular position of $\theta \approx 130^\circ$ is predicted well by the simulations, and the overall prediction of the pressure coefficient is also reasonable. Fig. 7.9 shows that the simulated mean streamwise velocity along the computational domain centerline (viz., at $y/D = 0$) also agrees well with the experimental results. The velocity difference in the wake field in Fig. 7.9b is presumed to originate from the issues with the grid quality of the wake region and RANS model used near the cylindrical surface.

Fig. 7.10 shows the PSD of the fluctuating surface pressure on both cylinders obtained from the BART experiments and from the present simulation. The dominant peak and weaker peak are correctly predicted by the present simulation on the front and rear cylinder surfaces, with slight amplitude differences. The primary vortex-shedding frequency of 179 Hz from the simulation is in good agreement with the BART experiments. The smaller peaks at frequencies of approximately 350 Hz, 550 Hz and 700 Hz, evident in the BART experimental fluctuating surface pressure PSD for the front and rear cylinders, are also captured well in the present simulation. The relatively high amplitude in the broadband part of the power spectral density, especially at the angular position of $\theta \approx 180^\circ$ for the front cylinder, is consistent with results reported by David et al. [24].

The Ffowcs Williams-Hawkings equation was used to predict the acoustic field based on the unsteady flow data. Three different FW-H surfaces were used to represent the sound (pressure fluctuation) source: namely, an impermeable FW-H surface coinciding with the walls of the cylinders and two permeable FW-H surfaces shown in Fig. 7.7(a) and designated as PS1 and PS2. The temporal duration used in the FW-H solver was the last 0.5 s of the numerical simulation—a duration that encompassed more than 80 vortex-shedding periods. The acoustic observer is located at the point $(x/D, y/D, z/D) = (-8.33, 27.815, 0)$ where the origin of the Cartesian coordinate system coincides with the center of the first cylinder (cf. Fig. 7.7(b)).

Fig. 7.11(a) exhibits the PSD of the sound pressure level. It is seen that a good agreement is obtained between the present results and the QFF measurements, with respect to both the amplitude and location of the peak values in the power spectra. Our simulation results are similar to the numerical simulations (using the lattice Boltzmann method) reported by Guillaume et al. [23]. Both of these numerical simulations improve on the simulations reported by David et al. [24] (which used unsteady RANS to predict the flow field). The present numerical simulations

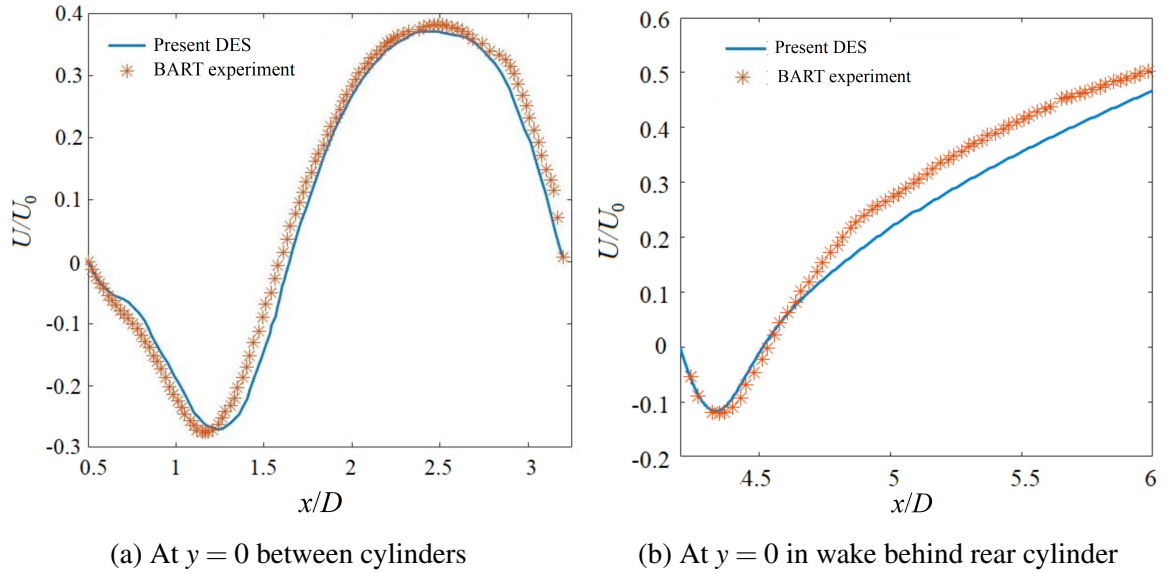


Figure 7.9: Mean streamwise velocity at $y = 0$ for downstream fetches in the range $0.5 \leq x/D \leq 3.3$ between the cylinders and in the range $4.0 \leq x/D \leq 6.0$ corresponding to the wake of the rear cylinder. The mean streamwise velocity is compared between the present numerical simulations and the experimental measurements reported by Jenkins et al. [20].

contain some noise owing to the small time step used for the acquisition of the sound pressure—and, moreover, no smoothing has been applied in the PSD processing. Fig. 7.11(b) compares the sound pressure level PSDs generated by the three FW-H surfaces (one impermeable and two permeable) to the experimental measurements. The overall shapes of the SPL PSDs from the three FW-H surfaces are consistent with the experimental results. However, the SPL PSD predicted using the two permeable FW-H surfaces exhibit weak peaks near 60 Hz, which may originate from the turbulence (quadrupole source) in the wakes of the tandem cylinders. These weak peaks increase with distance from the cylinder, especially in the high broadband and low-frequency ranges. Comparing the present simulations to the experimental results demonstrates that the sound pressure fluctuations provided by the impermeable FW-H surface (which coincides with the surfaces of the cylinders) leads to excellent predictions of the far-field noise.

7.2.3 Flow past oscillating tandem cylinders at a Reynolds number of 150

This sub-section will investigate the sound propagation from oscillating tandem cylinders in a laminar flow in order to further validate the present acoustic model for the simulation of the noise generated by a moving object. The results from the present work are compared to the DNS computations undertaken by Hattori and Komatsu [25]. Fig. 7.12 shows the setup for this tandem cylinder case. The streamwise distance between the centers of the two cylinders is $4D$ and the aspect ratio of each cylinder is 16.7. The front (upstream) cylinder is fixed, while the rear (downstream) cylinder oscillates with an amplitude of $0.2D$ and a non-dimensional frequency of $0.14U_0/D$. The inflow velocity is from left to right and the resulting flow has a Reynolds number of $Re = 150$ and a Mach number of $M_0 = 0.2$. The height of the first cell away from the cylindrical surface is consistent with the simulation in Section 7.2.1. The FW-H control surface is taken to be a rectangle with a streamwise (in-line) length of $6D$ and a transverse width of $2D$. The center of this rectangle coincides with the center of the tandem cylinder array (viz., the center of the

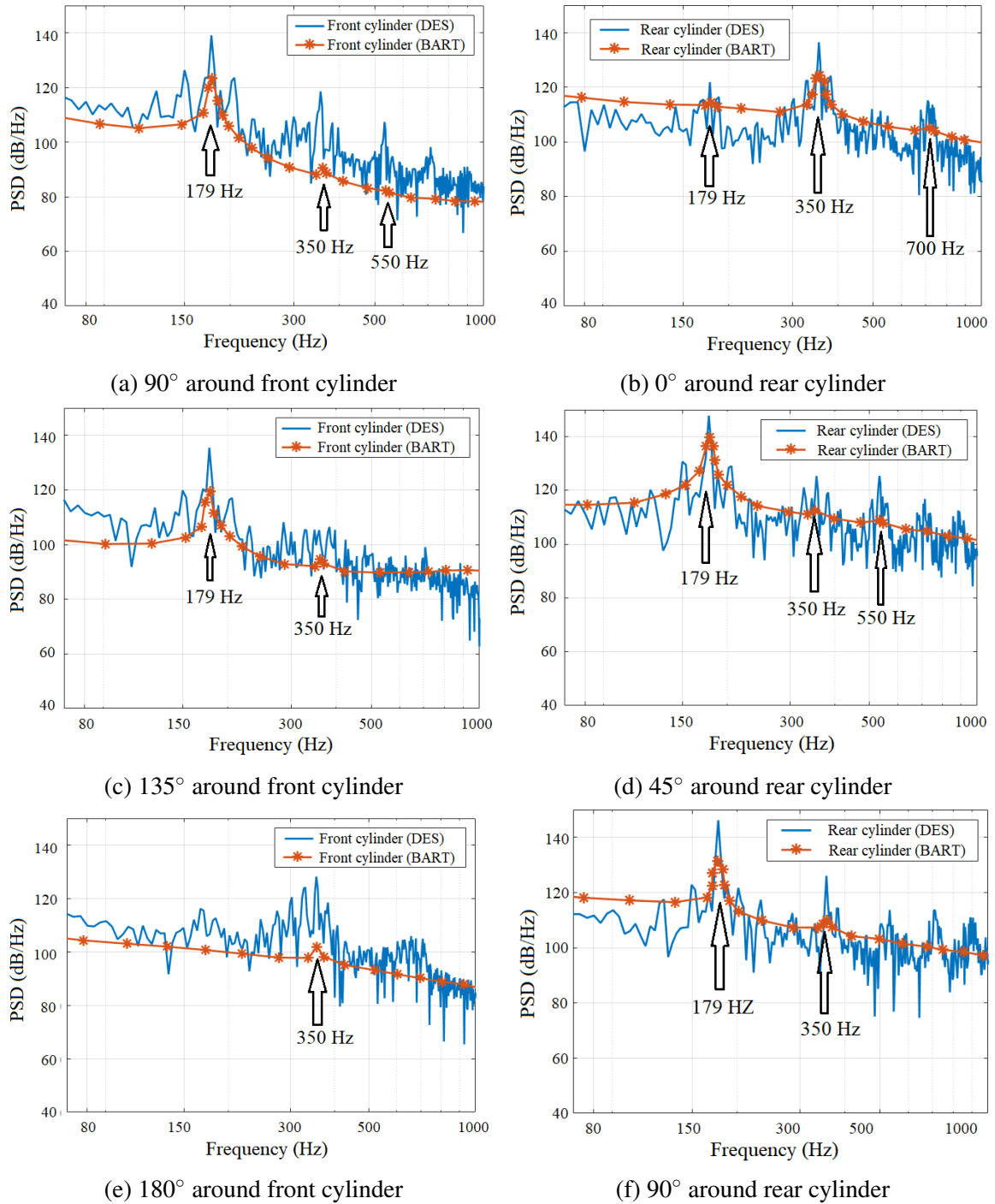


Figure 7.10: The PSD of the fluctuating surface pressure for the front (upwind) and rear (downwind) cylinders obtained from the present numerical simulations and from the BART experiments [22].

rectangle midway between the two cylinders in the streamwise direction and this is taken to be the origin of a Cartesian coordinate system used in the simulation).

Fig. 7.13 compares the present predictions of the SPL directivity in the x - y plane (at $z/D = 0$) at a radial distance of $80D$ from the midpoint between the two in-line cylinders for angular positions θ in the range $0^\circ \leq \theta \leq 180^\circ$ to the DNS results reported by Hattori and Komatsu [25].

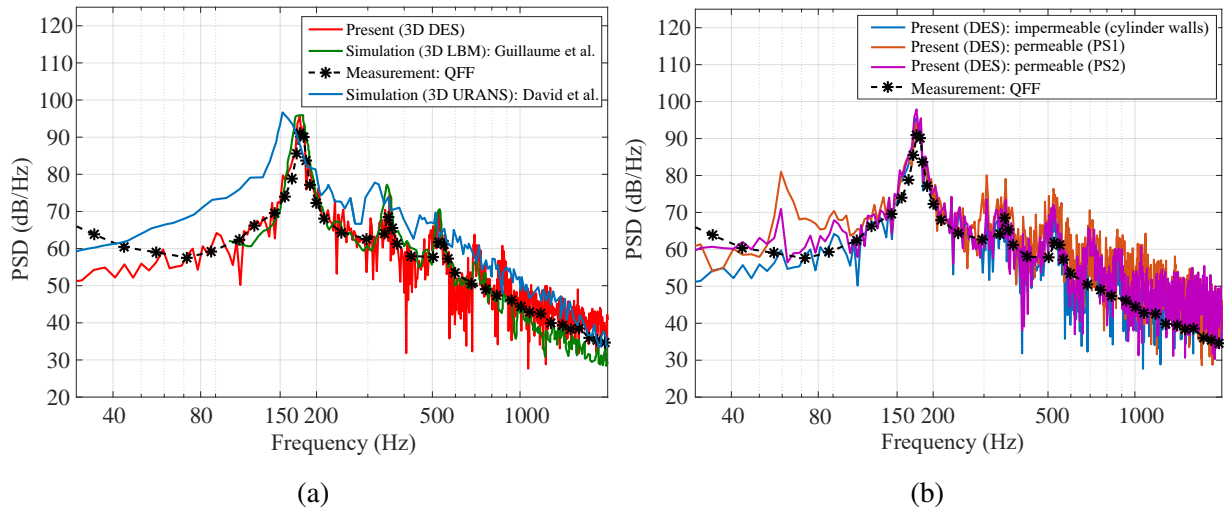


Figure 7.11: Power spectral density of the sound pressure level at the observer (microphone) location $(x/D, y/D, z/D) = (-8.33, 27.815, 0)$: (a) comparison of the present predictions of the SPL PSD with those obtained by Guillaume et al.[23] and David et al.[24] and with experimental measurements of the SPL PSD obtained from the QFF experiment [21]; and, (b) comparison of the present predictions of the SPL PSD obtained using three different FW-H surfaces (one impermeable surface coinciding with the walls of the cylinders and two permeable surfaces shown as PS1 and PS2 in Fig. 7.7(a)).

Overall, the general SPL directivity from the two methods is in excellent conformance with each other. The sound pressure intensity from the DNS is slightly smaller near $\theta = 180^\circ$ (viz., in the downstream direction) than that predicted by our present simulations. Hattori and Komatsu [25] also compared the results from the FW-H method and DNS and showed that a high degree of consistency between the two predictions was obtained.

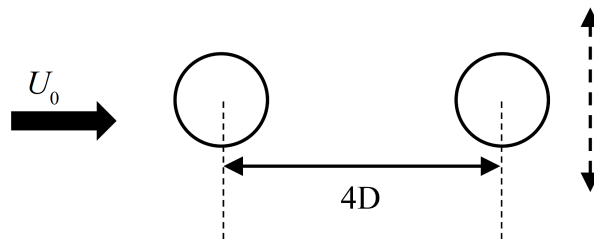


Figure 7.12: Configuration of tandem cylinders used in the DNS conducted by Hattori and Komatsu [25]—the front (upstream) cylinder is fixed and the rear (downstream) cylinder is oscillating in transverse (or, y -) direction. The center-to-center separation between the two cylinders in the streamwise (or, x -) direction is $L = 4D$.

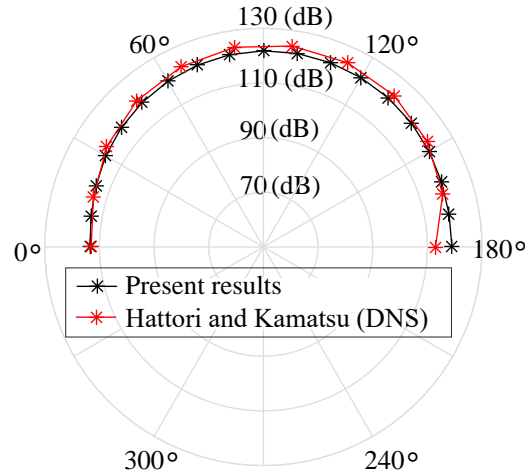


Figure 7.13: The SPL directivity for the configuration of tandem cylinders shown in Fig. 7.12 obtained in the x - y plane (at $z/D = 0$) at a radial distance of $80D$ from the midpoint between the two in-line cylinders for angular positions in the range $0^\circ \leq \theta \leq 180^\circ$. The prediction obtained from the present numerical simulation are compared to that obtained from the DNS conducted by Hattori and Komatsu [25].

7.3 Effect of Reynolds number and number of cylinders on the noise structure

In the previous section, the present hybrid model was validated using three test cases: namely, a turbulent flow past a stationary cylinder, a turbulent flow past stationary tandem cylinders, and a laminar flow past tandem cylinders one of which is oscillating in the transverse direction. This section will use the validated hybrid model to study high Reynolds number flows over stationary cylinders. Firstly, the effect of Re on the noise structure generated by the flow past tandem cylinders will be investigated. Secondly, the similarities and differences in the noise structure generated by the flow past a single cylinder and a pair of cylinders (tandem cylinders) will be studied for a fixed value of the Reynolds number Re .

7.3.1 Effect of Reynolds number on noise

Fig. 7.14(a) shows the computational domain, boundary conditions and inflow turbulence intensity for a tandem cylinder case. Both cylinders have a diameter D of 0.1 m and the distance between the centers of the two cylinders in the streamwise direction is $L = 3D$. The aspect ratio of the cylinders is five. Fig. 7.14(b) displays the mesh used to simulate this case for three different values of the Reynolds number: namely for $Re = 60,000$, $120,000$ and $240,000$. The maximum dimensionless wall-normal distance y^+ of the first cell above the cylinder wall is 2.5, 5.0, and 10.0 for $Re = 60,000$, $120,000$, and $240,000$, respectively. We note that y^+ varies because a constant (fixed) mesh condition is used for the three different values of Re . The time step was dynamically adjusted to maintain a maximum CFL number of 0.6, resulting in an higher temporal accuracy than those used for the validation case studies described previously.

The positions of the microphones (observers) used to monitor the sound pressure are displayed in Fig. 7.15. The microphones are located at angular positions θ of 0° , 45° , 90° , 135°

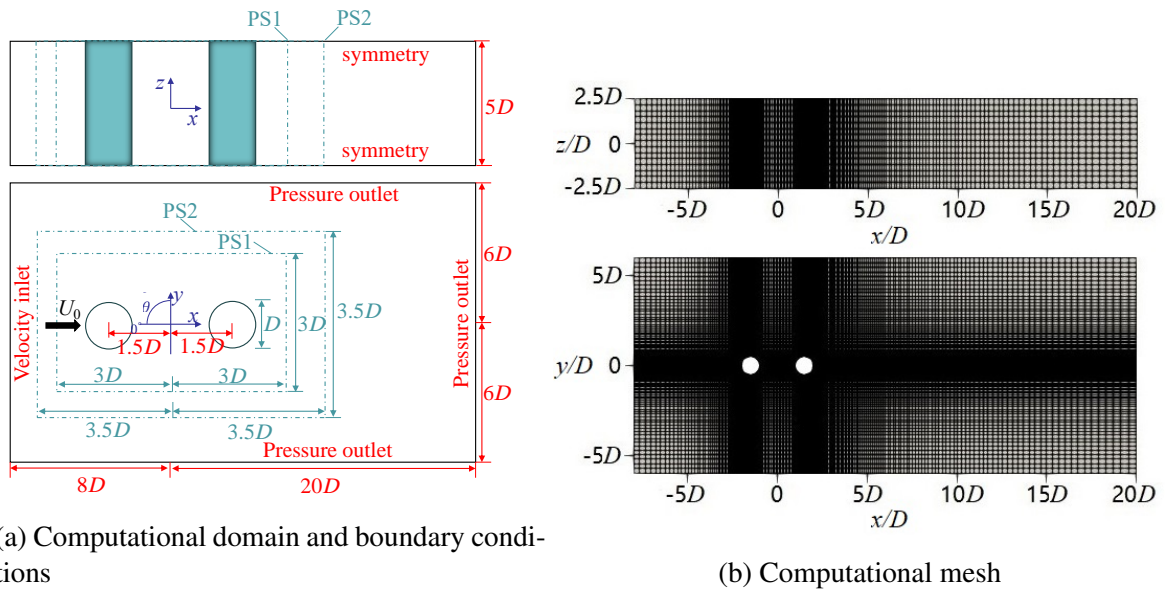


Figure 7.14: (a) The computational domain and boundary conditions and (b) the computational mesh used in the simulation of the tandem cylinders case. The permeable FW-H surfaces used in the prediction of the noise field are shown as PS1 and PS2 in (a).

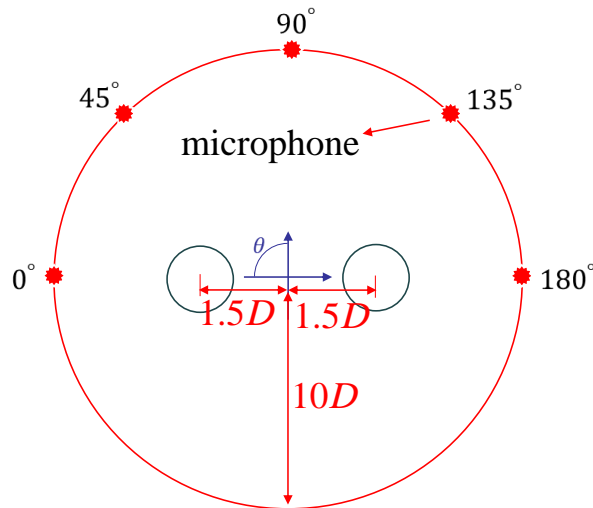
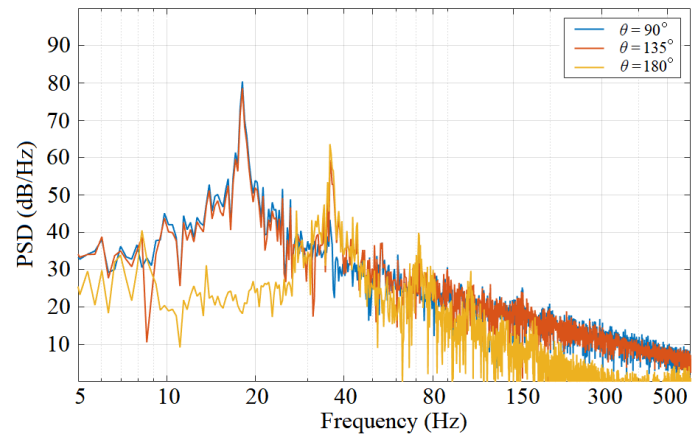
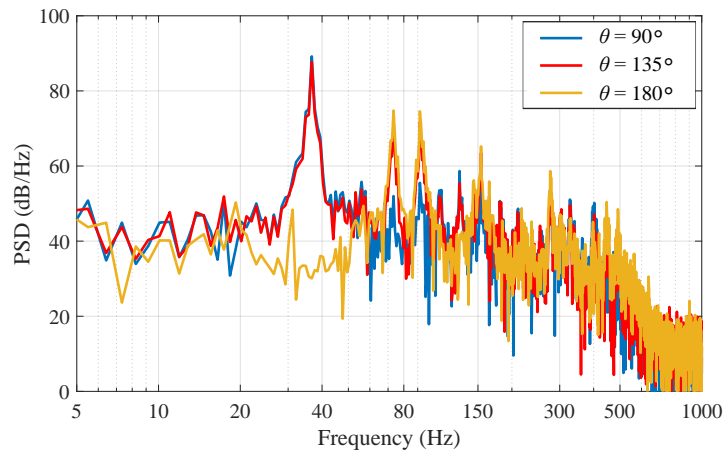


Figure 7.15: The location of the microphones used for monitoring the sound pressure from the noise field generated by a flow over tandem cylinders (viz., a pair of cylinders whose center-to-center separation in the streamwise direction is $L = 3D$).

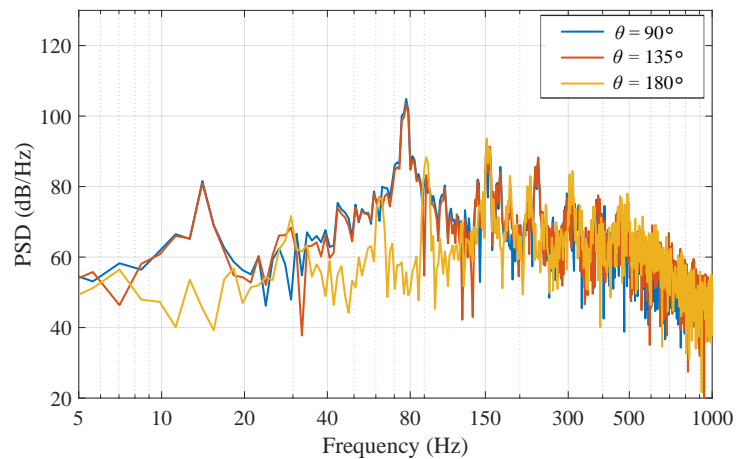
and 180° in the x - y plane (at $z/D = 0$) at a radial distance of $10D$ from the midpoint between the tandem cylinders in the streamwise direction (which coincides with the origin of the Cartesian coordinate system used to describe the computational domain as shown in Fig. 7.14). The walls of both cylinders are used as the impermeable FW-H surface for the determination of the noise field. Fig. 7.16 shows the PSD of the sound pressure level at the microphone locations for $Re = 60,000$, $120,000$, and $240,000$. The peak amplitudes of the sound pressure level PSD depend on the observer location. For $Re = 60,000$, the sound pressure level PSD at an angular position of 90° has a maximum value at a frequency of 19.2 Hz. Furthermore, it is seen that the sound pressure level PSD at an angular position of $\theta = 180^\circ$ has a maximum value at a frequency



(a) $Re = 60,000$



(b) $Re = 120,000$



(c) $Re = 240,000$

Figure 7.16: The sound pressure level PSD at different angular positions θ in the x - y plane (at $z/D = 0$) at a radial distance of $10D$ from the midpoint between the stationary tandem cylinders in the streamwise direction. The surfaces of the two cylinders are taken as the impermeable FW-H surface for determination of the noise field generated by a flow past the tandem cylinders.

of 35.8 Hz. In contrast, the sound pressure level PSD at an angular position of $\theta = 135^\circ$ exhibits spectral peaks at frequencies of 19.2 Hz and 35.8 Hz—these frequencies are related to the lift

force and drag force fluctuations, respectively. This characteristic feature is also exhibited in the SPL power spectra for the other two values of Re (viz., for $Re = 120,000$ and $240,000$), with the SPL PSD at the higher values of Re generally producing a richer set of harmonics.

The sound pressure level PSD at an angular position of $\theta = 135^\circ$ provides additional information, since it takes into account the pressure fluctuations in the transverse (lift) and in-line (drag) directions. Fig. 7.17(a) compares the sound pressure level PSD at an angular location of $\theta = 135^\circ$ for $Re = 60,000$, $120,000$ and $240,000$. The frequency corresponding to the largest (dominant) spectral peak increases with increasing values of Re . This increase is due to the fact that this frequency is associated with the vortex-shedding frequency which, in turn, is correlated with the value of Re . Furthermore, the peak amplitude and the overall spectral amplitudes also increase with increasing values of Re . The directivity pattern for the sound pressure level at three values of Re is shown in Fig. 7.17(b). The SPL directivity pattern is skewed (tilted) in the downwind direction and reaches its maximum value at an angular position θ of around 135° (approximately or better).

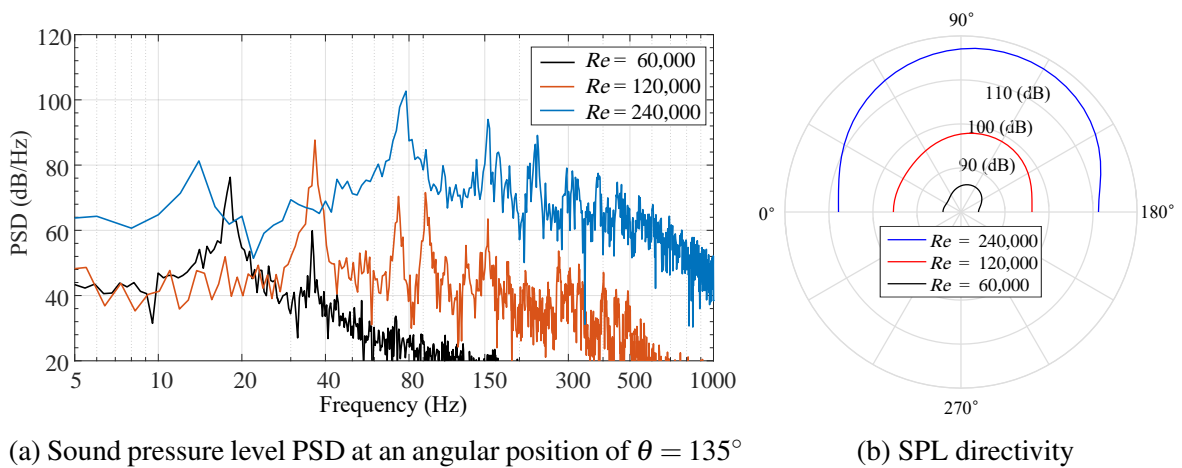


Figure 7.17: (a) The sound pressure level PSD at an angular position of $\theta = 135^\circ$ and (b) the SPL directivity pattern for angular positions in the range $0^\circ \leq \theta \leq 180^\circ$ for three different values of the Reynolds number Re . The sound pressure level is determined in the x - y plane (at $z/D = 0$) at a radial distance of $10D$ from the midpoint between the tandem cylinders in the streamwise direction. The surfaces of the two cylinders are taken as the impermeable FW-H surface for determination of the noise field generated by a flow past the tandem cylinders.

7.3.2 Effect of number of cylinders on noise

For a fixed Reynolds number of $120,000$, the effect of adding a second cylinder on the noise generation is investigated numerically. For the case of a single cylinder, the boundary conditions, domain, inflow turbulence intensity, and the maximum value of the dimensionless wall-normal distance y^+ of the first cell above the wall of the mesh used for the simulation are consistent with those used in sub-section 7.2.1. For the case of tandem cylinders, the boundary conditions, inflow turbulence intensity, and y^+ for the first grid cell above the wall are the same as those used in sub-section 7.3.1.

Fig. 7.18 exhibits the sound pressure level PSD for the flow past a single and tandem cylinder(s) in the x - y plane at $z/D = 0$ at a radial distance of $10D$ at three different angular positions;

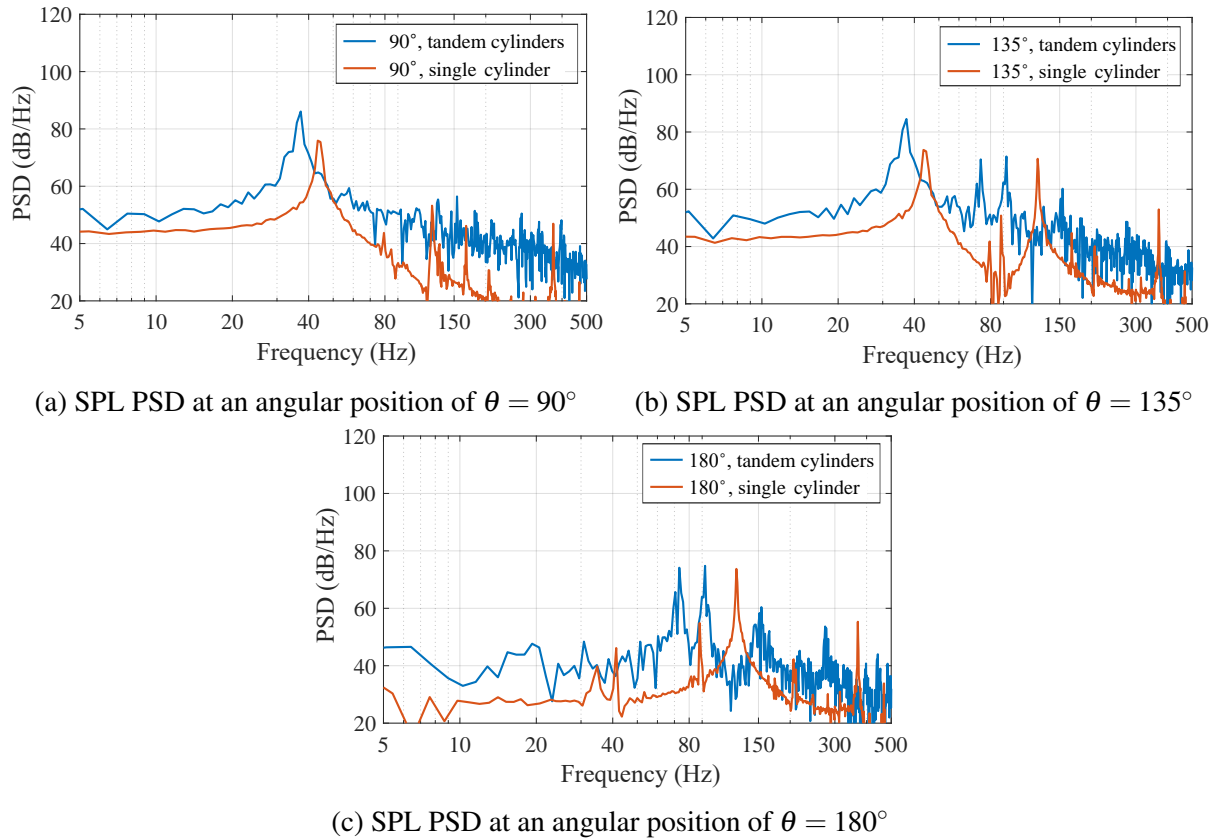


Figure 7.18: The sound pressure level PSD obtained in the x - y plane at $z/D = 0$ at a radial distance of $10D$ for three angular positions $\theta = 90^\circ$, 135° , and 180° for the flow past a single and tandem cylinder(s) at $Re = 120,000$. An impermeable FW-H surface coinciding with the surfaces of the cylinder(s) is used for the prediction of the noise field generated by the flow past a single or tandem cylinder(s).

namely, at $\theta = 90^\circ$, 135° , and 180° . Unless stated otherwise, the radial distance for the determination of the SPL PSD and/or SPL directivity is measured from the center of the cylinder for the single cylinder case or from the midpoint between the streamwise separation of the two cylinders for the tandem cylinders case. As shown in Fig. 7.18, the first tonal frequency of the noise generated by a flow past a single and tandem cylinder(s) is located at 44.56 Hz and 36.24 Hz, respectively. Furthermore, the second tonal frequency of this noise for a single and tandem cylinder(s) is located at 123.07 Hz and 80 Hz, respectively. The sound pressure level PSD for the tandem cylinders exhibits larger amplitudes than those for a single cylinder. In general, the peak frequency value of the SPL PSD for the single cylinder is larger than that of the tandem cylinders, but the spectral amplitude corresponding to this frequency is smaller. In conformance with these observations, a perusal of the SPL PSD for a single and tandem cylinder(s) shows that the acoustic energy at the angular positions of $\theta = 90^\circ$ and 180° is contained primarily in the first and second tones of the noise, respectively. Fig. 7.19 shows the SPL directivity in the x - y plane at $z/D = 0$ at a radial distance of $10D$ for angular positions in the range $0^\circ \leq \theta \leq 360^\circ$. The SPLs for the single and tandem cylinder(s) assume values of approximately 90 dB and 95 dB, respectively.

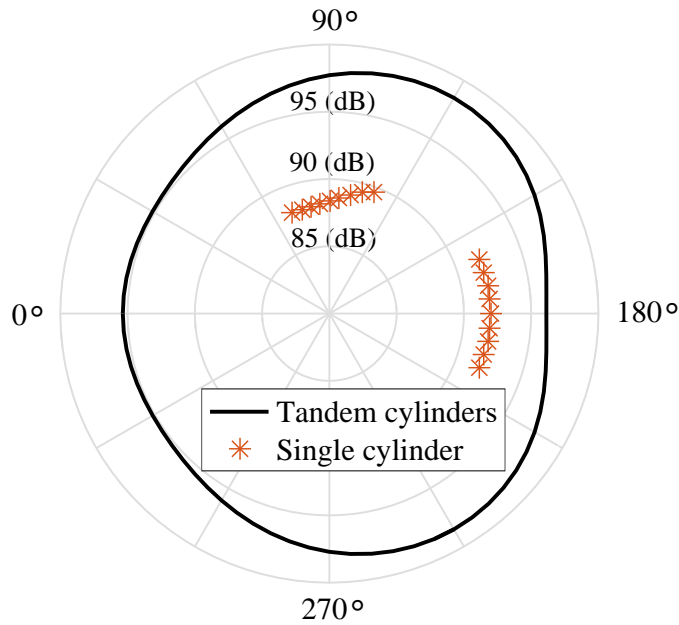


Figure 7.19: The SPL directivity pattern in the x - y plane at $z/D = 0$ at a radial distance of $10D$ obtained for the flow past a single and tandem cylinder(s) at $Re = 120,000$. An impermeable FW-H surface coinciding with the surfaces of the cylinder(s) is used for the prediction of the noise field generated by the flow past a single or tandem cylinder(s).

7.4 Single circular cylinder in forced transverse oscillation at varied frequencies

For the case of a laminar flow past an oscillating cylinder at $Re = 150$, the oscillation frequency significantly affects the aeroacoustic energy of the generated noise at a fixed value of the oscillation amplitude A . In this case, the aeroacoustic energy of an oscillating cylinder for $0.14 < Sc < 0.17$ is suppressed significantly compared to that of a stationary cylinder [25] (Sc is the Scruton number defined as $Sc \equiv fD/U_0$ where f is the oscillation frequency, D is the cylinder diameter, and U_0 is the inflow velocity). However, it is unknown whether the noise suppression arising from the oscillation of a cylinder occurs for a turbulent flow—a regime of flow that has engineering and practical relevance.

This section investigates the effect of the oscillation frequency on the aeroacoustic propagation of a turbulent flow past a transversely oscillating cylinder at a fixed Reynolds number of $Re = 120,000$ with an oscillation amplitude of $A = 0.2D$ and an oscillation frequency f ranging from 5 to 50 Hz (viz., $5 \text{ Hz} \leq f \leq 50 \text{ Hz}$). Five microphones (observers) are positioned in the x - y plane at $z/D = 0$ at a radial distance of $10D$ at angular positions of $\theta = 0^\circ, 45^\circ, 90^\circ, 135^\circ,$ and 180° . The root-mean-square (r.m.s.) values of the fluctuating pressure p' as a function of the Scruton number Sc is shown in Fig. 7.20. Here, the dashed horizontal lines in the figure correspond to the acoustic noise power generated by a flow past the stationary cylinder for the same value of the Reynolds number Re . Overall, the structure of the acoustic energy exhibits a symmetry about the angular position $\theta = 90^\circ$. More specifically, the r.m.s. values of p' as a function of Sc at angular positions of 0° and 45° are the same (approximately or better) as those at 180° and 135° , respectively. Additionally, the r.m.s. values of p' are smallest at the angular positions of $\theta = 0^\circ$ and 180° (viz., in the upstream and downstream directions, respectively). This largest

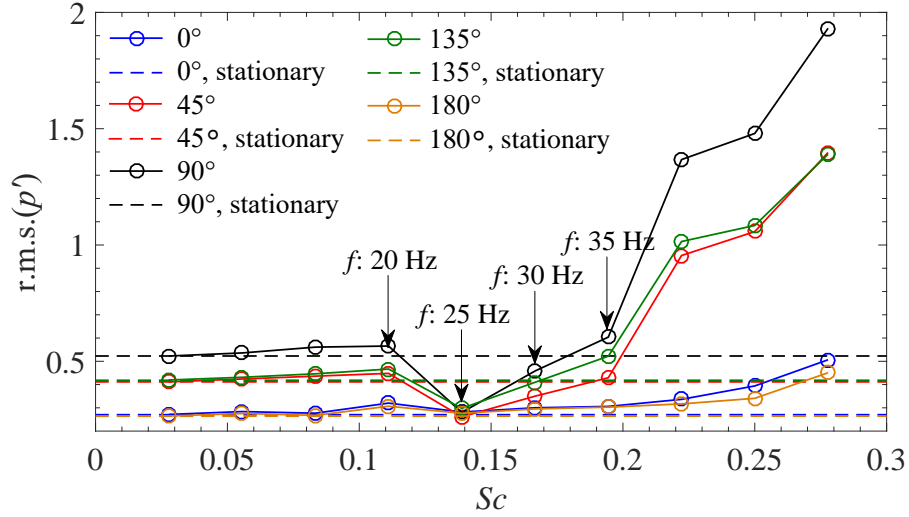


Figure 7.20: Root-mean-square (r.m.s.) values of the fluctuating pressure p' . The results correspond to the noise generated by the flow past a transversely oscillating cylinder at $Re = 120,000$ with an oscillation amplitude $A = 0.2D$ and an oscillation frequency f ranging from 5 to 50 Hz. The five microphones (observers) are positioned in the x - y plane at $z/D = 0$ at a radial distance of $10D$ at angular positions of $\theta = 0^\circ, 45^\circ, 90^\circ, 135^\circ,$ and 180° . The horizontal dashed lines correspond to the r.m.s. values of p' obtained for the stationary cylinder.

levels of the noise occur at an angular position of 90° . More significantly, the acoustic energy is minimum at $Sc \approx 0.15$ for the turbulent flow past an oscillating cylinder at $Re = 120,000$. This observation is consistent with the results reported by Hattori and Komatsu [25] for the case of a laminar flow past an oscillating cylinder at $Re = 150$. In particular, it appears that the observed reduction in the noise occurs when the oscillation frequency of the cylinder is about 57% of the vortex-shedding frequency of the stationary cylinder. For $Sc > 0.2$, the acoustic energy is seen to increase monotonically with increasing values of Sc .

Hattori and Komatsu [25] suggested that the synchronization between the lift force exerted on the cylinder and the inertial force leads to the reduction of the acoustic power. For $0.14 < Sc < 0.17$, the periodic lock-in to the cylinder oscillation reduces the lift force and, thereby, the acoustic power. However, the work did not discuss how the synchronization modifies the two aeroacoustic sources provided by the forced oscillation and the original vortex shedding (viz., the vortex shedding from the stationary cylinder). Such an analysis can provide deeper physical insights concerning the impact of the synchronization.

Fig. 7.21 displays the power spectrum of the fluctuating pressure p' obtained from a microphone (observer) in the x - y plane at $z/D = 0$ at a radial distance of $10D$ at an angular position of $\theta = 135^\circ$. For the case of a stationary cylinder, the power spectrum of p' has only one dominant peak at a frequency of 44 Hz with an amplitude of 0.42 Pa arising from the vortex shedding. For a cylinder with an oscillation frequency f of 20 Hz, the power spectrum of p' exhibits two dominant peaks with frequencies of 20 Hz and 44 Hz. These two frequencies correspond to the frequency of the forced oscillation (20 Hz) and to the frequency associated with the vortex shedding from the stationary cylinder (44 Hz). The amplitude of the spectral peak at 44 Hz (due to vortex shedding) is comparable to that for the stationary cylinder.

As the oscillation frequency f of the cylinder increases to 25 Hz ($Sc = 0.14$), the first peak in the p' power spectrum at 25 Hz (correlated with the structural motion) is enhanced in amplitude

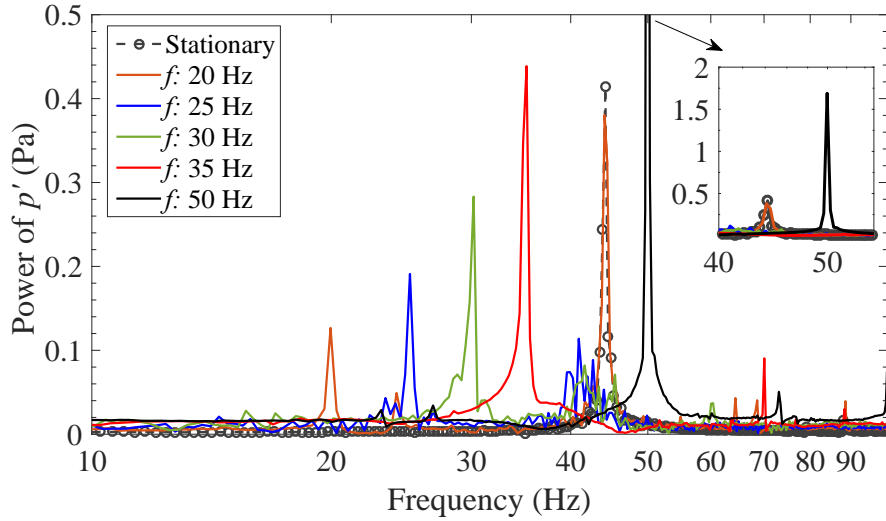


Figure 7.21: Power spectrum of the fluctuating pressure p' obtained from a microphone (observer) positioned in the x - y plane at $z/D = 0$ at a radial distance of $10D$ at an angular position of $\theta = 135^\circ$. The p' power spectrum for the stationary cylinder is compared with a cylinder with oscillation frequencies f of 20, 25, 30, 35, and 50 Hz.

relative to that of the p' power spectrum for the cylinder with an oscillation frequency of 20 Hz. In contrast, the second peak at 44 Hz (corresponding to the vortex shedding of the stationary cylinder) is reduced in amplitude relative to that for the p' power spectrum for the cylinder with $f = 20$ Hz. This reduction in the spectral peak amplitude is associated with an overall decrease in the total sound pressure (cf. Fig. 7.20).

As the cylinder oscillation frequency f increases further to 30 Hz ($Sc = 0.17$), the amplitudes of the first and second dominant peaks in the p' power spectrum are further increased and decreased (suppressed), respectively, relative to those for the p' power spectra for cylinders with smaller values of the oscillation frequency f . For cylinder oscillation frequencies $f \geq 35$ Hz, the total acoustic power (sound pressure) begins increasing again (cf. Fig. 7.20) owing to the increased amplitude of the (dominant) first peak in the p' power spectrum. Indeed, for cylinder oscillation frequencies greater than 35 Hz, the second peak in the p' power spectrum disappears altogether. The overall sound pressure exhibits a monotonic increase with increasing values of Sc (or, cylinder oscillation frequency f) owing to the fact that the amplitude of the first (dominant) peak in the p' power spectrum increases monotonically with f . More specifically, the monotonic increase in the overall sound pressure appears to be exponential with increasing values of Sc . In consequence, the effective value of the sound pressure already approaches 2.0 Pa when the cylinder oscillation frequency is 50 Hz ($Sc = 0.28$).

Based on the preceding discussion, the oscillation of the cylinder generates a thickness noise $p'_T(\mathbf{x}, t)$ (cf. Eq. (B.2)) arising from the periodic structural motion. To further understand the influence of the structural motion on the noise generation, we decompose the total noise into a loading $p'_L(\mathbf{x}, t)$ and a thickness $p'_T(\mathbf{x}, t)$ noise contribution and use the surface of the cylinder as the control surface for the application of the FW-H methodology (implying that there is no quadrupole noise contribution). To this purpose, we consider the noise generated by an oscillating cylinder with an oscillation frequency $f = 0$ Hz (stationary cylinder), 20 Hz, 25 Hz, and 50 Hz. The r.m.s. values of fluctuating pressure p' for the loading and thickness noise are summarized in Fig. 7.22. The loading and thickness noise are highlighted in the figure using blue and

f	Sc	0°	45°	90°	135°	180°			
0 Hz	0	0.2704	0.4115	0.5228	0.4184	0.2640			
		0.2704	0	0.4115	0	0.5228	0	0.4184	0
20 Hz	0.1111	0.3202	0.4481	0.5657	0.4667	0.3068			
		0.3192	0.0134	0.4465	0.0806	0.5592	0.1157	0.4613	0.0807
25 Hz	0.1389	0.2818	0.2614	0.2803	0.29785	0.2765			
		0.2824	0.0136	0.2445	0.1496	0.2322	0.2202	0.2706	0.1500
50 Hz	0.2778	0.5065	1.3977	1.9317	1.3900	0.4508			
		0.4613	0.1538	0.9323	0.9433	1.1999	1.4565	0.8574	0.9471

Figure 7.22: The r.m.s. value of the fluctuating pressure p' (Pa) obtained for an oscillating cylinder with oscillation frequency f (equivalently Sc) of 0 Hz (stationary cylinder), 20 Hz, 25 Hz and 50 Hz in the x - y plane at $z/D = 0$ at a radial distance of $10D$ at angular positions of 0° (upstream direction), 45° , 90° , 135° and 180° (downstream direction). An impermeable FW-H surface (cylinder walls) is used to determine the noise field generated by the flow past the cylinder. Under each column associated with a particular angular position, the total sound pressure, loading noise, and thickness noise are highlighted in the white, blue and yellow boxes, respectively.

yellow colours, respectively. The r.m.s value of the total sound pressure is not equal to the sum of the r.m.s values of the loading and thickness noise owing to the fact that the fluctuations of the loading and thickness noise involve phase differences. As a consequence, for the case of a cylinder oscillating with a frequency of $f = 20$ Hz, at a radial distance of $10D$ and an angular position of $\theta = 180^\circ$ (downstream direction), the value of the total sound pressure of 0.3068 Pa is smaller than the value of the loading noise (cf. the values shown in red in the column corresponding to an angular position of 180° in Fig. 7.22).

For the stationary cylinder (oscillation frequency $f = 0$ Hz), there are no components in the acoustic field arising from the thickness noise due to the fact that a fixed cylinder surface is used in the application of the FW-H methodology. As the cylinder starts to move to-and-fro (from side to side), the r.m.s. value of p' associated with the thickness noise (highlighted in yellow in Fig. 7.22) increases monotonically with an increasing cylinder oscillation frequency. However, the r.m.s. value of p' arising from the loading noise (highlighted in blue in Fig. 7.22) exhibits a sudden decrease at 25 Hz, after which it increases again. More specifically, a comparison of Fig. 7.21 with Fig. 7.22 shows that the loading noise is not related to the second peak in the p' power spectrum (which corresponds to the vortex shedding from the stationary cylinder). This is because the second peak is seen to disappear at a certain oscillation frequency and then re-appear again with an amplitude that increases with increasing cylinder oscillation frequency.

Fig. 7.23(a) shows the power spectrum of the fluctuating pressure p' for a cylinder with oscillation frequencies f of 20, 25, and 50 Hz. The microphone (observer) is positioned in the x - y plane at $z/D = 0$ at a radial distance of $10D$ and at an angular position of $\theta = 135^\circ$. It is noted that the noise generated by the stationary cylinder includes only the loading noise (with a dominant peak frequency of 44 Hz). For an oscillating cylinder with oscillation frequencies of 20, 25, and 50 Hz, both the loading and thickness components of the noise exist. This implies that the motion of the cylinder gives rise to both a loading and a thickness component of the noise. The energy associated with these two components of the noise is comparable in magnitude.

Next, we consider the quadrupole component of the noise arising from the turbulence of the

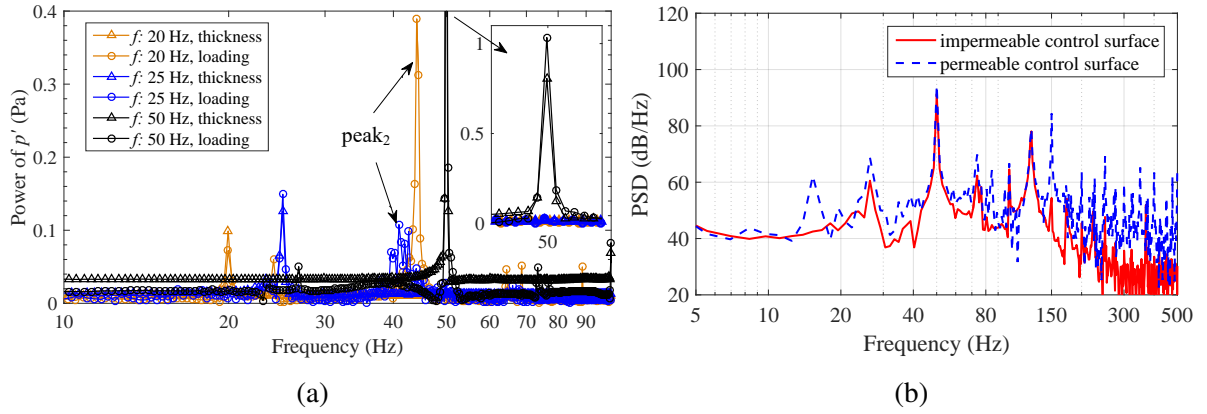


Figure 7.23: FW-H predictions of (a) the power spectrum of the fluctuating pressure p' obtained from a microphone (observer) positioned in the x - y plane at $z/D = 0$ at a radial distance of $10D$ and an angular position of $\theta = 135^\circ$ for a cylinder oscillating with frequencies f of 20, 25, and 50 Hz and (b) the power spectral density of the SPL obtained using an impermeable (cylinder walls) and a permeable (PS0) FW-H control surface for a cylinder oscillating with a frequency f of 50 Hz.

flow. The power spectral density of the SPL obtained at the microphone location (given above) for an oscillating cylinder with an oscillation frequency f of 50 Hz is shown in Fig. 7.23(b). In this figure, we compare the results obtained using the FW-H methodology for two different control surfaces: namely, an impermeable (cylinder walls) and a permeable FW-H surface (PS0) (see Fig. 7.2(a) for the delineation of PS0). The quadrupole noise resulting from the use of the permeable control surface appears to enhance the energy of the broadband noise relative to that obtained from the impermeable control surface. Nevertheless, the peak energy obtained using the two FW-H control surfaces is comparable. The broadband characteristics of the quadrupole noise are consistent with the chaotic nature of the turbulence.

7.5 Single circular cylinder with forced oscillations in the transverse or streamwise directions

This section will study the vortex structure and the noise characteristics for a flow past a single oscillating cylinder at $Re = 120,000$ that is free to vibrate in either the transverse or streamwise directions [262, 263]. The computational domain, boundary conditions, inflow turbulence intensity, and mesh are the same as those in sub-section 7.3.2. Fig. 7.24 displays the three cases investigated in this section: namely, a stationary cylinder, a cylinder oscillating in the transverse direction, and a cylinder oscillating in the streamwise direction. The amplitude and frequency of the cylinder oscillations are fixed to $A/D = 1$ and $f = 20$ Hz ($Sc = 0.111$). Thirty complete cycles of oscillations are used for the time-domain analysis.

7.5.1 Analysis of unsteady vortex structures

Vortex shedding from a cylinder is significant in the generation of noise. The use of vorticity is a popular method for the visualization of the vortex structure in a turbulent wake. Unfortu-

nately, the components of the vorticity vector depends on the coordinate system. Haller [264] proposed an objective description of a vortex using an invariant of the velocity gradient tensor:

$$Q = \frac{1}{4} (\omega_{ij}\omega_{ij} - 2S_{ij}S_{ij}) , \quad (7.4)$$

where Q is the second invariant of the velocity gradient tensor under a Galilean transformation, S_{ij} is the strain-rate tensor defined as $S_{ij} \equiv \frac{1}{2} \left(\frac{\partial u_i}{\partial x_j} + \frac{\partial u_j}{\partial x_i} \right)$, ω_{ij} is the rotation tensor defined as $\omega_{ij} \equiv \frac{1}{2} \left(\frac{\partial u_i}{\partial x_j} - \frac{\partial u_j}{\partial x_i} \right)$, and $i, j = 1, 2, 3$ represent the coordinate directions.

Eq. 7.4 implies that Q at a location in the flow is the difference between the rotation and the strain rate. If this difference is positive so that the rotation rate (or, swirling rate) is greater than the strain rate (or, axial deformation rate), then vortex structures dominate at this location in the flow. Therefore, the locations where $Q > 0$ can be used as a criterion for the identification of vortices in the flow. Another important invariant is the third invariant of the velocity gradient tensor under a Galilean transformation given by

$$R = \frac{1}{3} \left(S_{ij}S_{jk}S_{ki} + \frac{3}{4}\omega_i\omega_jS_{ij} \right) , \quad (7.5)$$

where ω_i are the components of the vorticity vector. Both Q and R can be used to distinguish vortex structures in the flow field. When Q is positive and large (implying that the rotation rate is greater than the strain rate), then the third invariant $R \approx 0.25\omega_i\omega_jS_{ij}$ represents the strength of vortex extension. When R is negative, the vortex structure is compressed and the vortex is weak. When R is positive, the vortex structure is stretched, and the vortex is strong. When Q is negative and large, the strain rate is greater than the rotation rate, and the flow field is mainly dominated by the strain. It is worth noting that both Q and R take values of zero near the wall and, as a result, the use of Q and R for the description of vortical motion avoids an over-prediction of vortices in the near-wall region.

Fig. 7.25 shows the velocity gradient tensor invariants for the stationary and oscillating single cylinder. The flow past a stationary cylinder exhibits regular vortices in the wake. Near the stationary cylinder surface, the value of Q is positive and large, implying that the vortex is already formed in this region of the flow. Additionally, the small absolute value of R at specific positions

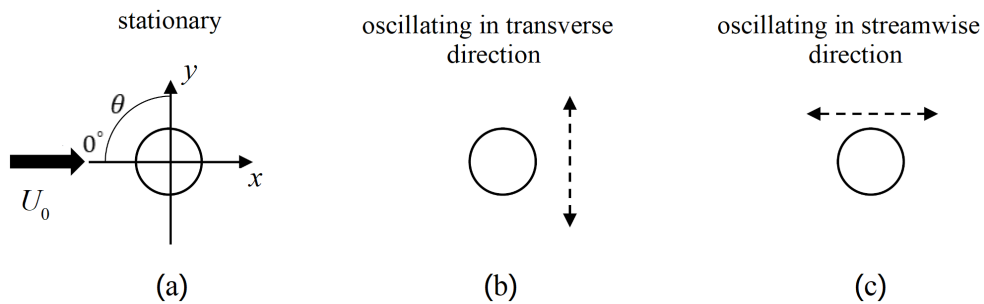


Figure 7.24: Three cases: (a) single stationary cylinder; (b) single cylinder oscillating in the transverse (or, y -) direction; and, (c) single cylinder oscillating in the streamwise (or, x -) direction. For cases (b) and (c), the cylinder is oscillating with an amplitude $A = D$ and a frequency $f = 20$ Hz.

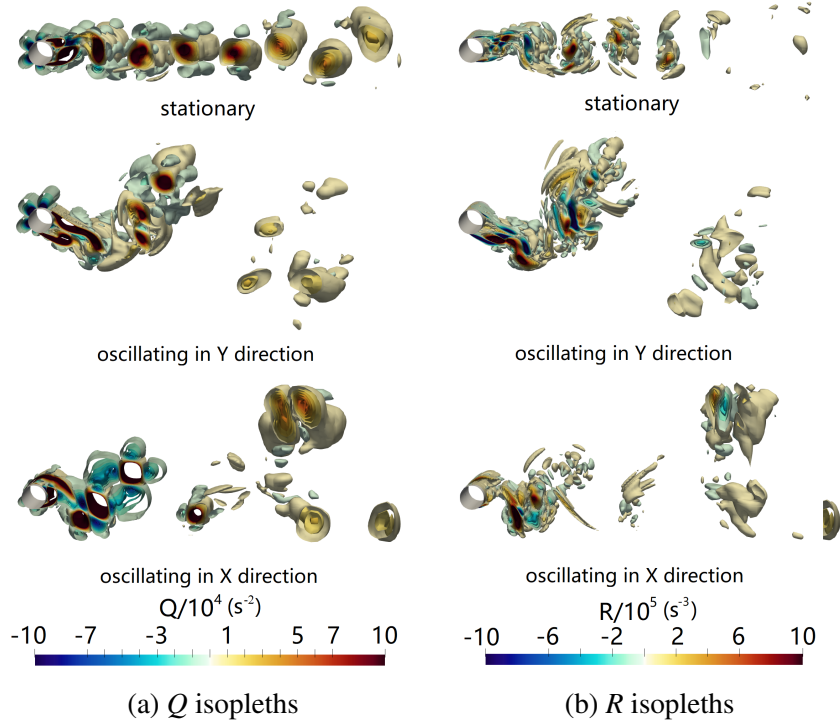


Figure 7.25: Isopleths of the (a) second invariant Q and (b) third invariant R obtained when the cylinder passes through the initial position (viz., the stationary position for the oscillating cylinder) after several oscillation cycles for three cases: namely, a stationary cylinder, a cylinder oscillating in the transverse (y -) direction, and a cylinder oscillating in the streamwise (x -) direction.

in the wake indicates flow regions where the vortex structure is relatively stable. When R is positive and large, the vortex is strengthened. The third invariant R has a large absolute value, but is positive near the lower surface and negative near the upper surface of the cylinder, implying that the vortex is strengthened near the lower surface.

When the cylinder vibrates in the transverse direction, the isopleths of Q in the wake become more complex. Overall, the positive and negative regions are staggered, indicating that the effects of rotation and strain jointly dominate the dynamics of the unsteady wake. Moreover, the large values of Q and R suggest that the vibration of the cylinder results in the detachment of the vortex from the cylinder surface, elongating and ejecting the vortex as a result of the transverse motion (velocity) of the cylinder. The vortices that are shed from the cylinder move downstream and these coherent structures are gradually smeared (dissipated) in the wake.

7.5.2 Analysis of the acoustic field

Figs 7.26(a) and (b) display the SPL PSD obtained at a microphone (observer) positioned in the x - y plane at $z/D = 0$ at a radial distance of $10D$ and at an angular position of $\theta = 135^\circ$. The results are shown for both the flow past a stationary and an oscillating cylinder (with an oscillation frequency $f = 20$ Hz) with $Re = 120,000$. For each case, the FW-H methodology is applied using an impermeable (cylinder walls) and a permeable (PS0) FW-H control surface. For the flow past a stationary cylinder, the SPL PSD obtained using the permeable FW-H surface exhibits larger values of the amplitude in the frequency range from 10 Hz to 80 Hz and is more

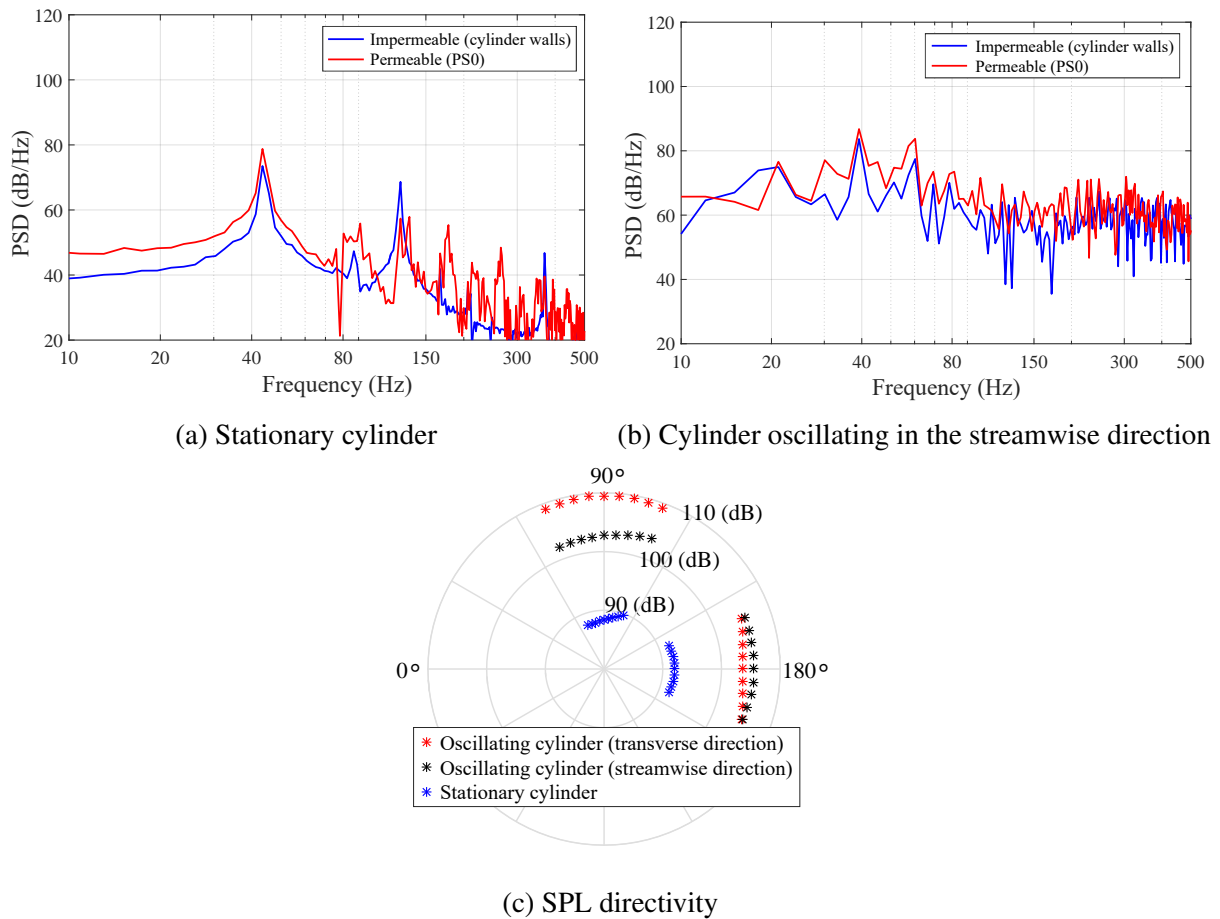


Figure 7.26: The SPL PSD obtained for (a) a stationary cylinder and (b) a cylinder oscillating in the streamwise (x -) direction at a microphone positioned in the x - y plane at $z/D = 0$ at a radial distance of $10D$ and at an angular position of $\theta = 135^\circ$. The FW-H methodology is applied in both cases for an impermeable (cylinder walls) and a permeable (PS0) FW-H surface. (c) The SPL directivity pattern obtained for a stationary cylinder, a cylinder oscillating in the transverse direction, and a cylinder oscillating in the streamwise direction at the same microphone location as in (a) and (b) using an impermeable FW-H surface coinciding with the cylinder walls.

complex (viz., exhibits a more complex structure in the spectral peaks) for frequencies greater than about 80 Hz. The dominant peak in the SPL PSD for the stationary cylinder corresponding to a frequency of 43 Hz is associated with the vortex-shedding frequency. In contrast, the SPL PSD for a flow past an oscillating cylinder exhibits characteristics that are consistent with those of broadband noise. Even so, the SPL PSD in this case still exhibits spectral peaks at 20, 40, and 60 Hz—frequencies that are associated with the various harmonics of the cylinder oscillation frequency (viz., 20 Hz).

Fig. 7.26(c) displays the SPL directivity pattern (with the cylinder surface used as the FW-H control surface) obtained for a stationary cylinder, a cylinder oscillating in the transverse (y -) direction, and a cylinder oscillating in the streamwise (x -) direction. A perusal of this figure shows that the sound pressure level from the flow past a stationary cylinder is smaller than that for the oscillating cylinder (in either the transverse or streamwise directions). In a direction orthogonal to the flow direction (viz., at an angular position θ of around 90°), the cylinder oscillating in the transverse direction exhibits a larger sound pressure level than the cylinder

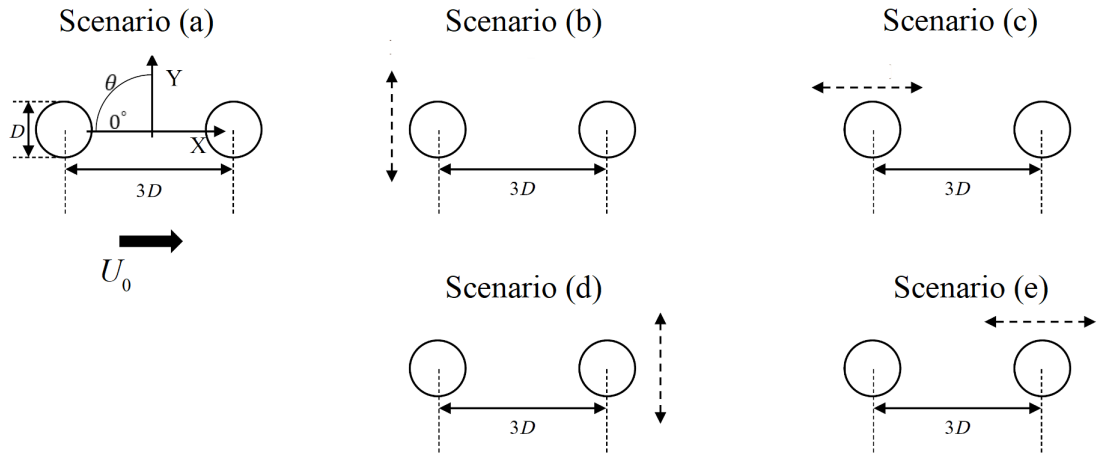


Figure 7.27: Five cases (scenarios) of tandem cylinders: (1) Scenario (a)—front and rear cylinders stationary; (2) Scenario (b)—front cylinder oscillating in transverse direction and rear cylinder stationary; (3) Scenario (c)—front cylinder oscillating in streamwise direction and rear cylinder stationary; (4) Scenario (d)—front cylinder stationary and rear cylinder oscillating in transverse direction; and, (5) Scenario (e)—front cylinder stationary and rear cylinder oscillating in streamwise direction.

oscillating in the streamwise direction. In contrast, the sound pressure level for the cylinder oscillating in the transverse and streamwise directions are comparable in the flow direction (viz., at an angular position θ of around 180°).

7.6 Tandem cylinders with forced oscillations in the transverse or streamwise directions

This section investigates the acoustic field for a flow past a stationary and oscillating tandem cylinder(s) at a Reynolds number $Re = 120,000$ for a number of different cases. The computational domain, boundary conditions, inflow turbulence intensity, and mesh are same as in Section 7.3. Fig. 7.27 shows the five cases (scenarios) that will be investigated here for the tandem cylinders. For the cases (scenarios) where one of the cylinders is oscillating, the amplitude and frequency of the oscillation are $A = D$ and $f = 20$ Hz, respectively. The five cases (scenarios) considered herein are as follows: (1) Scenario (a)—front (upstream) and rear (downstream) cylinders both stationary; (2) Scenario (b)—front cylinder oscillating in the transverse direction and rear cylinder stationary; (3) Scenario (c)—front cylinder oscillating in the streamwise direction and rear cylinder stationary; (4) Scenario (d)—front cylinder stationary and rear cylinder oscillating in the transverse direction; and, (5) Scenario (e)—front cylinder stationary and rear cylinder oscillating in the streamwise direction.

7.6.1 Analysis of average pressure on the cylinder surfaces

Fig. 7.28 displays the PSD of the average surface pressure on the front and rear cylinders. When both cylinders are stationary (cf. Fig. 7.28(a)), the peak values of the average surface

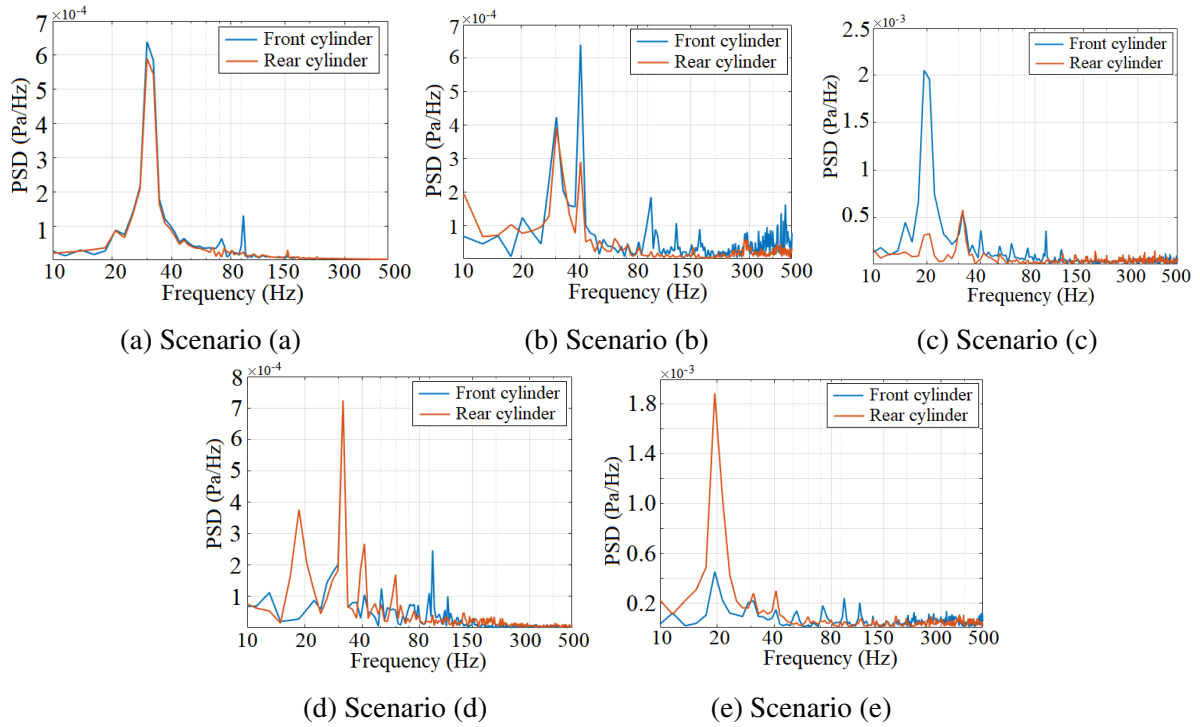


Figure 7.28: The average surface pressure PSD for the front and rear cylinders for five cases (scenarios): (a) front and rear cylinders stationary; (b) front cylinder oscillating in the transverse direction and rear cylinder stationary; (c) front cylinder oscillating in the streamwise (in-line) direction and rear cylinder stationary; (d) front cylinder stationary and rear cylinder oscillating in the transverse direction; and, (e) front cylinder stationary and rear cylinder oscillating in the streamwise (in-line) direction.

pressure PSD for the front cylinder occur at frequencies of about 35 Hz and 80 Hz—these two frequencies correspond to the lift and drag force fluctuations, respectively. Due to the vortex-shedding from the front cylinder, the average surface pressure PSD of the rear cylinder also exhibits a spectral peak at a frequency of about 35 Hz. However, the average surface pressure PSD of the rear cylinder does not exhibit a spectral peak at a frequency of 80 Hz implying that this cylinder is minimally influenced (impacted) by the drag force fluctuations arising from the front cylinder.

For Scenario (b), the average surface pressure PSD for the front cylinder exhibits a spectral peak value at a frequency of 20 Hz (fundamental frequency) and a second spectral peak value (corresponding to the first harmonic) at a frequency of 40 Hz. This second spectral peak (first harmonic) has a larger amplitude than the first peak (fundamental frequency). These characteristics of the average surface pressure PSD are also reflected generally in those of the rear cylinder. In Scenario (c), the amplitude of the first spectral peak (fundamental frequency at 20 Hz) is larger than that of the second spectral peak (first harmonic at 40 Hz) in the average surface pressure PSD of the front cylinder. Furthermore, vibrations in the streamwise (in-line) direction appears to weaken the vortex shedding and, as a result, the spectral peak amplitude of the rear cylinder sound pressure level PSD at a frequency of 30 Hz is smaller relative to that associated with fundamental frequency at 20 Hz. This phenomenon is observed for in-line oscillations of either the front or the rear cylinder. As can be seen from the amplitudes of the average surface pressure PSD, when either the front or rear cylinder is oscillating in the in-line direction (cf. Figs 7.28(c) and

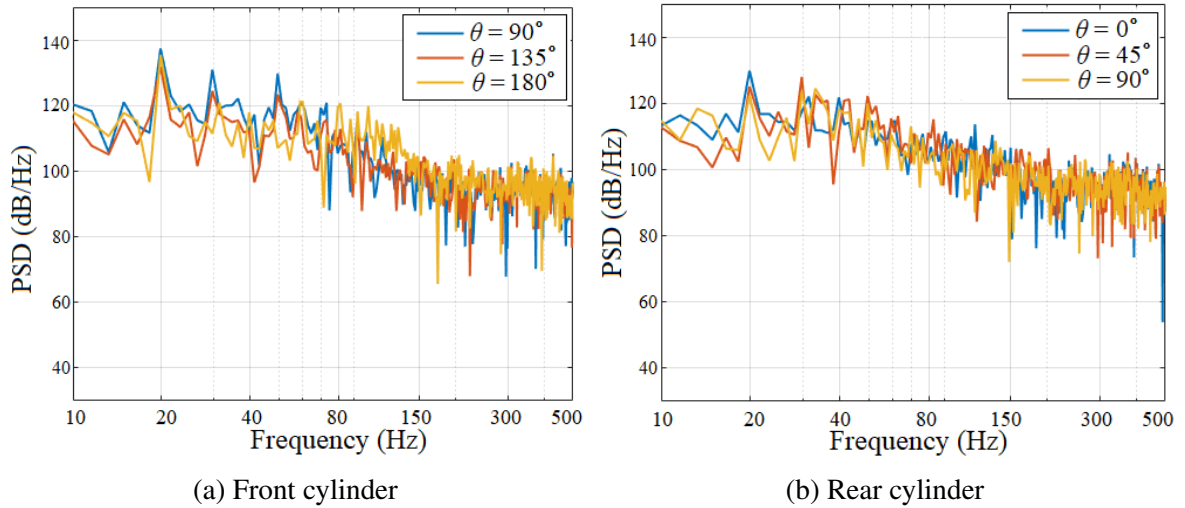


Figure 7.29: The sound pressure level PSD at various angular positions θ on the surface of the front (upstream) and rear (downstream) cylinders for the case where the front cylinder is oscillating in the streamwise (in-line) direction and the rear cylinder is stationary (Scenario (c)).

(e)), the amplitude of the spectral peak value at a frequency of 20 Hz is about $2 \times 10^{-3} \text{ Pa Hz}^{-1}$. However, the cases involving two stationary cylinders or one or the other cylinder oscillating in the transverse direction (cf. Figs 7.28(a), (b), and (d)), the amplitude of the spectral peak at a frequency of 20 Hz is less than $1 \times 10^{-3} \text{ Pa Hz}^{-1}$. The surface pressure fluctuations resulting from an in-line oscillation of either the front or rear cylinder is larger than those resulting from a transverse oscillation of either the front or rear cylinder.

We use Scenario (c) to analyze the variation of the sound pressure level along the cylinder surface. The SPL PSDs at three angular positions on the front cylinder (viz., at $\theta = 90^\circ$, 135° and 180°) and at three angular positions on the rear cylinder (viz., at $\theta = 0^\circ$, 45° and 90°) are exhibited in Fig. 7.29. The frequencies associated with the spectral peaks of the SPL at these angular positions are similar to those of the average surface pressure—in particular, there are dominant peaks corresponding to frequencies of around 20 Hz and 30 Hz. However, the amplitude of each peak varies depending on the angular position of the observer. These results are similar to the fluctuating surface pressure power spectra (cf. Fig. 7.10) on the cylinder measured in the NASA tandem cylinders experiment (see Section 7.2.2).

Fig. 7.30 shows the mean pressure coefficient C_p as a function of the arclength $s \equiv \pi D \theta / 360$ along two different circular arcs on the front and rear cylinders for the five scenarios summarized in Fig. 7.27. The reference pressure at the upwind stagnation point of the front cylinder for each of these scenarios is different. When both the front and rear cylinders are stationary, the mean pressure coefficient for the rear cylinder varies with the spanwise location of the circular arc (e.g., positions 1 and 2 shown in Fig. 7.30(a)) which is indicative of the effect of the strong three-dimensional nature of the flow around the rear cylinder. For the cases when one or the other cylinder oscillates, the mean pressure coefficient C_p is more uniform along the spanwise direction for the rear cylinder.

In general, the oscillatory motion of one or the other cylinder has a very small effect on the C_p distribution of the front cylinder, but significantly affects the C_p distribution of the rear cylinder. In particular, the location of the separation point on the front cylinder does not exhibit significant variations (viz., the separation point is located at $s \approx 0.065$, except for Scenario (b) where from

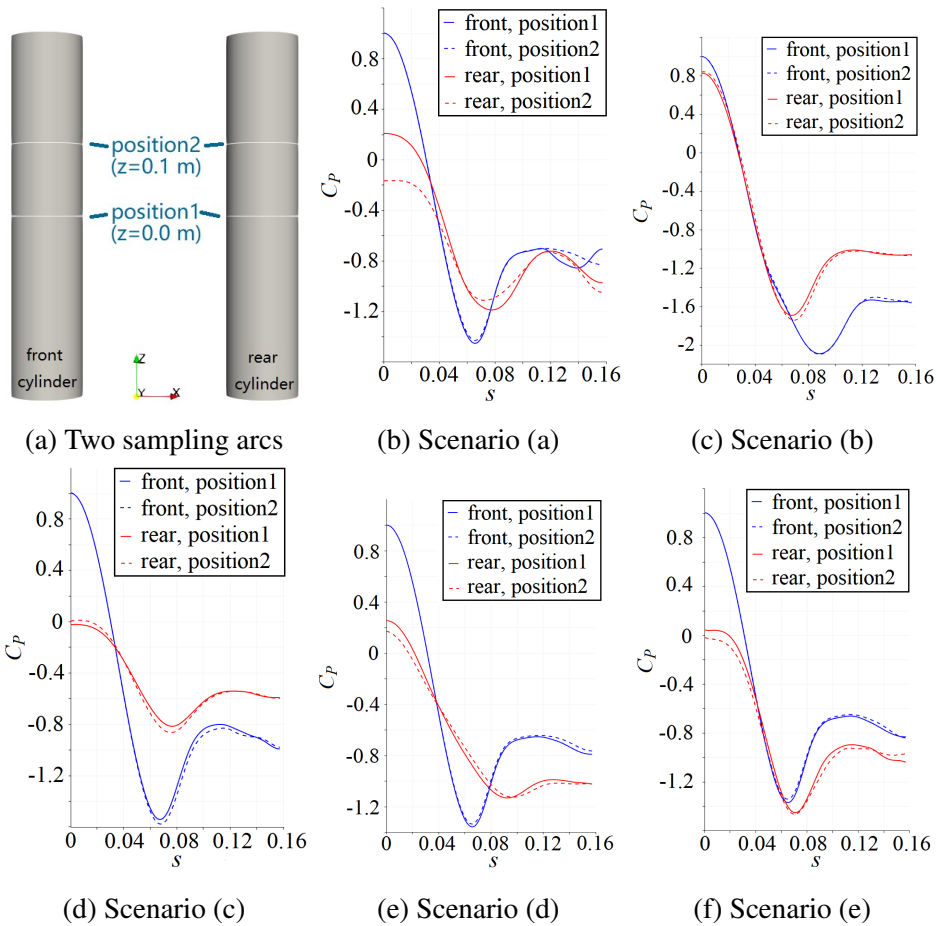


Figure 7.30: The mean pressure coefficient C_P as a function of the arclength $s \equiv \pi D\theta/360$ along circular arcs at (a) two spanwise positions on the surface of the front and rear cylinders. The dependence of C_P on s for the front and rear cylinders is summarized for five different scenarios: (b) Scenario (a)—front and rear cylinders stationary; (c) Scenario (b)—front cylinder oscillating in the transverse direction and rear cylinder stationary; (d) Scenario (c)—front cylinder oscillating in the streamwise (in-line) direction and rear cylinder stationary; (e) Scenario (d)—front cylinder stationary and rear cylinder oscillating in the transverse direction; and, (f) Scenario (e)—front cylinder stationary and rear cylinder oscillating in the streamwise (in-line) direction.

Fig. 7.30(c) it is seen that the separation point is located at $s \approx 0.085$). This insensitivity of the separation point location is due to the relative uniformity of the incident flow and to the stable and dominant vortex shedding from the front (upstream) cylinder. Nevertheless, the oscillation of the front cylinder in the transverse direction has a significant effect on the dynamics of the vortex shedding, leading to the movement of the separation point location as is evident from a careful examination of Fig. 7.30(c). In contrast to the front cylinder, the flow incident on the rear (downstream) cylinder is rather complex, and the oscillatory motion of the front cylinder appears to alter both the location of the separation point and the surface pressure distribution of the rear cylinder. When one or the other cylinder vibrates in the in-line direction, the pressure coefficient C_P at the stagnation point of the rear cylinder is approximately zero. The near vanishing of the pressure coefficient here may be due to the continuous stretching and squeezing of the fluid between the two cylinders as one of the cylinders oscillates in the streamwise (in-line) direction.

7.6.2 Analysis of unsteady vortex structures

Fig. 7.31 displays the isopleths of the velocity gradient tensor invariants Q and R for the tandem cylinders for the five scenarios summarized in Fig. 7.27. For the case where the front and rear cylinders are both stationary (cf. Fig. 7.31(a)), the value of Q near the center of the shed vortices is positive, indicating that the vortex structure plays a leading role in the advection of these structures at the given location. The downstream development of the wake of the front cylinder is suppressed owing to the presence of the rear cylinder. The vortex shedding from the rear cylinder is more regular than that of the front cylinder for all five scenarios studied. Near the stagnation point of the cylinder surfaces, the value of Q is large and negative, suggesting that the flow is dominated by strain at the stagnation point. The isopleths of R show that the flow is highly complex. When the vortex shed by the front cylinder collides with the rear cylinder, the value of R is negative with a large absolute value, implying that the strain dominates this region of the flow.

When the front cylinder begins to vibrate in the streamwise (in-line) direction (cf. Fig. 7.31(c)), it is seen from a careful perusal of the isopleths of Q and R that the vortices shed by the front (upstream) cylinder are squeezed between the two cylinders. This compression of the shed vortices from the upstream cylinder does not occur in the case of a single cylinder. When the front cylinder begins to vibrate in the transverse direction (cf. Fig. 7.31(b)), the large values of Q suggest that the vibration of the front cylinder ejects the detached vortex away from the region between the two cylinders. These ejected vortices are not as easily squeezed by the in-line motion of one or the other of the cylinders.

Furthermore, it can be observed from an examination of the isopleths of R that the oscillations of the rear cylinder generate more flow regions with large $|R|$ in the wake—this results in more instability of the flow in the wake region. An increased instability of the wake region, in turn, increases the sound level of the broadband noise. While the regularly shed vortices produce the dominant peaks in the noise power spectrum, the dynamical processes associated with wake instability and broken vortices increase the energy of the broadband noise.

7.6.3 Analysis of acoustic field

In this section, the SPL PSD for Scenario (d) (viz., front cylinder stationary and rear cylinder oscillating in transverse direction) is analyzed. To this purpose, the SPL PSDs acquired in the x - y plane at $z/D = 0$ at a radial distance of $10D$ at various angular positions θ are compared. The impermeable cylinder walls and the permeable surfaces designated previously as PS1 and PS2 are used as the FW-H surfaces. As a reminder for the reader, the two permeable FW-H surfaces PS1 and PS2 used here are shown in Fig. 7.14(a).

Fig. 7.32 shows the SPL PSDs at microphones (observers) positioned at angular positions of $\theta = 0^\circ, 45^\circ, 90^\circ, 135^\circ,$ and 180° at a radial distance of $10D$ from the midpoint of the streamwise separation between the pair of cylinders (where the front cylinder is stationary and the rear cylinder is oscillating in the streamwise direction). The SPL PSDs displayed in this figure, obtained using the two permeable FW-H control surfaces PS1 and PS2, are similar to each other and each has a larger amplitude than that obtained using the impermeable FW-H control surface, especially in the range of frequencies between 80 Hz and 500 Hz. This difference in amplitude suggests that the permeable FW-H control surface PS1 provides all the necessary information on the pressure required to model the noise produced by the flow over the tandem cylinders—whereas, the

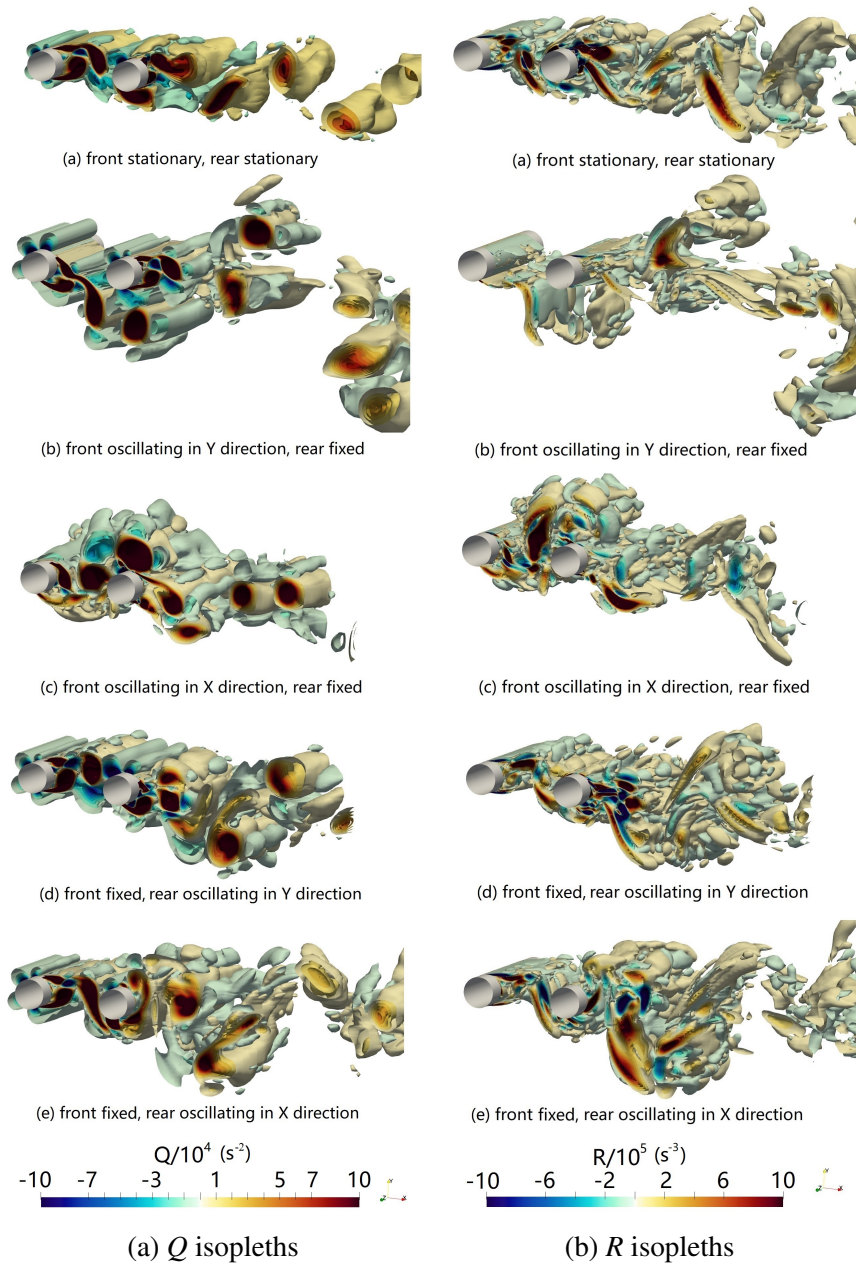
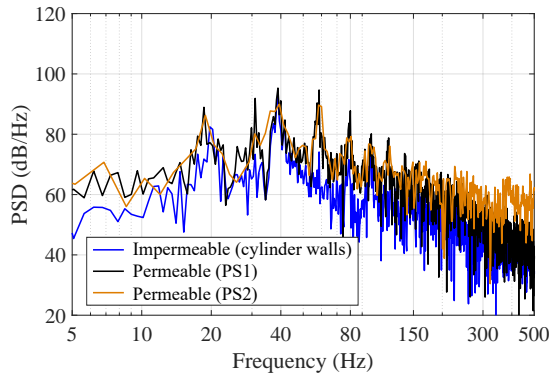
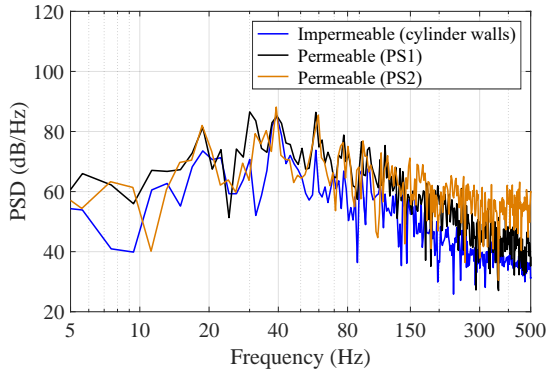


Figure 7.31: Isopleths of the two invariants Q and R taken when the cylinder passes through the initial position (viz., the stationary position for an oscillating cylinder) after several cycles of oscillations for five different scenarios of tandem cylinders.

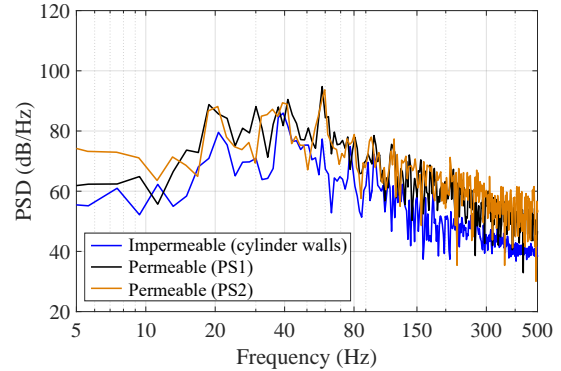
impermeable FW-H control surface coinciding with the cylinder walls does not provide sufficient information on the sound source to enable an accurate prediction of the noise field. This observation is contrary to the NASA QFF case shown in Fig. 7.11 in which it is seen that the noise field produced by the impermeable and permeable FW-H control surfaces are similar to each other, even in the high-frequency band. The difference between the present results and the NASA QFF case is due to the motion of the rear cylinder. This difference highlights the fact that the vibration of this cylinder generates a highly turbulent and unstable wake (yielding a quadrupole source contribution) which generates more noise in the wake than that for a pair of stationary cylinders.



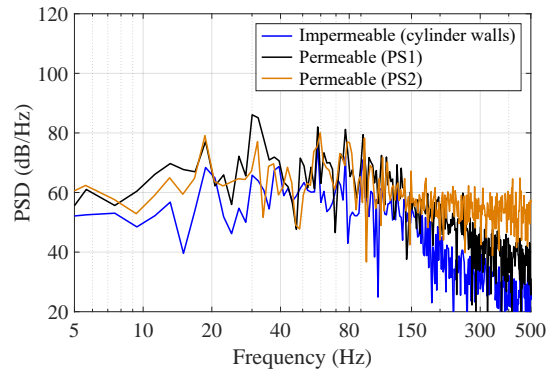
(a) SPL PSD at angular position 90°



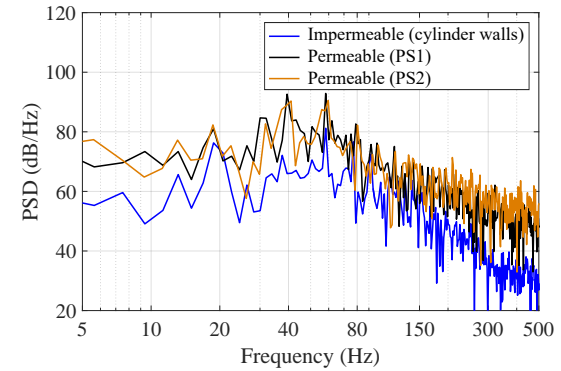
(b) SPL PSD at angular position 45°



(c) SPL PSD at angular position 135°



(d) SPL PSD at angular position 0°



(e) SPL PSD at angular position 180°

Figure 7.32: SPL PSDs obtained at various angular positions at a radial distance of $10D$ from the midpoint between the two cylinders with the front cylinder stationary and the rear cylinder oscillating in the transverse direction.

The oscillatory motion of one of the cylinders generates more broadband noise (which include the contributions in the high-frequency range with frequencies greater than about 80 Hz). The latter noise contribution cannot be captured using a FW-H impermeable control surface (viz., the cylinder walls). Finally, it is of interest to note the SPL PSDs for the impermeable and permeable FW-H control surfaces obtained at an angular position of $\theta = 90^\circ$ are similar to each other. This similarity may arise from the weak directivity of the broadband noise in the transverse direction.

Fig. 7.33 exhibits the SPL PSDs at a fixed angular location of $\theta = 135^\circ$ at a radial distance of $10D$ from the midpoint between the pair of cylinders for the five scenarios summarized in

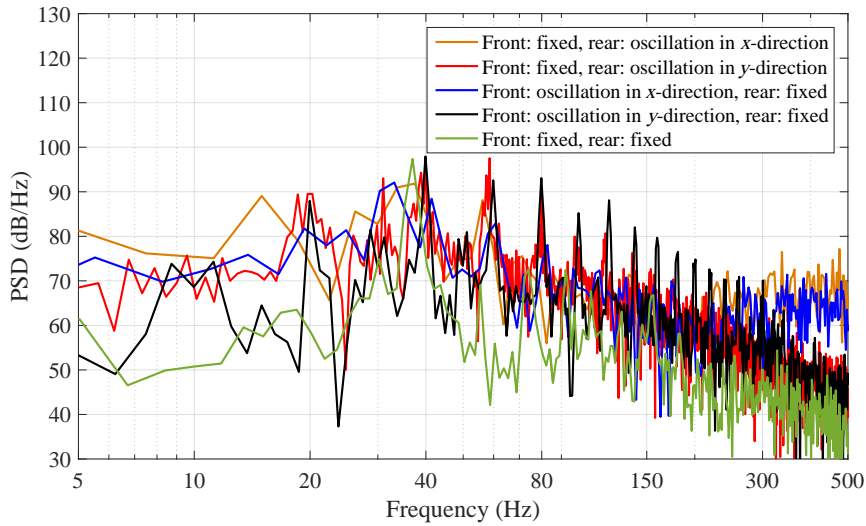


Figure 7.33: SPL PSD obtained at an angular position of $\theta = 135^\circ$ at radial distance of $10D$ from the midpoint between the two cylinders for five different scenarios.

Fig. 7.27. The permeable control surface PS1 is used in the FW-H methodology for the prediction of the noise field. The dominant peak in the SPL PSDs corresponds to a frequency between about 30 Hz and 40 Hz for all five scenarios—a frequency that corresponds (approximately or better) to the primary vortex-shedding frequency of the stationary tandem cylinders (shown as the black curve in Fig. 7.33). The vibration of one of the cylinders in the pair causes the primary vortex-shedding frequency to shift slightly which is consistent with the PSD characteristics of the average surface pressure displayed in Fig. 7.28. The PSD amplitude of the broadband noise increases when the cylinder vibrates, but the amplitude of the primary peak between 30 and 40 Hz remains relatively constant. There are also several harmonics corresponding to the vibration frequency, along with an overall global increase in the SPL amplitude evident from a careful examination of Fig. 7.34(b).

Fig. 7.34 exhibits the SPL directivity at a (fixed) radial distance $10D$ from the midpoint between the pair of cylinders for angular positions in the range $0^\circ \leq \theta \leq 180^\circ$ for the five scenarios of tandem cylinders depicted in Fig. 7.27. A comparison of Figs 7.34(a) and 7.34(b) shows that the SPLs obtained using the permeable FW-H control surface (PS1) are larger than those obtained using the impermeable FW-H control surface (viz., the cylinder walls), especially in the upwind ($\theta = 0^\circ$) and downwind ($\theta = 180^\circ$) directions of the tandem cylinders. A significant level of broadband noise (arising from the turbulence or quadrupole source) is incorporated using the permeable FW-H control surface (PS1)—an observation that is consistent with Fig. 7.32.

When an impermeable control surface (viz., the cylinder walls) is used in the FW-H methodology, a careful perusal of Fig. 7.34(a) shows that when one or the other cylinder is oscillating in the streamwise (in-line) direction, the overall SPL is significantly larger—especially in the upwind (0°) and downwind (180°) directions—than that when one of the cylinders is oscillating in the transverse direction. For the SPL directivity obtained using the permeable FW-H control surface, the oscillation of one or the other cylinder increases the overall SPL (especially in the range of angular positions $135^\circ \leq \theta \leq 180^\circ$) in comparison to the case of two stationary cylinders. This increase in the SPL directivity in the downwind direction agrees with the results reported earlier with regard to the fact that the oscillations of a cylinder increase the turbulent velocity fluctuations in the wake region. In particular, in-line (x -direction) oscillations of one or the other

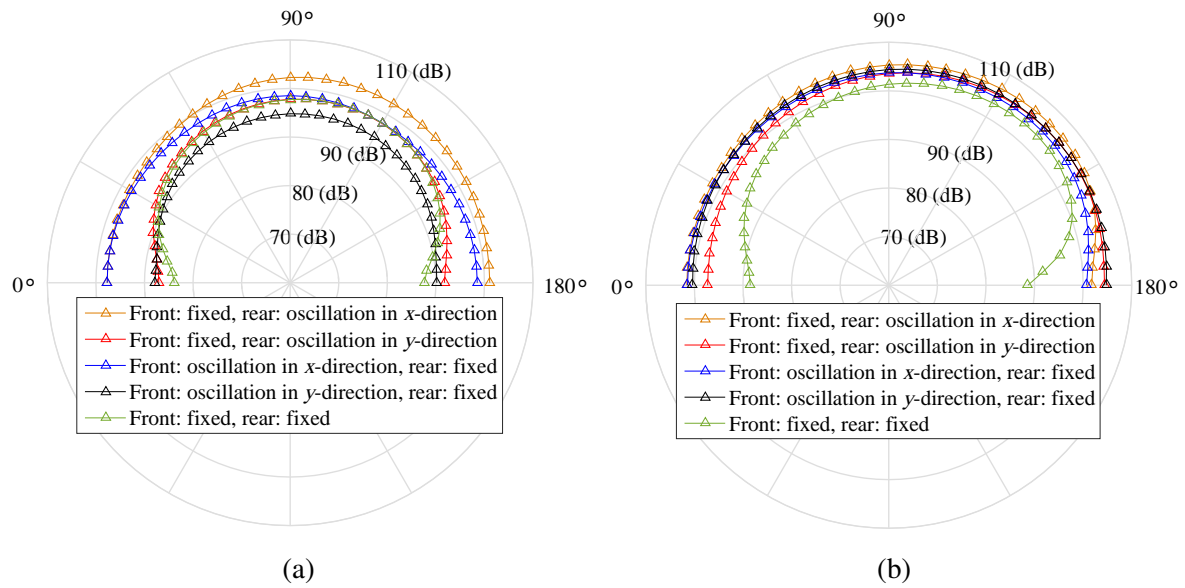


Figure 7.34: Directivity of the SPL obtained at a radial distance of $10D$ from the midpoint between the pair of cylinders for five different scenarios involving tandem cylinders: directivity predicted using (a) an impermeable FW-H control surface (taken as the cylinder walls) and (b) the permeable FW-H control surface PS1.

cylinder is seen to generate the largest noise levels—an observation that is consistent with the results obtained using the impermeable FW-H control surface.

In conclusion, the streamwise (in-line) oscillations of one or the other cylinder result in larger values of the SPL than the transverse oscillations of one or other cylinder (assuming the same oscillation amplitude and frequency for the two cases). This outcome is consistent with the power spectral analysis described earlier. The physical mechanism underpinning this observed difference resides in the fact that an in-line oscillation of one or the other cylinder results in a repeatedly (periodic) squeezing of the flow between the cylinders which, in turn, generates high levels of shear in the flow increasing the complexity of the flow field. Furthermore, oscillations of the rear (downstream) cylinder (in either the streamwise or transverse directions) increase the SPL more than comparable oscillations of the front (upstream) cylinder. When the rear cylinder is stationary, it blocks the wake of the front cylinder. However, when the rear cylinder oscillates, the noise increases through a combination of the more energetic oscillating wake of the rear cylinder and the repeated thrashing within the front cylinder wake. These observations agree the results reported by David et al. [24]—in this study, the researchers showed that noise production in a tandem cylinders array is attributed primarily to the motion of the rear cylinder.

7.7 Chapter summary

The work in this chapter uses a three-dimensional DES/FW-H simulation methodology to investigate the wake and noise generated by an oscillating single or tandem cylinder(s) at high Reynolds numbers. A comparison between previous experimental and numerical results and those obtained from our DES/FW-H simulation methodology is conducted for the stationary single and tandem cylinder(s) in a turbulent flow and for oscillating tandem cylinders in a laminar

flow. There is good conformance between the numerical and experimental results for the predictions of the surface pressure, the wake velocity profiles, and the sound generation—with very minor discrepancies observed only in the prediction of the location of the separation point of the rear cylinder in the tandem cylinders case. The validity of the SST-DES turbulence model, coupled with the FW-H equation solved using the Farassat time-domain integration methodology, for the prediction of the flow and noise fields is thereby demonstrated for the turbulent flow over a single or a pair of cylinder(s).

As the flow moves past the stationary tandem cylinders, the turbulent fluctuations and flow velocity increase both the amplitude of the broadband noise and the frequency of the dominant peak in the SPL PSD in comparison to that of a single cylinder. Furthermore, more spectral peaks are present in the SPL PSD for the tandem cylinders in comparison to that for a single cylinder. The PSD of the sound pressure has a strong dependence on the angular position (direction or directivity). The propagation of the sound pressure in the transverse direction is associated with the lift fluctuation which has a smaller frequency and a larger amplitude. The propagation of sound pressure in the streamwise (in-line) direction is associated with the drag fluctuations which has a larger frequency and a smaller amplitude.

The oscillation of a single cylinder leads to the suppression of the acoustic energy in comparison to that of a stationary cylinder (both at Reynolds number $Re = 120,000$)—indeed, this phenomenon occurs when the value of oscillation frequency approaches 57% of the vortex-shedding frequency for the stationary cylinder. This acoustic energy suppression is consistent with previous laminar simulations (at $Re = 150$) which concluded that the aerodynamics noise is significantly reduced if the fluid motion is locked in the frequency range below the original vortex-shedding frequency for the fixed (stationary) cylinder. Furthermore, the reduction of the noise here arises from the oscillations in the structure which, in turn, suppresses the source of noise caused by the vortex shedding from the stationary cylinder. The new source of noise arising from the cylinder oscillation does not compensate for this noise suppression. Moreover, the new noise source induced by the structural motion includes the loading and thickness noise—these two contributions to the noise have comparable energy. In contrast, the noise generated by the vortex shedding from the stationary cylinder embodies only the loading noise and this noise component disappears as the oscillation frequency increases.

Five different scenarios of tandem cylinders summarized in Fig. 7.27 were investigated in detail. When one or the other cylinder oscillates in either the transverse or streamwise directions, the use of an impermeable control surface in the FW-H method for the prediction of the noise field leads to an underprediction of the sound pressure level. The use of a permeable control surface (e.g., PS1) provides improved predictions of the noise field by capturing properly the higher broadband noise levels through the inclusion of a quadrupole source that represents the noise arising from the turbulent fluctuations in the wake. The noise energy provided by one or the other cylinder oscillating in the streamwise (in-line) direction is larger than that associated with one or the other cylinder oscillating in the transverse direction. In addition, the oscillation impacts the distribution of the mean pressure coefficient C_p on the rear cylinder more than on the front cylinder due primarily to the highly complex nature of the incident flow on the rear cylinder.

The second Q and third R invariants of the velocity gradient tensor were calculated for the five different scenarios of tandem cylinders studied herein. The isopleths associated with the distribution of Q in the wake are more complex when the front cylinder oscillates in the transverse direction. The flow is dominated by the strain near the stagnation point at the surfaces of the two

cylinders resulting in large negative values of Q . The oscillations of the rear cylinder increase the values of R in the wake more than the oscillations of the front cylinder. This increase in the values of R is associated with an increased broadband noise.

The oscillations of one or the other cylinder lead to an increase in the SPL directivity, especially in the upwind ($\theta = 0^\circ$) and downwind ($\theta = 180^\circ$) directions. A transverse oscillation of a single cylinder results in a higher SPL than a streamwise (in-line) oscillation of the same cylinder. In contrast, for tandem cylinders, an in-line oscillation of one or the other cylinder results in a higher SPL than a transverse oscillation of one or the other cylinder. Furthermore, the SPL is more sensitive to oscillations of the rear cylinder than the front cylinder. This sensitivity arises because the oscillation of the rear cylinder increases friction, collision, and extrusion of the flow, leading to stronger pressure fluctuations and higher noise levels. These studies will be of great implications to engineering issues such as the design and assessment of the noise problem originating from bladeless wind turbines.

Chapter 8

Conclusions and future work

In this thesis, to begin with, the effect of nonlinear restoring forces on the response of the flow-induced vibration system is studied. Secondly, the modal behavior and underlying mechanism of lock-in behavior are investigated with respect to the FIV system with uniform flow. Thirdly, this thesis tries to figure out the triggering mechanism of galloping phenomena for the FIV system with the uniform flow, and varied factors are considered in this part. Fourthly, to further explore the modal situation underpinning the locking interval of the FIV-based energy extractor in real physical scenarios, one new data-driven theory via the superposition of the 2-D ROMs (SROM) for the purpose of performing modal analysis and stability predictions of 3-D FIV of an elastically-mounted circular cylinder submerged in spanwise shear inflow at subcritical Reynolds numbers is introduced. Lastly, the aeroacoustics propagations of moving single and tandem cylinders with forced oscillation are investigated. The conclusions are summarized as follows:

(1) The numerical simulation of two-dimensional flows around an elastically-mounted circular cylinder on a linear/quadratic spring configuration at a low-Reynolds number is conducted in order to study the vortex-induced vibration. The Re extent ranged from 50 to 150. The equivalent natural frequency for a circular cylinder elastically supported on a nonlinear spring is derived and found to depend on the square root of the maximum amplitude of the displacement. The range of Re associated with the initial branch is increased and the upper and lower branches are suppressed for an elastically-mounted cylinder on a linear/quadratic spring configuration compared to that elastically supported on a linear spring. The detailed characteristics (e.g., vortex shedding modes, amplitude, oscillation frequency, etc.) of the nonlinear lock-in range and the transition out of this range for the FIV system as a function of increasing Re are studied using power spectrum, phase portrait, and dynamical mode decomposition analysis. The information is synthesized in order to investigate the different physical mechanisms and phenomena appearing in the FIV system and how these are linked to the underlying vortex shedding and amplitude response regimes of the dynamics of the fixed and elastically-mounted cylinder. Overall, the amplitude-emphasized range is extended by the nonlinear restoring forces.

(2) A reduced-order model for the fluid dynamics is obtained using the eigensystem realization algorithm (ERA), which is subsequently coupled to a linear structural equation to provide a state-space model for the coupled FIV system, in order to provide a simplified computationally inexpensive mathematical representation of the system. This methodology is used to study the dynamics of laminar flows past an elastically-mounted circular cylinder with Reynolds number Re ranging from 20 to 180, inclusive. A detailed analysis of the distribution of the eigenvalues

of the transfer (or, system) matrix of the reduced FIV system shows that the frequency range of the lock-in can be partitioned into resonance and flutter lock-in regimes. The resonance lock-in (lower branch of the FIV response) dominates the fluid-structure interaction. Furthermore, it is shown that when the structural natural frequency is close to one of the eigenfrequencies associated with the wake modes, resonance lock-in (rather than flutter lock-in) will be the primary mechanism governing the FIV response even though the real part of the eigenvalues associated with the structural mode is positive. With increasing Reynolds number, the instability of each wake mode is enhanced resulting in a transformation of the wake modes interacting with the structural mode. It is suggested herein that the weakened interaction between the wake modes and the structural mode at $Re = 180$ (associated with the greater separation between the root loci of the modes) results in the premature termination of the resonance lock-in at $F_s = 0.155$ with increasing U_r . The DMD and power spectral analysis of the time series of the transverse displacement and lift coefficient are used to support the results obtained from ROM/ERA and, more specifically, to provide a clear demonstration of the balanced interaction between the wake modes and the structural mode. This result is used to explain the beating phenomenon which occurs in the initial branch and the significant lag time that arises between the initial branch and the occurrence of a fully-developed response in the lower branch.

(3) The mechanisms that are important for the triggering of galloping in a system consisting of the flow past an elastically-mounted body with various cross-sectional geometries are investigated using three methodologies: high-fidelity full-order model, linear stability analysis based on the eigensystem realization algorithm, and the Den Hartog stability criterion. The results synthesis is used to study the effect of the Reynolds number, the mass ratio, the cross-sectional geometry, and the angle of attack on the suppression/initiation of galloping. In the LSA application to a flow-induced vibration system with coupled modes, the importance of identifying correctly which of the coupled modes correspond to the structure mode is stressed. LSA and the Den Hartog stability criterion are applied to explain the recently observed phenomenon of the collapse of galloping for a rectangular cylinder when the side ratio is decreased below a critical value. Galloping appears and disappears when the flat face of a body is directed into or away from the incident wind direction. Furthermore, it is found very small changes from a right angle in the windward interior angle of an isosceles-trapezoidal body can significantly provoke or suppress galloping.

(4) We present a novel data-driven theory for the stability analysis of a flow-induced vibration (FIV) system consisting of an elastically-mounted circular cylinder submerged in three-dimensional spanwise shear inflow at subcritical Reynolds number. The presented data-driven theory separates the cylinder into several elements along the spanwise direction and treats the aerodynamics of each element as a two-dimensional situation subject to uniform inflow. An eigensystem realization algorithm is constructed to obtain the separate 2-D flow reduced-order model for each element, then the SROM is processed to obtain the simplified 3-D flow ROM. The simplified 3-D flow ROM is coupled with the structural model to perform a linear stability analysis of the FIV system under study. The proposed data-driven technique demonstrates high consistency with the high-fidelity full-order model with regard to the prediction of the flutter lock-in boundaries while being more time-efficient, whereas the traditional direct 3-D data-driven analysis involves significant errors. The growth rate obtained using SROM is negatively correlated with the lagging time (reflected in the FOM calculation) for the FIV system to evolve from the initial stationary state to the final equilibrium state. The evolution of the structural instability range with the variation of the mass ratio is analyzed/predicted by the proposed data-driven

theory.

(5) The noise generated by a three-dimensional turbulent wake behind an oscillating single or tandem cylinder(s) is studied using detached eddy simulation and the Ffowcs Williams-Hawkings (FW-H) method. The drag force fluctuations result in the propagation of the sound pressure in the streamwise direction, whereas the lift force fluctuations result in the propagation of the sound pressure in the transverse direction. The second and third invariants of the velocity gradient tensor are used to visualize the distinct vortex structures in the wake for the five different scenarios of tandem cylinders. The fundamental frequency and the first harmonic in the sound pressure power spectrum are related to the oscillation frequency of the cylinder. For an oscillating cylinder at a fixed Reynolds number $Re = 120,000$, the sound energy is suppressed compared to that of a stationary cylinder provided the value of oscillation frequency approaches 57% of the original vortex-shedding frequency of the stationary cylinder. This noise reduction arises from the structural oscillations suppressing the noise generated by the vortex shedding from the stationary cylinder—the additional source of noise arising from the structural oscillations is too small to compensate for the mechanism responsible for the noise suppression. The noise generated by the cylinder motion includes contributions from the loading and thickness noise, whereas the noise generated by vortex shedding from the stationary cylinder only includes the loading noise. A single-cylinder oscillating in the transverse direction exhibits a larger sound pressure level (SPL) than the streamwise oscillation of the same cylinder. In contrast, the streamwise oscillation of one or the other cylinder in a tandem array results in a larger SPL than the transverse oscillation of one or the other cylinder. Finally, the SPL is more sensitive to the oscillations of the rear (downstream) cylinder than the front (upstream) cylinder.

In the future, the effect of nonlinear restoring force on FIV response will be investigated in turbulent situations and tandem (cylinder) configurations. Furthermore, applying the LSA methodology to the FIV system at higher Reynolds numbers will also be conducted. The features discrepancy of aeroacoustics propagation from moving cylinders with forced and self-excited vibration are also valuable to be further analyzed. The effect of turbulence models on aerodynamic noise propagation also deserves to be further explored. In addition, in future acoustic propagation studies of complex cylindrical arrays, a combination of actuator line models and acoustic models could be considered to reduce expensive computational costs.

References

- [1] H. J. Fernando. *Handbook of Environmental Fluid Dynamics, Volume Two: Systems, Pollution, Modeling, and Measurements*. CRC Press, 2012.
- [2] Aerospace Engineering Blog. Boundary layer separation and pressure drag. [EB/OL]. Accessed October 15, 2016.
- [3] J. H. Lienhard. *Synopsis of lift, drag, and vortex frequency data for rigid circular cylinders, Volume 300*. Technical Extension Service, Washington State University Pullman, WA, 1966.
- [4] C. C. Feng. *The measurement of vortex induced effects in flow past stationary and oscillating circular and D-section cylinders*. PhD thesis, University of British Columbia, 1968.
- [5] A. Khalak and C. Williamson. Investigation of relative effects of mass and damping in vortex-induced vibration of a circular cylinder. *Journal of Wind Engineering and Industrial Aerodynamics*, 69-71:341–350, 1997.
- [6] N. Jauvtis and C. Williamson. Vortex-induced vibration of a cylinder with two degrees of freedom. *Journal of Fluids and Structures*, 17(7):1035–1042, 2003.
- [7] N. Jauvtis and C. Williamson. The effect of two degrees of freedom on vortex-induced vibration at low mass and damping. *Journal of Fluid Mechanics*, 509:23–62, 2004.
- [8] R. Govardhan and C. Williamson. Modes of vortex formation and frequency response of a freely vibrating cylinder. *Journal of Fluid Mechanics*, 420:85–130, 2000.
- [9] C.H.K. Williamson and R. Govardhan. Vortex-induced vibrations. *Annual Review of Fluid Mechanics*, 36(1):413–455, 2004.
- [10] M. M. Bernitsas, K. Raghavan, Y. Ben-Simon, and E. Garcia. VIVACE (vortex induced vibration aquatic clean energy): A new concept in generation of clean and renewable energy from fluid flow. *Journal of Offshore Mechanics and Arctic Engineering*, 130(4):041101, 2008.
- [11] S. P. Singh and S. Mittal. Vortex-induced oscillations at low Reynolds numbers: Hysteresis and vortex-shedding modes. *Journal of Fluids and Structures*, 20(8):1085–1104, 2005.
- [12] W. Zhang, X. Li, Z. Ye, and Y. Jiang. Mechanism of frequency lock-in in vortex-induced vibrations at low Reynolds numbers. *Journal of Fluid Mechanics*, 783:72–102, 2015.

- [13] S. Mittal and S. Singh. Vortex-induced vibrations at subcritical Re. *Journal of Fluid Mechanics*, 534:185–194, 2005.
- [14] Navrose and S. Mittal. Lock-in in vortex-induced vibration. *Journal of Fluid Mechanics*, 794:565–594, 2016.
- [15] W. Yao and R. Jaiman. Model reduction and mechanism for the vortex-induced vibrations of bluff bodies. *Journal of Fluid Mechanics*, 827:357–393, 2017.
- [16] X. Li, Z. Lyu, J. Kou, and W. Zhang. Mode competition in galloping of a square cylinder at low Reynolds number. *Journal of Fluid Mechanics*, 867:516–555, 2019.
- [17] Y. Oguma, T. Yamagata, and N. Fujisawa. Measurement of sound source distribution around a circular cylinder in a uniform flow by combined particle image velocimetry and microphone technique. *Journal of Wind Engineering and Industrial Aerodynamics*, 118:1–11, 2013.
- [18] N. Fujisawa and G. Takeda. Flow control around a circular cylinder by internal acoustic excitation. *Journal of Fluids and Structures*, 17(7):903–913, 2003.
- [19] S. Dong, G. E. Karniadakis, A. Ekmekci, and D. Rockwell. A combined direct numerical simulation–particle image velocimetry study of the turbulent near wake. *Journal of Fluid Mechanics*, 569:185–207, 2006.
- [20] L. Jenkins, M. Khorrami, M. Choudhari, and C. McGinley. Characterization of unsteady flow structures around tandem cylinders for component interaction studies in airframe noise. *11th AIAA/CEAS Aeroacoustics Conference*, page 2812, 2005.
- [21] F. V. Hucheson and T. F. Brooks. Noise radiation from single and multiple rod configurations. *International Journal of Aeroacoustics*, 11(3-4):291–333, 2012.
- [22] L. Jenkins, D. Neuhart, C. McGinley, M. Khorrami, and M. Choudhari. Measurements of unsteady wake interference between tandem cylinders. In *36th AIAA Fluid Dynamics Conference and Exhibit*, page 3202, 2006.
- [23] G. Bres, F. Pérot, and D. Freed. A Ffowcs Williams-Hawkings solver for Lattice-Boltzmann based computational aeroacoustics. In *16th AIAA/CEAS Aeroacoustics Conference*, page 3711, 2010.
- [24] D. Lockard, M. Khorrami, M. Choudhari, F. Hucheson, T. Brooks, and D. Stead. Tandem cylinder noise predictions. In *13th AIAA/CEAS Aeroacoustics Conference (28th AIAA Aeroacoustics Conference)*, page 3450, 2007.
- [25] Y. Hattori and R. Komatsu. Mechanism of aeroacoustic sound generation and reduction in a flow past oscillating and fixed cylinders. *Journal of Fluid Mechanics*, 832:241–268, 2017.
- [26] X. Mao and H. M. Blackburn. The structure of primary instability modes in the steady wake and separation bubble of a square cylinder. *Physics of Fluids*, 26(7):074103, 2014.

- [27] SECC. The UK low carbon transition plan. https://assets.publishing.service.gov.uk/government/uploads/system/uploads/attachment_data/file/228752/9780108508394.pdf. Accessed 2009.
- [28] V. J. Modi and S. R. Munshi. An efficient liquid sloshing damper for vibration control. *Journal of Fluids and Structures*, 12(8):1055–1071, 1998.
- [29] O. J. Waals, A. C. Phadke, and S. Bultema. Flow induced motions on multi column floaters. In *ASME 2007 26th International Conference on Offshore Mechanics and Arctic Engineering, San Diego, California, USA*, volume 1: Offshore Technology; Special Symposium on Ocean Measurements and Their Influence on Design, page 669–678, 06 2007.
- [30] S. Chen. *Dynamic performance of bridges and vehicles under strong wind*. PhD thesis, Louisiana State University, Baton Rouge, USA, 2004.
- [31] J. Lee. *Hydrokinetic Power Harnessing Utilizing Vortex Induced Vibrations through a Virtual c-k VIVACE Model*. PhD thesis, University of Michigan, 2010.
- [32] J. H. Gerrard. The mechanics of the formation region of vortices behind bluff bodies. *Journal of Fluid Mechanics*, 25(2):401–413, 1966.
- [33] E. de Langre. Frequency lock-in is caused by coupled-mode flutter. *Journal of Fluids and Structures*, 22(6):783–791, 2006.
- [34] M. P. Païdoussis, S. J. Price, and E. De Langre. *Fluid-Structure Interactions: Cross-Flow-Induced Instabilities*. Cambridge University Press, 2010.
- [35] J. Zhao, K. Hourigan, and M. Thompson. An experimental investigation of flow-induced vibration of high-side-ratio rectangular cylinders. *Journal of Fluids and Structures*, 91:102580, 02 2019.
- [36] M. Zhao. Flow-induced vibrations of square and rectangular cylinders at low Reynolds number. *Fluid Dynamics Research*, 47(2):025502, 2015.
- [37] R. K. Jaiman, S. Sen, and P. S. Gurugubelli. A fully implicit combined field scheme for freely vibrating square cylinders with sharp and rounded corners. *Computers & Fluids*, 112:1–18, 2015.
- [38] H. Huang and X. Li. Experimental Study on the Influence Factors of Static Aerodynamic Characteristics of Ice-Coated Commonly Used Conductors. *Advanced Materials Research*, 774–776:1227–1231, 11 2013.
- [39] J. N. Newman. *Marine Hydrodynamics*. The MIT Press, 1977.
- [40] T. Sarpkaya. A critical review of the intrinsic nature of vortex-induced vibrations. *Journal of Fluids and Structures*, 19(4):389–447, 2004.
- [41] A. Khalak and C. Williamson. Dynamics of a hydroelastic cylinder with very low mass and damping. *Journal of Fluids and Structures*, 10:455–472, 1996.
- [42] A. Khalak and C. Williamson. Motions, forces and mode transitions in vortex-induced vibrations at low mass-damping. *Journal of Fluids and Structures*, 13(7-8):813–851, 1999.

- [43] R. Govardhan. *Vortex-induced Vibration of Two and Three-dimensional Bodies*. Cornell University, 2000.
- [44] R. Govardhan and C. Williamson. Resonance forever: existence of a critical mass and an infinite regime of resonance in vortex-induced vibration. *Journal of Fluid Mechanics*, 473:147–166, 2002.
- [45] D. Brika and A. Laneville. Vortex-induced vibrations of a long flexible circular cylinder. *Journal of Fluid Mechanics*, 250:481–481, 1993.
- [46] J. Zhao, K. Hourigan, and M. C. Thompson. Flow-induced vibration of D-section cylinders: An afterbody is not essential for vortex-induced vibration. *Journal of Fluid Mechanics*, 851:317–343, 2018.
- [47] M. Branković and P. W. Bearman. Measurements of transverse forces on circular cylinders undergoing vortex-induced vibration. *Journal of Fluids and Structures*, 22(6-7):829–836, 2006.
- [48] N. Ferguson and G. V. Parkinson. Surface and wake flow phenomena of the vortex-excited oscillation of a circular cylinder. *Journal of Manufacturing Science & Engineering*, 89(4):831–838, 1967.
- [49] G. Parkinson. Phenomena and modelling of flow-induced vibrations of bluff bodies. *Progress in Aerospace Sciences*, 26(2):169–224, 1989.
- [50] O. M. Griffin. Flow near self-excited and forced vibrating circular cylinders. *Journal of Manufacturing Science & Engineering*, 94(2):539–547, 1972.
- [51] O. M. Griffin and S. E. Ramberg. Some recent studies of vortex shedding with application to marine tubulars and risers. *Journal of Energy Resources Technology*, 104(1):2–13, 1982.
- [52] B. M. Sumer and J. Fredsøe. *Hydrodynamics Around Cylindrical Structures*. World Scientific, revised edition, 2006.
- [53] J. H. Gerrard. *Flow around Circular Cylinders; Volume 1. Fundamentals*. By MM Zdravkovich. Oxford Science Publications, 1997. 672 pp.£ 120. Cambridge University Press, 1997.
- [54] M. M. Zdravkovich. *Flow around circular cylinders: Volume 2: Applications*. Oxford University Press, 1997.
- [55] M. S. Pantazopoulos. *Vortex-induced vibration parameters: critical review*. American Society of Mechanical Engineers, New York, 1994.
- [56] P. W. Bearman. Vortex shedding from oscillating bluff bodies. *AnRFM*, 16:195–222, 1984.
- [57] R. D. Gabbai and H. Benaroya. An overview of modeling and experiments of vortex-induced vibration of circular cylinders. *Journal of Sound and Vibration*, 282(3-5):575–616, 2005.

- [58] B. Stappenbelt, A. D. Johnstone, and J. D. L. Anger. Vortex-induced vibration marine current energy harvesting. In *Fluid-Structure-Sound Interactions and Control*, pages 401–406. Springer, 2016.
- [59] A. B. Rostami and M. Armandei. Renewable energy harvesting by vortex-induced motions: Review and benchmarking of technologies. *Renewable and Sustainable Energy Reviews*, 70:193–214, 2017.
- [60] Y. Yoshitake, A. Sueoka, M. Yamasaki, Y. Sugimura, and T. Ohishi. Quenching of vortex-induced vibrations of towering structure and generation of electricity using hula-hoops. *Journal of Sound and Vibration*, 272(1-2):21–38, 2004.
- [61] M. M. Bernitsas, Y. Ben-Simon, K. Raghavan, and E. Garcia. The VIVACE converter: model tests at high damping and Reynolds number around 10^5 . *Journal of Offshore Mechanics and Arctic Engineering*, 131(1):011102, 2009.
- [62] E. S. Kim. *Synergy of Multiple Cylinders in Flow Induced Motion for Hydrokinetic Energy Harnessing*. PhD thesis, University of Michigan, 2013.
- [63] H. Sun, E. S. Kim, G. Nowakowski, E. Mauer, and M. M. Bernitsas. Effect of mass-ratio, damping, and stiffness on optimal hydrokinetic energy conversion of a single, rough cylinder in flow induced motions. *Renewable Energy*, 99:936–959, 2016.
- [64] H. Sun, C. Ma, E. S. Kim, G. Nowakowski, E. Mauer, and M. M. Bernitsas. Flow-induced vibration of tandem circular cylinders with selective roughness: Effect of spacing, damping and stiffness. *European Journal of Mechanics-B/Fluids*, 74:219–241, 2019.
- [65] H. Sun, C. Ma, E. S. Kim, G. Nowakowski, E. Mauer, and M. M. Bernitsas. Hydrokinetic energy conversion by two rough tandem-cylinders in flow induced motions: Effect of spacing and stiffness. *Renewable Energy*, 107:61–80, 2017.
- [66] J. Piñero. VORTEX Bladeless. [EB/OL]. <https://vortexbladeless.com/> Accessed April 4, 2021.
- [67] D. Zhao, X. Hu, T. Tan, Z. Yan, and W. Zhang. Piezoelectric galloping energy harvesting enhanced by topological equivalent aerodynamic design. *Energy Conversion and Management*, 222:113260, 2020.
- [68] S. Tucker Harvey, I. A. Khovanov, and P. Denissenko. A galloping energy harvester with flow attachment. *Applied Physics Letters*, 114(10):104103, 2019.
- [69] K. Zhao, Q. Zhang, and W. Wang. Optimization of Galloping Piezoelectric Energy Harvester with V-Shaped Groove in Low Wind Speed. *Energies*, 12(24), 2019.
- [70] C. Evangelinos, D. Lucor, and G. E. Karniadakis. DNS-derived force distribution on flexible cylinders subject to vortex-induced vibration. *Journal of Fluids and Structures*, 14(3):429–440, 2000.
- [71] H. M. Blackburn, R. N. Govardhan, and C. Williamson. A complementary numerical and physical investigation of vortex-induced vibration. *Journal of Fluids and Structures*, 15(3-4):481–488, 2001.

- [72] H. M. Blackburn and R. D. Henderson. A study of two-dimensional flow past an oscillating cylinder. *Journal of Fluid Mechanics*, 385:255–286, 1999.
- [73] X. Ma, G. S. Karamanos, and G. E. Karniadakis. Dynamics and low-dimensionality of a turbulent near wake. *Journal of Fluid Mechanics*, 410:29–65, 2000.
- [74] S. Dong and G. E. Karniadakis. DNS of flow past a stationary and oscillating cylinder at $Re=10000$. *Journal of Fluids and Structures*, 20(4):519–531, 2005.
- [75] S. George and A. Ducoin. A coupled Direct Numerical Simulation of 1DOF vibration approach to investigate the transition induced vibration over a hydrofoil. *Journal of Fluids and Structures*, 105:103345, 2021.
- [76] W. Chen, C. Ji, D. Xu, and Z. Zhang. Three-dimensional direct numerical simulations of vortex-induced vibrations of a circular cylinder in proximity to a stationary wall. *Physical Review Fluids*, 7:044607, Apr 2022.
- [77] A. N. Kolmogorov. The local structure of turbulence in incompressible viscous fluid for very large Reynolds numbers. *Comptes Rendus Chimie URSS*, 30:301–305, 1941.
- [78] A. N. Kolmogorov. Dissipation of energy in the locally isotropic turbulence. *Proceedings of the Royal Society of London. Series A: Mathematical and Physical Sciences*, 434(1890):15–17, 1991.
- [79] J. W. Deardorff. A numerical study of three-dimensional turbulent channel flow at large Reynolds numbers. *Journal of Fluid Mechanics*, 41(2):453–480, 1970.
- [80] J. Dalheim. Numerical prediction of VIV on deepwater risers subjected to shear currents and waves. In *Offshore Technology Conference, Houston, Texas*,, 1999.
- [81] K. Herfjord, S. O. Drange, and T. Kvamsdal. Assessment of vortex-induced vibrations on deepwater risers by considering fluid-structure interaction. *Journal of Offshore Mechanics and Arctic Engineering*, 121(4):207–212, 1999.
- [82] J. Zhang and C. Dalton. Interactions of vortex-induced vibrations of a circular cylinder and a steady approach flow at a Reynolds number of 13,000. *Computers & Fluids*, 25(3):283–294, 1996.
- [83] M. J. Janocha, M. C. Ong, and G. Yin. Large eddy simulations and modal decomposition analysis of flow past a cylinder subject to flow-induced vibration. *Physics of Fluids*, 34(4):045119, 2022.
- [84] Z. Pan, W. Cui, and Q. Miao. Numerical simulation of vortex-induced vibration of a circular cylinder at low mass-damping using RANS code. *Journal of Fluids and Structures*, 23(1):23–37, 2007.
- [85] E. Guilmineau and P. Queutey. Numerical simulation of vortex-induced vibration of a circular cylinder with low mass-damping in a turbulent flow. *Journal of Fluids and Structures*, 19(4):449–466, 2004.

- [86] J. B. Wanderley, S. H. Sphaier, and C. Levi. A numerical investigation of vortex induced vibration on an elastically mounted rigid cylinder. *International Conference on Offshore Mechanics and Arctic Engineering*, 48227:703–711, 2008.
- [87] M. Zhao, J. M. Murphy, and K. Kwok. Numerical Simulation of Vortex-Induced Vibration of Two Rigidly Connected Cylinders in Side-by-Side and Tandem Arrangements Using RANS Model. *Journal of Fluids Engineering*, 138(2), 09 2015. 021102.
- [88] P. Catalano, M. Wang, G. Iaccarino, and P. Moin. Numerical simulation of the flow around a circular cylinder at high Reynolds numbers. *International Journal of Heat and Fluid Flow*, 24(4):463–469, 2003.
- [89] J. Xu and R. Zhu. Numerical simulation of VIV for an elastic cylinder mounted on the spring supports with low mass-ratio. *Journal of Marine Science and Application*, 8(3):237–245, 2009.
- [90] N. B. Khan, Z. Ibrahim, L. T. T. Nguyen, M. F. Javed, and M. Jameel. Numerical investigation of the vortex-induced vibration of an elastically mounted circular cylinder at high Reynolds number ($Re = 10^4$) and low mass ratio using the RANS code. *PLOS ONE*, 12(10), 10 2017.
- [91] A. Barrero-Gil, S. Pindado, and S. Avila. Extracting energy from vortex-induced vibrations: a parametric study. *Applied mathematical modelling*, 36(7):3153–3160, 2012.
- [92] Z. M. Luo and L. X. Zhang. Numerical simulation on VIV of a spring-mounted rigid cylinder through fully coupling with fluid. *Applied Mechanics and Materials*, 444:363–368, 2014.
- [93] J. Wang, J. Ran, and Z. Zhang. Energy harvester based on the synchronization phenomenon of a circular cylinder. *Mathematical Problems in Engineering*, 2014: 567357, 2014.
- [94] R. Naseer, H. Dai, A. Abdelkefi, and L. Wang. Piezomagnetoelastic energy harvesting from vortex-induced vibrations using monostable characteristics. *Applied Energy*, 203:142–153, 2017.
- [95] F. Pan, Z. Xu, L. Jin, P. Pan, and X. Gao. Designed simulation and experiment of a piezoelectric energy harvesting system based on vortex-induced vibration. *IEEE Transactions on Industry Applications*, 53(4):3890–3897, 2017.
- [96] G. R. Franzini and L. O. Bunzel. A numerical investigation on piezoelectric energy harvesting from vortex-induced vibrations with one and two degrees of freedom. *Journal of Fluids and Structures*, 77:196–212, 2018.
- [97] W. Chen, C. Ji, M. M. Alam, D. Xu, H. An, F. i Tong, and Y. Zhao. Flow-induced vibrations of a D-section prism at a low Reynolds number. *Journal of Fluid Mechanics*, 941:A52, 2022.
- [98] W. Zhang, Z. Ye, C. Zhang, and F. Liu. Supersonic flutter analysis based on a local piston theory. *AIAA Journal*, 47(10):2321–2328, 2009.

- [99] D. J. Lucia, P. S. Beran, and W. A. Silva. Reduced-order modeling: new approaches for computational physics. *Progress in Aerospace Sciences*, 40(1-2):51–117, 2004.
- [100] M. Ghoreyshi, A. Jirasek, and R. M. Cummings. Reduced order unsteady aerodynamic modeling for stability and control analysis using computational fluid dynamics. *Progress in Aerospace Sciences*, 71:167–217, 2014.
- [101] E. H. Dowell, H. C. Curtiss, R. H. Scanlan, and F. Sisto. *A modern course in aeroelasticity, Volume 3*. Springer, 1989.
- [102] J. Juang and R. S. Pappa. An eigensystem realization algorithm for modal parameter identification and model reduction. *Journal of Guidance, Control, and Dynamics*, 8(5):620–627, 1985.
- [103] T. J. Cowan, A. S. Arena J., and K. K. Gupta. Accelerating computational fluid dynamics based aeroelastic predictions using system identification. *Journal of Aircraft*, 38(1):81–87, 2001.
- [104] B. Stappenbelt. The effect of non-linear mooring stiffness on the vortex-induced motion of cylindrical structures. *International Society of Offshore and Polar Engineers*, 3:1144–1150, 2010.
- [105] E. Wang, K. Ramesh, S. Killen, and I. M. Viola. On the nonlinear dynamics of self-sustained limit-cycle oscillations in a flapping-foil energy harvester. *Journal of Fluids and Structures*, 83:339–357, 2018.
- [106] K. Ramesh, J. Murua, and A. Gopalarathnam. Limit-cycle oscillations in unsteady flows dominated by intermittent leading-edge vortex shedding. *Journal of Fluids and Structures*, 55:84–105, 2015.
- [107] D. A. W. Barton, S. G. Burrow, and L. R. Clare. Energy Harvesting From Vibrations With a Nonlinear Oscillator. *Journal of Vibration and Acoustics*, 132(2):021009, 2010.
- [108] B. H. Huynh, T. Tjahjowidodo, Z. W. Zhong, Y. Wang, and N. Srikanth. Numerical and experimental investigation of nonlinear vortex induced vibration energy converters. *Journal of Mechanical Science and Technology*, 31(8):3715–3726, 2017.
- [109] H. Sun, C. Ma, and M. M. Bernitsas. Hydrokinetic power conversion using flow induced vibrations with nonlinear (adaptive piecewise-linear) springs. *Energy*, 143:1085–1106, 2018.
- [110] E. Wang, W. Xu, X. Gao, L. Liu, Q. Xiao, and K. Ramesh. The effect of cubic stiffness nonlinearity on the vortex-induced vibration of a circular cylinder at low Reynolds numbers. *Ocean Engineering*, 173:12–27, 2019.
- [111] R. Badhurshah, R. Bhardwaj, and A. Bhattacharya. Numerical simulation of vortex-induced vibration with bistable springs: Consistency with the equilibrium constraint. *Journal of Fluids and Structures*, 103:103280, 04 2021.
- [112] R. Mishra, A. Soti, R. Bhardwaj, S. Kulkarni, and M. Thompson. Transverse vortex-induced vibration of a circular cylinder on a viscoelastic support at low Reynolds number. *Journal of Fluids and Structures*, 95:102997, 05 2020.

- [113] C. Gao, W. Zhang, X. Li, Y. Liu, J. Quan, Z. Ye, and Y. Jiang. Mechanism of frequency lock-in in transonic buffeting flow. *Journal of Fluid Mechanics*, 818:528–561, 2017.
- [114] J. Sjöberg, Q. Zhang, L. Ljung, A. Benveniste, B. Deylon, P. Y. Glorennec, H. Hjalmarsson, and A. Juditsky. *Nonlinear black-box modeling in system identification: a unified overview*. Linköping University, 1995.
- [115] J. N. Juang and R. S. Pappa. An Eigensystem Realization Algorithm (ERA) for Modal Parameter Identification, NASA. In *JPL Workshop on Identification and Control of Flexible Space Structures, Pasadena, CA, USA*, 1984.
- [116] W. A. Silva and R. E. Bartels. Development of reduced-order models for aeroelastic analysis and flutter prediction using the CFL3Dv6.0 code. *Journal of Fluids and Structures*, 19(6):729–745, 2004.
- [117] W. A. Silva, P. Chwalowski, and B. Perry III. Evaluation of linear, inviscid, viscous, and reduced-order modelling aeroelastic solutions of the agard 445.6 wing using root locus analysis. *International Journal of Computational Fluid Dynamics*, 28(3-4):122–139, 2014.
- [118] S. L. Brunton, C. W. Rowley, and D. R. Williams. Reduced-order unsteady aerodynamic models at low Reynolds numbers. *Journal of Fluid Mechanics*, 724:203–233, 2013.
- [119] W. Yao and R. Jaiman. Feedback control of unstable flow and vortex-induced vibration using the eigensystem realization algorithm. *Journal of Fluid Mechanics*, 827:394–414, 2017.
- [120] A. Chizfahm and R. Jaiman. Data-driven stability analysis and near-wake jet control for the vortex-induced vibration of a sphere. *Physics of Fluids*, 33(4):044104, 2021.
- [121] X. Li, W. Zhang, and C. Gao. Proximity-interference wake-induced vibration at subcritical Re: Mechanism analysis using a linear dynamic model. *Physics of Fluids*, 30(3):033606, 2018.
- [122] A. Chizfahm and R. Jaiman. Deep learning for stability analysis of a freely vibrating sphere at moderate Reynolds number, 2021.
- [123] T. L. B. Flinois, A. S. Morgans, and P. J. Schmid. Projection-free approximate balanced truncation of large unstable systems. *Physical Review E*, 92(2):023012, 2015.
- [124] Z. Ma, S. Ahuja, and C. W. Rowley. Reduced-order models for control of fluids using the eigensystem realization algorithm. *Theoretical and Computational Fluid Dynamics*, 25(1-4):233–247, 2011.
- [125] Y. Nakamura and Y. Tomonari. Galloping of rectangular prisms in a smooth and in a turbulent flow. *Journal of Sound and Vibration*, 52(2):233–241, 1977.
- [126] H. Park, R. A. Kumar, and M. M. Bernitsas. Enhancement of flow-induced motion of rigid circular cylinder on springs by localized surface roughness at $3 \times 10^4 \leq \text{Re} \leq 1.2 \times 10^5$. *Ocean Engineering*, 72:403–415, 2013.

- [127] J. Lian, X. Yan, F. Liu, J. Zhang, Q. Ren, and X. Yang. Experimental investigation on soft galloping and hard galloping of triangular prisms. *Applied Sciences*, 7(2):198, 2017.
- [128] D.S. Weaver and I. Veljkovic. Vortex shedding and galloping of open semi-circular and parabolic cylinders in cross-flow. *Journal of Fluids and Structures*, 21(1):65–74, 2005.
- [129] M. Novak and H. Tanaka. Effect of turbulence on galloping instability. *Journal of Engineering Mechanics*, 100(1):27–47, 1974.
- [130] J. P. Den Hartog. Transmission line vibration due to sleet. *Transactions of the American Institute of Electrical Engineers*, 51(4):1074–1076, 1932.
- [131] J. P. Den Hartog. *Mechanical Vibrations*. McGraw–Hill, 1956.
- [132] G. Dimitriadis. *Introduction to Nonlinear Aeroelasticity*. John Wiley & Sons, 2017.
- [133] N. Nikitas and J. H. Macdonald. Misconceptions and generalizations of the Den Hartog galloping criterion. *Journal of Engineering Mechanics*, 140(4):04013005, 2014.
- [134] S. R. Bukka, A. R. Magee, and R. Jaiman. Stability analysis of passive suppression for vortex-induced vibration. *Journal of Fluid Mechanics*, 886:A12, 2020.
- [135] T. K. Prasanth and S. Mittal. Vortex-induced vibrations of a circular cylinder at low Reynolds numbers. *Journal of Fluid Mechanics*, 594:463–491, 2008.
- [136] M. Zhao, L. Cheng, H. An, and L. Lu. Three-dimensional numerical simulation of vortex-induced vibration of an elastically mounted rigid circular cylinder in steady current. *Journal of Fluids and Structures*, 50:292–311, 2014.
- [137] A. Sareen, J. Zhao, D. Lo Jacono, J. Sheridan, K. Hourigan, and M. C. Thompson. Vortex-induced vibration of a rotating sphere. *Journal of Fluid Mechanics*, 837:258–292, 2018.
- [138] J. Liu, X. Bai, and A. Guo. Drag and lift forces on a stationary cylinder in a linear shear flow at a low Reynolds number. *Journal of Fluids and Structures*, 94:102928, 2020.
- [139] J. D. Murray. Non-uniform Shear Flow Past Cylinders. *The Quarterly Journal of Mechanics and Applied Mathematics*, 10(4):406–424, 01 1957.
- [140] L. F. Chen and G. X. Wu. Boundary shear flow past a cylinder near a wall. *Applied Ocean Research*, 92:101923, 2019.
- [141] M. Kiya, H. Tamura, and M. Arie. Vortex shedding from a circular cylinder in moderate-Reynolds-number shear flow. *Journal of Fluid Mechanics*, 101(4):721–735, 1980.
- [142] M. Cheng, S. H. N. Tan, and K. C. Hung. Linear shear flow over a square cylinder at low Reynolds number. *Physics of Fluids*, 17(7):078103, 2005.
- [143] S. Kang. Uniform-shear flow over a circular cylinder at low Reynolds numbers. *Journal of Fluids and Structures*, 22(4):541–555, 2006.
- [144] C. R. Robertson and A. Acrivos. Low Reynolds number shear flow past a rotating circular cylinder. Part 1. Momentum transfer. *Journal of Fluid Mechanics*, 40(4):685–703, 1970.

- [145] H. J. Sung, C. K. Chun, and J. M. Hyun. Experimental Study of Uniform-Shear Flow Past a Rotating Cylinder. *Journal of Fluid Mechanics*, 117(1):62–67, 03 1995.
- [146] K. D. Housiadas and R. I. Tanner. Viscoelastic shear flow past an infinitely long and freely rotating cylinder. *Physics of Fluids*, 30(7):073101, 2018.
- [147] O. M. Griffin. Vortex Shedding From Bluff Bodies in a Shear Flow: A Review. *Journal of Fluids Engineering-T ASME*, 107(3):298–306, 09 1985.
- [148] S. Gsell, R. Bourguet, and M. Braza. Vortex-induced vibrations of a cylinder in planar shear flow. *Journal of Fluid Mechanics*, 825:353–384, 2017.
- [149] L. Ding, H. Kong, Q. Zou, J. Wang, and L. Zhang. 2-DOF vortex-induced vibration of rotating circular cylinder in shear flow. *Ocean Engineering*, 249:111003, 2022.
- [150] A. K. De and S. Sarkar. Wake events during early three-dimensional transition of a circular cylinder placed in shear flow. *Physics of Fluids*, 32(5):053603, 2020.
- [151] R. Bourguet, G. Karniadakis, and M. S. Triantafyllou. Vortex-induced vibrations of a long flexible cylinder in shear flow. *Journal of Fluid Mechanics*, 677:342–382, 2011.
- [152] R. Bourguet, G. E. Karniadakis, and M. S. Triantafyllou. Distributed lock-in drives broadband vortex-induced vibrations of a long flexible cylinder in shear flow. *Journal of Fluid Mechanics*, 717:361–375, 2013.
- [153] E. Wang and Q. Xiao. Numerical simulation of vortex-induced vibration of a vertical riser in uniform and linearly sheared currents. *Ocean Engineering*, 121:492–515, 2016.
- [154] M. Zhao. Numerical simulation of vortex-induced vibration of a circular cylinder in a spanwise shear flow. *Physics of Fluids*, 27(6):063101, 2015.
- [155] S. Mittal and S. Singh. Vortex-induced vibrations at subcritical Re. *Journal of Fluid Mechanics*, 534:185–194, 2005.
- [156] J. Kou, W. Zhang, Y. Liu, and X. Li. The lowest Reynolds number of vortex-induced vibrations. *Physics of Fluids*, 29(4):041701, 2017.
- [157] D. I. Dolci and B. S. Carmo. Bifurcation analysis of the primary instability in the flow around a flexibly mounted circular cylinder. *Journal of Fluid Mechanics*, 880:R5, 2019.
- [158] R. Bourguet. Vortex-induced vibrations of a flexible cylinder at subcritical Reynolds number. *Journal of Fluid Mechanics*, 902:R3, 2020.
- [159] R. Hollenbach, R. Kielb, and K. Hall. Extending a Van Der Pol-Based Reduced-Order Model for Fluid-Structure Interaction Applied to Non-Synchronous Vibrations in Turbomachinery. *Journal of Turbomachinery*, 144(3), 10 2021.
- [160] A. J. Sanders. Non-Synchronous Vibration (NSV) Due to a Flow-Induced Aerodynamic Instability in a Composite Fan Stator. *Turbo Expo: Power for Land, Sea, and Air*, 6:507–516, 06 2004.
- [161] F. Ge, W. Lu, L. Wang, and Y. Hong. Shear flow induced vibrations of long slender cylinders with a wake oscillator model. *Acta Mechanica Sinica*, 27:330–338, 2011.

- [162] Y. Gao, L. Zou, Z. Zong, S. Takagi, and Y. Kang. Numerical prediction of vortex-induced vibrations of a long flexible cylinder in uniform and linear shear flows using a wake oscillator model. *Ocean Engineering*, 171:157–171, 2019.
- [163] J. F. Manwell, J. G. McGowan, and A. L. Rogers. *Wind energy explained: theory, design and application*. John Wiley & Sons, 2010.
- [164] T. Burton, N. Jenkins, D. Sharpe, and E. Bossanyi. *Wind energy handbook*. John Wiley & Sons, 2011.
- [165] E. Hau. *Wind turbines: fundamentals, technologies, application, economics*. Springer Science & Business Media, 2013.
- [166] W. K. Blake. *Mechanics of flow-induced sound and vibration, Volume 2: Complex flow-structure interactions*. Academic Press, 1986.
- [167] V. Strouhal. Über eine besondere art der tonerregung. *Annalen der Physik*, 241(10):216–251, 1878.
- [168] J. W. S. B. Rayleigh. *The theory of sound, Volumes 1 and 2*. Macmillan, 1896.
- [169] J. H. Gerrard. Measurements of the sound from circular cylinders in an air stream. *Proceedings of the Physical Society. Section B*, 68(7):453–461, 1955.
- [170] Y. Xing, P. Liu, H. Guo, and L. Li. Effect of helical cables on cylinder noise control. *Applied Acoustics*, 122:152–155, 2017.
- [171] L. Ling, P. Liu, Y. Xing, and H. Guo. Experimental investigation on the noise reduction method of helical cables for a circular cylinder and tandem cylinders. *Applied Acoustics*, 152:79–87, 2019.
- [172] H. Yokoyama, A. Miki, H. Onitsuka, and A. Iida. Direct numerical simulation of fluid-acoustic interactions in a recorder with tone holes. *The Journal of the Acoustical Society of America*, 138:858, 2015.
- [173] N. Hildebrand, M. M. Choudhari, and L. Duan. Direct numerical simulations of acoustic disturbances in various rectangular nozzle configurations. *In AIAA Scitech 2020 Forum*, page 0587, 2020.
- [174] O. Inoue and N. Hatakeyama. Sound generation by a two-dimensional circular cylinder in a uniform flow. *Journal of Fluid Mechanics*, 471:285–314, 2002.
- [175] P. R. Spalart and M. L. Shur. Variants of the Ffowcs Williams-Hawkings equation and their coupling with simulations of hot jets. *International Journal of Aeroacoustics*, 8(5):477–491, 2009.
- [176] S. Mendez, M. Shoeybi, S. K. Lele, and P. Moin. On the use of the Ffowcs Williams-Hawkings equation to predict far-field jet noise from large-eddy simulations. *International Journal of Aeroacoustics*, 12(1-2):1–20, 2013.
- [177] A. E. Filios, N. S. Tachos, A. P. Fragias, and D. P. Margaris. Broadband noise radiation analysis for an HAWT rotor. *Renewable energy*, 32(9):1497–1510, 2007.

- [178] M. J. Lighthill. On sound generated aerodynamically I. General theory. *Proceedings of the Royal Society of London. Series A. Mathematical and Physical Sciences*, 211(1107):564–587, 1952.
- [179] M. J. Lighthill. On sound generated aerodynamically II. Turbulence as a source of sound. *Proceedings of the Royal Society of London. Series A. Mathematical and Physical Sciences*, 222(1148):1–32, 1954.
- [180] N. Curle. The influence of solid boundaries upon aerodynamic sound. *Proceedings of the Royal Society of London. Series A. Mathematical and Physical Sciences*, 231(1187):505–514, 1955.
- [181] J. F. Williams and D. L. Hawkings. Sound generation by turbulence and surfaces in arbitrary motion. *Philosophical Transactions for the Royal Society of London. Series A, Mathematical and Physical Sciences*, pages 321–342, 1969.
- [182] D. S. Pope. A viscous/acoustic splitting technique for aeolian tone prediction. *Proc. Second Computational Aeroacoustics (CAA) Workshop on Benchmark Problems.*, 3352:305–318, 1997.
- [183] W. Z. Shen and J. N. Sorensen. Comment on the aeroacoustic formulation of hardin and pope. *AIAA Journal*, 37(1):141–143, 1999.
- [184] S. A. Slimon, M. C. Soteriou, and D. W. Davis. Computational aeroacoustics simulations using the expansion about incompressible flow approach. *AIAA Journal*, 37(4):409–416, 1999.
- [185] W. Z. Shen, J. A. Michelsen, and J. Sørensen. A collocated grid finite volume method for aeroacoustic computations of low-speed flows. *Journal of Computational Physics*, 196(1):348–366, 2004.
- [186] T. P. h. Bui, W. Schröder, and M. Meinke. Numerical analysis of the acoustic field of reacting flows via acoustic perturbation equations. *Computers & Fluids*, 37(9):1157–1169, 2008.
- [187] J. H. Seo and R. Mittal. A high-order immersed boundary method for acoustic wave scattering and low-mach number flow-induced sound in complex geometries. *Journal of Computational Physics*, 230(4):1000–1019, 2011.
- [188] J. H. Seo and Y. J. Moon. Linearized perturbed compressible equations for low mach number aeroacoustics. *Journal of Computational Physics*, 218(2):702–719, 2006.
- [189] N. Yoshinor and T. Gotanda. Aerodynamic noise source localization system for wind turbine rotor blade. *Journal of Mechanical Engineering Laboratory*, 50(4):88–97, 1996.
- [190] M. Wolsink, M. Sprengers, A. Keuper, T. H. Pedersen, and C. A. Westra. Annoyance from wind turbine noise on sixteen sites in three countries. In *European Community Wind Energy Conference, Lübeck-Travemünde, Germany*, page 273–276, 8-12 March 1993.

- [191] G. D. Hastie, D. J. Russell, P. Lepper, J. Elliott, B. Wilson, S. Benjamins, and journal=Journal of Applied Ecology volume=55 number=2 pages=684–693 year=2018 publisher=Wiley Online Library Thompson, D. Harbour seals avoid tidal turbine noise: Implications for collision risk.
- [192] P. Schmitt, B. Elsaesser, M. Coffin, J. Hood, and R. Starzmann. Field testing a full-scale tidal turbine part 3: Acoustic characteristics. In *European Wave and Tidal Energy Conference, Nantes, France*, 9 September 2015.
- [193] G. H. Koopmann. The vortex wakes of vibrating cylinders at low Reynolds numbers. *Journal of Fluid Mechanics*, 28(3):501–512, 1967.
- [194] O. M. Griffin and S. E. Ramberg. The vortex-street wakes of vibrating cylinders. *Journal of Fluid Mechanics*, 66(3):553–576, 1974.
- [195] M. M. Zdravkovich. Modification of vortex shedding in the synchronization range. *Journal of Fluids Engineering*, 104(4):513–517, 12 1982.
- [196] A. Ongoren and D. Rockwell. Flow structure from an oscillating cylinder Part 1. Mechanisms of phase shift and recovery in the near wake. *Journal of Fluid Mechanics*, 191:197–223, 1988.
- [197] G. E. Karniadakis and G. S. Triantafyllou. Frequency selection and asymptotic states in laminar wakes. *Journal of Fluid Mechanics*, 199(1):441–469, 1989.
- [198] E. Guilmineau and P. Queutey. A numerical simulation of vortex shedding from an oscillating circular cylinder. *Journal of Fluids and Structures*, 16(6):773–794, 2002.
- [199] Z. Zheng and N. Zhang. Frequency effects on lift and drag for flow past an oscillating cylinder. *Journal of Fluids and Structures*, 24(3):382–399, 2008.
- [200] N. Ganta, B. Mahato, and Y. G. Bhumkar. Analysis of sound generation by flow past a circular cylinder performing rotary oscillations using direct simulation approach. *Physics of Fluids*, 31(2):026104, 2019.
- [201] N. Ganta, B. Mahato, and Y. G. Bhumkar. Characteristics of sound radiated due to flow around a rotationally oscillating cylinder. *INTER-NOISE and NOISE-CON Congress and Conference Proceedings*, 259(6):3341–3350, 2019.
- [202] OpenFOAM/v2006. OpenCFD Ltd., User Guide v2006. [Online]. Available: <https://www.openfoam.com/documentation/guides/latest/doc/>. 2019.
- [203] O. Penttinen, E. Yasari, and H. Nilsson. A pimplefoam tutorial for channel flow, with respect to different LES models. *Practice Periodical on Structural Design and Construction*, 23(2):1–23, 2011.
- [204] Y. N. Sankin and N. A. Yuganova. Longitudinal vibrations of elastic rods of stepwise-variable cross-section colliding with a rigid obstacle. *Journal of Applied Mathematics and Mechanics*, 65(3):427–433, 2001.
- [205] A. Dullweber, B. Leimkuhler, and R. McLachlan. Symplectic splitting methods for rigid body molecular dynamics. *The Journal of Chemical Physics*, 107(15):5840–5851, 1997.

- [206] E. Wang and Q. Xiao. Numerical simulation of vortex-induced vibration of a vertical riser in uniform and linearly sheared currents. *Ocean Engineering*, 121:492–515, 2016.
- [207] L. Lu, J. Qin, B. Teng, and Y. Li. Numerical investigations of lift suppression by feedback rotary oscillation of circular cylinder at low Reynolds number. *Physics of Fluids*, 23(3):033601, 2011.
- [208] R. Govardhan and C. H. K. Williamson. Modes of vortex formation and frequency response of a freely vibrating cylinder. *Journal of Fluid Mechanics*, 420(1):85–130, October 2000.
- [209] J. S. Leontini, M. C. Thompson, and K. Hourigan. The beginning of branching behaviour of vortex-induced vibration during two-dimensional flow. *Journal of Fluids and Structures*, 22(6):857–864, 2006.
- [210] A. Placzek, J. F. Sigrist, and A. Hamdouni. Numerical simulation of an oscillating cylinder in a cross-flow at low Reynolds number: Forced and free oscillations. *Computers & Fluids*, 38(1):80–100, 2009.
- [211] Y. Modarres-Sadeghi, F. Chasparis, M. S. Triantafyllou, M. Tognarelli, and P. Beynet. Chaotic response is a generic feature of vortex-induced vibrations of flexible risers. *Journal of Sound and Vibration*, 330(11):2565–2579, 2011.
- [212] J. A. Mitropolsky N. N. Bogoliubov. *Asymptotic methods in the theory of non-linear oscillations*, volume 10. CRC Press, Gordon and Breach, New York, 1961.
- [213] T. K. Caughey. Equivalent linearization techniques. *The Journal of the Acoustical Society of America*, 35(11):1706–1711, 1963.
- [214] W. E. Vander-Velde. *Multiple-input describing functions and nonlinear system design*. Citeseer, 1968.
- [215] D. P. Atherton and G. M. Siouris. Nonlinear control engineering. *IEEE transactions on systems, man, and cybernetics*, 7(7):567–568, 1977.
- [216] A. Gelb and R. S. Warren. Direct statistical analysis of nonlinear systems: Cadet. *AIAA Journal*, 11(5):689–694, 1973.
- [217] C. H. K. Williamson and A. Roshko. Vortex formation in the wake of an oscillating cylinder. *Journal of Fluids and Structures*, 2(4):355–381, 1988.
- [218] Z. Huang, M. Ong, and C. Larsen. Wake structures and vortex-induced forces of a controlled in-line vibrating circular cylinder. *Ocean Engineering*, 189:106319, 10 2019.
- [219] O. Paré-Lambert and M. Olivier. A parametric study of energy extraction from vortex-induced vibrations. *Transactions of the Canadian Society for Mechanical Engineering*, 42(4):359–369, 2018.
- [220] Y. Qu, J. Wang, M. Sun, L. Feng, C. Pan, Q. Gao, and G. He. Wake vortex evolution of square cylinder with a slot synthetic jet positioned at the rear surface. *Journal of Fluid Mechanics*, 812(2):940–965, 2017.

- [221] E. Konstantinidis, S. Balabani, and M. Yianneskis. Bimodal vortex shedding in a perturbed cylinder wake. *Physics of Fluids*, 19(1):011701, 2007.
- [222] M. S. Hemati, C. W. Rowley, E. A. Deem, and L. N. Cattafesta. De-biasing the dynamic mode decomposition for applied Koopman spectral analysis of noisy datasets. *Theoretical and Computational Fluid Dynamics*, 31:349–368, 2017.
- [223] S. Sarkar, S. Ganguly, A. Dalal, P. Saha, and S. Chakraborty. Mixed convective flow stability of nanofluids past a square cylinder by dynamic mode decomposition. *International Journal of Heat and Fluid Flow*, 44:624–634, 2013.
- [224] I. Kozlov, K. Dobrego, and N. Gn. Application of LES methods for computation of hydrodynamic flows by an example of a 2D flow past a circular cylinder for $Re = 5–200$. *International Journal of Heat and Mass Transfer*, 54:887–893, 01 2011.
- [225] L. Qu, C. Norberg, L. Davidson, S. Peng, and F. Wang. Quantitative numerical analysis of flow past a circular cylinder at Reynolds number between 50 and 200. *Journal of Fluids and Structures*, 39:347–370, 2013.
- [226] S. G. Siegel, J. Seidel, C. Fagley, D. M. Luchtenburg, K. Cohen, and T. McLaughlin. Low-dimensional modelling of a transient cylinder wake using double proper orthogonal decomposition. *Journal of Fluid Mechanics*, 610:1–42, 2008.
- [227] B. R. Noack, W. Stankiewicz, M. Morzyński, and P. J. Schmid. Recursive dynamic mode decomposition of transient and post-transient wake flows. *Journal of Fluid Mechanics*, 809:843–872, 2016.
- [228] D. Barkley. Linear analysis of the cylinder wake mean flow. *Europhysics Letters*, 75:750–756, 2006.
- [229] L.S. Shieh, H. Wang, and R.E. Yates. Discrete-continuous model conversion. *Applied Mathematical Modelling*, 4(6):449–455, 1980.
- [230] B. Loring, H. Karimabadi, and V. Rortershteyn. A screen space GPGPU surface LIC algorithm for distributed memory data parallel sort last rendering infrastructures. In *Proceedings of the 9th International Conference on Numerical Modeling of Space Plasma Flows (ASTRONUM-2014), Long Beach, CA, USA March, 2015*.
- [231] A. P. Petkov. Transparent Line Integral Convolution: A New Approach for Visualizing Vector Fields in OpenDX. Master’s thesis, The University of Montana, 2005.
- [232] F. Giannetti and P. Luchini. Structural sensitivity of the first instability of the cylinder wake. *Journal of Fluid Mechanics*, 581:167–197, 2007.
- [233] O. Marquet, D. Sipp, and L. Jacquin. Sensitivity analysis and passive control of cylinder flow. *Journal of Fluid Mechanics*, 615:221–252, 2008.
- [234] C. H. K. Williamson. Vortex Dynamics in the Cylinder Wake. *Annual Review of Fluid Mechanics*, 28(1):477–539, 1996.

- [235] C. Cossu and L. Morino. On the instability of a spring-mounted circular cylinder in a viscous flow at low Reynolds numbers. *Journal of Fluids and Structures*, 14(2):183–196, 2000.
- [236] Peter J. Schmid. Dynamic mode decomposition of numerical and experimental data. *Journal of Fluid Mechanics*, 656:5–28, 2010.
- [237] M. Hemati, E. Deem, M. Williams, C. W. Rowley, and L. N. Cattafesta. Improving separation control with noise-robust variants of dynamic mode decomposition. *AIAA 2016-1103. 54th AIAA Aerospace Sciences Meeting. January 2016*.
- [238] M. Kiewat, T. Indinger, and M. Tsubokura. *Streaming Modal Decomposition Approaches for Vehicle Aerodynamics*. PhD thesis, Universitätsbibliothek der TU München, 2019.
- [239] M. R. Jovanović, P. J. Schmid, and J. W. Nichols. Sparsity-promoting dynamic mode decomposition. *Physics of Fluids*, 26(2):024103, 2014.
- [240] M. Sahin and R. Owens. A numerical investigation of wall effects up to high blockage ratios on two-dimensional flow past a confined cylinder. *Physics of Fluids*, 16:1305, 05 2004.
- [241] M. Zhao, L. Cheng, and T. Zhou. Numerical simulation of vortex-induced vibration of a square cylinder at a low Reynolds number. *Physics of Fluids*, 25(2):023603, 2013.
- [242] P. N. H. Brooks. *Experimental investigation of the aeroelastic instability of bluff two-dimensional cylinders*. PhD thesis, University of British Columbia, Vancouver, BC, Canada, 1960.
- [243] J. Zhao, J. S. Leontini, D. Lo Jacono, and J. Sheridan. Fluid-structure interaction of a square cylinder at different angles of attack. *Journal of Fluid Mechanics*, 747:688–721, 2014.
- [244] Z. Cheng, F. S. Lien, E. Yee, and J. H. Zhang. Mode transformation and interaction in vortex-induced vibration of laminar flow past a circular cylinder. *Physics of Fluids*, 34(3):033607, 2022.
- [245] E. Buffoni. Vortex shedding in subcritical conditions. *Physics of Fluids*, 15(3):814–816, 2003.
- [246] A. H. Techet, F. S. Hover, and M. S. Triantafyllou. Vortical patterns behind a tapered cylinder oscillating transversely to a uniform flow. *Journal of Fluid Mechanics*, 363:79–96, 1998.
- [247] X. Li, W. Zhang, and C. Gao. Proximity-interference wake-induced vibration at subcritical Re: Mechanism analysis using a linear dynamic model. *Physics of Fluids*, 30(3):033606, 2018.
- [248] H. K. Versteeg and W. Malalasekera. *An introduction to computational fluid dynamics: the finite volume method*. Pearson Education, 2007.
- [249] W. R. Wolf, J. L. F. Azevedo, and S. K. Lele. Convective effects and the role of quadrupole sources for aerofoil aeroacoustics. *Journal of Fluid Mechanics*, 708:502–538, 2012.

- [250] M. Strelets. Detached eddy simulation of massively separated flows. In *39th Aerospace sciences meeting and exhibit*, page 879, 2001.
- [251] J. Sigrist. *Modélisation et simulation numérique d'un problème couplé fluide-structure non linéaire. Application au dimensionnement de structures nucléaires de propulsion navale*. PhD thesis, École Centrale de Nantes - Université de Nantes, Nantes, France, 2004.
- [252] F. Farassat and K. S. Brentner. The uses and abuses of the acoustic analogy in helicopter rotor noise prediction. *Journal of the American Helicopter Society*, 33(1):29–36, 1988.
- [253] M. Wang, J. B. Freund, and S. K. Lele. Computational prediction of flow-generated sound. *Annual Review of Fluid Mechanics*, 38:483–512, 2006.
- [254] F. Farassat. Derivation of Formulations 1 and 1A of Farassat. *NASA/TM-2007-214853, March 2007*.
- [255] F. Farassat. Linear acoustic formulas for calculation of rotating blade noise. *AIAA Journal*, 19(9):1122–1130, 1981.
- [256] F. Farassat. *Theory of Noise Generation From Moving Bodies With an Application to Helicopter Rotors*. NASA Langley Technical Report Server, 1975.
- [257] F. Farassat and K. S. Brentner. The acoustic analogy and the prediction of the noise of rotating blades. *Theoretical and Computational Fluid Dynamics*, 10(1-4):155–170, 1998.
- [258] E. Andrey, E. Ilya, K. Matvey, K. Michael, and S. Sergei. Development of a dynamic library for computational aeroacoustics applications using the OpenFOAM open source package. *Procedia Computer Science*, 66:150–157, 2015.
- [259] C. Norberg. Fluctuating lift on a circular cylinder: review and new measurements. *Journal of Fluids and Structures*, 17(1):57–96, 2003.
- [260] H. Gopalan and R. Jaiman. Numerical study of the flow interference between tandem cylinders employing non-linear hybrid URANS–LES methods. *Journal of Wind Engineering and Industrial Aerodynamics*, 142:111–129, 2015.
- [261] M. Weinmann, R. D. Sandberg, and C. Doolan. Tandem cylinder flow and noise predictions using a hybrid RANS/LES approach. *International Journal of Heat and Fluid Flow*, 50:263–278, 2014.
- [262] Y. Qu and A. Metrikine. A single van der Pol wake oscillator model for coupled cross-flow and in-line vortex-induced vibrations. *Ocean Engineering*, 220:108476, 01 2021.
- [263] N. Srinil and H. Zanganeh. Modelling of coupled cross-flow/in-line vortex-induced vibrations using double Duffing and van der Pol oscillators. *Ocean Engineering*, 57:256, 1 2013.
- [264] G. Haller. An objective definition of a vortex. *Journal of Fluid Mechanics*, 525:1–26, 2005.
- [265] H. M. Nikoo, K. Bi, and H. Hao. Vortex-induced vibration of a full-diamond textured cylinder at subcritical Reynolds numbers. *Marine Structures*, 83:103193, 2022.

- [266] C. H. K. Williamson and R. Govardhan. Vortex-induced vibrations. *Annual Review of Fluid Mechanics*, 36(1):413–455, 2004.
- [267] J. Wang, D. Fan, and K. Lin. A review on flow-induced vibration of offshore circular cylinders. *Journal of Hydrodynamics*, 32:415–440, 2020.
- [268] P. W. Bearman. Circular cylinder wakes and vortex-induced vibrations. *Journal of Fluids and Structures*, 27(5):648–658, 2011.
- [269] L. Ma, K. Lin, D. Fan, J. Wang, and M. S. Triantafyllou. Flexible cylinder flow-induced vibration. *Physics of Fluids*, 34(1):011302, 2022.
- [270] Z. Cheng, F.-S. Lien, E. Yee, and J.-H. Zhang. Mode transformation and interaction in vortex-induced vibration of laminar flow past a circular cylinder. *Physics of Fluids*, 34:033607, 2022.
- [271] E. Åkervik, L. Brandt, D. S. Henningson, J. Høpfner, O. Marxen, and P. Schlatter. Steady solutions of the Navier-Stokes equations by selective frequency damping. *Physics of Fluids*, 18(6):068102, 2006.
- [272] G. Brès, F. Pérot, and D. Freed. A Ffowcs Williams - Hawkings Solver for Lattice-Boltzmann Based Computational Aeroacoustics. In *16th AIAA/CEAS Aeroacoustics Conference, Stockholm, Sweden, 07 June 2010 - 09 June 2010*.
- [273] O. Paré-Lambert and M. Olivier. A parametric study of energy extraction from vortex-induced vibrations. *Transactions of the Canadian Society for Mechanical Engineering*, 42(4):359–369, 2018.
- [274] S. Mittal. Global linear stability analysis of time-averaged flows. *International Journal for Numerical Methods in Fluids*, 58(1):111–118, 2008.
- [275] J. Donea, A. Huerta, J. P. Ponthot, and A. Rodríguez-Ferran. *Arbitrary Lagrangian–Eulerian Methods*. In *Encyclopedia of Computational Mechanics*. American Cancer Society, 2004.
- [276] N. M. Newmark. A method of computation for structural dynamics. *Journal of Engineering Mechanics*, 85:67–94, 1959.
- [277] M. Devaud and T. Hocquet. An essay on the vibrating string and its nonlinearities (hal-01532358v2). working paper or preprint, June 2017.
- [278] R. Dan. Sound fields radiated by simple sources. [EB/OL]. <https://www.acs.psu.edu/drussell/Demos/rad2/mdq.html/> Accessed November 21, 2013.
- [279] L. Feng, J. Wang, and C. Pan. Proper orthogonal decomposition analysis of vortex dynamics of a circular cylinder under synthetic jet control. *Physics of Fluids*, 23(1):014106, 2011.
- [280] C. H. K. Williamson and R. Govardhan. Vortex-induced vibrations. *Annual Review of Fluid Mechanics*, 36(1):413–455, 2004.
- [281] M. M. Rajamuni, M. C. Thompson, and K. Hourigan. Transverse flow-induced vibrations of a sphere. *Journal of Fluid Mechanics*, 837:931–966, 2018.

- [282] H. Sun, C. Ma, E. S. Kim, G. Nowakowski, E. Mauer, and M. M. Bernitsas. Flow-induced vibration of tandem circular cylinders with selective roughness: Effect of spacing, damping and stiffness. *European Journal of Mechanics-B/Fluids*, 74:219–241, 2019.
- [283] J. Juang and R. S. Pappa. An eigensystem realization algorithm for modal parameter identification and model reduction. *Journal of Guidance, Control, and Dynamics*, 8(5):620–627, 1985.
- [284] A. Modir and N. Goudarzi. Experimental investigation of Reynolds number and spring stiffness effects on vortex induced vibrations of a rigid circular cylinder. *European Journal of Mechanics-B/Fluids*, 74:34–40, 2019.
- [285] T. Sarpkaya. Vortex-Induced Oscillations: A Selective Review. *Journal of Applied Mechanics*, 46(2):241–258, 1979.
- [286] K. Vikestad, J. K. Vandiver, and C. M. Larsen. Added mass and oscillation frequency for a circular cylinder subjected to vortex-induced vibrations and external disturbance. *Journal of Fluids and Structures*, 14(7):1071–1088, 2000.
- [287] C. M. Larsen, K. Vikestad, and J. K. Vandiver. On multi-frequency vortex induced vibrations of long marine risers. In *OCEANS 96 MTS/IEEE Conference Proceedings. The Coastal Ocean-Prospects for the 21st Century*, volume 1, pages 505–510. IEEE, 1996.
- [288] L. Zhang, A. Abdelkefi, H. Dai, R. Naseer, and L. Wang. Design and experimental analysis of broadband energy harvesting from vortex-induced vibrations. *Journal of Sound and Vibration*, 408:210–219, 2017.
- [289] W. F. King III. A précis of developments in the aeroacoustics of fast trains. *Journal of Sound and Vibration*, 193(1):349–358, 1996.
- [290] C. Talotte. Aerodynamic noise: a critical survey. *Journal of Sound and Vibration*, 231(3):549–562, 2000.
- [291] R. S. Raghunathan, H. D. Kim, and T. Setoguchi. Aerodynamics of high-speed railway train. *Progress in Aerospace sciences*, 38(6-7):469–514, 2002.
- [292] T. Kitagawa and K. Nagakura. Aerodynamic noise generated by shinkansen cars. *Journal of Sound and vibration*, 231(3):913–924, 2000.
- [293] T. Kurita, M. Hara, H. Yamada, Y. Wakabayashi, F. Mizushima, H. Satoh, and T. Shikama. Reduction of pantograph noise of high-speed trains. *Journal of Mechanical systems for Transportation and Logistics*, 3(1):63–74, 2010.
- [294] C. Talotte, P. E. Gautier, D. J. Thompson, and C. Hanson. Identification, modelling and reduction potential of railway noise sources: a critical survey. *Journal of Sound and Vibration*, 267(3):447–468, 2003.
- [295] F. R. Grosche and G. E. A. Meier. Research at dlr göttingen on bluff body aerodynamics, drag reduction by wake ventilation and active flow control. *Journal of Wind Engineering and Industrial Aerodynamics*, 89(14-15):1201–1218, 2001.

- [296] V. L. Blumenthal, J. M. Streckenbach, and R. B. Tate. Aircraft environmental problems. *Journal of Aircraft*, 10(9):529–537, 1973.
- [297] D. P. Lockard and G. M. Lilley. *The airframe noise reduction challenge*. Citeseer, 2004.
- [298] W. T. Ellison, B. L. Southall, C. W. Clark, and A. S. Frankel. A new context-based approach to assess marine mammal behavioral responses to anthropogenic sounds. *Conservation Biology*, 26(1):21–28, 2012.
- [299] M. B. Halvorsen, T. J. Carlson, and A. Copping. Effects of tidal turbine noise on fish. *PNNL Report-20787 for US Dept of Energy, WA, DC: by Pacific Northwest National Laboratory, Sequim, WA*, pages 1–41, 2011.
- [300] D. Risch, N. VAN G., D. Gillespie, and B. Wilson. Characterisation of underwater operational sound of a tidal stream turbine. *The Journal of the Acoustical Society of America*, 147(4):2547–2555, 2020.
- [301] W. K. Blake. *Mechanics of flow-induced sound and vibration, Volume 2: Complex flow-structure interactions*. Academic Press, 2017.
- [302] F. R. Menter, M. Kuntz, and R. Langtry. Ten years of industrial experience with the sst turbulence model. *Turbulence, Heat and Mass Transfer*, 4(1):625–632, 2003.
- [303] D. B. Hanson and M. R. Fink. The importance of quadrupole sources in prediction of transonic tip speed propeller noise. *Journal of Sound and Vibration*, 62(1):19–38, 1979.
- [304] F. H. Schmitz and Y. H. Yu. Transonic rotor noise-theoretical and experimental comparisons. Technical report, ARMY RESEARCH AND TECHNOLOGY LABS MOFFETT FIELD CA AEROMECHANICS LAB, 1980.
- [305] B. H. Huynh, T. Tjahjowidodo, Z. W. Zhong, Y. Wang, and N. Srikanth. Numerical and experimental investigation of nonlinear vortex induced vibration energy converters. *Journal of Mechanical Science and Technology*, 31(8):3715–3726, 2017.
- [306] J. Zhao, K. Hourigan, and M. C. Thompson. An experimental investigation of flow-induced vibration of high-side-ratio rectangular cylinders. *Journal of Fluids and Structures*, 91:102580, 2019.

Appendix A

Appendix: The simplify of one common engineering VIV system mounted by nonlinear restoring force

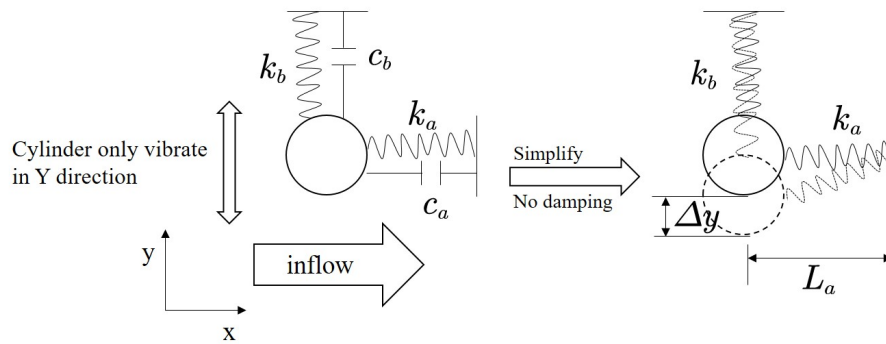


Figure A.1: VIV system oscillating in Y direction supported by two linear springs in X and Y direction.

For instance in Fig. A.1, the tandem-linear spring FSI system is very common in the engineering world. The cylinder motion is supported by two linear springs from X and Y direction, with k_a and k_b are stiffness of two linear springs in two direction, and the cylinder only move in Y direction. Then the integral springs force acted on the cylinder in Y direction $force_y$ will be:

$$force_y = k_b \cdot \Delta y + k_a \cdot \Delta y \cdot \frac{(\sqrt{L_a^2 + \Delta y^2} - L_a)}{\sqrt{L_a^2 + \Delta y^2}}, \quad (\text{A.1})$$

if $k_b = 0$, force from k_a part will change as Fig. A.2 with different k_a and L_a . As can be seen, the relationship of force changing with distance is not linear, and the larger k_a and smaller L_a are related to higher degree of nonlinearity.

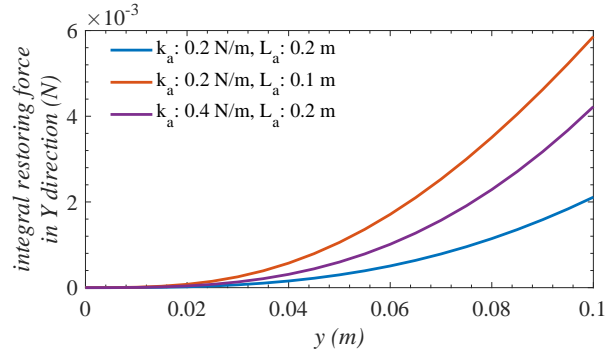


Figure A.2: Integral spring forces in Y direction with different k_a and L_a .

To have a better study of nonlinear spring's effect on VIV, most nonlinear system could be transferred to simple form, approximately equal to the form of a polynomial. Then the equation could be expanded into polynomial form by Taylor formula,

$$\begin{aligned} force_y &= k_b \cdot \Delta y + k_a \cdot \Delta y \cdot \frac{\left(\sqrt{L_a^2 + \Delta y^2} - L_a\right)}{\sqrt{L_a^2 + \Delta y^2}}, \\ &= (k_b + k_a) \cdot \Delta y - k_a L_a \cdot \frac{\Delta y}{\sqrt{L_a^2 + \Delta y^2}}, \end{aligned} \quad (\text{A.2})$$

after Taylor expands,

$$force_y = (k_b + k_a) \cdot \Delta y - k_a \left(\Delta y - \frac{1}{2L_a^2} \Delta y^3 + \frac{3}{8L_a^4} \Delta y^5 + o(\Delta y^5) \right), \quad (\text{A.3})$$

if $k_b=0$, omitting high order terms,

$$force_y = k_a \left(\frac{1}{2L_a^2} \Delta y^3 - \frac{3}{8L_a^4} \Delta y^5 \right), \quad (\text{A.4})$$

thus, if the small effects of higher-order terms is ignored, nonlinear spring can be transformed into polynomial form. This is a relatively simple case of nonlinear restoring force in engineering. In some other practical applications, such as automobile damping, complex nonlinear restoring force will be involved to meet the requirements. The nonlinear terms of Taylor expansion of engineering relations start from the second or third order. Here, one kind of simple nonlinear spring with force value $force_s$ is defined as equation A.5, and use it in the study of present work. This kind of nonlinear equation is the classical nonlinear spring expression in the vibration theory, and study on this will be valuable and representative. The spring is linear while k_2 and k_3 is equal to 0. Quadratic nonlinearity is the starting point of nonlinear system, so this thesis mainly studies the characteristics of VIV under quadratically nonlinear spring with hardening

spring ($k_2 > 0, k_3 = 0$) characteristics.

$$\begin{aligned}
 force_s &= k_1 \cdot \Delta L + k_2 \cdot \Delta L \cdot |\Delta L| + k_3 \cdot \Delta L^3, \\
 \Delta L &= \sqrt{\Delta x^2 + \Delta y^2}.
 \end{aligned}
 \tag{A.5}$$

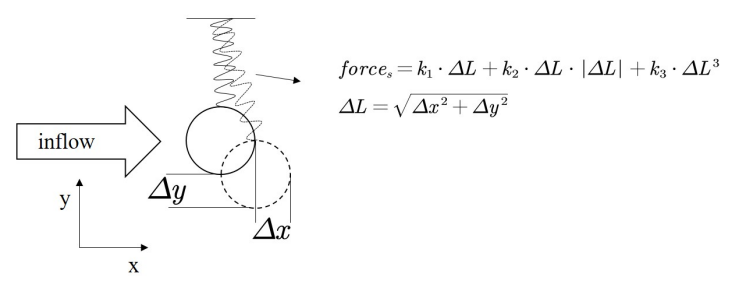


Figure A.3: VIV system with nonlinear restoring force of quadratic and cubic orders, structural damping is zero.

Appendix B

Appendix: Ffowcs Williams-Hawkings (FW-H) equation with Farassat's formulation 1A

In Farassat's formulation 1A, the quadrupole term is neglected, and the sound pressure p' at the observer position \mathbf{x} and time t from a subsonic moving source can be expressed as follows:

$$p'(\mathbf{x}, t) = p'_T(\mathbf{x}, t) + p'_L(\mathbf{x}, t), \quad (\text{B.1})$$

where the subscripts T and L denote the thickness and loading components of the noise. The thickness p'_T and loading p'_L noise are given, respectively, by

$$4\pi p'_T(\mathbf{x}, t) = \int_{f=0} \left[\frac{\dot{Q}_n + Q_{\dot{n}}}{r(1-M_r)^2} \right]_{\text{ret}} dS + \int_{f=0} \left[\frac{Q_n (r\dot{M}_r + c_0 (M_r - M^2))}{r^2 (1-M_r)^3} \right]_{\text{ret}} dS, \quad (\text{B.2})$$

and

$$4\pi p'_L(\mathbf{x}, t) = \frac{1}{c_0} \int_{f=0} \left[\frac{\dot{L}_r}{r(1-M_r)^2} \right]_{\text{ret}} dS + \int_{f=0} \left[\frac{L_r - L_M}{r^2 (1-M_r)^2} \right]_{\text{ret}} dS + \frac{1}{c_0} \int_{f=0} \left[\frac{L_r (r\dot{M}_r + c_0 (M_r - M^2))}{r^2 (1-M_r)^3} \right]_{\text{ret}} dS. \quad (\text{B.3})$$

Here, $M_i = v_i/c_0$ with $i = 1, 2, 3$ are the components of the Mach vector where c_0 is the speed of sound; M is the length (magnitude) of the Mach vector, and the dot above a variable indicates a time derivative. The terms in the equation are defined as follows (Einstein summation convention for repeated indices implied):

$$\begin{aligned} M_r &= M_i \hat{r}_i, \quad \dot{M}_r = \frac{\partial M_i}{\partial \tau} \hat{r}_i, \\ Q_n &= Q_i \hat{n}_i, \quad \dot{Q}_n = \frac{\partial Q_i}{\partial \tau} \hat{n}_i, \quad Q_{\dot{n}} = Q_i \frac{\partial \hat{n}_i}{\partial \tau}, \\ L_i &= L_{ij} \hat{n}_j, \quad \dot{L}_r = \frac{\partial L_i}{\partial \tau} \hat{r}_i, \quad L_r = L_i \hat{r}_i, \quad L_M = L_i M_i, \end{aligned} \quad (\text{B.4})$$

where Q_n and L_i are defined as

$$\begin{aligned} Q_n &= Q_i \hat{n}_i \equiv [\rho_0 v_i + \rho (u_i - v_i)] \hat{n}_i , \\ L_i &= L_{ij} \hat{n}_j \equiv [P_{ij} + \rho u_i (u_j - v_j)] \hat{n}_j . \end{aligned} \quad (\text{B.5})$$

Here, the velocity v_i defines the motion of the surface f .

The moving surface is described by $f(\mathbf{x}, t) = 0$ such that $\hat{n} = \nabla f$ is the unit outward normal to the surface. $P_{ij} = (p - p_0) \delta_{ij} - \tau_{ij}$ is the compressible stress tensor, and δ_{ij} is the Kronecker delta. In general, the viscous term in P_{ij} is negligible. In consequence, the stress tensor simplifies to $P_{ij} = (p - p_0) \delta_{ij}$. Additionally, in the region away from the source area, the perturbation of the density is small and $c^2 (\rho - \rho_0)$ can be replaced by the sound pressure p' . The subscript “ret” on a quantity refers to that quantity evaluated at the retarded time t_{ret} (viz., at the time at which the source was emitted):

$$t_{\text{ret}} = t - \frac{r}{c_0} , \quad (\text{B.6})$$

where $r = |\mathbf{x} - \mathbf{y}|$ denotes the distance from the sound source at \mathbf{y} at the time of emission t_{ret} of the sound to the observer at \mathbf{x} at the time of observation t .

Appendix C

Appendix: Parameters of turbulence models used in present work

The equations for turbulence kinetic energy and turbulence specific dissipation rate in k-omega Shear Stress Transport (SST) turbulence model are shown as:

$$\frac{\partial(\rho k)}{\partial t} + \frac{\partial(\rho u_i k)}{\partial x_i} = P_k - \rho \beta^* k \omega + \frac{\partial}{\partial x_i} \left[\left(\mu + \frac{\mu_t}{\sigma_k} \right) \frac{\partial k}{\partial x_i} \right], \quad (\text{C.1})$$

$$\frac{\partial(\rho \omega)}{\partial t} + \frac{\partial(\rho u_i \omega)}{\partial x_i} = P_\omega - \rho \beta_\omega \omega^2 + \frac{\partial}{\partial x_i} \left[\left(\mu + \frac{\mu_t}{\sigma_\omega} \right) \frac{\partial \omega}{\partial x_i} \right] + 2\rho(1 - F_1) \frac{1}{\sigma_{\omega,2} \omega} \frac{\partial k}{\partial x_i} \frac{\partial \omega}{\partial x_i}, \quad (\text{C.2})$$

with u_i as the velocity along the i th coordinate, ρ as the density, ω as the turbulence specific dissipation rate, k as the turbulence kinetic energy, P_k is the production term for k , μ as the dynamic viscosity, μ_t as the turbulent viscosity, and F_1 is the blending factor.

$$P_k = \min \left(-\tau_{ij} \frac{\partial u_i}{\partial x_j}, 10\rho \beta^* k \omega \right), \quad (\text{C.3})$$

$$P_\omega = \frac{\alpha \omega}{k} P_k, \quad (\text{C.4})$$

$$\alpha = \left(\frac{\beta_{i,1}}{\beta^*} - \frac{0.41^2}{\sigma_{\omega,1} \sqrt{\beta^*}} \right) F_1 + \left(\frac{\beta_{i,2}}{\beta^*} - \frac{0.41^2}{\sigma_{\omega,2} \sqrt{\beta^*}} \right) (1 - F_1), \quad (\text{C.5})$$

$$\mu_t = \frac{\rho k}{\max \left(\omega, \frac{SF_2}{a_1} \right)}, \quad (\text{C.6})$$

$$F_1 = \tanh \left\langle \left\{ \min \left[\max \left(\frac{\sqrt{k}}{\beta' \omega d}, \frac{500\mu_t}{\rho \omega d^2} \right) \frac{4k\rho\sigma_{\omega 2}}{d^2 CD_{k\omega}} \right] \right\}^4 \right\rangle, \quad (\text{C.7})$$

$$F_2 = \tanh \left\{ \left[\max \left(\frac{2\sqrt{k}}{\beta^* \omega d}, \frac{500\mu_t}{\rho \omega d^2} \right) \right]^2 \right\}, \quad (\text{C.8})$$

$$CD_{k\omega} = \max \left[2\rho\sigma_{\omega 2} \frac{1}{\omega} \left(\frac{\partial k}{\partial x_i} \right) \left(\frac{\partial \omega}{\partial x_i} \right), 10^{-10} \right], \quad (\text{C.9})$$

$$\sigma_k = \frac{1}{\left(\frac{F_1}{\sigma_{k,1}} \right) + ((1 - F_1) / \sigma_{k,2})}, \quad (\text{C.10})$$

$$\sigma_{\omega} = \frac{1}{\left(\frac{F_1}{\sigma_{\omega,1}} \right) + ((1 - F_1) / \sigma_{\omega,2})}, \quad (\text{C.11})$$

$$\beta_{\omega} = \beta_{i,1}F_1 + \beta_{i,2}(1 - F_1), \quad (\text{C.12})$$

with τ_{ij} as the turbulence shear stress, S as strain rate magnitude, and d as the distance to the surface. The constants' value in present research are:

$$\beta^* = 0.09, a_1 = 0.31, \sigma_{k,1} = 0.85, \sigma_{k,2} = 1.0, \quad (\text{C.13})$$

$$\sigma_{\omega,1} = 0.5, \sigma_{\omega,2} = 0.856, \beta_{i,1} = 0.075, \beta_{i,2} = 0.0828. \quad (\text{C.14})$$

Appendix D

Appendix: Derivation of equivalent natural frequency

We focus on development of an equivalent linearization for the following differential equation describing a cylinder of mass m supported by a linear/nonlinear spring configuration with no structural damping ($c = 0$):

$$m\ddot{y} + k_1 y + k_n l_n(y, \dot{y}) = F_y, \quad (\text{D.1})$$

where k_1 is the linear spring constant and k_n is the nonlinear spring constant for an n -th order nonlinear spring. Dividing Eq. D.1 by m gives

$$\ddot{y} + \omega_1^2 y + \frac{k_n}{m} l_n(y, \dot{y}) = f_y, \quad (\text{D.2})$$

where $\omega_1 \equiv \sqrt{k_1/m}$, and $f_y \equiv F_y/m$. Now, let us try to recast Eq. D.2 in the following form

$$\ddot{y} + \omega_{\text{eq}}^{(n)2} y = f_y, \quad (\text{D.3})$$

where the equivalent frequency $\omega_{\text{eq}}^{(n)} \equiv \sqrt{k_{\text{eq}}^{(n)}/m}$, and $k_{\text{eq}}^{(n)}$ is the “equivalent linear spring constant”. The problem reduces to the determination of the equivalent frequency $\omega_{\text{eq}}^{(n)}$ for n -th order nonlinear spring.

To this purpose, it is useful to define $\varepsilon_n \equiv k_n/k_1$. Now, the equivalent linearization method described by Caughey [213] can be used to determine $\omega_{\text{eq}}^{(n)}$. Towards this objective, the transverse displacement of the cylinder can be approximated by a sinusoid with a slow modulation in the amplitude and phase, so

$$y(t) = a(t) \sin\left(\omega_{\text{eq}}^{(n)} t + \phi(t)\right) \equiv a \sin(\theta). \quad (\text{D.4})$$

Following the equivalent linearization method described by Caughey [213], we obtain the following key result (Eq. (1.15) in [213]) which in terms of our current notation gives

$$\omega_{\text{eq}}^{(n)2} = \omega_1^2 + 2 \frac{k_n}{m} \frac{\langle S^{(n)}(a) \rangle}{\langle a^2 \rangle}, \quad (\text{D.5})$$

where

$$S^{(n)}(a) \equiv \frac{1}{2\pi} \int_0^{2\pi} a \sin(\theta) l_n(y, \dot{y}) d\theta, \quad (\text{D.6})$$

and $\langle \cdot \rangle$ denotes an ensemble-averaging operation. To compute the ensemble averages in equation D.5, we follow Caughey [213] and assume that the distribution of the envelope (slow modulation in the transverse displacement oscillations of the cylinder) follows a Rayleigh distribution for the amplitude peaks $a(t)$ (cf. Eq. D.4), so the probability density function for a is modeled in accordance to

$$p(a) = \frac{a}{\langle y^2 \rangle} \exp\left(-\frac{a^2}{2\langle y^2 \rangle}\right), \quad (\text{D.7})$$

where $\langle y^2 \rangle$ is the mean-square displacement of the transverse oscillations.

With this assumption, the ensemble averages in Eq. D.5 can be explicitly evaluated. Firstly, the mean-square amplitude of the transverse oscillations $\langle a^2 \rangle$ is given by

$$\langle a^2 \rangle = \int_0^\infty \frac{a^3}{\langle y^2 \rangle} \exp\left(-\frac{a^2}{2\langle y^2 \rangle}\right) da = 2\langle y^2 \rangle. \quad (\text{D.8})$$

Secondly, we can evaluate $\langle S^{(n)}(a) \rangle$ in Eq. D.5 as follows. The nonlinear spring function ($n \geq 2$) is given by

$$l_n(y, \dot{y}) = y|y^{n-1}|. \quad (\text{D.9})$$

Substituting Eq. D.9 into Eq. D.6 and evaluating the integral, we get

$$S^{(n)}(a) = \frac{1}{\sqrt{\pi}} \frac{\Gamma((n+2)/2)}{\Gamma((n+3)/2)} a^{n+1}, \quad n = 2, 3, \dots, \quad (\text{D.10})$$

where $\Gamma(x)$ is the gamma function. Now, we can use Eq. D.10 to compute $\langle S^{(n)}(a) \rangle$ which is required in Eq. D.5 to determine the equivalent frequency. This leads to

$$\langle S^{(n)}(a) \rangle = \sqrt{\frac{2^{1+n}}{\pi}} \Gamma((n+2)/2) \langle y^2 \rangle^{(n+3)/2-1}, \quad n = 2, 3, \dots. \quad (\text{D.11})$$

Finally, substituting Eqs D.11 and D.8 into Eq. D.5, we get a general expression for the equivalent frequency for an n -th order nonlinear spring:

$$\omega_{eq}^{(n)2} = \omega_1^2 \left(1 + \varepsilon_n \frac{2}{\sqrt{\pi}} \Gamma((n+2)/2) \langle a^2 \rangle^{(n-1)/2} \right), \quad n = 2, 3, \dots. \quad (\text{D.12})$$

In the preceding analysis, it was assumed that the transverse displacement of the cylinder can be modeled as a sinusoid with a slowly varying amplitude and phase as given in equation D.4. However, in certain regimes of operation (e.g., lock-in), the amplitude and phase of the sinusoid is constant (approximately or better) in time. For this case, the probability distribution of the amplitude $p(a)$ reduces to a delta function, so $p(a) = \delta(a)$. In view of this, the equivalent frequency in Eqs D.5 and D.6 simplifies to

$$\omega_{eq}^{(n)2} = \omega_1^2 \left(1 + 2\varepsilon_n \frac{S_n(a)}{a^2} \right), \quad n = 2, 3, \dots, \quad (\text{D.13})$$

which in view of Eq. D.10 results in

$$\omega_{\text{eq}}^{(n)2} = \omega_1^2 \left(1 + \varepsilon_n \frac{2}{\sqrt{\pi}} \frac{\Gamma((n+2)/2)}{\Gamma((n+3)/2)} a^{n-1} \right), \quad n = 2, 3, \dots \quad (\text{D.14})$$

Appendix E

Published, accepted, and submitted papers

The papers where I am the principal/first author (i.e. at least 90% of the paper is based on my own research work) are marked with an asterisk *.

1*: Zhi Cheng, Fue-Sang Lien, Eugene Yee, Ji Hao Zhang, Mode transformation and interaction in vortex-induced vibration of laminar flow past a circular cylinder, *Physics of Fluids* 34 (2022) 033607.

2*: Zhi Cheng, Fue-Sang Lien, Eugene Yee, Hang Meng, A unified framework for aeroacoustics simulation of wind turbines, *Renewable Energy* 188 (2022) 299-319.

3*: Zhi Cheng, Fue-Sang Lien, Eugene Yee, Guang Chen, Vortex-induced vibration of a circular cylinder with nonlinear restoring forces at low-Reynolds number, *Ocean Engineering* 266 (2022) 113197.

4*: Zhi Cheng, Fue-Sang Lien, Earl H. Dowell, Ryne Wang, Ji Hao Zhang, Data-driven stability analysis via the superposition of reduced-order models for the flutter of circular cylinder submerged in three-dimensional spanwise shear inflow at subcritical Reynolds number, *Physics of Fluids* 34 (2022) 123606.

5*: Zhi Cheng, Ryley McConkey, Eugene Yee, Fue-Sang Lien, Numerical investigation of noise suppression and amplification in forced oscillations of single and tandem cylinders in high Reynolds number turbulent flows, *Applied Mathematical Modelling* 117 (2023) 652-686.

6: Ying Wu, Zhi Cheng, Ryley McConkey, Fue-Sang Lien, Eugene Yee, Modelling of Flow-Induced Vibration of Bluff Bodies: A Comprehensive Survey and Future Prospects, *Energies* 15 (22) (2022) 8719.

7*: Zhi Cheng, Fue-Sang Lien, Eugene Yee, Hang Meng, Computational Schema for Wind Turbine Noise Prediction, in *CFDSC Congress 2021 At: Memorial University, St. John's Newfoundland and Labrador, Canada, July 2021*.

8*: Zhi Cheng, Fue-Sang Lien, Earl H. Dowell, Eugene Yee, Triggering of galloping in structures at low Reynolds numbers, Submitted to "*Journal of Fluids and Structures*" (in Oct 2022) with feedback decision of "minor revision".

9*: Zhi Cheng, Ji Hao Zhang, Ryne Wang, Fue-Sang Lien, Eugene Yee, Earl H. Dowell, Critical effect of geometrical contraction trend on galloping triggering for trapezoidal body, Submitted to "*Journal of Fluid Mechanics*" (in Dec 2022).

10: Guang Chen, Xiao-Bai Li, Kan He, Zhi Cheng, Dan Zhou, Xi-Feng Liang, Effect of the free-stream turbulence on the bi-modal wake dynamics of square-back bluff body, Accepted by "Physics of Fluids" (In press) (2023).